Supplementary Material

# Diffusing Uphill with James Clerk Maxwell and Josef Stefan

Rajamani Krishna

Van ‘t Hoff Institute for Molecular Sciences

University of Amsterdam

Science Park 904

1098 XH Amsterdam, The Netherlands

email: r.krishna@contact.uva.nl

## Table of Contents

# 1 Preamble

This Supplementary Material accompanying our article *Diffusing Uphill with James Clerk Maxwell and Josef Stefan* provides detailed derivations of the Maxwell-Stefan diffusion equations, along with solutions to the model equations describing transient equilibration in gaseous mixtures, multicomponent distillation, ternary liquid-liquid extraction, mixed electrolyte solutions, ion exchange processes, reverse osmosis, solid crystals, metal alloys, silicates, and microporous materials. All the necessary data inputs, and calculation methodologies are provided in the Supplementary Material. Procedures for estimation of diffusivities are discussed. This should enable the interested reader to reproduce all the calculations and results presented and discussed in the review article.

For ease of reading, this Supplementary Material is written as a stand-alone document; as a consequence, there is some overlap of material with the main manuscript.

# 2 Phenomenological relations for *n*-component diffusion

Before setting up the proper phenomenological relations between the diffusion fluxes and the driving forces, we first consider the various choices of concentration measures, and reference velocities. The treatment below is essentially a summary of Chapter 1 of Taylor and Krishna.[1]

## 2.1 Concentration measures

A summary of the wide variety of concentration measures for *n*-component mixtures that are encountered in practice are summarized in Table 2-1.

## 2.2 Diffusion fluxes and reference velocities

If $u_i$ denotes the ensemble average velocity of component *i* with respect to a laboratory-fixed (i.e. stationary) coordinate reference frame, the molar flux of component $i$ in the laboratory-fixed reference frame is $N_i = c_i u_i$ and the molar flux of the mixture is $N_t = \sum_{i=1}^{n} N_i$. The modelling and design of separation and reaction equipment requires calculation of the diffusion fluxes, $J_i$; these are defined with respect to an arbitrarily chosen reference velocity of the fluid mixture, $u$:

$$J_i \equiv c_i(u_i - u); \quad i = 1,2,..n \tag{2-1}$$

Most commonly, we choose $u$ as the molar average velocity of the mixture

$$u = \sum_{i=1}^{n} x_i u_i = x_1 u_1 + x_2 u_2 + \cdots x_n u_n \tag{2-2}$$

Only *n*-1 of the fluxes $J_i$ are independent because the diffusion fluxes sum to zero

$$\sum_{i=1}^{n} J_i = 0 \tag{2-3}$$

The molar fluxes $N_i$ in the laboratory fixed reference frame are related to the diffusion fluxes $J_i$ by

$$N_i \equiv c_i u_i = J_i + x_i N_t; \quad N_t = \sum_{i=1}^{n} N_i \tag{2-4}$$

The molar diffusion flux can also be defined with respect to other reference velocities; some commonly used ones are summarized in Table 2-2.

For ideal gas mixtures, the molar average mixture velocity equals the volume average mixture velocity. The mass average reference velocity frame is convenient to use when the equations of conservation of mass need to be solved in conjunction with the momentum balance relations. For diffusion of ions in dilute aqueous solutions, it is convenient to define the diffusion fluxes with respect to water (the *n*th component). The volume average mixture velocity is convenient for liquid mixtures.

## 2.3 The Generalized Fick's law for *n*-component diffusion

Choosing the mole fraction gradients as the driving forces, the diffusion fluxes $J_i \equiv c_i(u_i - u); \quad i = 1,2,..n$ with respect to the molar average reference velocity may expressed as linear functions of the ($n$-1) independent driving forces, by defining a ($n$-1) × ($n$-1) dimensional Fick diffusivity matrix $[D]$

$$(J) = -c_t [D] \frac{d(x)}{dz} = -\frac{1}{\overline{V}} [D] \frac{d(x)}{dz} \tag{2-5}$$

where $\overline{V} = \sum_{k=1}^{n} x_k \overline{V_k}$ is the mean molar volume of the mixture.

## 2.4 Other choices of reference velocities in the definition of [*D*]

The Fick diffusivity matrix $[D]$ is defined in equation (2-5) in terms of molar diffusion fluxes, $J_i$, that are, in turn, defined with respect to the molar average reference velocity frame $u$. Other choice of fluxes and reference velocities are encountered in the chemical engineering literature; see Section 3.2.2 of Taylor and Krishna.[1] See also Table 2-2.

**Phenomenological relations for n-component diffusion**

For mass diffusion fluxes, $j_i \equiv \rho_i (u_i - v); \quad i = 1,2,..n; \quad \sum_{i=1}^{n} j_i = 0$ defined with respect the mass average mixture velocity $v = \sum_{i=1}^{n} \omega_i u_i$, we write $(j) = -\rho_t [D^{mass}] \frac{d(\omega)}{dz}$.

The mass fractions are related to the mole fractions $x_i$ $\omega_i = \frac{\rho_i}{\rho_t} = \frac{x_i M_i}{\sum_{i=1}^{n} x_i M_i} = \frac{x_i M_i}{\overline{M}}; \quad x_i = \frac{c_i}{c_t} = \frac{\frac{\omega_i}{M_i}}{\sum_{i=1}^{n} \frac{\omega_i}{M_i}} = \frac{\omega_i}{M_i} \overline{M}$, where $M_i$ is the molar mass of species *i*, with the units kg mol$^{-1}$, and $\overline{M}$ is the mean molar mass of the mixture is $\overline{M} = \sum_{i=1}^{n} x_i M_i = \frac{1}{\sum_{i=1}^{n} \frac{\omega_i}{M_i}}$. The mixture mass density is related to the total molar concentration of the mixture $\rho_t = c_t \overline{M} = \frac{1}{\overline{V}} \overline{M}$.

For molar diffusion fluxes, $J_i^{volume} \equiv c_i (u_i - u^{volume}); \quad i = 1,2,..n; \quad \sum_{i=1}^{n} \overline{V}_i J_i^{volume} = 0$ defined with respect the volume average mixture velocity $u^{volume} = \sum_{i=1}^{n} c_i \overline{V}_i u_i$, we write $(J^{volume}) = -[D^{volume}] \frac{d(c)}{dz}$. This is a common choice in the experimental determination of diffusivities.

For *n*-component mixtures, the numerical values of the elements of $[D]$, $[D^{mass}]$, and $[D^{volume}]$ are different. However, the determinants of the corresponding matrices are equal to one another.[1]

$$|D| = |D^{mass}| = |D^{volume}| \tag{2-6}$$

For the special case of a binary mixture, *n* = 2, $dx_1 = \frac{\frac{1}{M_1 M_2}}{\left(\frac{\omega_1}{M_1} + \frac{\omega_2}{M_2}\right)^2} d\omega_1; \quad d\omega_1 = \frac{M_1 M_2}{(x_1 M_1 + x_2 M_2)^2} dx_1,$

and the Fick diffusivity is the same for the three different choice of reference velocity frames[1]

**Phenomenological relations for n-component diffusion**

$$j_1 \equiv \rho_1 \left(u_1 - v\right) = -\rho_t D_{12} \frac{d\omega_1}{dz}$$
$$J_1 \equiv c_1 \left(u_1 - u\right) = -c_t D_{12} \frac{dx_1}{dz} \tag{2-7}$$
$$J_1^{volume} \equiv c_i \left(u_1 - u^{volume}\right) = -D_{12} \frac{dc_1}{dz}$$

The inter-relationship between $J_1$ and $j_1$ is summarized in Table 2-3.

The formulae for transformation of the Fick diffusivity matrix from one reference frame to another are provided in Section 3.2.4 of Taylor and Krishna.[1] For example, for a ternary mixture, $n$ = 3, the transformation between $[D]$, and $[D^{mass}]$ is

$$[D^{mass}] = [A][D][A]^{-1}; \quad [D] = [A]^{-1}[D^{mass}][A];$$
$$[A] \equiv \begin{bmatrix} 1-\omega_1\left(1-\dfrac{\omega_3 x_1}{x_3\omega_1}\right) & -\omega_1\left(1-\dfrac{\omega_3 x_2}{x_3\omega_2}\right) \\ -\omega_2\left(1-\dfrac{\omega_3 x_1}{x_3\omega_1}\right) & 1-\omega_2\left(1-\dfrac{\omega_3 x_2}{x_3\omega_2}\right) \end{bmatrix} \begin{bmatrix} \omega_1 & 0 \\ 0 & \omega_2 \end{bmatrix} \begin{bmatrix} x_1 & 0 \\ 0 & x_2 \end{bmatrix}^{-1} \tag{2-8}$$

For the ternary mixture of $nC_8H_{18}$(1)/$nC_{10}H_{22}$(2)/1-methylnapthalene(3) with mass fractions $\omega_1$ = 0.3333, $\omega_2$ = 0.3333, $\omega_3$ = 0.3333 at 295.65 K, Leahy-Dios et al.[2] report experimental data on the Fick diffusivity matrix in the mass average reference velocity frame: $[D^{mass}] = \begin{bmatrix} 1.99 & -0.93 \\ -0.42 & 2.4 \end{bmatrix} \times 10^{-9}$ m$^2$s$^{-1}$; the large magnitudes of the off-diagonal elements are particular noteworthy. The corresponding mole fractions of the three components are $x_1$ = 0.384, $x_2$ = 0.308, $x_3$ = 0.308. On transformation using equation (2-8), we obtain the matrix of Fick diffusivities in the molar average reference velocity frame $[D] = \begin{bmatrix} 1.92 & -1.07 \\ -0.333 & 2.47 \end{bmatrix} \times 10^{-9}$ m$^2$s$^{-1}$.

For a ternary mixture, $n$ = 3, the transformation between $[D]$, and $[D^{volume}]$ is given by equation (2-9). Alimadadian and Colver;[3] report the elements of the Fick matrix $[D^{volume}]$ in the volume average reference velocity frame for acetone(1)/benzene(2)/methanol(3) mixtures at 9 different compositions. At

$x_1 = 0.350$, $x_2 = 0.302$, $x_3 = 0.348$, $\left[D^{volume}\right] = \begin{bmatrix} 3.819 & 0.42 \\ -0.561 & 2.133 \end{bmatrix} \times 10^{-9}$ $m^2 s^{-1}$. The partial molar volumes are $\overline{V_1} = 74.1 \times 10^{-6}$; $\overline{V_2} = 89.4 \times 10^{-6}$; $\overline{V_3} = 40.7 \times 10^{-6}$ $m^3$ $mol^{-1}$. Using equation (2-9), we can convert to the molar average reference velocity frame to obtain $[D] = \begin{bmatrix} 3.651 & -0.069 \\ -0.300 & 2.303 \end{bmatrix} \times 10^{-9}$ $m^2 s^{-1}$; see Example 3.2.1 of Taylor and Krishna[1] for further calculation details.

$$\left[D^{volume}\right] = [A][D][A]^{-1}; \quad [D] = [A]^{-1}\left[D^{volume}\right][A];$$

$$[A] \equiv \begin{bmatrix} 1 - \frac{x_1}{\overline{V}}\left(\overline{V_1} - \overline{V_3}\right) & -\frac{x_1}{\overline{V}}\left(\overline{V_2} - \overline{V_3}\right) \\ -\frac{x_2}{\overline{V}}\left(\overline{V_1} - \overline{V_3}\right) & 1 - \frac{x_2}{\overline{V}}\left(\overline{V_2} - \overline{V_3}\right) \end{bmatrix}; \quad \overline{V} = \sum_{k=1}^{3} x_k \overline{V_k} \tag{2-9}$$

## 2.5 The Onsager relations for *n*-component diffusion

Lars Onsager was amongst the first to recognize the limitations of Fick's law. In his classic paper published in 1945 entitled *Theories and Problems of Liquid Diffusion*, Onsager[4] wrote *The theory of liquid diffusion is relatively undeveloped… It is a striking symptom of the common ignorance in this field that not one of the phenomenological schemes which are fit to describe the general case of diffusion is widely known*. In the Onsager formalism for *n*-component mixture diffusion, the diffusion fluxes $J_i$ are postulated to be linearly dependent on the chemical potential gradients, $d\mu_i/dz$, of each of the species present in the mixture. Only (*n*-1) of the chemical potential gradients $\frac{d\mu_i}{dz}$ are independent, because of the Gibbs-Duhem relationship

$$x_1 \frac{d\mu_1}{dz} + x_2 \frac{d\mu_2}{dz} + \cdots x_n \frac{d\mu_n}{dz} = 0 \tag{2-10}$$

It is convenient, therefore, to choose the (*n*-1) independent chemical potential gradients $\frac{d(\mu_i - \mu_n)}{dz}$ as driving forces for diffusion. In (*n*-1) dimensional matrix notation, the Onsager formulation is written as

$$(J) = -\frac{1}{\overline{V}}[L]\frac{1}{RT}\left(\frac{d(\mu - \mu_n)}{dz}\right) \tag{2-11}$$

where $\overline{V} = \sum_{k=1}^{n} x_k \overline{V_k}$ is the mean molar volume of the mixture. For example, for an ideal gas mixture $\overline{V} = RT/p_t$. The units of the elements $L_{ij}$ are the same as those for Fick diffusivities, i.e. $m^2\ s^{-1}$. The matrix of Onsager coefficients $[L]$ is symmetric because of the Onsager Reciprocal Relations (ORR)[5]

$$L_{ij} = L_{ji} \tag{2-12}$$

For insightful and robust discussions on the validity of the Onsager relations, see Truesdell.[6]

In proceeding further, we define a ($n$-1) dimensional matrix $[\Theta]$, that is the Hessian of the molar Gibbs free energy, $G$

$$\Theta_{ij} = \frac{1}{RT}\frac{\partial^2 G}{\partial x_i \partial x_j} = \frac{1}{RT}\frac{\partial^2 G}{\partial x_i \partial x_i} = \Theta_{ji}; \qquad i, j = 1, 2 \ldots n-1 \tag{2-13}$$

where $G$, the molar Gibbs free energy for the $n$-component mixture, is the sum of two contributions

$$G = G^{ex} + RT\sum_{i=1}^{n} x_i \ln(x_i); \quad G^{ex} = RT\sum_{i=1}^{n} x_i \ln(\gamma_i) \tag{2-14}$$

where $\gamma_i$ is the activity coefficient of component $i$. Equation (2-14) can also be written in terms of the $\mu_i$, that is the chemical potential or partial molar Gibbs free energy:

$$G = \sum_{i=1}^{n} x_i \mu_i \tag{2-15}$$

When carrying out the partial differentiations of $G$, required in equation (2-13), it is important to note that all $n$ of the mole fractions cannot be varied independently. So, we re-write equation (2-15) in terms of the $n$-1 independent mole fractions

$$G = \sum_{i=1}^{n} x_i \mu_i = \sum_{i=1}^{n-1} x_i (\mu_i - \mu_n) + \mu_n \tag{2-16}$$

In view of equations (2-13) and (2-16), we obtain

$$\Theta_{ij} = \frac{1}{RT}\frac{\partial\left(\mu_i - \mu_n\right)}{\partial x_j} = \frac{1}{RT}\frac{\partial\left(\mu_j - \mu_n\right)}{\partial x_i} = \Theta_{ji}; \qquad i, j = 1, 2 \ldots n-1 \tag{2-17}$$

Combining equations (2-11), and (2-17) we get

$$(J) = -\frac{1}{\overline{\overline{V}}}\,[L][\Theta]\frac{d(x)}{dz} \tag{2-18}$$

The inter-relationship between the Fick, and Onsager formulations are

$$(J) = -\frac{1}{\overline{\overline{V}}}\,[L][\Theta]\frac{d(x)}{dz} = -\frac{1}{\overline{\overline{V}}}[D]\frac{d(x)}{dz} \tag{2-19}$$

and therefore

$$[D] = [L][\Theta] \tag{2-20}$$

## 2.6 The Maxwell-Stefan formulation for *n*-component diffusion

The Maxwell-Stefan approach, that we adopt in this article, has its origins in the pioneering works of James Clerk Maxwell [7] and Josef Stefan [8] who analyzed diffusion in *ideal gas mixtures*. The Maxwell-Stefan (M-S) formulation is best understood by considering *z*-directional diffusion in a binary gas mixture consisting of species 1 and 2, contained within the control volume shown schematically in Figure 2-1. The cross-sectional area available for diffusion is 1 $m^2$ and the length of the diffusion path is $dz$. If the change in the partial pressure of component *i* across the diffusion distance $dz$ is $-dp_i$, the force acting on species *i* per $m^3$ is $-\frac{dp_i}{dz}$. The number of moles of species *i* per $m^3$, $c_i = \frac{p_i}{RT}$, and therefore the force acting per mole of species *i* is $-\frac{RT}{p_i}\frac{dp_i}{dz}$ which for an ideal gas mixture at constant temperature also equals the chemical potential gradient $-\frac{d\mu_i}{dz}$. This force is balanced by friction between the diffusing species 1 and 2, each diffusing with a velocity $u_i$ (cf. Figure 2-2). We may expect that the frictional drag to be proportional to the velocity difference $(u_1 - u_2)$, and we write $-\frac{d\mu_1}{dz} = \frac{RT}{Đ_{12}}x_2\left(u_1 - u_2\right)$ where the term $\frac{RT}{Đ_{12}}$ is to be interpreted as the drag coefficient. The multiplier

$x_2$ in the right member represents the mole fraction of component 2; this factor is introduced because we expect the friction to be dependent on the number of molecules of component 2 relative to that of component 1. The Maxwell-Stefan diffusivity $Đ_{12}$ has the units $m^2\ s^{-1}$ and the physical significance of an inverse drag coefficient. The extension to *n*-component mixtures is intuitively obvious and can be written for component 1, for example as follows

$$-\frac{d\mu_1}{dz} = \frac{RT}{Đ_{12}} x_2 \left(u_1 - u_2\right) + \frac{RT}{Đ_{13}} x_3 \left(u_1 - u_3\right) + ..... + \frac{RT}{Đ_{1n}} x_n \left(u_1 - u_n\right) \tag{2-21}$$

The corresponding relations for components 2, 3, ..*n* are written down in an analogous manner. The left member of equation (2-21)) is the negative of the gradient of the chemical potential, with the units N $mol^{-1}$; it represents the driving force acting per mole of species 1. The term $RT/Đ_{ij}$ is interpreted as the drag coefficient for the *i-j* pair. The multiplier $x_j$ in each of the right members represents the mole fraction of component *j*; this factor is introduced because we expect the friction to be dependent on the number of molecules of *j* relative to that of component 1. The M-S diffusivity $Đ_{ij}$ has the units $m^2\ s^{-1}$ and the physical significance of an *inverse* drag coefficient. The magnitudes of the M-S diffusivities $Đ_{ij}$ do not depend on the choice of the mixture reference velocity because Equation (2-21) is set up in terms of velocity differences. Equation (2-21) may be re-written as

$$-\frac{1}{RT}\frac{d\mu_i}{dz} = \sum_{\substack{j=1 \\ j\neq i}}^{n} \frac{x_j\left(u_i - u_j\right)}{Đ_{ij}} \tag{2-22}$$

Multiplying both sides of equation (2-22) by $x_i$ we get

$$-\frac{x_i}{RT}\frac{d\mu_i}{dz} = \sum_{\substack{j=1 \\ j\neq i}}^{n} \frac{x_i x_j\left(u_i - u_j\right)}{Đ_{ij}} = \sum_{\substack{j=1 \\ j\neq i}}^{n} \frac{\left(x_j x_i u_i - x_i x_j u_j\right)}{Đ_{ij}} = \sum_{\substack{j=1 \\ j\neq i}}^{n} \frac{\left(x_j c_i u_i - x_i c_j u_j\right)}{c_t Đ_{ij}} \tag{2-23}$$

Introducing the expressions for fluxes $N_i = c_i u_i = c_t x_i u_i$ and $J_i = N_i - x_i N_t$ in equation (2-23), we get

$$-\frac{x_i}{RT}\frac{d\mu_i}{dz} = \sum_{\substack{j=1 \\ j\neq i}}^{n} \frac{x_j N_i - x_i N_j}{c_t Đ_{ij}} = \sum_{\substack{j=1 \\ j\neq i}}^{n} \frac{x_j J_i - x_i J_j}{c_t Đ_{ij}}; \quad i = 1,2,\ldots n \tag{2-24}$$

**Phenomenological relations for n-component diffusion**

The Maxwell-Stefan diffusion formulation (2-24) is consistent with the Onsager formulation; the Onsager Reciprocal Relations imply that the M-S pair diffusivities are symmetric

$$Đ_{ij} = Đ_{ji}; \quad i, j = 1,2...n \tag{2-25}$$

The second law of thermodynamics dictates that the rate of entropy production must be positive

$$\sigma = -\frac{1}{T}\sum_{i=1}^{n}\frac{d\mu_i}{dz}J_i = -\frac{1}{T}\sum_{i=1}^{n-1}\frac{d(\mu_i - \mu_n)}{dz}J_i \geq 0 \tag{2-26}$$

Insertion of the Maxwell-Stefan equation (2-24) into equation (2-26) we obtain on re-arrangement[9]

$$\sigma = \frac{1}{2}c_t R\sum_{i=1}^{n}\sum_{j=1}^{n}\frac{x_i x_j}{Đ_{ij}}\left|u_i - u_j\right|^2 \geq 0 \tag{2-27}$$

The term $\frac{x_i}{RT}\frac{d\mu_i}{dz}$ on the left hand member of equation (2-24) is the generalization of the mole fraction gradients, used as driving forces for ideal gas mixtures.

For non-ideal liquid mixtures, the chemical potential of component *i*, $\mu_i$ are related to the gradients of the component activities, $a_i = \gamma_i x_i$, where $\gamma_i$ is the activity coefficient:

$$\mu_i = \mu_i^0 + RT\ln(a_i) = \mu_i^0 + RT\ln(\gamma_i x_i) \tag{2-28}$$

For gaseous mixtures at high pressure, the chemical potential of component *i*, $\mu_i$ are related to the gradients of the component fugacities, $f_i = \phi_i p_i = \phi_i x_i p$:

$$\mu_i = \mu_i^0 + RT\ln(f_i) = \mu_i^0 + RT\ln(\phi_i x_i p_t) \tag{2-29}$$

where $\phi_i$ is the fugacity coefficient and $p_t$ is the total gas pressure.

In proceeding further, it is convenient to express the left member of equation (2-24) in terms of the mole fraction gradients by introducing an (*n*-1) × (*n*-1) matrix of thermodynamic correction factors $[\Gamma]$:

$$\frac{x_i}{RT}\frac{d\mu_i}{dz} = x_i\frac{d\ln a_i}{dz} = \sum_{j=1}^{n-1}\Gamma_{ij}\frac{dx_j}{dz}; \quad \Gamma_{ij} = \delta_{ij} + x_i\frac{\partial\ln\gamma_i}{\partial x_j}; \quad i, j = 1,2\ldots n-1 \tag{2-30}$$

For non-ideal ternary liquid mixtures, the elements of $[\Gamma]$ can be calculated from Van Laar, Wilson, UNIQUAC or NRTL models describing phase equilibrium thermodynamics.[1, 10]

The analogous expression for high pressure gaseous mixtures is

$$\frac{x_i}{RT}\frac{d\mu_i}{dz} = x_i\frac{d\ln f_i}{dz} = \sum_{j=1}^{n-1}\Gamma_{ij}\frac{dx_j}{dz}; \quad \Gamma_{ij} = \delta_{ij} + x_i\frac{\partial \ln \phi_i}{\partial x_j}; \quad i,j = 1,2\ldots n-1 \tag{2-31}$$

In this case, the elements of $[\Gamma]$ can be calculated by analytic differentiation of an Equation of State (EOS) such as the Peng-Robinson (PR) EOS; for further details see Krishna and van Baten.[11] For binary mixtures, explicit analytic expressions for $\Gamma = x_1\frac{\partial \ln f_1}{\partial x_1} = \delta_{ij} + x_1\frac{\partial \ln \phi_1}{\partial x_1}$ for PR EOS are provided in the paper by Tuan et al.[12]

We also define a ($n$-1) × ($n$-1) matrix of inverse M-S diffusivities $[B]$ whose elements are given by

$$B_{ii} = \frac{x_i}{Đ_{in}} + \sum_{\substack{k=1\\k\neq i}}^{n}\frac{x_k}{Đ_{ik}}; \quad B_{ij(i\neq j)} = -x_i\left(\frac{1}{Đ_{ij}} - \frac{1}{Đ_{in}}\right); \quad i,j = 1,2\ldots n-1 \tag{2-32}$$

Combining equations (2-24), (2-30), (2-31), and (2-32), we can re-cast equation (2-24) into ($n$-1) dimensional matrix notation

$$-[\Gamma]\frac{d(x)}{dz} = \frac{1}{c_t}[B](J); \quad (J) = -c_t[B]^{-1}[\Gamma]\frac{d(x)}{dz} = -c_t[\Lambda][\Gamma]\frac{d(x)}{dz} = -\frac{1}{\overline{\overline{V}}}[\Lambda][\Gamma]\frac{d(x)}{dz} \tag{2-33}$$

where we have additionally defined

$$[\Lambda] = [B]^{-1} \tag{2-34}$$

The inter-relationships between the Fick, Onsager, and the Maxwell-Stefan diffusivities is

$$\begin{aligned}&[D] = [B]^{-1}[\Gamma] = [\Lambda][\Gamma] = [L][\Theta];\\ &(J) = -\frac{1}{\overline{\overline{V}}}\,[L][\Theta]\frac{d(x)}{dz} = -\frac{1}{\overline{\overline{V}}}[D]\frac{d(x)}{dz} = -\frac{1}{\overline{\overline{V}}}[\Lambda][\Gamma]\frac{d(x)}{dz}\end{aligned} \tag{2-35}$$

Equation (2-35) underscores the direct influence of mixture thermodynamics on the elements $D_{ij}$ of the matrix of Fick diffusivities $[D]$.

For an ideal gas mixture, the thermodynamic correction factors $\Gamma_{ij} = \delta_{ij}$ and equation (2-35) reduces to

$$[\Lambda]=[B]^{-1}=[D];\quad \text{idealgas mixture} \tag{2-36}$$

For a binary mixture, $n = 2$, equation (2-24) simplifies to

$$-\frac{x_1}{RT}\frac{d\mu_1}{dz}=\frac{\left(x_2J_1-x_1J_2\right)}{c_t\text{Đ}_{12}} \tag{2-37}$$

Introducing the constraints $J_2=-J_1$, and $x_2=1-x_1$, equation (2-37) yields

$$J_1=-c_t\text{Đ}_{12}\frac{x_1}{RT}\frac{d\mu_1}{dz}=-c_t\text{Đ}_{12}\Gamma\frac{dx_1}{dz}=-c_tD_{12}\frac{dx_1}{dz} \tag{2-38}$$

in which the Fick diffusivity for binary mixture is

$$D_{12}=\text{Đ}_{12}\Gamma \tag{2-39}$$

For a ternary mixture, $n = 3$, equation (2-35) gives the following explicit expression for the four elements of the Fick diffusivity matrix

$$\begin{bmatrix} D_{11} & D_{12} \\ D_{21} & D_{22} \end{bmatrix}=\begin{bmatrix} \dfrac{x_2}{\text{Đ}_{23}}+\dfrac{x_1}{\text{Đ}_{12}}+\dfrac{x_3}{\text{Đ}_{23}} & x_1\left(\dfrac{1}{\text{Đ}_{12}}-\dfrac{1}{\text{Đ}_{13}}\right) \\ x_2\left(\dfrac{1}{\text{Đ}_{12}}-\dfrac{1}{\text{Đ}_{23}}\right) & \dfrac{x_1}{\text{Đ}_{13}}+\dfrac{x_2}{\text{Đ}_{12}}+\dfrac{x_3}{\text{Đ}_{13}} \end{bmatrix}^{-1}\begin{bmatrix} \Gamma_{11} & \Gamma_{12} \\ \Gamma_{21} & \Gamma_{22} \end{bmatrix} \tag{2-40}$$

The matrix inversion in equation (2-40) can performed explicity and we obtain

$$\begin{bmatrix} D_{11} & D_{12} \\ D_{21} & D_{22} \end{bmatrix}=\begin{bmatrix} \Lambda_{11} & \Lambda_{12} \\ \Lambda_{21} & \Lambda_{22} \end{bmatrix}\begin{bmatrix} \Gamma_{11} & \Gamma_{12} \\ \Gamma_{21} & \Gamma_{22} \end{bmatrix};$$

$$\begin{bmatrix} \Lambda_{11} & \Lambda_{12} \\ \Lambda_{21} & \Lambda_{22} \end{bmatrix}=\frac{\begin{bmatrix} \text{Đ}_{13}\left(x_1\text{Đ}_{23}+\left(1-x_1\right)\text{Đ}_{12}\right) & x_1\text{Đ}_{23}\left(\text{Đ}_{13}-\text{Đ}_{12}\right) \\ x_2\text{Đ}_{13}\left(\text{Đ}_{23}-\text{Đ}_{12}\right) & \text{Đ}_{23}\left(x_2\text{Đ}_{13}+\left(1-x_2\right)\text{Đ}_{12}\right) \end{bmatrix}}{x_1\text{Đ}_{23}+x_2\text{Đ}_{13}+x_3\text{Đ}_{12}} \tag{2-41}$$

The determinant of $[B]$ for a ternary mixture is

$$|B|=\frac{x_1}{\text{Đ}_{12}\text{Đ}_{13}}+\frac{x_2}{\text{Đ}_{12}\text{Đ}_{23}}+\frac{x_3}{\text{Đ}_{13}\text{Đ}_{23}}=\frac{1}{|\Lambda|};\quad |\Lambda|=\frac{\text{Đ}_{12}\text{Đ}_{13}\text{Đ}_{23}}{x_1\text{Đ}_{23}+x_2\text{Đ}_{13}+x_3\text{Đ}_{12}} \tag{2-42}$$

The quantity $|\Lambda|^{1/2}=\sqrt{\dfrac{\text{Đ}_{12}\text{Đ}_{13}\text{Đ}_{23}}{x_1\text{Đ}_{23}+x_2\text{Đ}_{13}+x_3\text{Đ}_{12}}}$ can be interpreted as a measure of the "average" magnitude of M-S diffusivity in the ternary mixture.

For stable single phase fluid mixtures, we must have $|\Gamma| \geq 0$ . In view of equation (2-35) the condition of phase stability translates to

$$|D| \geq 0; \quad |\Gamma| \geq 0; \quad \text{phase stability} \tag{2-43}$$

Equation (2-43) implies that all the eigenvalues of the Fick matrix [$D$] are positive definite. It is interesting to note that thermodynamic stability considerations do not require the diagonal elements $D_{ii}$ to be positive. If recourse is made to the kinetic theory of gases, it can be shown that the diagonal elements $D_{ii}$ are individually positive for mixtures of ideal gases. The off-diagonal elements $D_{ij}(i \neq j)$ can be either positive or negative, even for ideal gas mixtures. Indeed, the sign of $D_{ij}(i \neq j)$ also depends on the component numbering.

The condition for phase stability in a binary fluid mixture is

$$D_{12} \geq 0; \quad \Gamma \geq 0; \quad \text{phase stability} \tag{2-44}$$

The occurrence of $\Gamma < 0$ implies vapor/liquid or liquid/solid phase transitions.

## 2.7 List of Tables for Phenomenological relations for n-component diffusion

Table 2-1. Concentration measures

| Concentration measure | units | Inter-relation, constraint |
|---|---|---|
| $x_i$, mole fraction of species $i$ | - | $x_i = \frac{c_i}{c_t} = \frac{\frac{\omega_i}{M_i}}{\sum_{i=1}^{n} \frac{\omega_i}{M_i}} = \frac{\omega_i}{M_i}\overline{M}; \sum_{i=1}^{n} x_i = 1$ |
| $\omega_i$, mole fraction of species $i$ | - | $\omega_i = \frac{\rho_i}{\rho_t} = \frac{x_i M_i}{\sum_{i=1}^{n} x_i M_i} = \frac{x_i M_i}{\overline{M}}; \sum_{i=1}^{n} \omega_i = 1$ |
| $c_i$, molar density of species $i$ | mol m$^{-3}$ | $c_i = \frac{\rho_i}{M_i}; \sum_{i=1}^{n} c_i = c_t =$ mixture molar density$= \frac{1}{\overline{V}}$ |
| $\rho_i$, mass density of species $i$ | kg m$^{-3}$ | $\rho_i = c_i M_i; \sum_{i=1}^{n} \rho_i = \rho_t =$ mixture mass density |
| $M_i$, molar mass of species $i$ | kg mol$^{-1}$ | $\overline{M} = \sum_{i=1}^{n} x_i M_i =$ mean molar mass of mixture |
| $\overline{V_i}$, partial molar volume of $i$ | m$^3$ mol$^{-1}$ | $\overline{V} = \sum_{i=1}^{n} x_i \overline{V_i} = \frac{1}{c_t} =$ mean molar volume of mixture |
| $\phi_i$, volume fraction of species $i$ | - | $\phi_i = c_i \overline{V_i}$ |
| $f_i$, fugacity of species $i$ | Pa | $\sum_{i=1}^{n} f_i = f_t =$ total mixture fugacity |
| $\mu_i$, molar chemical potential of species $i$ | J mol$^{-1}$ | $\mu_i = \mu_i^0 + RT \ln f_i$ |

Table 2-2. Choice of reference velocity frame.

| Reference velocity | Constraint on molar fluxes |
|---|---|
| $u = \sum_{i=1}^{n} x_i u_i =$ molar average mixture velocity | $\sum_{i=1}^{n} J_i = 0$ |
| $v = \sum_{i=1}^{n} \omega_i u_i =$ mass average mixture velocity | $\sum_{i=1}^{n} \frac{\omega_i}{x_i} J_i = 0$ |
| $u^V = \sum_{i=1}^{n} c_i \overline{V}_i u_i = \sum_{i=1}^{n} \phi_i u_i =$ volume average mixture velocity | $\sum_{i=1}^{n} \overline{V}_i J_i = 0$ |
| $u_n = \sum_{i=1}^{n} \delta_{in} u_i =$ velocity of component $n$ | $J_n = 0$ |

Table 2-3. Inter-relation between $J_1$ and $j_1$ for binary mixture

| Molar fluxes | Mass fluxes |
|---|---|
| $J_1 = c_t x_1 (u_1 - u); u = x_1 u_1 + x_2 u_2$<br>$J_1 = c_t x_1 (u_1 - x_1 u_1 - x_2 u_2) = c_t x_1 x_2 (u_1 - u_2)$<br>$x_1 = \frac{\omega_1}{M_1}\overline{M}; x_2 = \frac{\omega_2}{M_2}\overline{M}; c_t = \frac{\rho_t}{\overline{M}}$<br>$J_1 = c_t x_1 x_2 (u_1 - u_2)$<br>$J_1 = \rho_t \omega_1 \omega_2 \frac{\overline{M}}{M_1 M_2}(u_1 - u_2) = \frac{\overline{M}}{M_1 M_2} j_1$ | $j_1 = \rho_t \omega_1 (u_1 - v); v = \omega_1 u_1 + \omega_2 u_2$<br>$j_1 = \rho_t \omega_1 (u_1 - \omega_1 u_1 - \omega_2 u_2) = \rho_t \omega_1 \omega_2 (u_1 - u_2)$<br>$\omega_i = \frac{\rho_i}{\rho_t} = \frac{x_i M_i}{\sum_{i=1}^{n} x_i M_i} = \frac{x_i M_i}{\overline{M}}; \rho_t = c_t \overline{M}$<br>$j_1 = \rho_t \omega_1 \omega_2 (u_1 - u_2) = c_t x_1 x_2 (u_1 - u_2)$<br>$j_1 = c_t x_1 x_2 \frac{M_1 M_2}{\overline{M}}(u_1 - u_2) = \frac{M_1 M_2}{\overline{M}} J_1$ |
| $dx_1 = \frac{\frac{1}{\overline{M_1 M_2}}}{\left(\frac{\omega_1}{M_1} + \frac{\omega_2}{M_2}\right)^2} d\omega_1; \quad d\omega_1 = \frac{M_1 M_2}{(x_1 M_1 + x_2 M_2)^2} dx_1$<br>$\frac{1}{\overline{M}} = \frac{\omega_1}{M_1} + \frac{\omega_2}{M_2}; \overline{M} = x_1 M_1 + x_2 M_2$<br>$dx_1 = \frac{\overline{M}^2}{M_1 M_2} d\omega_1; \quad d\omega_1 = \frac{M_1 M_2}{\overline{M}^2} dx_1$<br>$\frac{c_t}{\rho_t}\frac{x_1 x_2}{\omega_1 \omega_2} = \frac{\overline{M}}{M_1 M_2}$ | |
| $J_1 = -c_t D_{12} \frac{dx_1}{dz};$<br>$dx_1 = \frac{\overline{M}^2}{M_1 M_2} d\omega_1; c_t = \frac{\rho_t}{\overline{M}}$<br>$J_1 = -\rho_t D_{12} \frac{\overline{M}}{M_1 M_2} \frac{d\omega_1}{dz}$<br>$\frac{M_1 M_2}{\overline{M}} J_1 = -\rho_t D_{12} \frac{d\omega_1}{dz} = j_1$ | $j_1 = -\rho_t D_{12} \frac{d\omega_1}{dz}$<br>$d\omega_1 = \frac{M_1 M_2}{\overline{M}^2} dx_1; \rho_t = c_t \overline{M}$<br>$j_1 = -c_t D_{12} \frac{M_1 M_2}{\overline{M}} \frac{dx_1}{dz}$<br>$\frac{\overline{M}}{M_1 M_2} j_1 = -c_t D_{12} \frac{dx_1}{dz} = J_1$ |

## 2.1 List of Figures for Phenomenological relations for n-component diffusion

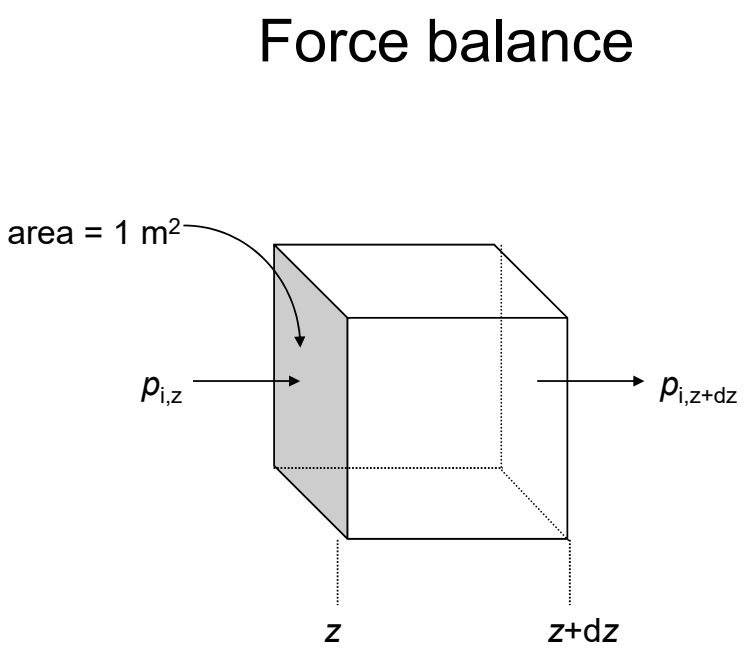


Figure 2-1. A force balance on a control volume containing an ideal gas mixture.

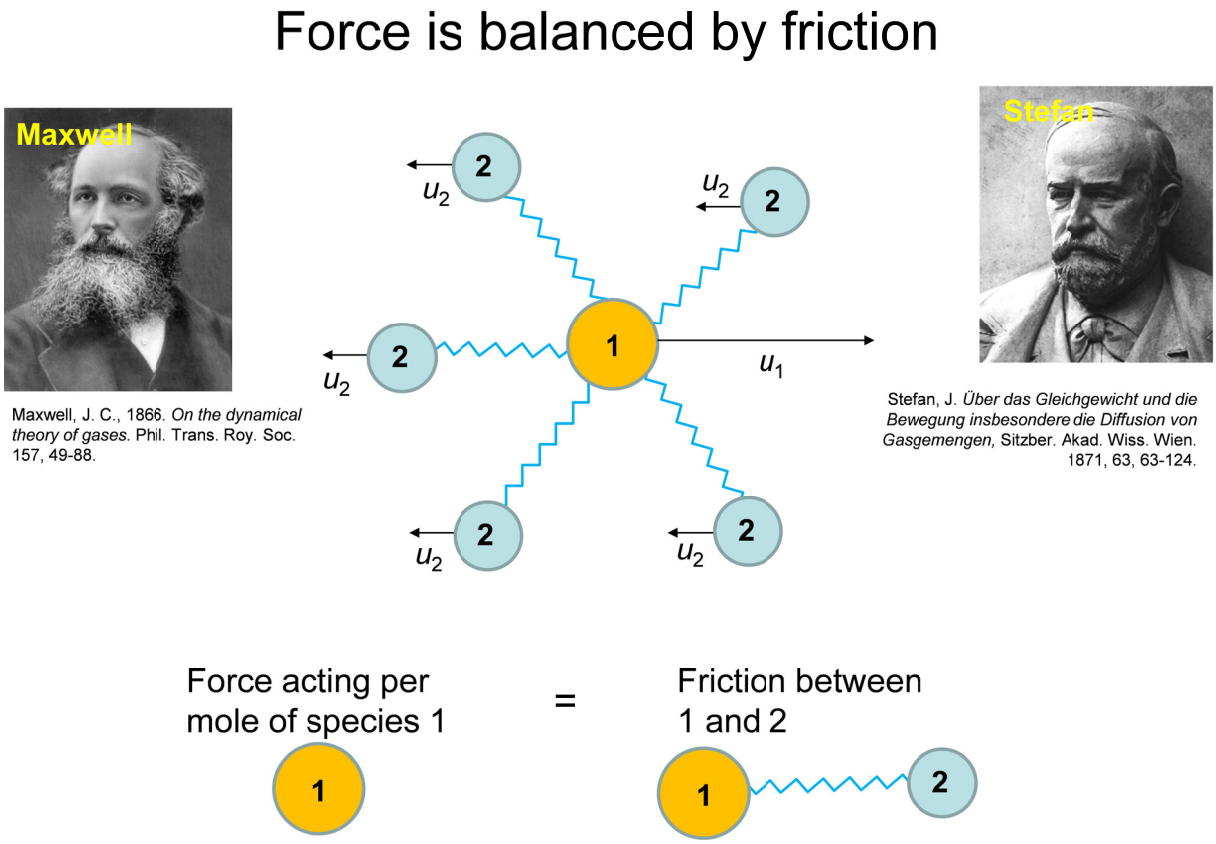


Figure 2-2. The force acting on each of the species in the diffusing binary mixture of species 1 and 2 is balanced by friction between the species 1 and 2.

# 3 Diffusion in Ideal Gas Mixtures

For an ideal gas mixture, the thermodynamic correction factors $\Gamma_{ij} = \delta_{ij}$ and the Maxwell-Stefan diffusion equations

$$-\frac{x_i}{RT}\frac{d\mu_i}{dz} = \sum_{\substack{j=1 \\ j\neq i}}^{n} \frac{x_j N_i - x_i N_j}{c_t Đ_{ij}} = \sum_{\substack{j=1 \\ j\neq i}}^{n} \frac{x_j J_i - x_i J_j}{c_t Đ_{ij}}; \quad i = 1,2,\ldots n \tag{3-1}$$

simplify to yield

$$-\frac{dy_i}{dz} = \sum_{\substack{j=1 \\ j\neq i}}^{n} \frac{y_j N_i - y_i N_j}{c_t Đ_{ij}} = \sum_{\substack{j=1 \\ j\neq i}}^{n} \frac{y_j J_i - y_i J_j}{c_t Đ_{ij}}; \quad i = 1,2,\ldots n \tag{3-2}$$

For mixtures of ideal gases for which the $Đ_{ij}$ are independent of composition the second-law requirement

$$\sigma = \frac{1}{2} c_t R \sum_{i=1}^{n}\sum_{j=1}^{n} \frac{x_i x_j}{Đ_{ij}} \left| u_i - u_j \right|^2 \geq 0 \tag{3-3}$$

can only be satisfied if

$$Đ_{ij} \geq 0; \quad (\text{ideal gas mixtures}) \tag{3-4}$$

Equation (3-4) was first derived by Hirschfelder, Curtiss and Bird.[13] For non-ideal fluid mixtures the $Đ_{ij}$ are composition dependent in general and a result analogous to equation (3-4) cannot be derived.[9]

## 3.1 The M-S pair diffusivities $Đ_{ij}$ in gaseous mixtures

The M-S pair diffusivities $Đ_{ij}$ for gaseous mixtures at low pressures, below about 10 bar, can be estimated to a good level of accuracy using the Fuller-Schettler-Giddings (FSG)[14] method.

$$Đ_{12} = \frac{1.43 \times 10^{-7} T^{1.75}}{p\sqrt{M_{12}}\left[\left(v_1^{1/3}\right) + \left(v_2^{1/3}\right)\right]^2} \quad \text{m}^2\text{s}^{-1} \tag{3-5}$$

where $p$ is the pressure (expressed in bars), $M_{12} = \dfrac{2}{\dfrac{1}{M_1}+\dfrac{1}{M_2}}$ is the mean molecular weight of the mixture (expressed in g mol$^{-1}$), $v_1$, and $v_2$ are the diffusion volumes (expressed in cm$^3$ mol$^{-1}$) whose values are obtained by summing the contributions of the volumes of the constituent atoms in the molecular species (the values are tabulated in Table 11.1 of Reid, Prausnitz, and Poling[15]). According to the FSG estimation procedure, the product of $Đ_{12}$ and the total pressure, $p$, is a function only of temperature and is also independent of composition.

In generalizing the FSG method to dense gas mixtures, it is important realize that equation (3-5) implies that, *at constant temperature*, the M-S diffusivity is *inversely* proportional to the molar density of the gas phase. For dense gases, the total mixture molar density of the gas phase is $c_t = \dfrac{p}{ZRT}$ where $Z$ is the compressibility factor. Consequently, the M-S diffusivity for dense gases can be estimated by correcting the original FSG equation by introducing the compressibility factor $Z$; see Krishna and van Baten[11] for further details

$$Đ_{12} = \frac{1.43\times 10^{-7} T^{1.75}}{p\sqrt{M_{12}}\left[\left(v_1^{1/3}\right)+\left(v_2^{1/3}\right)\right]^2} Z \tag{3-6}$$

Due to the introduction of the compressibility factor, $Z$, the M-S diffusivity $Đ_{12}$ becomes dependent on mixture composition. The molar density of the mixture is $c_t = \dfrac{p}{ZRT}$, and therefore Equation (3-6) anticipates that $c_t Đ_{12}$ is constant at constant temperature $T$.

## 3.2 The Loschmidt tube experiments of Arnold and Toor

Arnold and Toor[16] report experimental data on the transient equilibration of $CH_4(1)/Ar(2)/H_2(3)$ gas mixtures of two different compositions in the top and bottom compartments of a Loschmidt tube of total length; see Figure 3-1. The temperature is 307 K and the total pressures is 101.3 kPa. Each compartment has a length, $\delta = 0.4$ m. The initial compositions in the two compartments are

top compartment (+) : $0 \le z \le \delta; y_1 = 0.0; y_2 = 0.509; y_3 = 0.491$

botttom compartment (-) : $-\delta \le z \le 0; y_1 = 0.515; y_2 = 0.485; y_3 = 0.0$

The final equilibrated compositions are $y_{1,eq} = 0.2575$, $y_{2,eq} = 0.497$ and $y_{3,eq} = 0.2455$. For the ternary $CH_4(1)/Ar(2)/H_2(3)$ gas mixture, the binary pair diffusivities calculated using the Fuller-Schettler-Giddings (FSG)[14] method for $T = 307$ K and $p_t = 101.3$ kPa. are:

$$Đ_{12} = 2.16\times10^{-5}; \quad Đ_{13} = 7.72\times10^{-5}; \quad Đ_{23} = 8.33\times10^{-5} \quad \text{m}^2\ \text{s}^{-1}.$$

At the equilibrium composition, $y_{1,eq} = 0.2575$, $y_{2,eq} = 0.497$ and $y_{3,eq} = 0.2455$, the elements of the Fick diffusivity matrix $[D]$ can be calculated using (cf. Equation (2-41), with $\begin{bmatrix}\Gamma_{11} & \Gamma_{12}\\ \Gamma_{21} & \Gamma_{22}\end{bmatrix} = \begin{bmatrix}1 & 0\\ 0 & 1\end{bmatrix}$)

$$\begin{bmatrix}D_{11} & D_{12}\\ D_{21} & D_{22}\end{bmatrix} = \frac{\begin{bmatrix}Đ_{13}\left(x_1 Đ_{23} + (1-x_1)Đ_{12}\right) & x_1 Đ_{23}\left(Đ_{13} - Đ_{12}\right)\\ x_2 Đ_{13}\left(Đ_{23} - Đ_{12}\right) & Đ_{23}\left(x_2 Đ_{13} + (1-x_2)Đ_{12}\right)\end{bmatrix}}{x_1 Đ_{23} + x_2 Đ_{13} + x_3 Đ_{12}} \tag{3-7}$$

The result is $[D] = \begin{bmatrix}4.45895 & 1.784055\\ 3.63675 & 6.40716\end{bmatrix}\times10^{-5}$ $\text{m}^2\ \text{s}^{-1}$. The large off-diagonal elements indicate strong diffusional coupling for transfer of all components.

We note that the driving force for Ar is significantly lower than that of its two partner species. The analytic solution for transient equilibration trajectories in the two compartments is given in Section 5.5 of Taylor and Krishna.[1] In two-dimensional matrix notation, the equilibration trajectories are described by

$$\begin{pmatrix}y_1(\eta,t) - y_{1-}\\ y_2(\eta,t) - y_{2-}\end{pmatrix} = [Q(\eta,t]\begin{pmatrix}y_{1+} - y_{1-}\\ y_{2+} - y_{2-}\end{pmatrix}$$

$$[Q(\eta,t] = f(\eta,t,\lambda_1)\frac{[[D] - \lambda_2[I]]}{(\lambda_1 - \lambda_2)} + f(\eta,t,\lambda_2)\frac{[[D] - \lambda_1[I]]}{(\lambda_2 - \lambda_1)} \tag{3-8}$$

$$f(\eta,t,\lambda_i) = \frac{1}{2} + \frac{1}{\pi}\sum_{k=0}^{\infty}\frac{1}{\left(k+\frac{1}{2}\right)}\sin\left(\left(k+\frac{1}{2}\right)\pi\eta\right)\exp\left(-\left(k+\frac{1}{2}\right)^2\left(\frac{\pi}{\delta}\right)^2\lambda_i t\right)$$

In equation (3-8), the dimensionless distance coordinate $\eta = \frac{z}{\delta}$ where $\delta$ is the length of each of the two tube segments; $\lambda_1$ and $\lambda_2$ are distinct eigenvalues of the 2-dimensional Fick diffusivity square matrix $[D]$, that may be evaluated at the final equilibrated composition. We also note in passing that there are two typographical errors in Equation (5.5.6) of Taylor and Krishna;[1] Equation (3-8) is the correct one to use. See also Ravi[17] for further clarifications on this topic.

Figure 3-1(a) shows the composition profiles at time $t$ = 0.05 h from the start of the equilibration process. Due to strong coupling effects, the composition profile of Ar shows both overshoot (top compartment) and undershoot (bottom compartment).

At any time $t$, the integral averaged compositions in the bottom compartment are described by

$$\begin{pmatrix} y_1(t) - y_{1-} \\ y_2(t) - y_{2-} \end{pmatrix} = [Q(t] \begin{pmatrix} y_{1+} - y_{1-} \\ y_{2+} - y_{2-} \end{pmatrix}$$
$$[Q(t] = f(t,\lambda_1)\frac{[[D] - \lambda_2[I]]}{(\lambda_1 - \lambda_2)} + f(t,\lambda_2)\frac{[[D] - \lambda_1[I]]}{(\lambda_2 - \lambda_1)} \qquad (3\text{-}9)$$
$$f(t,\lambda_i) = \frac{1}{2} - \frac{1}{\pi^2}\sum_{k=0}^{\infty}\frac{1}{\left(k+\frac{1}{2}\right)^2}\exp\left(-\left(k+\frac{1}{2}\right)^2\left(\frac{\pi}{\delta}\right)^2\lambda_i t\right)$$

Figure 3-1(b) compares the transient equilibration trajectories calculated using equation (3-9) with the experimental data of Arnold and Toor;[16] there is excellent agreement between the two sets. The transient equilibration processes for $CH_4$, and $H_2$ are "normal", inasmuch as their equilibration are monotonous. The equilibration of Ar, however, shows an overshoot (in top compartment) and an undershoot (in bottom compartment). Such over- and under-shoots signal the occurrence of uphill diffusion engendered by diffusional coupling effects. In ternary composition space, the equilibration process follow serpentine trajectories; see Figure 3-1(c)

## 3.3 Two-bulb experiments of Duncan and Toor

One of the first set of experiments to demonstrate uphill diffusion were reported by Duncan and Toor[18] for ternary $H_2(1)/N_2(2)/CO_2(3)$ gas mixtures. The experimental set-up consisted of a two bulb

diffusion cell, pictured in Figure 3-2. The two bulbs are connected by means of an 86 mm long capillary tube. The length of the diffusion path, $\delta = 0.086$ m. Since the two bulbs are sealed there is no net transfer flux out of or into the system, i.e. we have conditions corresponding to equimolar diffusion

$$u = 0; \qquad N_1 + N_2 + N_3 = 0; \quad N_i = J_i .$$

The initial compositions (mole fractions in the two bulbs, Bulb A and Bulb B, are

$$\text{Bulb A}: y_1 = 0.0; y_2 = 0.5; y_3 = 0.5$$
$$\text{Bulb B}: y_1 = 0.5; y_2 = 0.5; y_3 = 0.0$$

The experimental data on the transient approach to equilibration are indicated by the symbols in Figure 3-3Figure 3-2.(a). We note that despite the fact that the driving force for nitrogen is practically zero, it does transfer from one bulb to the other, exhibiting over-shoot and under-shoot phenomena when approaching equilibrium. The transient equilibration trajectories of $H_2$, and $CO_2$ are "normal", with their compositions in the two bulbs approaching equilibrium in a monotonous manner.

The Maxwell-Stefan equations (3-2) allow a quantitative explanation of the experimental data; the model calculations are presented in Example 5.4.1 of Taylor and Krishna.[1] The M-S diffusivities calculated using the Fuller-Schettler-Giddings (FSG)[14] method for the three binary pairs at $T$ = 308.3 K are $Đ_{12} = 8.33\times10^{-5}$ m$^2$ s$^{-1}$; $Đ_{13} = 6.8\times10^{-5}$ m$^2$ s$^{-1}$; $Đ_{23} = 1.68\times10^{-5}$ m$^2$ s$^{-1}$.

The compositions in the two bulbs equilibrate after several hours to $y_{1,eq}$ = 0.25, $y_{2,eq}$ = 0.5 and $y_{3,eq}$ = 0.25. At this equilibrium composition the elements of the Fick diffusivity matrix [$D$] can be calculated using Equation (3-7); the result is $[D] = \begin{bmatrix} 7.68 & -0.11 \\ -3.83 & 2.15 \end{bmatrix} \times 10^{-5}$ m$^2$ s$^{-1}$. The large magnitude of the off-diagonal element $D_{21}$ indicate strong diffusional coupling for transfer of nitrogen.

If the Fick diffusivity matrix is assumed constant during the entire equilibration process, the transient equilibration trajectories can be expressed in two-dimensional matrix notation

$$\begin{pmatrix} y_1(t) - y_{1,eq} \\ y_2(t) - y_{2,eq} \end{pmatrix} = \exp\left[ -\beta \begin{bmatrix} D_{11} & D_{12} \\ D_{21} & D_{22} \end{bmatrix} t \right] \begin{pmatrix} y_{10} - y_{1,eq} \\ y_{20} - y_{2,eq} \end{pmatrix} = [Q] \begin{pmatrix} y_{10} - y_{1,eq} \\ y_{20} - y_{2,eq} \end{pmatrix} \tag{3-10}$$

where $\beta$ is the cell constant. From the information provided by Duncan and Toor,[18] the value of the cell constant is calculated as $\beta = 0.9895$ m$^{-2}$.

The Sylvester theorem, detailed in Appendix A of Taylor and Krishna,[1] is required for explicit calculation of the 2×2 square matrix $[Q] = \exp\left[-\beta \begin{bmatrix} D_{11} & D_{12} \\ D_{21} & D_{22} \end{bmatrix} t\right]$. For the case of distinct eigenvalues, $\lambda_1$ and $\lambda_2$ of the 2-dimensional square matrix $[D]$, the Sylvester theorem yields

$$[Q] = \exp[-\beta\lambda_1 t]\frac{[[D]-\lambda_2[I]]}{(\lambda_1-\lambda_2)} + \exp[-\beta\lambda_2 t]\frac{[[D]-\lambda_1[I]]}{(\lambda_2-\lambda_1)} \tag{3-11}$$

In equation (3-11), $[I]$ is the identity matrix with elements $\delta_{ik}$.

The continuous solid lines in Figure 3-3(a) are the calculations of the composition trajectories using Equations (3-10) and (3-11); these calculations are performed using MathCad 15.[19] There is excellent agreement with the experimental data of Duncan and Toor;[18] this validates the assumption of constant Fick diffusivity matrix, calculated at the final equilibrated composition. In ternary composition space, the equilibration trajectories follow serpentine paths in either of the two bulbs; see Figure 3-3(b)

At any time *t*, the instantaneous fluxes may be calculated $\begin{pmatrix} N_1(t) \\ N_2(t) \end{pmatrix} = \frac{c_t}{\delta}[D]\begin{pmatrix} y_{1A}(t) - y_{1B}(t) \\ y_{2A}(t) - y_{2B}(t) \end{pmatrix}$. Figure 3-3(c) presents the calculations of the instantaneous fluxes. At time $t = 0$, there is no driving force of species 2 (nitrogen), but its flux is non-zero because of the non-zero contribution of $\frac{c_t}{\delta} D_{21}\left(y_{1A}(t=0) - y_{1B}(t=0)\right)$.

The composition of $N_2$ in Bulb A continues to decrease during the time interval $0 < t < t_1$; concomitantly, the composition of $N_2$ in Bulb B continues to increase; the diffusion of nitrogen is in an up-hill direction. The occurrence of uphill diffusion is not in violation of the second law of thermodynamics; the second law requires that the total rate of entropy produced by all diffusing species should be positive definite

$$\sigma = -\frac{1}{T}\sum_{i=1}^{n}\frac{d\mu_i}{dz}J_i \geq 0 \tag{3-12}$$

For equimolar diffusion of ideal ternary gas mixtures, equation (3-12) simplifies to

$$\sigma = -R\left[N_1\frac{1}{y_1}\frac{dy_1}{dz} + N_2\frac{1}{y_2}\frac{dy_2}{dz} + N_3\frac{1}{y_3}\frac{dy_3}{dz}\right] \geq 0 \tag{3-13}$$

For diffusion across a film thickness $\delta$, with boundary conditions $\begin{matrix}\eta = 0; & z = 0; & (y) = (y_0)\\ \eta = 1; & z = \delta; & (y) = (y_\delta)\end{matrix}$, the integral average rate of entropy production can be approximated as follows

$$\sigma = -R\int_{z=0}^{z=\delta}\left[N_1\frac{1}{y_1}\frac{dy_1}{dz} + N_2\frac{1}{y_2}\frac{dy_2}{dz} + N_3\frac{1}{y_3}\frac{dy_3}{dz}\right]dz \approx \frac{R}{\delta}\sum_{i=1}^{3}N_i\frac{1}{(y_{iA}(t)+y_{iB})/2}(y_{iA}(t)-y_{iB}(t)) \geq 0 \tag{3-14}$$

In equation (3-14), we use the arithmetic average vapor compositions $y_{i,av} = \frac{y_{i0}+y_{i\delta}}{2}$ as a good approximation. The *individual* rates of the instantaneous entropy production $\sigma_i = \frac{R}{\delta}N_i\frac{1}{(y_{iA}(t)+y_{iB})/2}(y_{iA}(t)-y_{iB}(t))$ are plotted in Figure 3-3(c). We note that the rate of entropy production by nitrogen (species 2) is negative during the time interval $0<t<t_1$. However, the second law of thermodynamics is not violated because the other two species, hydrogen and carbon dioxide produce entropy at significantly higher rates, ensuring that $\sigma \geq 0$ is satisfied during the entire time duration.

## 3.4 Two-bulb experiments of Taviera, Cruz and Mendes

Taveira et al.[20] report experimental results for transient equilibration of He(1)/$N_2$(2)/$CO_2$(3) gas mixtures, in a two-bulb diffusion cell that are similar to that used by Duncan and Toor.[18] Figure 3-4 the Taveira set-up; the two bulbs are connected by means of a 153 mm long capillary tube; i.e. the length of the diffusion path, $\delta = 0.153$ m. The temperature, $T$ = 298 K and total pressure, $p_t$ = 40 kPa. The initial compositions (mole fractions in the two bulbs, Bulb A and Bulb B, are

$$\text{Bulb A}: y_1 = 0.5; y_2 = 0.5; y_3 = 0.0$$
$$\text{Bulb B}: y_1 = 0.0; y_2 = 0.5; y_3 = 0.5$$

Since the two bulbs are sealed there is no net transfer flux out of or into the system, i.e. we have conditions corresponding to equimolar diffusion: $u = 0; \quad N_1 + N_2 + N_3 = 0; \quad N_i = J_i$.

The experimental data on the transient approach to equilibration are indicated by the symbols in Figure 3-5(a). We note that despite the fact that the driving force for nitrogen is zero, it does transfer from one bulb to the other, exhibiting over-shoot and under-shoot phenomena when approaching equilibrium. The transient equilibration trajectories of He, and $CO_2$ are "normal", with their compositions in the two bulbs approaching equilibrium in a monotonous manner.

The Maxwell-Stefan equations (3-2) allow a quantitative explanation of the experimental data. The M-S diffusivities calculated using the Fuller-Schettler-Giddings (FSG)[14] method for the three binary pairs at $T = 298$ K are

$$Đ_{12} = 17.8\times10^{-5} \quad \text{m}^2\ \text{s}^{-1}; Đ_{13} = 14.7\times10^{-5} \quad \text{m}^2\ \text{s}^{-1}; Đ_{23} = 4.1\times10^{-5} \quad \text{m}^2\ \text{s}^{-1}$$

The compositions in the two bulbs equilibrate after several hours to $y_{1,\text{eq}} = 0.25$, $y_{2,\text{eq}} = 0.5$ and $y_{3,\text{eq}} = 0.25$. At this equilibrium composition the elements of the Fick diffusivity matrix [$D$] can be calculated using Equation (3-7); the result is $[D] = \begin{bmatrix} 16.45 & -0.25 \\ -7.83 & 5.2 \end{bmatrix} \times 10^{-5}$ $\text{m}^2\ \text{s}^{-1}$. The large magnitude of $D_{21}$ indicate strong diffusional coupling for transfer of nitrogen.

If the Fick diffusivity matrix is assumed constant during the entire equilibration process, the transient equilibration trajectories are described by Equations (3-10) and (3-11);. From the details provided by Taveira et al.,[20] the value of the cell constant is calculated as $\beta = 4.38\ \text{m}^{-2}$.

The continuous solid lines in Figure 3-5(a) are the explicit calculations of the composition trajectories using Equations (3-10) and (3-11); these calculations are performed using MathCad 15.[19] There is excellent agreement with the experimental data of Taveira et al.;[20] this validates the assumption of constant Fick diffusivity matrix, calculated at the final equilibrated composition. In ternary composition space, the equilibration trajectories follow serpentine paths in either of the two bulbs; see Figure 3-5(b).

At any time *t*, the instantaneous fluxes may be calculated from $\begin{pmatrix} N_1(t) \\ N_2(t) \end{pmatrix} = \frac{c_t}{\delta}[D]\begin{pmatrix} y_{1A}(t) - y_{1B}(t) \\ y_{2A}(t) - y_{2B}(t) \end{pmatrix}$;

Figure 3-5(c) presents the calculations of the instantaneous fluxes. At time $t = 0$, there is no driving force of species 2 (nitrogen), but its flux is non-zero because of the non-zero contribution of $\frac{c_t}{\delta} D_{21}\left(y_{1A}(t=0) - y_{1B}(t=0)\right)$.

The composition of $N_2$ in Bulb A continues to increase during the time interval $0 < t < t_1$; concomitantly, the composition of $N_2$ in Bulb B continues to deccrease; the diffusion of nitrogen is in an up-hill direction. The occurrence of uphill diffusion is not in violation of the second law of thermodynamics; the second law requires that the total rate of entropy produced by all diffusing species should be positive definite. The individual rates of entropy production $\sigma_i = \frac{R}{\delta} N_i \frac{1}{\left(y_{iA}(t) + y_{iB}\right)/2}\left(y_{iA}(t) - y_{iB}(t)\right)$ are plotted in Figure 3-5(d). We note that the rate of entropy production by nitrogen (species 2) is negative during the time interval $0 < t < t_1$. However, the second law of thermodynamics is not violated because the other two species, helium and carbon-dioxide produce entropy at significantly higher rates, ensuring that $\sigma \geq 0$ is satisfied during the entire time duration.

## 3.5 Composition profiles within the capillary connecting bulbs

The analysis of the diffusion process at time $t = 0$ in the Duncan and Toor[18] and Taveira et al.[20] experiments for ternary $H_2(1)/N_2(2)/CO_2(3)$ and $He(1)/N_2(2)/CO_2(3)$ gas mixtures are of particular interest, because this situation triggers uphill diffusion of $N_2$ in both these systems. We analyze the ternary diffusion process at time $t = 0$ under the assumption of *quasi-steady state* for the compositions at either end of the capillary maintained at the initial bulb compositions. In the Duncan-Toor experiments,

the initial compositions are $\begin{matrix}\text{Bulb A}: y_1 = 0.0; y_2 = 0.5; y_3 = 0.5 \\ \text{Bulb B}: y_1 = 0.5; y_2 = 0.5; y_3 = 0.00000\end{matrix}$. In the Taveira experiments, the initial compositions are $\begin{matrix}\text{Bulb A}: y_1 = 0.5; y_2 = 0.5; y_3 = 0.0 \\ \text{Bulb B}: y_1 = 0.0; y_2 = 0.5; y_3 = 0.5\end{matrix}$.

Krishna and Standart[21] have developed exact solutions to the Maxwell-Stefan equations (3-2) for explicit evaluation of the fluxes for *steady-sta*te transfer across a film of thickness $\delta$. The Krishna-Standart solution, as applied to equimolar diffusion of ternary gas mixtures is detailed hereunder; see also the Supplementary Material accompanying the paper by Krishna.[22]

We define a dimensionless distance: $\eta = \frac{z}{\delta}$ and re-write Maxwell-Stefan equations (3-2) in two-dimensional matrix notation as follows

$$\frac{d(y)}{d\eta} = [\Phi](y) + (\phi) \tag{3-15}$$

In equation (3-15) we define a two-dimensional square matrix of dimensionless fluxes $[\Phi] = \frac{\delta}{c_t}\begin{bmatrix} \frac{N_2}{Đ_{12}} + \frac{N_1}{Đ_{13}} + \frac{N_3}{Đ_{13}} & -N_1\left(\frac{1}{Đ_{12}} - \frac{1}{Đ_{13}}\right) \\ -N_2\left(\frac{1}{Đ_{12}} - \frac{1}{Đ_{23}}\right) & \frac{N_1}{Đ_{12}} + \frac{N_2}{Đ_{23}} + \frac{N_3}{Đ_{23}} \end{bmatrix}$. We also define a column matrix of dimensionless fluxes $(\phi) = -\frac{\delta}{c_t}\begin{pmatrix} \frac{N_1}{Đ_{13}} \\ \frac{N_2}{Đ_{23}} \end{pmatrix}$. The boundary conditions are $\begin{matrix}\eta = 0; \quad z = 0; \quad (y) = (y_0) \\ \eta = 1; \quad z = \delta; \quad (y) = (y_\delta)\end{matrix}$.

For steady-state transfer across a film, the matrices $[\Phi]$ and $(\phi)$ are both $\eta$-invariant. Therefore (3-15) represents a system of coupled *ordinary* differential equations with *constant coefficients* $[\Phi]$ and $(\phi)$. The system of equations can be solved analytically to obtain the mole fraction profiles within the length of the capillary connecting the two tubes $(y_\eta - y_0) = -[\exp[\Phi]\eta - [I]][\exp[\Phi] - [I]]^{-1}(y_0 - y_\delta)$ where $[I]$ is the identity matrix with Kronecker delta $\delta_{ik}$ as elements.

The Sylvester theorem, detailed in Equation (A.5.17) of Taylor and Krishna,[1] is required for explicit calculation of $[\exp[\Phi]\eta - [I]][\exp[\Phi] - [I]]^{-1}$. For equimolar diffusion, one of the eigenvalues of $[\Phi] = \frac{\delta}{c_t}\begin{bmatrix} \frac{N_2}{Đ_{12}} + \frac{N_1}{Đ_{13}} + \frac{N_3}{Đ_{12}} & -N_1\left(\frac{1}{Đ_{12}} - \frac{1}{Đ_{13}}\right) \\ -N_2\left(\frac{1}{Đ_{12}} - \frac{1}{Đ_{23}}\right) & \frac{N_1}{Đ_{12}} + \frac{N_2}{Đ_{23}} + \frac{N_3}{Đ_{23}} \end{bmatrix}$ vanishes; see Krishna and Standart[21] for details. Explicitly, the two eigenvalues are $\lambda_1 = \left[N_1\left(\frac{1}{Đ_{12}} - \frac{1}{Đ_{23}}\right) + N_2\left(\frac{1}{Đ_{12}} - \frac{1}{Đ_{13}}\right)\right]\frac{\delta}{c_t}$ and $\lambda_2 = 0$. The application of Sylvester's theorem for evaluation of $[\Phi][\exp[\Phi] - [I]]^{-1}$ has to be done with care, because $\frac{\lambda_2}{\exp(\lambda_2) - 1}$ needs to be evaluated by use of L'Hôpital's rule: $\frac{\lambda_2}{\exp(\lambda_2) - 1} \to 1$. So,

$$[\Phi][\exp[\Phi] - [I]]^{-1} = \left(\frac{\lambda_1}{\exp(\lambda_1) - 1}\right)\frac{[\Phi]}{(\lambda_1)} - \frac{[\Phi] - \lambda_1[I]}{(\lambda_1)}$$

. The two independent fluxes can be evaluated explicitly

$$\begin{pmatrix} N_1 \\ N_2 \end{pmatrix} = -\frac{c_t}{\delta}[D_{\eta=0}]\left.\frac{d(y)}{d\eta}\right|_{\eta=0} = \frac{c_t}{\delta}[D_{\eta=0}][\Phi][\exp[\Phi] - [I]]^{-1}(y_0 - y_\delta) \tag{3-16}$$

The Fick diffusivity matrix $[D_{\eta=0}]$ is evaluated at $\eta = 0;\quad z = 0;\quad (y) = (y_0)$. The *quasi-steady-state* fluxes in the Duncan-Toor experiments are $\begin{pmatrix} N_1 \\ N_2 \end{pmatrix} = \begin{pmatrix} -17.5 \\ 8.17 \end{pmatrix};\quad N_3 = 9.35$ mmol m$^{-2}$ s$^{-1}$. The *quasi-steady-state* fluxes in the Taveira experiments are $\begin{pmatrix} N_1 \\ N_2 \end{pmatrix} = \begin{pmatrix} 8.62 \\ -3.88 \end{pmatrix};\quad N_3 = -4.74$ mmol m$^{-2}$ s$^{-1}$.

For the determination of the composition profiles, we need to evaluate $[\exp[\Phi]\eta - [I]][\exp[\Phi] - [I]]^{-1}$; by use of L'Hôpital's rule: $\left(\frac{\exp(\lambda_2\eta) - 1}{\exp(\lambda_2) - 1}\right) \to \eta$. So

$$[\exp[\Phi]\eta - [I]][\exp[\Phi] - [I]]^{-1} = \left(\frac{\exp(\lambda_1\eta) - 1}{\exp(\lambda_1) - 1}\right)\frac{[\Phi]}{(\lambda_1)} - \eta\frac{[\Phi] - \lambda_1[I]}{(\lambda_1)} \tag{3-17}$$

The composition profiles within the capillary in the Duncan-Toor and Taveira experiments are shown in Figure 3-6. In both sets of experiments, the variation of the compositions of $N_2$ is not monotonic, but shows a sharp minimum; this maximum is a direct result of uphill diffusion at $t = 0$.

## 3.6 Uphill diffusion in $He/N_2/O_2$ mixtures: Heliox therapy

In diffusion processes in lung airways, normally four gases are involved: $O_2$, $CO_2$, $N_2$, and $H_2O$; the Maxwell-Stefan equations (3-2) are commonly used to model pulmonary gas transport.[23-29] The transport of the fresh breathed-in air towards the acini of human beings with chronic obstructive bronchopneumopathy, such as asthma, is rendered difficult due to bronchoconstriction and other factors.[29-31] Such patients need some respiratory support to allow the oxygen to be transported through the proximal bronchial tree and then diffused in the distal one. One such support system consists of the inhalation of a mixture of heliox (20% $O_2$; 80% He), that facilitates the transport of oxygen, and exhalation of $CO_2$.

We now demonstrate the phenomena of uphill diffusion of $O_2$ in ternary He(1)/$N_2$(2)/$O_2$(3) mixtures. For purposes of demonstration we use the same set-up as in the Taveira experiments; see Figure 3-7. The two bulbs are connected by means of a 153 mm long capillary tube, i.e. the length of the diffusion path $\delta = 0.153$ m. The temperature, $T = 298$ K and total pressure, $p_t = 100$ kPa. The initial compositions (mole fractions in the two bulbs, Bulb A and Bulb B, are taken as $\begin{matrix}\text{Bulb A}: y_1 = 0.8\; y_2 = 0.0; y_3 = 0.2 \\ \text{Bulb B}: y_1 = 0.0; y_2 = 0.8; y_3 = 0.2\end{matrix}$. This implies that the driving forces for transfer of $O_2$ is zero at time $t = 0$. Since the two bulbs are sealed there is no net transfer flux out of or into the system, i.e. we have conditions corresponding to equimolar diffusion: $u = 0; \quad N_1 + N_2 + N_3 = 0; \quad N_i = J_i$.

Using the Fuller-Schettler-Giddings (FSG) estimation procedure,[14] the M-S diffusivities of the constituent binary pairs are $Đ_{12} = 7.1; \quad Đ_{13} = 7.45; \quad Đ_{23} = 2.08\times10^{-5}$ m$^2$ s$^{-1}$. The compositions in the

two bulbs equilibrate after several hours to $y_{1,eq} = 0.4$, $y_{2,eq} = 0.4$, and $y_{3,eq} = 0.2$. At this equilibrium composition the elements of the Fick diffusivity matrix [$D$] can be calculated using Equation (3-7); the result is $[D] = \begin{bmatrix} 7.2533 & 0.0546 \\ -2.8584 & 2.8839 \end{bmatrix} \times 10^{-5}$ m$^2$ s$^{-1}$. The large magnitude of $D_{21}$ indicate strong diffusional coupling for transfer of nitrogen.

If the Fick diffusivity matrix is assumed constant during the entire equilibration process, the transient equilibration trajectories are described by are described by Equations (3-10) and (3-11); the value of the cell constant is calculated as $\beta = 4.38$ m$^{-2}$. The continuous and dashed lines in Figure 3-8(a) are the explicit calculations of the composition trajectories using Equations (3-10) and (3-11); these calculations are performed using MathCad 15.[19] Particularly noteworthy are the transient overshoot and undershoot experienced by $O_2$ during transient equilibration. The overshoot arises because $O_2$ gets dragged uphill during the early transience; In ternary composition space, the equilibration trajectories follow serpentine paths in either of the two bulbs; see Figure 3-8(b).

At any time $t$, the instantaneous fluxes may be calculated from $\begin{pmatrix} N_1(t) \\ N_2(t) \end{pmatrix} = \frac{c_t}{\delta}[D]\begin{pmatrix} y_{1A}(t) - y_{1B}(t) \\ y_{2A}(t) - y_{2B}(t) \end{pmatrix}$; Figure 3-8(c) presents the calculations of the instantaneous fluxes. At time $t$ = 0, there is no driving force of species 3 (oxygen), but its flux is non-zero because of coupled transfers.

The occurrence of uphill $O_2$ diffusion is not in violation of the second law of thermodynamics; the second law requires that the total rate of entropy produced by all diffusing species should be positive definite. The individual rates of entropy production $\sigma_i = \frac{R}{\delta} N_i \frac{1}{(y_{iA}(t) + y_{iB})/2}(y_{iA}(t) - y_{iB}(t))$ are plotted in Figure 3-8(d). We note that the rate of entropy production by oxygen (species 2) is negative during the time interval $0 < t < t_1$. However, the second law of thermodynamics is not violated because the other two species, helium and nitrogen produce entropy at significantly higher rates, ensuring that $\sigma \geq 0$ is satisfied during the entire time duration.

An alternative way to demonstrate the phenomenon of uphill $O_2$ diffusion is to model the ternary He(1)/$N_2$(2)/$O_2$(3) mixture diffusion as inter-diffusion between two cylindrical Loschmidt tubes each of length $\delta$ as pictured in Figure 3-9. For comparison with the experimental data as reported in Figure 3 of Bres and Hatzfeld,[23] we take the tube length, $\delta = 1$ m. The initial compositions in the two compartments are $\begin{matrix} \text{bottom compartment}\,(-): -\delta \le z \le 0;; y_1 = 0.8; y_2 = 0.0; y_3 = 0.2 \\ \text{top compartment}\,(+): 0 \le z \le \delta; y_1 = 0.0; y_2 = 0.8; y_3 = 0.2 \end{matrix}$.

The final equilibrated compositions are $y_{1,eq}$ = 0.4, $y_{2,eq}$ = 0.4 and $y_{3,eq}$ = 0.2. At this equilibrium composition the elements of the Fick diffusivity matrix [$D$] can be calculated using Equation (3-7); the result is $[D] = \begin{bmatrix} 7.2533 & 0.0546 \\ -2.8584 & 2.8839 \end{bmatrix} \times 10^{-5}$ $\text{m}^2\ \text{s}^{-1}$. Coupling effects appear to be non-negligible.

Figure 3-9(a,b) show the transient equilibration of $O_2$ in the (a) top, and (b) bottom compartments at the positions $z/\delta = \pm 0.35$, and $z/\delta = \pm 0.5$, calculated using equation (3-8). The overshoot of $O_2$ composition in the bottom compartment signals uphill diffusion; this overshoot has been verified in the experimental data presented in Figure 3 of Bres and Hatzfeld.[23] The corresponding transient equilibration of $O_2$ in the top compartment tube displays undershoots. If coupling effects are ignored entirely, no oxygen transport in feasible. Put another way, the efficacy of heliox therapy relies on uphill transfer of oxygen.

In ternary composition space, the equilibration trajectories at $z/\delta = \pm 0.5$ follow serpentine trajectories as shown in Figure 3-10. The equilibration trajectories are practically indistinguishable from those determined using the two-bulb diffusion set-up; see Figure 3-8(b).

## 3.7 Uphill diffusion in He/$N_2$/$O_2$/$CO_2$ mixtures: Heliox therapy

We now demonstrate the phenomena of uphill diffusion of *both* $O_2$ and $CO_2$ in quaternary He(1)/$N_2$(2)/$O_2$(3)/$CO_2$(4) mixtures. For purposes of demonstration we use the same set-up as in the Taveira experiments; see Figure 3-11. The two bulbs are connected by means of a 153 mm long capillary tube, i.e. the length of the diffusion path $\delta = 0.153$ m. The temperature, $T$ = 298 K and total

pressure, $p_t$ = 100 kPa. The initial compositions (mole fractions in the two bulbs, Bulb A and Bulb B, are taken as $\begin{matrix}\text{Bulb A}: y_1 = 0.79; y_2 = 0.0; y_3 = 0.15; y_4 = 0.06 \\ \text{Bulb B}: y_1 = 0.0; y_2 = 0.79; y_3 = 0.15; y_4 = 0.06\end{matrix}$. This implies that the driving forces for transfer of both $O_2$ and $CO_2$ are zero at time $t = 0$. Since the two bulbs are sealed there is no net transfer flux out of or into the system, i.e. we have conditions corresponding to equimolar diffusion: $u = 0; \quad N_1 + N_2 + N_3 = 0; \quad N_i = J_i$. Using the Fuller-Schettler-Giddings (FSG) estimation procedure,[14] the M-S diffusivities of the constituent binary pairs are

$$\begin{matrix}Đ_{12} = 7.1; & Đ_{13} = 7.45; & Đ_{14} = 5.87; \\ Đ_{23} = 2.08; & Đ_{24} = 1.64; & \times 10^{-5}\ \text{m}^2\ \text{s}^{-1}. \\ Đ_{34} = 1.64; & & \end{matrix}$$

The compositions in the two bulbs equilibrate after several hours to $y_{1,eq}$ = 0.395, $y_{2,eq}$ = 0.39, $y_{3,eq}$ = 0.15, and $y_{4,eq}$ = 0.06. At this equilibrium composition the elements of the Fick diffusivity matrix [$D$] can be calculated using $[D] = [B]^{-1}$; the result is

$$\begin{bmatrix} D_{11} & D_{12} & D_{13} \\ D_{21} & D_{22} & D_{23} \\ D_{31} & D_{32} & D_{33} \end{bmatrix} = \begin{bmatrix} 6.8633 & -0.1863 & -0.2377 \\ -2.9906 & 2.5687 & -0.2391 \\ -1.1633 & -0.0989 & 2.757 \end{bmatrix} \times 10^{-5} \quad \text{m}^2\ \text{s}^{-1}.$$

If the Fick diffusivity matrix is assumed constant during the entire equilibration process, the transient equilibration trajectories, written in 3-dimensional matrix form, are

$$\begin{pmatrix} y_1(t) - y_{1,eq} \\ y_2(t) - y_{2,eq} \\ y_3(t) - y_{3,eq} \end{pmatrix} = \exp\left[ -\beta \begin{bmatrix} D_{11} & D_{12} & D_{13} \\ D_{21} & D_{22} & D_{23} \\ D_{31} & D_{32} & D_{33} \end{bmatrix} t \right] \begin{pmatrix} y_{10} - y_{1,eq} \\ y_{20} - y_{2,eq} \\ y_{30} - y_{3,eq} \end{pmatrix} = [Q] \begin{pmatrix} y_{10} - y_{1,eq} \\ y_{20} - y_{2,eq} \\ y_{30} - y_{3,eq} \end{pmatrix} \tag{3-18}$$

where $\beta = 4.38\ \text{m}^{-2}$ is the cell constant. The Sylvester theorem, detailed in Appendix A of Taylor and Krishna,[1] is required for explicit calculation of the 3×3 square matrix $[Q] = \exp\left[ -\beta \begin{bmatrix} D_{11} & D_{12} & D_{13} \\ D_{21} & D_{22} & D_{23} \\ D_{31} & D_{32} & D_{33} \end{bmatrix} t \right]$.

For the case of distinct eigenvalues, $\lambda_1$, $\lambda_2$, and $\lambda_3$ of the 3-dimensional square matrix $[D]$, the Sylvester theorem yields

$$[Q]=\exp[-\beta\lambda_1 t]\frac{[[\Phi]-\lambda_2[I]]}{(\lambda_1-\lambda_2)}\frac{[[\Phi]-\lambda_3[I]]}{(\lambda_1-\lambda_3)}++\exp[-\beta\lambda_2 t]\frac{[[\Phi]-\lambda_1[I]]}{(\lambda_2-\lambda_1)}\frac{[[\Phi]-\lambda_3[I]]}{(\lambda_2-\lambda_3)}+$$
$$+\exp[-\beta\lambda_3 t]\frac{[[\Phi]-\lambda_1[I]]}{(\lambda_3-\lambda_1)}\frac{[[\Phi]-\lambda_2[I]]}{(\lambda_3-\lambda_1)} \tag{3-19}$$

where $[I]$ is the identity matrix with elements $\delta_{ik}$.

Figure 3-12(a,b) presents the composition trajectories in Bulb A, and Bulb B during transient approach to equilibrium in the two-bulb diffusion apparatus for He(1)/$N_2$(2)/$O_2$(3)/$CO_2$(4) mixtures. We note that both $O_2$ and $CO_2$ exhibit overshoots and undershoots during transient equilibration; uphill diffusion manifest during the time interval $0<t<t_1$. On the other hand, the equilibration trajectories of He and $N_2$ are both monotonous.

Figure 3-13(a,b) present calculations of the instantaneous fluxes $\begin{pmatrix}N_1(t)\\N_2(t)\\N_3(t)\end{pmatrix}=\frac{c_t}{\delta}\begin{bmatrix}D_{11}&D_{12}&D_{13}\\D_{21}&D_{22}&D_{23}\\D_{31}&D_{32}&D_{33}\end{bmatrix}\begin{pmatrix}y_{1A}(t)-y_{1B}(t)\\y_{2A}(t)-y_{2B}(t)\\y_{3A}(t)-y_{3B}(t)\end{pmatrix}$ during transient approach to equilibrium in the two-bulb diffusion apparatus for He(1)/$N_2$(2)/$O_2$(3)/$CO_2$(4) mixtures. During the time interval $0<t<t_1$, the fluxes of both $O_2$ and $CO_2$ are negative, signaling the phenomena of uphill diffusion. Uphill diffusion contributes significantly to inhalation/exhalation of $O_2$ and $CO_2$ for patients with breathing difficulties.

Figure 3-14 (a,b) show calculations of the individual rates of entropy production $\sigma_i=\frac{R}{\delta}N_i\frac{1}{(y_{iA}(t)+y_{iB})/2}(y_{iA}(t)-y_{iB}(t))$. During the time interval $0<t<t_1$, both $O_2$ and $CO_2$ consume entropy, i.e. $\sigma_3\le 0;\sigma_4\le 0$. The other two components produce entropy at a such a high rate as to prevent the violation of the second law requirement $\sigma=\sigma_1+\sigma_2+\sigma_3+\sigma_4\ge 0$.

Replacing Helium with either Argon or $SF_6$, leads to equilibration trajectories for which the phenomena of uphill diffusion is imperceptibly small. This is evidenced in Figure 3-15 (a,b)that present comparisons of the composition trajectories of (a) $O_2$, and (b) $CO_2$ in Bulb A for transient equilibration of He(1)/$N_2$(2)/$O_2$(3)/$CO_2$(4), Ar(1)/$N_2$(2)/$O_2$(3)/$CO_2$(4), and $SF_6$(1)/$N_2$(2)/$O_2$(3)/$CO_2$(4) mixtures. This

leads us to conclude that the uphill diffusion phenomena is engendered by large differences in the binary pair M-S diffusivities.

## 3.8 List of Figures for Diffusion in Ideal Gas Mixtures

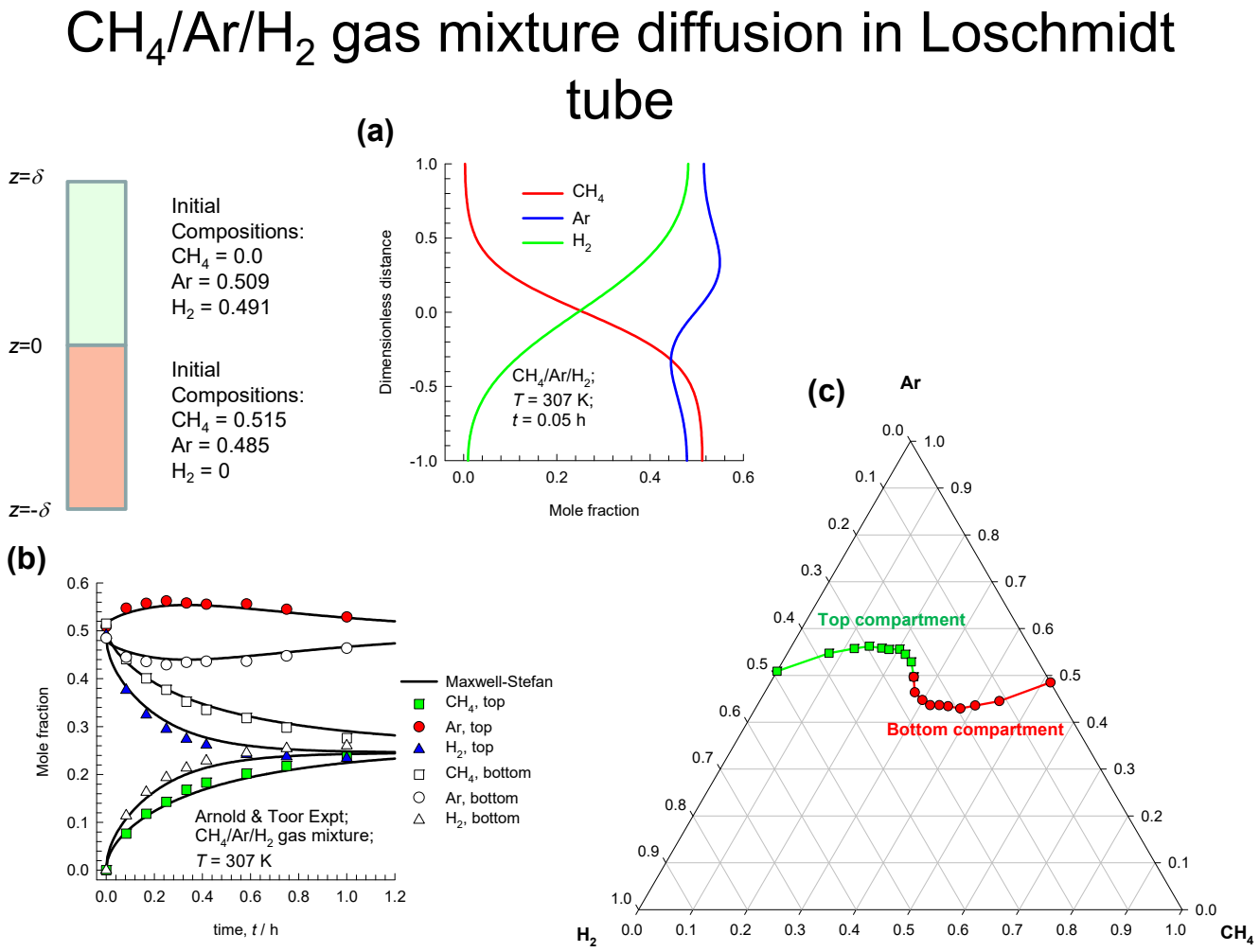


Figure 3-1. (a, b) The Loschmidt tube experiment of Arnold and Toor[16] on the transient approach to equilibrium for $CH_4(1)/Ar(2)/H_2(3)$ gas mixtures. The plotted data (symbols) are spatially averaged compositions in the top and bottom compartments. The continuous solid lines are the model calculations as presented in Example 5.5.1 of Taylor and Krishna.[1] (c) The equilibration trajectories plotted in ternary composition space.

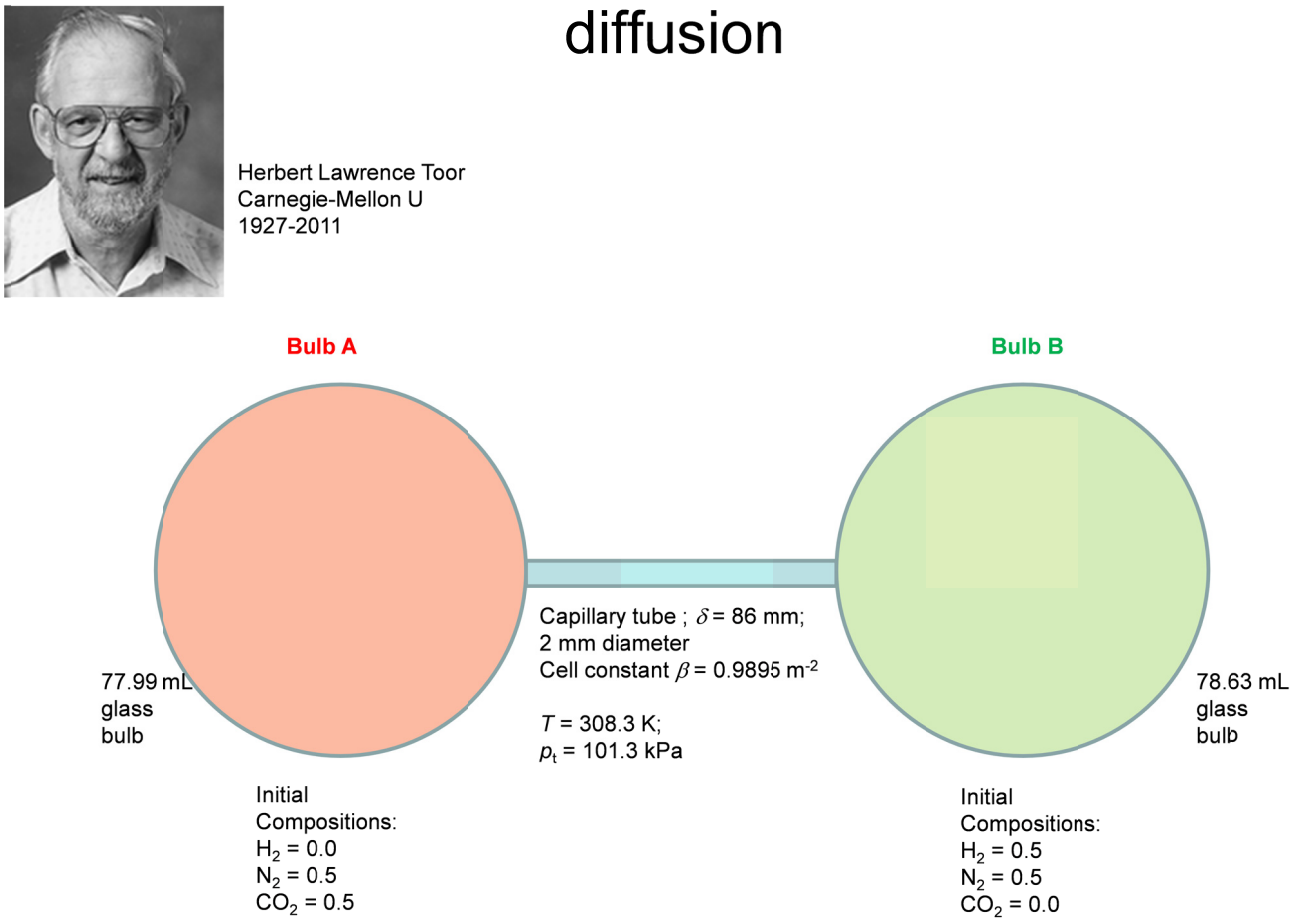


Figure 3-2. The two-bulb diffusion experimental set-up of Duncan and Toor[18] for $H_2(1)/N_2(2)/CO_2(3)$ gas mixture.

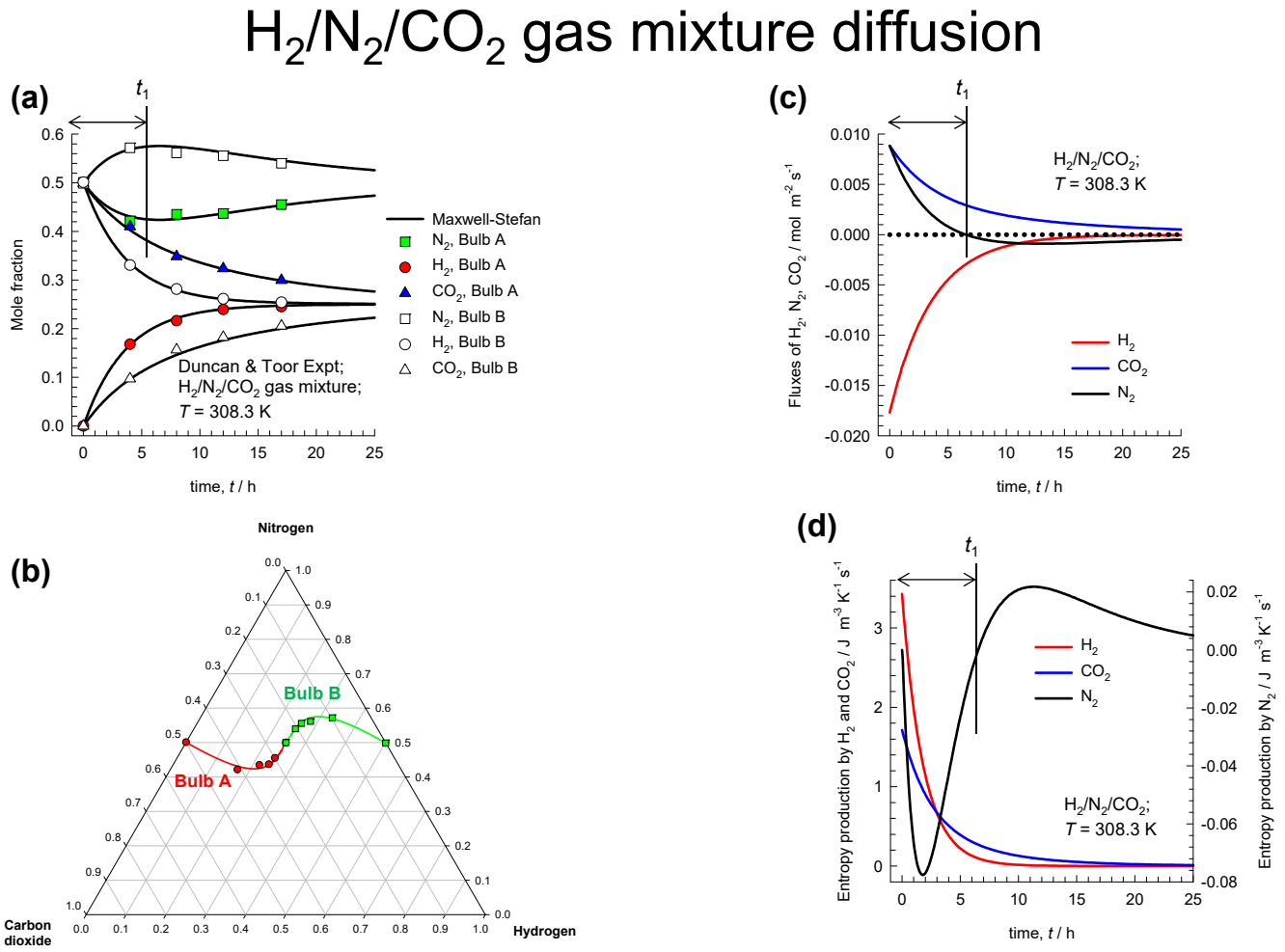


Figure 3-3. (a) Experimental data of Duncan and Toor[18] on the transient approach to equilibrium in the two-bulb diffusion experiments for $H_2(1)/N_2(2)/CO_2(3)$ mixtures. The continuous solid lines are the transient equilibration trajectories calculated using the Maxwell-Stefan equations, as presented in Example 5.4.1 of Taylor and Krishna.[1] (b) The equilibration trajectories plotted in ternary composition space. (c) Calculations of the instantaneous fluxes of the three components as a function of time. (d) Calculations of the individual rates of entropy production of the three species.

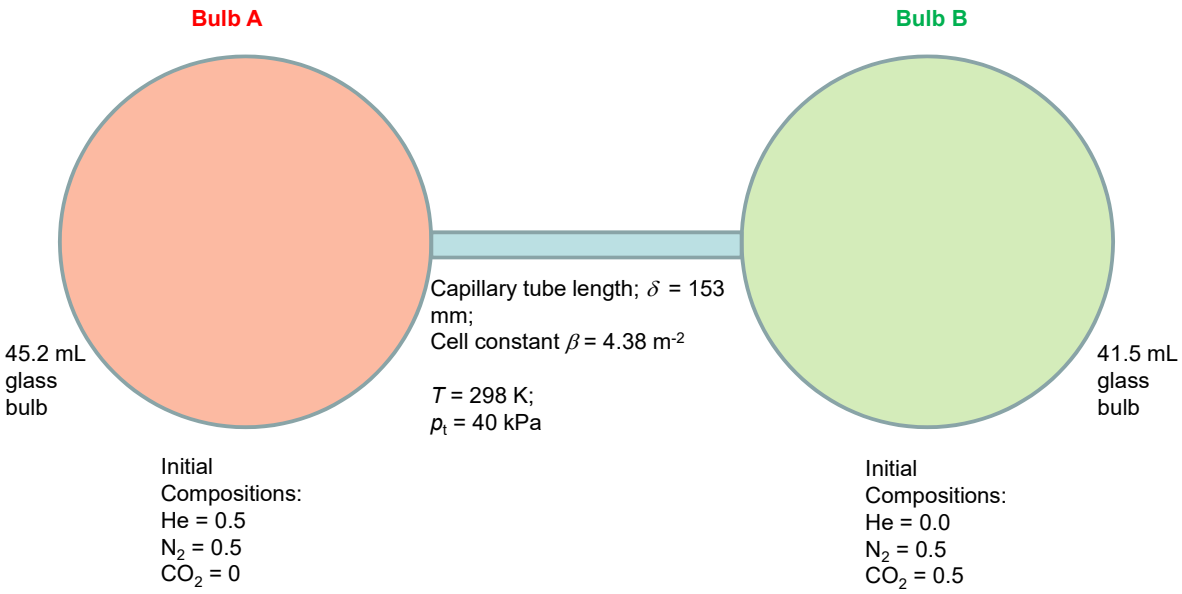


Figure 3-4. The two-bulb diffusion experimental set-up of Taveira et al.[20] with He(1)/$N_2$(2)/$CO_2$(3) gas mixtures.

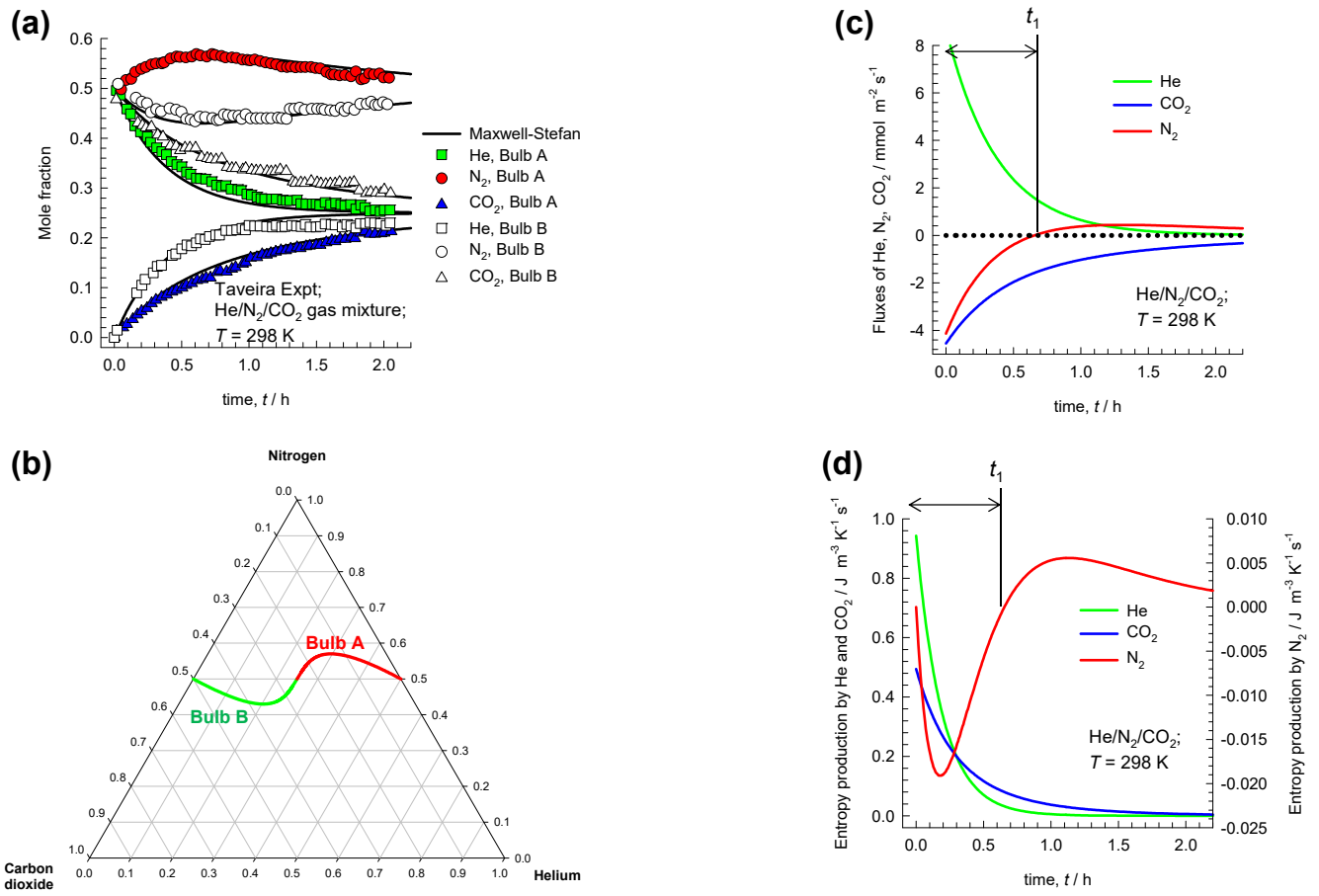


Figure 3-5. (a) Experimental data of Taveira et al.[20] on the transient approach to equilibrium in the two-bulb diffusion experiments for He(1)/$N_2$(2)/$CO_2$(3) mixtures. The continuous solid lines are the transient equilibration trajectories calculated using the Maxwell-Stefan equations. (b) The equilibration trajectories plotted in ternary composition space. (c) Calculations of the instantaneous fluxes of the three components as a function of time. (d) Calculations of the individual rates of entropy production of the three species as a function of time.

# Composition profiles within the capillary

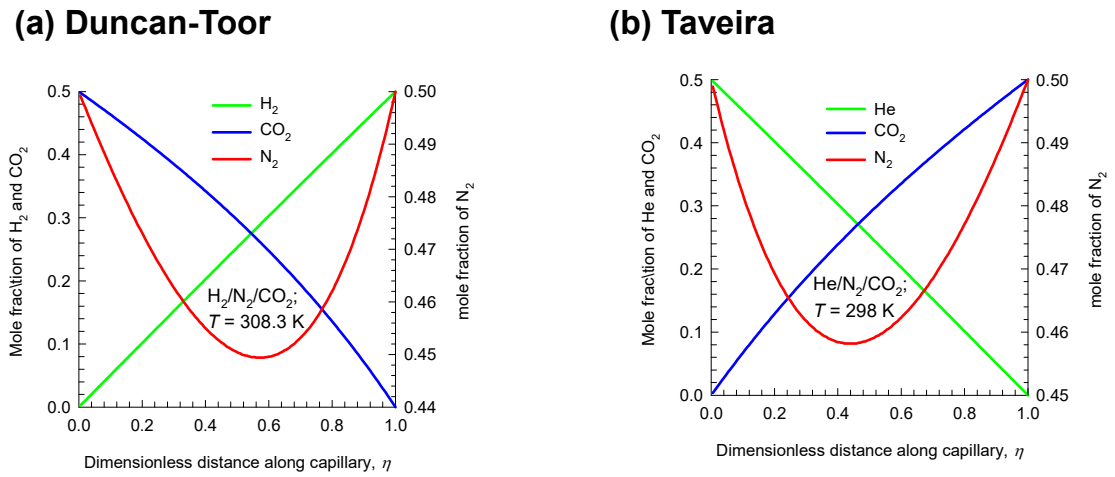


Figure 3-6. Quasi-steady compositions profiles within the capillary connecting the two bulbs in the experiments of (a) Duncan and Toor[18] on the transient approach to equilibrium in the two-bulb diffusion experiments for $H_2(1)/N_2(2)/CO_2(3)$ mixtures, and (b) Taveira et al.[20] on the transient approach to equilibrium in the two-bulb diffusion experiments for $He(1)/N_2(2)/CO_2(3)$ mixtures.

# $He/N_2/O_2$ gas mixture diffusion: Heliox therapy

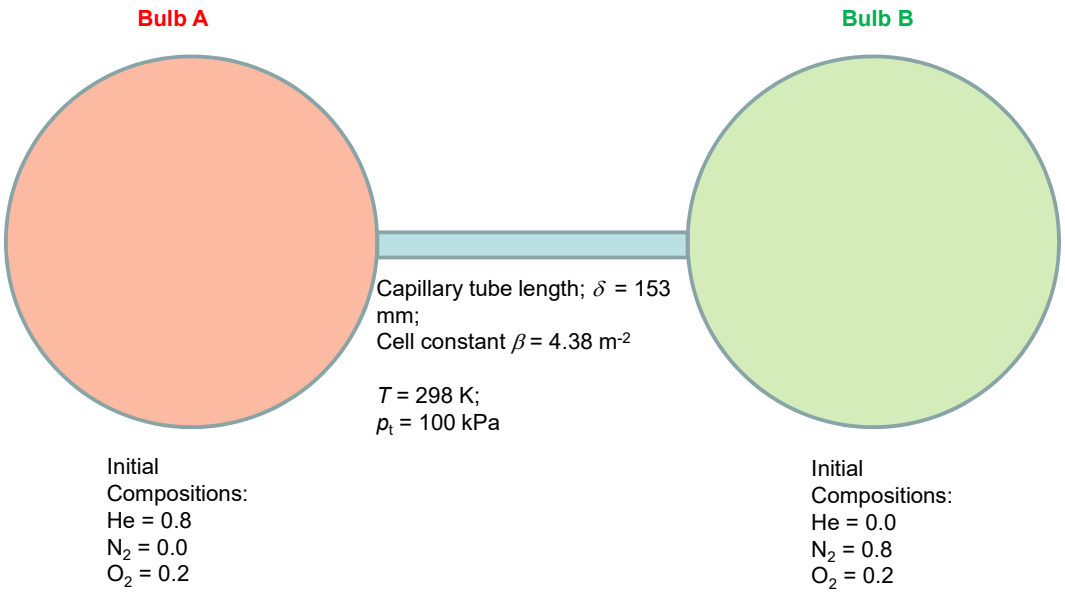


Figure 3-7. The two-bulb diffusion set-up for $He(1)/N_2(2)/O_2(3)$ mixtures.

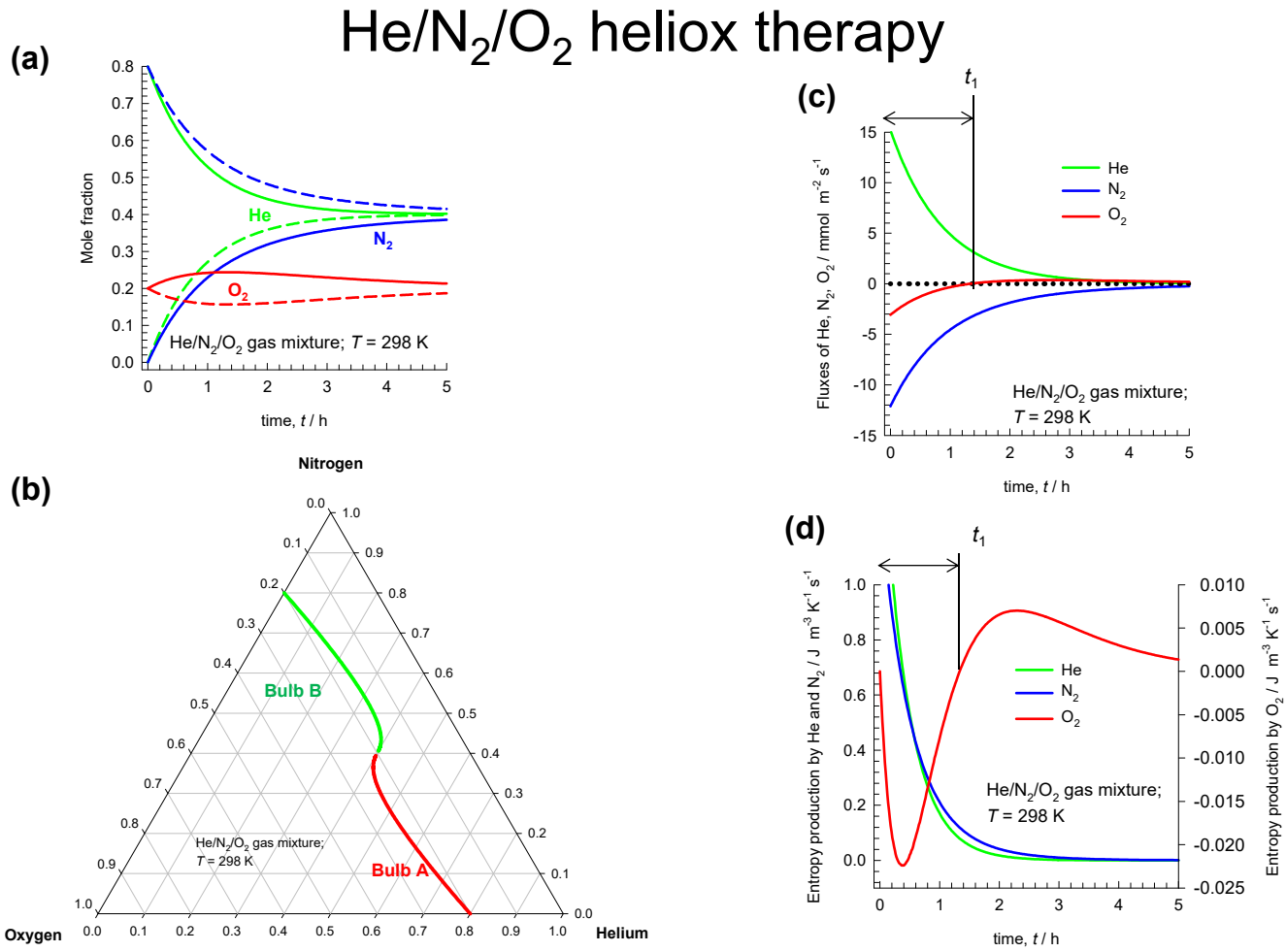


Figure 3-8. (a) Transient approach to equilibrium for He(1)/$N_2$(2)/$O_2$(3) mixtures in the two-bulb diffusion set-up, calculated using the Maxwell-Stefan equations. (b) The equilibration trajectories plotted in ternary composition space. (c) Calculations of the instantaneous fluxes of the three components. (d) Calculations of the individual rates of entropy production of the three species.

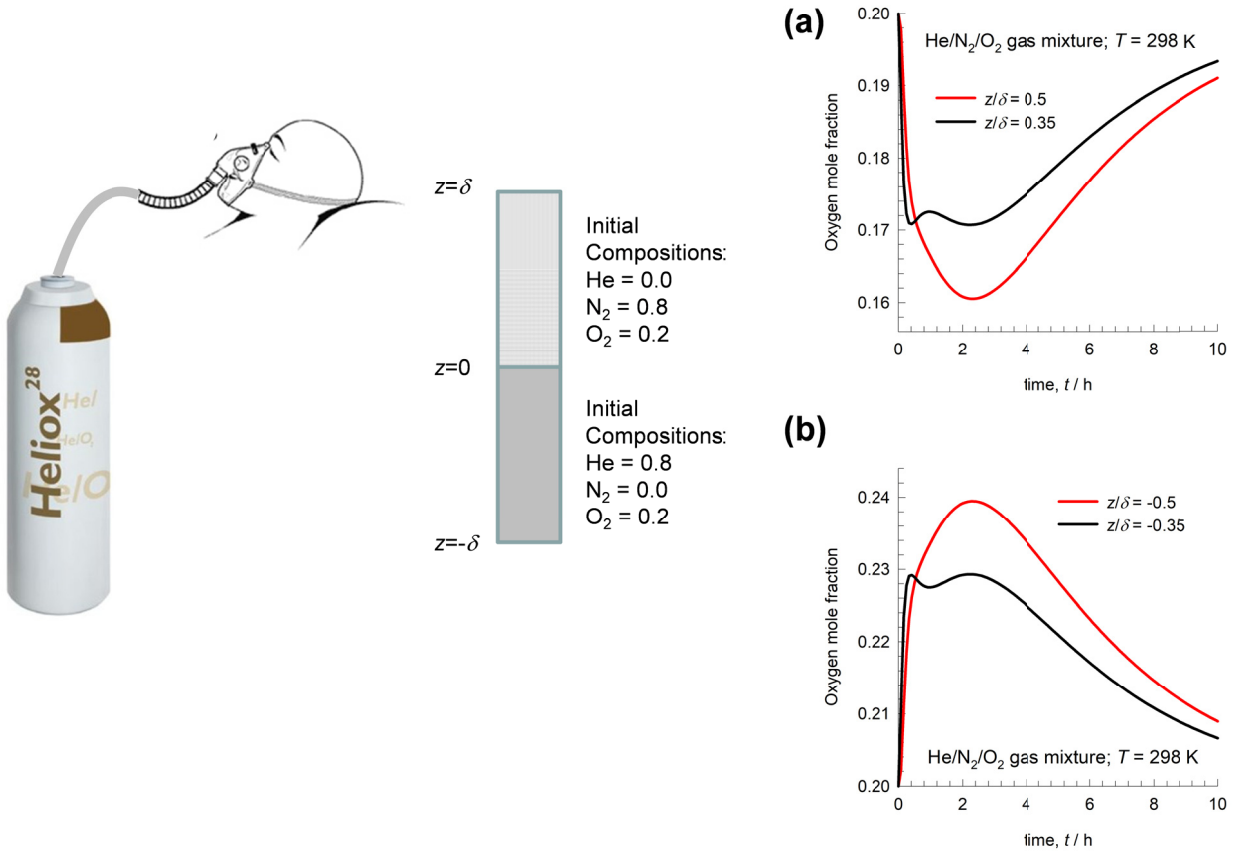


Figure 3-9. Heliox therapy modeled as inter-diffusion of He(1)/$N_2$(2)/$O_2$(3) mixtures between two cylindrical Loschmidt tubes. (a, b) The transient equilibration trajectories $O_2$ in the (a) top, and (b) bottom compartments at the positions $z/\delta = \pm 0.35$, and $z/\delta = \pm 0.5$.

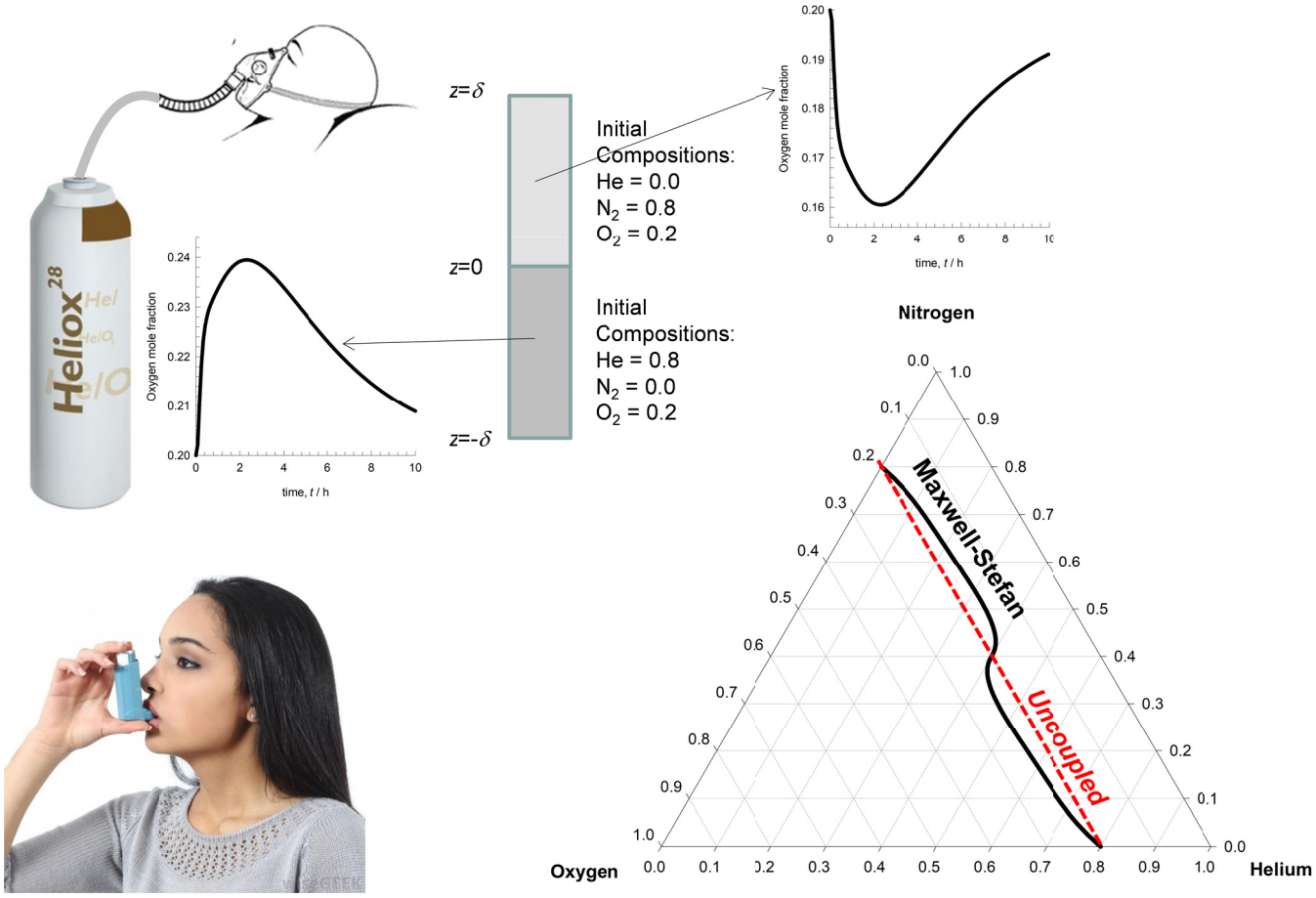


Figure 3-10. Heliox therapy modeled as inter-diffusion of He(1)/$N_2$(2)/$O_2$(3) mixtures between two cylindrical Loschmidt tubes. The transient equilibration trajectories at $z/\delta = \pm 0.5$ in the top and bottom compartments, are shown in ternary composition space.

# $He/N_2/O_2/CO_2$ gas mixture diffusion: Heliox therapy

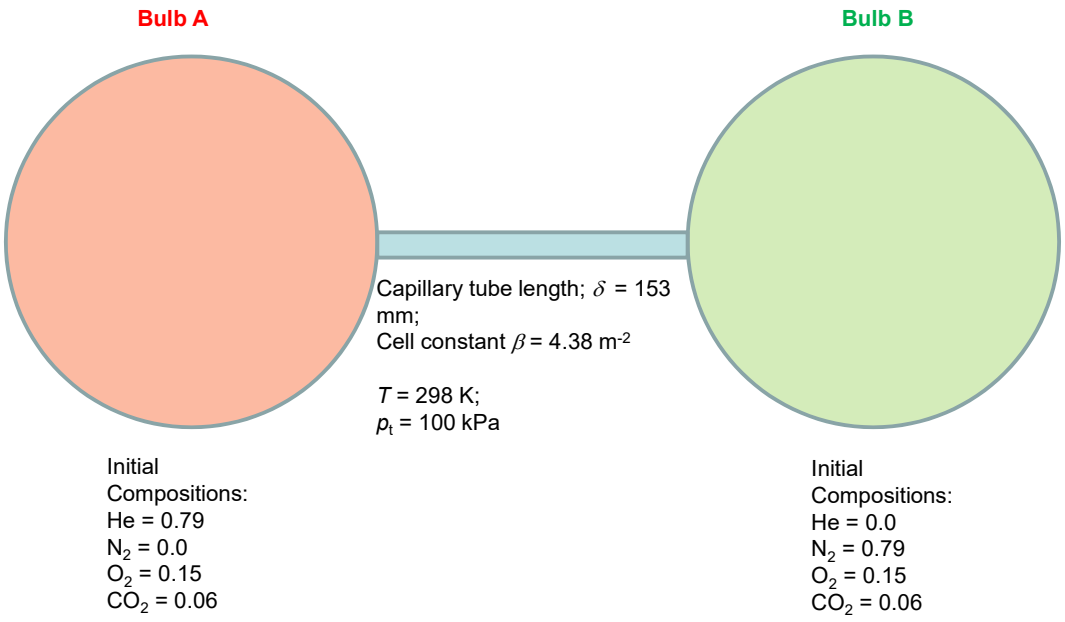


Figure 3-11. The two-bulb diffusion set-up for $He(1)/N_2(2)/O_2(3)/CO_2(4)$ mixtures.

# $He/N_2/O_2/CO_2$ gas mixture diffusion

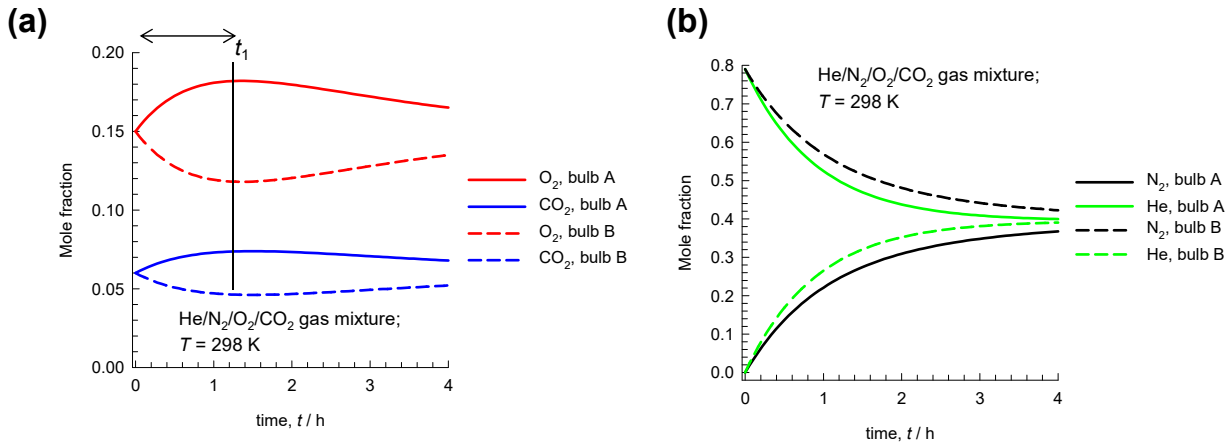


Figure 3-12. Composition trajectories in Bulb A, and Bulb B during transient approach to equilibrium in the two-bulb diffusion apparatus for $He(1)/N_2(2)/O_2(3)/CO_2(4)$ mixtures.

# $He/N_2/O_2/CO_2$ gas mixture diffusion

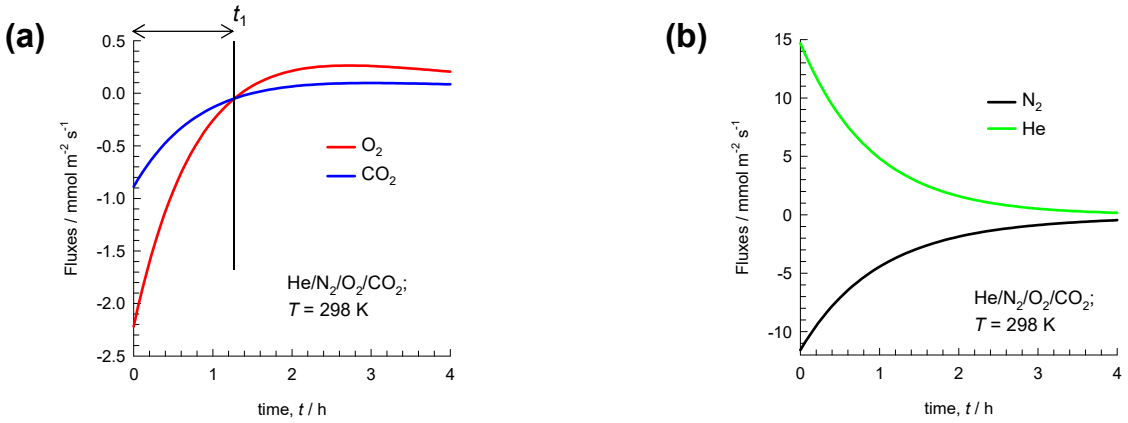


Figure 3-13.Instantaneous fluxes during transient approach to equilibrium in the two-bulb diffusion apparatus for He(1)/$N_2$(2)/$O_2$(3)/$CO_2$(4) mixtures.

# $He/N_2/O_2/CO_2$ gas mixture diffusion

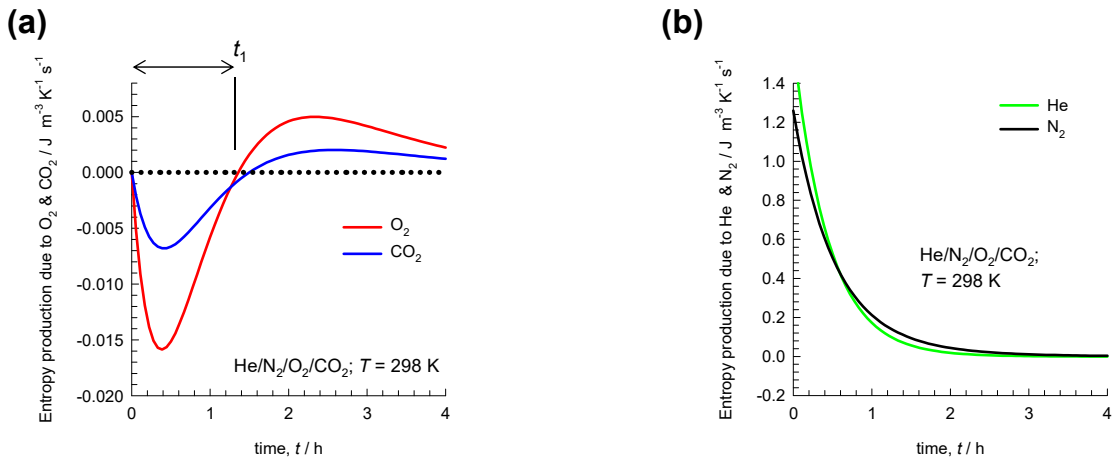


Figure 3-14. The individual rates of entropy production during transient approach to equilibrium in the two-bulb diffusion apparatus for $He(1)/N_2(2)/O_2(3)/CO_2(4)$ mixtures.

# Inert/$N_2$/$O_2$/$CO_2$ gas mixture diffusion

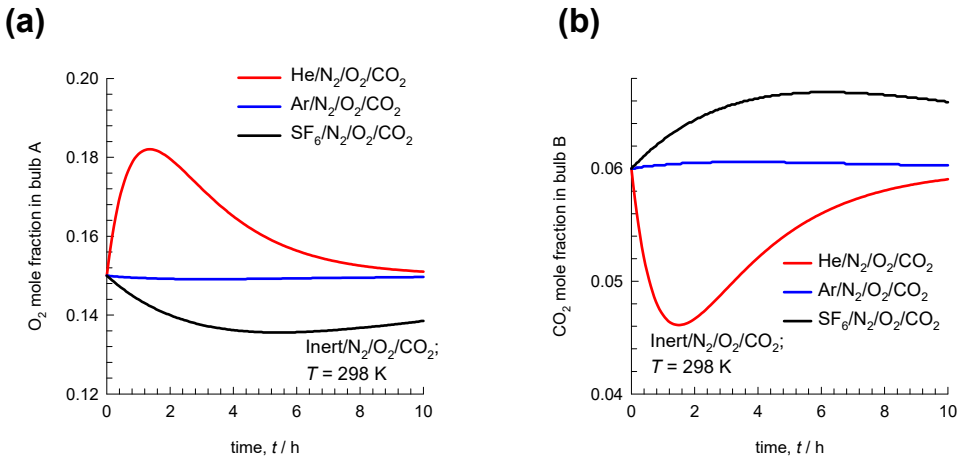


Figure 3-15. Comparison of the composition trajectories of (a) $O_2$, and (b) $CO_2$ in Bulb A for transient equilibration of He(1)/$N_2$(2)/$O_2$(3)/$CO_2$(4), Ar(1)/$N_2$(2)/$O_2$(3)/$CO_2$(4), and $SF_6$(1)/$N_2$(2)/$O_2$(3)/$CO_2$(4) mixtures.

# 4 Multicomponent Distillation

## 4.1 Murphree point efficiencies

Design and simulation procedures for distillation are commonly based on the equilibrium stage model, developed by Sorel more than a hundred years ago.[32] Departures from thermodynamic equilibrium between the vapor and liquid phases on a distillation tray are commonly accounted for by introducing the component Murphree point efficiencies

$$E_i = \frac{y_{iE} - y_{iL}}{y_{iE} - y_{i,eq}} = 1 - \frac{y_{iL} - y_{i,eq}}{y_{iE} - y_{i,eq}} = 1 - \frac{\Delta y_{iL}}{\Delta y_{iE}}; \quad i = 1,2,...n \tag{4-1}$$

where $y_{iE}$, and $y_{iL}$ are, respectively, the vapor phase mole fractions, entering and leaving a tray, and $y_{i,eq}$ is the vapor composition in thermodynamic equilibrium with the liquid leaving the tray. See schematic in Figure 4-1. For a tray in thermodynamic equilibrium, the component efficiencies are 100% for each component. Mass transfer resistances on either side of the vapor/liquid interface reduce the component efficiencies to values below 100%. For binary distillation, the Murphree component efficiencies are bounded, i.e. $0 \le E_{1,} = E_2 \le 1$. For multicomponent distillation, with the number of species $n \ge 3$, coupled diffusion effects in either vapor or liquid phases cause the component efficiencies to be distinctly different from one another, $E_1 \ne E_2 \ne E_3$. Phenomena such as osmotic diffusion, diffusion barrier, and uphill diffusion lead to component efficiencies that are unbounded ( $E_i \to \pm\infty$), zero ( $E_i = 0$ ), or negative ( $E_i < 0$ ); this has been demonstrated in several experimental and theoretical studies.[33-41] The values of the component Murphree efficiencies influence the composition profiles along the height of distillation columns.

Levy et al.[42] have put forward the following two "rules" regarding that are applicable to continuous azeotropic distillation columns operating with each stage in thermodynamic equilibrium:

- Rule 1: If the simple distillation boundary is perfectly linear, then the steady-state composition profile in a continuous distillation column cannot cross the boundary from either side.
- Rule 2: If the simple distillation boundary is curved, then the steady-state composition profile in a continuous distillation column cannot cross the boundary from the concave side but may cross the boundary from the convex side when moving from the product compositions inward.

Consider, for example, the system water/methanol/2-propanol; the residue curve maps for this system are shown in Figure 4-2(a). A straight-line distillation boundary connects the binary water/2-propanol azeotrope with pure methanol and divides the composition space into two regions. According to Rule 1, the column composition trajectories cannot cross this straight line distillation boundary, whichever side the feed is located. For either of the two feed locations, F1 and F2 in Figure 4-2(a)m boundary crossing is forbidden.

For the system acetone/chloroform/methanol we have three binary and one ternary azeotrope dividing the composition space into four regions by means of four distillation boundaries, that are all curved; see the residue curve map shown in Figure 4-2(b). According to Rule 2, the column trajectory obtained for operation with the feed located on the concave side of a boundary, with say composition indicated by F1 is able to cross that boundary. This has been demonstrated experimentally by Li et al.[43] Conversely, if the feed is located on the convex side, with say composition indicated by F2 the boundary cannot be crossed.[42]

In a series of papers, Springer et al. [35, 37, 39, 40] have reported a set of experiments in a bubble-cap tray column operating at total reflux for homogeneous azeotropic distillation using mixtures: water/ethanol/acetone, water/ethanol/methanol, water/ethanol/methylacetate, water/ethanol/methanol/acetone to demonstrate that the Levy rules are violated. The experimental set-up used by Springer can be viewed at: http://krishna.amsterchem.com/distillation/. A schematic of the experimental set-up is shown in Figure 4-3. The set-up consists of a 12-stage distillation column wherein all the experiments were conducted under total-reflux conditions at 101.3 kPa. The condenser

is a total condenser, and is considered to be stage 1. The numbering of the stages is downwards, and the Stage 12 is the partial reboiler. Stages 2, to 11 are bubble-cap trays.

For rationalization and quantitative description of the observed experimental boundary crossing phenomena, Springer et al.[35, 37, 39, 40] used rigorous non-equilibrium (NEQ) stage-wise contacting model, as implemented in ChemSep.[32, 44] The NEQ model uses the Maxwell-Stefan formulation for diffusion in the vapor and the two liquid phases. The important conclusion reached in their work is that boundary crossing effects are primarily attributable to diffusional coupling effects, that cause the component Murphree efficiencies to be unequal to one another. Unequal component efficiencies cause column composition trajectories to deviate from those of the residue curve maps. Put another way, the NEQ model does not follow the tramline guides of the RCM.

Our earlier detailed analysis of the Springer experiments show that the interphase mass transfer process is dominated by molecular diffusion in the gaseous mixture inside the dispersed bubbles on the tray.[45] For demonstrating the phenomenon of (a) uphill diffusion and (b) boundary crossing, we adopt the Geddes model for transient equilibration of vapor bubbles rising through the liquid on a tray.[46]

## 4.2 Geddes model for transient equilibration inside vapor bubble

For a ternary mixture, the diffusion, in either the dispersed vapor bubbles or in the continuous liquid phase surrounding the bubbles, is described by the generalized Fick's law $(J) = -c_t [D] \frac{d(x)}{dz}$ in which the two-dimensional matrix of Fick diffusivities [$D$] is a product of two matrices $[D] = [\Lambda][\Gamma]$. The vapor phase can often be considered to thermodynamically ideal; in this event, the matrix of thermodynamic factor degenerates to the identity matrix $\Gamma_{ij} = \delta_{ij}; \quad i, j = 1,2$. The matrix $[\Lambda]$ to be expressed explicitly in terms of the M-S diffusivities of the constituent binary pairs in the ternary mixture: $\begin{bmatrix} \Lambda_{11} & \Lambda_{12} \\ \Lambda_{21} & \Lambda_{22} \end{bmatrix} = \frac{\begin{bmatrix} Đ_{13}\left(x_1 Đ_{23} + (1-x_1) Đ_{12}\right) & x_1 Đ_{23}\left(Đ_{13} - Đ_{12}\right) \\ x_2 Đ_{13}\left(Đ_{23} - Đ_{12}\right) & Đ_{23}\left(x_2 Đ_{13} + (1-x_2) Đ_{12}\right) \end{bmatrix}}{x_1 Đ_{23} + x_2 Đ_{13} + x_3 Đ_{12}}$.

Let us consider the dispersion to consist of uniform and rigid vapor bubbles of diameter, $d_{bubble}$. The transient equilibration process within a rigid spherical bubble is described by Geddes model that was originally developed for describing binary diffusion inside vapor bubbles on distillation trays.[46] For ternary mixtures, the Geddes model can be written in two-dimensional matrix equation[1, 47]

$$\left(y - y_{eq}\right) = [Q]\left(y_0 - y_{eq}\right); \quad [Q] \equiv \frac{6}{\pi^2}\sum_{m=1}^{\infty}\frac{1}{m^2}\exp\left[-m^2\pi^2\frac{4[D]t}{d_{bubble}^2}\right] \tag{4-2}$$

In equation (4-2), $\left(y_0\right)$ denotes the vapor composition entering the tray. The Sylvester theorem, detailed in Appendix A of Taylor and Krishna,[1] is required for explicit calculation of the composition trajectories described by the Geddes model. For the case of two distinct eigenvalues, $\lambda_1$, $\lambda_2$ of the 2-dimensional square matrix $[D]$, the Sylvester theorem yields

$$[Q] = f(\lambda_1)\frac{[[D]-\lambda_2[I]]}{(\lambda_1-\lambda_2)} + f(\lambda_2)\frac{[[D]-\lambda_1[I]]}{(\lambda_2-\lambda_1)} \tag{4-3}$$

In equation (4-3), $[I]$ is the identity matrix with elements $\delta_{ik}$. The functions $f(\lambda_i)$ are calculated from

$$f(\lambda_i) = \frac{6}{\pi^2}\sum_{m=1}^{\infty}\frac{1}{m^2}\exp\left[-m^2\pi^2\frac{4\lambda_i t}{d_{bubble}^2}\right] \tag{4-4}$$

For diffusion in quaternary mixtures, the Fick diffusivity matrix is 3-dimensional. For the case of three distinct eigenvalues, $\lambda_1$, $\lambda_2$, and $\lambda_3$ of the 3-dimensional square matrix $[D]$, the Sylvester theorem yields

$$[Q] = \frac{f(\lambda_1)[[D]-\lambda_2[I]][[D]-\lambda_3[I]]}{(\lambda_1-\lambda_2)(\lambda_1-\lambda_3)} + \frac{f(\lambda_2)[[D]-\lambda_1[I]][[D]-\lambda_3[I]]}{(\lambda_2-\lambda_1)(\lambda_2-\lambda_3)} + \frac{f(\lambda_3)[[D]-\lambda_1[I]][[D]-\lambda_2[I]]}{(\lambda_3-\lambda_1)(\lambda_3-\lambda_2)} \tag{4-5}$$

For vapor bubbles rising on a sieve or bubble-cap tray, the effective contact time of the dispersed phase bubbles with the surrounding continuous phase is $t = h_f / V_{bubble}$, where $h_f$ is the froth dispersion

height, and $V_{bubble}$ is the bubble rise velocity. The fractional approaches to equilibrium for contact time *t*, also termed as the Murphree efficiencies,[48-50] are calculated from

$$E_i = \frac{y_{i0} - y_{iL}}{y_{i0} - y_{i,eq}}; \quad i = 1,2,..n \tag{4-6}$$

We now apply the Geddes model to rationalize the boundary crossing effects for water(1)/ethanol(2)/acetone(3), water(1)/ethanol(2)/methanol(3), and water(1)/ethanol(2)/methylacetate(3), and water(1)/ethanol(2)/methanol(3)/acetone(4) mixtures.

## 4.3 Boundary crossing in water/ethanol/acetone mixture

As an example of boundary crossing in homogeneous azeotropic distillation, we present the experimental results for Run T2-26 for water(1)/ethanol(2)/acetone(3) mixture in Figure 4-4. In Run T2-26, the condenser composition is left of the distillation boundary. Therefore, the residue curves dictate that the reboiler composition should be in the top left corner, rich in ethanol. The measured compositions along the column operating at total reflux shows that the reboiler composition is towards the right of the distillation boundary, and is rich in water. Boundary crossing occurs at stage 2, just below the total condenser.

For Run T2-26, the values of $\Delta y_{2E} = \left(y_{2E} - y_{2,eq}\right)$ are plotted in Figure 4-5(a). We note that the ethanol driving force $\Delta y_{2E} = \left(y_{2E} - y_{2,eq}\right) > 0$ for Stages 2 – 9, $\Delta y_{2E} = \left(y_{2E} - y_{2,eq}\right) \approx 0$ for Stage 10, and $\Delta y_{2E} = \left(y_{2E} - y_{2,eq}\right) < 0$ for Stage 11. The values of the Murphree efficiency $E_2$ for ethanol is negative on Stage 10; on Stage 11, $E_2 > 1$; see in Figure 4-5(b). This implies reverse or uphill diffusion on stages 10 and 11; the transfer of ethanol is dictated by the driving forces of the other two components $\Delta y_{1E} = \left(y_{1E} - y_{1,eq}\right)$, and $\Delta y_{3E} = \left(y_{3E} - y_{3,eq}\right)$, that are both finite.[35]

We shall demonstrate below that the boundary crossing is primarily due to the factor that the Murphree efficiency of water is higher than that of ethanol, i.e. $E_1 > E_2$.

To rationalize and quantify the phenomena of boundary crossing, consider a specific tray for which the composition of the vapor entering is $y_{10} = 0.075$, $y_{20} = 0.5$, and $y_{30} = 0.425$. This composition is right of the distillation boundary. For total reflux operations, the compositions of the liquid leaving that stage will be equal to that of the vapor entering the stage, i.e. $x_1 = 0.075$, $x_2 = 0.5$, and $x_3 = 0.425$. The composition of vapor in equilibrium with the liquid leaving the tray can be determined using the NRTL parameters provided in Table 4-1. The bubble point temperature is 336.6 K and the equilibrium composition is $y_{1,eq} = 0.04869$, $y_{2,eq} = 0.29898$, and $y_{3,eq} = 0.65233$. The equilibrium composition is also right of the distillation boundary, as is to be expected. The driving forces are $\Delta y_1 = y_{10} - y_{1,eq} = 0.02631$, and $\Delta y_2 = y_{20} - y_{2,eq} = 0.20102$. Both driving forces are positive, i.e. directed from vapor to the liquid phase.

The values of the vapor phase M-S diffusivities of the binary pairs, calculated using the Fuller-Schettler-Giddings (FSG)[14] method, are $Đ_{12} = 1.98$; $Đ_{13} = 1.72$; $Đ_{23} = 0.856 \times 10^{-5}$ $m^2 s^{-1}$. These diffusivities are independent of composition. The differences in the binary pair diffusivities cannot be ignored, as we demonstrate below. At the average composition between the entering compositions and the equilibrated compositions, use of the Fick diffusivity matrix $[D] = \dfrac{\begin{bmatrix} Đ_{13}\left(x_1 Đ_{23} + (1-x_1)Đ_{12}\right) & x_1 Đ_{23}\left(Đ_{13} - Đ_{12}\right) \\ x_2 Đ_{13}\left(Đ_{23} - Đ_{12}\right) & Đ_{23}\left(x_2 Đ_{13} + (1-x_2)Đ_{12}\right) \end{bmatrix}}{x_1 Đ_{23} + x_2 Đ_{13} + x_3 Đ_{12}}$ results in $[D] = \begin{bmatrix} 1.82109 & -0.00765 \\ -0.42848 & 0.88913 \end{bmatrix} \times 10^{-5}$ $m^2\ s^{-1}$ in which the $D_{21}$ is seen to non-negligible in comparison with $D_{22}$. We can also determine a "magnitude" of the Fick diffusivity for use in the calculation of the Fourier number: $|D|^{1/2} = 1.27 \times 10^{-5}$ $m^2\ s^{-1}$ in order to plot the results in terms of dimensionless Fourier number $\dfrac{4|D|^{1/2} t}{d_{bubble}^2}$.

The diffusion equilibration trajectory, calculated using the Geddes model is shown in Figure 4-6(a). The curvilinear equilibration trajectory crosses the distillation boundary during a portion of this traject. Figure 4-6(b) presents a plot of the component Murphree efficiencies, $E_i$, as function of the Fourier

number $\frac{4|D|^{1/2}t}{d_{bubble}^2}$. The Murphree point efficiency of ethanol, $E_2$, is the lowest; this is because of the negative contribution of $D_{21}\Delta y_1$; the Murphree point efficiency of water, $E_1$, is higher than that of ethanol: $E_1 > E_2$. Due to $E_1 > E_2$, a larger proportion of water is transferred to the liquid phase as compared to ethanol; this implies that the vapor phase is poorer in water than predicted by calculations based on equal component efficiencies. The hierarchy of point efficiencies $E_1 > E_2 \approx E_3$ is in agreement with the experimentally determined values for Stages 2 to 9; see Figure 4-5(b).

The contact time of the bubble with the liquid phase is finite. For a 4.5 mm bubble, with a rise velocity of 0.2 m $s^{-1}$ in a dispersion of height 9.2 mm, the contact time $t$ = 0.046 s; these are the input parameters used by Springer et al. in the NEQ model implementation.[37] For this contact time, the composition of the vapor bubble leaving the tray is $y_1$ =0.05212, $y_2$ = 0.35762, and $y_3$ = 0.59026. This vapor composition is on the left side of the distillation boundary, and is indicated by the circle with cross-hair in Figure 4-6(a). Such boundary crossing is observed in Run T2-26 of the experiments of Springer et al.;[35, 37, 39, 40] cf. Figure 4-4.

For various vapor compositions entering any given stage, we have plotted in Figure 4-6(c) the actual composition vector $\left(y_i - y_{i,0}\right)$, calculated from the Geddes model (taking bubble diameter of 4.5 mm, and contact time $t$ = 0.046 s) along with the equilibrium vector $\left(y_i^* - y_{i,0}\right)$. The angle between the Geddes trajectory, also called the NEQ (non-equilibrium) trajectory (blue line) and the EQ trajectory (pink line) increases when the differences in the component efficiencies increases.[51] If all the component efficiencies were equal to one another, the angle between the NEQ and EQ vectors would be zero. We also note from Figure 4-6(c) that for entering vapor compositions that lie to the left of the distillation boundary, no boundary crossing is observed.

As illustration, consider a specific tray for which the composition of the vapor entering is $y_{10}$ = 0.075, $y_{20}$ = 0.7, and $y_{30}$ = 0.225; this composition is left of the distillation boundary. For total reflux operations, the compositions of the liquid leaving that stage will be equal to that of the vapor entering

the stage, i.e. $x_1 = 0.075$, $x_2 = 0.7$, and $x_3 = 0.225$. The composition of vapor in equilibrium with the liquid leaving the tray can be determined using the NRTL parameters provided in Table 4-1. The bubble point temperature is 335.5 K and the equilibrium composition is $y_{1,\text{eq}} = 0.05487$, $y_{2,\text{eq}} = 0.4719$, and $y_{3,\text{eq}} = 0.47322$. The equilibrium composition is also left of the distillation boundary, as is to be expected. The driving forces are $\Delta y_1 = y_{10} - y_{1,eq} = 0.02013$, and $\Delta y_2 = y_{20} - y_{2,eq} = 0.2281$. Both driving forces are positive, i.e. directed from vapor to the liquid phase.

The values of the vapor phase M-S diffusivities of the binary pairs, calculated using the Fuller-Schettler-Giddings (FSG)[14] method, are $Đ_{12} = 2.03$; $Đ_{13} = 1.76$; $Đ_{23} = 0.877\times10^{-5}$ $\text{m}^2\text{s}^{-1}$. These diffusivities are independent of composition. The differences in the binary pair diffusivities cannot be ignored, as we demonstrate below. At the average composition between the entering compositions and the equilibrated compositions, the Fick diffusivity matrix is calculated

$$[D] = \frac{\begin{bmatrix} Đ_{13}\left(x_1 Đ_{23} + (1-x_1)Đ_{12}\right) & x_1 Đ_{23}\left(Đ_{13} - Đ_{12}\right) \\ x_2 Đ_{13}\left(Đ_{23} - Đ_{12}\right) & Đ_{23}\left(x_2 Đ_{13} + (1-x_2)Đ_{12}\right) \end{bmatrix}}{x_1 Đ_{23} + x_2 Đ_{13} + x_3 Đ_{12}} = \begin{bmatrix} 1.91742 & -0.00847 \\ -0.66293 & 0.913543 \end{bmatrix} \times 10^{-5} \quad \text{m}^2 \quad \text{s}^{-1} \quad \text{in}$$

which the $D_{21}$ is seen to non-negligible in comparison with $D_{22}$. We can also determine a "magnitude" of the Fick diffusivity for use in the calculation of the Fourier number: $|D|^{1/2} = 1.32\times10^{-5}$ $\text{m}^2$ $\text{s}^{-1}$ in order to plot the results in terms of dimensionless Fourier number $\frac{4|D|^{1/2}t}{d_{bubble}^2}$.

The diffusion equilibration trajectory, calculated using the Geddes model is shown in Figure 4-7(a). The curvilinear equilibration trajectory remains to the left the distillation boundary during the entire traject. see Figure 4-7(b) presents a plot of the component Murphree efficiencies, $E_i$, as function of the Fourier number $\frac{4|D|^{1/2}t}{d_{bubble}^2}$. The Murphree point efficiency of ethanol, $E_2$, is the lowest; this is because of the negative contribution of $D_{21}\Delta y_1$; the Murphree point efficiency of water, $E_1$, is higher than that of ethanol: $E_1 > E_2$. Due to $E_1 > E_2$, a larger proportion of water is transferred to the liquid phase as compared to ethanol; this implies that the vapor phase is poorer in water than predicted by calculations

based on equal component efficiencies. The hierarchy of point efficiencies $E_1 > E_2 \approx E_3$ is in agreement with the experimentally determined values for Stages 2 to 9; see Figure 4-5(b).

The contact time of the bubble with the liquid phase is finite. For a 4.5 mm bubble, with a rise velocity of 0.2 m $s^{-1}$ in a dispersion of height 9.2 mm, the contact time $t$ = 0.046 s; these are the input parameters used by Springer et al. in the NEQ model implementation.[37] For this contact time, the composition of the vapor bubble leaving the tray is $y_1$ = 0.05751, $y_2$ = 0.53831, and $y_3$ = 0.40418. This vapor composition is also the left side of the distillation boundary, and is indicated by the circle with cross-hair. No boundary crossing possible for the chosen vapor composition entering the tray.

## 4.4 Boundary crossing in water/ethanol/methanol mixture

The experimental data for Run T4-13 with water(1)/ethanol(2)/methanol(3) mixture are shown in Figure 4-8, In Run T4-13, the condenser composition is left of the distillation boundary. Therefore, the residue curves dictate that the reboiler composition should be in the top left corner, rich in ethanol. The measured compositions along the column operating at total reflux shows that the reboiler composition is towards the right of the distillation boundary, and is rich in water. Also shown in Figure 4-8, are the Murphree component efficiencies along the column for Run T4-13. We shall demonstrate below that the boundary crossing is primarily due to the factor that the Murphree efficiency of water is higher than that of ethanol, i.e. $E_1 > E_2$.

Consider distillation of water(1)/ethanol(2)/methanol(3) mixture in a tray column operating at total reflux at a total pressure of 101.3 kPa. For a specified tray, the composition of the vapor entering the tray is $y_{10}$ = 0.082, $y_{20}$ = 0.68, and $y_{30}$ = 0.238. This composition is right of the distillation boundary. For total reflux operations, the compositions of the liquid leaving that stage will be equal to that of the vapor entering the stage, i.e. $x_1$ = 0.082, $x_2$ = 0.68, and $x_3$ = 0.238. The composition of vapor in equilibrium with the liquid leaving the tray can be determined using the NRTL parameters provided in provided in Table 4-1. The bubble point temperature is 348 K and the equilibrium composition is $y_{1,eq}$ = 0.06767, $y_{2,eq}$ = 0.59691, and $y_{3,eq}$ = 0.33542. The final equilibrated composition is also right of the distillation

boundary, as is to be expected. The driving forces are $\Delta y_1 = y_{10} - y_{1,eq} = 0.01433$, and $\Delta y_2 = y_{20} - y_{2,eq} = 0.08309$. Both driving forces are positive, i.e. directed from vapor to the liquid phase.

The values of the vapor phase M-S diffusivities of the binary pairs, calculated using the Fuller-Schettler-Giddings (FSG)[14] method, are $Đ_{12} = 2.1$; $Đ_{13} = 2.72$; $Đ_{23} = 1.36 \times 10^{-5}$ $m^2 s^{-1}$. These diffusivities are independent of composition. The differences in the binary pair diffusivities cannot be ignored, as we demonstrate below. At the average composition between the entering compositions and the equilibrated compositions, the Fick diffusivity matrix is calculated $[D] = \begin{bmatrix} 2.28276 & 0.02578 \\ -0.52706 & 1.39446 \end{bmatrix} \times 10^{-5}$ $m^2$ $s^{-1}$ in which the $D_{21}$ is seen to non-negligible in comparison with $D_{22}$. We can also determine a "magnitude" of the Fick diffusivity for use in the calculation of the Fourier number: $|D|^{1/2} = 1.8 \times 10^{-5}$ $m^2$ $s^{-1}$ in order to plot the results in terms of dimensionless Fourier number $\frac{4|D|^{1/2} t}{d_{bubble}^2}$.

The diffusion equilibration trajectory, calculated using the Geddes model is shown in Figure 4-9(a). The curvilinear equilibration trajectory crosses the distillation boundary during a portion of this traject. Figure 4-9(b) presents a plot of the component Murphree efficiencies, $E_i$, as function of the Fourier number. The Murphree point efficiency of ethanol, $E_2$, is the lowest; this is because of the negative contribution of $D_{21}\Delta y_1$; the Murphree point efficiency of water, $E_1$, is higher than that of ethanol: $E_1 > E_2$. Due to $E_1 > E_2$, a higher proportion of water is transferred to the liquid phase as compared to ethanol; this implies that the vapor phase is poorer in water than predicted by calculations based on equal component efficiencies. The hierarchy of point efficiencies $E_1 > E_2 \approx E_3$ is in agreement with the experimentally determined values shown in Figure 4-8(b).

The contact time of the bubble with the liquid phase is finite. For a 4.5 mm bubble, with a rise velocity of 0.2 m $s^{-1}$ in a dispersion of height 9.2 mm, the contact time $t$ = 0.046 s; these are the input

parameters used by Springer et al.[35, 37, 39, 40] in the NEQ model implementation.[37] For this contact time, the composition of the vapor bubble leaving the tray is$y_1$ =0.06856, $y_2$ = 0.61221, and $y_3$ = 0.31943. This vapor composition is on the left side of the distillation boundary. Such boundary crossing is observed in Run T4-13 of the experiments of Springer et al.[37] (cf. Figure 4-8).

For various vapor compositions entering any given stage, we have plotted in Figure 4-9(c) the actual composition vector $\left(y_i - y_{i,0}\right)$, calculated from the Geddes model (taking bubble diameter of 4.5 mm, and contact time $t$ = 0.046 s) along with the equilibrium vector $\left(y_i^* - y_{i,0}\right)$. The angle between the NEQ trajectory (blue line) and the EQ trajectory (pink line) increases when the differences in the component efficiencies increase. If all the component efficiencies were equal to unit, the NEQ and EQ trajectories would coincide. We see from Figure 4-9(c) that the NEQ trajectory has a tendency to cut across to the right of the EQ trajectory, precisely as has been observed in Run T4-13; cf. Figure 4-8.

## 4.5 Boundary crossing in water/ethanol/methylacetate mixture

The experimental data for Run T3-23 with water(1)/ethanol(2)/methylacetate(3) mixture are shown in Figure 4-10. In Run T3-23, the condenser composition is left of the distillation boundary. Therefore, the residue curves dictate that the reboiler composition should be in the top left corner, rich in ethanol. The measured compositions along the column operating at total reflux shows that the reboiler composition is towards the right of the distillation boundary, and is rich in water. Also shown in Figure 4-10 are the Murphree component efficiencies along the column for Run T4-13. We shall demonstrate later that the boundary crossing is primarily due to the factor that the Murphree efficiency of water is higher than that of ethanol, i.e. $E_1 > E_2$.

Consider distillation of water(1)/ethanol(2)/methylacetatel(3) mixture in a tray column operating at total reflux at a total pressure of 101.3 kPa. For a specified tray, the composition of the vapor entering the tray is $y_{10}$ = 0.095, $y_{20}$ = 0.6345, and $y_{30}$ = 0.2705. The chosen vapor composition is right of the distillation boundary. For total reflux operations, the compositions of the liquid leaving that stage will be equal to that of the vapor entering the stage, i.e. $x_1$ = 0.095, $x_2$ = 0.6345, and $x_3$ = 0.2705. The

composition of vapor in equilibrium with the liquid leaving the tray can be determined using the NRTL parameters provided in Table 4-1. The bubble point temperature is 337 K and the equilibrium composition is $y_{1,eq} = 0.06324$, $y_{2,eq} = 0.36863$, and $y_{3,eq} = 0.56813$. The final equilibrated composition is also right of the distillation boundary, as is to be expected. The driving forces are $\Delta y_1 = y_{10} - y_{1,eq} = 0.03176$, and $\Delta y_2 = y_{20} - y_{2,eq} = 0.26587$.

The values of the vapor phase M-S diffusivities of the binary pairs, calculated using the Fuller-Schettler-Giddings (FSG)[14] method, are $Đ_{12} = 2$; $Đ_{13} = 1.62$; $Đ_{23} = 0.791 \times 10^{-5}$ $m^2 s^{-1}$; these diffusivities are independent of composition. The differences in the binary pair diffusivities cannot be ignored, as we demonstrate below. At the average composition between the entering compositions and the equilibrated compositions, the Fick diffusivity matrix is calculated $[D] = \begin{bmatrix} 1.79479 & -0.01346 \\ -0.56871 & 0.83543 \end{bmatrix} \times 10^{-5}$ $m^2$ $s^{-1}$ in which the $D_{21}$ is seen to non-negligible in comparison with $D_{22}$. We can also determine a "magnitude" of the Fick diffusivity for use in the calculation of the Fourier number: $|D|^{1/2} = 1.22 \times 10^{-5}$ $m^2$ $s^{-1}$ in order to plot the results in terms of dimensionless Fourier number $\frac{4|D|^{1/2} t}{d_{bubble}^2}$.

The diffusion equilibration trajectory, calculated using Geddes model is shown in Figure 4-11(a). The curvilinear equilibration trajectory crosses the distillation boundary during a portion of this traject. Figure 4-11(b) presents a plot of the component Murphree efficiencies, $E_i$, as function of the Fourier number. The Murphree point efficiency of ethanol is the lowest; this is because of the negative contribution of the $D_{21}\Delta y_1$. The hierarchy of point efficiencies $E_1 > E_2 \approx E_3$ is in agreement with the experimentally determined values shown in Figure 4-10. A lower amount of ethanol is transferred to the liquid phase than predicted by an uncoupled equation; i.e. the vapor phase is richer in ethanol. The component efficiency of water is higher than that of partner species; see Figure 4-11(b). Water is the least volatile of the three components, and its transfer is directed from vapor to the liquid phase; a

higher efficiency of water ensures that the liquid phase is richer in water than anticipated on the basis of equal component efficiencies.

The contact time of the bubble with the liquid phase is finite. For a 4.5 mm bubble, with a rise velocity of 0.2 m $s^{-1}$ in a dispersion of height 9.2 mm, the contact time $t$ = 0.046 s; these are the input parameters used by Springer et al. in the NEQ model implementation.[37] For this contact time, the composition of the vapor bubble leaving the tray is $y_1$ =0.06778, $y_2$ = 0.45057, and $y_3$ = 0.48165. This vapor composition is on the left side of the distillation boundary. Such boundary crossing is observed in Run T3-23 of the experiments of Springer et al.[35, 37, 39, 40] (cf. Figure 4-10). The component efficiency of water is higher than that of partner species; see Figure 4-11(b). Water is the least volatile of the three components, and its transfer is directed from vapor to the liquid phase; a higher efficiency of water ensures that the liquid phase is richer in water than anticipated on the basis of equal component efficiencies.

For various vapor compositions entering any given stage, we have plotted in Figure 4-11(c), the actual composition vector $\left(y_i - y_{i,0}\right)$, calculated from the Geddes model (taking bubble diameter of 4.5 mm, and contact time $t$ = 0.046 s) along with the equilibrium vector $\left(y_i^* - y_{i,0}\right)$. The angle between the NEQ trajectory (blue line) and the EQ trajectory (pink line) increases when the differences in the component efficiencies increase. If all the component efficiencies were equal to unity, the NEQ and EQ trajectories would coincide. We see from Figure 4-11(c) that the NEQ trajectory has a tendency to cut across to the right of the EQ trajectory, precisely as has been observed in Run T3-23; cf. Figure 4-10.

We also note from Figure 4-11(c) that for entering vapor compositions that lie to the left of the distillation boundary, no boundary crossing is observed. As illustration, consider a specific tray for which the composition of the vapor entering is $y_{10}$ = 0.075, $y_{20}$ = 0.6, and $y_{30}$ = 0.325; this composition is left of the distillation boundary. For total reflux operations, the compositions of the liquid leaving that stage will be equal to that of the vapor entering the stage, i.e. $x_1$ = 0.075, $x_2$ = 0.6, and $x_3$ = 0.325. The composition of vapor in equilibrium with the liquid leaving the tray can be determined using the NRTL

parameters provided in Table 4-1. The bubble point temperature is 336 K and the equilibrium composition is $y_{1,\text{eq}} = 0.0508$, $y_{2,\text{eq}} = 0.34186$, and $y_{3,\text{eq}} = 0.60735$. The equilibrium composition is also left of the distillation boundary, as is to be expected. The driving forces are $\Delta y_1 = y_{10} - y_{1,eq} = 0.0242$, and $\Delta y_2 = y_{20} - y_{2,eq} = 0.25814$. Both driving forces are positive, i.e. directed from vapor to the liquid phase.

The values of the vapor phase M-S diffusivities of the binary pairs, calculated using the Fuller-Schettler-Giddings (FSG)[14] method, are $Đ_{12} = 1.98$; $Đ_{13} = 1.61$; $Đ_{23} = 0.787 \times 10^{-5}$ $\text{m}^2\text{s}^{-1}$. These diffusivities are independent of composition. The differences in the binary pair diffusivities cannot be ignored, as we demonstrate below. At the average composition between the entering compositions and the equilibrated compositions, the Fick diffusivity matrix is calculated

$$[D] = \frac{\begin{bmatrix} Đ_{13}\left(x_1 Đ_{23} + (1-x_1)Đ_{12}\right) & x_1 Đ_{23}\left(Đ_{13} - Đ_{12}\right) \\ x_2 Đ_{13}\left(Đ_{23} - Đ_{12}\right) & Đ_{23}\left(x_2 Đ_{13} + (1-x_2)Đ_{12}\right) \end{bmatrix}}{x_1 Đ_{23} + x_2 Đ_{13} + x_3 Đ_{12}} = \begin{bmatrix} 1.77081 & -0.010457 \\ -0.52149 & 0.821 \end{bmatrix} \times 10^{-5} \quad \text{m}^2 \quad \text{s}^{-1} \quad \text{in}$$

which the $D_{21}$ is seen to non-negligible in comparison with $D_{22}$. We can also determine a "magnitude" of the Fick diffusivity for use in the calculation of the Fourier number: $|D|^{1/2} = 1.2 \times 10^{-5}$ $\text{m}^2$ $\text{s}^{-1}$ in order to plot the results in terms of dimensionless Fourier number $\frac{4|D|^{1/2} t}{d_{bubble}^2}$.

The diffusion equilibration trajectory, calculated using the Geddes model is shown in Figure 4-12(a). The curvilinear equilibration trajectory remains to the left the distillation boundary during the entire traject. Figure 4-12(b) presents a plot of the component Murphree efficiencies, $E_i$, as function of the Fourier number $\frac{4|D|^{1/2} t}{d_{bubble}^2}$. The Murphree point efficiency of ethanol, $E_2$, is the lowest; this is because of the negative contribution of $D_{21}\Delta y_1$; the Murphree point efficiency of water, $E_1$, is higher than that of ethanol: $E_1 > E_2$. Due to $E_1 > E_2$, a larger proportion of water is transferred to the liquid phase as compared to ethanol; this implies that the vapor phase is poorer in water than predicted by calculations

based on equal component efficiencies. The hierarchy of point efficiencies $E_1 > E_2 \approx E_3$ is in agreement with the experimentally determined values shown in cf. Figure 4-10.

The contact time of the bubble with the liquid phase is finite. For a 4.5 mm bubble, with a rise velocity of 0.2 m $s^{-1}$ in a dispersion of height 9.2 mm, the contact time $t$ = 0.046 s; these are the input parameters used by Springer et al. in the NEQ model implementation.[37] For this contact time, the composition of the vapor bubble leaving the tray is $y_1$ = 0.05432, $y_2$ = 0.42158, and $y_3$ = 0.5241. This vapor composition is also the left side of the distillation boundary, and is indicated by the circle with cross-hair. No boundary crossing possible for the chosen vapor composition entering the tray.

## 4.6 Boundary crossing in water/ethanol/methanol/acetone mixtures

Experimental data for Murhpree efficiencies for quaternary water(1)/ethanol(2)/methanol(3)/acetone(4) mixtures were determined by Springer et al.[39] The experiments were carried out in a 12-stage bubble cap distillation column wherein all the experiments were conducted under total-reflux conditions at 101.3 kPa. Table 4-3 provides the data on the liquid compositions leaving each stage for Run Q6. The experimental composition trajectories in the column are indicated by the blue circles in Figure 4-13. The data are plotted in ternary composition space by combining the mole fractions of methanol and acetone in the left bottom vertex in Figure 4-13. Table 4-2 provides the NRTL parameters used in the calculation of the vapor/liquid phase equilibrium.

Two distillation boundaries are shown in Figure 4-13: the “acetone” boundary is the same as for the water/ethanol/acetone mixture; the “methanol” boundary is the same as for the water/ethanol/methanol mixture. The experimental data shows that both the “acetone” and “methanol” boundaries are crossed in Run Q6. Also shown as insets are the Murphree component efficiencies and component driving forces. The component Murphree efficiency of methanol is negative on stage 3, and slightly exceeds unity on stage 4. This implies that uphill diffusion of methanol manifests on stage 4. The reason is to found in the fact that the driving force of methanol is practically zero on these two stages; the direction of transport of methanol is dictated by the transfer of the three partner species in the mixture: water,

ethanol, and acetone. The boundary crossing is primarily due to the fact that the Murphree efficiency of water is higher than that of ethanol, i.e. $E_1 > E_2$.

We now demonstrate that the phenomenon of uphill diffusion on stage 4 can be rationalized on the basis of the Geddes model for transient diffusion within a spherical bubble. The bubble diameter used in the simulations correspond to the value determined experimentally to be 4.5 mm. In the experimental set-up of Springer et al.[39] the vapor/liquid contact time on the tray is 0.046 s.

The composition of the vapor entering the tray is $y_{10}$ = 0.0614, $y_{20}$ = 0.5527, $y_{30}$ = 0.1868, and $y_{40}$ = 0.199. For total reflux operations, the compositions of the liquid leaving that stage will be equal to that of the vapor entering the stage, i.e. $x_1$ = 0.0614, $x_2$ = 0.5527, $x_3$ = 0.1868, and $x_4$ = 0.199. The composition of vapor in equilibrium with the liquid leaving the tray can be determined using the NRTL parameters provided in Table 4-2. The bubble point temperature is 337 K and the equilibrium composition is $y_{1,eq}$ = 0.03846, $y_{2,eq}$ = 0.35035, $y_{3,eq}$ = 0.19685, and $y_{4,eq}$ = 0.41435. The driving forces are $\Delta y_1 = y_{10} - y_{1,eq} = 0.02294$, $\Delta y_2 = y_{20} - y_{2,eq} = 0.20235$, and $\Delta y_3 = y_{30} - y_{3,eq} = -0.01005$.

The values of the vapor phase M-S diffusivities of the binary pairs, calculated using the Fuller-Schettler-Giddings (FSG)[14] method, are provided in Table 4-4. The differences in the binary pair diffusivities cannot be ignored, as we demonstrate below. At the average composition between the entering compositions and the equilibrated compositions, the Fick diffusivity matrix is calculated from $[D] = [B]^{-1}$: $\begin{bmatrix} D_{11} & D_{12} & D_{13} \\ D_{21} & D_{22} & D_{23} \\ D_{31} & D_{32} & D_{33} \end{bmatrix} = \begin{bmatrix} 2.08543 & -0.00713 & -0.02297 \\ -0.55018 & 1.00661 & -0.20879 \\ -0.23304 & -0.02717 & 1.30245 \end{bmatrix} \times 10^{-5}$ $m^2\ s^{-1}$; the off-diagonal elements are non-negligible. We can also determine a "magnitude" of the Fick diffusivity for use in the calculation of the Fourier number: $|D|^{1/3} = 1.394 \times 10^{-5}$ $m^2\ s^{-1}$ in order to plot the results in terms of in terms of dimensionless Fourier number $\frac{4|D|^{1/2} t}{d_{bubble}^2}$. Figure 4-14 presents the Geddes model calculations for the Murphree point efficiencies on Stage 4. The inlet compositions on the stages are as specified in

Table 4-3. The *x*-axis is dimensionless Fourier number $\frac{4|D|^{1/3}t}{d_{bubble}^2}$. For stage 4, we note that the efficiency of methanol exceeds unity, indicating uphill diffusion. This is in accord with the data of Springer et al.[39] in Figure 4-13.

Figure 4-15 shows the equilibration trajectory for water(1)/ethanol(2)/methanol(3)/acetone(4) mixtures for entering vapor compositions $y_{1E} = 0.111; y_{1E} = 0.79; y_{1E} = 0.08; y_{1E} = 0.019$. We note that the equilibration trajectory has crossed the water/ethanol/acetone "distillation boundary". These calculations provide a rationalization of the experimental observation of boundary crossing in Figure 4-13.

## 4.7 Boundary crossing in water/methanol/2-propanol mixtures

Let us consider the system: water(1)/methanol(2)/2-propanol(3) has one binary azeotrope, as indicated in Figure 4-16(a). We note that the boundary is very nearly a straight line. According to boundary crossing rules of Levy et al.[42] it is not possible to cross a straight-line boundary. But these remarks regarding boundary crossing are based on the use of the EQ stage model.

In order to see whether the introduction of mass transfer resistance has an influence on the column composition trajectories (a boundary crossing phenomenon) for this homogeneous ternary azeotropic system, we carried out the simulations with both EQ and NEQ stage models for a 12-stage column operating at total reflux. The feed composition was chosen to be $x_1 = 0.05$, $x_2 = 0.8$ which is located in on the left side of the distillation boundary, see Figure 4-16(b) and fixed on stage 1 (condenser). The EQ (green triangular markers) and NEQ (red circular markers) composition trajectories are seen to follow completely different composition trajectories; see see Figure 4-16(b). The NEQ model predicts that the bottom product composition corresponds to (nearly) pure water whereas the EQ model predicts the bottom product to consist of (nearly) pure 2-propanol. The NEQ model crosses the distillation boundary.

We shall demonstrate below that the boundary crossing is primarily due to the factor that the Murphree efficiency of water is higher than that of ethanol, i.e. $E_1 > E_2$.

**Multicomponent Distillation**

Consider distillation of water(1)/methanol(2)/2-propanol(3) mixture in a tray column operating at total reflux at a total pressure of 101.3 kPa. For a specified tray, the composition of the vapor entering the tray is $y_{10}$ = 0.12, $y_{20}$ = 0.62, and $y_{30}$ = 0.26. The chosen vapor composition is right of the distillation boundary. For total reflux operations, the compositions of the liquid leaving that stage will be equal to that of the vapor entering the stage, i.e. $x_1$ = 0.12, $x_2$ = 0.62, and $x_3$ = 0.26. The composition of vapor in equilibrium with the liquid leaving the tray can be determined using the NRTL parameters provided in Table 4-1. The bubble point temperature is 344 K and the equilibrium composition is $y_{1,eq}$ = 0.0742, $y_{2,eq}$ = 0.76109, and $y_{3,eq}$ = 0.1647. The final equilibrated composition is also right of the distillation boundary, as is to be expected.The driving forces are $\Delta y_1 = y_{10} - y_{1,eq} = 0.0458$, and $\Delta y_2 = y_{20} - y_{2,eq} = -0.14109$.

The values of the vapor phase M-S diffusivities of the binary pairs, calculated using the Fuller-Schettler-Giddings (FSG)[14] method, are $Đ_{12} = 2.67$; $Đ_{13} = 1.73$; $Đ_{23} = 1.12\times10^{-5}$ $m^2s^{-1}$; these diffusivities are independent of composition. At the average composition between the entering compositions and the equilibrated compositions, the Fick diffusivity matrix is calculated $[D] = \begin{bmatrix} 2.33042 & -0.0543 \\ -0.98755 & 1.21223 \end{bmatrix} \times 10^{-5}$ $m^2$ $s^{-1}$ in which the $D_{21}$ is seen to non-negligible in comparison with $D_{22}$. We can also determine a "magnitude" of the Fick diffusivity for use in the calculation of the Fourier number: $|D|^{1/2} = 1.66\times10^{-5}$ $m^2$ $s^{-1}$ in order to plot the results in terms of dimensionless Fourier number $\frac{4|D|^{1/2}t}{d_{bubble}^2}$.

The diffusion equilibration trajectory, calculated using Geddes model is shown in Figure 4-17(a). The curvilinear equilibration trajectory crosses the distillation boundary during a portion of this traject. The contact time of the bubble with the liquid phase is finite. For a 4.5 mm bubble, with a rise velocity of 0.2 m $s^{-1}$ in a dispersion of height 9.2 mm, the contact time $t$ = 0.046 s. For this contact time, the composition of the vapor bubble leaving the tray is $y_1$ =0.07685, $y_2$ = 0.73677, and $y_3$ = 0.18638. The

composition of the vapor leaving the tray is to the left of the distillation boundary. The vapor phase is poorer in methanol than predicted by the equilibrium model.

Figure 4-17(b) presents a plot of the component Murphree efficiencies, $E_i$, as function of the Fourier number. The Murphree point efficiency of methanol is the lower than that of water; this is because of the negative contribution of the $D_{21}\Delta y_1$. The driving force of methanol is directed from the vapor to the liquid phase. Due to the lower efficiency of methanol, a smaller amount of methanol is transferred to the liquid phase than predicted by a model that assumes equal component efficiencies for all components; i.e. in other words, the vapor phase is poorer in methanol.

Figure 4-17(c) compares the NEQ and EQ vector trajectories.

Pelkonen et al.[52] performed total reflux experiments with the system water/methanol/2-propanol in a packed distillation column and showed that if the composition at the top of the column is located on the distillation boundary (i.e. the line connecting pure methanol with the methanol/2-propanol binary azeotrope) the experimentally measured composition profiles end up with a reboiler composition that is rich in water. The measured composition trajectories can be simulated very well using a nonequilibrium (NEQ) stage model incorporating the Maxwell-Stefan diffusion equations. On the other hand, an equilibrium (EQ) stage model (i.e. a model in which the component efficiencies are each taken to 100%) predicts that the reboiler compositions corresponds to pure 2-propanol. Pelkonen et al.[52, 53] also performed similar experiments with the quaternary system acetone-methanol-isopropanol-water, with the composition near the top of the column chosen to lie on the distillation boundary and obtained the same dramatic differences between the predictions of the NEQ and EQ models. The NEQ model predictions were in accord with the experiments.

## 4.8 Uphill diffusion in acetone/chloroform/methanol mixtures

For the system acetone/chloroform/methanol we have three binary and one ternary azeotrope dividing the composition space into four regions by means of four distillation boundaries, that are all curved; see the residue curve map shown in Figure 4-18(a). According to Rule 2 of Levy et al.[42], boundary crossing

is *not* forbidden if the feed is located on the concave side of the distillation boundary, say as indicated in Figure 4-18(a).

We now demonstrate the possibility of uphill diffusion in this system.

Consider distillation of acetone(1)/chloroform(2)/methanol(3) mixture in a sieve tray column operating at total reflux at a total pressure of 101.3 kPa. For a specified tray, the composition of the vapor entering the tray is $y_{10} = 0.486$, $y_{20} = 0.46$, and $y_{30} = 0.054$. The chosen vapor composition lies on the concave side of the distillation boundary. For total reflux operations, the compositions of the liquid leaving that stage will be equal to that of the vapor entering the stage, i.e. $x_1 = 0.486$, $x_2 = 0.46$, and $x_3 = 0.054$. The composition of vapor in equilibrium with the liquid leaving the tray can be determined using the NRTL parameters provided in Table 4-1. The bubble point temperature is 334.6 K and the equilibrium composition is $y_{1,\text{eq}} = 0.49042$, $y_{2,\text{eq}} = 0.38374$, and $y_{3,\text{eq}} = 0.12584$. The final equilibrated composition is on the convex side of the distillation boundary; boundary crossing is not forbidden. The driving forces are $\Delta y_1 = y_{10} - y_{1,eq} = -4.41582 \times 10^{-3}$, and $\Delta y_2 = y_{20} - y_{2,eq} = 0.07626$.

The values of the vapor phase M-S diffusivities of the binary pairs, calculated using the Fuller-Schettler-Giddings (FSG)[14] method, are $Đ_{12} = 0.59$; $Đ_{13} = 1.1$; $Đ_{23} = 0.93 \times 10^{-5}$ $\text{m}^2\text{s}^{-1}$; these diffusivities are independent of composition. At the average composition between the entering compositions and the equilibrated compositions, the Fick diffusivity matrix is calculated $[D] = \begin{bmatrix} 0.85691 & 0.23788 \\ 0.16128 & 0.77088 \end{bmatrix} \times 10^{-5}$ $\text{m}^2$ $\text{s}^{-1}$ in which both off-diagonal elements are seen to non-negligible in comparison with the diagonal elements. We can also determine a "magnitude" of the Fick diffusivity for use in the calculation of the Fourier number: $|D|^{1/2} = 0.79 \times 10^{-5}$ $\text{m}^2$ $\text{s}^{-1}$ in order to plot the results in terms of dimensionless Fourier number $\frac{4|D|^{1/2} t}{d_{bubble}^2}$.

The diffusion equilibration trajectory, calculated using Geddes model is shown in Figure 4-18(b). The contact time of the bubble with the liquid phase is finite. For a 4.5 mm bubble, with a rise velocity of

0.2 m $s^{-1}$ in a dispersion of height 9.2 mm, the contact time $t$ = 0.046 s. For this contact time, the composition of the vapor bubble leaving the tray is $y_1$ = 0.48372, $y_2$ = 0.40845, and $y_3$ = 0.10783. The composition of the vapor leaving the tray remains on the concave side off the distillation boundary.

Figure 4-18(c) presents a plot of the component Murphree efficiencies, $E_i$, as function of the Fourier number. The Murphree point efficiency of acetone is negative because the positive contribution of $D_{12}\Delta y_2$ is opposite in sign to the diagonal contribution $D_{11}\Delta y_1$. Put another way, uphill diffusion of acetone occurs.

## 4.9 Uphill diffusion in water/ethanol/tert-butanol mixtures

For the system water/ethanol/tert-butanol (=2-methyl-2-propanol) there are two binary azeotropes dividing the composition space into two distinct regions boundaries, that are all curved; see the residue curve map shown in Figure 4-19(a). Experimental data of Krishna et al.[33] for distillation of water/ethanol/tert-butanol mixtures in a sieve tray distillation column, operating under total reflux conditions, have demonstrated the occurrence of negative component efficiencies. Our objective here is to investigate the origins of negative efficiencies by using the Geddes model for vapor phase equilibrium within a spherical bubble. We now demonstrate the possibility of uphill diffusion in this system.

Consider distillation of water(1)/ethanol(2)/tert-butanol(3) mixture in a sieve tray column operating at total reflux at a total pressure of 101.3 kPa. For a specified tray, the composition of the vapor entering the tray is $y_{10}$ = 0.3089, $y_{20}$ = 0.5558, and $y_{30}$ = 0.436. The chosen vapor composition corresponds to Run M46 of Krishna et al.[33] For total reflux operations, the compositions of the liquid leaving that stage will be equal to that of the vapor entering the stage, i.e. $x_1$ = 0.3089, $x_2$ = 0.5558, and $x_3$ = 0.436. The composition of vapor in equilibrium with the liquid leaving the tray can be determined using the NRTL parameters provided in Table 4-1. The bubble point temperature is 352 K and the equilibrium composition is $y_{1,eq}$ = 0.27405, $y_{2,eq}$ = 0.59176, and $y_{3,eq}$ = 0.13419. The driving forces are $\Delta y_1 = y_{10} - y_{1,eq} = 0.03485$, $\Delta y_2 = y_{20} - y_{2,eq} = -0.03596$, and $\Delta y_3 = y_{30} - y_{3,eq} = 0.001108$. Particularly

noteworthy is the fact that the driving force of tert-butanol is about one order of magnitude lower than that of water, and ethanol.

The values of the vapor phase M-S diffusivities of the binary pairs, calculated using the Fuller-Schettler-Giddings (FSG)[14] method, are $Đ_{12} = 2.14$; $Đ_{13} = 1.59$; $Đ_{23} = 0.79 \times 10^{-5}$ $m^2 s^{-1}$; these diffusivities are independent of composition. At the average composition between the entering compositions and the equilibrated compositions, the Fick diffusivity matrix is calculated $[D] = \begin{bmatrix} 1.9443 & -0.09042 \\ -0.86633 & 1.00673 \end{bmatrix} \times 10^{-5}$ $m^2$ $s^{-1}$ in which the $D_{21}$ is seen to non-negligible in comparison with $D_{22}$. In other words, the flux of ethanol is strongly coupled to the flux of water. We can also determine a "magnitude" of the Fick diffusivity for use in the calculation of the Fourier number: $|D|^{1/2} = 1.37 \times 10^{-5}$ $m^2$ $s^{-1}$ in order to plot the results in terms of dimensionless Fourier number $\frac{4|D|^{1/2} t}{d_{bubble}^2}$.

The diffusion equilibration trajectory, calculated using Geddes model is shown in Figure 4-19(b). The contact time of the bubble with the liquid phase is finite. For a 4.5 mm bubble, with a rise velocity of 0.2 m $s^{-1}$ in a dispersion of height 9.2 mm, the contact time $t$ = 0.046 s. For this contact time, the composition of the vapor bubble leaving the tray is $y_1$ = 0.27742, $y_2$ = 0.58721, and $y_3$ = 0.13537; see Figure 4-19(b). It is remarkable that the composition of tert-butanol leaving the tray higher than the entering tray composition, whereas the EQ model anticipates that the tert-butanol composition should be lower than the entering composition.

Figure 4-19(c) presents a plot of the component Murphree efficiencies, $E_i$, as function of the Fourier number. The Murphree point efficiency of tert-butanol is negative because it is being dragged uphill by the two partners: water and ethanol. Further explanation of this is provided in Example 12.2.2 of Taylor and Krishna.[1]

## 4.10 List of Tables for Multicomponent Distillation

Table 4-1. NRTL parameters for homogeneous ternary mixtures at 101.3 kPa (Gmehling & Onken, 1977). These parameters are used along with $G_{ij} = \exp(-\alpha_{ij}\tau_{ij})$ and $\tau_{ij} = B_{ij}/T$

| **Ternary systems** | | | | |
|---|---|---|---|---|
| Component *i* | Component *j* | $B_{ij}$ / [K] | $B_{ji}$ / [K] | $\alpha_{ij}$ / [-] |
| Water | Methanol | 594.6299 | -182.6052 | 0.297 |
| Water | 2-propanol | 729.2208 | 70.6619 | 0.288 |
| Methanol | 2-propanol | 65.71121 | -89.74272 | 0.304 |
| Acetone | Chloroform | -327.6945 | 151.8924 | 0.3054 |
| Acetone | Methanol | 59.42076 | 149.0765 | 0.3003 |
| Chloroform | Methanol | 671.975 | -53.0728 | 0.2873 |
| Water | Ethanol | 624.9174 | -29.169 | 0.2937 |
| Water | Acetone | 602.6252 | 330.4768 | 0.5103 |
| Ethanol | Acetone | 188.8983 | 22.83319 | 0.3006 |
| Water | Ethanol | 624.9174 | -29.169 | 0.2937 |
| Water | Methanol | 594.6299 | -182.605 | 0.297 |
| Ethanol | Methanol | 73.413 | -79.1718 | 0.3029 |
| Water | Ethanol | 624.9174 | -29.169 | 0.2937 |
| Water | Methylacetate | 796.8165 | 334.6706 | 0.35 |
| Ethanol | Methylacetate | 198.9705 | 134.162 | 0.3 |
| Water | Methanol | 594.629 | -182.605 | 0.297 |
| Water | Methylacetate | 860.2462 | 442.4 | 0.383 |

| | | | | |
|---|---|---|---|---|
| Methanol | Methylacetate | 229.9405 | 284.8969 | 1.0293 |
| Water | Ethanol | 620.17 | −20.46 | 0.3194 |
| Water | Tert-butanol | 1122.14 | 209.54 | 0.4917 |
| Ethanol | Tert-butanol | 250.99 | −335.37 | -0.1382 |

Table 4-2. The NRTL parameters for the quaternary mixture water (1) – ethanol (2) – methanol (3) – acetone (4) at 101.3 kPa (Gmehling & Onken, 1977). These parameters are used along with $G_{ij} = \exp(-\alpha_{ij}\tau_{ij})$ and $\tau_{ij} = B_{ij}/T$

| **Quaternary system (homogeneous)** | | | | |
|---|---|---|---|---|
| Component *i* | Component *j* | $B_{ij}$ / [K] | $B_{ji}$ / [K] | $\alpha_{ij}$ / [-] |
| Water | Ethanol | 624.9174 | -29.169 | 0.2937 |
| Water | Methanol | 594.6299 | -182.6052 | 0.297 |
| Water | Acetone | 602.6252 | 330.4768 | 0.5103 |
| Ethanol | Methanol | 73.413 | -79.1718 | 0.3029 |
| Ethanol | Acetone | 188.8983 | 22.83319 | 0.3006 |
| Methanol | Acetone | 97.78178 | 107.83 | 0.3008 |

Table 4-3. Compositions of the liquid leaving each stage for Run Q6 of Springer. At total reflux, the compositions leaving each stage equals the vapor entering each stage. These compositions were determined by a non-equilibrium stage model that matched the column composition profiles that were determined in the experiments.

| Stage number | $x_{1E}$ | $x_{2E}$ | $x_{3E}$ | $x_{4E}$ |
|---|---|---|---|---|
| 1 | 0.0205 | 0.2865 | 0.1956 | 0.4974 |
| 2 | 0.0307 | 0.3658 | 0.1986 | 0.4049 |
| 3 | 0.0446 | 0.4576 | 0.197 | 0.3008 |
| 4 | 0.0614 | 0.5527 | 0.1868 | 0.199 |
| 5 | 0.0787 | 0.6374 | 0.167 | 0.1169 |
| 6 | 0.094 | 0.7026 | 0.1412 | 0.0622 |
| 7 | 0.1064 | 0.748 | 0.1147 | 0.031 |
| 8 | 0.1163 | 0.778 | 0.0908 | 0.0149 |
| 9 | 0.1245 | 0.7977 | 0.0709 | 0.006964 |
| 10 | 0.1316 | 0.8103 | 0.0549 | 0.003223 |
| 11 | 0.1381 | 0.818 | 0.0424 | 0.00148 |
| 12 | 0.1462 | 0.825 | 0.0284 | 0.0003942 |

Table 4-4. M-S vapor phase diffusivities for the binary pairs in the quaternary Water (1) – Ethanol (2) – Methanol (3) – Acetone (4) system. The values are calculated using the FSG correlation at the temperature 340 K, the average temperature in Run Q6 in the Springer experiments.

| Parameter | units | i-j pair | | | | | |
|---|---|---|---|---|---|---|---|
| | | 1-2 pair | 1-3 pair | 1-4 pair | 2-3 pair | 2-4 pair | 3-4 pair |
| $Đ_{ij}$ | $10^{-5}$ $m^2$ $s^{-1}$ | 2.1 | 2.72 | 1.82 | 1.36 | 0.908 | 1.18 |

## 4.11 List of Figures for Multicomponent Distillation

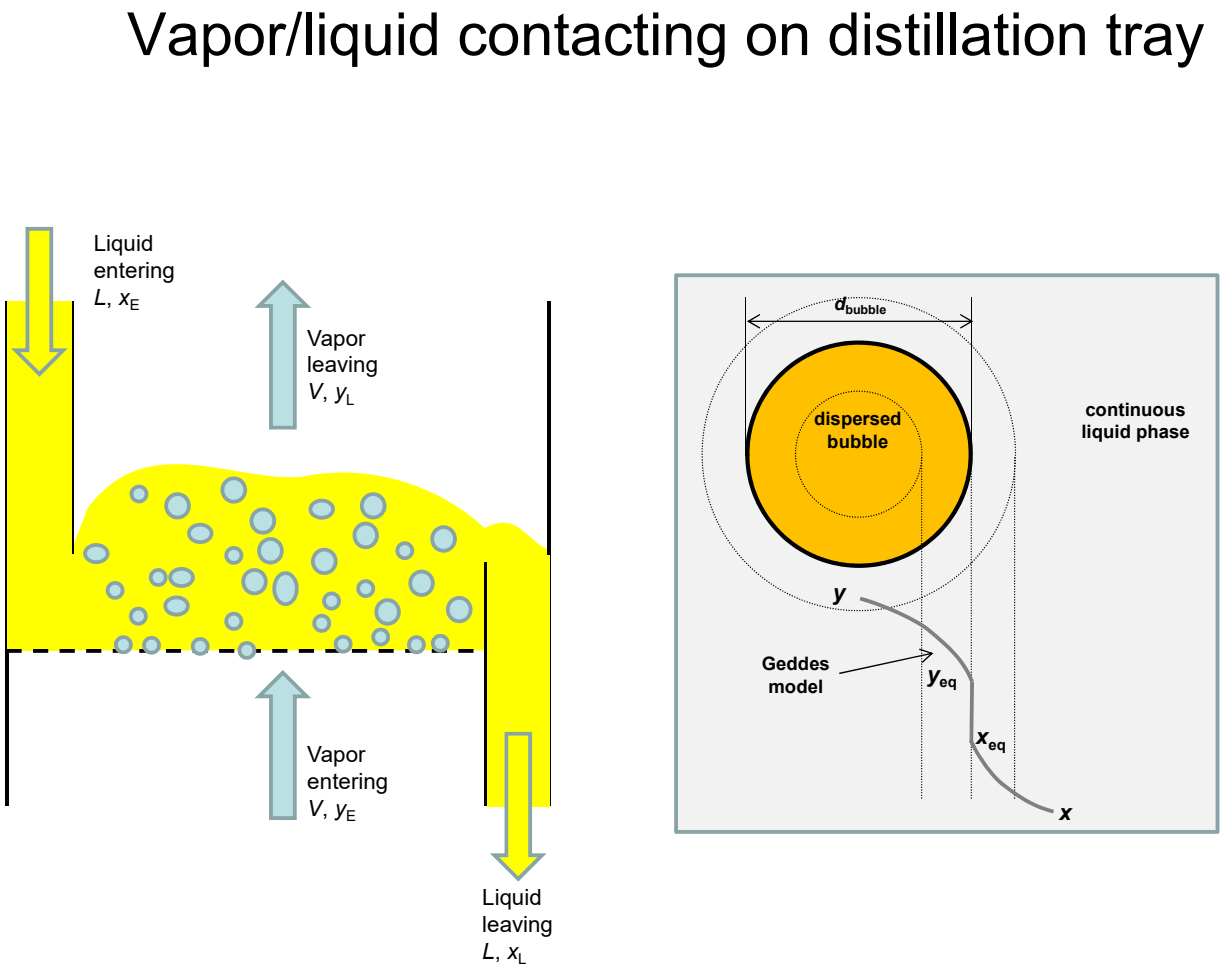


Figure 4-1. Schematic of vapor/liquid contacting on a distillation tray, indicating transfer resistances.

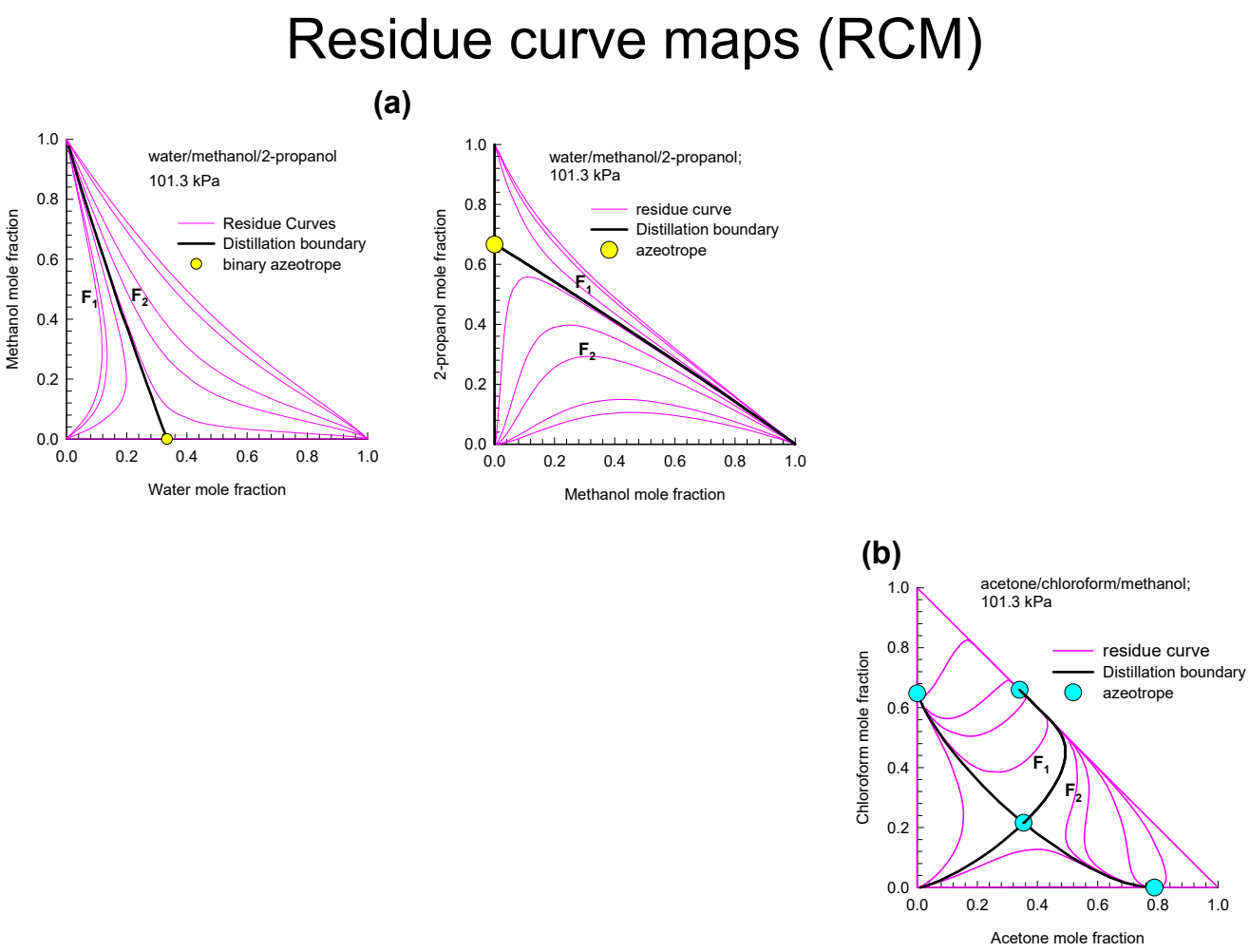


Figure 4-2. (a) Residue curve map for the water/methanol/2-propanol system, showing a straight-line distillation boundary and feed locations F1 and F2 on either side of the distillation boundary. (b) Residue curve map for the acetone/chloroform/methanol system, showing feed locations F1 and F2 on the concave and convex sides of the highlighted distillation boundary respectively.

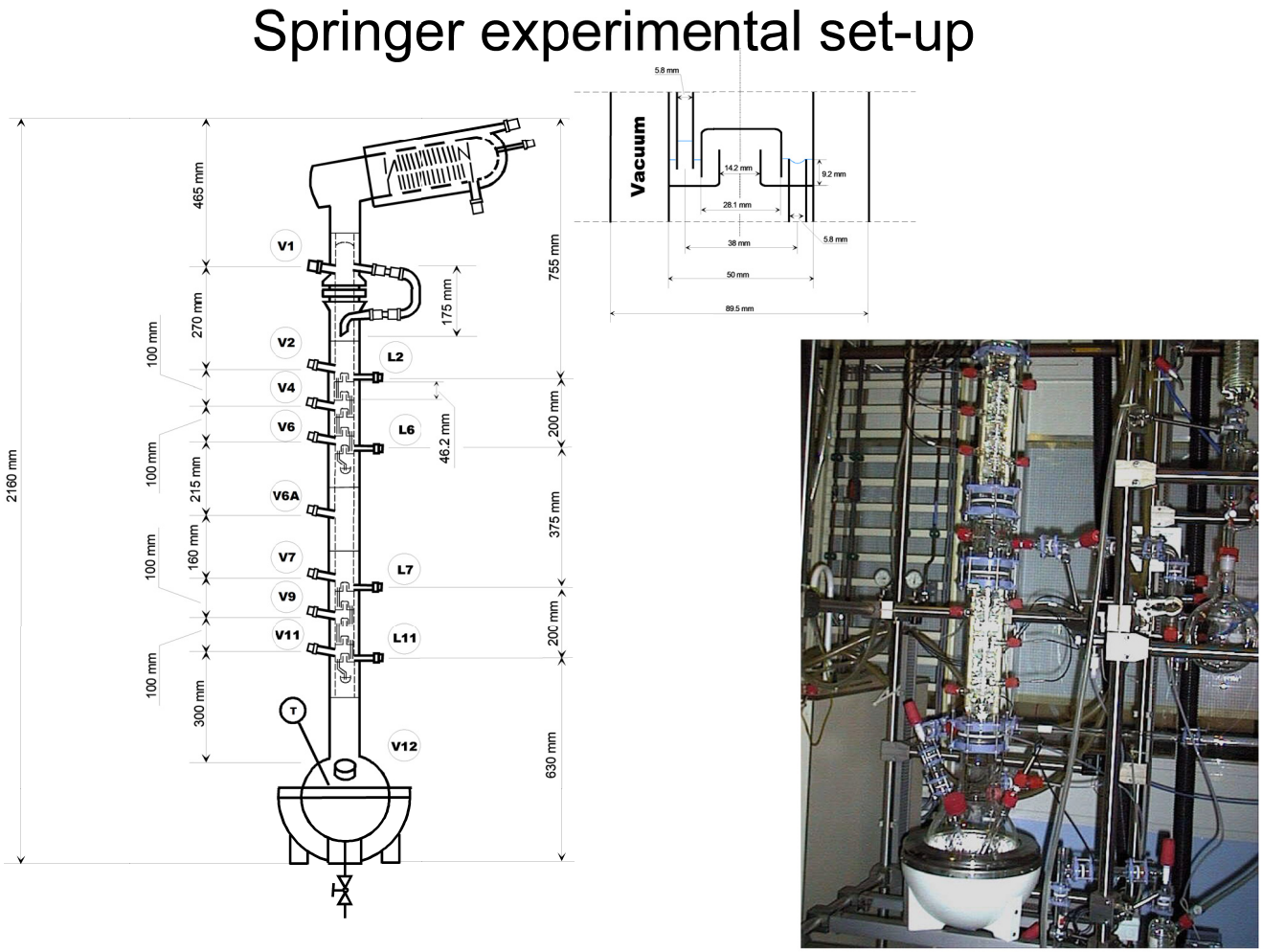


Figure 4-3. (a) Schematic of a laboratory-scale distillation column used in the experiments of Springer et al.[35, 37] which includes a total condenser (1), a partial reboiler (12), 10 bubble-cap trays (2-11), and 13 draw-off faucets, 9 for vapor samples and 4 for liquid samples.

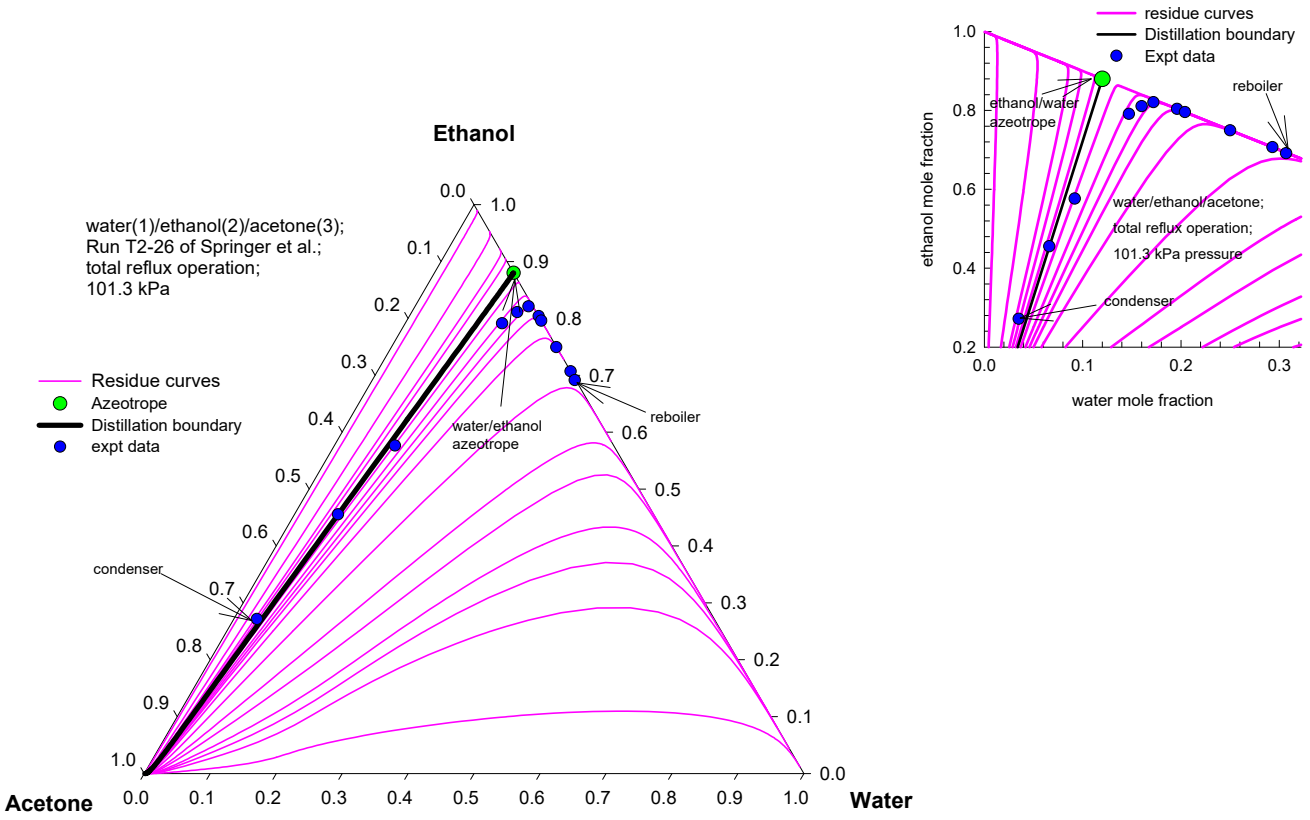


Figure 4-4. Residue curve maps for distillation of water(1)/ethanol(2)/acetone(3) mixtures. The blue circles represent the experimental data for T2-26 of Springer et al.[35, 37, 39, 40] on composition trajectories in a bubble-cap tray column operating at total reflux implying $x_i = y_i$.

# Murphree component efficiencies

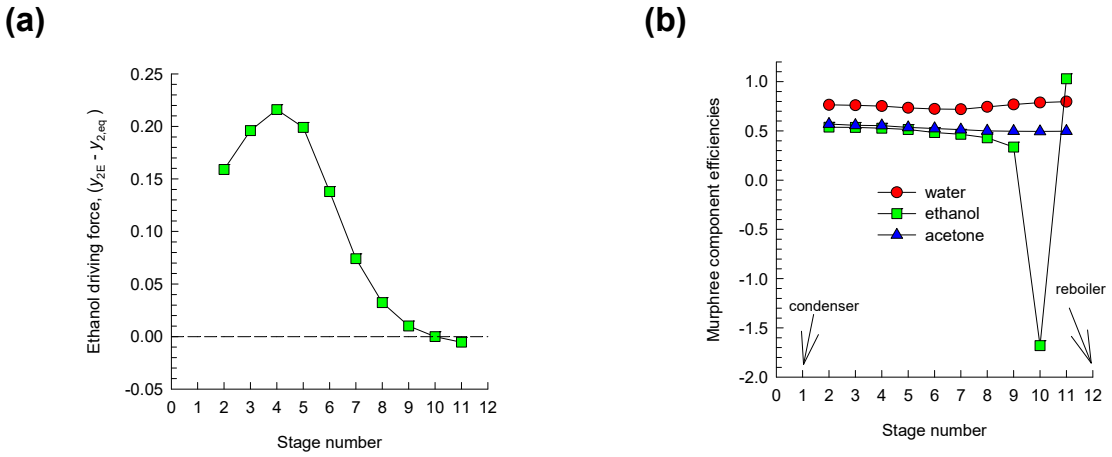


Figure 4-5. (a) Ethanol driving force $\Delta y_{2E} = \left(y_{2E} - y_{2,eq}\right)$ on each stage for the system water(1)/ethanol(2)/acetone(3). (b) Murphree component efficiencies for the system water(1)/ethanol(2)/acetone(3).

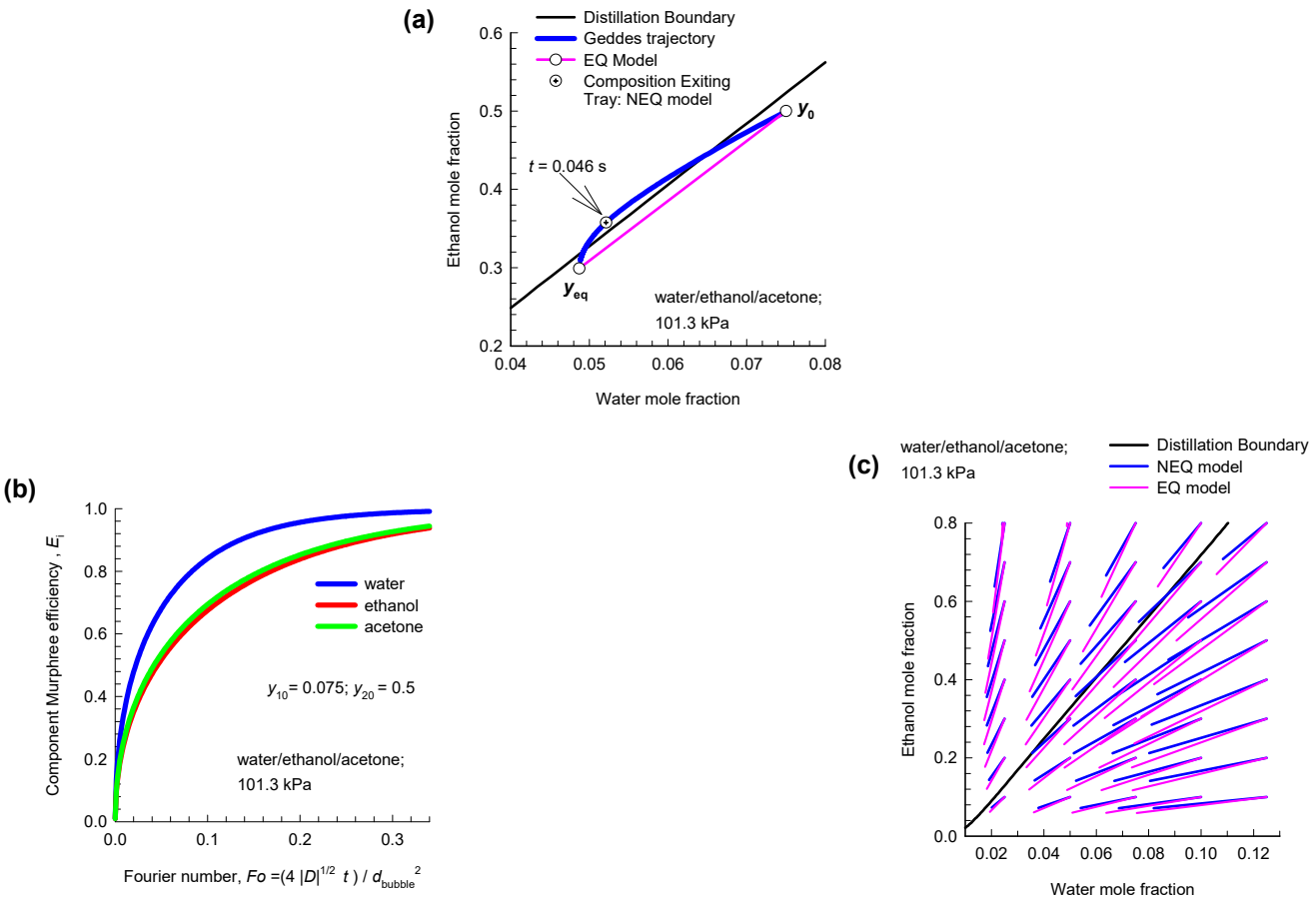


Figure 4-6. (a) Transient equilibration trajectories for the system water(1)/ethanol(2)/acetone(3) at 101.3 kPa. The initial mole fractions in the rigid spherical vapor bubble are $y_{10}$ = 0.075, $y_{20}$ = 0.5, and $y_{30}$ = 0.425; the final equilibrium compositions are $y_{1,eq}$ = 0.04869, $y_{2,eq}$ = 0.29898, and $y_{3,eq}$ = 0.65233. (b) Plot of the component Murphree efficiencies, $E_i$, as function of the Fourier number. (c) NEQ and EQ trajectory vectors for various entering tray compositions for the system water(1)/ethanol(2)/acetone(3) at 101.3 kPa.

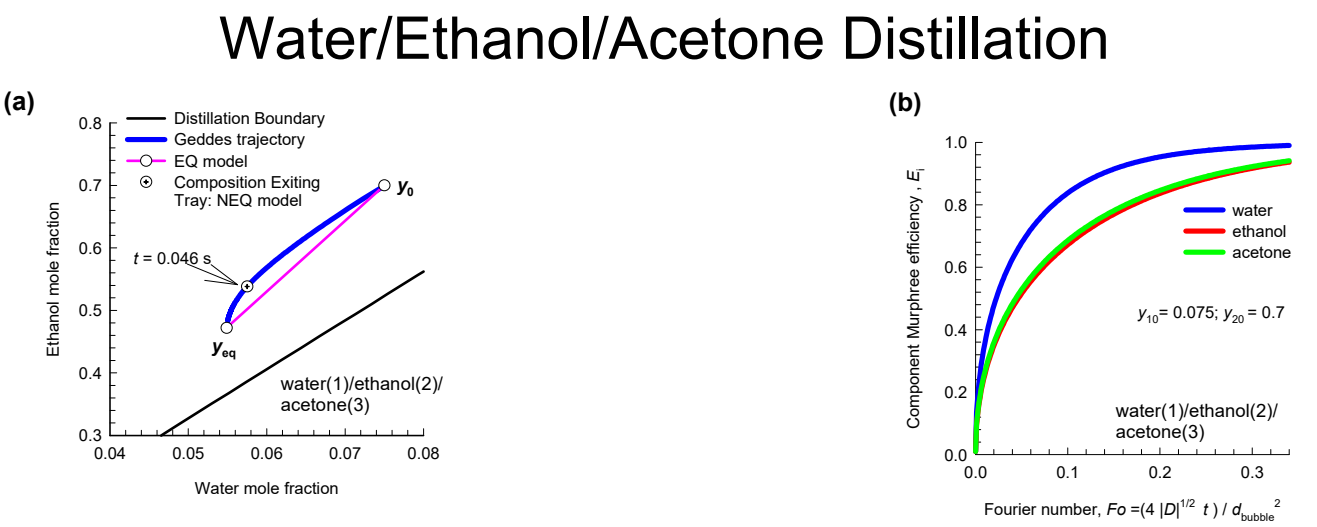


Figure 4-7. (a) Transient equilibration trajectories for the system water(1)/ethanol(2)/acetone(3) at 101.3 kPa. The initial mole fractions in the rigid spherical vapor bubble are $y_{10}$ = 0.075, $y_{20}$ = 0.7, and $y_{30}$ = 0.225; the final equilibrium compositions are $y_{1,eq}$ = 0.05487, $y_{2,eq}$ = 0.4719, and $y_{3,eq}$ = 0.47322. (b) Plot of the component Murphree efficiencies, $E_i$, as function of the Fourier number.

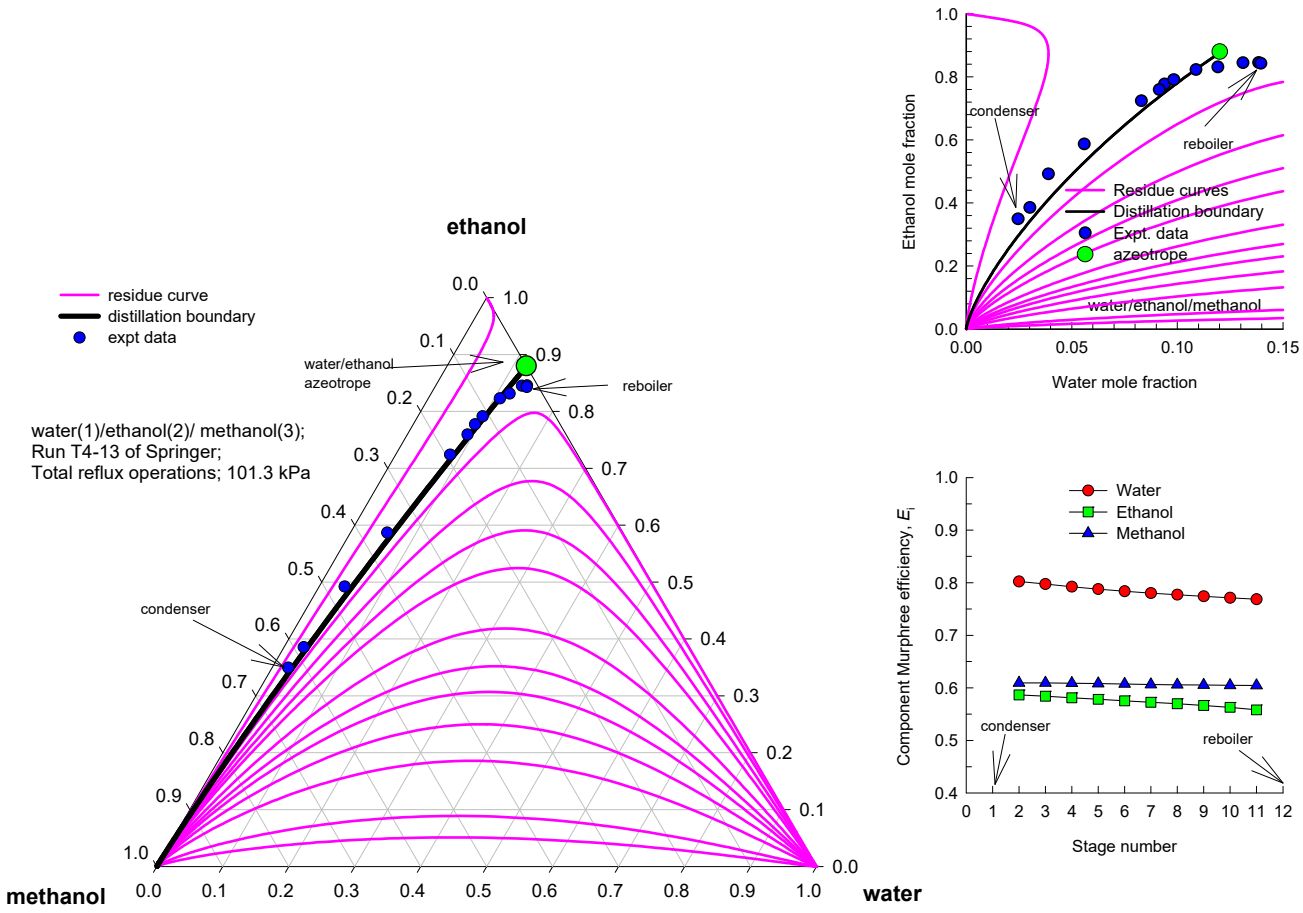


Figure 4-8.Residue curve maps for distillation of water(1)/ethanol(2)/methanol(3) mixtures. The blue circles represent the experimental data for T4-13 of Springer et al.[35, 37, 39, 40] on composition trajectories in a bubble-cap tray column operating at total reflux implying $x_i = y_i$.

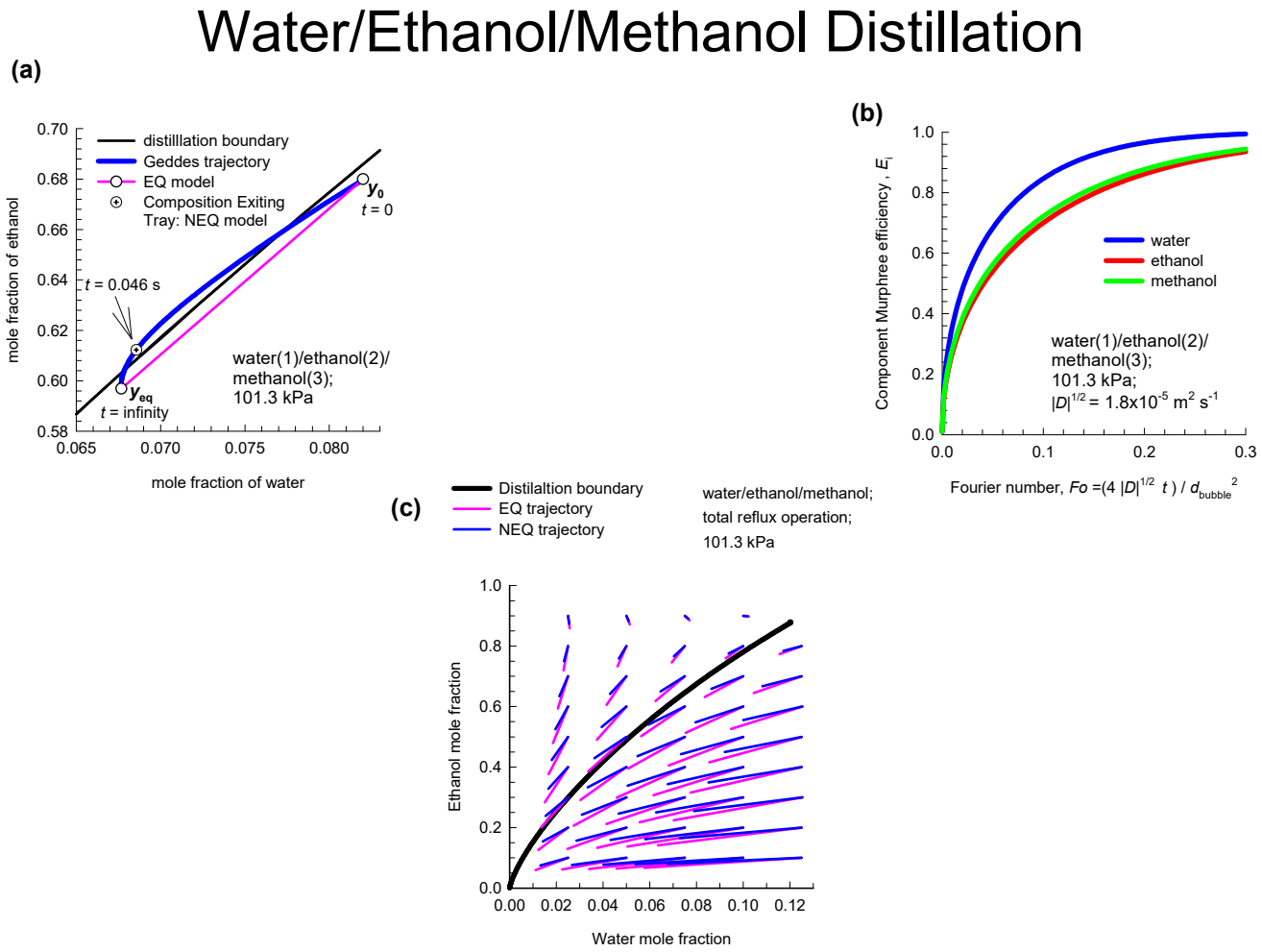


Figure 4-9. (a) Transient equilibration trajectories for the system water(1)/ethanol(2)/methanol(3) at 101.3 kPa. The initial mole fractions in the rigid spherical vapor bubble are $y_{10}$ = 0.082, $y_{20}$ = 0.68, and $y_{30}$ = 0.238; the final equilibrium compositions are $y_{1,eq}$ = 0.06767, $y_{2,eq}$ = 0.59691, and $y_{3,eq}$ = 0.33542. (b) Plot of the component Murphree efficiencies, $E_i$, as function of the Fourier number. (c) NEQ and EQ trajectory vectors for various entering tray compositions for the system water(1)/ethanol(2)/methanol(3) at 101.3 kPa.

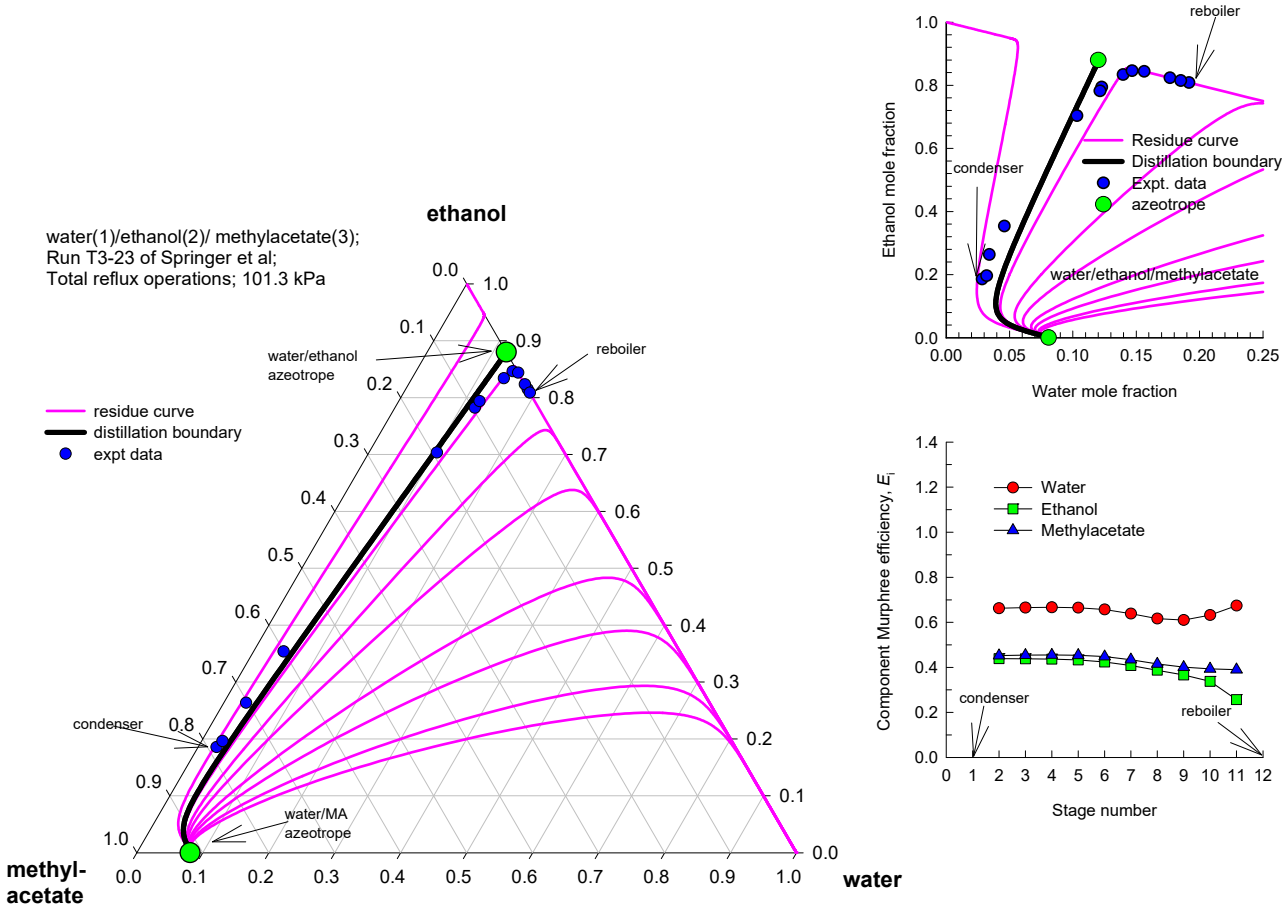


Figure 4-10. Residue curve maps for distillation of water(1)/ethanol(2)/methylacetate(3) mixtures. The blue circles represent the experimental data for T3-23 of Springer et al.[35, 37, 39, 40] on composition trajectories in a bubble-cap tray column operating at total reflux implying $x_i = y_i$.

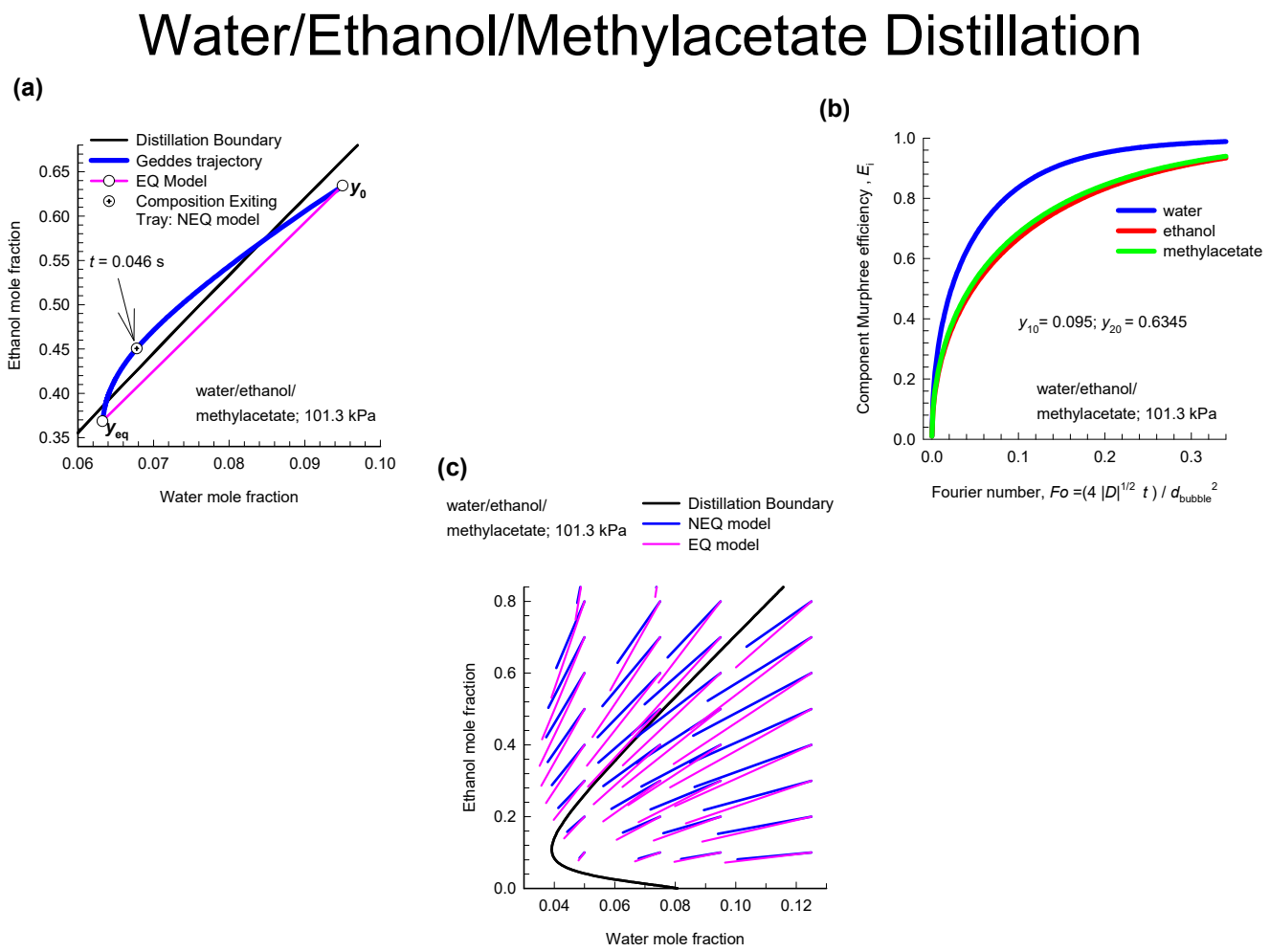


Figure 4-11. (a) Transient equilibration trajectories for the system water(1)/ethanol(2)/methylacetate(3) at 101.3 kPa. The initial mole fractions in the rigid spherical vapor bubble are $y_{10} = 0.095$, $y_{20} = 0.6345$, and $y_{30} = 0.2705$; the final equilibrium compositions are $y_{1,eq} = 0.06324$, $y_{2,eq} = 0.36863$, and $y_{3,eq} = 0.56813$. (b) Plot of the component Murphree efficiencies, $E_i$, as function of the Fourier number. (c) NEQ and EQ trajectory vectors for various entering tray compositions for the system water(1)/ethanol(2)/methylacetate(3) at 101.3 kPa.

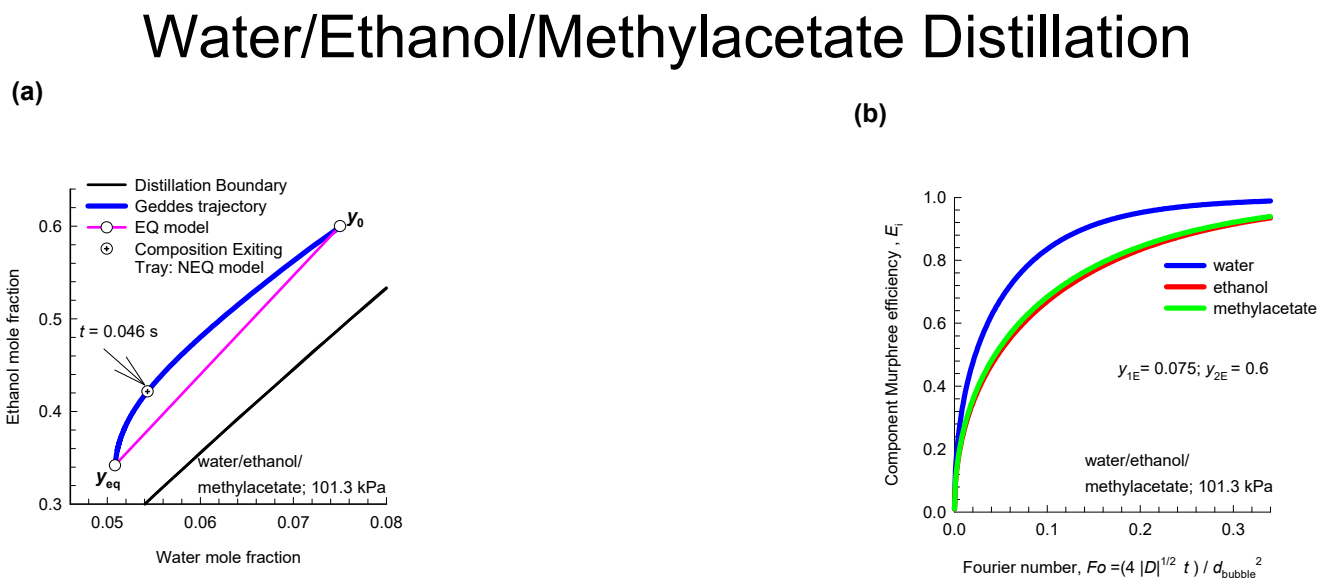


Figure 4-12. (a) Transient equilibration trajectories for the system water(1)/ethanol(2)/methylacetate(3) at 101.3 kPa. The initial mole fractions in the rigid spherical vapor bubble are $y_{10}$ = 0.075, $y_{20}$ = 0.6, and $y_{30}$ = 0.325; the final equilibrium compositions are $y_{1,eq}$ = 0.0508, $y_{2,eq}$ = 0.34186, and $y_{3,eq}$ = 0.60735. (b) Plot of the component Murphree efficiencies, $E_i$, as function of the Fourier number.

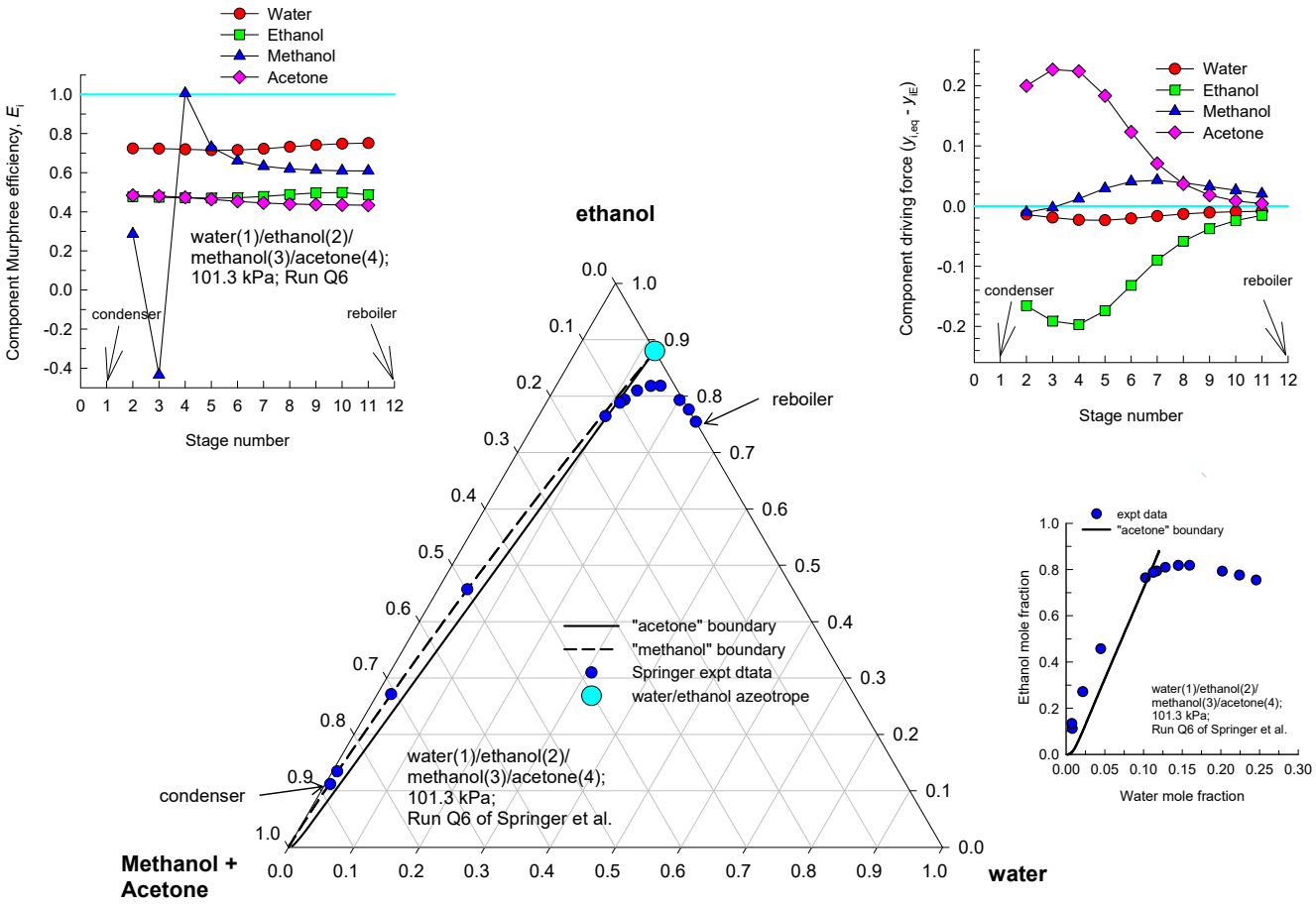


Figure 4-13. Experimental data (blue circles) of Springer et al.[39] for Run Q6 with quaternary water(1)/ethanol(2)/methanol(3)/acetone(4) mixtures. Also shown as insets are the Murphree component efficiencies and component driving forces.

# Murphree Point Efficiencies: Geddes model

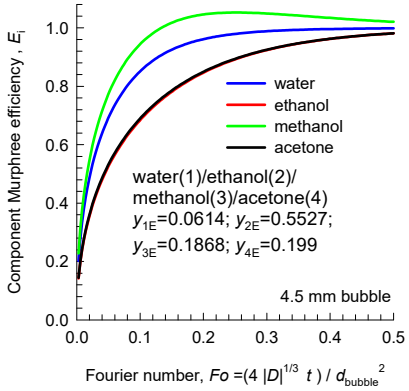


Figure 4-14. Geddes model calculations for the Murhpree point efficiencies on Stage 4. The liquid compositions leaving each stage (= vapor composition entering that stage) are as specified in Table 4-3. The bubble size is taken to be 4.5 mm.

# Boundary crossing with Geddes model

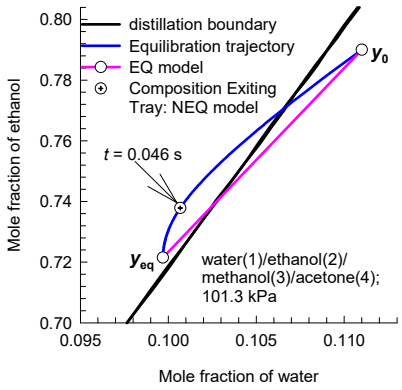


Figure 4-15. Equilibration trajectory for water(1)/ethanol(2)/methanol(3)/acetone(4) mixtures calculated with the Geddes model.[46]

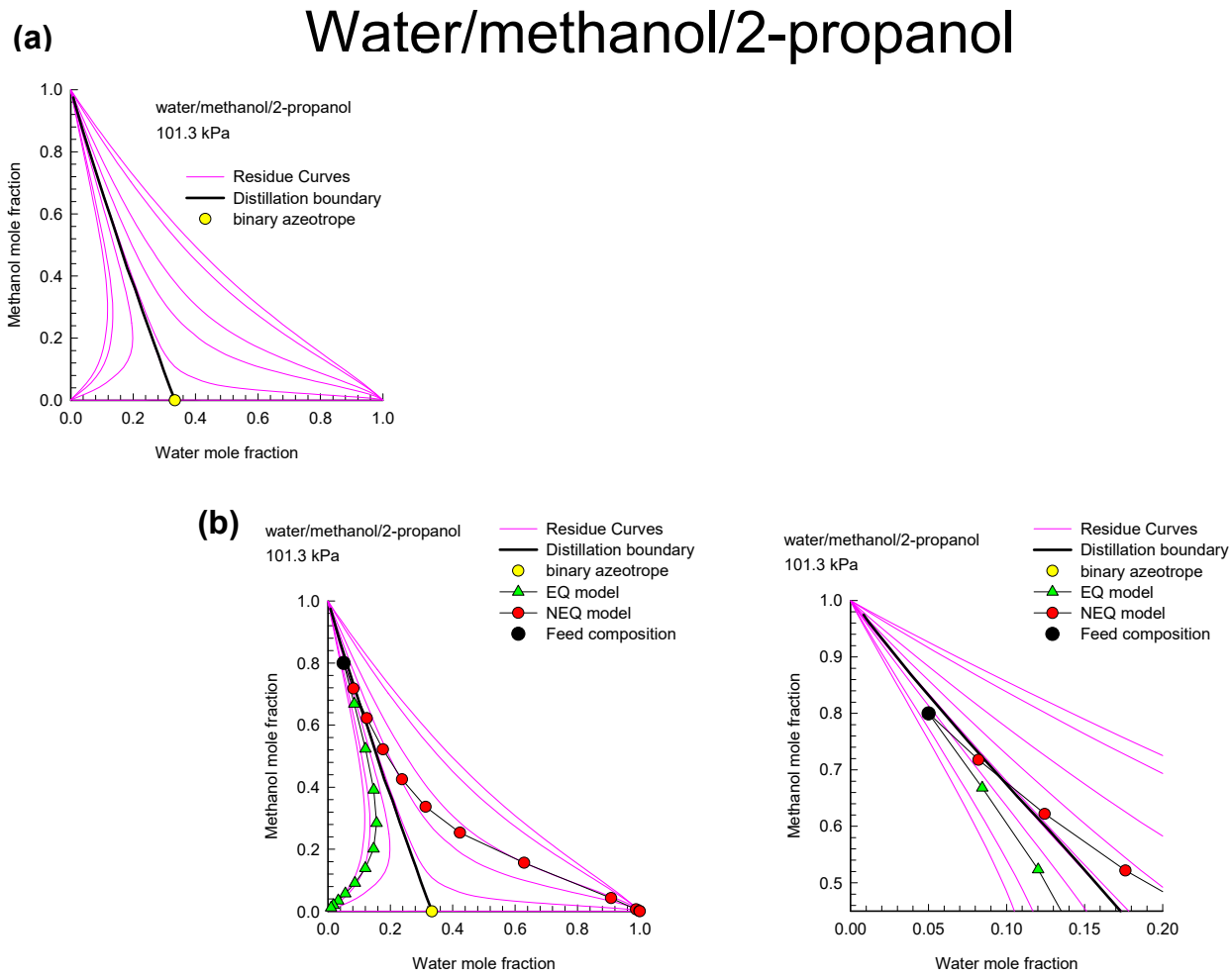


Figure 4-16. (a) Residue curve map for the water/methanol/2-propanol system, showing a straight-line distillation boundary and feed locations F1 and F2 on either side of the distillation boundary. (b) Comparison of EQ and NEQ distillation trajectories.

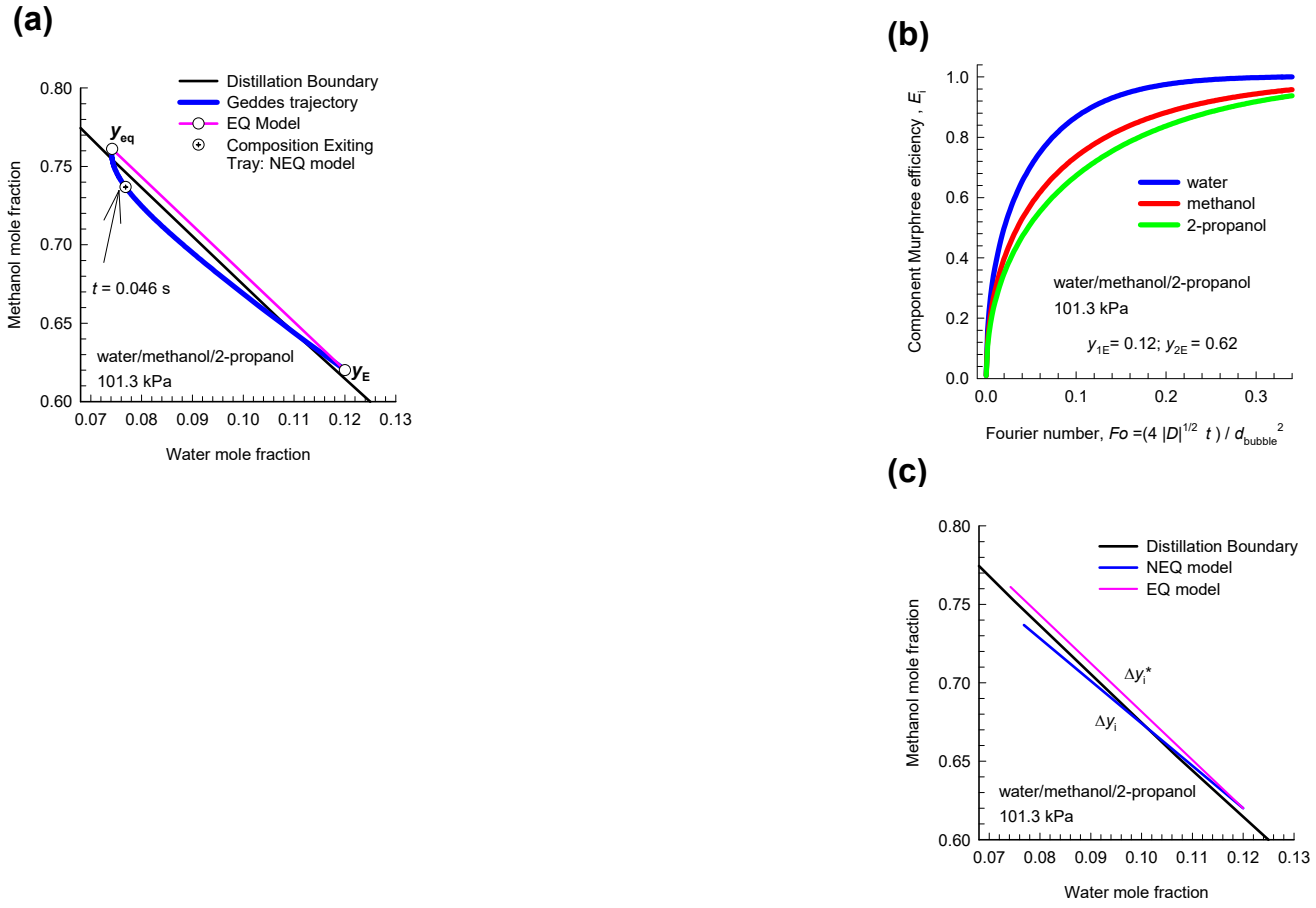


Figure 4-17. (a) Transient equilibration trajectories for the system water(1)/methanol(2)/2-propanol(3) at 101.3 kPa. The initial mole fractions in the rigid spherical vapor bubble are $y_{10}$ = 0.12, $y_{20}$ = 0.62, and $y_{30}$ = 0.26. The final equilibrium compositions are $y_{1,eq}$ = 0.0742, $y_{2,eq}$ = 0.76109, and $y_{3,eq}$ = 0.1647. (b) Plot of the component Murphree efficiencies, $E_i$, as function of the Fourier number. (c) Comparison of the NEQ and EQ trajectory vectors.

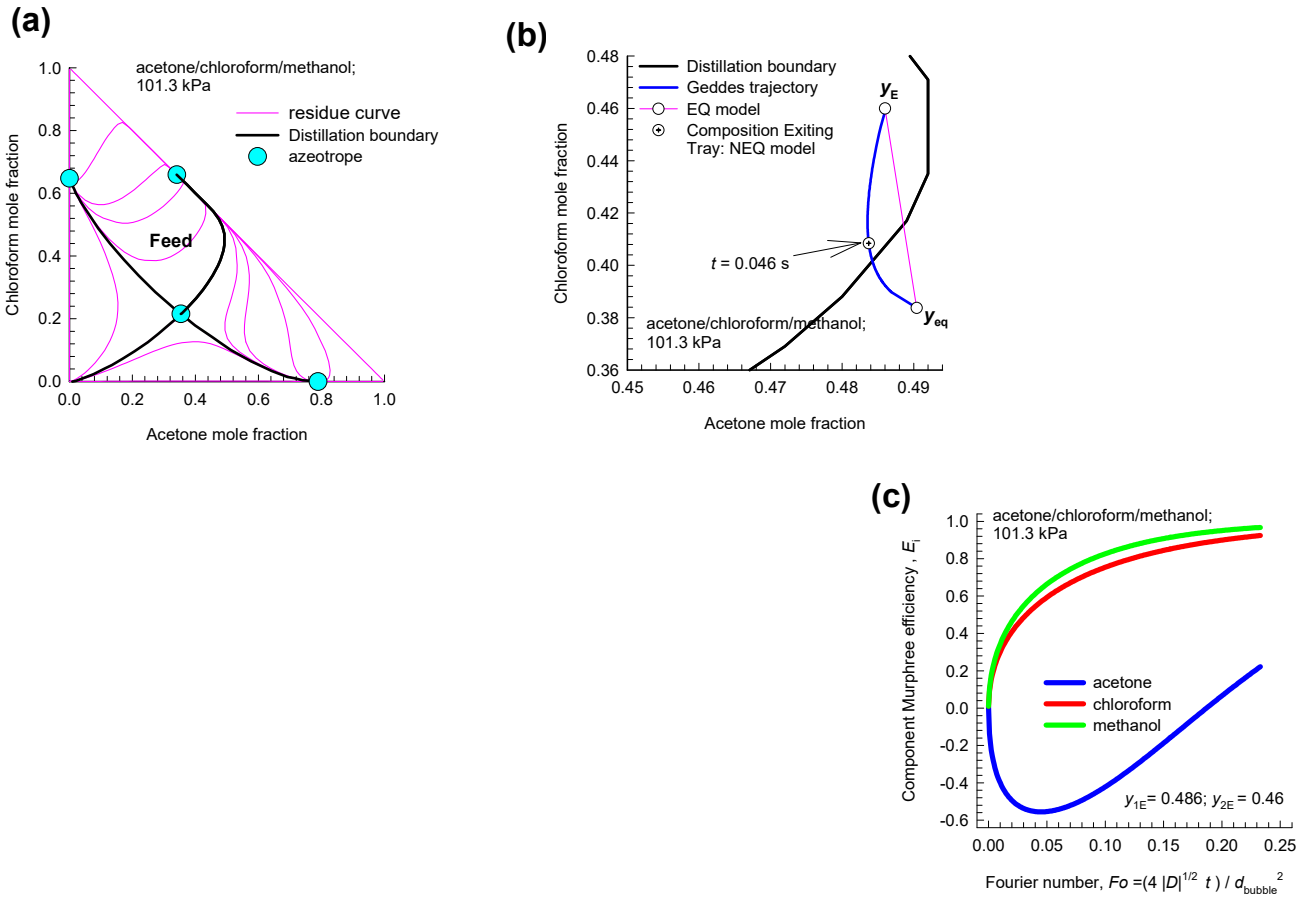


Figure 4-18. (a) Residue curve map for the acetone/chloroform/methanol system. (b) Transient equilibration trajectories for the system acetone(1)/chloroform(2)/methanol(3) at 101.3 kPa. The initial mole fractions in the rigid spherical vapor bubble are $y_{10}$ = 0.486, $y_{20}$ = 0.46, and $y_{30}$ = 0.054. The final equilibrium compositions are $y_{1,eq}$ = 0.49042, $y_{2,eq}$ = 0.38374, and $y_{3,eq}$ = 0.12584. (c) Plot of the component Murphree efficiencies, $E_i$, as function of the Fourier number.

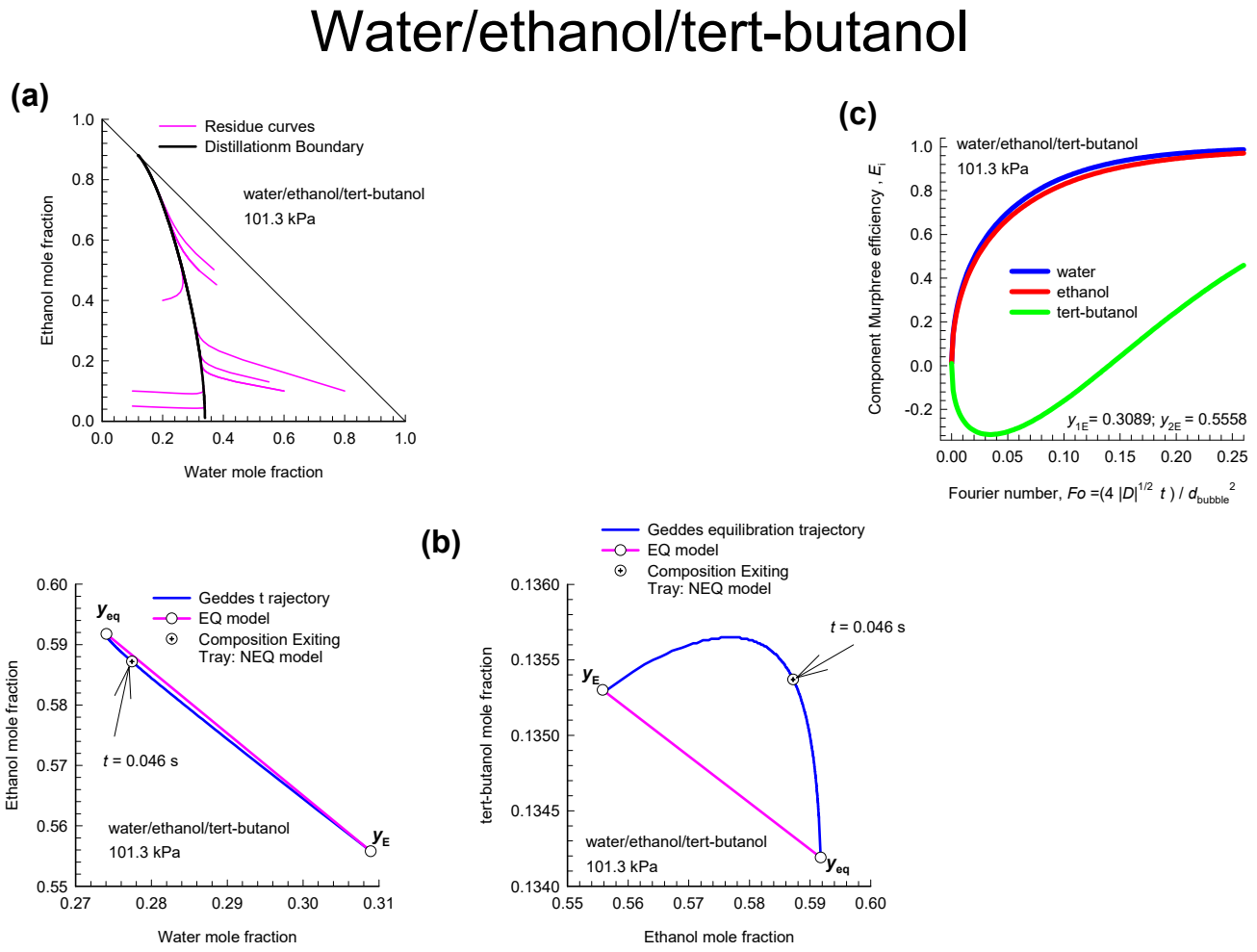


Figure 4-19. (a) Residue curve map for the water(1)/ethanol(2)/tert-butanol(3) system. (b) Transient equilibration trajectories for the system water(1)/ethanol(2)/tert-butanol(3) at 101.3 kPa. The initial mole fractions in the rigid spherical vapor bubble are $y_{10}$ = 0.3089, $y_{20}$ = 0.5558, and $y_{30}$ = 0.436. The final equilibrium compositions are $y_{1,eq}$ = 0.27405, $y_{2,eq}$ = 0.59176, and $y_{3,eq}$ = 0.13419. (c) Plot of the component Murphree efficiencies, $E_i$, as function of the Fourier number.

# 5 Influence of Phase Stability on Diffusivities

The phase equilibrium thermodynamics has a significant influence on the diffusion characteristics. This is illustrated below for a variety of binary and ternary mixtures.

## 5.1 The Darken correction factor for non-ideal thermodynamics

For binary fluid mixtures, the Fick, Maxwell-Stefan, and Onsager diffusivities are inter-related:

$$D_{12} = Đ_{12}\Gamma = L_{12}\Theta = L_{12}\frac{1}{x_1 x_2}\Gamma; \quad \Gamma = \left(1 + \frac{\partial \ln \gamma_1}{\partial \ln x_1}\right) \tag{5-1}$$

In the pioneering papers by Darken[54, 55] the following expression is postulated for the composition dependence of the Fick diffusivity $D_{12}$

$$D_{12} = \left(x_2 D_1^* + x_1 D_2^*\right)\left(1 + \frac{\partial \ln \gamma_1}{\partial \ln x_1}\right) = \left(x_2 D_{1,self} + x_1 D_{2,self}\right)\left(1 + \frac{\partial \ln \gamma_1}{\partial \ln x_1}\right) \tag{5-2}$$

where $D_1^* \equiv D_{1,self}$, and $D_2^* \equiv D_{2,self}$ are the tracer diffusivities (also named *self*-diffusivities, $D_{1,\mathrm{self}}$ and $D_{2,\mathrm{self}}$) in the binary mixture. Darken[54, 55] was one of the first to recognize the need to use activity gradients as proper driving forces when setting up the phenomenological relations to describe diffusion. The thermodynamic factor $\Gamma$ is also referred to as the "Darken correction factor". Combining equations equations , and we obtain the following expression for the composition dependence of the M-S diffusivity $Đ_{12}$ for a binary mixture

$$Đ_{12} = x_2 D_{1,self} + x_1 D_{2,self} \tag{5-3}$$

The tracer or *self*-diffusivities, $D_1^* \equiv D_{1,self}$, and $D_2^* \equiv D_{2,self}$ are more easily accessible, both experimentally[56-58] and from Molecular Dynamics (MD) simulations,[59] than the $Đ_{12}$.

A somewhat more accurate interpolation formula is the empirical Vignes relation[59, 60]

$$Đ_{12} = \left(Đ_{12}^{x_1 \to 1}\right)^{x_1} \left(Đ_{12}^{x_2 \to 1}\right)^{x_2} \tag{5-4}$$

where the limiting values of the M-S diffusivities are

$$D_{2,self}^{x_1 \to 1} = Đ_{12}^{x_1 \to 1}; \quad D_{1,self}^{x_2 \to 1} = Đ_{12}^{x_2 \to 1} \tag{5-5}$$

Generally speaking, the factoring out of the effects of non-ideal mixture thermodynamics (by use of $\frac{D_{12}}{\Gamma} = Đ_{12}$) results in a milder variation of the M-S diffusivity as compared to the Fick diffusivity.

The Vignes interpolation formula (5-4) offers the possibility of interpolation using data at either ends of the composition scale. To verify this, Figure 5-1(a,b,c) present comparison of the Fick, and M-S, and Onsager diffusivities for (a) acetone (1) – water (2), (b) ethanol (1) – water (2) and (c) methanol(1)/n-hexane (2) mixtures along with the estimations using using the Vignes interpolation formula (5-4). We see that that the interpolation formula is of good accuracy. Further examination of the validity of the Vignes interpolation formula in available in published works.[1, 61-65]

The Onsager diffusivity is related to the M-S diffusivity by

$$L_{12} = x_1 x_2 Đ_{12} = \frac{D_{12}}{\Gamma} \tag{5-6}$$

The $L_{12}$ vanishes at either ends of the composition scale (cf. Figure 5-1) and this characteristic makes it less desirable for use in practical applications.[1, 9, 34, 66, 67]

## 5.2 Thermodynamic corrections for dense gaseous mixtures

The M-S pair diffusivities $Đ_{ij}$ for gaseous mixtures at low pressures, below about 10 bar, can be estimated to a good level of accuracy using the Fuller-Schettler-Giddings (FSG)[14] method.

$$Đ_{12} = \frac{1.43 \times 10^{-7} T^{1.75}}{p\sqrt{M_{12}}\left[\left(v_1^{1/3}\right) + \left(v_2^{1/3}\right)\right]^2} \quad \mathrm{m^2 s^{-1}} \tag{5-7}$$

where $p$ is the pressure (expressed in bars), $M_{12} = \frac{2}{\frac{1}{M_1} + \frac{1}{M_2}}$ is the mean molecular weight of the mixture (expressed in g $\mathrm{mol^{-1}}$), $v_1$, and $v_2$ are the diffusion volumes (expressed in $\mathrm{cm^3\ mol^{-1}}$) whose

values are obtained by summing the contributions of the volumes of the constituent atoms in the molecular species (the values are tabulated in Table 11.1 of Reid, Prausnitz, and Poling[15]). According to the FSG estimation procedure, the product of $Đ_{12}$ and the total pressure, $p$, is a function only of temperature and is also independent of composition. In generalizing the FSG method to dense gas mixtures, it is important realize that equation (3-5) implies that, *at constant temperature*, the M-S diffusivity is *inversely* proportional to the molar density of the gas phase. For dense gases, the total mixture molar density of the gas phase is $c_t = \frac{p}{ZRT}$ where $Z$ is the compressibility factor. Consequently, the M-S diffusivity for dense gases can be estimated by correcting the original FSG equation by introducing the compressibility factor $Z$; see Krishna and van Baten[11] for further details

$$Đ_{12} = \frac{1.43\times 10^{-7} T^{1.75}}{p\sqrt{M_{12}}\left[\left(v_1^{1/3}\right)+\left(v_2^{1/3}\right)\right]^2} Z \tag{5-8}$$

Due to the introduction of the compressibility factor, $Z$, the M-S diffusivity $Đ_{12}$ becomes dependent on mixture composition. The molar density of the mixture is $c_t = \frac{p}{ZRT}$, and therefore Equation (3-6) anticipates that $c_t Đ_{12}$ is constant at constant temperature $T$.

The Fick diffusivity for dense gas mixtures can be estimated by multiplying M-S diffusivity $Đ_{12}$, determined from Equation (3-6), with the thermodynamic correction factor $\Gamma$

$$D_{12} = Đ_{12}\Gamma = D_{12}^{FSG} Z\Gamma; \quad \Gamma \equiv \left(1+\frac{\partial \ln \phi_1}{\partial \ln x_1}\right) \tag{5-9}$$

The thermodynamic correction factor is determinable by analytic differentiation of an Equation of State (EOS) such as the Peng-Robinson (PR) EOS; for further details see Krishna and van Baten.[11] For binary mixtures, explicit analytic expressions for $\Gamma = x_1 \frac{\partial \ln f_1}{\partial x_1} = \delta_{ij} + x_1 \frac{\partial \ln \phi_1}{\partial x_1}$ for PR EOS are provided in the paper by Tuan et al.[12]

Figure 5-2(a) presents the experimental data of Nishiumi and Kubota[68] for diffusivity of benzene in supercritical $CO_2$ as a function of the reduced pressure, $p/p_c$. The deep well in the experimental Fick

diffusivity at the reduced pressure, $p/p_c \approx 1$ can be rationalized by equation (5-9) taking:

$D_{12} = \frac{8\times10^{-7}}{p} Z\left(1+\frac{\partial \ln \phi_1}{\partial \ln x_1}\right)$ $\mathrm{m^2 s^{-1}}$ for $x_1$ = 0.005, 0.007, 0.01, 0.013, and 0.017; Figure 5-2(b).

## 5.3 Diffusivities in PbTe/PbS crystalline mixtures

Consider the phase equilibrium thermodynamics for PbTe(1)/PbS(2) crystalline mixtures on its diffusion characteristics. This mixture may also be represented as $Pb(Te_{x1}S_{x2})$, with $x_1 + x_2 = 1$. Consequently, are the mole fractions of the cations Te, and S in the $Pb(Te_{x1}\ S_{x2})$ crystalline matrix.

The molar Gibbs free energy

$$\frac{G}{RT} = \frac{G^{ex}}{RT} + \left(x_1 \ln x_1 + x_2 \ln x_2\right); \quad \frac{G^{ex}}{RT} = \left(x_1 \ln \gamma_1 + x_2 \ln \gamma_2\right) \tag{5-10}$$

can be calculated using using the sub-regular solution model with parameters provided in Table 1 of Leute.[69] The vanishing of the second derivative of the Gibbs free energy

$$\frac{\partial^2 G}{\partial x_1^2} = 0 \tag{5-11}$$

delineates the limits of phase instability; this defines the spinodal curve. The second derivative of the Gibbs free energy is simply related to the thermodynamic factor, $\Gamma$,

$$\frac{1}{RT}\frac{\partial^2 G}{\partial x_1^2} = \frac{\Gamma}{x_1 x_2}; \quad \Gamma = \left(1+\frac{\partial \ln \gamma_1}{\partial \ln x_1}\right); \quad x_2 = 1 - x_1 \tag{5-12}$$

Figure 5-3(a) shows the calculations of the spinodal curve. The critical temperature is 1074 K, and the critical composition is $x_1$ = 0.38. Figure 5-3(b) shows calculations of the thermodynamic correction factor, $\Gamma$, at various temperatures. For temperatures below 1074 K, there is a range of compositions for which $\Gamma < 0$; within this region, the mixture is unstable and will undergo spinodal decomposition.

For binary $Pb(Te_{x1}\ S_{x2})$ mixtures, the Fick diffusivity, $D$, is the product of the Maxwell-Stefan diffusivity, $Đ$, and the thermodynamic factor, $\Gamma$

$$D = Đ\Gamma \tag{5-13}$$

The strong influence of the thermodynamic factor on the composition dependence of the Fick diffusivity is underscored by the experimental data of Leute[69] on the Fick diffusivity, $D$, for inter-diffusion of Te and S cations in PbTe(1)/PbS(2) crystalline mixtures of varying compositions at different temperatures: 973 K, 998 K, 1023 K, 1048 K, 1073 K, and 1098 K; see Figure 5-4(a,b,c), and Figure 5-5(a,b,c). Also plotted (continuous solid blue lines) using the right $y$-axis in Figure 5-4(a,b,c), and Figure 5-5(a,b,c) are the thermodynamic correction factor, $\Gamma$, at the corresponding temperatures. The Fick diffusivity is seen to reduce by one to two orders of magnitude as the critical composition is approached, in line with the calculations of $\Gamma$. For more detailed discussions, see Leute.[69]

## 5.4 Diffusivities in aqueous glycine and urea solution

Figure 5-6(a) shows the experimental data of Chang and Myerson[70] for the diffusivity of glycine in aqueous solutions at temperatures of 298.15 K and 308.15 K. The Fick diffusivity plummets to vanishingly low values as the spinodal compositions are reached. Figure 5-6(b) shows analogous Fick diffusivity data for urea as a function of solute concentration in aqueous solutions at $T$ =298.15 K.[71] The strong concentration dependence of the Fick diffusivity $D_{12}$ is dictated by the thermodynamic factor $\Gamma$.

## 5.5 Darken and Vignes interpolation formulae for ternary liquid mixtures

For diffusion in $n$-component non-ideal liquid mixtures, the matrix of Fick diffusivities $[D]$ has significant non-diagonal contributions caused by (a) differences in the binary pair M-S diffusivities, $Đ_{ij}$, and (b) strong coupling introduced by the matrix of thermodynamic factors $[\Gamma]$.

The description of the composition dependence of the M-S diffusivities $Đ_{ij}$ in liquid mixtures containing three or more species is much less developed. Krishna and van Baten[59] postulate that the M-S diffusivity of the $i$-$j$ pair in the ternary $i$-$j$-$k$ mixture depends on $D_{i,self}$ and $D_{j,self}$ in this mixture, but weighted with mole fractions on a $k$-free basis, i.e.

$$Đ_{ij} = \frac{x_i}{x_i + x_j} D_{j,self} + \frac{x_j}{x_i + x_j} D_{i,self} \tag{5-14}$$

Each of the three M-S pair diffusivities $Đ_{ij}$ depends on six infinite dilution parameters

$$Đ_{12}^{x_1 \to 1}; \quad Đ_{12}^{x_2 \to 1}; \quad Đ_{13}^{x_1 \to 1}; \quad Đ_{13}^{x_3 \to 1}; \quad Đ_{23}^{x_2 \to 1}; \quad Đ_{23}^{x_3 \to 1} \tag{5-15}$$

These limiting values of $Đ_{ij}$ at the edges of the ternary composition space are

$$\begin{aligned}
&Đ_{12}^{x_1 \to 1} = D_{2,self}^{x_1 \to 1}; \quad Đ_{12}^{x_2 \to 1} = D_{1,self}^{x_2 \to 1}; \quad Đ_{12}^{x_3 \to 1} = \frac{x_1}{x_1 + x_2} D_{2,self}^{x_3 \to 1} + \frac{x_2}{x_1 + x_2} D_{1,self}^{x_3 \to 1}; \\
&Đ_{13}^{x_1 \to 1} = D_{3,self}^{x_1 \to 1}; \quad Đ_{13}^{x_3 \to 1} = D_{1,self}^{x_3 \to 1}; \quad Đ_{13}^{x_2 \to 1} = \frac{x_1}{x_1 + x_3} D_{3,self}^{x_2 \to 1} + \frac{x_3}{x_1 + x_3} D_{1,self}^{x_2 \to 1}; \\
&Đ_{23}^{x_2 \to 1} = D_{3,self}^{x_2 \to 1}; \quad Đ_{23}^{x_3 \to 1} = D_{2,self}^{x_3 \to 1}; \quad Đ_{23}^{x_3 \to 1} = \frac{x_2}{x_2 + x_3} D_{3,self}^{x_1 \to 1} + \frac{x_3}{x_2 + x_3} D_{2,self}^{x_1 \to 1};
\end{aligned} \tag{5-16}$$

Noting that the following limiting values hold

$$\begin{aligned}
&Đ_{12}^{x_1 \to 1} = D_{2,self}^{x_1 \to 1}; \quad Đ_{12}^{x_2 \to 1} = D_{1,self}^{x_2 \to 1}; \\
&Đ_{13}^{x_1 \to 1} = D_{3,self}^{x_1 \to 1}; \quad Đ_{13}^{x_3 \to 1} = D_{1,self}^{x_3 \to 1}; \\
&Đ_{23}^{x_2 \to 1} = D_{3,self}^{x_2 \to 1}; \quad Đ_{23}^{x_3 \to 1} = D_{2,self}^{x_3 \to 1};
\end{aligned} \tag{5-17}$$

we derive

$$\begin{aligned}
&Đ_{12}^{x_1 \to 1} = D_{2,self}^{x_1 \to 1}; \quad Đ_{12}^{x_2 \to 1} = D_{1,self}^{x_2 \to 1}; \quad Đ_{12}^{x_3 \to 1} = \frac{x_1}{x_1 + x_2} Đ_{23}^{x_3 \to 1} + \frac{x_2}{x_1 + x_2} Đ_{13}^{x_3 \to 1}; \\
&Đ_{13}^{x_1 \to 1} = D_{3,self}^{x_1 \to 1}; \quad Đ_{13}^{x_3 \to 1} = D_{1,self}^{x_3 \to 1}; \quad Đ_{13}^{x_2 \to 1} = \frac{x_1}{x_1 + x_3} Đ_{23}^{x_2 \to 1} + \frac{x_3}{x_1 + x_3} Đ_{12}^{x_2 \to 1}; \\
&Đ_{23}^{x_2 \to 1} = D_{3,self}^{x_2 \to 1}; \quad Đ_{23}^{x_3 \to 1} = D_{2,self}^{x_3 \to 1}; \quad Đ_{23}^{x_3 \to 1} = \frac{x_2}{x_2 + x_3} Đ_{13}^{x_1 \to 1} + \frac{x_3}{x_2 + x_3} Đ_{12}^{x_1 \to 1};
\end{aligned} \tag{5-18}$$

Equation (5-18) is the proper estimation procedure for $Đ_{ij}^{x_j \to 1}$ that is consistent with the Darken equation (5-3).

For a ternary mixture, Wesselingh and Bollen[72] have suggested the following extension of the Vignes interpolation formula (5-4)

$$Đ_{ij} = \left(Đ_{ij}^{x_i \to 1}\right)^{x_i} \left(Đ_{ij}^{x_j \to 1}\right)^{x_j} \left(Đ_{ij}^{x_k \to 1}\right)^{x_k} \tag{5-19}$$

For the estimation of $Đ_{ij}^{x_k \to 1}$, the *i* - *j* pair diffusivity when both *i* and *j* are present in infinitely dilute concentrations. Krishna and van Baten[59] suggest the following extension of equation (5-16)

$$
\begin{aligned}
Đ_{12}^{x_3\to 1} &= \left(Đ_{13}^{x_3\to 1}\right)^{x_1/(x_1+x_2)}\left(Đ_{23}^{x_3\to 1}\right)^{x_2/(x_1+x_2)}\\
Đ_{13}^{x_2\to 1} &= \left(Đ_{12}^{x_2\to 1}\right)^{x_1/(x_1+x_3)}\left(Đ_{23}^{x_2\to 1}\right)^{x_3/(x_1+x_3)}\\
Đ_{23}^{x_1\to 1} &= \left(Đ_{12}^{x_1\to 1}\right)^{x_2/(x_2+x_3)}\left(Đ_{13}^{x_1\to 1}\right)^{x_3/(x_2+x_3)}
\end{aligned}
\tag{5-20}
$$

For the special case of an equimolar mixture we obtain

$$
\begin{aligned}
Đ_{12}^{x_3\to 1} &= \sqrt{\left(Đ_{13}^{x_3\to 1}Đ_{23}^{x_3\to 1}\right)}\\
Đ_{13}^{x_2\to 1} &= \sqrt{\left(Đ_{12}^{x_2\to 1}Đ_{23}^{x_2\to 1}\right)}\\
Đ_{23}^{x_3\to 1} &= \sqrt{\left(Đ_{12}^{x_1\to 1}Đ_{13}^{x_1\to 1}\right)}
\end{aligned}
\tag{5-21}
$$

The simplified interpolation formula (5-21) was proposed by Wesselingh and Bollen.[72]

The square root of the determinant $|\Lambda|^{1/2}$ may be viewed as a measure of the "magnitude" of the M-S diffusivity that characterizes diffusion in a ternary mixture.

$$
|\Lambda|^{1/2} = \sqrt{\frac{Đ_{12}Đ_{13}Đ_{23}}{x_1Đ_{23}+x_2Đ_{13}+x_3Đ_{12}}}
\tag{5-22}
$$

Close to the regions of phase splitting, the thermodynamic coupling effects predominate and a simple procedure for the estimation of the Fick diffusivity matrix has been proposed[73]

$$
[D] = |\Lambda|^{1/2}[\Gamma]
\tag{5-23}
$$

The accuracy of the estimates using equation (5-23) has been verified by comparison with a very wide range of MD simulations and experimental data. [73]

## 5.6 Diffusivities in partially miscible glycerol/acetone/water mixtures

We examine the influence of phase stability on diffusion in glycerol(1)/acetone(2)/water(3) mixtures for which the liquid-liquid phase equilibrium data has been provided by Krishna et al;[10] see Table 5-1. The binodal and spinodal curves are shown in Figure 5-7. The composition of the plait point is $x_{\text{glycerol}}$= 0.1477, $x_{\text{acetone}}$= 0.4163 and $x_{\text{water}}$= 0.4360. At the plait point, the binodal and spinodal curves converge. Outside the region delineated by the binodal curve, we have the requirement that needs to be fulfilled for phase stability in homogeneous liquid mixtures

$$|\Gamma| > 0; \quad \text{phase stability} \tag{5-24}$$

Within the region delineated by the spinodal curve, there is the region of phase instability

$$|\Gamma| < 0; \quad |D| < 0; \quad \text{phase instability} \tag{5-25}$$

Equation (5-25) implies that one of eigenvalues of the Fick diffusivity matrix [$D$] must be negative. The region between the binodal and spinodal curves is meta-stable. At the plait point, and along the spinodal curve we must have

$$|\Gamma| = 0; \quad |D| = |\Lambda||\Gamma| = 0; \quad \text{spinodal curve} \tag{5-26}$$

So, the determinant $|\Gamma|$ also vanishes along the spinodal curve, and at the plait point, i.e. $|\Gamma| = 0$ .

Grossmann and Winkelmann[74-76] have reported data on the Fick diffusivity matrix [$D$] for glycerol(1)/acetone(2)/water(3) mixtures at 75 different compositions, in the acetone-rich and water-rich regions. To demonstrate the influence of phase stability on the elements of the matrix of Fick diffusivities, we examine a set of four experimental data sets, all measured at a constant glycerol mole fraction: (A) $x_1$= 0.1, $x_2$ = 0.1, $x_3$ = 0.8; (B) $x_1$= 0.1, $x_2$ = 0.3, $x_3$ = 0.6; (C) $x_1$= 0.1, $x_2$ = 0.432, $x_3$ = 0.468; (D) $x_1$= 0.1, $x_2$ = 0.48, $x_3$ = 0.42.

The elements of the Fick diffusivity matrix are indicated in Figure 5-7. At composition A, the experimental data on the elements of the Fick diffusivity are $[D] = \begin{bmatrix} 0.3868 & 0.0184 \\ 0.1477 & 0.407 \end{bmatrix} \times 10^{-9}$ $\text{m}^2\ \text{s}^{-1}$. The importance of diffusional coupling can be quantified by the ratio $\frac{D_{12}D_{21}}{D_{11}D_{22}} = 0.01725$. The matrix of thermodynamic factors at the composition $x_1$= 0.1, $x_2$ = 0.1, $x_3$ = 0.8 is calculated from the NRTL parameters to be $[\Gamma] = \begin{bmatrix} 1.552124 & 0.361702 \\ 0.262193 & 0.656544 \end{bmatrix}$. The importance of thermodynamic coupling is quantified by the factor $\frac{\Gamma_{12}\Gamma_{21}}{\Gamma_{11}\Gamma_{22}} = 0.093064$.

At composition B, $x_1$= 0.1, $x_2$ = 0.3, $x_3$ = 0.6, the experimental data on the elements of the Fick diffusivity are $[D]=\begin{bmatrix}0.4513 & 0.1618\\ 0.2512 & 0.3075\end{bmatrix}\times 10^{-9}$ $m^2\ s^{-1}$. The importance of diffusional coupling can be quantified by the ratio $\frac{D_{12}D_{21}}{D_{11}D_{22}}=0.292879$. The matrix of thermodynamic factors at the composition $x_1$= 0.1, $x_2$ = 0.3, $x_3$ = 0.6 is calculated from the NRTL parameters to be $[\Gamma]=\begin{bmatrix}1.49091 & 0.47104\\ 0.739491 & 0.412104\end{bmatrix}$. The importance of thermodynamic coupling is quantified by the factor $\frac{\Gamma_{12}\Gamma_{21}}{\Gamma_{11}\Gamma_{22}}=0.566933$.

At composition C, $x_1$= 0.1, $x_2$ = 0.432, $x_3$ = 0.468, the experimental data on the elements of the Fick diffusivity are $[D]=\begin{bmatrix}0.495 & 0.2306\\ 0.4839 & 0.4025\end{bmatrix}\times 10^{-9}$ $m^2\ s^{-1}$. The importance of diffusional coupling can be quantified by the ratio $\frac{D_{12}D_{21}}{D_{11}D_{22}}=0.560072$. The matrix of thermodynamic factors at the composition $x_1$= 0.1, $x_2$ = 0.432, $x_3$ = 0.468 is calculated from the NRTL parameters to be $[\Gamma]=\begin{bmatrix}1.442111 & 0.533204\\ 0.95815 & 0.409655\end{bmatrix}$. The importance of thermodynamic coupling is quantified by the factor $\frac{\Gamma_{12}\Gamma_{21}}{\Gamma_{11}\Gamma_{22}}=0.864789$.

At composition D, $x_1$= 0.1, $x_2$ = 0.48, $x_3$ = 0.42, the experimental data on the elements of the Fick diffusivity are $[D]=\begin{bmatrix}0.5684 & 0.30466\\ 0.3476 & 0.3195\end{bmatrix}\times 10^{-9}$ $m^2\ s^{-1}$. The importance of diffusional coupling can be quantified by the ratio $\frac{D_{12}D_{21}}{D_{11}D_{22}}=0.583022$. The matrix of thermodynamic factors at the composition $x_1$= 0.1, $x_2$ = 0.48, $x_3$ = 0.42 is calculated from the NRTL parameters to be $[\Gamma]=\begin{bmatrix}1.422299 & 0.556079\\ 1.007783 & 0.420284\end{bmatrix}$. The importance of thermodynamic coupling is quantified by the factor $\frac{\Gamma_{12}\Gamma_{21}}{\Gamma_{11}\Gamma_{22}}=0.937496$.

As the compositions approach the region of phase instability, the extent of diffusion coupling and thermodynamic coupling both increase; see Figure 5-7. Figure 5-8(a) presents a plot of the ratio $\frac{D_{12}D_{21}}{D_{11}D_{22}}$ of the elements of the Fick diffusivity matrix [$D$] for glycerol(1)/acetone(2)/water(3) mixtures as a function of the ratio $\frac{\Gamma_{12}\Gamma_{21}}{\Gamma_{11}\Gamma_{22}}$. We see a unique dependence between the two sets of data. Along the spinodal curve, both of these ratios tend to unity values, in view of equation (5-26). The important message emerging from Figure 5-8(a) is that diffusional coupling effects become of increasing importance as the compositions approach values corresponding to the spinodal curve.

Figure 5-8(b) presents a plot of $|D|^{1/2}$, that is an appropriate measure of the magnitude of the Fick diffusvity matrix, as a function of the mole fraction of glycerol, $x_1$. We note that $|D|^{1/2}$ tends to vanish as the plait point composition is approached, in conformity with the restraint imposed by equation (5-26). Krishna[45, 73] has demonstrated that the Fick diffusivity matrix [$D$] for glycerol(1)/acetone(2)/water(3) mixtures can be estimated with reasonably good accuracy taking $[D]=|\Lambda|^{1/2}[\Gamma]$ using $|\Lambda|^{1/2}=(D_{1,self})^{x_1}(D_{2,self})^{x_2}(D_{3,self})^{x_3}$, taking $D_{1,\text{self}}$= 0.01, $D_{2,\text{self}}$= 3.2, $D_{3,\text{self}}$= 0.5 with units $10^{-9}$ m$^2$ s$^{-1}$.

## 5.7 Diffusivities in partially miscible water/chloroform/acetic acid mixtures

Figure 5-9 shows the experimental data for liquid/liquid equilibrium in water(1)/chloroform(2)/acetic-acid(3) mixtures. The binodal curve is indicated in green. The spinodal curve is indicated by the red line. The experimental data of Vitagliano et al.[77] for Fick diffusivity matrix [$D$] of water(1)/chloroform(2)/acetic-acid(3) mixtures at five different compositions are shown in Figure 5-9.We note that the influence of diffusional coupling, quantified by $\frac{D_{12}D_{21}}{D_{11}D_{22}}$ progressively increases in magnitude as the compositions become increasingly poorer in acetic acid and the two-phase region is approached. At the plait point (composition: $x_1$ = 0.375, $x_2$ = 0.261 and $x_3$ = 0.364) the matrix of Fick diffusivities determined by Vitagliano et al.[77] by extrapolation of their data is

$[D]=\begin{bmatrix}0.92 & 0.40\\ 0.37 & 0.161\end{bmatrix}\times 10^{-9}$ $m^2\ s^{-1}$. It can be confirmed that the determinant vanishes, i.e. $|D|=0$ because $\frac{\Gamma_{12}\Gamma_{21}}{\Gamma_{11}\Gamma_{22}}=1;\quad |\Gamma|=0;\quad |D|=|\Lambda||\Gamma|=0$.

More recent measurements reported by Buzatu et al.[78] for Fick diffusivity matrix [$D$] of water(1)/chloroform(2)/acetic-acid(3) mixtures at five different compositions are shown in Figure Figure 5-10. A similar trend is observed and the degree of coupling, quantified by $\frac{D_{12}D_{21}}{D_{11}D_{22}}$, increases as the two-phase region is approached.

Figure 5-11(a) presents a plot of $|D|^{1/2}$ as a function of (1- $x_3$) for water(1)/chloroform(2)/acetic-acid(3) mixtures for the two data sets. The magnitude of $|D|^{1/2}$ reduces progressively as the plait point composition is approached; this is in conformity with the restraint imposed by equation (5-26).

In order to demonstrate that the coupling effects in the Fick diffusivity matrix have their origins in the coupling effects of the matrix of thermodynamic factors, Figure 5-11(b) presents a plot of the ratio $\frac{D_{12}D_{21}}{D_{11}D_{22}}$ of the elements of the Fick diffusivity matrix [$D$] for water(1)/chloroform(2)/acetic-acid(3) mixtures as a function of the ratio $\frac{\Gamma_{12}\Gamma_{21}}{\Gamma_{11}\Gamma_{22}}$. We see a unique dependence between the two sets of data. Along the spinodal curve, both of these ratios tend to unity values, in view of equation (5-26). The important message emerging from Figure 5-11 is that diffusional coupling effects become of increasing importance as the compositions approach values corresponding to the spinodal curve.

Krishna[45, 73] has demonstrated that the Fick diffusivity matrix [$D$] for water(1)/chloroform(2)/acetic-acid(3) mixtures can be estimated with reasonably good accuracy taking $[D]=|\Lambda|^{1/2}[\Gamma]$ using $|\Lambda|^{1/2}=\left(D_{1,self}\right)^{x_1}\left(D_{2,self}\right)^{x_2}\left(D_{3,self}\right)^{x_3}$, taking taking $D_{1,self}$= 0.4, $D_{2,self}$= 0.8, $D_{3,self}$= 1.1 with units $10^{-9}$ $m^2\ s^{-1}$.

## 5.8 Diffusivities in partially miscible acetone/water/ethylacetate mixtures

Figure 5-12 shows the phase equilibrium diagram for partially miscible acetone/water/ethylacetate mixtures at 293 K. Pertler[79] reports the values of the elements of the Fick diffusivity matrix in both the ethylacetate-rich and water-rich regions. In each of these two cases, he adopts a different numbering for the components. For the ethylacetate-rich region, the values of the elements of Fick diffusivity matrix [$D$] are reported using the component number acetone(1)/water(2)/ethylacetate(3); the values are plotted in Figure 5-12. Particularly noteworthy is the extremely large negative value of $D_{21}$. The large negative value of $D_{21}$ is caused by the corresponding large negative value of $\Gamma_{21}$, as is evident in the plot on the right upper side of Figure 5-12.

Figure 5-13 presents the experimental data of Pertler[79] for the elements of the Fick diffusivity matrix in the water-rich region of the phase diagram; these values correspond to the component numbering: acetone(1)/ethylacetate(2)/water(3). The negative value of $D_{12}$ is caused by the corresponding large negative value of $\Gamma_{12}$, as is evident in the plot on the left upper side of Figure 5-13.

## 5.9 Diffusivities in glycine/L-valine/water solutions

Lo and Myerson[80] report data on the Fick diffusivity matrix $[D]$ for glycine(1)/L-valine(2)/water(3) solutions. The data were measured as a function of the molar concentration of glycine, $c_1$, at three different L-valine concentrations ($c_2$ = 0.1, 0.3, 0.05 mol L$^{-1}$). Figure 5-14 presents a plot of $|D|^{1/2}$ as a function of the molar concentration of glycine, $c_1$. The magnitude of $|D|^{1/2}$ tends to vanish as the spinodal compositions are approached.

## 5.10 List of Tables for Influence of Phase Stability on Diffusivities

Table 5-1. NRTL parameters for glyercol(1)/acetone(2)/water(3) at 298 K. These parameters are from Krishna et al.[10]

| | $\tau_{ij} = A_{ij}/T$ | $\tau_{ji} = A_{ji}/T$ | $\alpha_{ij} = \alpha_{ji}$ |
|---|---|---|---|
| | dimensionless | dimensionless | dimensionless |
| glycerol(1)/acetone(2) | 0.868 | 2.467 | 0.2 |
| glycerol(1)/water(3) | -1.29 | -1.52 | 0.2 |
| acetone(2)/water(3) | -0.665 | 2.095 | 0.2 |

Table 5-2. UNIQUAC parameters for water(1)/chloroform(2)/acetic-acid(3) at 298 K. These parameters are from Pertler.[79] These parameters needed re-adjustment in order to match the experimental solubility data of Othmer and Ku.[81] The following are the adjusted values used in the calculations.

| | $r_i$ | $q_i$ |
|---|---|---|
| | dimensionless | dimensionless |
| water(1) | 0.92 | 1.4 |
| chloroform(2) | 2.87 | 2.41 |
| acetic-acid(3) | 2.2024 | 2.072 |

| | $\tau_{ij} = \exp(-A_{ij}/T)$ | $\tau_{ji} = \exp(-A_{ji}/T)$ |
|---|---|---|
| | dimensionless | dimensionless |
| water(1)/chloroform(2) | 0.4285 | 0.229 |
| water(1)/acetic-acid(3) | 1.274 | 1.312 |
| chloroform(2)/acetic-acid(3) | 1.388 | 0.885 |

Table 5-3. UNIQUAC parameters for acetone(1)/ethyl-acetate(2)/water(3) at 293 K. These parameters are from Pertler.[79]

| | $r_i$ | $q_i$ |
|---|---|---|
| | dimensionless | dimensionless |
| acetone(1) | 2.5735 | 2.336 |
| ethyl-acetate(2) | 3.4786 | 3.116 |
| water(3) | 0.92 | 1.4 |

| | $\tau_{ij} = \exp(-A_{ij}/T)$ | $\tau_{ji} = \exp(-A_{ji}/T)$ |
|---|---|---|
| | dimensionless | dimensionless |
| acetone(1)/ethyl-acetate(2) | 1.3068 | 0.827 |
| acetone(1)/water(3) | 0.488 | 1.328 |
| ethyl-acetate(2)/water(3) | 0.2538 | 0.7705 |

## 5.11 List of Figures for Influence of Phase Stability on Diffusivities

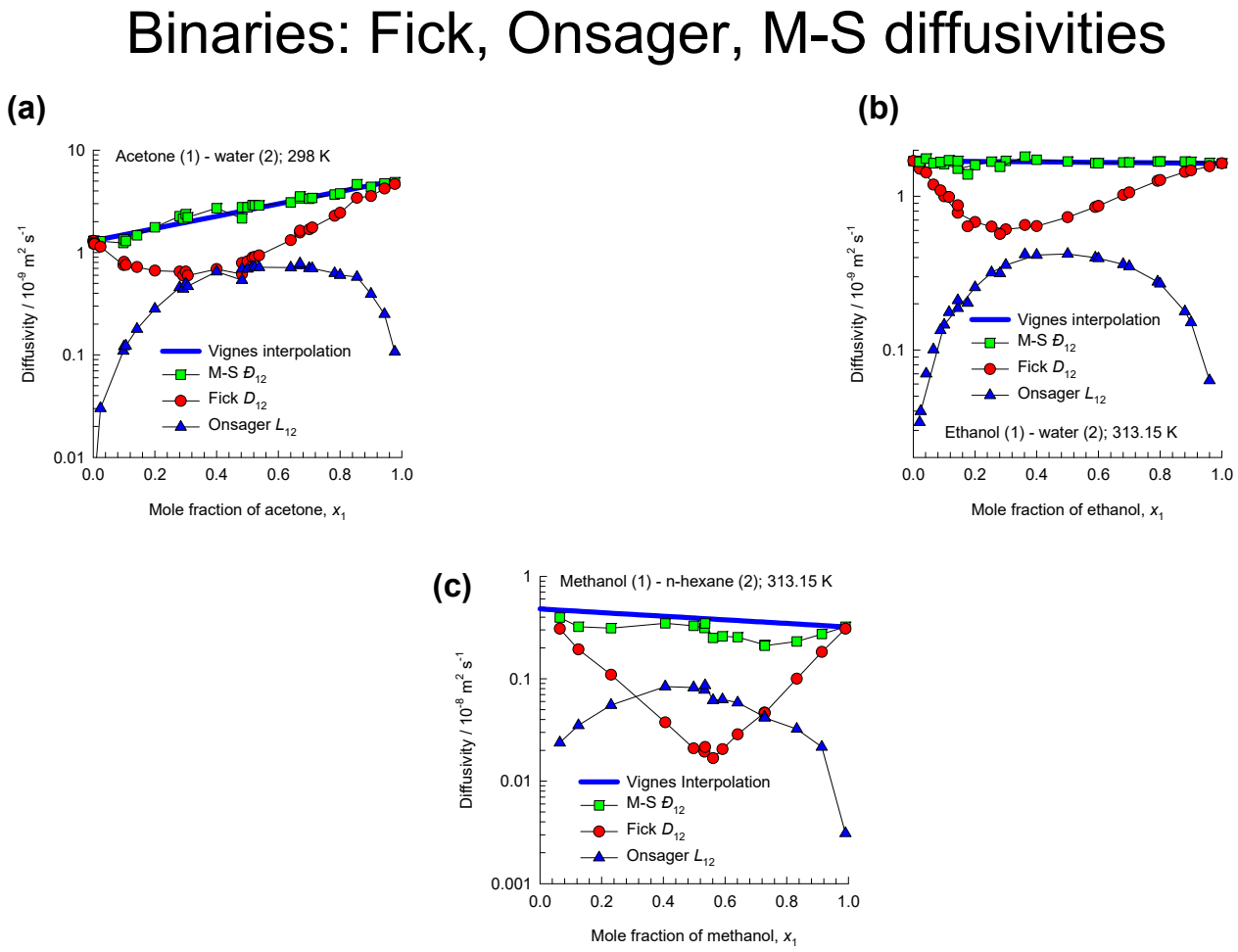


Figure 5-1. Comparison of the Fick diffusivities, $D_{12}$, with the Maxwell-Stefan, $Đ_{12}$, and Onsager, $L_{12}$, diffusivities for (a) acetone (1) – water (2), (b) ethanol(1)-water(2), and (c) methanol(1)-n-hexane (2) mixtures. The experimental data on $D_{12}$ are from Tyn and Calus,[82] Grossmann and Winkelmann,[74] Königer et al,[83] and Clark and Rowley[84] The $Đ_{12}$ are obtained by correcting for the thermodynamic factor $Đ_{12} = \dfrac{D_{12}}{\Gamma}$. Also shown are the calculations using the Vignes interpolation formula (5-4). The Onsager coefficients $L_{12}$ are calculated using equation (5-6).

# Fick diffusivity in benzene/$CO_2$ mixtures

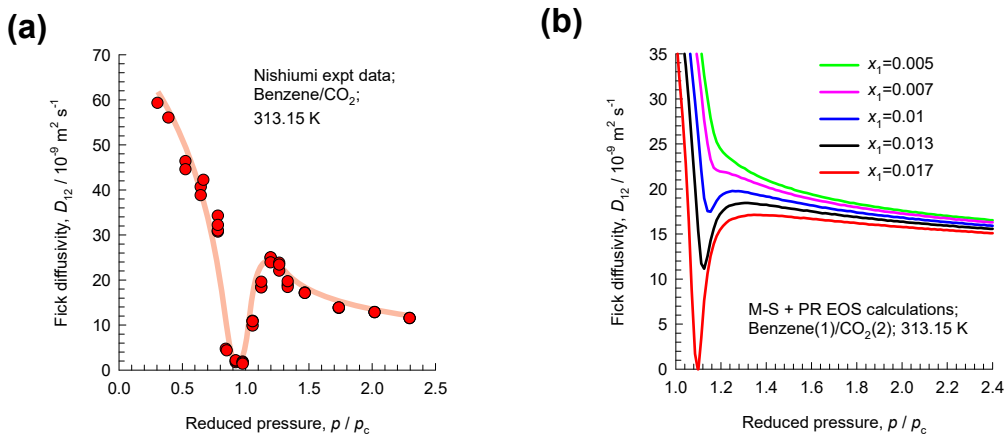


Figure 5-2. (a) Experimental data of Nishiumi and Kubota[68] for diffusivity of benzene (component 1) in supercritical $CO_2$ (component 2) as a function of the reduced pressure, $p_r = \frac{p}{P_{c2}}$ where $P_{c2}$ = 7.28 MPa is the critical pressure of $CO_2$. The measurements were made in a Taylor dispersion tube with varying amounts of benzene injection into the tube. (b) The solid lines are the calculations of the Fick diffusivities as a function of $p/p_c$ and composition of benzene in the mixture using the PR EOS. The PR EOS calculations presented here use a binary interaction parameter $k_{12}$ = 0.0774; for further details see Krishna and van Baten.[11]

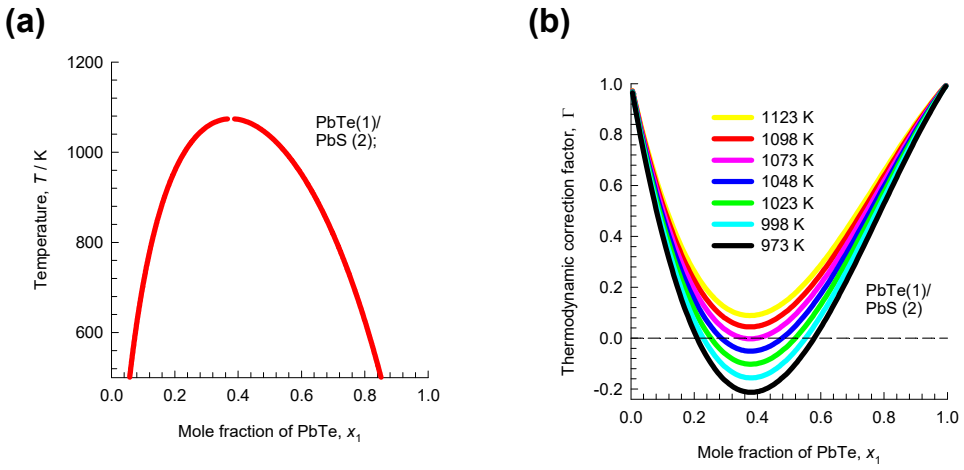


Figure 5-3. Phase equilibrium thermodynamics for PbTe(1)/PbS(2) crystalline mixtures, calculated using the sub-regular solution model with parameters provided in Table 1 of Leute.[69] (a) Spinodal curve $T$-$x_1$ curve. (b) Thermodynamic correction factor, $\Gamma$, at various temperatures.

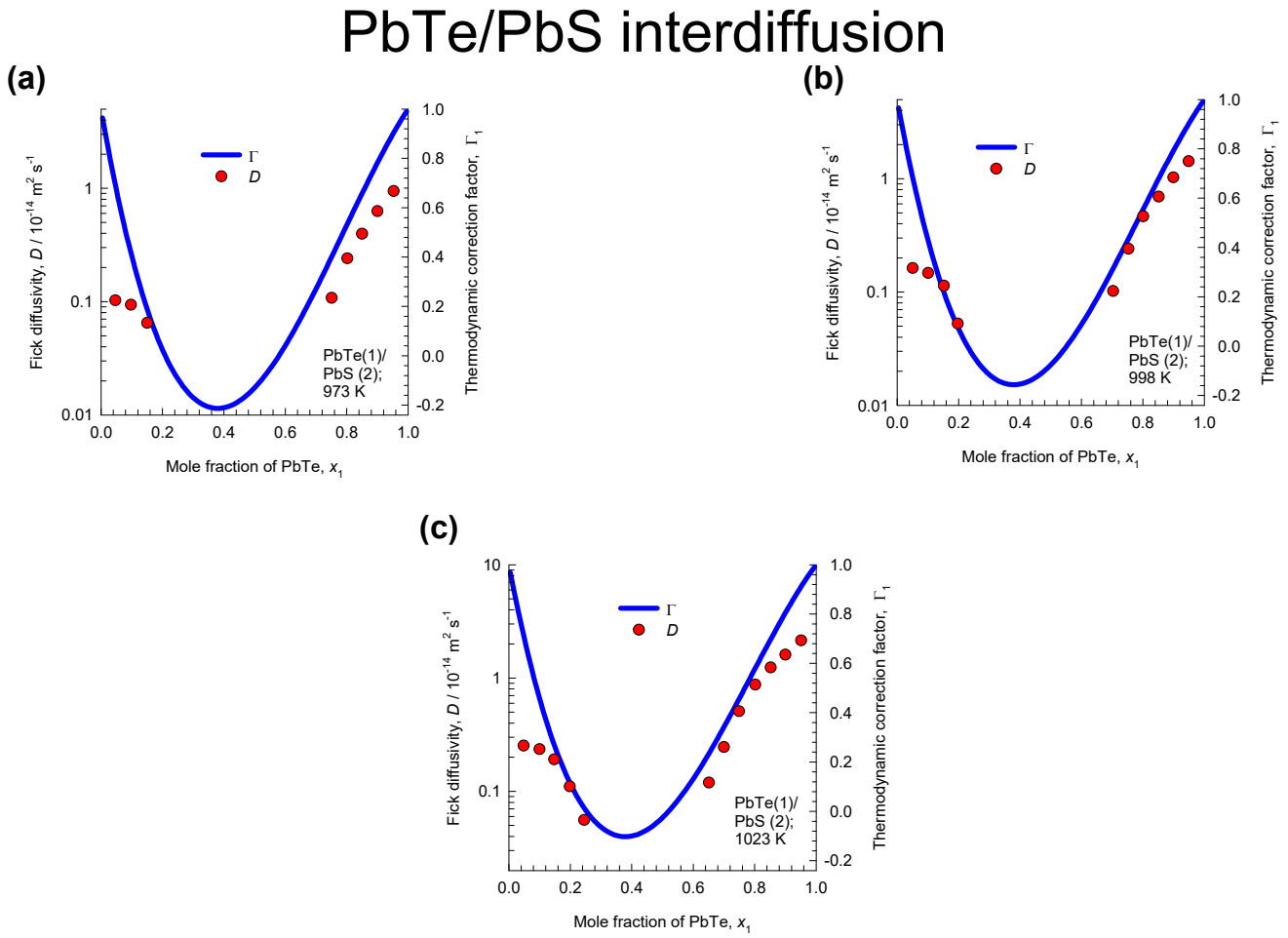


Figure 5-4. Fick diffusivity, $D$, for inter-diffusion of Te and S cations in PbTe(1)/PbS(2) crystalline mixtures of varying compositions at three different temperatures: 973 K, 998 K, and 1023 K; these data are re-plotted using the data scanned from Figure 1a of Leute.[69] Also plotted (continuous solid blue lines) using the right $y$-axis are the thermodynamic correction factor, $\Gamma$, at the corresponding temperatures.

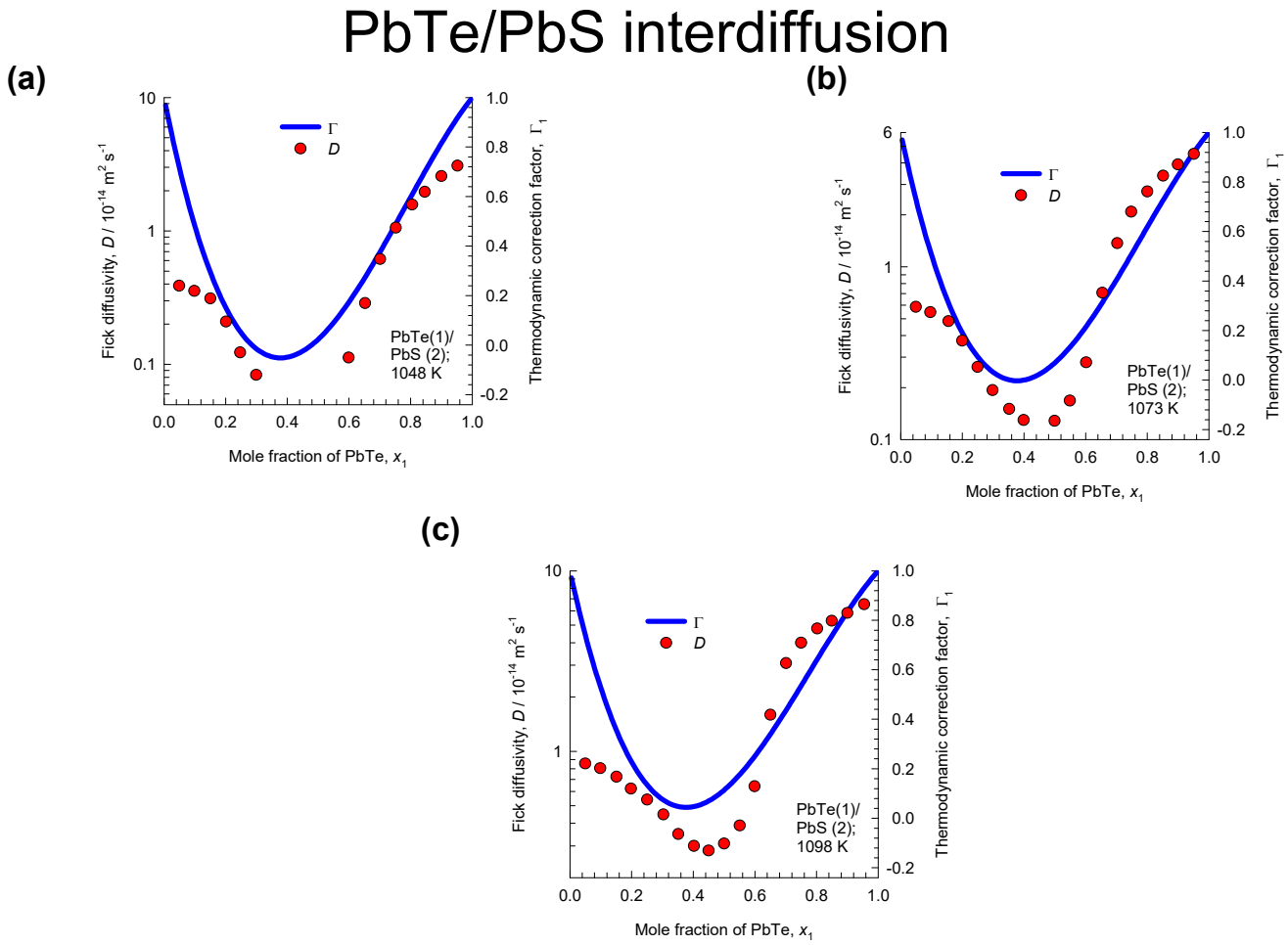


Figure 5-5. Fick diffusivity, $D$, for inter-diffusion of Te and S cations in PbTe(1)/PbS(2) crystalline mixtures of varying compositions at three different temperatures: 1048 K, 1073 K, and 1098 K; these data are re-plotted using the data scanned from Figure 1a of Leute.[69] Also plotted (continuous solid blue lines) using the right $y$-axis are the thermodynamic correction factor, $\Gamma$, at the corresponding temperatures.

# Diffusivity of glycine in water

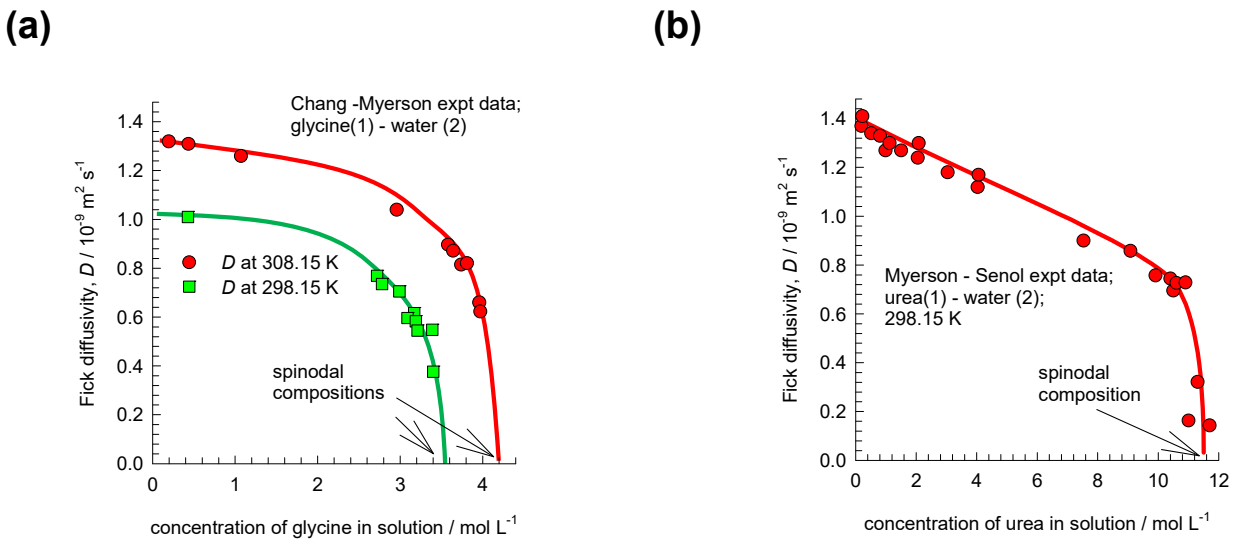


Figure 5-6. (a) Fick diffusivity of glycine as a function of solute concentration in aqueous solutions, at $T$ =298.15 K and 308.15 K.[70] (b) Fick diffusivity of urea as a function of solute concentration in aqueous solutions, at $T$ =298.15 K.[71]

# Fick diffusivity matrix in Glycerol/Acetone/Water

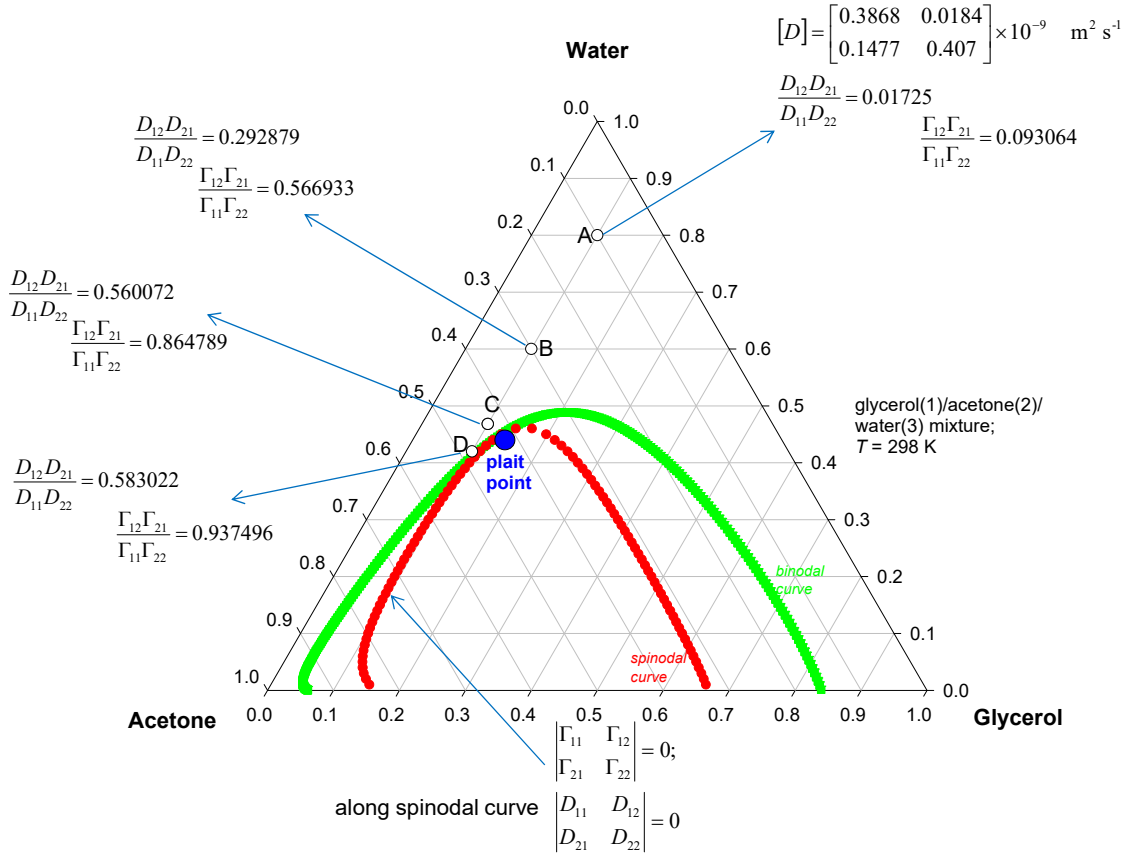


Figure 5-7. The phase equilibrium diagram for glycerol(1)/acetone(2)/water(3) mixtures at 298 K.[10] The composition of the plait point is: $x_{\text{glycerol}}$= 0.1477, $x_{\text{acetone}}$= 0.4163 and $x_{\text{water}}$= 0.4360. Also indicated are the four different compositions for which Grossmann and Winkelmann[74-76] have measured the Fick diffusivity matrix [$D$] for glycerol(1)/acetone(2)/water(3) mixtures. The spinodal curve is calculated using the constraint $|\Gamma| = 0$; for this purpose the phase equilibrium is determined from the NRTL parameters in Table 5-1.

# Coupling effects in Glycerol/Acetone/Water

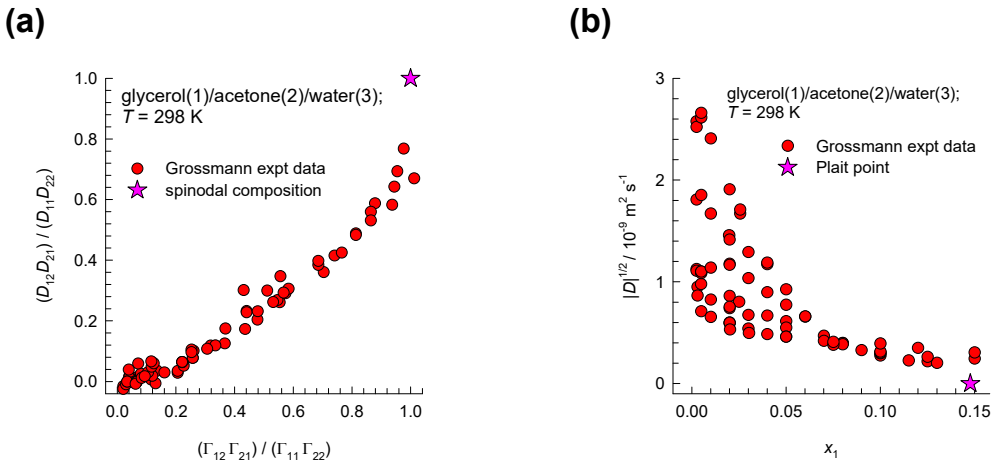


Figure 5-8. (a) The ratio $\frac{D_{12}D_{21}}{D_{11}D_{22}}$ of the elements of the Fick diffusivity matrix [$D$] for glycerol(1)/acetone(2)/water(3) mixtures plotted against the corresponding value of the ratio $\frac{\Gamma_{12}\Gamma_{21}}{\Gamma_{11}\Gamma_{22}}$.(b) Plot of $|D|^{1/2}$ for glycerol(1)/acetone(2)/water(3) mixtures as a function of the mole fraction of glycerol, $x_1$.

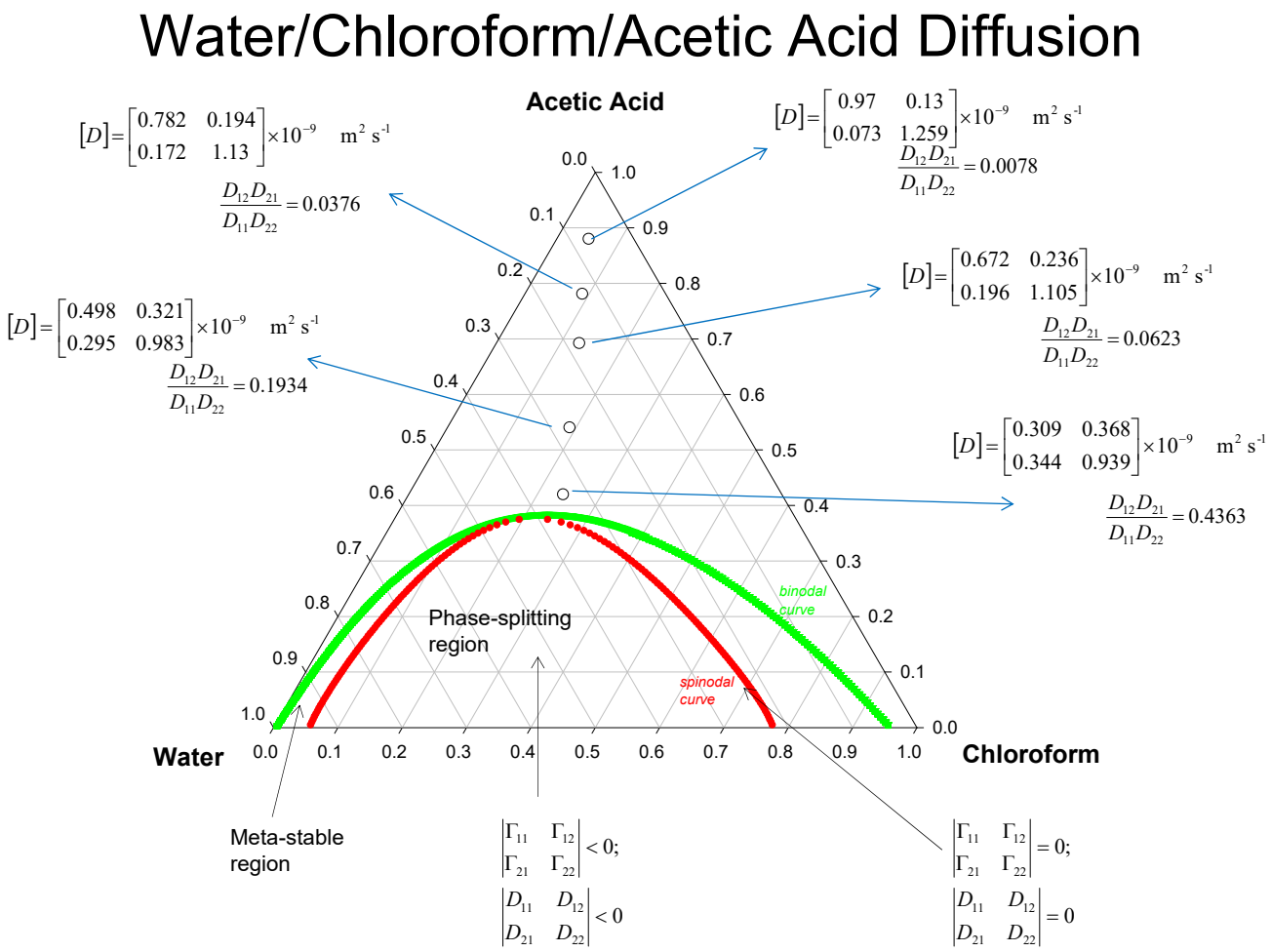


Figure 5-9. Experimental data of Vitagliano et al.[77] for Fick diffusivity matrix [$D$] of water(1)/chloroform(2)/acetic-acid(3) mixtures at six different compositions. The measured values of the Fick matrix [$D$], in units of $10^{-9}$ m$^2$ s$^{-1}$, are indicated. The composition of the plait point is $x_1$ = 0.375, $x_2$= 0.262, $x_3$= 0.363. The binodal curve is from the experimental data of Othmer and Ku.[81] The spinodal curve is obtained from the criterion of phase stability; the UNIQUAC parameters are provided in Table 5-2.

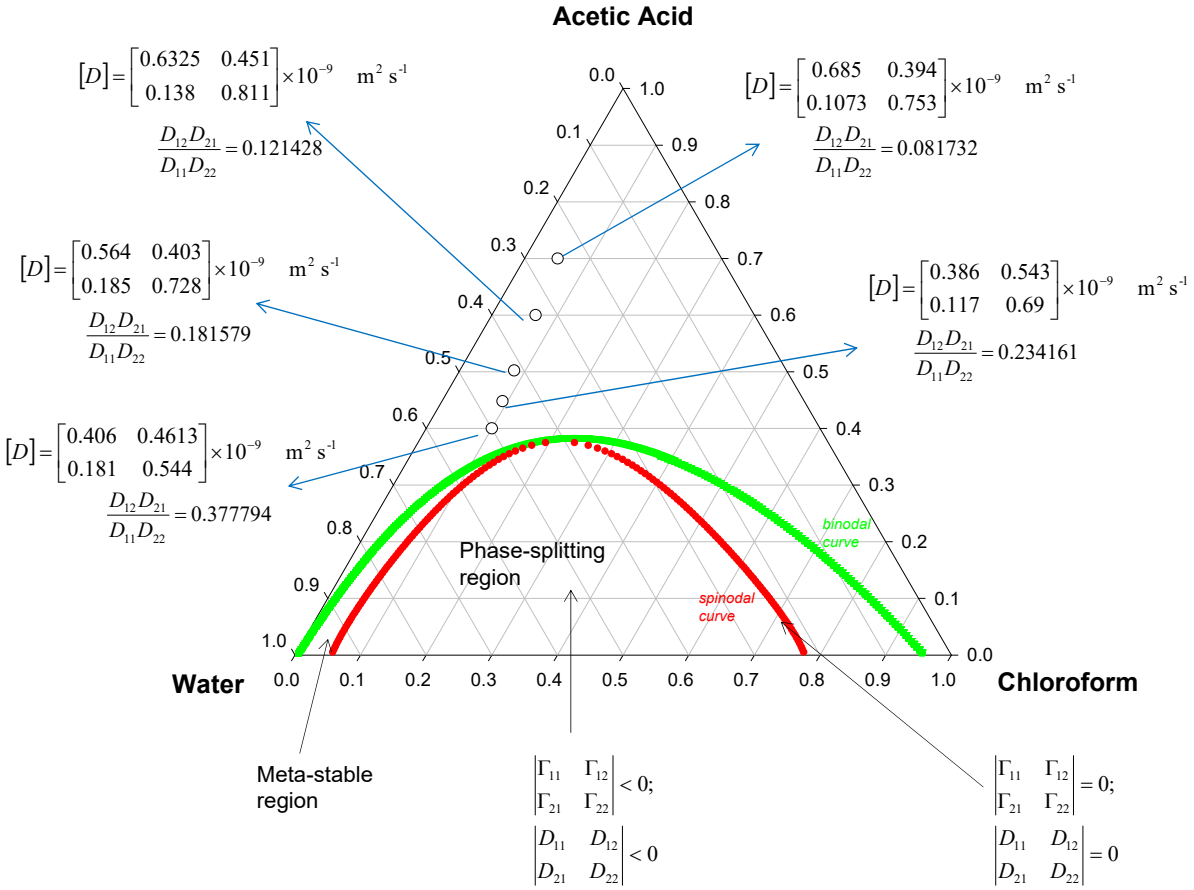


Figure 5-10. Experimental data of Buzatu et al.[78] for Fick diffusivity matrix [$D$] of water(1)/chloroform(2)/acetic-acid(3) mixtures at six different compositions. The measured values of the Fick matrix [$D$], in units of $10^{-9}$ m$^2$ s$^{-1}$, are indicated. The composition of the plait point is $x_1$ = 0.375, $x_2$= 0.262, $x_3$= 0.363. The binodal curve is from the experimental data of Othmer and Ku.[81] The spinodal curve is obtained from the criterion of phase stability; the UNIQUAC parameters are provided in Table 5-2.

# Water/Chloroform/Acetic Acid: Coupling effects in Diffusion

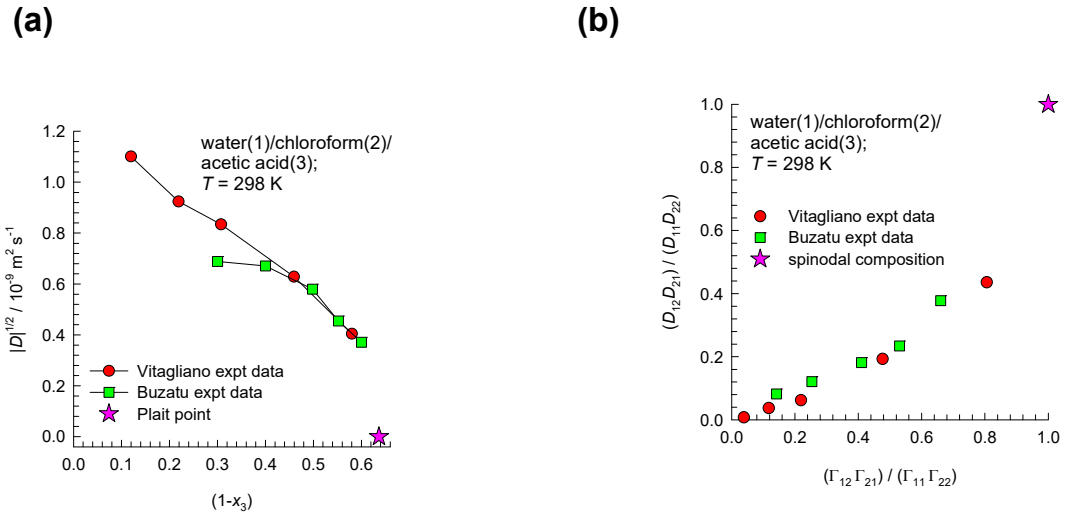


Figure 5-11. (a) Plot of $|D|^{1/2}$ as a function of (1- $x_3$) for water(1)/chloroform(2)/acetic-acid(3) mixtures. (b) The ratio $\frac{D_{12}D_{21}}{D_{11}D_{22}}$ of the elements of the Fick diffusivity matrix [$D$] for water(1)/chloroform(2)/acetic-acid(3) mixtures plotted against the corresponding value of the ratio $\frac{\Gamma_{12}\Gamma_{21}}{\Gamma_{11}\Gamma_{22}}$.

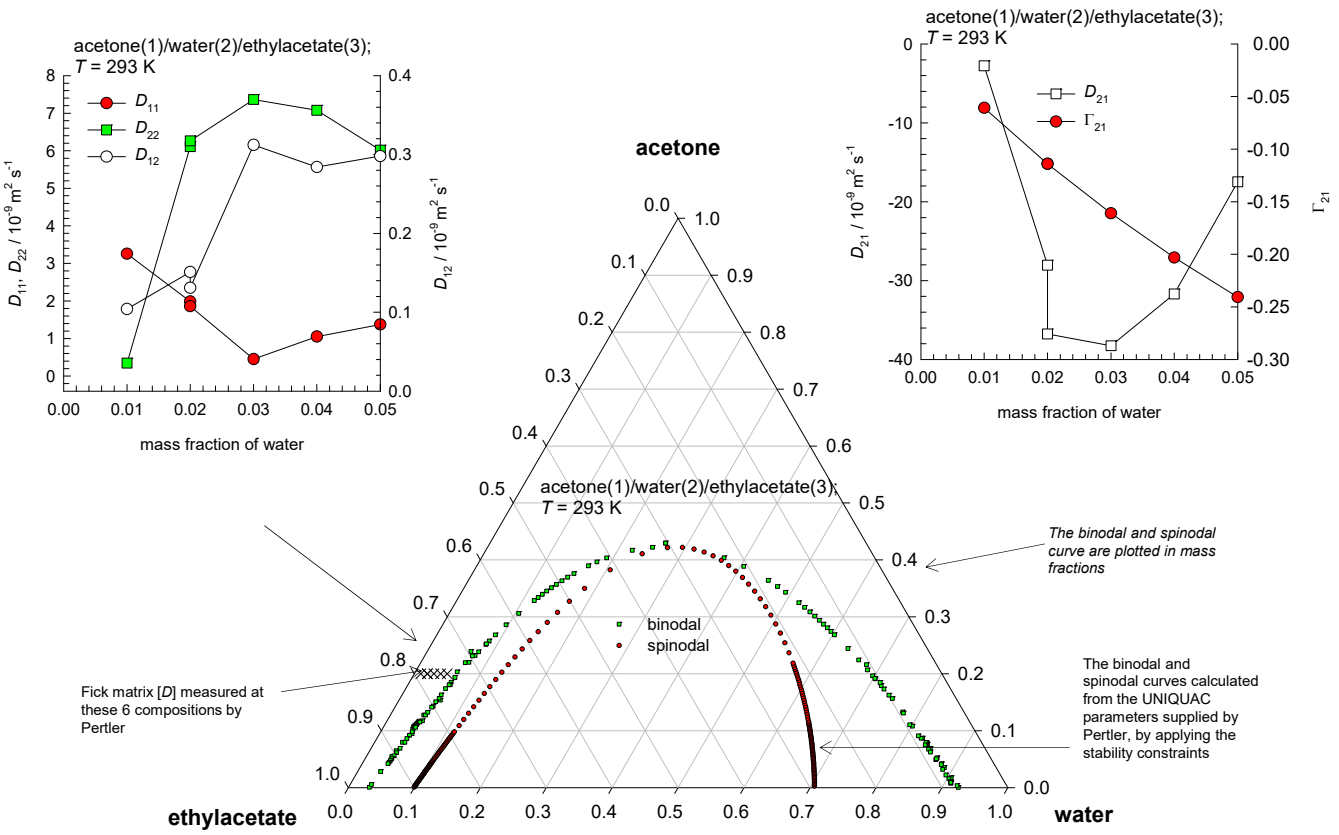


Figure 5-12. Phase equilibrium diagram for acetone/water/ethylacetate mixtures at 293 K. The binodal curve data is from Haeberl and Blass.[85] The spinodal curve is obtained from the criterion of phase stability; the UNIQUAC parameters are provided Table 5-3. Also indicated are the six experimental values of of Pertler[79] for the elements of the Fick diffusivity matrix in the ethylacetate-rich region of the phase diagram; these values correspond to the component numbering: acetone(1)/water(2)/ethylacetate(3). Note that the phase diagram is plotted in mass fractions.

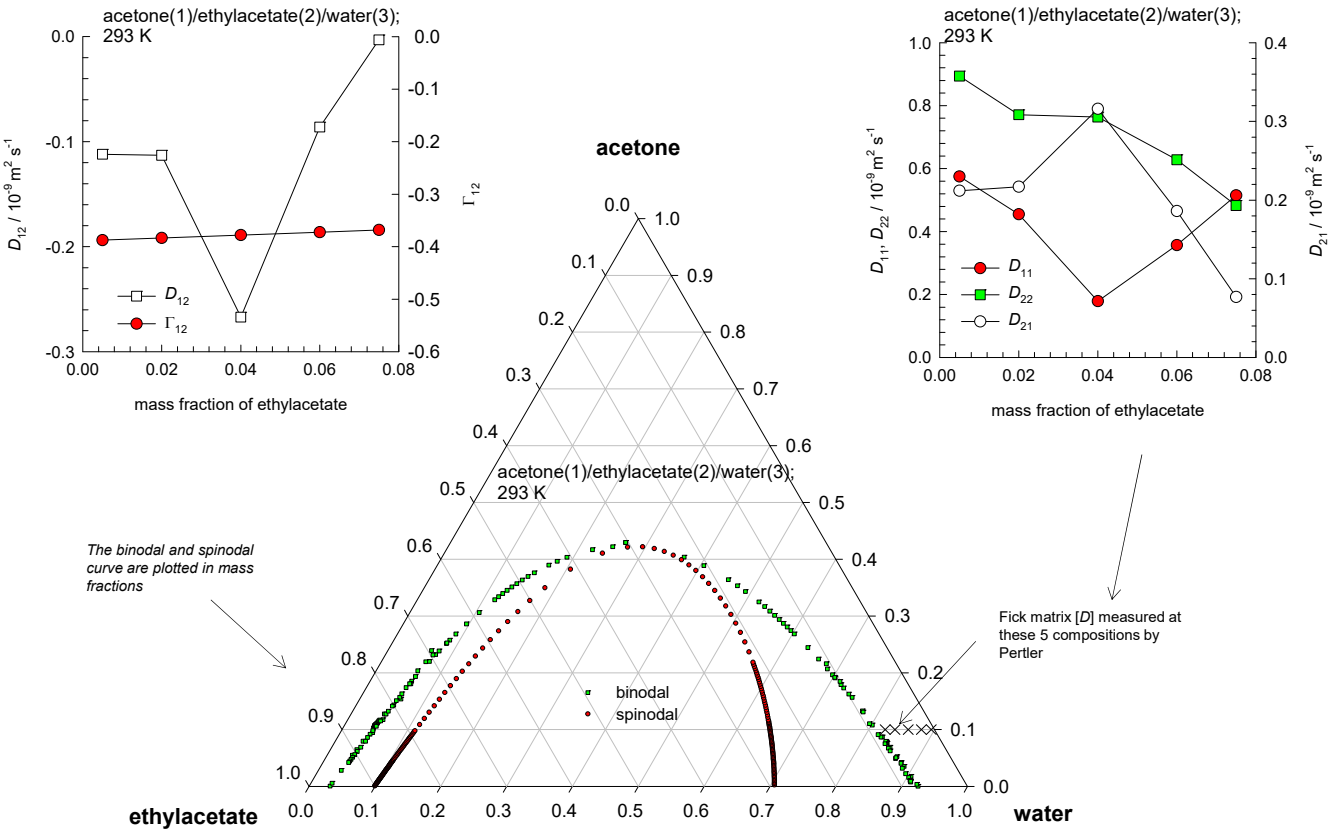


Figure 5-13. Experimental data of Pertler[79] for the elements of the Fick diffusivity matrix in the water-rich region of the phase diagram; these values correspond to the component numbering: acetone(1)/ethylacetate(2)/water(3). Note that the phase diagram is plotted in mass fractions.

# Diffusivities in glycine(1)/L-valine(2)/water(3) solutions

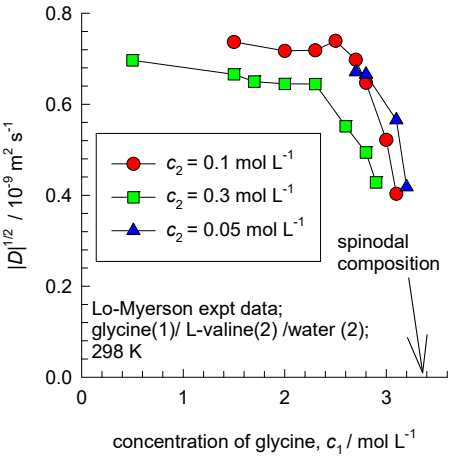


Figure 5-14. Plot of $|D|^{1/2}$ for glycine(1)/L-valine(2)/water(3) solutions as a function of the molar concentration of glycine, $c_1$. The data on the Fick diffusivity matrix $[D]$, measured at three different L-valine concentrations ($c_2$ = 0.1, 0.3, 0.05 mol L$^{-1}$) are culled from Table 1, Table 2, and Table 3 of Lo and Myerson.[80]

# 6 Ternary Liquid-Liquid Extraction

## 6.1 Preamble on technology of liquid-liquid extraction

Liquid extraction[86] is often used in the chemical and petroleum industries to separate mixtures that have boiling points close to one another, making distillation operations difficult and energy-intensive.[48-50, 87-89] With the rapid development of a vast variety of ionic liquids[90, 91], and eutectic[92] solvents, there is renewed interest in extractive separations for a variety of applications. An important application of liquid extraction involves the selective removal of aromatics from mixtures of hydrocarbons for the purposes of improving the properties of kerosene, diesel, and lube-oils, and manufacture of food-grade hexane.[50, 91, 93, 94] Solvents such as sulfolane, NMP (N-methyl pyrrolidone), ionic liquids, and eutectics, allow the reduction of aromatics of hydrocarbon mixtures. As illustration, consider the separation a 50/50 propylbenzene/dodecane feed mixture, indicated by F in Figure 6-1. Addition of the extraction agent, N-methyl pyrrolidone (NMP = solvent S) to the feed mixture F results in a mixture of composition M that falls within the unstable region of the phase diagram. The mixture M separates into two phases with compositions E (Extract) and R (Raffinate) at either ends of the tie-line shown. The composition of the extract phase is $x_{1,eq}$ = 0.682507484, $x_{2,eq}$ = 0.195546114, and $x_{3,eq}$ = 0.1219464; the composition of the raffinate phase, at the other end of the tie-line is: $x_{1,eq}$ = 0.338353679, $x_{2,eq}$ = 0.238690456, and $x_{3,eq}$ = 0.42295586. The feed phase F will equilibrate to R, and the solvent phase S will equilibrate to E. In the extract phase E, the propylbenzene/dodecane ratio is 1.6, whereas this ratio is reduced to 0.56 in the raffinate phase R.

Figure 6-2 shows the corresponding phase equilibrium diagram for the system NMP(1)/propylbenzene(2)/tetradecane(3). We consider the separation a 50/50 propylbenzene/tetradecane feed mixture, indicated by F by addition of NMP as solvent. For this system, the composition of the extract phase is $x_{1,eq}$ = 0.689463372, $x_{2,eq}$ = 0.208896097, and $x_{3,eq}$ = 0.101640532; the composition of the raffinate phase, at the other end of the tie-line is: $x_{1,eq}$ = 0.329380812, $x_{2,eq}$ = 0.250774108, and $x_{3,eq}$ = 0.41984508. The feed phase F will equilibrate to R, and

the solvent phase S will equilibrate to E. In the extract phase E, the propylbenzene/dodecane ratio is 2.06, whereas this ratio is reduced to 0.6 in the raffinate phase R.

The design and development of liquid-liquid extraction processes is crucially dependent on our ability to describe (a) liquid-liquid phase equilibrium thermodynamics, and (b) composition trajectories and fluxes in both the adjoining phases as these approach equilibrium or stationary states. The design and sizing of appropriate liquid-liquid contacting devices such as stirred vessels, sieve-tray columns, and rotating disc contactors (RDC) are crucially dependent on accurate estimation of the interphase transfer fluxes, and stage efficiencies, for achieving S-E, and F-R equilibration.[44, 50, 87-89, 95] The equilibration trajectories are dependent on the diffusivities, that are strongly influenced by considerations of phase stability.

## 6.2 Murphree point efficiencies in ternary liquid-liquid extraction processes

Figure 6-3 is a schematic of liquid-liquid contacting in a sieve-tray column. This principle also applies to other stage-wise operations. On a given stage, the continuous liquid phase can be considered to be well-mixed; this is a reasonably good approximation.

For a ternary mixture, the diffusion fluxes in either continuous or dispersed phase is described by the generalized Fick's law

$$(J) = -c_t \left[D\right] \frac{d\left(x\right)}{dz} = -\frac{1}{\overline{V}} \left[D\right] \frac{d\left(x\right)}{dz} \tag{6-1}$$

in which the two-dimensional matrix of Fick diffusivities [$D$] is a product of two matrices

$$\begin{bmatrix} D_{11} & D_{12} \\ D_{21} & D_{22} \end{bmatrix} = \begin{bmatrix} \Lambda_{11} & \Lambda_{12} \\ \Lambda_{21} & \Lambda_{22} \end{bmatrix} \begin{bmatrix} \Gamma_{11} & \Gamma_{12} \\ \Gamma_{21} & \Gamma_{22} \end{bmatrix} \tag{6-2}$$

The $2 \times 2$ matrix of thermodynamic factors $\left[\Gamma\right]$

$$\frac{x_i}{RT} \frac{d\mu_i}{dz} = \sum_{j=1}^{2} \Gamma_{ij} \frac{dx_j}{dz}; \quad \Gamma_{ij} = \delta_{ij} + x_i \frac{\partial \ln \gamma_i}{\partial x_j}; \quad i, j = 1,2 \tag{6-3}$$

can be calculated from UNIQUAC or NRTL models describing phase equilibrium thermodynamics.[1, 10] The matrix $[\Lambda]$ can be expressed explicitly in terms of the M-S diffusivities of the constituent binary pairs in the ternary mixture:

$$\begin{bmatrix} \Lambda_{11} & \Lambda_{12} \\ \Lambda_{21} & \Lambda_{22} \end{bmatrix} = \frac{\begin{bmatrix} Đ_{13}\left(x_1 Đ_{23}+(1-x_1)Đ_{12}\right) & x_1 Đ_{23}\left(Đ_{13}-Đ_{12}\right) \\ x_2 Đ_{13}\left(Đ_{23}-Đ_{12}\right) & Đ_{23}\left(x_2 Đ_{13}+(1-x_2)Đ_{12}\right) \end{bmatrix}}{x_1 Đ_{23}+x_2 Đ_{13}+x_3 Đ_{12}} \tag{6-4}$$

For partially miscible ternary mixtures, the coupling effects in the Fick matrix are primarily due to the thermodynamic factors; this has been demonstrated in the foregoing sections, and in earlier works.[45, 73] For the calculations presented in this article, we use the following, simplified expression for the calculation of the Fick matrix

$$\begin{bmatrix} D_{11} & D_{12} \\ D_{21} & D_{22} \end{bmatrix} = |\Lambda|^{1/2} \begin{bmatrix} \Gamma_{11} & \Gamma_{12} \\ \Gamma_{21} & \Gamma_{22} \end{bmatrix} \tag{6-5}$$

with the scalar diffusivity $|\Lambda|^{1/2}$ calculated from

$$|\Lambda|^{1/2} = \sqrt{\frac{Đ_{12} Đ_{13} Đ_{23}}{x_1 Đ_{23}+x_2 Đ_{13}+x_3 Đ_{12}}} \tag{6-6}$$

Let us consider the dispersion to consist of uniform and rigid droplets of diameter, $d_{drop}$. The transient equilibration process within a rigid spherical droplet is described by Geddes model that was originally developed for describing binary diffusion inside vapor bubbles on distillation trays.[46] For ternary mixtures, the Geddes model can be written in two-dimensional matrix differential equation[1]

$$\left(x-x_{eq}\right)=[Q]\left(x_0-x_{eq}\right); \quad [Q]\equiv\frac{6}{\pi^2}\sum_{m=1}^{\infty}\frac{1}{m^2}\exp\left[-m^2\pi^2\frac{4[D]t}{d_{drop}^2}\right] \tag{6-7}$$

The Sylvester theorem, detailed in Appendix A of Taylor and Krishna,[1] is required for explicit calculation of the composition trajectories described by equation (6-7). For extraction equipment such as a sieve tray or rotating disc contactors, the effective contact time of the dispersed phase droplets with

the surrounding continuous phase is $t = h_f / V_{drop}$, where $h_f$ is the liquid/liquid dispersion height, and $V_{drop}$ is the droplet rise velocity.[96]

The fractional approaches to equilibrium for contact time $t$, also termed as the Murphree efficiencies,[48-50] are calculated from

$$E_1 = \frac{x_{10} - x_1}{x_{10} - x_{1eq}} = 1 - Q_{11} - Q_{12}\frac{\Delta x_2}{\Delta x_1};$$
$$E_2 = \frac{x_{20} - x_2}{x_{20} - x_{2eq}} = 1 - Q_{22} - Q_{21}\frac{\Delta x_1}{\Delta x_2};$$
$$E_3 = \frac{x_{30} - x_3}{x_{30} - x_{3eq}} = \frac{\frac{\Delta x_1}{\Delta x_2}E_1 + E_2}{\frac{\Delta x_1}{\Delta x_2} + 1} \tag{6-8}$$

In equation (6-8), $\Delta x_1 = x_{10} - x_{1,eq}$, and $\Delta x_2 = x_{20} - x_{2,eq}$.

## 6.3 Uphill diffusion in partially miscible glycerol/acetone/water mixtures

The experimental data (indicated by the white circles) on transient equilibration of glycerol-rich and acetone-rich phases of the glycerol/acetone/water mixture were measured in a stirred Lewis cell by Krishna et al.;[97] see Figure 6-4. For the acetone-rich phase (left hand side), the initial mole fractions are $x_{10}$ = 0.0, $x_{20}$ = 0.77, and $x_{30}$ = 0.23; the final equilibrium composition is $x_{1,eq}$ = 0.042, $x_{2,eq}$ = 0.894, and $x_{3,eq}$ = 0.064. For the glycerol-rich phase (right hand side), the initial mole fractions are $x_{10}$ = 0.85, $x_{20}$ = 0.0, and $x_{30}$ = 0.15; the final equilibrium composition is $x_{1,eq}$ = 0.552, $x_{2,eq}$ = 0.164, and $x_{3,eq}$ = 0.284. In our previous works,[45, 97] the equilibration trajectories in either the glycerol-rich or the acetone-rich phase were calculated using the exponential decay model

$$\left(x - x_{eq}\right) = [Q]\left(x_0 - x_{eq}\right); \quad [Q] \equiv \exp[-\beta[D]t] \tag{6-9}$$

where $\beta$ is the Lewis cell constant. The value of the constant used in our calculations is $\beta = 10^7$. The precise choice of the value of this constant has no influence on the trajectories in composition space. The calculated equilibration trajectories are indicated by the blue lines in Figure 6-4.

We now apply the Geddes equilibration model to investigate the equilibration of a single droplet of 2 mm diameter in the dispersed phase. The initial mole fractions of the dispersed phase droplet is $x_{10}$ = 0.85, $x_{20}$ = 0.0, and $x_{30}$ = 0.15. The final equilibrated composition is $x_{1,eq}$ = 0.552, $x_{2,eq}$ = 0.164, and $x_{3,eq}$ = 0.284. The continuous phase is the acetone-rich phase with the composition at the other end of the tie-line: $x_{1,eq}$ = 0.042, $x_{2,eq}$ = 0.894, and $x_{3,eq}$ = 0.064. In our calculations we assume that the mass transfer resistance resides predominantly within the dispersed phase; this is a common occurrence.[45, 98]

The matrix of thermodynamic factors, calculated at the arithmetic average composition of the dispersed phase droplets between the initial and final equilibrated compositions ($x_{1,av}$ = 0.701, $x_{2,av}$ = 0.082, and $x_{3,av}$ = 0.217) is $[\Gamma]=\begin{bmatrix} 2.1516171 & 1.171495 \\ 0.019193 & 0.687462 \end{bmatrix}$. For calculation of the transient equilibration trajectories in the dispersed phase, the scalar diffusivity $|\Lambda|^{1/2}$ is calculated from $|\Lambda|^{1/2} = \left(D_{1,self}\right)^{x_1}\left(D_{2,self}\right)^{x_2}\left(D_{3,self}\right)^{x_3}$, taking $D_{1,\text{self}}$ = 0.01, $D_{2,\text{self}}$ = 3.2, $D_{3,\text{self}}$ = 0.5 with units $10^{-9}$ m$^2$ s$^{-1}$; this yields $|\Lambda|^{1/2} = 3.75\times10^{-11}$ m$^2$s$^{-1}$; therefore, $[D]=|\Lambda|^{1/2}[\Gamma]=\begin{bmatrix} 8.069819 & 4.39379 \\ 0.071986 & 2.578383 \end{bmatrix}\times10^{-11}\text{m}^2\text{s}^{-1}$. The off-diagonal element $D_{12}$ are significantly large in comparison to the diagonal element $D_{12}$, indicating strongly coupled diffusion process for transfer of glycerol (1). We can also determine a "magnitude" of the Fick diffusivity $|D|^{1/2} = 4.53\times10^{-11}$ m$^2$ s$^{-1}$ for use in the calculation of the Fourier number.

The component driving forces for transfer of glycerol (1) and acetone (2) are $\Delta x_1 = x_{10} - x_{1,eq} = 0.298$, $\Delta x_2 = x_{20} - x_{2,eq} = -0.164$. Particularly noteworthy is that the magnitude of the driving force for acetone transfer is lower than that for glycerol, and opposite in sign.

The transient Geddes equilibration trajectory follows a highly curvilinear path to equilibrium; see Figure 6-5(a), and is in good agreement with the experimental data. If coupling effects are completely ignored, the equilibration trajectory follows a linear path in composition space. Figure 6-5(b) presents a plot of component Murphree efficiencies as a function of the dimensionless Fourier number $\frac{4|D|^{1/2}t}{d_{drop}^2}$ where the

droplet diameter is taken as $d_{\text{drop}}$ = 2 mm. During the later stages of the equilibration process, the Murphree point efficiency of water (component 3) has values exceeding unity, indicative of uphill diffusion.

Let us examine the trajectory followed during equilibration of homogenous mixtures of two different compositions, indicated by L and R in Figure 6-6, for the system glycerol(1)/acetone(2)/water(3). The composition of the equilibrated mixture is $x_{1,\text{eq}} = 0.5$, $x_{2,\text{eq}} = 0.17$ and $x_{3,\text{eq}} = 0.33$, which point lies on the binodal curve. At the average composition, the matrix of thermodynamic factors is calculated from phase equilibrium thermodynamics: $[\Gamma]=\begin{bmatrix} 2.3 & 1.37 \\ 0.149 & 0.464 \end{bmatrix}$. The "magnitude" of the M-S diffusivity is estimated from $|\Lambda|^{1/2} = (D_{1,self})^{x_1}(D_{2,self})^{x_2}(D_{3,self})^{x_3}$ taking $D_{1,\text{self}}$= 0.01, $D_{2,\text{self}}$= 3.2, $D_{3,\text{self}}$= 0.5 with units $10^{-9}$ m$^2$ s$^{-1}$; the value $|\Lambda|^{1/2} = 0.095\times10^{-9}$ m$^2$ s$^{-1}$. We assume that the matrix of Fick diffusivities is $[D]=|\Lambda|^{1/2}[\Gamma]$; the calculated value is i.e. $[D]=\begin{bmatrix} 0.223 & 0.133 \\ 0.0144 & 0.045 \end{bmatrix}\times10^{-9}$ m$^2$ s$^{-1}$. Using this diffusivity estimate, we calculated the equilibration trajectory using

$$\begin{pmatrix} x_1 \\ x_2 \end{pmatrix} = \frac{1}{2}\begin{pmatrix} x_{1L}+x_{1,R} \\ x_{2L}+x_{2,R} \end{pmatrix} + \frac{1}{2}erf\left[\frac{z}{\sqrt{4t}}\begin{bmatrix} D_{11} & D_{12} \\ D_{21} & D_{22} \end{bmatrix}^{-1/2}\right]\begin{pmatrix} x_{1R}-x_{1L} \\ x_{2R}-x_{2L} \end{pmatrix} \tag{6-10}$$

We note that the serpentine trajectory has penetrated the binodal envelope; see Figure 6-6. This indicates the spontaneous emulsification is feasible. A linear equilibration trajectory (shown by pink line) does not foray into the meta-stable zone.

In the foregoing example, an important consequence of uphill diffusion is emulsification.

## 6.4 Uphill diffusion in water(1)/chloroform(2)/acetic acid(3) mixtures

We now apply the Geddes equilibration model to investigate the equilibration of a single droplet of 2 mm diameter in water(1)/chloroform(2)/acetic-acid(3) mixtures mixtures in the dispersed phase; see Figure 6-7. The initial mole fractions of the dispersed phase droplet (the droplet diameter is taken as $d_{\text{drop}}$ = 2 mm) is $x_{10}$ = 0.0, $x_{20}$ = 0.3, and $x_{30}$ = 0.7. The final equilibrated composition is $x_{1,\text{eq}}$ =

0.267383532, $x_{2,eq}$ = 0.382190021, and $x_{3,eq}$ = 0.350426. The continuous phase has the compositions at the other end of the tie-line: $x_{1,eq}$ = 0.609997518, $x_{2,eq}$ = 0.081651022, and $x_{3,eq}$ = 0.308351. In our calculations we assume that the mass transfer resistance resides predominantly within the dispersed phase; this is a common occurrence.[45, 98]

The matrix of thermodynamic factors, calculated at the arithmetic average composition of the dispersed phase droplets between the initial and final equilibrated compositions ($x_{1,av}$ = 0.133692, $x_{2,av}$ = 0.341095, and $x_{3,av}$ = 0.525213) is $[\Gamma]=\begin{bmatrix} 1.0364 & 0.419067 \\ 0.83488 & 1.0914296 \end{bmatrix}$. For calculation of the transient equilibration trajectories in the dispersed phase, the scalar diffusivity $|\Lambda|^{1/2}$ is calculated from $|\Lambda|^{1/2} = (D_{1,self})^{x_1} (D_{2,self})^{x_2} (D_{3,self})^{x_3}$, taking $D_{1,self}$= 0.4, $D_{2,self}$= 0.8, $D_{3,self}$= 1.1 with units $10^{-9}$ m$^2$ s$^{-1}$; this yields $|\Lambda|^{1/2} = 8.62\times10^{-10}$ m$^2$s$^{-1}$; therefore, $[D] = |\Lambda|^{1/2}[\Gamma] = \begin{bmatrix} 0.893327 & 0.361215 \\ 0.719626 & 0.94076 \end{bmatrix} \times 10^{-9}\,\mathrm{m^2 s^{-1}}$. The off-diagonal elements are significantly large, indicating strongly coupled diffusion process. The experimental data on the Fick diffusivity matrix, as reported by Vitagliano et al.[77], and Buzatu et al.[78] confirm the significance of diffusional coupling effects arising primarily from thermodynamic coupling.[99] We can also determine the "magnitude" of the Fick diffusivity $|D|^{1/2} = 7.62\times10^{-10}$ m$^2$ s$^{-1}$ for use in the calculation of the Fourier number.

The component driving forces for transfer of water (1) and chloroform (2) are $\Delta x_1 = x_{10} - x_{1,eq}$ = -0.267384, $\Delta x_2 = x_{20} - x_{2,eq}$ = -0.08219. Particularly noteworthy is that the magnitude of the driving force for chloroform transfer is significantly lower than that for water.

The transient Geddes equilibration trajectory follows a highly curvilinear path to equilibrium; see Figure 6-7. If coupling effects are completely ignored, the equilibration trajectory follows a linear path in composition space. Figure 6-8(a) presents a plot of component Murphree efficiencies as a function of the dimensionless Fourier number $\frac{4|D|^{1/2} t}{d_{drop}^2}$ where the droplet diameter is taken as $d_{drop}$ = 2 mm. During

the early stages of the equilibration process, the Murphree point efficiency of chloroform (component 2) exhibits values exceeding unity, indicative of uphill diffusion. As a consequence of uphill diffusion, the transient equilibration of chloroform exhibits a pronounced overshoot during its approach to equilibration; see Figure 6-8(b).

Figure 6-8(c) plots the corresponding activities, $a_i = \gamma_i x_i$, of water, chloroform and acetic acid as a function of the Fourier number. It is noteworthy that the transient equilibration process in terms of component activities is monotonic; this implies that the composition overshoots have their origins in the thermodynamic influences engendered by the off-diagonal elements of $[\Gamma]$.

We now demonstrate that uphill diffusion may open up the possibility of emulsification for water(1)/chloroform(2)/acetic-acid(3) mixtures. Consider inter-diffusion between two compartments maintained at two different compositions, indicated by L and R in Figure 6-9. The initial composition of the left compartment is: $x_{1,L}$ = 0.3, $x_{2,L}$ = 0.3 and $x_{3,L}$ = 0.4; the initial composition of the right compartment is: $x_{1,R}$ = 0.1, $x_{2,R}$ = 0.7 and $x_{3,R}$ = 0.2. The composition at equilibrium is $x_{1,eq}$ = 0.2, $x_{2,eq}$ = 0.5 and $x_{3,eq}$ = 0.3; this point lies on the binodal curve. The matrix of thermodynamic factors, calculated at the arithmetic average compositions is $[\Gamma] = \begin{bmatrix} 0.9907682 & 0.6232338 \\ 0.90262047 & 0.87687646 \end{bmatrix}$. For calculation of the transient equilibration trajectories in the dispersed phase, the scalar diffusivity $|\Lambda|^{1/2}$ is calculated from $|\Lambda|^{1/2} = (D_{1,self})^{x_1} (D_{2,self})^{x_2} (D_{3,self})^{x_3}$, ttaking $D_{1,self}$= 0.4, $D_{2,self}$= 0.8, $D_{3,self}$= 1.1 with units $10^{-9}$ m$^2$ s$^{-1}$; this yields $|\Lambda|^{1/2} = 7.66 \times 10^{-10}$ m$^2$s$^{-1}$; therefore, $[D] = |\Lambda|^{1/2}[\Gamma] = \begin{bmatrix} 0.75918367 & 0.47755764 \\ 0.6916398 & 0.67191325 \end{bmatrix} \times 10^{-9}$ m$^2$s$^{-1}$. The off-diagonal elements are significantly large in comparison to the diagonal elements, indicating strongly coupled diffusion process. The equilibration trajectory, calculated using equation (6-10), is plotted by the blue line in Figure 6-9. We note that composition trajectory in the left chamber has forayed into the meta-stable region. A linear equilibration trajectory, shown by the pink line in Figure 6-9, remains in the

homogeneous single-phase region. Uphill diffusion opens up the possibility of emulsification during mixing of homogeneous liquid mixtures.

## 6.5 Uphill diffusion in water(1)/acetone(2)/ethylacetate(3) mixtures

We now apply the Geddes equilibration model to investigate the equilibration of a single droplet of 2 mm diameter in water(1)/acetone(2)/ethylacetate(3) mixtures in the dispersed phase; see Figure 6-10. The initial mole fractions of the dispersed phase droplet is $x_{10} = 0.87$, $x_{20} = 0.13$, and $x_{30} = 0.0$. The final equilibrated composition is $x_{1,eq} = 0.4049748$, $x_{2,eq} = 0.146113283$, and $x_{3,eq} = 0.045392$. The continuous phase has the compositions at the other end of the tie-line: $x_{1,eq} = 0.4049748$, $x_{2,eq} = 0.317548401$, and $x_{3,eq} = 0.277477$. In our calculations we assume that the mass transfer resistance resides predominantly within the dispersed phase; this is a common occurrence.[45, 98]

The matrix of thermodynamic factors, calculated at the arithmetic average composition of the dispersed phase droplets between the initial and final equilibrated compositions ($x_{1,av} = 0.839247$, $x_{2,av} = 0.138057$, and $x_{3,av} = 0.022696$) is $[\Gamma] = \begin{bmatrix} -0.173928 & -0.584424 \\ 0.937821 & 1.518296 \end{bmatrix}$. For calculation of the transient equilibration trajectories in the dispersed phase, the scalar diffusivity $|\Lambda|^{1/2}$ is calculated from $|\Lambda|^{1/2} = \sqrt{\frac{Đ_{12}Đ_{13}Đ_{23}}{x_1Đ_{23} + x_2Đ_{13} + x_3Đ_{12}}}$; this yields; this yields $|\Lambda|^{1/2} = 1.16 \times 10^{-9}\ \mathrm{m^2 s^{-1}}$; therefore, $[D] = |\Lambda|^{1/2}[\Gamma] = \begin{bmatrix} -0.20228 & -0.67969 \\ 1.090695 & 1.765792 \end{bmatrix} \times 10^{-9}\ \mathrm{m^2 s^{-1}}$. The off-diagonal elements are significantly large in comparison to the diagonal elements, indicating strongly coupled diffusion process. The experimental data on the Fick diffusivity matrix, as reported by Pertler[79] (see Figure 5-12 and Figure 5-13) confirm the significance of diffusional coupling effects arising primarily from thermodynamic coupling.[99] We can also determine the "magnitude" of the Fick diffusivity $|D|^{1/2} = 6.2 \times 10^{-10}\ \mathrm{m^2\ s^{-1}}$ for use in the calculation of the Fourier number $\frac{4|D|^{1/2} t}{d_{drop}^2}$. The component driving forces for transfer of

water (1) and acetone (2) are $\Delta x_1 = x_{10} - x_{1,eq} = 0.061505$, $\Delta x_2 = x_{20} - x_{2,eq} = -0.016113$. Particularly noteworthy is that the magnitude of the driving force for acetone transfer is significantly lower than that for water, and opposite in sign.

The transient Geddes equilibration trajectory follows a highly curvilinear path to equilibrium; see Figure 6-10. The experimental data obtained by Haeberl and Blass[85] confirms that the equilibration tends to "hug" the binodal curve rather than follow a straight-line equilibration path. If coupling effects are completely ignored, the equilibration trajectory follows a linear path in composition space.

Figure 6-11(a) presents a plot of component Murphree efficiencies as a function of the dimensionless Fourier number $\frac{4|D|^{1/2} t}{d_{drop}^2}$ where the droplet diameter is taken as $d_{\text{drop}} = 2$ mm. During the early stages of the equilibration process, the Murphree point efficiency of acetone (component 2) exhibits negative values, indicative of uphill diffusion. As a consequence of uphill diffusion, the transient equilibration of acetone exhibits a pronounced undershoot during its approach to equilibration; see Figure 6-11(b).

We now demonstrate that uphill diffusion may open up the possibility of emulsification for water(1)/acetone(2)/ethylacetate(3) mixtures. Consider inter-diffusion between two compartments maintained at two different compositions. The initial composition of the left compartment is: $x_{1,\text{L}} = 0.05$, $x_{2,\text{L}} = 0.1$ and $x_{3,\text{L}} = 0.85$; the initial composition of the right compartment is: $x_{1,\text{R}} = 0.55$, $x_{2,\text{R}} = 0.45$ and $x_{3,\text{R}} = 0.0$; see Figure 6-12. The composition at equilibrium is $x_{1,\text{eq}} = 0.3$, $x_{2,\text{eq}} = 0.275$ and $x_{3,\text{eq}} = 0.425$; this point lies on the binodal curve. The matrix of thermodynamic factors, calculated at the arithmetic average compositions is $[\Gamma] = \begin{bmatrix} 0.169614 & -0.365349 \\ 0.085606 & 1.270447 \end{bmatrix}$. For calculation of the transient equilibration trajectories in the dispersed phase, scalar diffusivity $|\Lambda|^{1/2}$ is calculated from $|\Lambda|^{1/2} = \sqrt{\frac{Đ_{12} Đ_{13} Đ_{23}}{x_1 Đ_{23} + x_2 Đ_{13} + x_3 Đ_{12}}}$; this yields $|\Lambda|^{1/2} = 2.06 \times 10^{-9}\ \text{m}^2\text{s}^{-1}$. Therefore, $[D] = |\Lambda|^{1/2}[\Gamma] = \begin{bmatrix} 0.34674 & -0.746879 \\ 0.175003 & 2.59716 \end{bmatrix} \times 10^{-9}\ \text{m}^2\text{s}^{-1}$. The off-diagonal element $D_{12}$ is a significantly

large fraction of the diagonal element $D_{11}$, indicating strongly coupled diffusion flux of water with acetone driving force. The equilibration trajectory, calculated using equation (6-10), is plotted by the blue line in Figure 6-12. We note that composition trajectory in the right chamber has forayed into the meta-stable region. A linear equilibration trajectory, shown by the pink line in Figure 6-12 remains in the homogeneous single-phase region. Uphill diffusion opens up the possibility of emulsification during mixing of homogeneous liquid mixtures.

## 6.6 Uphill diffusion in water(1)/caprolactam(2)/toluene(3) mixtures

The extraction of caprolactam from aqueous solutions by toluene is an important processing step in the manufacture of Nylon-66. Let us examine the diffusion equilibration trajectories for water(1)/caprolactam(2)/toluene(3) mixtures at 298K; see Figure 6-13. The UNIQUAC parameters for calculation of the phase equilibrium thermodynamics are provided in Table 6-3.The initial mole fractions in the drop are $x_{10} = 0.0$, $x_{20} = 0.12$, and $x_{30} = 0.88$. The final equilibrium composition of the dispersed phase droplets is $x_{1,eq} = 0.108182718$, $x_{2,eq} = 0.130183682$, and $x_{3,eq} = 0.7616336$, corresponding to one end of the tie-line; the other end of the tie-line, corresponding to the compositions of the continuous phase (assumed to be of constant composition) has the compositions $x_{1c,eq} = 0.725244955$, $x_{2c,eq} = 0.226323187$, and $x_{3c,eq} = 0.0484319$. In our calculations we assume that the mass transfer resistance resides predominantly within the dispersed phase; this is a common occurrence.[45, 98]

The matrix of thermodynamic factors, calculated at the arithmetic average composition of the dispersed phase droplets between the initial and final equilibrated compositions ($x_{1,av} = 0.0540914$, $x_{2,av} = 0.1250918$, and $x_{3,av} = 0.8208168$) is $[\Gamma] = \begin{bmatrix} 0.8548921 & -0.481726 \\ -0.979743 & 1.2381142 \end{bmatrix}$. The off-diagonal elements are significantly large in comparison to the diagonal elements, indicating strongly coupled diffusion process. For calculation of the transient equilibration trajectories in the dispersed phase, the scalar diffusivity $|\Lambda|^{1/2}$ is assumed to have the value $|\Lambda|^{1/2} = 1\times10^{-9}\ \mathrm{m^2 s^{-1}}$; therefore,

$[D]=|\Lambda|^{1/2}[\Gamma]=\begin{bmatrix}0.8548921 & -0.481726\\ -0.979743 & 1.2381142\end{bmatrix}\times 10^{-9}$. We can also determine a "magnitude" of the Fick diffusivity $|D|^{1/2}=7.66\times 10^{-10}$ for use in the calculation of the Fourier number $\frac{4|D|^{1/2}t}{d_{drop}^2}$ where the droplet diameter is taken as $d_{\text{drop}}$ = 2 mm. The component driving forces for transfer of water (1) and caprolactam (2) are $\Delta x_1 = x_{10} - x_{1,eq} = -0.1081827$, $\Delta x_2 = x_{20} - x_{2,eq} = -0.0101837$. It is particularly noteworthy that the driving force for caprolactam is significantly smaller, by about an order of magnitude than that of water.

The transient Geddes equilibration trajectory follows a highly curvilinear path to equilibrium; see Figure 6-13. If coupling effects are completely ignored, the equilibration trajectory follows a linear path in composition space.

Figure 6-14(a) presents a plot of component Murphree efficiencies as a function of the dimensionless Fourier number $\frac{4|D|^{1/2}t}{d_{drop}^2}$ where $|D|^{1/2}=7.66\times 10^{-10}$ m$^2$ s$^{-1}$ and the droplet diameter is taken as $d_{\text{drop}}$ = 2 mm. During the initial stages of the equilibration process, the Murphree point efficiency of caprolactam (component 2) is strongly negative, indicative of uphill diffusion. As a consequence of uphill diffusion, the transient equilibration of caprolactam exhibits a pronounced undershoot during its approach to equilibration; see Figure 6-14(b).

Figure 6-15 plots the Geddes equilibration trajectories for different values of the initial droplet compositions: $x_{10}$ = 0.0, $x_{20}$ = 0.0; $x_{10}$ = 0.0, $x_{20}$ = 0.1; $x_{10}$ = 0.0, $x_{20}$ = 0.2; $x_{10}$ = 0.0, $x_{20}$ = 0.3; $x_{10}$ = 0.0, $x_{20}$ = 0.4; $x_{10}$ = 0.0, $x_{20}$ = 0.5; $x_{10}$ = 0.0, $x_{20}$ = 0.6. In all these six cases, the Geddes equilibration trajectories follow curvilinear paths.

## 6.7 Uphill diffusion in water(1)/ethanol(2)/benzene(3) mixtures

We apply the Geddes equilibration model to investigate the equilibration of a single droplet of 2 mm diameter in water(1)/ethanol(2)/benzene(3) mixtures in the dispersed phase. The initial mole fractions of

the dispersed phase droplet is $x_{10}$ = 0.0, $x_{20}$ = 0.2, and $x_{30}$ = 0.8; see Figure 6-16. The final equilibrated composition is $x_{1,eq}$ = 0.082641058, $x_{2,eq}$ = 0.231828339, and $x_{3,eq}$ = 0.685531. The continuous phase has the compositions at the other end of the tie-line: $x_{1,eq}$ = 0.548327987, $x_{2,eq}$ = 0.370735283, and $x_{3,eq}$ = 0.080937. In our calculations we assume that the mass transfer resistance resides predominantly within the dispersed phase; this is a common occurrence.[45, 98]

The matrix of thermodynamic factors, calculated at the arithmetic average composition of the dispersed phase droplets between the initial and final equilibrated compositions ($x_{1,av}$ = 0.041321, $x_{2,av}$ = 0.215914, and $x_{3,av}$ = 0.742765) is $[\Gamma]=\begin{bmatrix} 0.834875 & -0.257899 \\ -1.1304071 & 0.709572 \end{bmatrix}$. For calculation of the transient equilibration trajectories in the dispersed phase, the scalar diffusivity $|\Lambda|^{1/2}$ is assumed to have the value $|\Lambda|^{1/2} = 1\times10^{-9}\ \mathrm{m^2 s^{-1}}$; therefore, $[D]=|\Lambda|^{1/2}[\Gamma]=\begin{bmatrix} 0.834875 & -0.257899 \\ -1.1304071 & 0.709572 \end{bmatrix}\times10^{-9}\mathrm{m^2 s^{-1}}$. The off-diagonal elements are significantly large in comparison to the diagonal elements, indicating strongly coupled diffusion process. We can also determine the "magnitude" of the Fick diffusivity $|D|^{1/2} = 5.49\times10^{-10}\ \mathrm{m^2\ s^{-1}}$ for use in the calculation of the Fourier number $\frac{4|D|^{1/2}t}{d_{drop}^2}$. The component driving forces for transfer of water (1) and ethanol (2) are $\Delta x_1 = x_{10} - x_{1,eq} = -0.082641$, $\Delta x_2 = x_{20} - x_{2,eq} = -0.031828$. Particularly noteworthy is that the driving force for ethanol transfer is lower than that for water.

The transient Geddes equilibration trajectory follows a highly curvilinear path to equilibrium; see Figure 6-16. If coupling effects are completely ignored, the equilibration trajectory follows a linear path in composition space.

Figure 6-17(a) presents a plot of component Murphree efficiencies as a function of the dimensionless Fourier number $\frac{4|D|^{1/2}t}{d_{drop}^2}$ where the droplet diameter is taken as $d_{drop}$ = 2 mm. During the early stages of

the equilibration process, the Murphree point efficiency of ethanol (component 2) exhibits negative values, indicative of uphill diffusion. As a consequence of uphill diffusion, the transient equilibration of ethanol exhibits a pronounced undershoot during its approach to equilibration; see Figure 6-17(b).

## 6.8 Uphill diffusion in water(1)/ethyl acetate (2)/ethanol(3) mixtures

We apply the Geddes equilibration model to investigate the equilibration of a single droplet of 2 mm diameter in water(1)/ethyl acetate(2) /ethanol(3) mixtures in the dispersed phase. The initial mole fractions of the dispersed phase droplet is $x_{10} = 0.0$, $x_{20} = 0.85$, and $x_{30} = 0.15$; see Figure 6-18. The final equilibrated composition is $x_{1,eq} = 0.359190924$, $x_{2,eq} = 0.499644619$, and $x_{3,eq} = 0.141164$. The continuous phase has the compositions at the other end of the tie-line: $x_{1,eq} = 0.929439886$, $x_{2,eq} = 0.018683455$, and $x_{3,eq} = 0.051877$. In our calculations we assume that the mass transfer resistance resides predominantly within the dispersed phase; this is a common occurrence.[45, 98]

The matrix of thermodynamic factors, calculated at the arithmetic average composition of the dispersed phase droplets between the initial and final equilibrated compositions ($x_{1,av} = 0.179595$, $x_{2,av} = 0.674822$, and $x_{3,av} = 0.145582$) is $[\Gamma] = \begin{bmatrix} 1.327858 & 0.650985 \\ 0.929704 & 1.279449 \end{bmatrix}$. For calculation of the transient equilibration trajectories in the dispersed phase, the scalar diffusivity $|\Lambda|^{1/2}$ is assumed to have the value $|\Lambda|^{1/2} = 1\times10^{-9}\ \mathrm{m^2 s^{-1}}$; therefore, $[D] = |\Lambda|^{1/2}[\Gamma] = \begin{bmatrix} 1.327858 & 0.650985 \\ 0.929704 & 1.279449 \end{bmatrix} \times 10^{-9}\ \mathrm{m^2 s^{-1}}$. The off-diagonal elements are significantly large in comparison to the diagonal elements, indicating strongly coupled diffusion process. We can also determine the "magnitude" of the Fick diffusivity $|D|^{1/2} = 1.05\times10^{-9}$ m$^2$ s$^{-1}$ for use in the calculation of the Fourier number $\dfrac{4|D|^{1/2} t}{d_{drop}^2}$.The component driving forces for transfer of water (1) and ethyl acetate (2) are $\Delta x_1 = x_{10} - x_{1,eq} = -0.359191$, $\Delta x_2 = x_{20} - x_{2,eq} = 0.350355$. Particularly noteworthy is that the driving forces for transfer of ethanol transfer is practically nil: $\Delta x_3 = x_{30} - x_{3,eq} = 0.0088$.

The transient Geddes equilibration trajectory follows a curvilinear path to equilibrium; see Figure Figure 6-18. If coupling effects are completely ignored, the equilibration trajectory follows a linear path in composition space.

Figure 6-19(a) presents a plot of component Murphree efficiencies as a function of the dimensionless Fourier number $\frac{4|D|^{1/2}t}{d_{drop}^2}$ where the droplet diameter is taken as $d_{\text{drop}} = 2$ mm. During the early stages of the equilibration process, the Murphree point efficiency of ethanol (component 3) exhibits value exceeding unity, indicative of uphill diffusion. As a consequence of uphill diffusion, the transient equilibration of ethanol exhibits a pronounced undershoot during its approach to equilibration; see Figure 6-19(b).

## 6.9 Uphill diffusion in furfural(1)/formic acid(2)/water(3) mixtures

We apply the Geddes equilibration model to investigate the equilibration of a single droplet of 2 mm diameter in furfural(1)/formic acid(2)/water (3) mixtures in the dispersed phase. The initial mole fractions of the dispersed phase droplet is $x_{10} = 0.98$, $x_{20} = 0.02$, and $x_{30} = 0.0$; see Figure 6-20. The final equilibrated composition is $x_{1,\text{eq}} = 0.519537719$, $x_{2,\text{eq}} = 0.068252025$, and $x_{3,\text{eq}} = 0.41221026$. The continuous phase is the water-rich phase with the composition at the other end of the tie-line: $x_{1,\text{eq}} = 0.033873374$, $x_{2,\text{eq}} = 0.037692034$, and $x_{3,\text{eq}} = 0.92843459$. In our calculations we assume that the mass transfer resistance resides predominantly within the dispersed phase; this is a common occurrence.[45, 98]

The matrix of thermodynamic factors, calculated at the arithmetic average composition of the dispersed phase droplets between the initial and final equilibrated compositions ($x_{1,\text{av}} = 0.74976886$, $x_{2,\text{av}} = 0.04412601$, and $x_{3,\text{av}} = 0.20610513$) is $[\Gamma] = \begin{bmatrix} 0.50802915 & 0.90511575 \\ 0.40555182 & 1.653920 \end{bmatrix}$. For calculation of the transient equilibration trajectories in the dispersed phase, the scalar diffusivity $|\Lambda|^{1/2}$ is assumed to have the value $|\Lambda|^{1/2} = 1\times10^{-9}\ \text{m}^2\text{s}^{-1}$; therefore, $[D] = |\Lambda|^{1/2}[\Gamma] = \begin{bmatrix} 0.50802915 & 0.90511575 \\ 0.40555182 & 1.653920 \end{bmatrix} \times 10^{-9}\,\text{m}^2\text{s}^{-1}$. The

off-diagonal elements are significantly large in comparison to the diagonal elements, indicating strongly coupled diffusion process. We can also determine the "magnitude" of the Fick diffusivity $|D|^{1/2} = 6.9\times10^{-10}$ m$^2$ s$^{-1}$ for use in the calculation of the Fourier number $\frac{4|D|^{1/2}t}{d_{drop}^2}$.The component driving forces for transfer of furfural (1) and formic acid (2) are $\Delta x_1 = x_{10} - x_{1,eq} = 0.46046228$, $\Delta x_2 = x_{20} - x_{2,eq} = -0.0482520$2. Particularly noteworthy is that the driving force for formic acid transfer is significantly lower in magnitude than that of furfural, and opposite in sign.

The transient Geddes equilibration trajectory follows a highly curvilinear path to equilibrium, hugging the binodal curve; see Figure 6-20. If coupling effects are completely ignored, the equilibration trajectory follows a linear path in composition space.

Figure 6-21(a) presents a plot of component Murphree efficiencies as a function of the dimensionless Fourier number $\frac{4|D|^{1/2}t}{d_{drop}^2}$ where the droplet diameter is taken as $d_{drop}$ = 2 mm. During the early stages of the equilibration process, the Murphree point efficiency of formic acid (component 2) exhibits negative values, indicative of uphill diffusion. As a consequence of uphill diffusion, the transient equilibration of formic acid exhibits a pronounced undershoot during its approach to equilibration; see Figure 6-21(b).

## 6.10 Uphill diffusion in NMP(1)/propylbenzene(2)/dodecane(3) mixtures

Consider the separation a 50/50 propylbenzene/dodecane feed mixture, indicated by F in Figure Figure 6-1. Addition of the extraction agent, N-methyl pyrrolidone (NMP = solvent S) to the feed mixture F results in a mixture of composition M that falls within the unstable region of the phase diagram. The mixture M separates into two phases with compositions E (Extract) and R (Raffinate) at either ends of the tie-line shown. The composition of the extract phase is $x_{1,eq}$ = 0.682507484, $x_{2,eq}$ = 0.195546114, and $x_{3,eq}$ = 0.1219464; the composition of the raffinate phase, at the other end of the tie-line is: $x_{1,eq}$ = 0.338353679, $x_{2,eq}$ = 0.238690456, and $x_{3,eq}$ = 0.42295586. The feed phase F will

equilibrate to R, and the solvent phase S will equilibrate to E. In the extract phase E, the propylbenzene/dodecane ratio is 1.6, whereas this ratio is reduced to 0.56 in the raffinate phase R.

We first investigate the F-R equilibration trajectory, using the assumption that the 50/50 propylbenzene/dodecane feed mixture is dispersed as droplets of 2 mm diameter in a continuous phase consisting of solvent rich phase; see Figure 6-22. The initial mole fractions in the drop are $x_{10} = 0.0$, $x_{20} = 0.5$, and $x_{30} = 0.5$. The final equilibrated composition is $x_{1,eq} = 0.338353679$, $x_{2,eq} = 0.238690456$, and $x_{3,eq} = 0.42295586$. The final equilibrated composition is $x_{1,eq} = 0.682507484$, $x_{2,eq} = 0.195546114$, and $x_{3,eq} = 0.1219464$, corresponding to one end of the tie line. The continuous phase has the composition at the other end of the tie-line: $x_{1,eq} = 0.338353679$, $x_{2,eq} = 0.238690456$, and $x_{3,eq} = 0.42295586$. In our calculations we assume that the mass transfer resistance resides predominantly within the dispersed phase; this is a common occurrence.[45, 98]

The matrix of thermodynamic factors, calculated at the arithmetic average composition of the dispersed phase droplets between the initial and final equilibrated compositions ($x_{1,av} = 0.16917684$, $x_{2,av} = 0.36934523$, and $x_{3,av} = 0.46147793$) is $[\Gamma] = \begin{bmatrix} 0.51513196 & -0.29198399 \\ -0.17794847 & 1.20329934 \end{bmatrix}$. For calculation of the transient equilibration trajectories in the dispersed phase, the scalar diffusivity $|\Lambda|^{1/2}$ is assumed to have the value $|\Lambda|^{1/2} = 1\times10^{-9}\ \mathrm{m^2 s^{-1}}$; therefore, $[D] = |\Lambda|^{1/2}[\Gamma] = \begin{bmatrix} 0.51513196 & -0.29198399 \\ -0.17794847 & 1.20329934 \end{bmatrix} \times 10^{-9}\ \mathrm{m^2 s^{-1}}$. The off-diagonal element $D_{12}$ has the same order of magnitude as the diagonal element $D_{11}$, indicating that coupled diffusion phenomena cannot be ignored. We can also determine the "magnitude" of the Fick diffusivity $|D|^{1/2} = 7.54\times10^{-10}\ \mathrm{m^2\ s^{-1}}$ for use in the calculation of the Fourier number $\dfrac{4|D|^{1/2} t}{d_{drop}^2}$. The component driving forces for transfer of NMP (1) and propylbenzene (2) are $\Delta x_1 = x_{10} - x_{1,eq} = -0.33835368$, $\Delta x_2 = x_{20} - x_{2,eq} = 0.26130954$.

Particularly noteworthy is that the driving force for propylbenzene transfer is of the same order of magnitude as that of NMP, but opposite in sign.

The transient Geddes equilibration trajectory follows a highly curvilinear path to equilibrium, hugging the binodal curve; see Figure 6-22. If coupling effects are completely ignored, the equilibration trajectory follows a linear path in composition space.

Figure 6-23(a) presents a plot of component Murphree efficiencies as a function of the dimensionless Fourier number $\frac{4|D|^{1/2}t}{d_{drop}^2}$ where the droplet diameter is taken as $d_{\text{drop}}$ = 2 mm. During the early stages of the equilibration process, the Murphree point efficiency of dodecane (component 2) exhibits negative values, indicative of uphill diffusion. As a consequence of uphill diffusion, the transient equilibration of dodecane exhibits a slight, yet perceptible, composition overshoot during its approach to equilibration; see Figure 6-23(b).

We now apply the Geddes equilibration model to investigate the equilibration of a single droplet of 2 mm diameter in the system N-methylpyrrolidone (NMP)(1)/propylbenzene(2)/dodecane(3) mixtures in which the the dispersed phase is rich in the solvent NMP. The initial mole fractions in the drop are assumed to be $x_{10}$ = 0.82, $x_{20}$ = 0.18, and $x_{30}$ = 0.0; see Figure 6-24. The final equilibrated composition is $x_{1,\text{eq}}$ = 0.682507484, $x_{2,\text{eq}}$ = 0.195546114, and $x_{3,\text{eq}}$ = 0.1219464.The continuous phase has the composition at the other end of the tie-line: $x_{1,\text{eq}}$ = 0.338353679, $x_{2,\text{eq}}$ = 0.238690456, and $x_{3,\text{eq}}$ = 0.42295586. In our calculations we assume that the mass transfer resistance resides predominantly within the dispersed phase; this is a common occurrence.[45, 98]

The matrix of thermodynamic factors, calculated at the arithmetic average composition of the dispersed phase droplets between the initial and final equilibrated compositions ($x_{1,\text{av}}$ = 0.75125374, $x_{2,\text{av}}$ = 0.18777306, and $x_{3,\text{av}}$ = 0.0609732) is $[\Gamma]=\begin{bmatrix} 0.03813646 & -0.73226404 \\ 0.51435241 & 1.5112041 \end{bmatrix}$. For calculation of the transient equilibration trajectories in the dispersed phase, the scalar diffusivity $|\Lambda|^{1/2}$ is assumed to have

the value $|\Lambda|^{1/2} = 1\times10^{-9}\ \mathrm{m^2 s^{-1}}$; therefore, $[D] = |\Lambda|^{1/2}[\Gamma] = \begin{bmatrix} 0.03813646 & -0.73226404 \\ 0.51435241 & 1.5112041 \end{bmatrix} \times 10^{-9}\ \mathrm{m^2 s^{-1}}$.

Both off-diagonal elements are significantly large in comparison to the diagonal elements, indicating strongly coupled diffusion process. We can also determine the "magnitude" of the Fick diffusivity $|D|^{1/2} = 6.9\times10^{-10}\ \mathrm{m^2\ s^{-1}}$ for use in the calculation of the Fourier number $\frac{4|D|^{1/2}t}{d_{drop}^2}$.The component driving forces for transfer of NMP (1) and propylbenzene (2) are $\Delta x_1 = x_{10} - x_{1,eq} = 0.13749252$, $\Delta x_2 = x_{20} - x_{2,eq} = -0.0155461$1. Particularly noteworthy is that the driving force for propylbenzene transfer is significantly lower in magnitude than that of NMP, and opposite in sign.

The transient Geddes equilibration trajectory follows a highly curvilinear path to equilibrium, hugging the binodal curve; see Figure 6-24. If coupling effects are completely ignored, the equilibration trajectory follows a linear path in composition space.

Figure 6-25(a) presents a plot of component Murphree efficiencies as a function of the dimensionless Fourier number $\frac{4|D|^{1/2}t}{d_{drop}^2}$ where the droplet diameter is taken as $d_{\mathrm{drop}}$ = 2 mm. During the early stages of the equilibration process, the Murphree point efficiency of propylbenzene (component 2) exhibits negative values, indicative of uphill diffusion. As a consequence of uphill diffusion, the transient equilibration of propylbenzene exhibits a pronounced composition undershoot during its approach to equilibration; see Figure 6-25(b).

## 6.11 Uphill diffusion in NMP(1)/propylbenzene(2)/tetradecane(3) mixtures

We investigate the F-R equilibration trajectory, using the assumption that the 50/50 propylbenzene/tetradecane feed mixture is dispersed as droplets of 2 mm diameter in a continuous phase consisting of solvent rich phase; see Figure 6-26. The initial mole fractions in the drop are $x_{10}$ = 0.0, $x_{20}$ = 0.5, and $x_{30}$ = 0.5. The final equilibrated composition is $x_{1,\mathrm{eq}}$ = 0.329380812, $x_{2,\mathrm{eq}}$ = 0.250774108, and $x_{3,\mathrm{eq}}$ = 0.41984508, corresponding to one end of the tie line. The continuous phase has the composition

at the other end of the tie-line: $x_{1,eq} = 0.329380812$, $x_{2,eq} = 0.250774108$, and $x_{3,eq} = 0.41984508$. In our calculations we assume that the mass transfer resistance resides predominantly within the dispersed phase; this is a common occurrence.[45, 98]

The matrix of thermodynamic factors, calculated at the arithmetic average composition of the dispersed phase droplets between the initial and final equilibrated compositions ($x_{1,av} = 0.16469041$, $x_{2,av} = 0.37538705$, and $x_{3,av} = 0.45992254$) is $[\Gamma] = \begin{bmatrix} 0.52331466 & -0.51132939 \\ -0.13074844 & 2.17166685 \end{bmatrix}$. For calculation of the transient equilibration trajectories in the dispersed phase, the scalar diffusivity $|\Lambda|^{1/2}$ is assumed to have the value $|\Lambda|^{1/2} = 1\times10^{-9}\ \mathrm{m^2 s^{-1}}$; therefore, $[D] = |\Lambda|^{1/2}[\Gamma] = \begin{bmatrix} 0.52331466 & -0.51132939 \\ -0.13074844 & 2.17166685 \end{bmatrix} \times 10^{-9}\ \mathrm{m^2 s^{-1}}$. The off-diagonal element $D_{12}$ is the same order of magnitude as the diagonal element $D_{11}$, indicating that coupling effects are perhaps not negligible process. We can also determine the "magnitude" of the Fick diffusivity $|D|^{1/2} = 1.03\times10^{-9}\ \mathrm{m^2\ s^{-1}}$ for use in the calculation of the Fourier number $\dfrac{4|D|^{1/2}t}{d_{drop}^2}$. The component driving forces for transfer of NMP (1) and propylbenzene (2) are $\Delta x_1 = x_{10} - x_{1,eq} = -0.32938081$, $\Delta x_2 = x_{20} - x_{2,eq} = 0.24922589$. Particularly noteworthy is that the driving force for propylbenzene transfer is of the same order of magnitude as that of NMP, but opposite in sign.

The transient Geddes equilibration trajectory follows a highly curvilinear path to equilibrium, hugging the binodal curve; see Figure 6-26. If coupling effects are completely ignored, the equilibration trajectory follows a linear path in composition space.

Figure 6-27(a) presents a plot of component Murphree efficiencies as a function of the dimensionless Fourier number $\dfrac{4|D|^{1/2}t}{d_{drop}^2}$ where the droplet diameter is taken as $d_{drop} = 2$ mm. During the early stages of the equilibration process, the Murphree point efficiency of tetradecane (component 3) exhibits negative

values, indicative of uphill diffusion. As a consequence of uphill diffusion, the transient equilibration of tetradecane exhibits a slight, yet perceptible, composition overshoot during its approach to equilibration; see Figure 6-27(b).

## 6.12 List of Tables for Ternary Liquid-Liquid Extraction

Table 6-1. NRTL parameters for NMP(1)/propylbenzene(2)/dodecane(3) at 298 K. The parameters are from Al-Jimaz et al.[94]

| | $A_{ij}$ | $A_{ji}$ | $\alpha_{ij} = \alpha_{ji}$ |
|---|---|---|---|
| | K | K | dimensionless |
| NMP(1)/ propylbenzene(2) | 16.061 | 52.731 | 0.2 |
| NMP(1)/dodecane(3) | 875.58 | 161 | 0.2 |
| propylbenzene(2)/ dodecane(3) | 271.23 | -299.3 | 0.2 |

Table 6-2. NRTL parameters for NMP(1)/propylbenzene(2)/tetradecane(3) at 298.15 K. The parameters are from Al-Jimaz et al.[94]

| | $A_{ij}$ | $A_{ji}$ | $\alpha_{ij} = \alpha_{ji}$ |
|---|---|---|---|
| | K | K | dimensionless |
| NMP(1)/ propylbenzene(2) | -854.09 | 474.73 | 0.2 |
| NMP(1)/tetradecane(3) | 1035.4 | 122.26 | 0.2 |
| propylbenzene(2)/ tetradecane(3) | 84.968 | -797.95 | 0.2 |

Table 6-3. UNIQUAC parameters for water(1)/caprolactam(2)/toluene(3) at 298.15 K. These parameters are from Table 1, Chapter 7 of the PhD dissertation of Bollen.[100]

| | $r_i$ | $q_i$ |
|---|---|---|
| | dimensionless | dimensionless |
| water(1) | 0.92 | 1.4 |
| caprolactam(2) | 4.6106 | 3.724 |
| toluene(3) | 3.9928 | 2.968 |

| | $\tau_{ij} = A_{ij}/T$ | $\tau_{ji} = A_{ji}/T$ |
|---|---|---|
| | dimensionless | dimensionless |
| water(1)/caprolactam(2) | 0.1027043 | 3.647516849 |
| water(1)/ toluene(3) | 0.2563201 | 0.0964476 |
| caprolactam(2)/toluene(3) | 0.3324973 | 1.4351863 |

Table 6-4. UNIQUAC parameters for water (1)/ethanol(2)/benzene(3) at 298.15 K. These parameters are taken from Example 05.20 of Gmehling et al.[101]

| | $r_i$ | $q_i$ |
|---|---|---|
| | dimensionless | dimensionless |
| water(1) | 0.92 | 1.4 |
| ethanol(2) | 2.105 | 1.972 |
| benzene(3) | 3.1878 | 2.4 |

| | $\tau_{ij} = A_{ij}/T$ | $\tau_{ji} = A_{ji}/T$ |
|---|---|---|
| | dimensionless | dimensionless |
| water(1)/ethanol(2) | 0.1713 | 2.9060 |
| Water(1)/benzene(3) | 0.354 | 0.0117 |
| ethanol(2)/benzene(3) | 1.359 | 0.3625 |

Table 6-5. UNIQUAC parameters for water (1)/ethyl acetate(2)/ethanol(3). These parameters are taken from Table 3 of Resa and Goenaga.[102]

| | $r_i$ | $q_i$ |
|---|---|---|
| | dimensionless | dimensionless |
| water(1) | 0.92 | 1.4 |
| Ethyl acetate (2) | 3.4786 | 3.116 |
| ethanol(3) | 2.105 | 1.972 |

| | $A_{ij}$ | $A_{ji}$ |
|---|---|---|
| | $K^{-1}$ | $K^{-1}$ |
| water(1)/ethyl acetate(2) | 176.158 | 320.83 |
| Water(1)/ethanol(3) | -109.102 | -137.836 |
| Ethyl acetate(2)/ethanol(3) | 390.218 | -355.791 |

Table 6-6. NRTL parameters for furfural(1)/formic acid(2)/water (3) at 298 K. These parameters are taken from Table 2 of Reyes-Labarta et al.[103]

| | $\tau_{ij} = A_{ij}/T$ | $\tau_{ji} = A_{ji}/T$ | $\alpha_{ij} = \alpha_{ji}$ |
|---|---|---|---|
| | dimensionless | dimensionless | dimensionless |
| Furfural(1)/ formic acid(2) | 3.0959 | -1.662 | 0.2 |
| Furfural(1)/ water(3) | 0.1044 | 4.126 | 0.2 |
| Formic acid (2)/ water(3) | 1.386 | -3.523 | 0.2 |

## 6.13 List of Figures for Ternary Liquid-Liquid Extraction

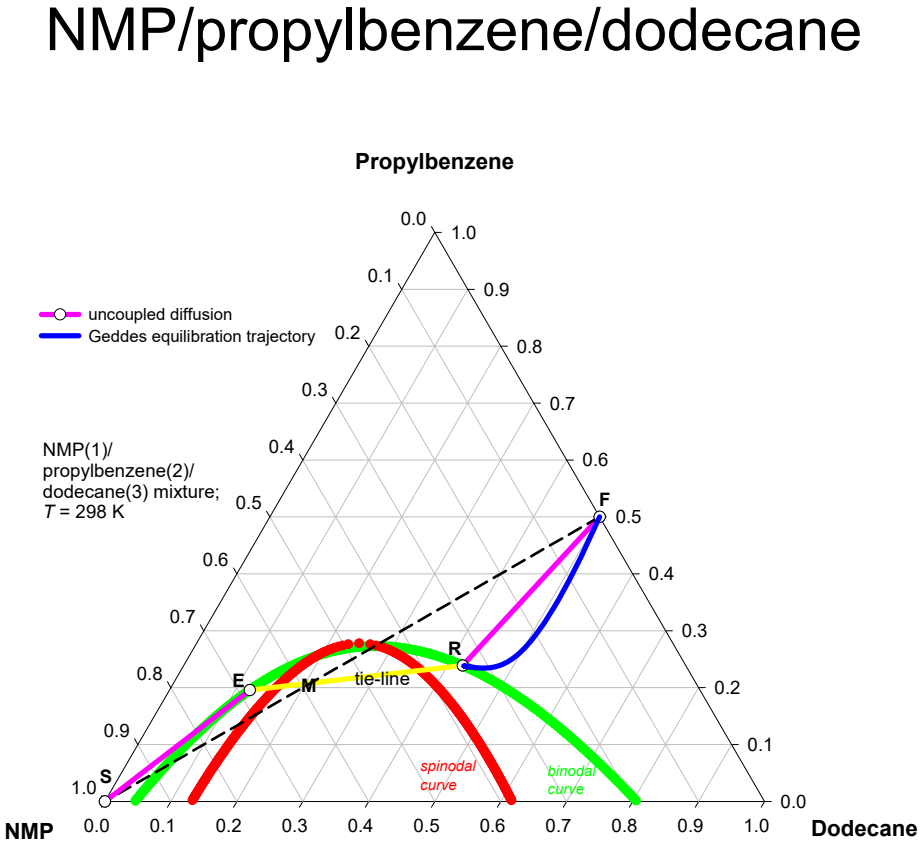


Figure 6-1.The phase equilibrium diagram for the system NMP(1)/propylbenzene(2)/dodecane(3) at 298 K. Pure N-methyl pyrrolidone (NMP, S = solvent) is mixed with a 50/50 propylbenzene/dodecane feed mixture (F) to yield mixture M that lies in the two phase region. The plait point is indicated by P. The mixture separates into two phases with compositions E (Extract) and R (Raffinate) at either ends of the tie-line shown. The feed phase F will equilibrate to R, and the solvent phase S will equilibrate to E. The NRTL parameters for calculation of the phase equilibrium thermodynamics are provided in Table 6-1.

# NMP/propylbenzene/tetradecane

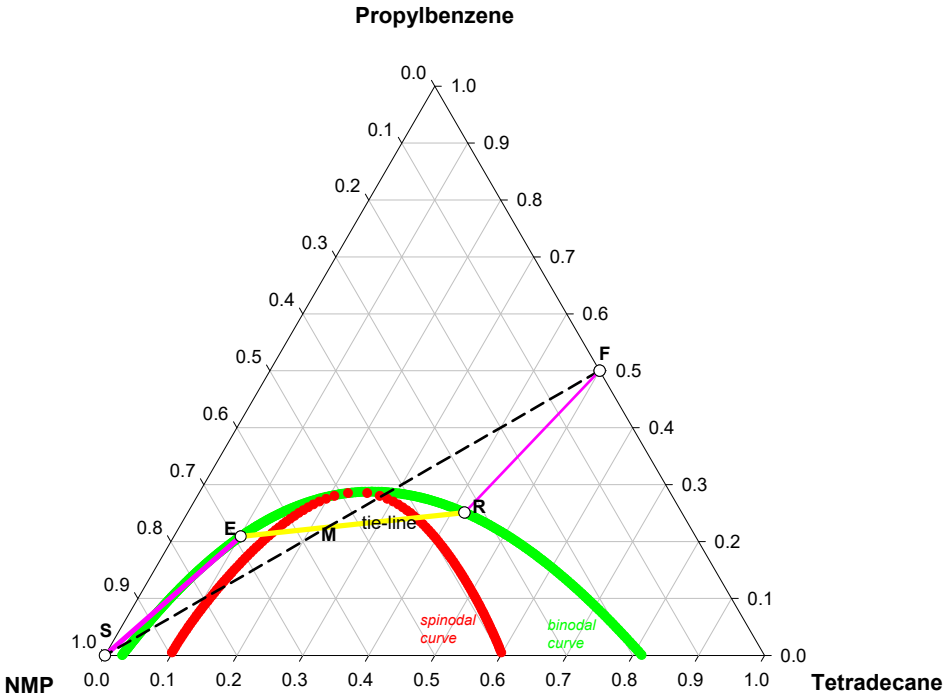


Figure 6-2.The phase equilibrium diagram for the system NMP(1)/propylbenzene(2)/tetradecane(3) at 298 K. Pure N-methyl pyrrolidone (NMP, S = solvent) is mixed with a 50/50 propylbenzene/dodecane feed mixture (F) to yield mixture M that lies in the two phase region. The plait point is indicated by P. The mixture separates into two phases with compositions E (Extract) and R (Raffinate) at either ends of the tie-line shown. The feed phase F will equilibrate to R, and the solvent phase S will equilibrate to E. The NRTL parameters for calculation of the phase equilibrium thermodynamics are provided in Table 6-2.

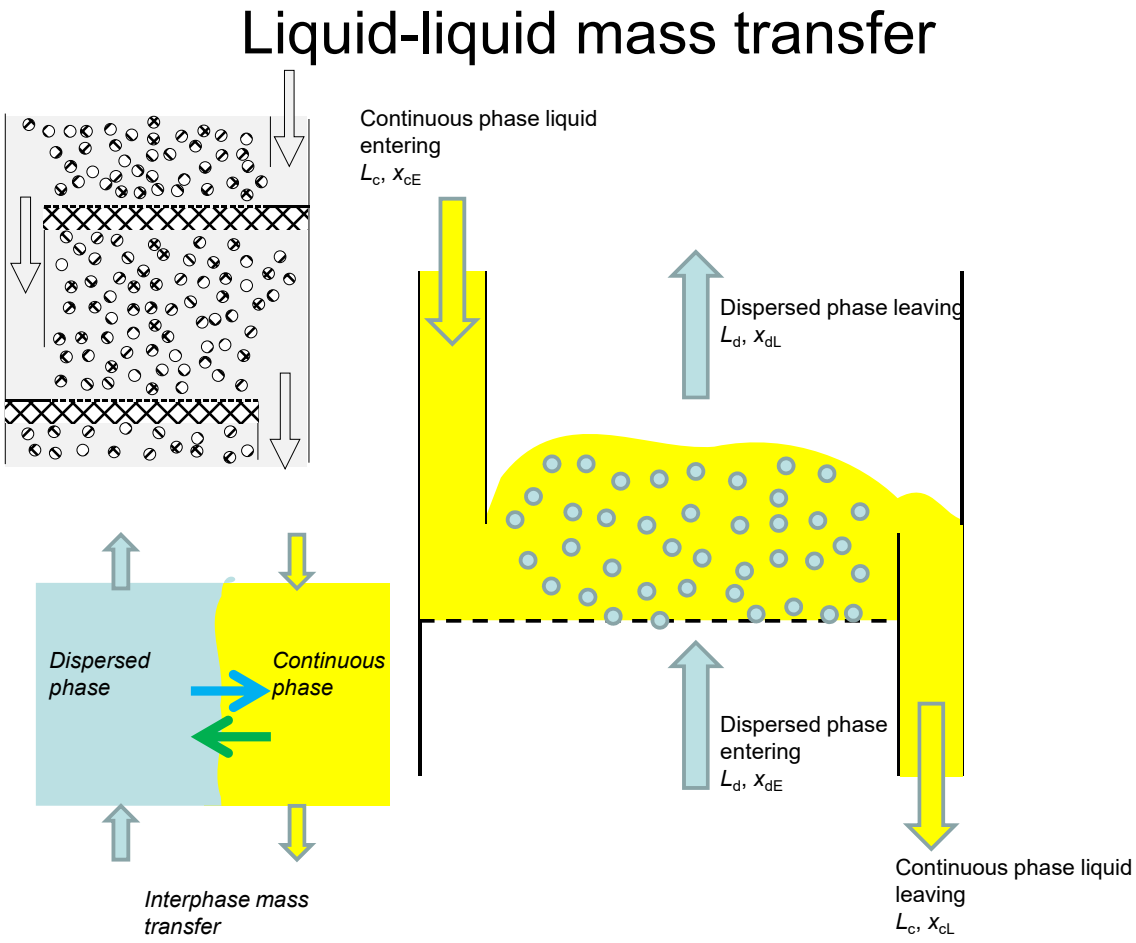


Figure 6-3. Schematic of single-stage contacting in sieve-tray column.

# Glycerol/Acetone/Water Equilibration

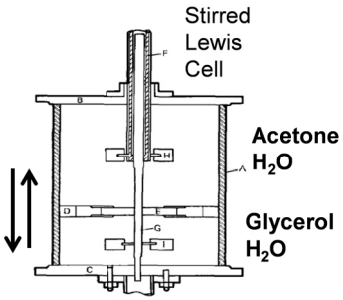


George Lenell Standart
University of Manchester
1921-1978

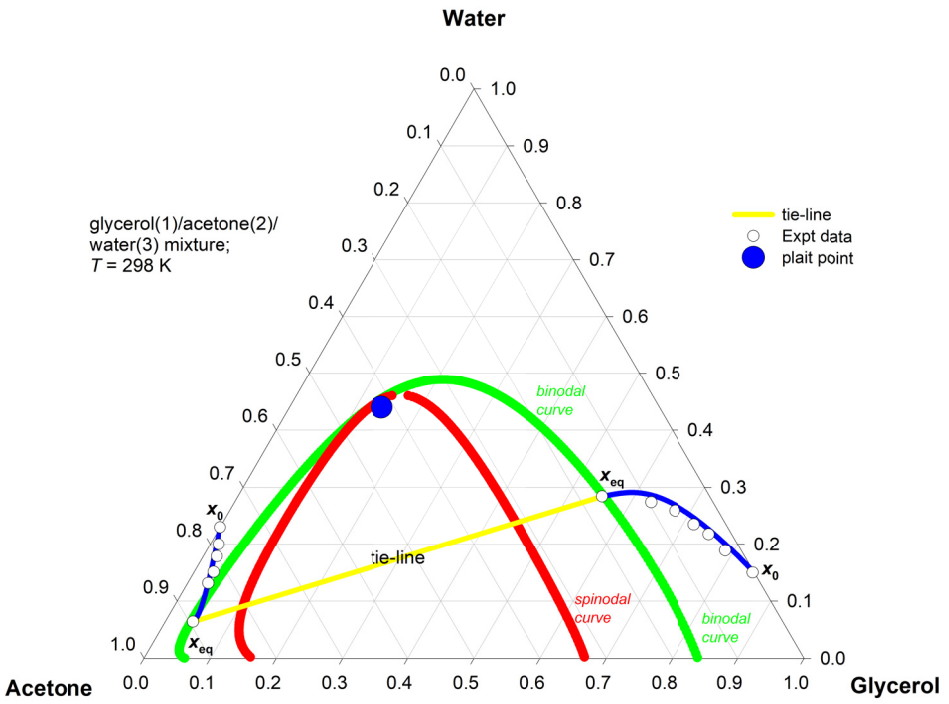


Figure 6-4. Transient equilibration trajectories for the system glycerol(1)/acetone(2)/water(3) mixtures at 298 K. For the acetone-rich phase (left hand side), the initial mole fractions drop are $x_{10}$ = 0.0, $x_{20}$ = 0.77, and $x_{30}$ = 0.23; the final equilibrium composition is $x_{1,eq}$ = 0.042, $x_{2,eq}$ = 0.894, and $x_{3,eq}$ = 0.064. For the glycerol-rich phase (right hand side), the initial mole fractions are $x_{10}$ = 0.85, $x_{20}$ = 0.0, and $x_{30}$ = 0.15; the final equilibrium composition is $x_{1,eq}$ = 0.552, $x_{2,eq}$ = 0.164, and $x_{3,eq}$ = 0.284. The experimental data for the equilibration paths for glycerol(1)/acetone(2)/water(3) mixture measured in a stirred Lewis cell by Krishna et al.[97] are also indicated. The two trajectories are calculated using $[D]=|\Lambda|^{1/2}[\Gamma]$ with $|\Lambda|^{1/2}=(D_{1,self})^{x_1}(D_{2,self})^{x_2}(D_{3,self})^{x_3}$, taking $D_{1,self}$= 0.01, $D_{2,self}$= 3.2, $D_{3,self}$= 0.5 with units $10^{-9}$ m$^2$ s$^{-1}$; this diffusivity information has been derived from our earlier work.[73] The calculation details are provided by Krishna.[45]

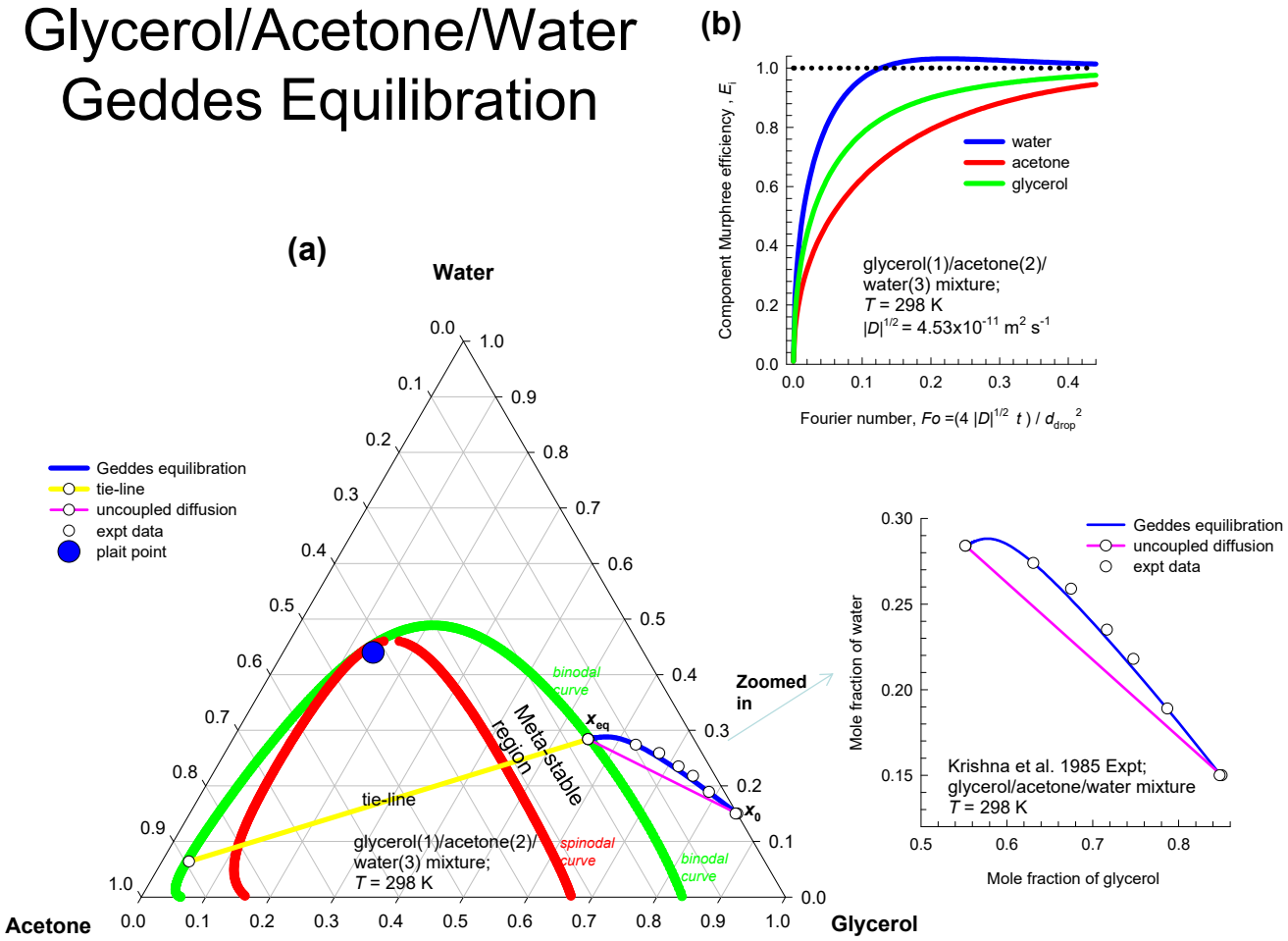


Figure 6-5. (a) Transient equilibration trajectories for glycerol(1)/acetone(2)/water(3) mixture at 298 K, calculated using the Geddes model. The initial mole fractions of the dispersed phase droplets of 2 mm diameter is $x_{10} = 0.85$, $x_{20} = 0.0$, and $x_{30} = 0.15$. The final equilibrated composition is $x_{1,eq} = 0.552$, $x_{2,eq} = 0.164$, and $x_{3,eq} = 0.284$. (b) Plot of the component Murphree efficiencies, $E_i$, as function of the Fourier number. The phase equilibrium is determined from the NRTL parameters in Table 5-1.

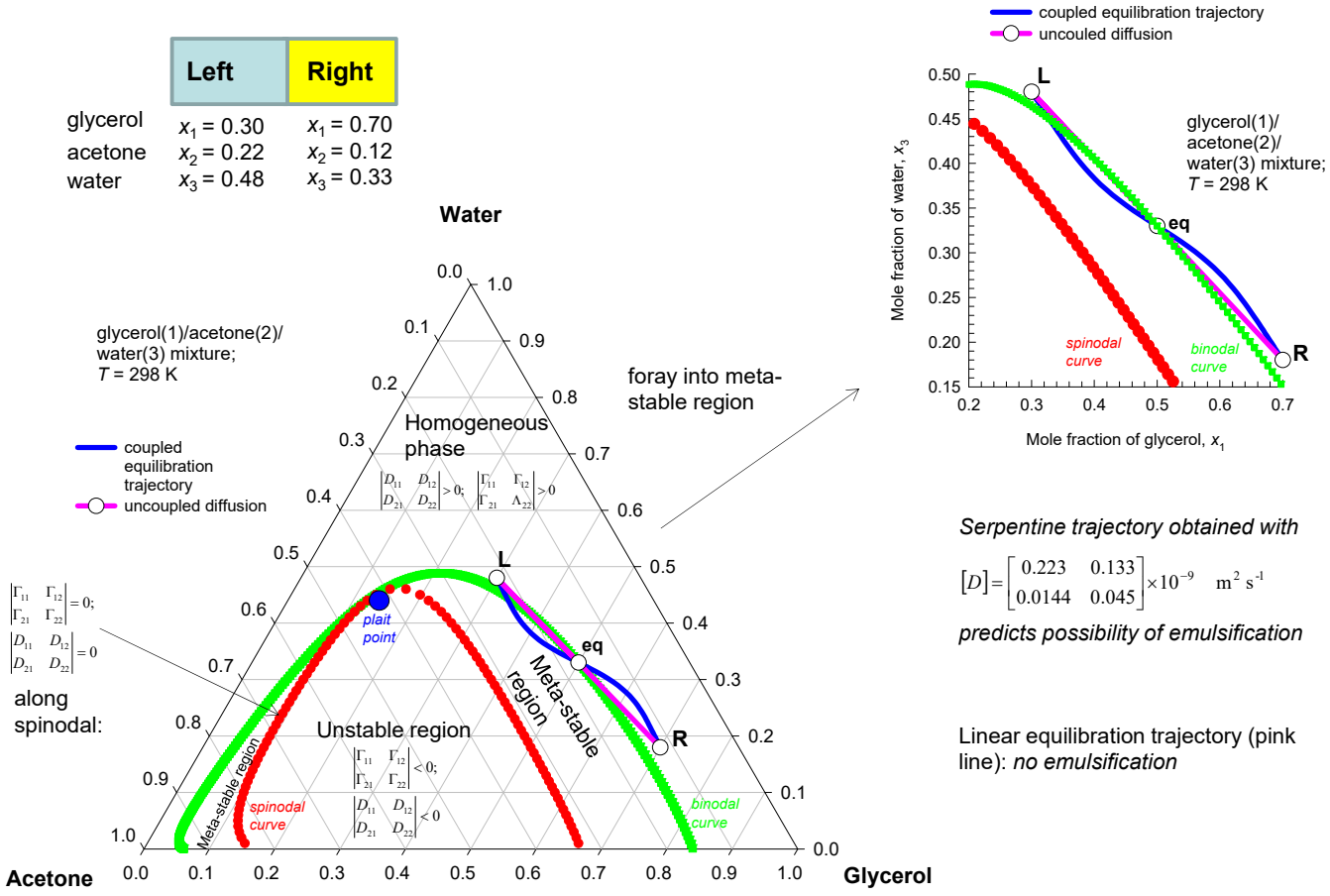


Figure 6-6. Trajectory followed during equilibration of homogenous mixtures of two different compositions for the system glycerol(1)/acetone(2)/water(3); the equilibrium composition $x_{1,eq}$ = 0.5, $x_{2,eq}$ = 0.17 and $x_{3,eq}$ = 0.33. The NRTL parameters for calculation of the phase equilibrium thermodynamics are provided in Table 5-1.

# Water/chloroform/acetic acid: equilibration trajectory

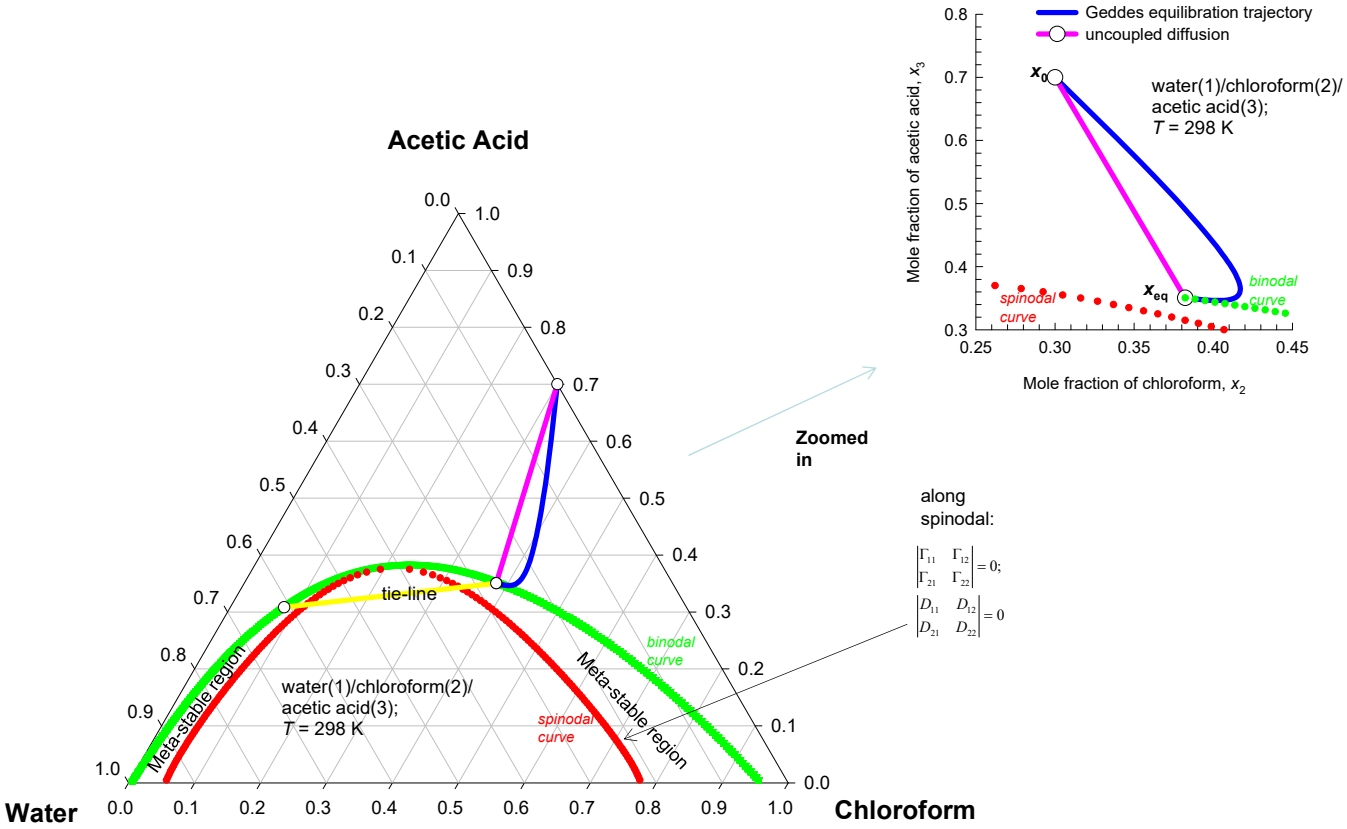


Figure 6-7. Transient equilibration trajectories for water(1)/chloroform(2)/acetic-acid(3) mixture, calculated using the Geddes model, plotted in composition space. The initial mole fractions of the dispersed phase droplet is $x_{10} = 0.0$, $x_{20} = 0.3$, and $x_{30} = 0.7$. The final equilibrated composition is $x_{1,eq} = 0.267383532$, $x_{2,eq} = 0.382190021$, and $x_{3,eq} = 0.350426$. The UNIQUAC parameters are provided in Table 5-2.

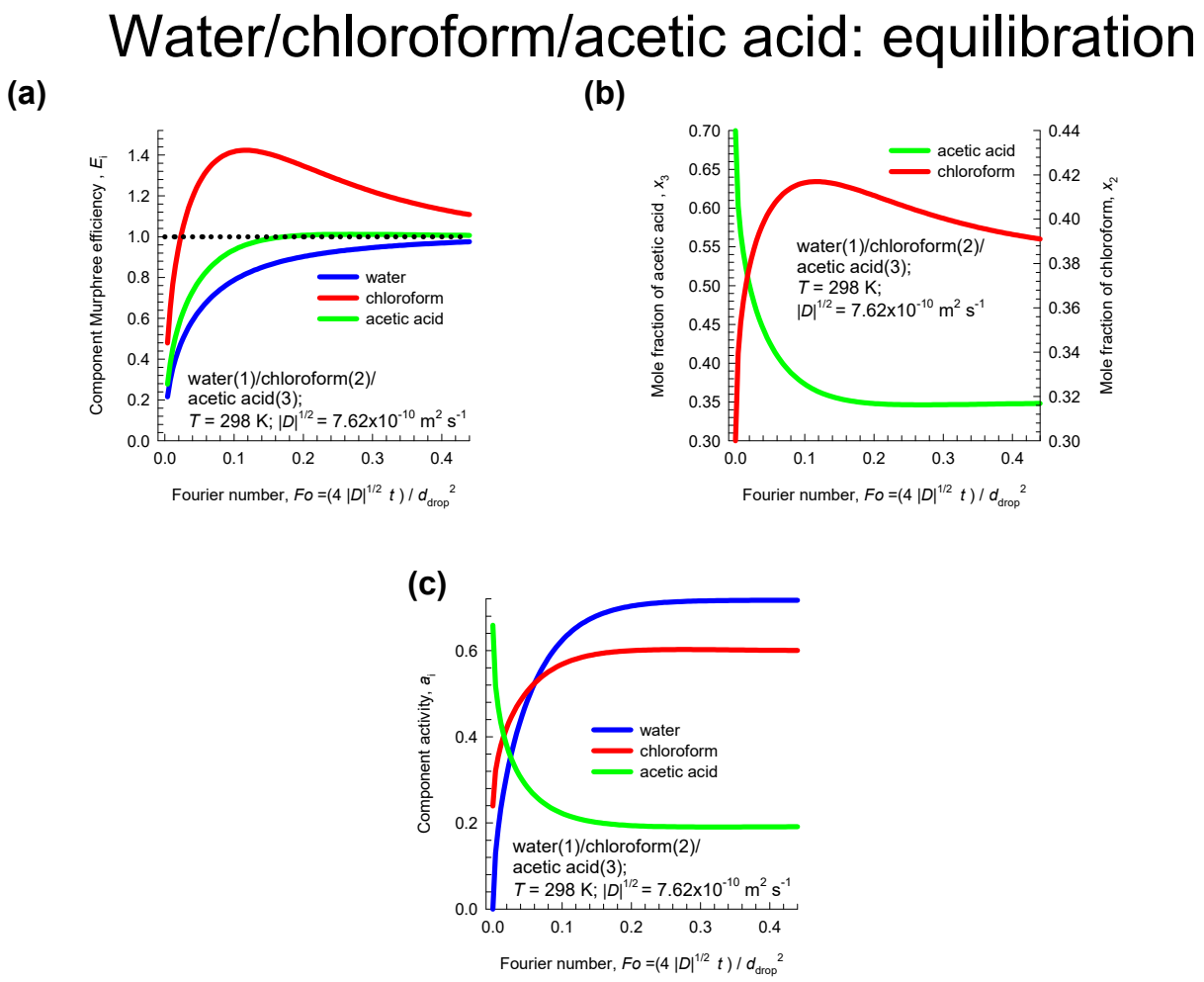


Figure 6-8. Transient equilibration trajectories for water(1)/chloroform(2)/acetic-acid(3) mixture. (a) Plot of the component Murphree efficiencies, $E_i$, as function of the Fourier number. (b) Plot of the transient equilibration compositions (mole fractions) of chloroform and acetic acid as a function of the Fourier number. (c) Plot of the transient equilibration activities of water, chloroform and acetic acid as a function of the Fourier number.

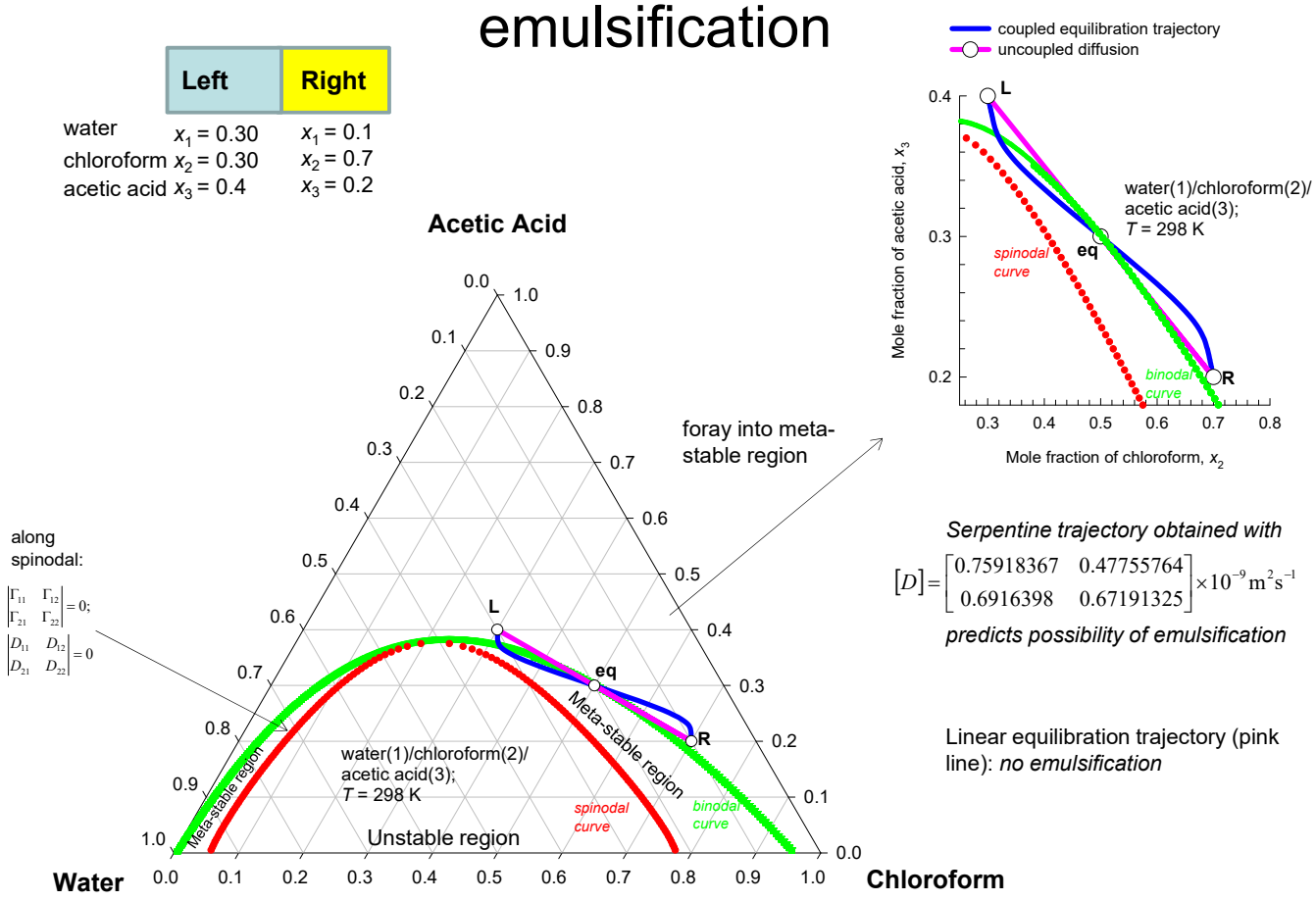


Figure 6-9. Transient inter-diffusion in a diffusion couple consisting of water(1)/chloroform(2)/acetic-acid(3) mixtures.

# Water/Acetone/Ethylacetate: equilibration trajectory

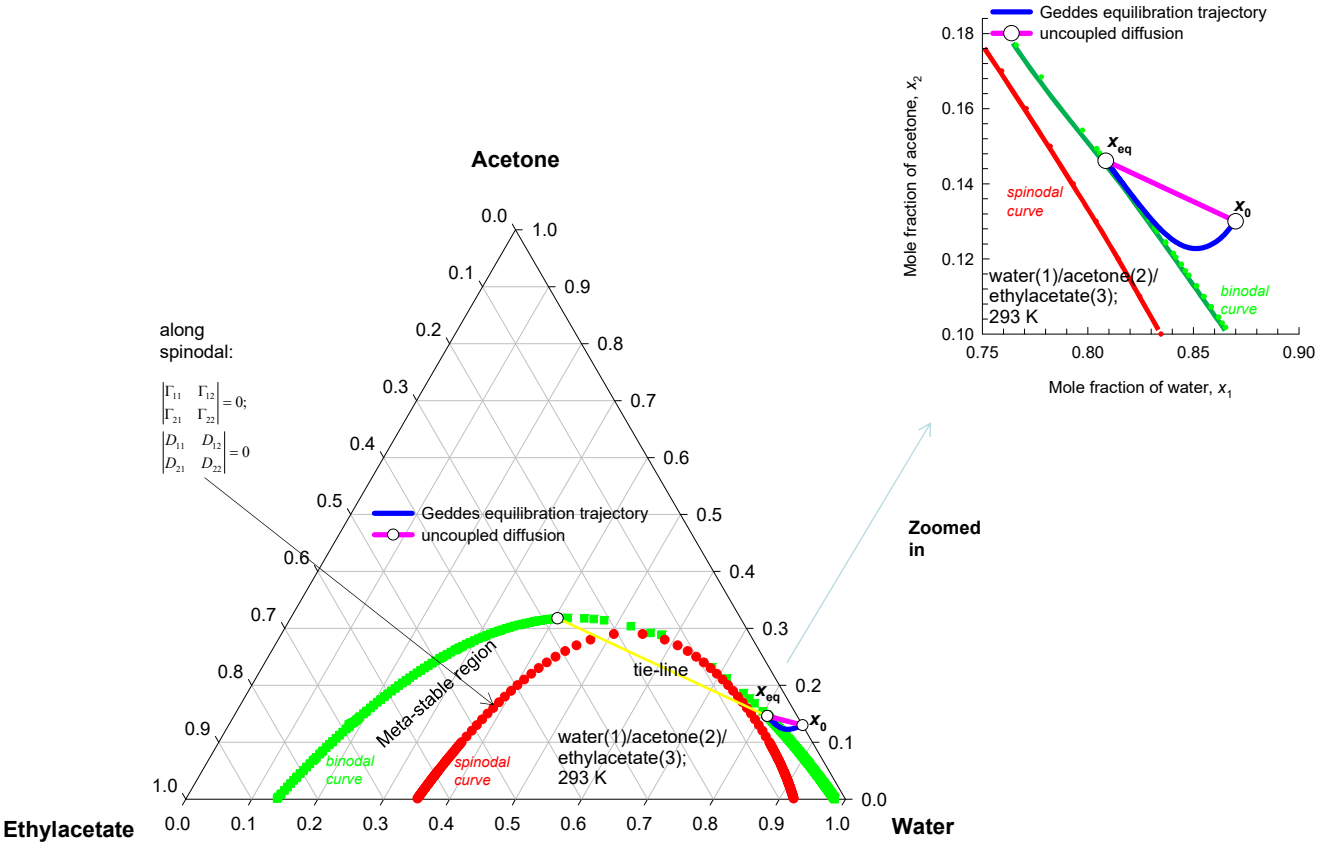


Figure 6-10. Transient equilibration trajectories for water(1)/acetone(2)/ethylacetate(3) mixture, calculated using the Geddes model, plotted in composition space. The initial mole fractions of the dispersed phase droplet of 2 mm diameter is $x_{10} = 0.87$, $x_{20} = 0.13$, and $x_{30} = 0.0$. The final equilibrated composition is $x_{1,eq} = 0.4049748$, $x_{2,eq} = 0.146113283$, and $x_{3,eq} = 0.045392$. The UNIQUAC parameters for calculation of the phase equilibrium thermodynamics are provided in Table 5-3.

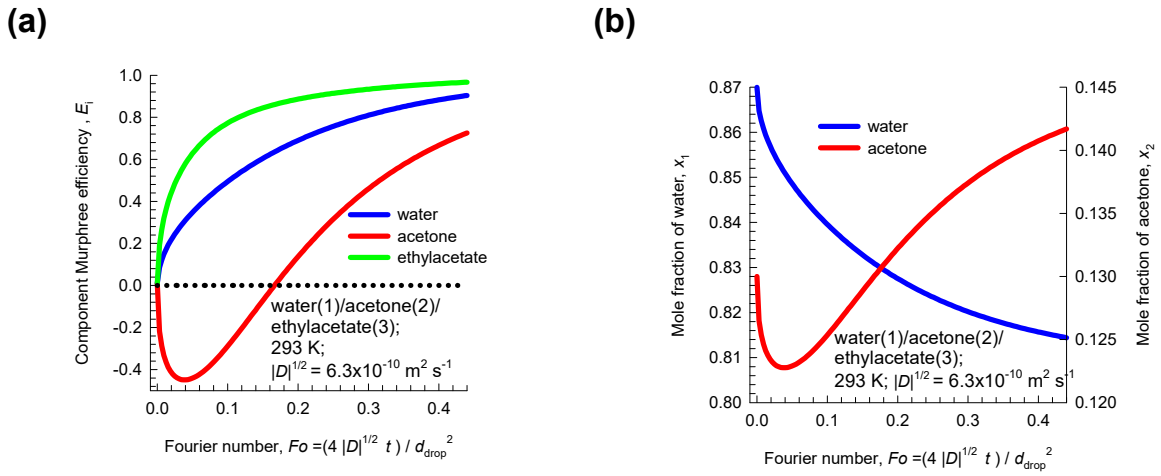


Figure 6-11. Transient equilibration trajectories for water(1)/acetone(2)/ethylacetate(3) mixture. (a) Plot of the component Murphree efficiencies, $E_i$, as function of the Fourier number. (b) Plot of the transient equilibration compositions of water and acetone as a function of the Fourier number.

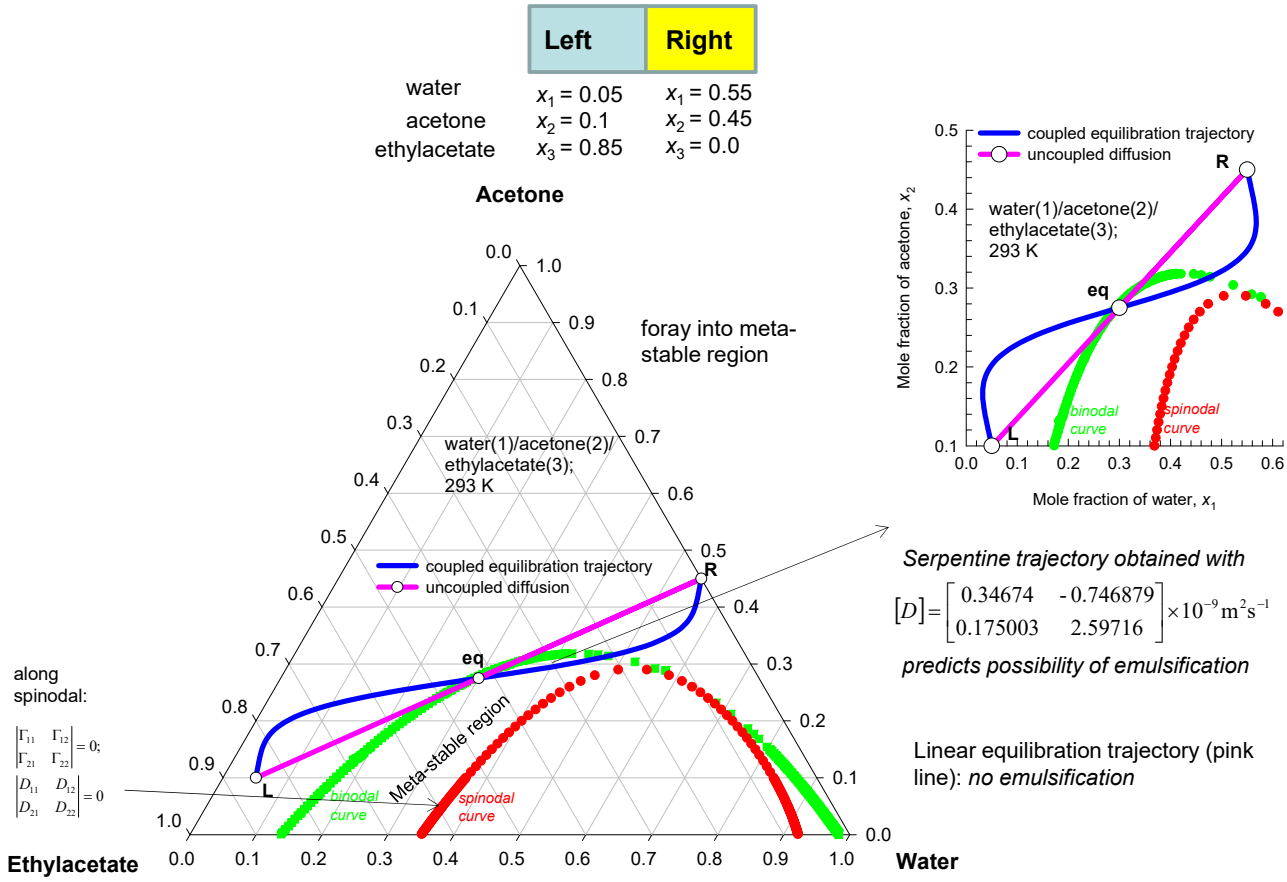


Figure 6-12. Trajectory followed during equilibration of homogenous mixtures of two different compositions for the system water(1)/acetone(2)/ethylacetate(3); the equilibrium composition $x_{1,eq}$ = 0.30, $x_{2,eq}$ = 0.275 and $x_{3,eq}$ = 0.425. The UNIQUAC parameters for calculation of the phase equilibrium thermodynamics are provided in Table 5-3.

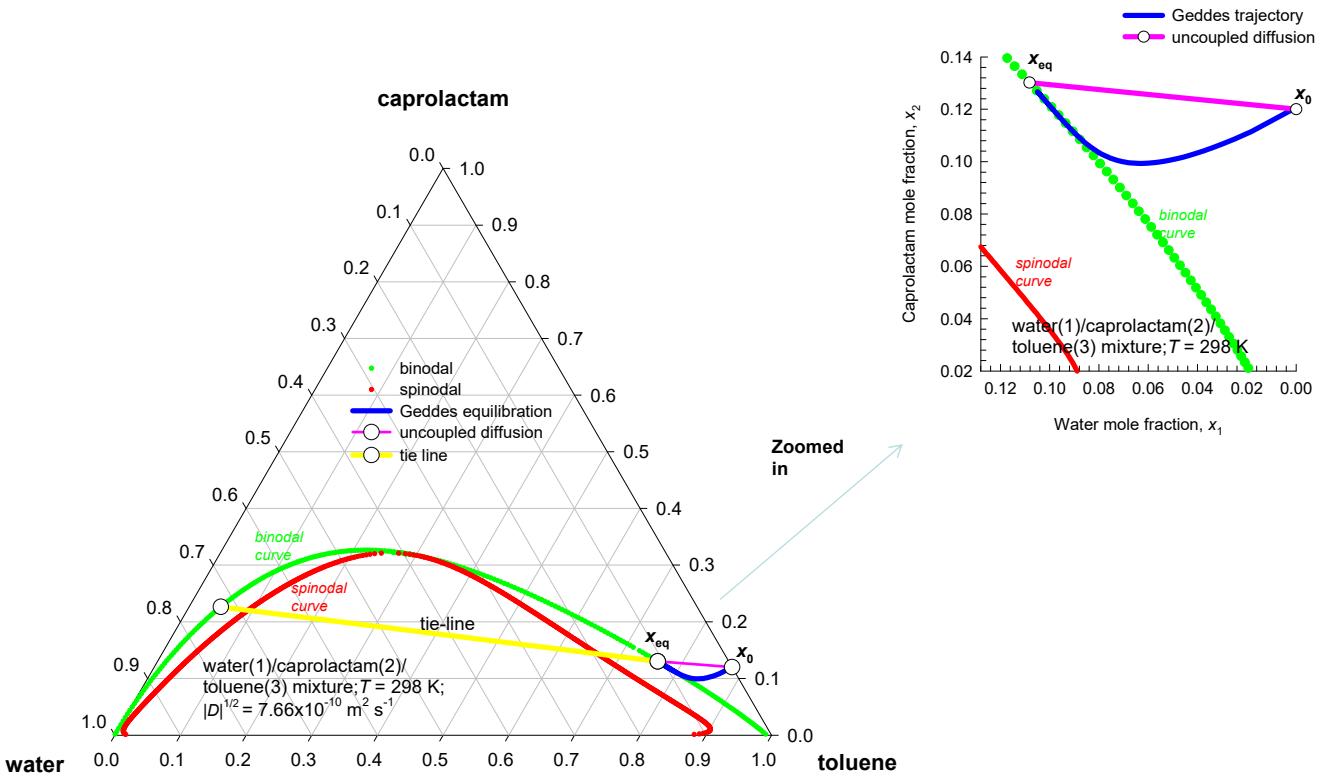


Figure 6-13. Transient equilibration trajectories for the system water(1)/caprolactam(2)/toluene(3) at 298 K. The initial mole fractions in the drop are $x_{10}$ = 0.0, $x_{20}$ = 0.12, and $x_{30}$ = 0.88. The final equilibrium composition is $x_{1,eq}$ = 0.108182718, $x_{2,eq}$ = 0.130183682, and $x_{3,eq}$ = 0.7616336. The UNIQUAC parameters for calculation of the phase equilibrium thermodynamics are provided in Table 6-3.

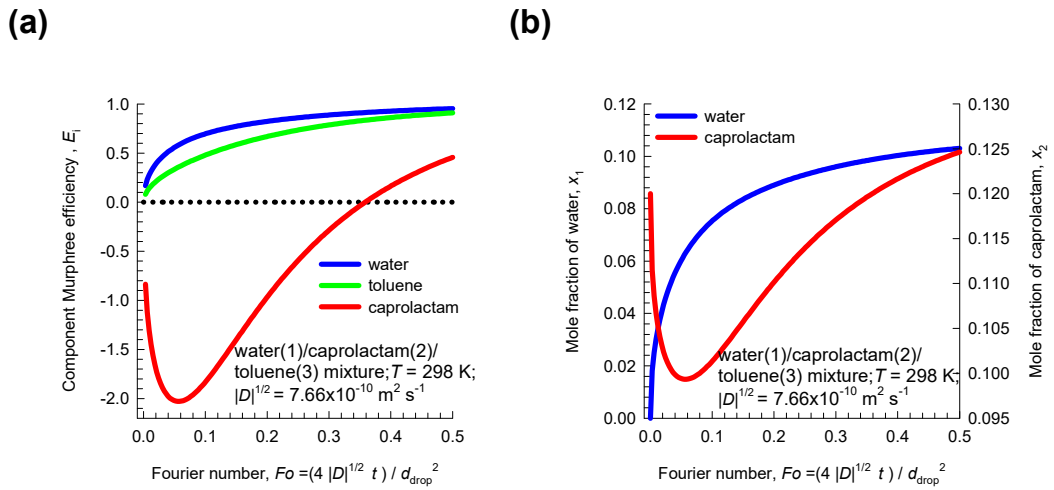


Figure 6-14. Transient equilibration trajectories for the system water(1)/caprolactam(2)/toluene(3) at 298 K. (a) Plot of the component Murphree efficiencies, $E_i$, as function of the Fourier number. (b) Plot of the transient equilibration compositions of water and caprolactam as a function of the Fourier number.

# Water/Caprolactam/Toluene equilibration

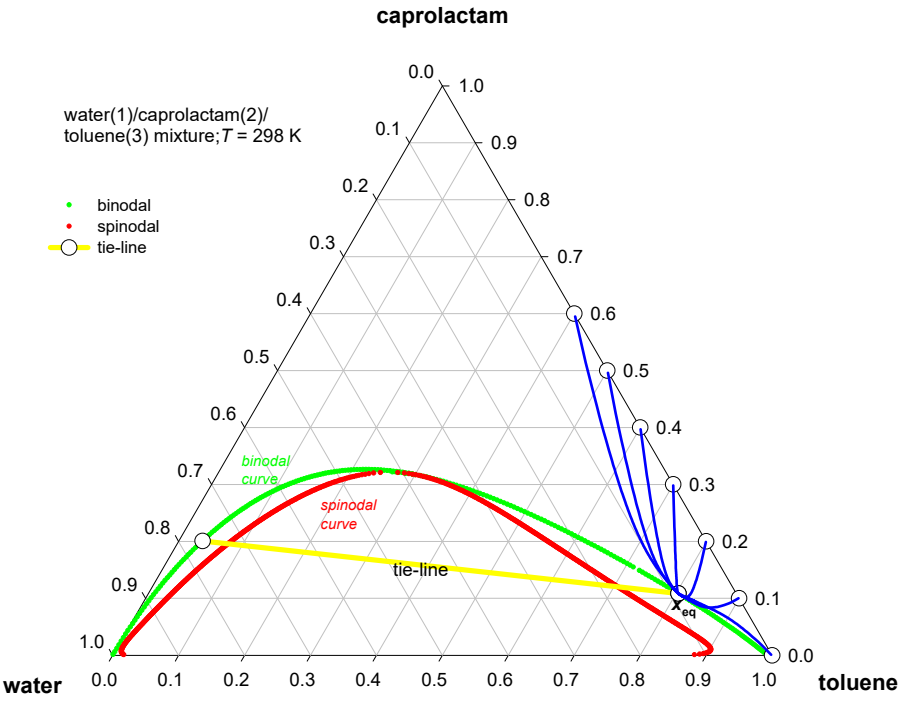


Figure 6-15.Transient equilibration trajectories for the system water(1)/caprolactam(2)/toluene(3) at 298 K. The initial mole fractions in the drop are binary caprolactam(2)/toluene(3) mixtures of varying compositions. The final equilibrium composition is $x_{1,eq}$ = 0.76316675, $x_{2,eq}$ = 0.200866022, and $x_{3,eq}$ = 0.035967228. The UNIQUAC parameters for calculation of the phase equilibrium thermodynamics are provided in Table 6-3.

# Water/ethanol/benzene equilibration

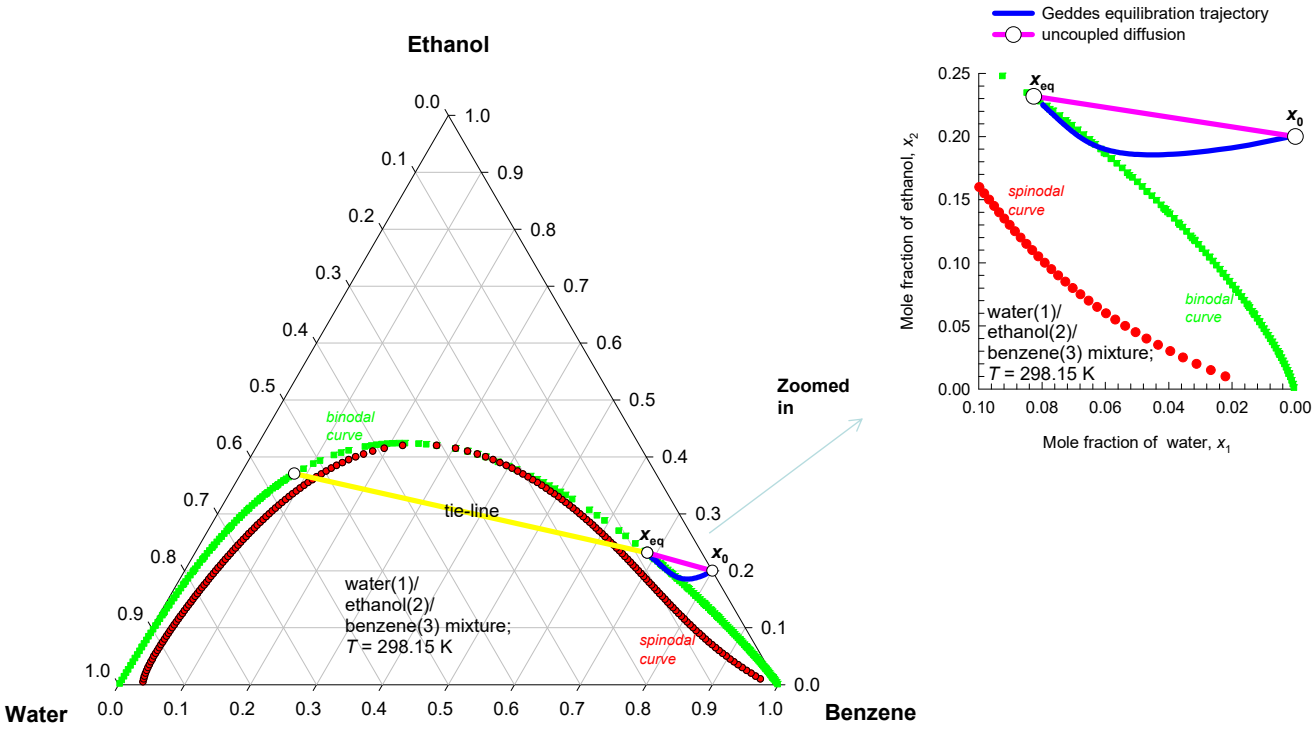


Figure 6-16. Transient equilibration trajectories for the system water(1)/ethanol(2)/benzene(3) at 298 K. The initial mole fractions in the drop are $x_{10}$ = 0.0, $x_{20}$ = 0.2, and $x_{30}$ = 0.88. The final equilibrated composition is $x_{1,eq}$ = 0.082641058, $x_{2,eq}$ = 0.231828339, and $x_{3,eq}$ = 0.685531. The UNIQUAC parameters are provided in Table 6-4.

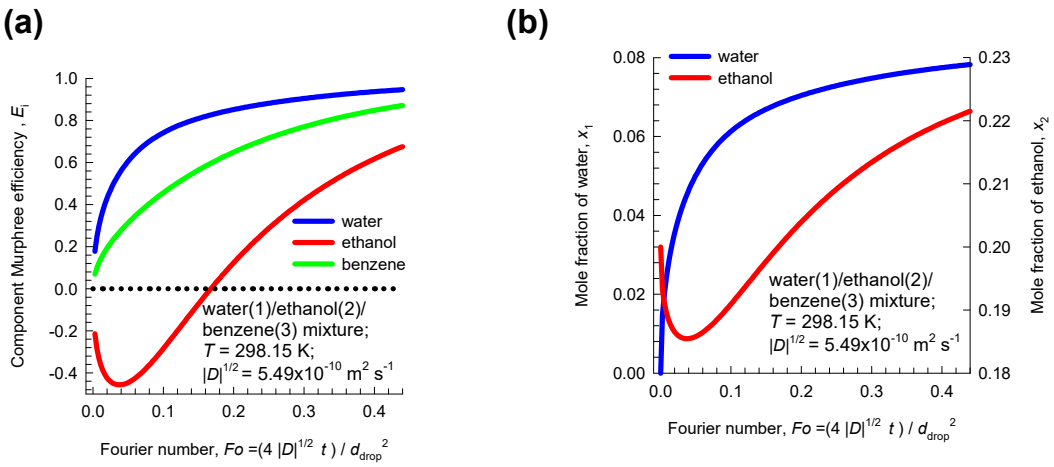


Figure 6-17. Transient equilibration trajectories for the system water(1)/ethanol(2)/benzene(3) at 298 K. (a) Plot of the component Murphree efficiencies, $E_i$, as function of the Fourier number. (b) Plot of the transient equilibration compositions of water (1) and ethanol (2) as a function of the Fourier number.

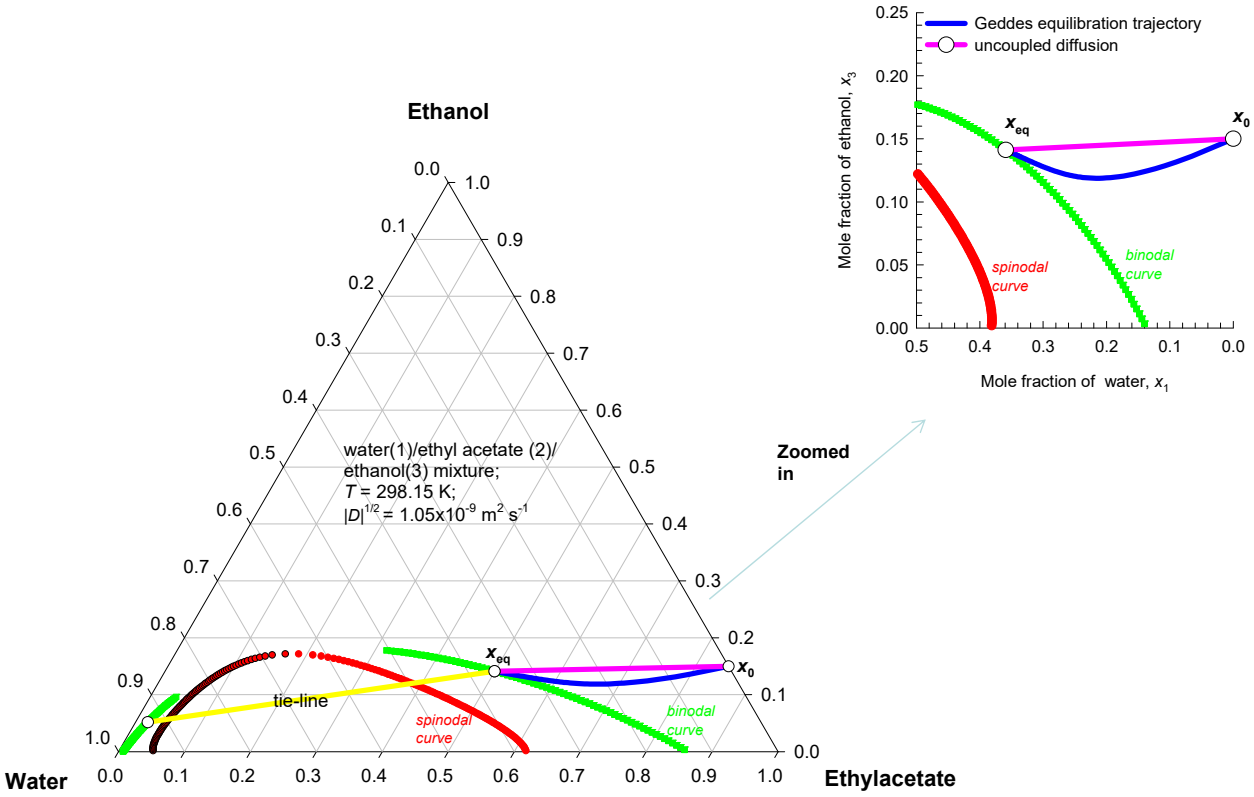


Figure 6-18. Transient equilibration trajectories for the system water(1)/ethyl acetate(2)/ethanol(3) at 298 K. The initial mole fractions in the drop are $x_{10}$ = 0.0, $x_{20}$ = 0.85, and $x_{30}$ = 0.15. The final equilibrated composition is $x_{1,eq}$ = 0.359190924, $x_{2,eq}$ = 0.499644619, and $x_{3,eq}$ = 0.141164. The UNIQUAC parameters are provided in Table 6-5.

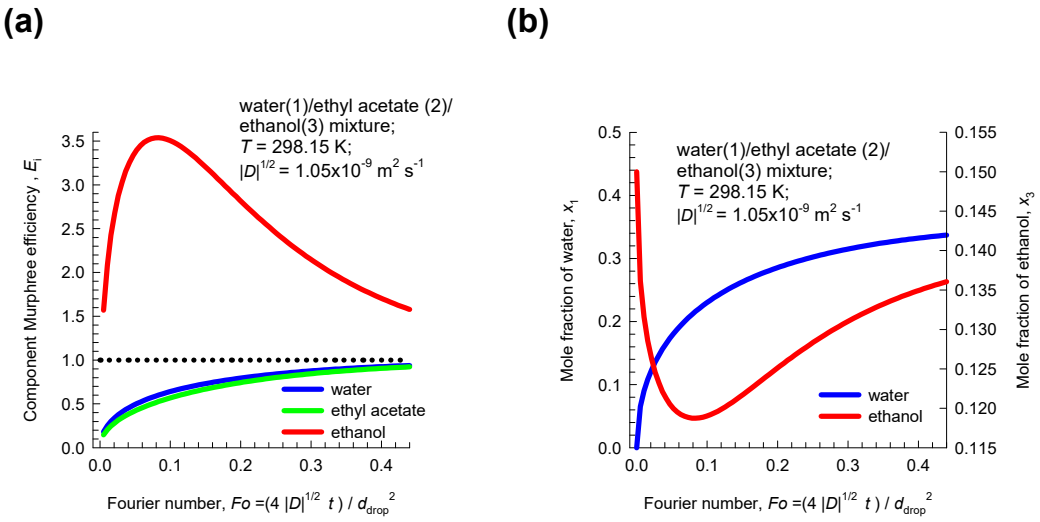


Figure 6-19. Transient equilibration trajectories for the system water(1)/ethyl acetate(2) /ethanol(3) at 298 K. (a) Plot of the component Murphree efficiencies, $E_i$, as function of the Fourier number. (b) Plot of the transient equilibration compositions of water (1) and ethanol (3) as a function of the Fourier number.

# Furfural/formic acid/water equilibration

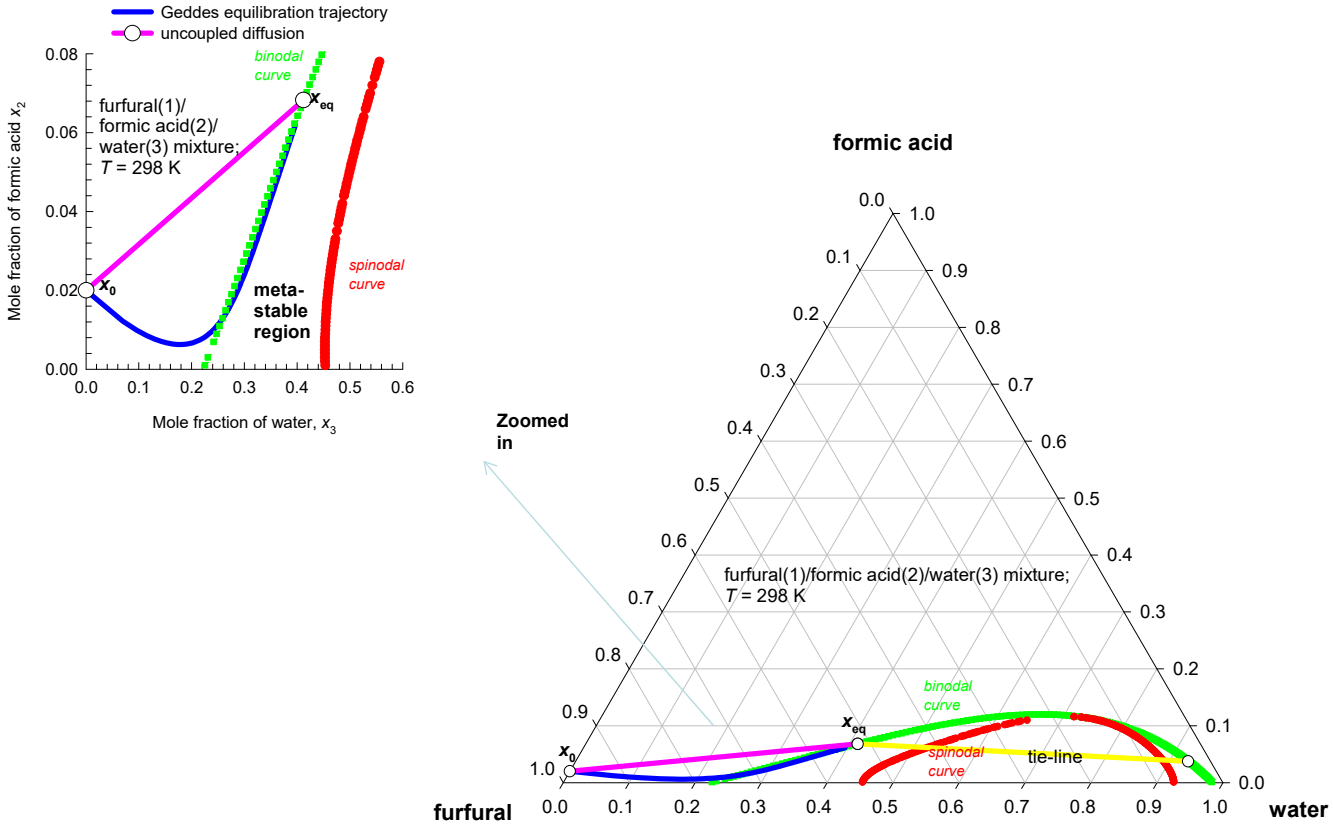


Figure 6-20.Transient equilibration trajectories for the system furfural(1)/formic acid(2)/water (3) at 298 K. The initial mole fractions in the drop are $x_{10}$ = 0.98, $x_{20}$ = 0.02, and $x_{30}$ = 0.0. The final equilibrated composition is $x_{1,eq}$ = 0.519537719, $x_{2,eq}$ = 0.068252025, and $x_{3,eq}$ = 0.41221026. The NRTL parameters for calculation of the phase equilibrium thermodynamics are provided in Table 6-6.

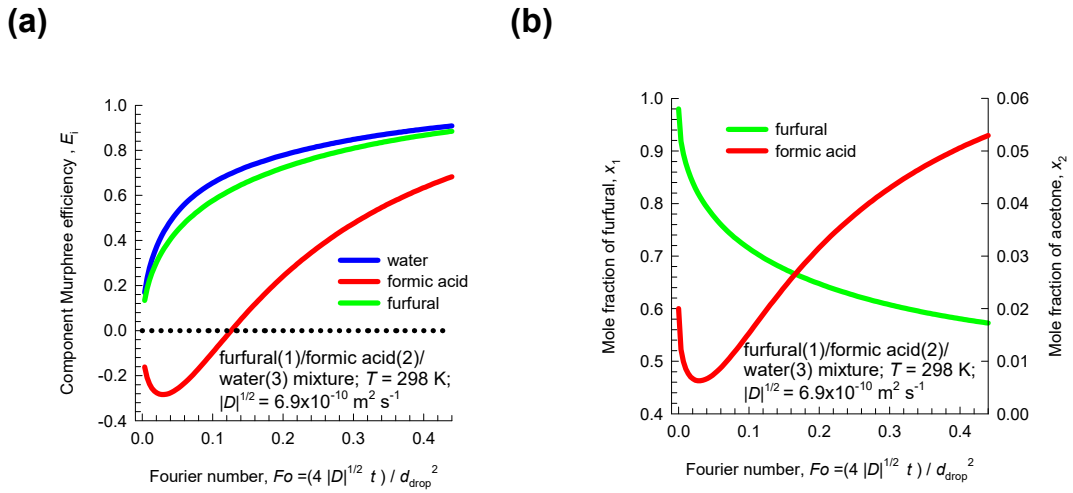


Figure 6-21.Transient equilibration trajectories for the system furfural(1)/formic acid(2)/water (3) at 298 K. (a) Plot of the component Murphree efficiencies, $E_i$, as function of the Fourier number. (b) Plot of the transient equilibration compositions of furfural and formic acid as a function of the Fourier number.

# NMP/propylbenzene/dodecane equilibration

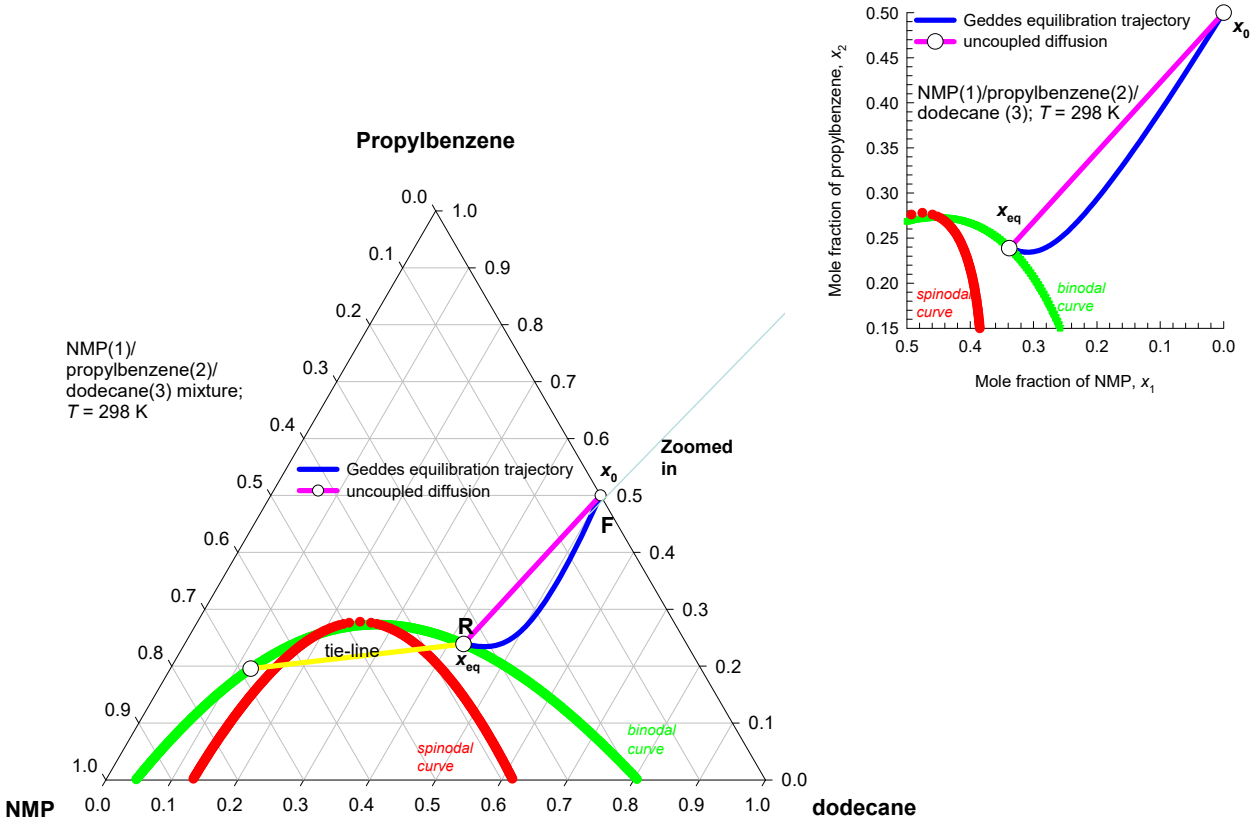


Figure 6-22. Transient equilibration trajectories for the system NMP(1)/propylbenzene(2)/dodecane(3) at 298 K. The initial mole fractions in the drop are $x_{10} = 0.0$, $x_{20} = 0.5$, and $x_{30} = 0.5$. The final equilibrated composition is $x_{1,eq} = 0.338353679$, $x_{2,eq} = 0.238690456$, and $x_{3,eq} = 0.42295586$. The NRTL parameters are provided in Table 6-1.

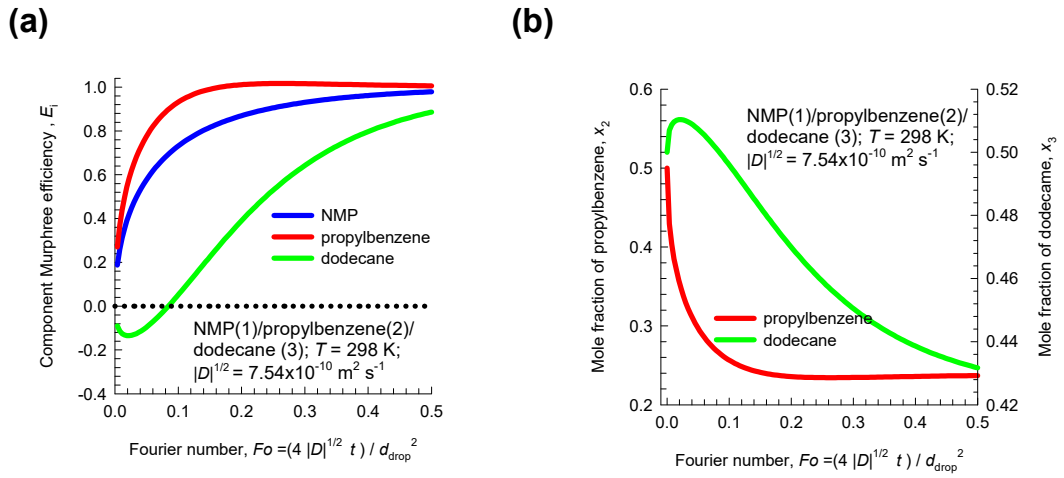


Figure 6-23. Transient equilibration in the system NMP(1)/propylbenzene(2)/dodecane(3) at 298 K. (a) Plot of the component Murphree efficiencies, $E_i$, as function of the Fourier number. (b) Plot of the transient equilibration compositions of propylbenzene and dodecane as a function of the Fourier number.

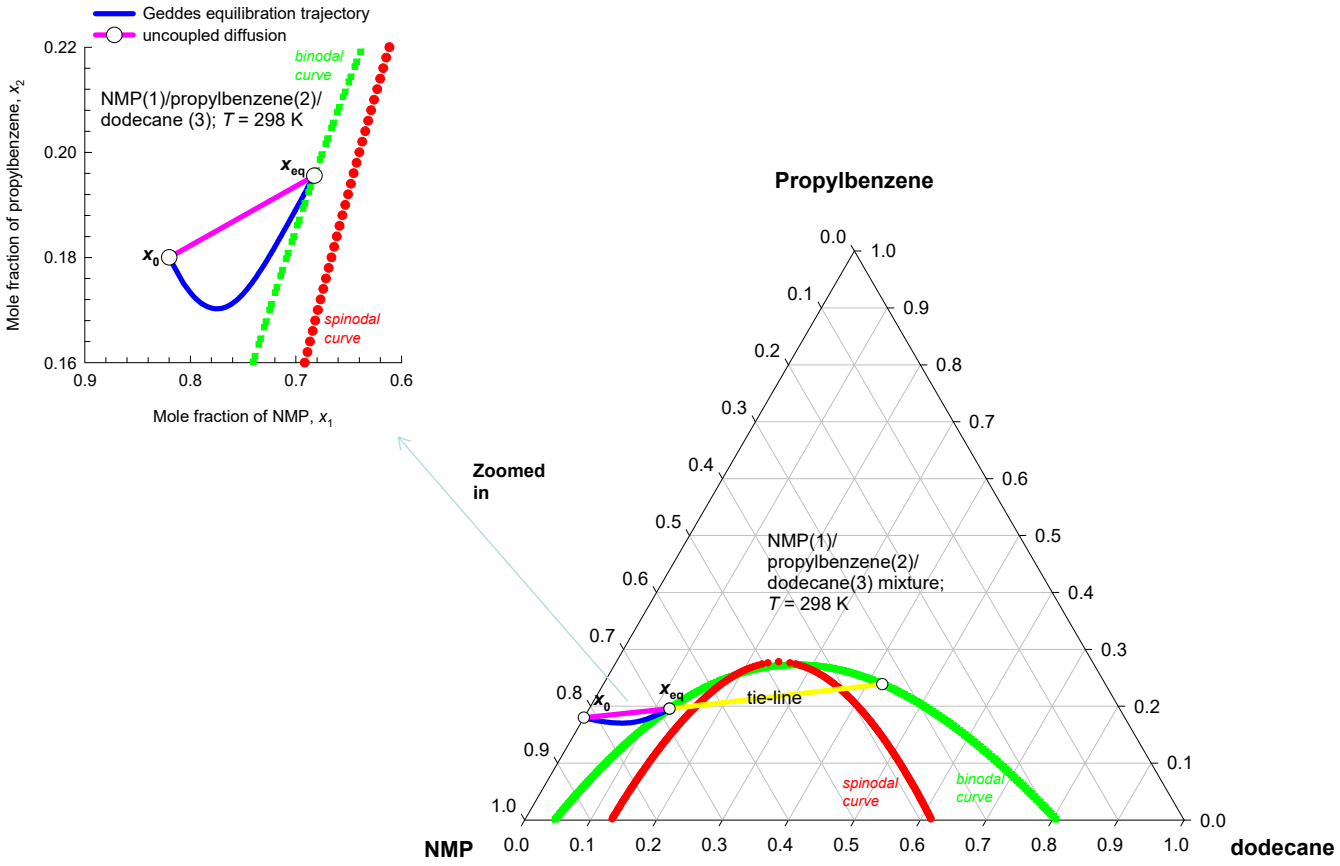


Figure 6-24. Transient equilibration trajectories for the system NMP(1)/propylbenzene(2)/dodecane(3) at 298 K. The initial mole fractions in the drop are $x_{10} = 0.82$, $x_{20} = 0.18$, and $x_{30} = 0.0$. The final equilibrated composition is $x_{1,eq} = 0.682507484$, $x_{2,eq} = 0.195546114$, and $x_{3,eq} = 0.1219464$. The NRTL parameters are provided in Table 6-1.

# NMP/propylbenzene/dodecane equilibration

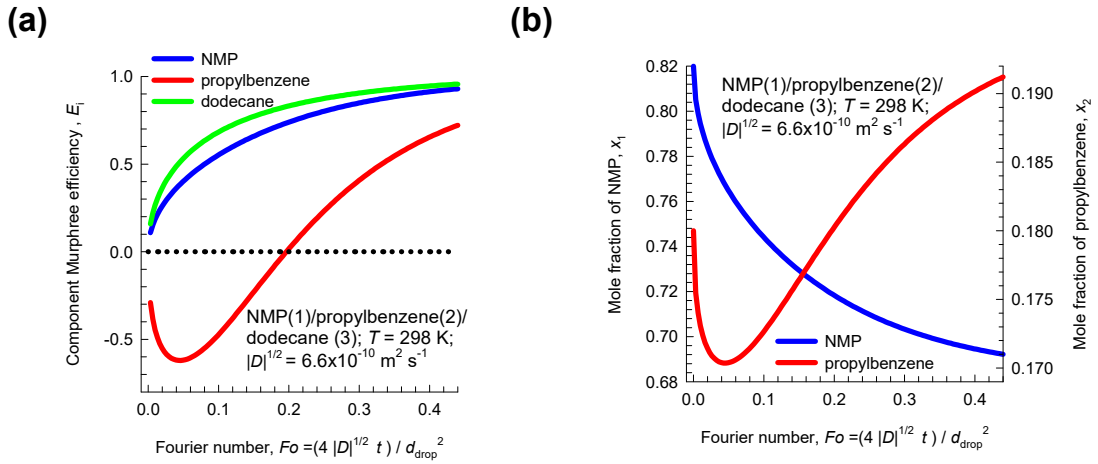


Figure 6-25. Transient equilibration trajectories for the system NMP(1)/propylbenzene(2)/dodecane(3) at 298 K. (a) Plot of the component Murphree efficiencies, $E_i$, as function of the Fourier number. (b) Plot of the transient equilibration compositions of NMP and propylbenzene as a function of the Fourier number.

# NMP/propylbenzene/tetradecane equilibration

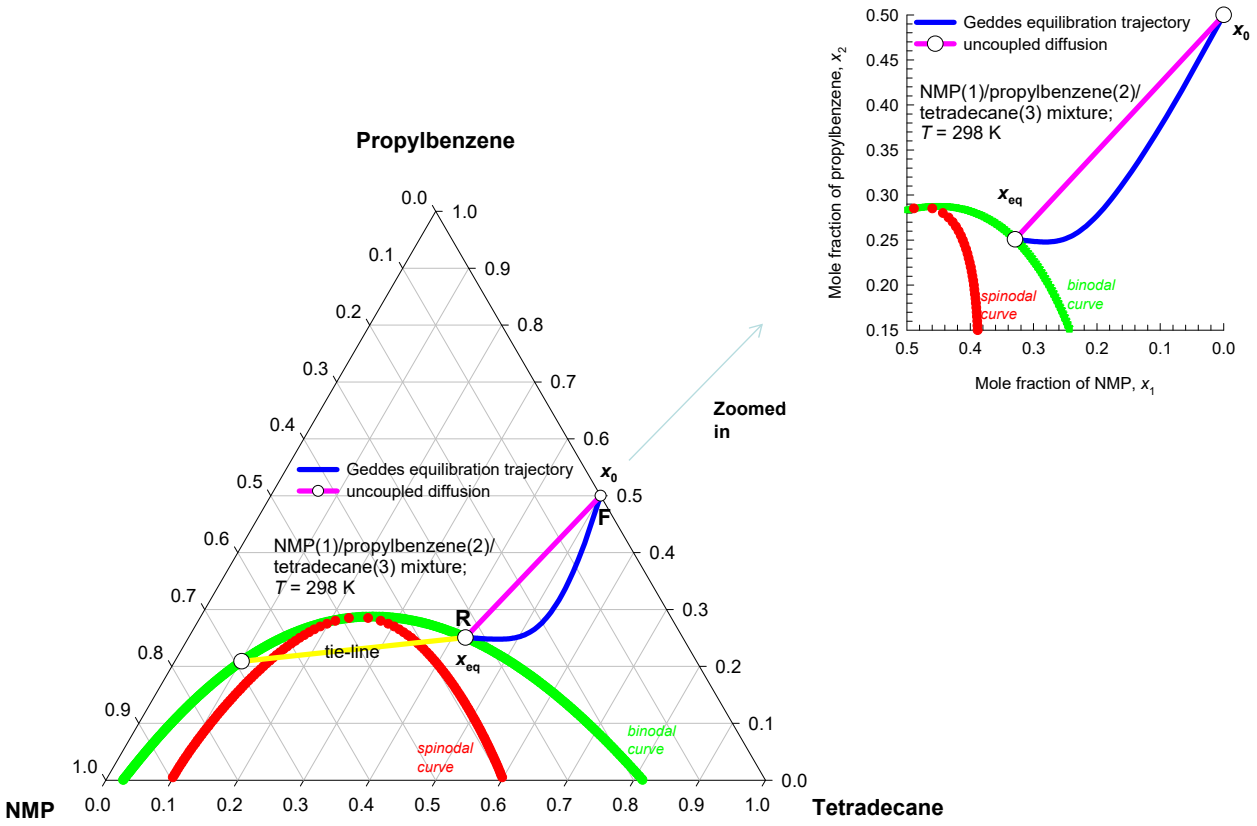


Figure 6-26. Transient equilibration trajectories for the system NMP(1)/propylbenzene(2)/tetradedecane(3) at 298 K. The initial mole fractions in the drop are $x_{10}$ = 0.0, $x_{20}$ = 0.5, and $x_{30}$ = 0.5. The final equilibrated composition is $x_{1,eq}$ = 0.329380812, $x_{2,eq}$ = 0.250774108, and $x_{3,eq}$ = 0.41984508. The NRTL parameters for calculation of the phase equilibrium thermodynamics are provided in Table 6-2.

# NMP/propylbenzene/tetradecane equilibration

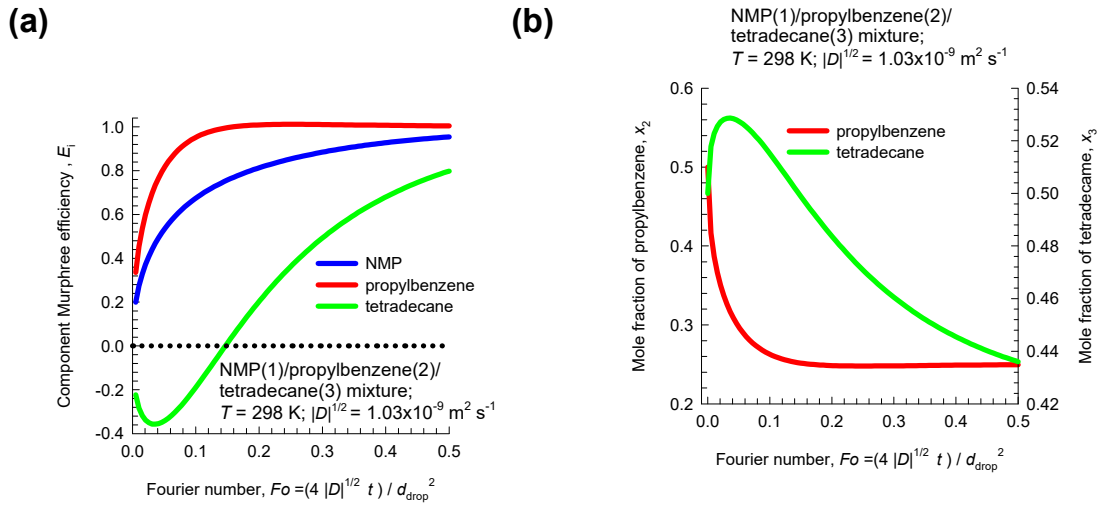


Figure 6-27. Transient equilibration in the system NMP(1)/propylbenzene(2)/tetradedecane(3) at 298 K. (a) Plot of the component Murphree efficiencies, $E_i$, as function of the Fourier number. (b) Plot of the transient equilibration compositions of propylbenzene and tetradecane as a function of the Fourier number.

# 7 Diffusion in Polymeric Systems

For modelling mixture diffusion in polymeric systems, we need to reformulate the Maxwell-Stefan equations using volume fractions instead of mole fractions.[104-108] The use of volume fractions facilitates the application of the Flory-Huggins model for the calculation of the phase equilibrium thermodynamics and the matrix of thermodynamic correction factors $[\Gamma]$. For detailed derivations, see our earlier publications.[107, 108] The M-S equations written in terms of volume fractions take the form (m = polymer)

$$\begin{aligned} -\frac{1}{RT}\frac{d\mu_i}{dz} &= \sum_{\substack{j=1\\ j\neq i}}^{n}\frac{\phi_j\left(u_i-u_j\right)}{Đ_{ij}^{V}}+\frac{\phi_m\left(u_i\right)}{Đ_{im}^{V}};\quad i=1,2,...n \\ -\phi_i\frac{1}{RT}\frac{d\mu_i}{dz} &= \sum_{\substack{j=1\\ j\neq i}}^{n}\frac{\phi_i\phi_j\left(u_i-u_j\right)}{Đ_{ij}^{V}}+\frac{\phi_i\phi_m\left(u_i\right)}{Đ_{im}^{V}};\quad i=1,2,...n \end{aligned} \tag{7-1}$$

The modified M-S diffusivities $Đ_{ij}^{V}$ are related to the M-S diffusivities $Đ_{ij}=Đ_{ji}$, defined in terms of mole fractions, by: $c_t Đ_{ij}\overline{V_j}=\frac{Đ_{ij}\overline{V_j}}{\overline{\overline{V}}}=Đ_{ij}^{V}$, and $c_t Đ_{im}\overline{V_m}=\frac{Đ_{im}\overline{V_m}}{\overline{\overline{V}}}=Đ_{im}^{V}$. The symmetry constraint imposed by the Onsager Reciprocal Relations is $Đ_{ij}=\frac{Đ_{ij}^{V}}{\overline{\overline{V_j}}}\overline{V}=Đ_{ji}=\frac{Đ_{ji}^{V}}{\overline{\overline{V_i}}}\overline{V};\quad \frac{Đ_{ji}^{V}}{\overline{\overline{V_i}}}=\frac{Đ_{ij}^{V}}{\overline{\overline{V_j}}}$. It is important to note that the M-S diffusivities $Đ_{ij}^{V}$ are *not* symmetric.

## 7.1 Immersion precipitation process for membrane preparation

Diffusion close to phase transition regions is of importance in membrane preparation by immersion precipitation.[109, 110] In order to illustrate this, let us consider diffusion in the ternary mixture consisting of water (non-solvent, component 1), acetone (solvent, component 2) and cellulose acetate (polymer, component m); a detailed analysis of phase equilibria and diffusion in polymer solutions is available in our earlier publications.[107, 108] The binodal and spinodal curves for this ternary mixture are shown in

Figure 7-1; the calculations are based on the Flory-Huggins equations that relate the component activities to volume fractions, $\phi_i$.[107, 108] The spinodal curve defines the limit of phase stability, and along the spinodal curve, the condition $|\Gamma| = 0$ must be satisfied, i.e. we must have $\Gamma_{11}\Gamma_{22} = \Gamma_{12}\Gamma_{21}$, the product of the off-diagonal elements is equal in magnitude to the product of the diagonal elements.[45, 73] This situation implies a significant degree of thermodynamic coupling.

Curvilinear equilibration trajectories for water/acetone/CA have been reported in the immersion precipitation process for membrane preparation.[109, 110] Figure 7-1 shows the transient equilibration trajectory when a 10% solution of Cellulose Acetate (CA) in acetone is immersed in a bath of water-rich aqueous solution of water/acetone; we note the curvilinear trajectory has entered the meta-stable region. This foray into the meta-stable region impacts on the membrane structure.[109, 110] Tsay and McHugh[111] present detailed modelling of the transient equilibration trajectories for water/acetone/CA systems; see also Krishna.[107, 108]

In order to demonstrate the foray into the meta-stable region, we consider transient diffusion within a spherical droplet of 2 mm diameter in a continuous solvent-rich phase that is representative of the coagulation bath. The initial volume fractions in the drop are $\phi_{10} = 0.2$, $\phi_{20} = 0.7$, and $\phi_{30} = 0.1$. The final equilibrated composition is $\phi_{1,eq} = 0.18067$, $\phi_{2,eq} = 0.10078$, and $\phi_{3,eq} = 0.71855$; this composition is at one end of the tie-line with the coagulation bath of constant composition $\phi_1 = 0.928$, $\phi_2 = 0.072$, and $\phi_3 = 0.0$.

The matrix of thermodynamic factors, calculated at the arithmetic average volume fractions of the dispersed phase droplets between the initial and final equilibrated compositions ($\phi_{1,av} = 0.19034$, $\phi_{2,av} = 0.40039$, and $\phi_{3,av} = 0.40927$) is $[\Gamma] = \begin{bmatrix} 0.34018 & -0.06198 \\ -0.78883 & 0.60362 \end{bmatrix}$.

For consistency with the Flory-Huggins description of mixture thermodynamics, the Maxwell-Stefan equations are formulated in terms of the volume fractions; see Krishna[107, 108] Following the work of

Mulder et al.[112] we take $[D]=\begin{bmatrix} Đ_{1m}^{V} & 0 \\ 0 & Đ_{2m}^{V} \end{bmatrix}[\Gamma]$, where the modified Maxwell-Stefan diffusivities for permeation of penetrants water (component 1) and acetone (Component 2) are taken to be the same as for water/ethanol/CA system: $\begin{matrix} Đ_{1m}^{V} = 8.8\times10^{-12}\exp(7.3\phi_1 + 7.3\phi_2) & \text{m}^2\ \text{s}^{-1} \\ Đ_{2m}^{V} = 6\times10^{-12}\exp(7.3\phi_1 + 7.3\phi_2) & \text{m}^2\ \text{s}^{-1} \end{matrix}$. Evaluated at the arithmetic average volume fractions of the dispersed phase, we obtain $[D]=\begin{bmatrix} Đ_{1m}^{V} & 0 \\ 0 & Đ_{2m}^{V} \end{bmatrix}[\Gamma]=\begin{bmatrix} 2.23353 & -0.40692 \\ -3.53135 & 2.7022 \end{bmatrix}\times10^{-10}\,\text{m}^2\text{s}^{-1}$. The off-diagonal element $D_{21}$ is the same order of magnitude as the diagonal element $D_{22}$, indicating that coupling effects are significant. We can also determine the "magnitude" of the Fick diffusivity $|D|^{1/2} = 2.144\times10^{-10}$ m$^2$ s$^{-1}$ for use in the calculation of the Fourier number.

The component driving forces for transfer of water (1) and acetone (2) are $\Delta\phi_1 = \phi_{10} - \phi_{1,eq} = 0.01933$, $\Delta\phi_2 = \phi_{20} - \phi_{2,eq} = 0.59922$. Particularly noteworthy is that the driving force for acetone transfer is significantly larger than the driving force for transfer of water.

The transient Geddes equilibration trajectory follows a highly curvilinear path to equilibrium, and exhibits a foray into the meta-stable region; see Figure 7-2(a). If coupling effects are completely ignored, the equilibration trajectory follows a linear path in composition space, and no foray into the meta-stable region is feasible.

Figure 7-2(b) presents a plot of component Murphree efficiencies as a function of the dimensionless Fourier number $\dfrac{4|D|^{1/2}t}{d_{drop}^2}$ where the droplet diameter is taken as $d_{\text{drop}}$ = 2 mm. During the early stages of the equilibration process, the Murphree point efficiency of water (component 1) exhibits negative values, indicative of uphill diffusion. As a consequence of uphill diffusion, the transient equilibration of water exhibits a distinct composition overshoot during its approach to equilibration; see Figure 7-2(c).

## 7.2 List of Tables for Diffusion in Polymeric Systems

Table 7-1. The Flory-Huggins parameters for penetrants water (anti-solvent, component 1) and acetone (solvent, Component 2) in cellulose acetate (CA) (polymer, indicated by subscript m) at $T$ = 298.15 K. The Flory-Huggins parameters are taken from Altena and Smolders[113] and Altinkaya and Ozbas.[114]

$$\chi_{12} = a + b(u_2) + c(u_2)^2 + d(u_2)^3 + e(u_2)^4; \quad u_2 = \frac{\phi_2}{\phi_1 + \phi_2}$$

$$a = 1.1; b = -0.42; c = 4.09; d = -6.7; e = 4.28;$$

$$\chi_{1m} = 1.4; \chi_{2m} = 0.45;$$

$$\overline{V_1} = 18 \times 10^{-6} \text{ m}^3 \text{ mol}^{-1}$$

$$\overline{V_2} = 73.92 \times 10^{-6} \text{ m}^3 \text{ mol}^{-1}$$

$$\overline{V_m} = 0.030532 \text{ m}^3 \text{ mol}^{-1}$$

Modified Maxwell-Stefan diffusivities for permeation of penetrants water (component 1) and acetone (Component 2) are taken to be the same as for water/ethanol/CA system.[112]

$$Đ_{1m}^{V} = 8.8 \times 10^{-12} \exp(7.3\phi_1 + 7.3\phi_2) \quad \text{m}^2 \text{ s}^{-1}$$

$$Đ_{2m}^{V} = 6 \times 10^{-12} \exp(7.3\phi_1 + 7.3\phi_2) \quad \text{m}^2 \text{ s}^{-1}$$

The 1-2 friction is considered to be negligible.

## 7.3 List of Figures for Diffusion in Polymeric Systems

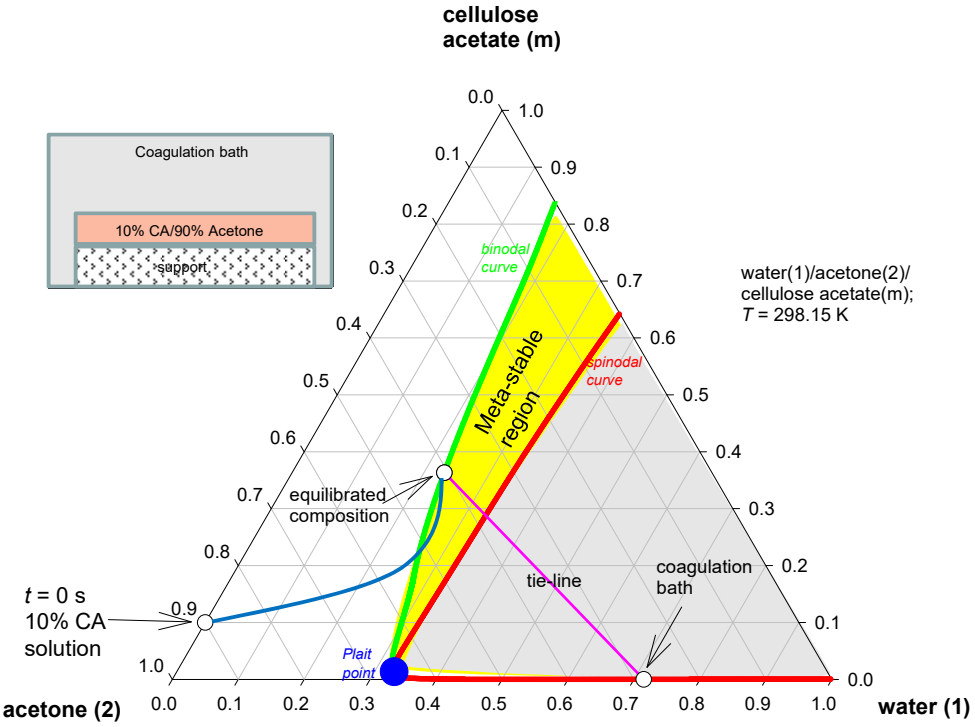


Figure 7-1. Diffusion trajectories during the immersion precipitation process for membrane preparation; adapted from the papers of van den Berg and Smolders,[109] and Reuvers and Smolders.[110] A 10% solution of Cellulose Acetate (CA) in acetone is immersed in a bath of pure water. The transient equilibration trajectory is indicated in a qualitative manner.

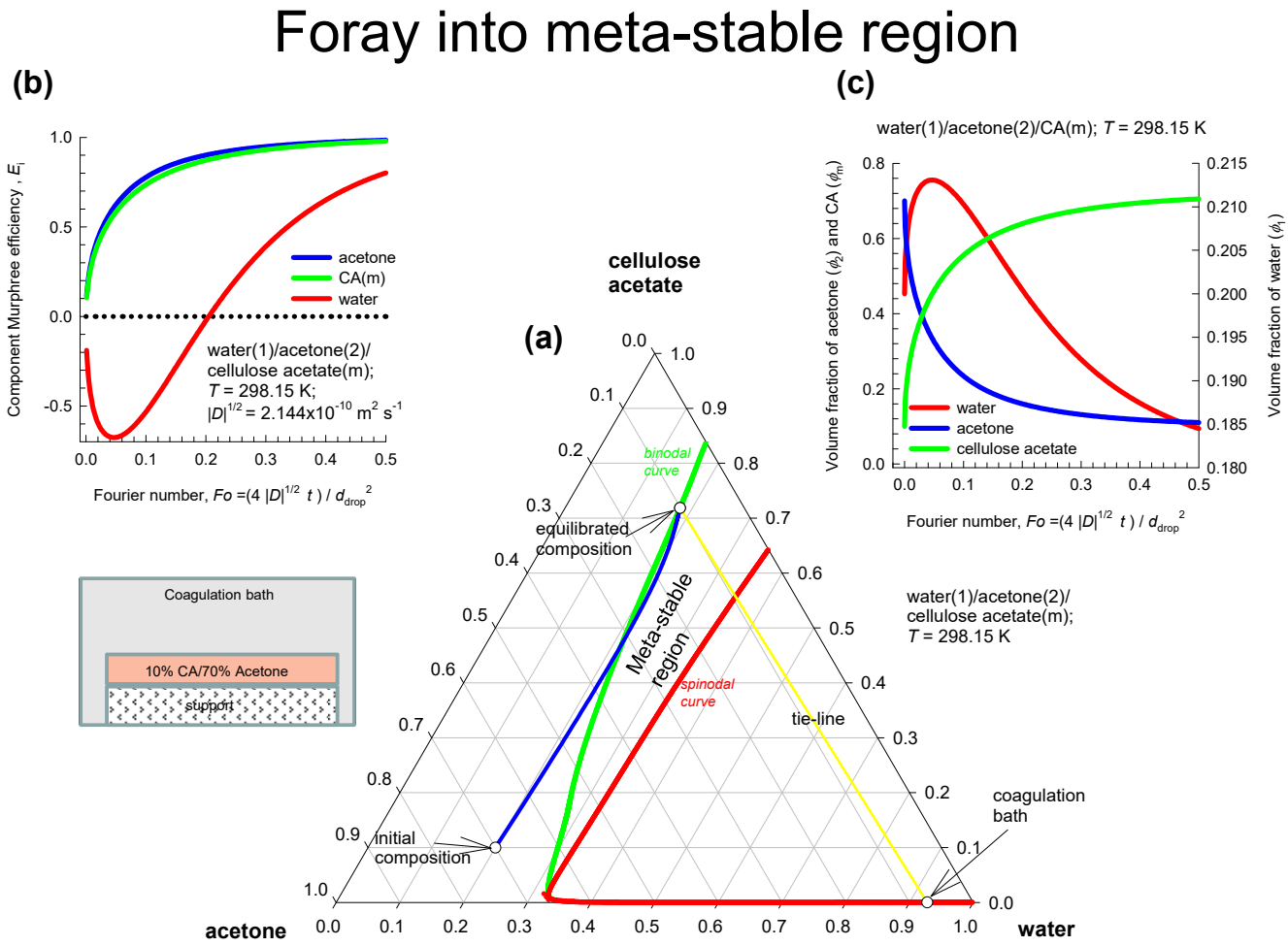


Figure 7-2. (a) Geddes equilibration trajectory in a ternary system consisting of water (non-solvent, component 1), acetone (solvent, component 2) and cellulose acetate (polymer, component m). The plotted data in ternary composition space are in terms of volume fractions. The equilibration trajectory is indicated by the blue line in ternary composition space. (b) Plot of the component Murphree efficiencies, $E_i$, as function of the Fourier number. (c) Transient volume fraction profiles in the polymer solution, as function of the Fourier number. The Flory-Huggins parameters and diffusivity data are provided in Table 7-1.

# 8 Diffusion in crystalline solids and alloys

The proper description of multicomponent diffusion in metals, glasses, steels, alloys, and composites is important in a wide variety of processes such as bonding, cladding, controlled heat treatments, and surface modification. [54, 115-122] The phenomenological description of diffusion in crystalline solids and alloys is described in a number of texts and articles;[54, 115-121] in all cases, the description is based on the Onsager formulation of irreversible thermodynamics.[4]

For the specific case of a ternary mixture consisting of components 1, 2, and 3, the Onsager formulation for the diffusion fluxes in a *lattice-fixed reference frame* may be written as

$$\begin{pmatrix} J_1 \\ J_2 \end{pmatrix} = -\frac{1}{\overline{\overline{V}}} \begin{bmatrix} L_{11} & L_{12} \\ L_{21} & L_{22} \end{bmatrix} \frac{1}{RT} \begin{pmatrix} \dfrac{d\left(\mu_1 - \mu_3\right)}{dz} \\ \dfrac{d\left(\mu_2 - \mu_3\right)}{dz} \end{pmatrix} = -\frac{1}{\overline{\overline{V}}} \begin{bmatrix} \dfrac{L_{11}}{x_1} & \dfrac{L_{12}}{x_2} \\ \dfrac{L_{12}}{x_1} & \dfrac{L_{22}}{x_2} \end{bmatrix} \frac{1}{RT} \begin{pmatrix} x_1 \dfrac{d\left(\mu_1 - \mu_3\right)}{dz} \\ x_2 \dfrac{d\left(\mu_2 - \mu_3\right)}{dz} \end{pmatrix} \tag{8-1}$$

The Gibbs-Duhem relations constrain the chemical potential gradients: $x_1 \dfrac{d\mu_1}{dz} + x_2 \dfrac{d\mu_2}{dz} + x_3 \dfrac{d\mu_3}{dz} = 0$.

The chemical potential gradients are related to the mole fraction gradients

$$\frac{1}{RT} \begin{pmatrix} \dfrac{d\left(\mu_1 - \mu_3\right)}{dz} \\ \dfrac{d\left(\mu_2 - \mu_3\right)}{dz} \end{pmatrix} = \begin{bmatrix} \Theta_{11} & \Theta_{12} \\ \Theta_{21} & \Theta_{22} \end{bmatrix} \begin{pmatrix} \dfrac{dx_1}{dz} \\ \dfrac{dx_2}{dz} \end{pmatrix} \tag{8-2}$$

So, the diffusion fluxes can be related to the mole fraction gradients

$$(J) = -\frac{1}{\overline{\overline{V}}} [L][\Theta] \frac{d(x)}{dz}; \quad \begin{pmatrix} J_1 \\ J_2 \end{pmatrix} = -\frac{1}{\overline{\overline{V}}} \begin{bmatrix} L_{11} & L_{12} \\ L_{21} & L_{22} \end{bmatrix} [\Theta] \begin{pmatrix} \dfrac{dx_1}{dz} \\ \dfrac{dx_2}{dz} \end{pmatrix} = -\frac{1}{\overline{\overline{V}}} \begin{bmatrix} D_{11} & D_{12} \\ D_{21} & D_{22} \end{bmatrix} \begin{pmatrix} \dfrac{dx_1}{dz} \\ \dfrac{dx_2}{dz} \end{pmatrix} \tag{8-3}$$

The Hessian of the Gibbs free-energy $[\Theta]$ is related to the thermodynamic correction factors $\Gamma_{ij} = \delta_{ij} + x_i \dfrac{\partial \ln \gamma_i}{\partial x_j}; \qquad i, j = 1, 2$ as follows

$$\begin{bmatrix} \Theta_{11} & \Theta_{12} \\ \Theta_{21} & \Theta_{22} \end{bmatrix} = \frac{1}{x_3} \begin{bmatrix} \dfrac{(1-x_2)}{x_1} & 1 \\ 1 & \dfrac{(1-x_1)}{x_2} \end{bmatrix} \begin{bmatrix} \Gamma_{11} & \Gamma_{12} \\ \Gamma_{21} & \Gamma_{22} \end{bmatrix} \tag{8-4}$$

The inter-relation between the Fick, Onsager and Maxwell-Stefan formulations are

$$\begin{bmatrix} D_{11} & D_{12} \\ D_{21} & D_{22} \end{bmatrix} = \begin{bmatrix} L_{11} & L_{12} \\ L_{21} & L_{22} \end{bmatrix} \begin{bmatrix} \Theta_{11} & \Theta_{12} \\ \Theta_{21} & \Theta_{22} \end{bmatrix} = [L] \frac{1}{x_3} \begin{bmatrix} \dfrac{(1-x_2)}{x_1} & 1 \\ 1 & \dfrac{(1-x_1)}{x_2} \end{bmatrix} \begin{bmatrix} \Gamma_{11} & \Gamma_{12} \\ \Gamma_{21} & \Gamma_{22} \end{bmatrix} =$$

$$\begin{bmatrix} \dfrac{1-x_2}{Đ_{13}} + \dfrac{x_2}{Đ_{12}} & -\dfrac{x_1}{Đ_{12}} + \dfrac{x_1}{Đ_{13}} \\ -\dfrac{x_2}{Đ_{12}} + \dfrac{x_2}{Đ_{23}} & \dfrac{1-x_1}{Đ_{23}} + \dfrac{x_1}{Đ_{12}} \end{bmatrix}^{-1} \begin{bmatrix} \Gamma_{11} & \Gamma_{12} \\ \Gamma_{21} & \Gamma_{22} \end{bmatrix} = \tag{8-5}$$

$$= \frac{\begin{bmatrix} Đ_{13}\left(x_1 Đ_{23} + (1-x_1) Đ_{12}\right) & x_1 Đ_{23}\left(Đ_{13} - Đ_{12}\right) \\ x_2 Đ_{13}\left(Đ_{23} - Đ_{12}\right) & Đ_{23}\left(x_2 Đ_{13} + (1-x_2) Đ_{12}\right) \end{bmatrix}}{x_1 Đ_{23} + x_2 Đ_{13} + x_3 Đ_{12}} \begin{bmatrix} \Gamma_{11} & \Gamma_{12} \\ \Gamma_{21} & \Gamma_{22} \end{bmatrix}$$

The inter-relationship between the Fick, Onsager and Maxwell-Stefan formulations are summarized in Figure 8-1, and Figure 8-2.

## 8.1 The Maxwell-Stefan formulation of tracer diffusion in crystalline solids and alloys

Consider the specific example of vacancy mediated tracer diffusion in a crystalline solid; see Figure 8-3. The three species may be identified as follows: 1 = tagged species 1*; 2 = untagged species 1; 3 = vacancy (V). The elements of the Onsager matrix is given by[121]

$$[L] = \frac{a^2 \nu x_3}{1-x_3} \begin{bmatrix} x_1(1-x_3) - x_1 x_2 (1-f) & x_1 x_2 (1-f) \\ x_1 x_2 (1-f) & x_2(1-x_3) - x_1 x_2 (1-f) \end{bmatrix} \tag{8-6}$$

In equation (8-6), $a$ is the jump distance, $\nu$ is the jump frequency, and $f$ is the correlation factor. For a BCC crystal, for example, $f = 0.727$. Combining equations (2-35), (8-5), and (8-6) we obtain

$$[B]^{-1} = \frac{a^2 \nu}{1-x_3} \begin{bmatrix} (1-x_3)(1-x_2) - x_2 x_3 (1-f) & x_1 (1-x_3) + x_1 x_3 (1-f) \\ x_2 (1-x_3) + x_2 x_3 (1-f) & (1-x_1)(1-x_3) - x_1 x_3 (1-f) \end{bmatrix} \tag{8-7}$$

Performing the matrix inversion of the right member of equation (8-7), we obtain

$$[B]=\begin{bmatrix} B_{11} & B_{12} \\ B_{21} & B_{22} \end{bmatrix}=\begin{bmatrix} \frac{1-x_2}{Đ_{13}}+\frac{x_2}{Đ_{12}} & -\frac{x_1}{Đ_{12}}+\frac{x_1}{Đ_{13}} \\ -\frac{x_2}{Đ_{12}}+\frac{x_2}{Đ_{23}} & \frac{1-x_1}{Đ_{23}}+\frac{x_1}{Đ_{12}} \end{bmatrix}=\frac{1}{x_3(1-x_3)a^2\nu f}\begin{bmatrix} x_2+x_1x_3f & -x_1(1-x_3f) \\ -x_2(1-x_3f) & x_1+x_2x_3f \end{bmatrix} \tag{8-8}$$

The Maxwell-Stefan pair diffusivities can be determined as follows

$$\frac{1}{Đ_{13}}=B_{11}+\frac{x_2B_{12}}{x_1}=\frac{1}{a^2\nu};\quad \frac{1}{Đ_{23}}=B_{22}+x_1\frac{B_{21}}{x_2}=\frac{1}{a^2\nu};\quad \frac{1}{Đ_{12}}=\frac{1}{Đ_{13}}-\frac{B_{12}}{x_1}$$

$$Đ_{13}=a^2\nu;\quad Đ_{23}=a^2\nu;\quad Đ_{12}=\frac{x_3(1-x_3)f}{1-x_3x_3f}a^2\nu \tag{8-9}$$

The M-S pair diffusivity $Đ_{12}$ quantifies the correlations between jumps.

The following expression for the tracer diffusivity $D^*$ has been derived by Krishna[123]

$$\frac{1}{D^*}=\frac{(1-x_3)}{Đ_{12}}+\frac{x_3}{Đ_{13}} \tag{8-10}$$

Therefore, we derive

$$\frac{a^2\nu}{D^*}=\frac{1-x_3x_3f}{x_3f}+x_3=\frac{1}{x_3f};\quad D^*=x_3fa^2\nu \tag{8-11}$$

The self-diffusivity is strongly influenced by correlations.

## 8.2 Vacancy mediated diffusion in binary alloys

Consider the specific example of vacancy mediated diffusion in binary crystalline solids. The three species may be identified as follows: 1 = species 1; 2 = species 2; 3 = vacancy (V). The fluxes in the lattice-fixed reference frame are

$$\begin{pmatrix} J_1 \\ J_2 \end{pmatrix}=-\frac{1}{\overline{\overline{V}}}\begin{bmatrix} \frac{L_{11}}{x_1} & \frac{L_{12}}{x_2} \\ \frac{L_{12}}{x_1} & \frac{L_{22}}{x_2} \end{bmatrix}\frac{1}{RT}\begin{pmatrix} x_1\frac{d\mu_1}{dz} \\ x_2\frac{d\mu_2}{dz} \end{pmatrix} \tag{8-12}$$

The vacancy flux is $J_1+J_2=-J_V$. The fluxes in the laboratory-fixed reference velocity frame are

$$N_1 = J_1 - x_1\left(J_1 + J_2\right); \quad N_2 = J_2 - x_2\left(J_1 + J_2\right) \tag{8-13}$$

In 2-dimensional matrix notation, the fluxes in the laboratory-fixed reference frame are

$$\begin{pmatrix} N_1 \\ N_2 \end{pmatrix} = \begin{bmatrix} 1-x_1 & -x_1 \\ -x_2 & 1-x_2 \end{bmatrix}\begin{pmatrix} J_1 \\ J_2 \end{pmatrix} = -\frac{1}{\overline{\overline{V}}}\begin{bmatrix} 1-x_1 & -x_1 \\ -x_2 & 1-x_2 \end{bmatrix}\begin{bmatrix} \frac{L_{11}}{x_1} & \frac{L_{12}}{x_2} \\ \frac{L_{12}}{x_1} & \frac{L_{22}}{x_2} \end{bmatrix}\frac{1}{RT}\begin{pmatrix} x_1\frac{d\mu_1}{dz} \\ x_2\frac{d\mu_2}{dz} \end{pmatrix}$$

$$\begin{pmatrix} N_1 \\ N_2 \end{pmatrix} = -\frac{1}{\overline{\overline{V}}}\begin{bmatrix} \left(1-x_1\right)\frac{L_{11}}{x_1} - L_{12} & \left(1-x_1\right)\frac{L_{12}}{x_2} - x_1\frac{L_{22}}{x_2} \\ -x_2\frac{L_{11}}{x_1} + \left(1-x_2\right)\frac{L_{12}}{x_1} & \left(1-x_2\right)\frac{L_{22}}{x_2} - L_{12} \end{bmatrix}\frac{1}{RT}\begin{pmatrix} x_1\frac{d\mu_1}{dz} \\ x_2\frac{d\mu_2}{dz} \end{pmatrix} \tag{8-14}$$

Following Belova and Murch,[118, 119] we will make the usual assumption that vacancies are produced and annihilated during an inter-diffusion process in such a way that

$$\frac{d\mu_3}{dz} = 0; \quad x_1\frac{d\mu_1}{dz} + x_2\frac{d\mu_2}{dz} = 0; \quad \frac{d\mu_2}{dz} = -\frac{x_1}{x_2}\frac{d\mu_1}{dz} \tag{8-15}$$

Therefore, the fluxes of components 1, and 2 in the laboratory-fixed reference frame can be written in the simplified form

$$\begin{aligned} N_1 &= -\frac{1}{\overline{\overline{V}}}\left(\left(\frac{1-x_1}{x_1}\right)L_{11} - \frac{\left(1+x_2-x_1\right)}{x_2}L_{12} + \frac{x_1}{x_2}L_{22}\right)\frac{1}{RT}x_1\frac{d\mu_1}{dz} \\ N_2 &= -\frac{1}{\overline{\overline{V}}}\left(\frac{\left(1-x_2\right)}{x_2}L_{22} - \frac{\left(1+x_1-x_2\right)}{x_1}L_{12} + \frac{x_2}{x_1}L_{11}\right)\frac{1}{RT}x_2\frac{d\mu_2}{dz} \end{aligned} \tag{8-16}$$

The following expression can be derived for the inter-diffusion coefficient in a binary alloy

$$\begin{aligned} &N_1 = -\frac{1}{\overline{\overline{V}}}Đ_{Inter}\frac{1}{RT}x_1\frac{d\mu_1}{dz}; \quad N_2 = -\frac{1}{\overline{\overline{V}}}Đ_{Inter}\frac{1}{RT}x_2\frac{d\mu_2}{dz}; \\ &Đ_{Inter} = \left(\frac{1-x_1}{x_1}\right)L_{11} - \frac{\left(1+x_2-x_1\right)}{x_2}L_{12} + \frac{x_1}{x_2}L_{22} = \frac{\left(1-x_2\right)}{x_2}L_{22} - \frac{\left(1+x_1-x_2\right)}{x_1}L_{12} + \frac{x_2}{x_1}L_{11} \end{aligned} \tag{8-17}$$

In the Manning approach,[120] the phenomenological coefficients are directly related to the tracer diffusion coefficients $D_1^*, D_2^*$ by

$$L_{11} = x_1D_1^*\left(1 + \frac{2x_1D_1^*}{M_0\left(x_1D_1^* + x_2D_2^*\right)}\right); L_{22} = x_2D_2^*\left(1 + \frac{2x_2D_2^*}{M_0\left(x_1D_1^* + x_2D_2^*\right)}\right); L_{12} = \frac{2x_1x_2D_1^*D_2^*}{M_0\left(x_1D_1^* + x_2D_2^*\right)} \tag{8-18}$$

where $M_0 = \frac{2f}{1-f}$, and f is the correlation factor. For a BCC crystal, for example, $f = 0.727$.

The following expression can be derived for the inter-diffusion coefficient in a binary alloy

$$Đ_{Inter} = \left(x_2 D_1^* + x_1 D_2^*\right) S; \quad S = \left(1 + \frac{2x_1 x_2 \left(D_1^* - D_2^*\right)^2}{M_0 \left(x_1 D_1^* + x_2 D_2^*\right)\left(x_2 D_1^* + x_1 D_2^*\right)}\right) \tag{8-19}$$

where $S$ is the vacancy-wind correction factor. [118-120]

## 8.3 The Maxwell-Stefan-Darken formulation for inter-diffusion in a binary alloy

Darken[54] derived a relation for the inter-diffusion flux of the components 1 and 2 in a binary alloy, in a *laboratory-fixed reference frame*

$$N_1 = -\frac{1}{\overline{V}} D_{\text{int}er} \frac{dx_1}{dz}; \quad D = Đ_{Inter} \Gamma; \quad \Gamma = \left(1 + \frac{\partial \ln \gamma_1}{\partial \ln x_1}\right); \quad Đ_{Inter} = x_2 D_1^* + x_1 D_2^* \tag{8-20}$$

The Maxwell-Stefan inter-diffusivity may be interpolated using the information on the unary tracer diffusivities of the two constituents of the alloy, $D_1^*, D_2^*$. The thermodynamic correction factor, $\Gamma = \left(1 + \frac{\partial \ln \gamma_1}{\partial \ln x_1}\right)$, is also referred to as the Darken correction factor. Essemtially, the Darken expression for the inter-diffusion coefficient in binary alloys is a special, limiting, case of the Manning approach[118-120] in which correlation effects are neglected and the matrix of Onsager coefficients is assumed to be diagonal

$$L_{11} = x_1 D_1^*; \quad L_{22} = x_2 D_2^*; \quad L_{12} = 0; \quad Đ_{Inter} = \left(x_2 D_1^* + x_1 D_2^*\right); \quad S = 1 \tag{8-21}$$

As illustration of the accuracy of the Maxwell-Stefan-Darken equation (8-21). Figure 8-4 presents a re-analysis of the experimental data of Reynolds et al.[124] for inter-diffusion in Au(1)-Ni(2) alloy. The predictions of the Fick inter-diffusivity from data on the unary tracer diffusivities of the two constituents of the alloy, $D_1^*, D_2^*$, along with the thermodynamic correction factor, $\Gamma = \left(1 + \frac{\partial \ln \gamma_1}{\partial \ln x_1}\right)$, is in good agreement with the experimental data on the Fick inter-diffusion coefficient.

## 8.4 The Maxwell-Stefan formulation for inter-diffusion in a ternary alloy

Consider the vacancy mediated diffusion in ternary crystalline solids. The four species may be identified as follows: 1 = species 1; 2 = species 2; 3 = species 3; 4 = vacancy (V). Following Belova and Murch,[118, 119] we will make the usual assumption that vacancies are produced and annihilated during an inter-diffusion process in such a way that

$$\frac{d\mu_4}{dz}=0;\quad x_1\frac{d\mu_1}{dz}+x_2\frac{d\mu_2}{dz}+x_3\frac{d\mu_3}{dz}=0;\quad \frac{d\mu_3}{dz}=-\frac{x_1}{x_3}\frac{d\mu_1}{dz}-\frac{x_2}{x_3}\frac{d\mu_2}{dz} \tag{8-22}$$

In the *lattice-fixed reference frame*, we write the Onsager relations for the diffusion fluxes as

$$\begin{pmatrix}J_1\\J_2\\J_3\end{pmatrix}=-\frac{1}{\overline{\overline{V}}}\begin{bmatrix}\frac{L_{11}}{x_1} & \frac{L_{12}}{x_2} & \frac{L_{13}}{x_3}\\ \frac{L_{21}}{x_2} & \frac{L_{22}}{x_2} & \frac{L_{23}}{x_3}\\ \frac{L_{31}}{x_3} & \frac{L_{32}}{x_3} & \frac{L_{33}}{x_3}\end{bmatrix}\frac{1}{RT}\begin{pmatrix}x_1\frac{d\mu_1}{dz}\\ x_2\frac{d\mu_2}{dz}\\ x_3\frac{d\mu_3}{dz}\end{pmatrix} \tag{8-23}$$

The vacancy flux is

$$\begin{aligned}&J_1+J_2+J_3=-J_V=-\frac{1}{\overline{\overline{V}}}L_1\frac{d\mu_1}{dz}-\frac{1}{\overline{\overline{V}}}L_2\frac{d\mu_2}{dz}-\frac{1}{\overline{\overline{V}}}L_3\frac{d\mu_3}{dz}\\ &L_1=L_{11}+L_{21}+L_{31}\\ &L_2=L_{12}+L_{22}+L_{32}\\ &L_3=L_{13}+L_{23}+L_{33}\end{aligned} \tag{8-24}$$

The fluxes in the laboratory-fixed reference velocity frame are

$$N_1=J_1-x_1\left(J_1+J_2+J_3\right);\quad N_2=J_2-x_2\left(J_1+J_2+J_3\right);\quad N_3=J_3-x_3\left(J_1+J_2+J_3\right)=-N_1-N_2 \tag{8-25}$$

Combining equations (8-23), (8-24), and (8-25), we obtain

$$\begin{pmatrix}N_1\\N_2\\N_3\end{pmatrix}=\begin{bmatrix}1-x_1 & -x_1 & -x_1\\ -x_2 & 1-x_2 & -x_2\\ -x_3 & -x_3 & 1-x_3\end{bmatrix}\begin{pmatrix}J_1\\J_2\\J_3\end{pmatrix}=-\frac{1}{\overline{\overline{V}}}\begin{bmatrix}1-x_1 & -x_1 & -x_1\\ -x_2 & 1-x_2 & -x_2\\ -x_3 & -x_3 & 1-x_3\end{bmatrix}\begin{bmatrix}\frac{L_{11}}{x_1} & \frac{L_{12}}{x_2} & \frac{L_{13}}{x_3}\\ \frac{L_{21}}{x_2} & \frac{L_{22}}{x_2} & \frac{L_{23}}{x_3}\\ \frac{L_{31}}{x_3} & \frac{L_{32}}{x_3} & \frac{L_{33}}{x_3}\end{bmatrix}\frac{1}{RT}\begin{pmatrix}x_1\frac{d\mu_1}{dz}\\ x_2\frac{d\mu_2}{dz}\\ x_3\frac{d\mu_3}{dz}\end{pmatrix} \tag{8-26}$$

Invoking $x_1 \frac{d\mu_1}{dz} + x_2 \frac{d\mu_2}{dz} = -x_3 \frac{d\mu_3}{dz}$, we derive the following relations for the two independent fluxes in the laboratory-fixed reference frame

$$\begin{pmatrix} N_1 \\ N_2 \end{pmatrix} = -\frac{1}{\overline{\overline{V}}} \begin{bmatrix} \frac{L_{11}}{x_1} - \frac{L_{13}}{x_3} - L_1 + \frac{x_1 L_3}{x_3} & \frac{L_{12}}{x_2} - \frac{L_{13}}{x_3} - \frac{x_1 L_2}{x_2} + \frac{x_1}{x_3} L_3 \\ \frac{L_{21}}{x_1} - \frac{L_{23}}{x_3} - \frac{x_2 L_1}{x_1} + \frac{x_2 L_3}{x_3} & \frac{L_{22}}{x_{21}} - \frac{L_{23}}{x_3} - L_2 + \frac{x_2 L_3}{x_3} \end{bmatrix} \frac{1}{RT} \begin{pmatrix} x_1 \frac{d\mu_1}{dz} \\ x_2 \frac{d\mu_2}{dz} \end{pmatrix} \tag{8-27}$$

where

$$L_1 = L_{11} + L_{21} + L_{31}$$
$$L_2 = L_{12} + L_{22} + L_{32}$$
$$L_3 = L_{13} + L_{23} + L_{33}$$

The inter-diffusion fluxes in a ternary alloy, in a *laboratory-fixed reference frame* are described by a matrix of Fickian inter-diffusivities

$$\begin{pmatrix} N_1 \\ N_2 \end{pmatrix} = -\frac{1}{\overline{\overline{V}}} \begin{bmatrix} D_{11} & D_{12} \\ D_{21} & D_{22} \end{bmatrix} \begin{pmatrix} \frac{dx_1}{dz} \\ \frac{dx_2}{dz} \end{pmatrix} = -\frac{1}{\overline{\overline{V}}} \begin{bmatrix} \frac{1-x_2}{Đ_{13}} + \frac{x_2}{Đ_{12}} & -\frac{x_1}{Đ_{12}} + \frac{x_1}{Đ_{13}} \\ -\frac{x_2}{Đ_{12}} + \frac{x_2}{Đ_{23}} & \frac{1-x_1}{Đ_{23}} + \frac{x_1}{Đ_{12}} \end{bmatrix}^{-1} [\Gamma] \begin{pmatrix} \frac{dx_1}{dz} \\ \frac{dx_2}{dz} \end{pmatrix} \tag{8-28}$$

$$N_3 = -N_1 - N_2$$

From experimental data on the matrix of Fickian inter-diffusivities, [$D$], the Maxwell-Stefan pair diffusivities $Đ_{ij}$ can be backed-out using the following relations

$$[B] = \begin{bmatrix} B_{11} & B_{12} \\ B_{21} & B_{22} \end{bmatrix} = \begin{bmatrix} \frac{1-x_2}{Đ_{13}} + \frac{x_2}{Đ_{12}} & -\frac{x_1}{Đ_{12}} + \frac{x_1}{Đ_{13}} \\ -\frac{x_2}{Đ_{12}} + \frac{x_2}{Đ_{23}} & \frac{1-x_1}{Đ_{23}} + \frac{x_1}{Đ_{12}} \end{bmatrix} = \begin{bmatrix} \Gamma_{11} & \Gamma_{12} \\ \Gamma_{21} & \Gamma_{22} \end{bmatrix} \begin{bmatrix} D_{11} & D_{12} \\ D_{21} & D_{22} \end{bmatrix}^{-1} \tag{8-29}$$

$$\frac{1}{Đ_{13}} = B_{11} + \frac{x_2 B_{12}}{x_1}; \quad \frac{1}{Đ_{23}} = B_{22} + \frac{x_1 B_{21}}{x_2}; \quad \frac{1}{Đ_{12}} = \frac{1}{Đ_{13}} - \frac{B_{12}}{x_1} = \frac{1}{Đ_{23}} - \frac{B_{21}}{x_2}$$

As illustration of the backing-out procedure for determining the Maxwell-Stefan pair diffusivities $Đ_{ij}$ we consider the published experimental inter-diffusivity data for Cu(1)/Fe(2)/Ni(3) system at 1273 K; [119, 125, 126] see Figure 8-5. The thermodynamic correction factors are determined from the regular solution model $G^{ex} = A_{12} x_1 x_2 + A_{23} x_2 x_3 + A_{31} x_3 x_1$; $A_{12} = 33$; $A_{23} = -5$; $A_{31} = 5$ kJ mol$^{-1}$. The backed-out data on the Maxwell-Stefan pair diffusivities $Đ_{ij}$ for Cu(1)/Fe(2)/Ni(3) system at 1273 K

using equation (8-29) are shown in Figure 8-6, in which the *x*-axis is $|D|^{1/2}$, i.e. the square-root of the experimental data on the Fick inter-diffusivity matrix, that is independent of the component numbering. The backed-out Maxwell-Stefan pair diffusivities $Đ_{ij}$ show only a small spread in values over a wide range of compositions.

The extension of the Darken analysis to inter-diffusion in ternary alloys is provided by Belova and Murch;[118, 119] these allow the determination of the Fick inter-diffusivity matrix on the basis of the information of the unary tracer diffusivities of components 1, 2 and 3. For the special case in which the Onsager matrix is diagonal, and the Darken approximation $\frac{L_{11}}{x_1} = D_1^*; \quad \frac{L_{22}}{x_2} = D_2^*; \quad \frac{L_{33}}{x_3} = D_3^*$ holds, the inter-diffusion fluxes are calculable from the tracer diffusivities of the individual species

$$\begin{pmatrix} N_1 \\ N_2 \end{pmatrix} = -\frac{1}{\overline{\overline{V}}} \begin{bmatrix} D_1^* - x_1 D_1^* + x_1 D_3^* & -x_1 D_2^* + x_1 D_3^* \\ -x_2 D_1^* + x_2 D_3^* & D_2^* - x_2 D_2^* + x_2 D_3^* \end{bmatrix} \begin{bmatrix} \Gamma_{11} & \Gamma_{12} \\ \Gamma_{21} & \Gamma_{22} \end{bmatrix} \begin{pmatrix} \frac{dx_1}{dz} \\ \frac{dx_2}{dz} \end{pmatrix} = -\frac{1}{\overline{\overline{V}}} [B]^{-1} [\Gamma] \begin{pmatrix} \frac{dx_1}{dz} \\ \frac{dx_2}{dz} \end{pmatrix} \tag{8-30}$$

$$N_3 = -N_1 - N_2$$

Combining equations (8-29), and (8-30) we obtain

$$[B] = \begin{bmatrix} B_{11} & B_{12} \\ B_{21} & B_{22} \end{bmatrix} = \begin{bmatrix} \frac{1-x_2}{Đ_{13}} + \frac{x_2}{Đ_{12}} & -\frac{x_1}{Đ_{12}} + \frac{x_1}{Đ_{13}} \\ -\frac{x_2}{Đ_{12}} + \frac{x_2}{Đ_{23}} & \frac{1-x_1}{Đ_{23}} + \frac{x_1}{Đ_{12}} \end{bmatrix} = \begin{bmatrix} D_1^* - x_1 D_1^* + x_1 D_3^* & -x_1 D_2^* + x_1 D_3^* \\ -x_2 D_1^* + x_2 D_3^* & D_2^* - x_2 D_2^* + x_2 D_3^* \end{bmatrix}^{-1} \tag{8-31}$$

$$= \frac{1}{x_3 D_1^* D_2^* + x_2 D_1^* D_3^* + x_1 D_3^* D_2^*} \begin{bmatrix} D_2^* - x_2 D_2^* + x_2 D_3^* & x_1 D_2^* - x_1 D_3^* \\ x_2 D_1^* - x_2 D_3^* & D_1^* - x_1 D_1^* + x_1 D_3^* \end{bmatrix}$$

The Maxwell-Stefan pair diffusivities $Đ_{ij}$ can be estimated from the tracer diffusivities $D_1^*, D_2^*, D_3^*$ from the following interpolation formulae

$$Đ_{12} = x_2 D_1^* + x_1 D_2^* + x_3 \frac{D_1^* D_2^*}{D_3^*}$$
$$Đ_{13} = x_3 D_1^* + x_1 D_3^* + x_2 \frac{D_1^* D_3^*}{D_2^*} \quad (8\text{-}32)$$
$$Đ_{23} = x_3 D_2^* + x_2 D_3^* + x_1 \frac{D_2^* D_3^*}{D_1^*}$$

Figure 8-7 presents a comparison of the experimental data on the square-root of the experimental data for Cu(1)/Fe(2)/Ni(3) system at 1273 K.[119, 125, 126] on the Fick inter-diffusivity matrix, $|D|^{1/2}$, with the estimations using the Maxwell-Stefan-Darken model, using equations (8-28), and (8-32). The agreement with the experimental data on $|D|^{1/2}$ is reasonably good; no significant improvements result when using the more complete model of Belova and Murch[118, 119] that includes the vacancy-wind corrections.

## 8.5 Uphill diffusion in PbS(1)/PbTe(2)/PbSe(3) mixtures

For ternary PbS(1)/PbTe(2)/PbSe(3) crystalline mixtures, also represented as $Pb(S_{x1}Te_{x2}Se_{x3})$ with $x_1 + x_2 + x_3 = 1$, the spinodal curve is described by the vanishing of the determinant of the matrix of thermodynamic factors, i.e. $|\Gamma| = 0$. The matrix of thermodynamic factors $[\Gamma]$ may be calculated using the sub-regular solution model with parameters provided in Table 1 of Kokkonis and Leute.[127] For $T$ = 823 K, the spinodal curve is plotted in Figure 8-8.

In homogeneous single-phase regions, sizable magnitudes of cross-coefficients of the Fick diffusivity matrix $[D] = |\Lambda|^{1/2}[\Gamma]$ often lead to serpentine equilibration trajectories and uphill diffusion.[99] To demonstrate this let us consider inter-diffusion of PbS(1)/PbTe(2)/PbSe(3) mixtures that ensues when two different compositions (in the left and right compartments in Figure 8-8 are brought in contact. The initial composition of the left compartment is: $x_{1,L}$ = 0.3, $x_{2,L}$= 0.0 and $x_{3,L}$ = 0.7. The initial composition of the right compartment is: $x_{1,R}$ = 0.2, $x_{2,R}$ = 0.5, and $x_{3,R}$ = 0.3. The composition at equilibrium is $x_{1,eq}$ = 0.25, $x_{2,eq}$ = 0.25 and $x_{3,eq}$ = 0.5. The transient equilibration process is described by the coupled two-dimensional matrix equation

$$\begin{pmatrix} x_1 \\ x_2 \end{pmatrix} = \frac{1}{2}\begin{pmatrix} x_{1L} + x_{1,R} \\ x_{2L} + x_{2,R} \end{pmatrix} + \frac{1}{2} erf\left[ \frac{z}{\sqrt{4t}} \begin{bmatrix} D_{11} & D_{12} \\ D_{21} & D_{22} \end{bmatrix}^{-1/2} \right] \begin{pmatrix} x_{1R} - x_{1L} \\ x_{2R} - x_{2L} \end{pmatrix} \tag{8-33}$$

At the equilibrated composition, $x_{1,\text{eq}} = 0.25$, $x_{2,\text{eq}} = 0.25$ and $x_{3,\text{eq}} = 0.5$, the values of the elements of the matrix of thermodynamic factors is $[\Gamma] = \begin{bmatrix} 0.832 & 0.52 \\ 0.499 & 0.77 \end{bmatrix}$. The scalar diffusivity $|\Lambda|^{1/2}$ is assumed to have the value $|\Lambda|^{1/2} = 1 \times 10^{-14}$ m$^2$s$^{-1}$; therefore, $[D] = |\Lambda|^{1/2}[\Gamma] = \begin{bmatrix} 0.832 & 0.52 \\ 0.499 & 0.77 \end{bmatrix} \times 10^{-14}$ m$^2$s$^{-1}$. Due to the large values of the off-diagonal elements, the transient equilibration trajectories follow curvilinear trajectories in either compartment. Particularly noteworthy is the transient overshoot (left compartment) and undershoot (right compartment) of the PbTe composition.

## 8.6 Uphill diffusion of C in austenite: Darken experiments

One of the very first experimental evidence of uphill diffusion is available in the classic experiments reported by Lawrence Stamper Darken,[55] who was one of the first to recognize the need to use activity gradients as proper driving forces when setting up the phenomenological relations to describe diffusion. Two austenite bars of different compositions (0.48% C, 3.8% Si), and (0.45% C, 0.05% Si) are welded together. The Carbon in the high-Si bar has a higher activity than the bar with the lower Si content; the calculated values of these activities are 0.051, and 0.024 respectively.[128] Carbon was allowed to diffuse for 13 days at 1323 K; after this period the bars are quenched and the composition profiles determined as shown in Figure 8-9(a). The high C content near the surface of the austenite bar on the right, imparts the required "hardness" to steel. The process of hardening of steel by "carburizing" is reliant on uphill transport of carbon from the high-Si bar to the low-Si bar, despite the fact that the initial compositions of carbon are practically the same in the two adjoining bars.

Figure 8-9(b) shows the corresponding profiles of the activity of C, calculated using the regular solution theory, the transport of C is down the gradient of the component activity.

Three quotes from the Darken paper,[55] summarize the foregoing arguments (see Figure 8-10):

"*the driving force in an isothermal diffusion process may be regarded as the gradient of the chemical potential,*",

"*for a system with more than two components it is no longer necessarily true that a given element tends to diffuse toward a region of lower concentration even within a single phase region*", and

"*departure from the behavior of an ideal solution may be so great that the concentration gradient and the chemical potential gradient, or activity gradient, may be of different sign, thus giving rise to uphill diffusion*".

The over- and under-shoots in the %C are adequately modelled by equation (8-33) that is based on the work of Kirkaldy[129] with the values of the Fick diffusivity matrix $[D] = \begin{bmatrix} 480 & 34 \\ 0 & 2.3 \end{bmatrix} \times 10^{-13}$ $m^2\ s^{-1}$. The finite value of the off-diagonal element $D_{12}$ reflects the dependence of the activity of C (species 1) on the composition of Si (component 2).

## 8.7 Uphill diffusion of Ni in Co/Fe/Ni ternary alloys

Another convincing confirmation of the conclusions reached in the Darken experiments are provided by the experimental data of Vignes and Sabatier[130, 131] for inter-diffusion between the left and right compartments of Co(1)/Fe(2)/Ni(3) mixture, annealed to a temperature of 1588 K. The initial atom fraction of Ni in the left and right bars are identical and equal 0.5. The arithmetic averaged atom fractions of Co(1)/Fe(2)/Ni(3) mixture are $x_{1,eq} = 0.25$, $x_{2,eq} = 0.25$ and $x_{3,eq} = 0.5$. However, the absence of differences in the Ni compositions is no hindrance to transport of Ni, engendered by diffusional coupling effects. Their experimental data, demonstrating uphill diffusion can be simulated with excellent accuracy using equation (8-33); the results of these simulations, but not the experiments, are presented in Figure 8-11. The atom fraction of each component is measured on either side of the Matano plane, at $t$ = 17 h after the start of the simulation are shown. In the simulations, the value of the Fick diffusivity matrix is chosen to be $[D] = \begin{bmatrix} 0.7 & 0.02 \\ 0.026 & 1.7 \end{bmatrix} \times 10^{-14}\ m^2 s^{-1}$; this choice is on the basis of

the experimental data presented in Table 2b of Divya et al.[132] The experimental trajectory, plotted in ternary composition space, follows a serpentine path.

## 8.8 Uphill diffusion in $K_2O/SrO/SiO_2$ mixtures

To illustrate the diffusional characteristics of multicomponent glasses, let us consider a set of experiments reported by Varshneya and Cooper.[133] Two glass slabs with different compositions of $K_2O/SrO/SiO_2$ were brought into contact at time $t$=0 and the transient concentration distributions determined. The wt% of each component is measured on either side of $z = z_0$ =0, measured at $t$ = 4.55 h after the start of the experiment are shown in Figure 8-12(a). The over- and under-shoots in the SrO concentrations are adequately modelled by equation (8-33), wherein the matrix of Fick diffusivities have the values $[D] = \begin{bmatrix} 1 & -0.267 \\ -1.22 & 0.33 \end{bmatrix} \times 10^{-13}$ m$^2$ s$^{-1}$.

The transient equilibration trajectories, plotted in 2D and 3D composition space follow serpentine trajectories; see Figure 8-12(b). The non-monotonous equilibration trajectory observed for SrO in Figure 8-12( signals uphill diffusion; such phenomena are of importance in the processing of ceramics, cements, alloys, steels, and composites.[122, 134] We note that the transient equilibration becomes monotonic for the uncoupled diffusion process.

## 8.9 Uphill diffusion in Fe/Mg/Ca in garnet

Let us examine the experimental data of Vielzeuf and Saúl[135] for inter-diffusion of Fe/Mg/Ca mixtures in garnet, a precious stone consisting of a deep red vitreous silicate mineral. Garnets are nesosilicates having the general formula $X_3Y_2(SiO_4)_3$. The $X$ site is usually occupied by divalent cations (Ca, Mg, Fe, Mn)$^{2+}$ and the $Y$ site by trivalent cations (Al, Fe, Cr)$^{3+}$ in an octahedral/tetrahedral framework with [SiO4]$^{4-}$ occupying the tetrahedra. A diffusion "couple" with two different compositions are brought into contact at time $t$ = 0; see Figure 8-13(a). The driving forces for the three components are (in atom fractions): $\Delta x_1 = -0.15; \quad \Delta x_2 = 0.01; \quad \Delta x_3 = 0.14$. The composition profiles on either side of the interface marker ($z$ = 0) are monitored at various time intervals. The composition

profiles at $t$ = 100 h (cf. Figure 8-13(a)) shows spatial over- and under-shoot in the composition profile for Mg, whose driving force is significantly lower than that of the two partner atoms. In ternary composition space, the equilibration trajectory is serpentine in shape; see Figure 8-13(b).

The modelling of the experimental data Vielzeuf and Saúl[135] for inter-diffusion of Fe/Mg/Ca mixtures in garnet proceeds along similar lines to the foregoing examples. The overshoot in the equilibration of Mg is adequately modelled using the values of the Fick diffusivity matrix $[D] = \begin{bmatrix} 5.86 & -1.02 \\ -5.5 & 1.18 \end{bmatrix} \times 10^{-19}$ m$^2$ s$^{-1}$ in equation (8-33); see Figure 8-13(a). Neglect of diffusion coupling effects results in linear, monotonic, equilibration. The non-monotonous equilibration trajectory observed for Mg in Figure 8-13(a) signals uphill diffusion; such phenomena are of importance in the processing of ceramics, cements, alloys, steels, and composites.[122, 134]

## 8.10 List of Figures for Diffusion in crystalline solids and alloys

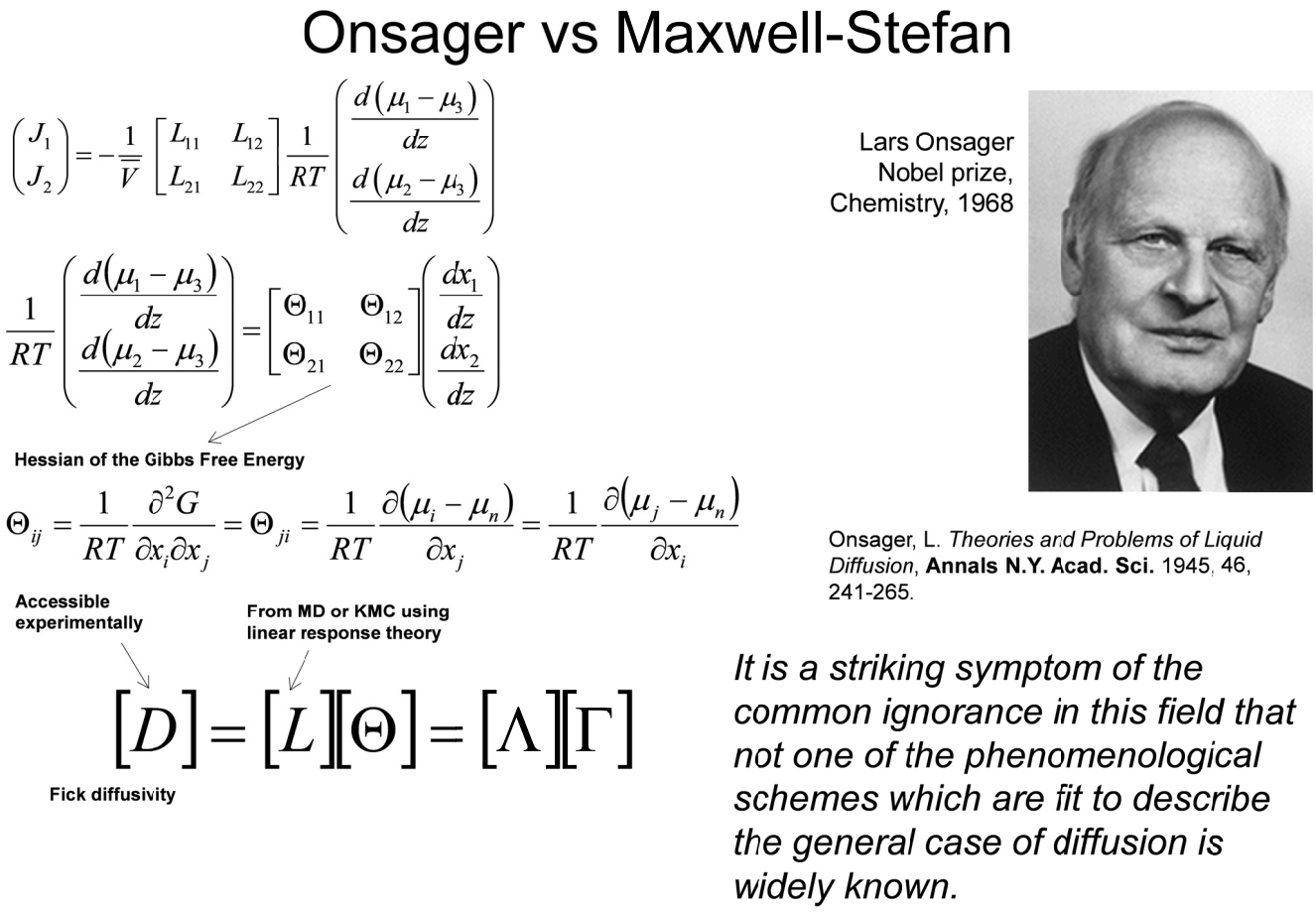


Figure 8-1. Onsager formulation for diffusion in ternary mixtures.

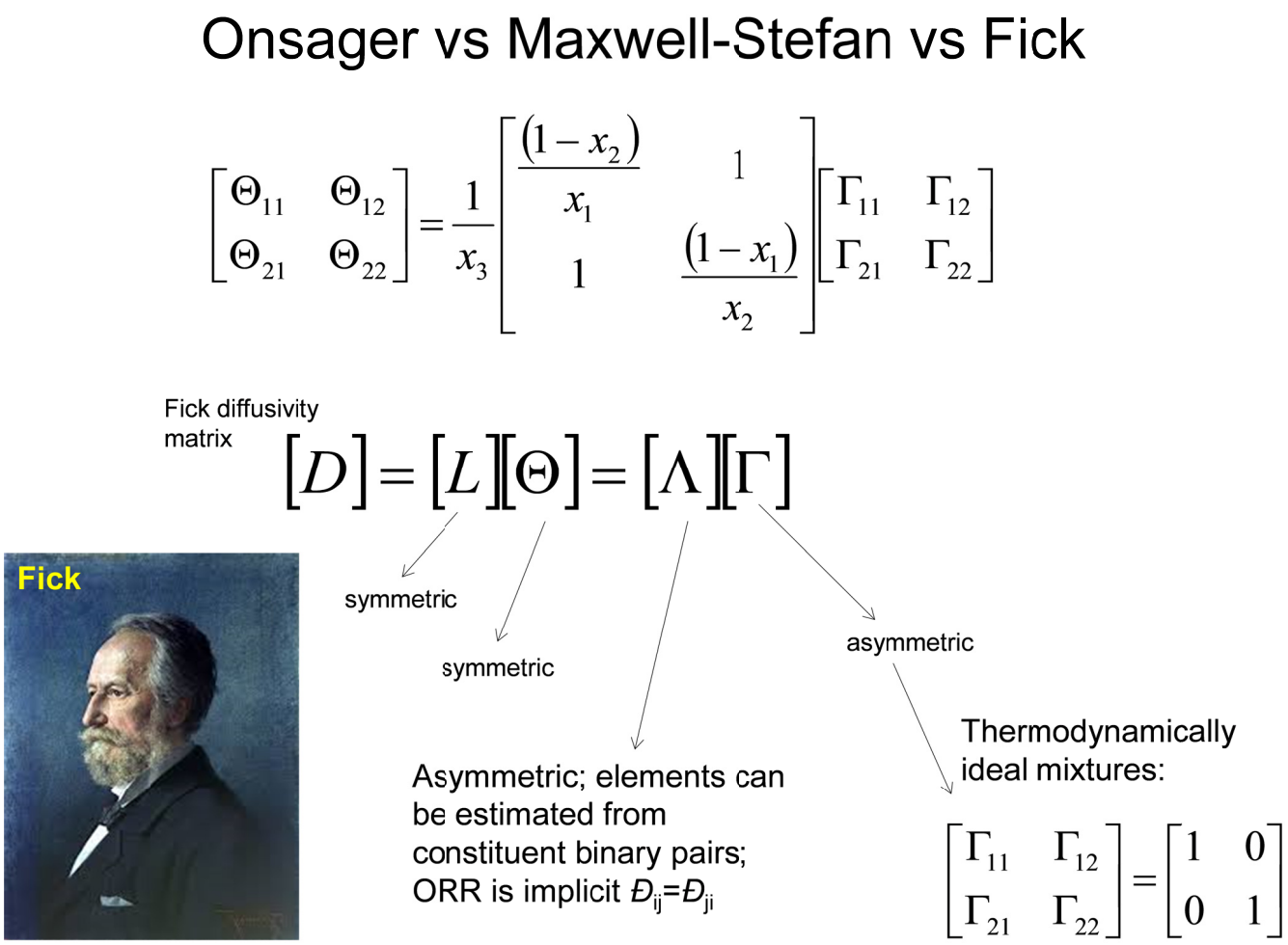


Figure 8-2. Inter-relation between the Onsager, and Maxwell-Stefan formulations.

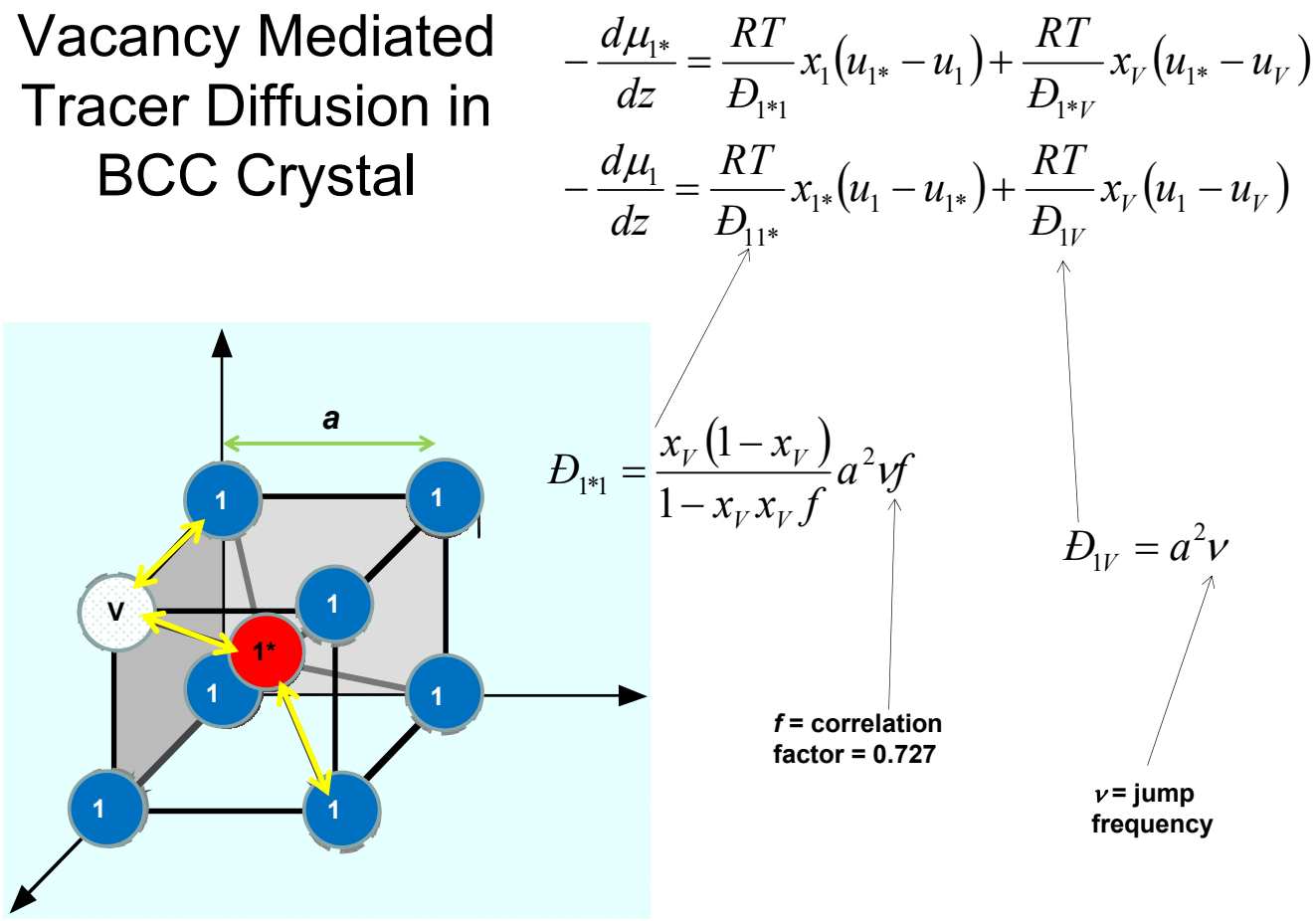


Figure 8-3. The Maxwell-Stefan formulation of vacancy-mediated tracer diffusion in BCC crystal.

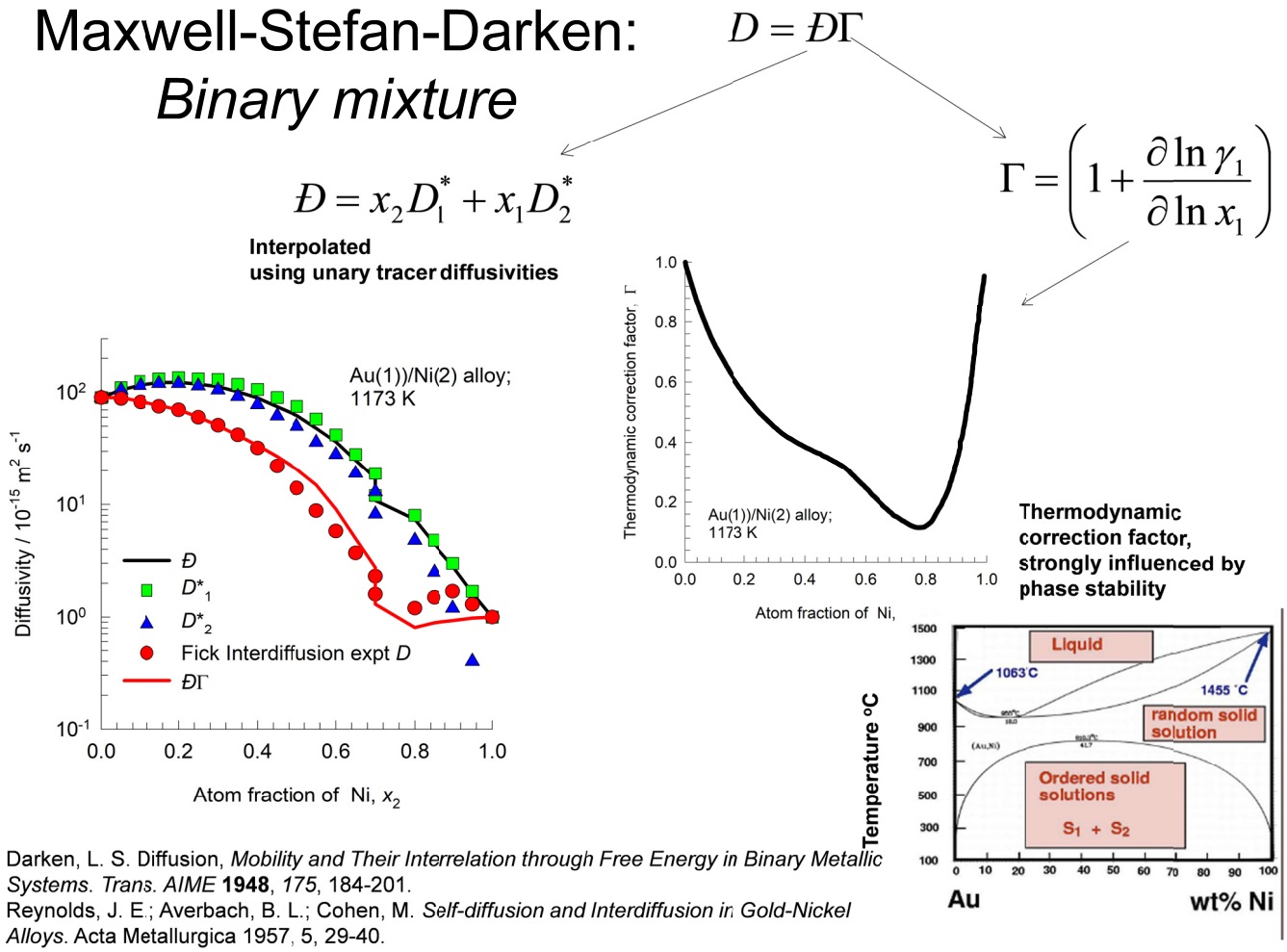


Darken, L. S. Diffusion, *Mobility and Their Interrelation through Free Energy in Binary Metallic Systems. Trans. AIME* **1948**, *175*, 184-201.
Reynolds, J. E.; Averbach, B. L.; Cohen, M. *Self-diffusion and Interdiffusion in Gold-Nickel Alloys*. Acta Metallurgica 1957, 5, 29-40.

Figure 8-4. The Maxwell-Stefan-Darken description of inter-diffusion in Au(1)-Ni(2) alloy. The experimental data are from Reynolds et al.[124]

# Inter-Diffusivity in Cu/Fe/Ni alloys

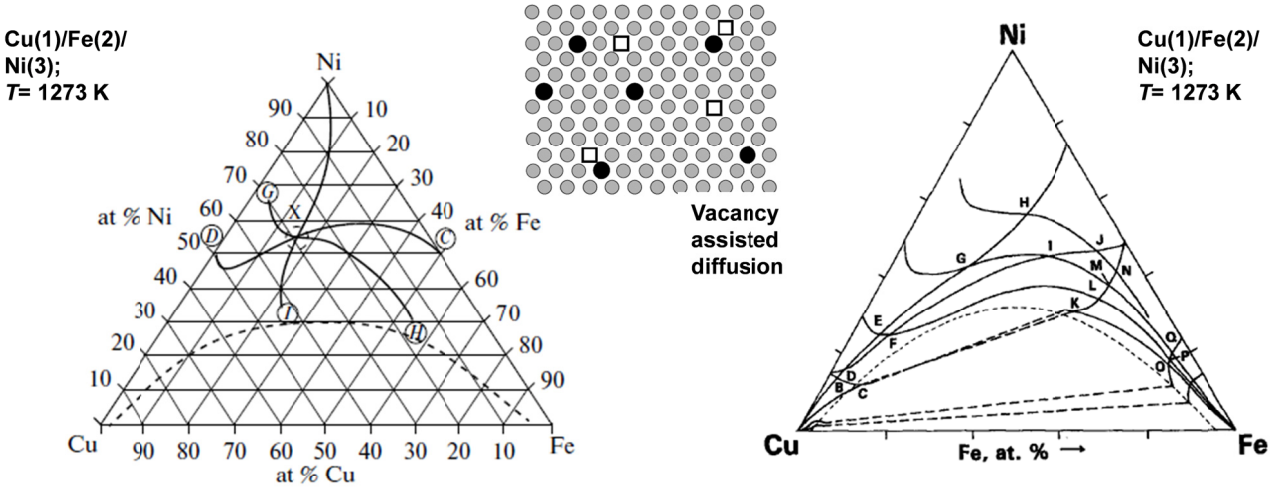


Ugaste, Ü.; Kodentsov, A. A.; Van Loo, F. J. J. *Concentration Dependence of Interdiffusion Coefficients in Cu–Fe–Ni System.* The Physics of Metals and Metallography 2013, 114, 54-62.

Rönkä, K. J.; Kodentsov, A. A.; Van Loon, P. J. J.; Kivilahti, J. K.; Van Loo, F. J. J. *Thermodynamic and Kinetic Study of Diffusion Paths in the System Cu-Fe-Ni.* Metall. Mater. Trans. A 1996, 27A, 2229-2238.

**Laboratory-fixed reference frame for inter-diffusion fluxes**
**[*D*] determined from ternary couples with common intersection compositions**

Figure 8-5. Published experimental inter-diffusivity data for Cu(1)/Fe(2)/Ni(3) system at 1273 K.[119, 125, 126]

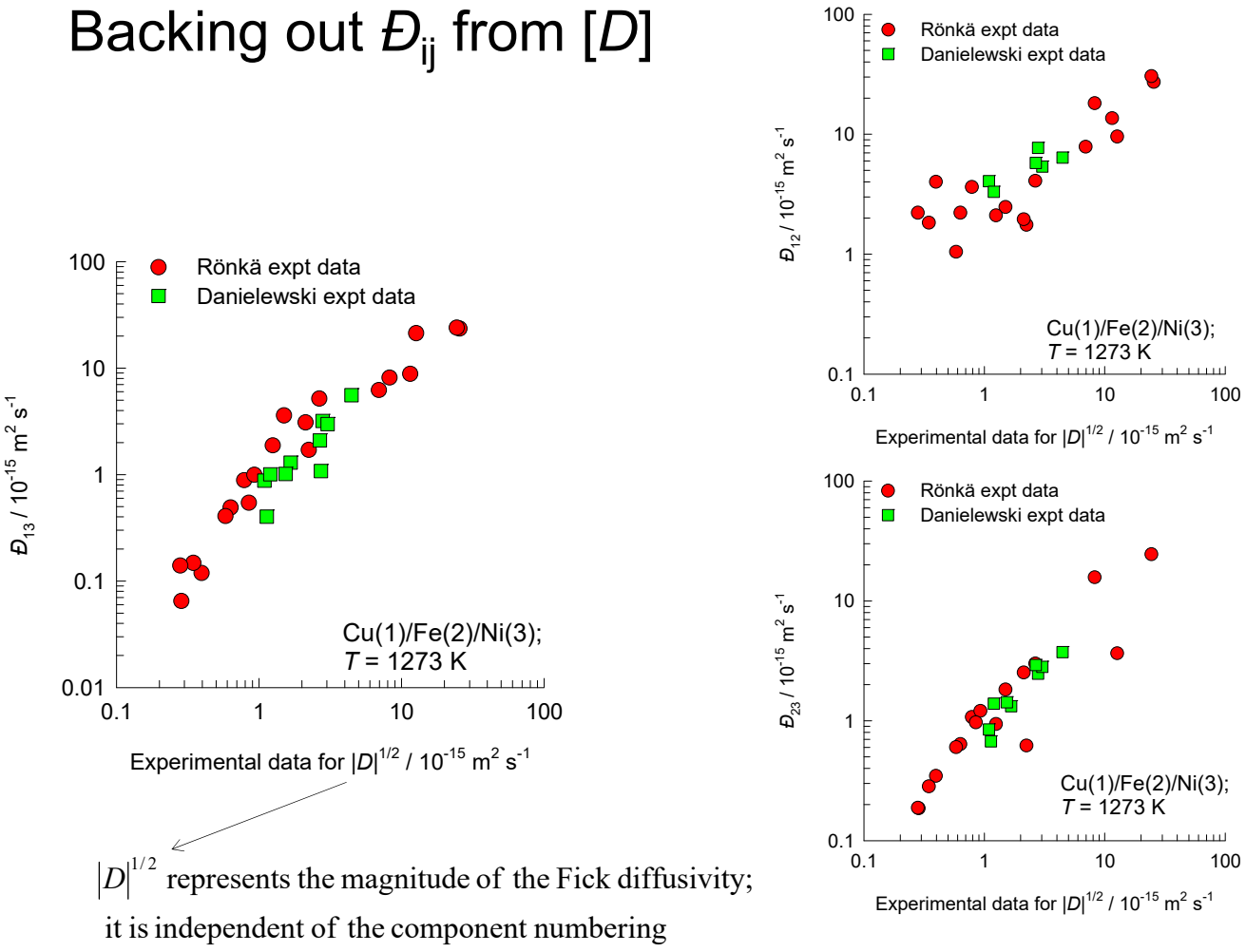


Figure 8-6. Backed-out data on the Maxwell-Stefan pair diffusivities for Cu(1)/Fe(2)/Ni(3) system at 1273 K.[119, 125, 126] The Danielewski data are those reported by Belova et al.[119] as Sample 6 – Sample 15. The *x*-axis is $|D|^{1/2}$, i.e. the square-root of the experimental data on the Fick inter-diffusivity matrix, that is independent of the component numbering.

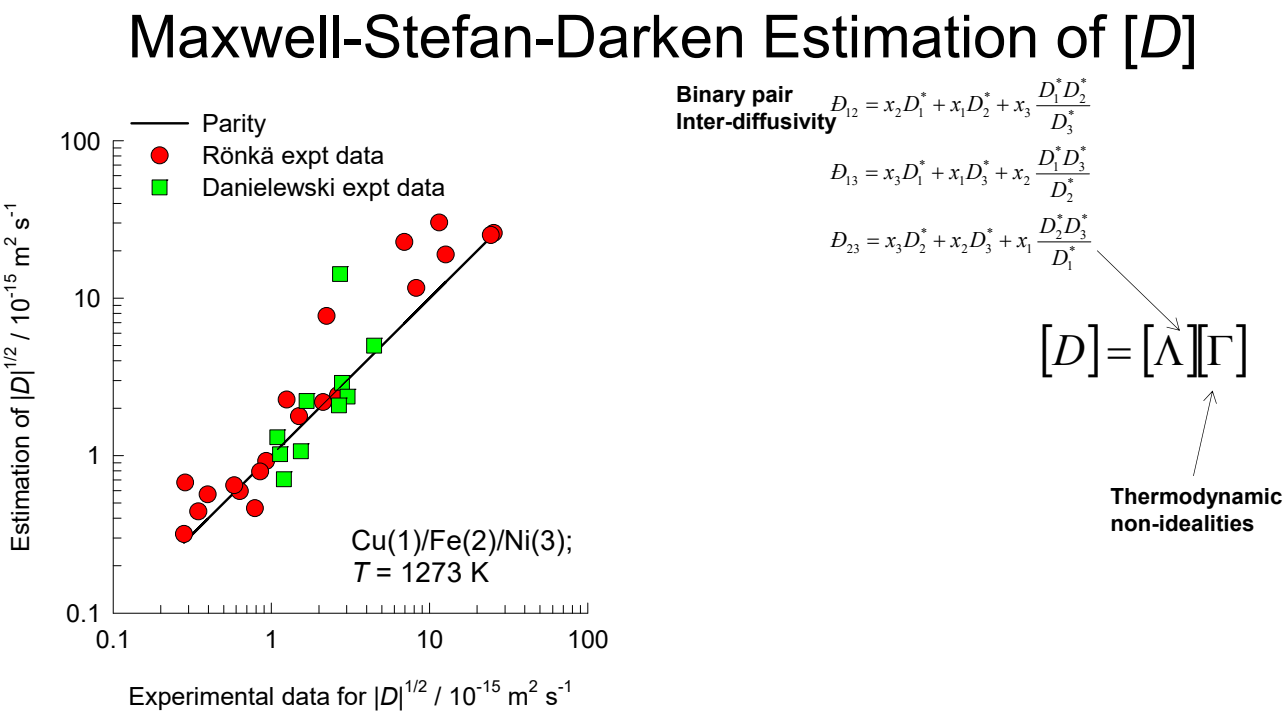


Figure 8-7. Comparison of the experimental data for Cu(1)/Fe(2)/Ni(3) system at 1273 K.[119, 125, 126] on the square root of the Fick inter-diffusivity matrix, $|D|^{1/2}$, with the estimations using the Maxwell-Stefan-Darken model.

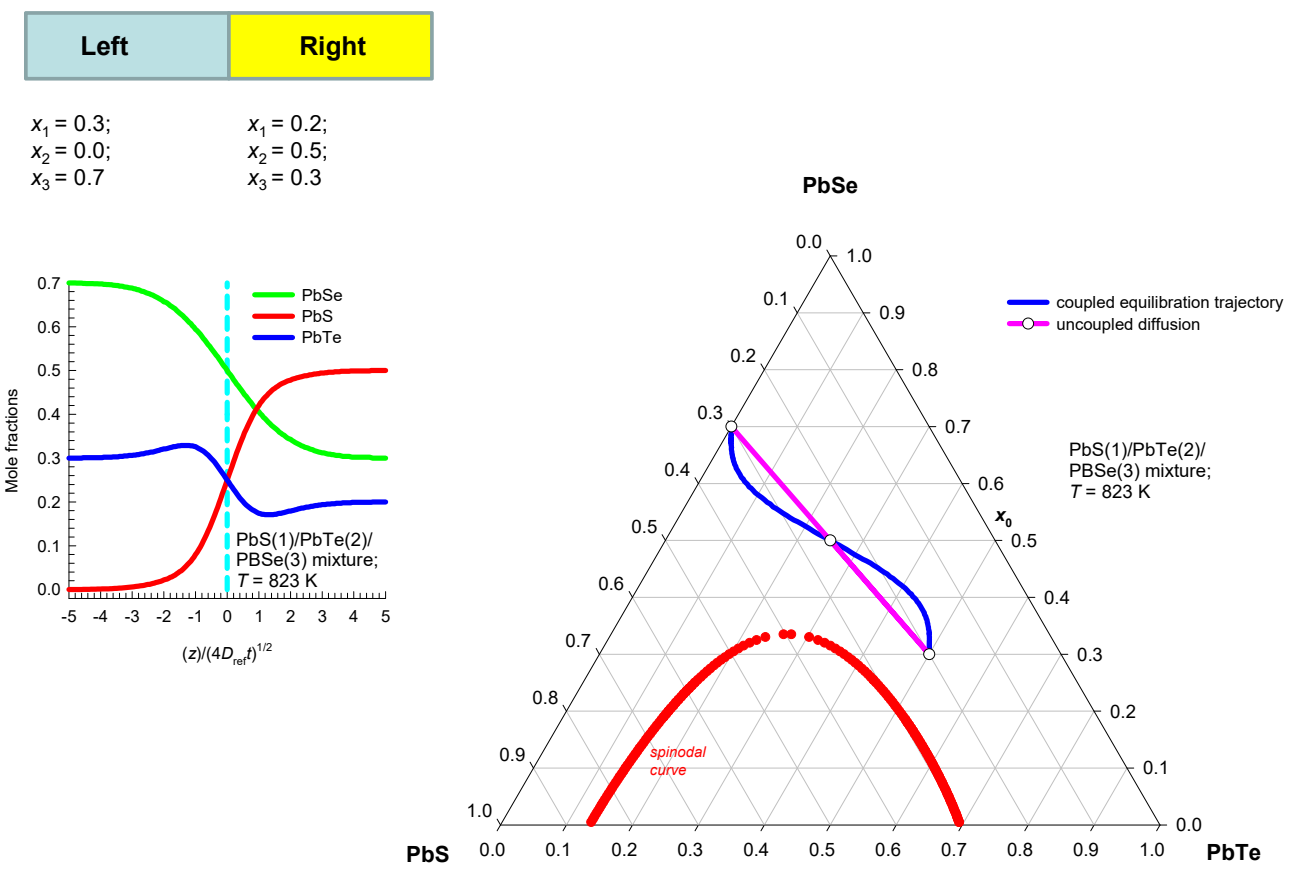


Figure 8-8. The equilibration trajectory for inter-diffusion in ternary PbS(1)/PbTe(2)/PbSe(3) crystalline mixtures at 823 K. The left and right compartments of a diffusion couple are maintained at two different compositions as indicated. Also plotted (continuous red line) is the spinodal curve, calculated at 823 K. The matrix of thermodynamic factors $[\Gamma]$ is calculated using the sub-regular solution model with parameters provided in Table 1 of Kokkonis and Leute.[127]

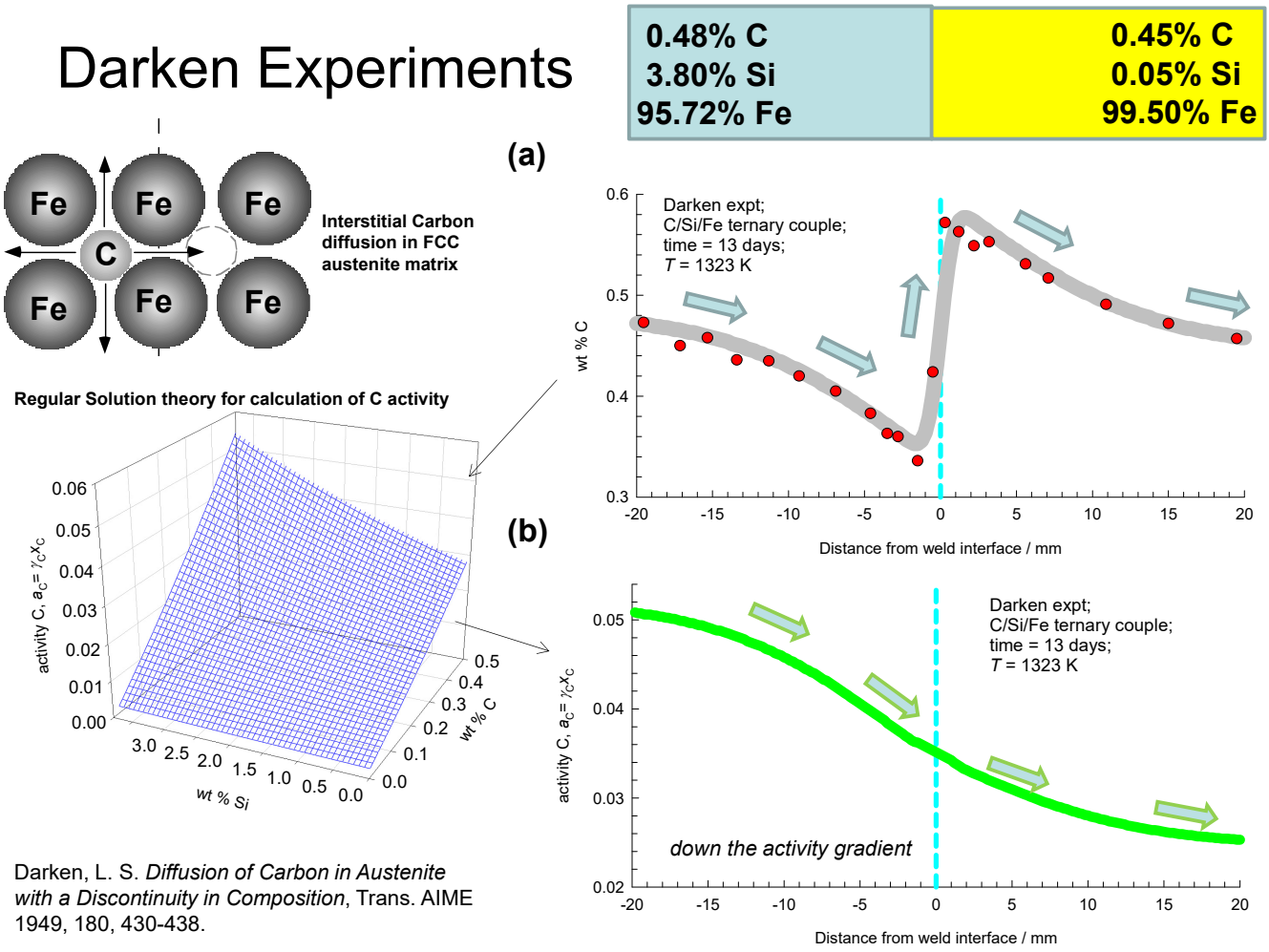


Darken, L. S. *Diffusion of Carbon in Austenite with a Discontinuity in Composition*, Trans. AIME 1949, 180, 430-438.

Figure 8-9. (a) Experimental data of Darken[55] for inter-diffusion between the left and right austenite bars consisting of C/Si/Fe mixtures, annealed to a temperature of 1323 K. The wt% of each component is measured on either side of the Matano plane, at $t$ = 13 days after the start of the experiment are shown. The calculations of the coupled diffusion model are based on the Fick diffusivity matrix determined by Kirkaldy for this experiment.[129] (b) The corresponding profiles of the activity of C, calculated using the regular solution theory,

# Takeaways from Lawrence Stamper Darken (1909 – 1978)

Darken, L. S. *Diffusion of Carbon in Austenite with a Discontinuity in Composition*, Trans. AIME 1949, 180, 430-438.

*..the driving force in an isothermal diffusion process may be regarded as the gradient of the chemical potential…*

*..for a system with **more than two components** it is no longer necessarily true that a given element tends to diffuse toward a region of lower concentration even within a **single phase** region…*

*..departure from the behavior of an ideal solution may be so great that the concentration gradient and the chemical potential gradient, or activity gradient, may be of different sign, thus giving rise to **uphill diffusion**…*

Figure 8-10.Three key take-aways from the classic paper of Darken.[55]

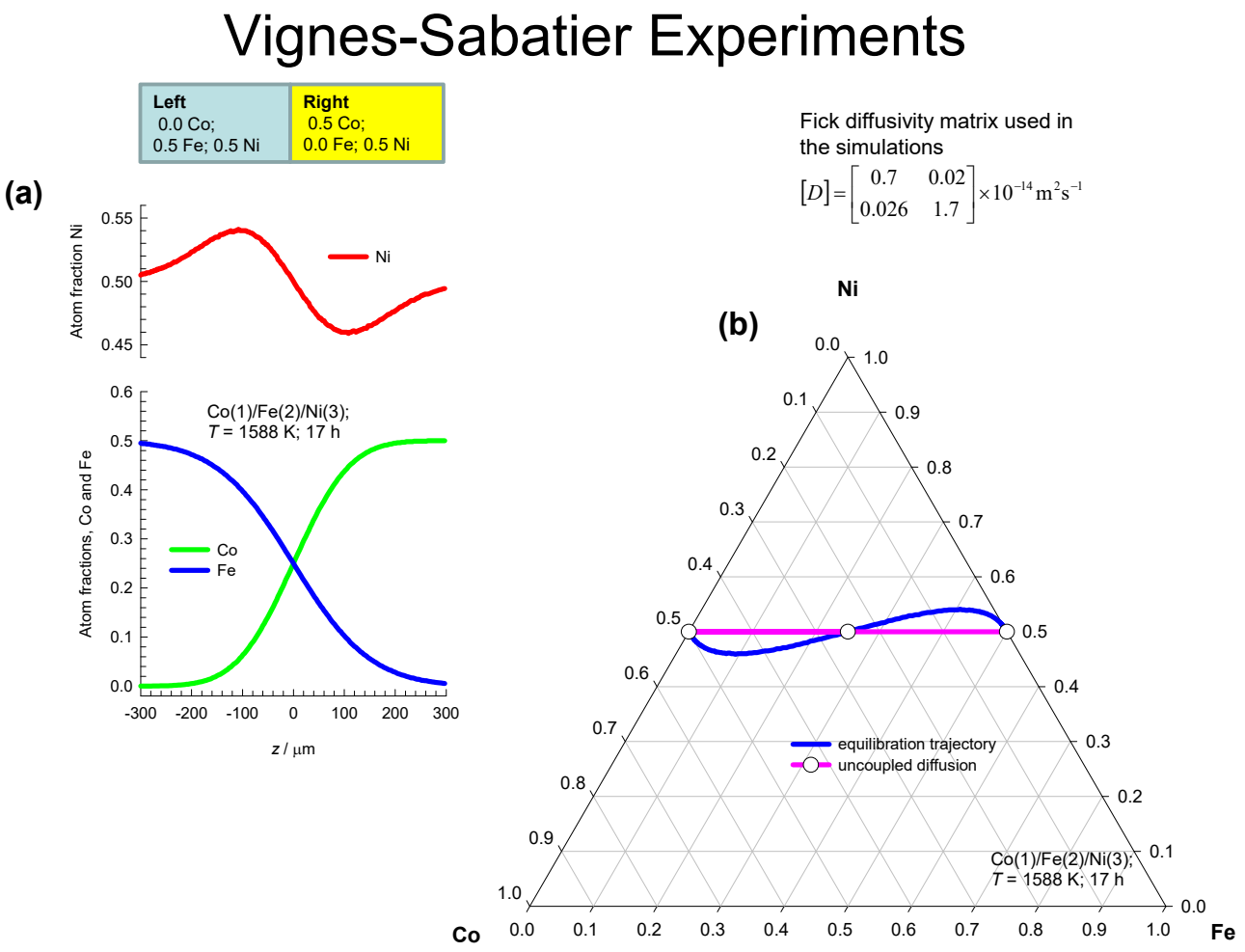


Figure 8-11. (a) Simulations of transient inter-diffusion between the left and right compartments of Co/Fe/Ni mixture, annealed to a temperature of 1588 K. The atom fraction of each component on either side of the Matano plane, at $t$ = 17 h after the start of the simulation are shown. (b) Equilibration trajectories in composition space. These simulations are designed to match the experimental data of Vignes and Sabatier[130, 131]

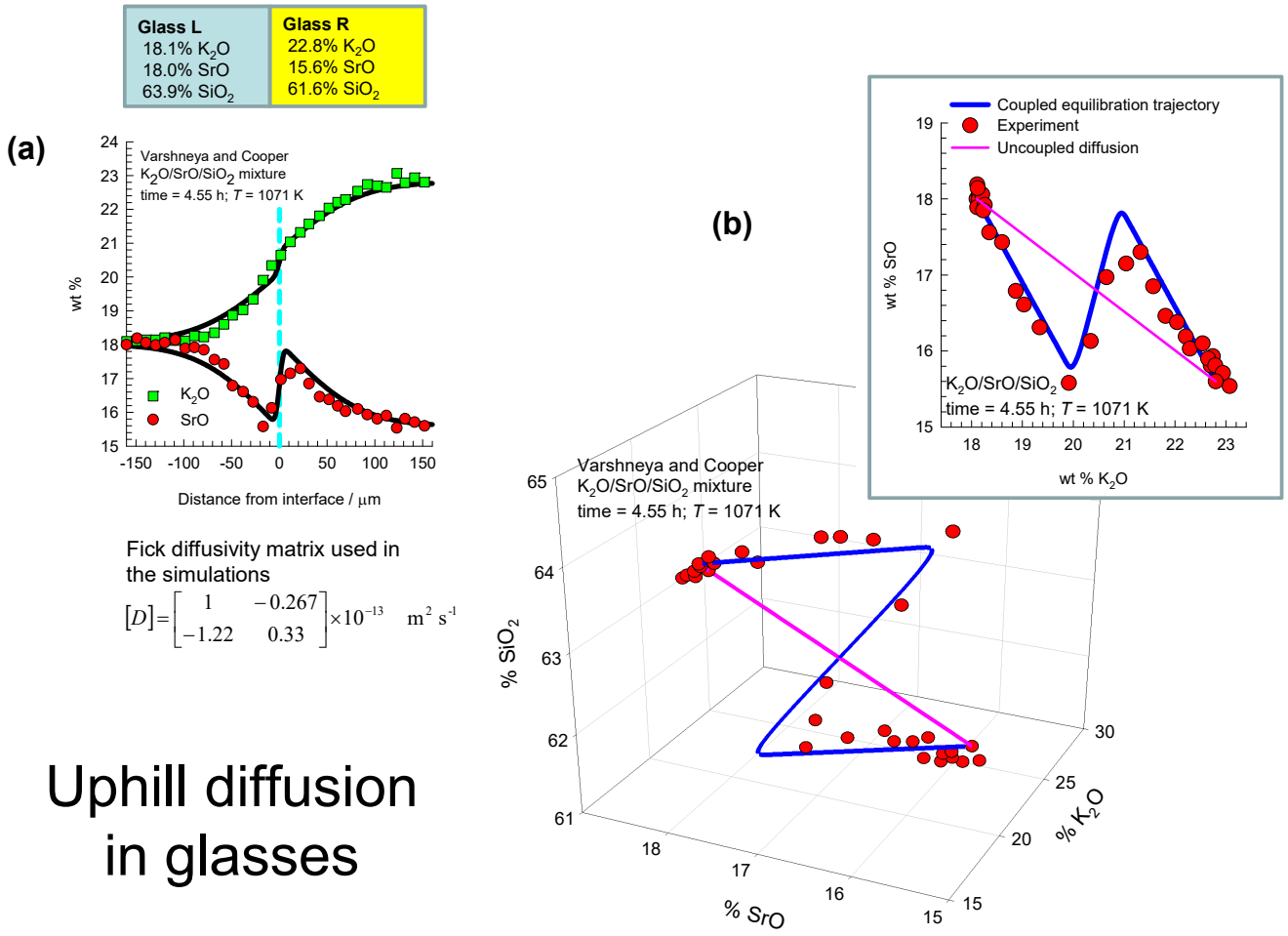


Figure 8-12. (a) Experimental data of Varshneya and Cooper[133] for inter-diffusion between the left and right slabs consisting of $K_2O/SrO/SiO_2$ mixtures. The wt% of each component is measured on either side of the Matano plane, measured at $t$ = 4.55 h after the start of the experiment are shown. (b) Equilibration trajectories in 2D and 3D composition space.

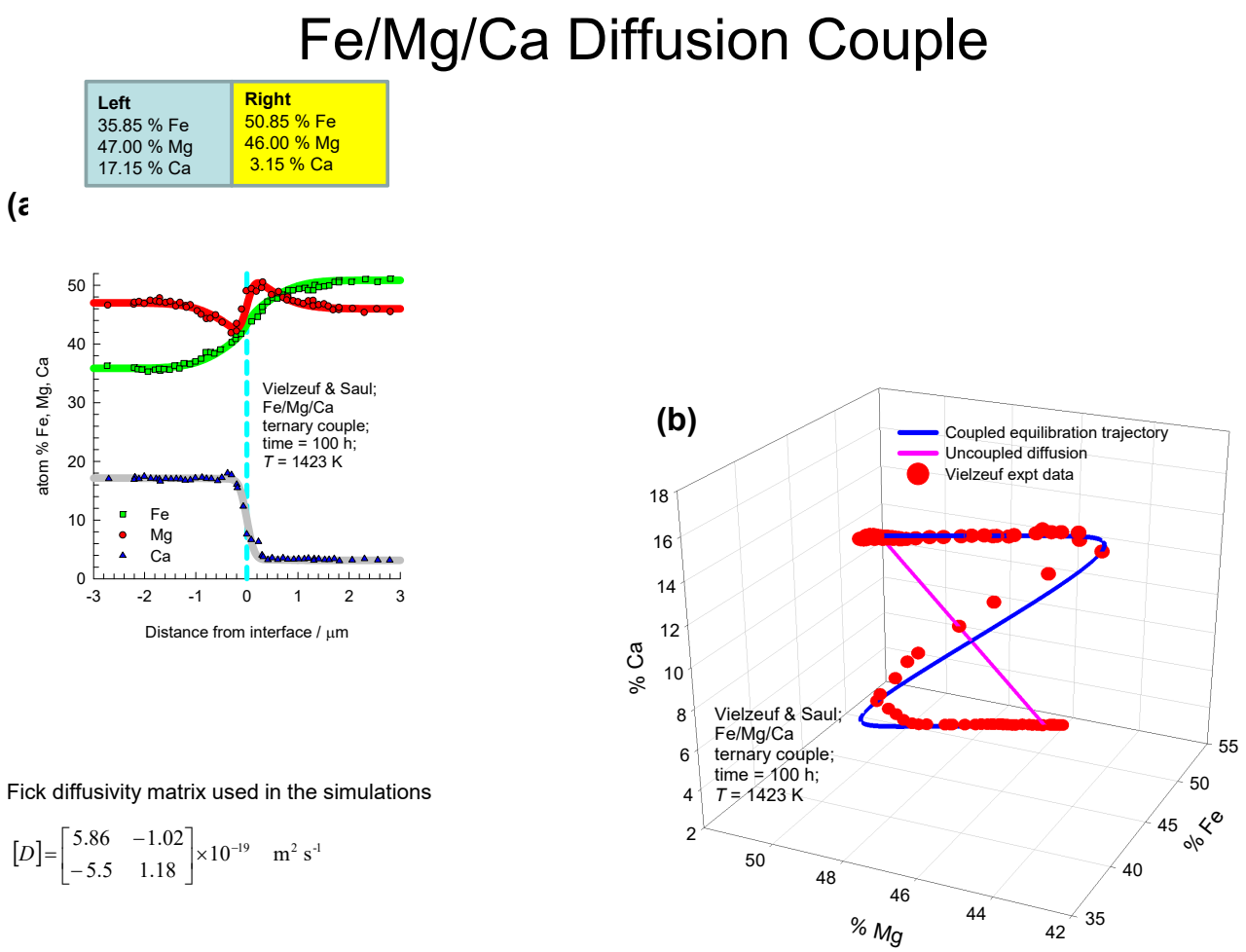


Fick diffusivity matrix used in the simulations

$$[D]=\begin{bmatrix}5.86 & -1.02\\ -5.5 & 1.18\end{bmatrix}\times 10^{-19} \quad \mathrm{m^2\ s^{-1}}$$

Figure 8-13. (a) Experimental data of Vielzeuf and Saúl[135] for inter-diffusion between the left and right slabs containing Fe/Mg/Ca mixtures. The atom % of each component is measured on either side of the Matano plane, measured at $t$ = 100 h after the start of the experiment are shown as function of the distance. (b) Equilibration trajectories in 3D composition space.

# 9 M-S formulation with generalized driving force

The analysis of the diffusion processes in the foregoing sections were restricted to isothermal, isobaric systems in the absence of external body forces such as centrifugal forces and electrostatic potential gradients. The important persuasive advantage of the Maxwell-Stefan formulation

$$-\frac{x_i}{RT}\nabla_{T,p}\mu_i = \sum_{j=1}^{n}\frac{x_i x_j}{Đ_{ij}}\left(\mathbf{u}_i - \mathbf{u}_j\right) = \sum_{\substack{j=1\\ j\neq i}}^{n}\frac{x_j\mathbf{N}_i - x_i\mathbf{N}_j}{c_t Đ_{ij}} = \sum_{j=1}^{n}\frac{x_j\mathbf{J}_i - x_i\mathbf{J}_j}{c_t Đ_{ij}};\quad i=1,2,...n \tag{9-1}$$

is that equation (9-1) can be extended, elegantly, to include the contribution of pressure gradients, and external body forces. The treatment below follows earlier works.[1, 136, 137]

## 9.1 Irreversible Thermodynamics and the M-S equation

The theory or irreversible thermodynamics is described in several excellent texts.[5, 137-139] Our treatment essentially follows that of Lightfoot,[137] and Standart et al.[1, 9] The starting point for our analysis is the rate of entropy production due to *n*-component diffusion; see Equation (2.3.1) of Taylor and Krishna.[1] The rate of entropy production is a product of the "flux" $\mathbf{j}_i$ and the driving force $\left(\nabla_T \tilde{\mu}_i - \tilde{\mathbf{F}}_i\right)$.

$$\sigma = -\frac{1}{T}\sum_{i=1}^{n}\left(\nabla_T \tilde{\mu}_i - \tilde{\mathbf{F}}_i\right)\bullet \mathbf{j}_i \geq 0 \tag{9-2}$$

where $\mathbf{j}_i = \rho_i\left(\mathbf{u}_i - \mathbf{v}\right) = \rho_t x_i\left(\mathbf{u}_i - \mathbf{v}\right)$ is the mass diffusion flux of species *i* with respect to the mass average reference velocity $\mathbf{v}$; $\tilde{\mu}_i = \frac{\mu_i}{M_i}$ is the specific chemical potential of species *i* with units of J kg$^{-1}$; $M_i$ is the molar mass of of species *i* with units kg mol$^{-1}$; $\nabla_T \tilde{\mu}_i$ is the isothermal gradient of the specific chemical potential; $\tilde{\mathbf{F}}_i$ represents the force acting per kg of species *i*. $\tilde{\mathbf{F}}_i$ represents the body force

acting per mole of species *i*, $\rho_i \tilde{\mathbf{F}}_i = c_i \mathbf{F}_i$; $\tilde{\mathbf{F}}_i = \frac{\mathbf{F}_i}{M_i}$. The requirement $\sigma \geq 0$ follows from the second law of thermodynamics.

Under the action of external body forces, linear momentum will be conserved

$$\begin{aligned} &-\nabla p + \sum_{i=1}^{n} \rho_i \tilde{\mathbf{F}}_i = \rho_t \frac{d\mathbf{v}}{dt} + \nabla \bullet \tau = \text{conservation of linear momentum} \\ &\frac{d}{dt} \equiv \frac{\partial}{\partial t} + \mathbf{v} \bullet \nabla = \text{material derivative following mixture velocity} \\ &-\frac{1}{\rho_t} \nabla p + \sum_{i=1}^{n} \omega_i \tilde{\mathbf{F}}_i = \frac{d\mathbf{v}}{dt} + \frac{1}{\rho_t} \nabla \bullet \tau \end{aligned} \tag{9-3}$$

where $\mathbf{v}$ is the mass average mixture velocity, $\boldsymbol{\tau}$ is the stress tensor and $\omega_i$ is the mass fraction of species *i*.

In diffusion processes of relevance to chemical engineering mechanical equilibrium is established far quicker than thermodynamic equilibrium and we may safely assume

$$\frac{d\mathbf{v}}{dt} + \frac{1}{\rho_t} \nabla \bullet \tau \approx 0 = -\frac{1}{\rho_t} \nabla p + \sum_{i=1}^{n} \omega_i \tilde{F}_i \tag{9-4}$$

Adding the vanishing quantity $0 = -\frac{1}{\rho_t} \nabla p + \sum_{i=1}^{n} \omega_i \tilde{F}_i$ to the driving forces in equation (9-2):

$$\begin{aligned} \sigma &= -\frac{1}{T} \sum_{i=1}^{n} \left( \nabla_T \tilde{\mu}_i - \tilde{\mathbf{F}}_i - \frac{1}{\rho_t} \nabla p + \sum_{i=1}^{n} \omega_i \tilde{F}_i \right) \bullet \mathbf{j}_i \\ \sigma &= -\frac{1}{T} \sum_{i=1}^{n} \rho_i \left( \nabla_T \tilde{\mu}_i - \tilde{\mathbf{F}}_i - \frac{1}{\rho_t} \nabla p + \sum_{i=1}^{n} \omega_i \tilde{F}_i \right) \bullet \left( \mathbf{u}_i - \mathbf{v} \right) \\ \sigma &= -\frac{1}{T} \sum_{i=1}^{n} \left( \rho_i \nabla_T \tilde{\mu}_i - \omega_i \nabla p - \rho_i \left( \tilde{\mathbf{F}}_i - \sum_{i=1}^{n} \omega_i \tilde{F}_i \right) \right) \bullet \left( \mathbf{u}_i - \mathbf{v} \right) \geq 0 \end{aligned} \tag{9-5}$$

The chemical potential gradient term may be expanded to explicitly include the contribution of the pressure gradient $\nabla_T \mu_i = \nabla_{T,p} \mu_i + \overline{V_i} \nabla p$ where $\overline{V_i}$ is the partial molar volume of species *i* with units $m^3$ $mol^{-1}$, and $\nabla_{T,p} \mu_i$ is the isothermal, isobaric gradient of the molar chemical potential. The isothermal

gradient of the specific chemical potential is $\nabla_T \tilde{\mu}_i = \frac{1}{M_i}\nabla_{T,p}\mu_i + \frac{\overline{V}_i}{M_i}\nabla p$. Expressed in terms of the gradients of the molar chemical potential, equation (9-5) takes the form

$$\sigma = -\frac{1}{T}\sum_{i=1}^{n}\left( c_i\nabla_{T,p}\mu_i + \left(c_i\overline{V}_i - \omega_i\right)\nabla p - \rho_i\left(\tilde{\mathbf{F}}_i - \sum_{i=1}^{n}\omega_i\tilde{F}_i\right)\right)\bullet\left(\mathbf{u}_i - \mathbf{v}\right) \geq 0 \tag{9-6}$$

It is convenient to define the generalized driving force $\mathbf{d}_i$:

$$\begin{aligned} c_t RT\mathbf{d}_i &\equiv c_i\nabla_{T,p}\mu_i + \left(c_i\overline{V}_i - \omega_i\right)\nabla p - \rho_i\left(\tilde{\mathbf{F}}_i - \sum_{i=1}^{n}\omega_i\tilde{\mathbf{F}}_i\right) \\ \mathbf{d}_i &\equiv \frac{x_i}{RT}\nabla_{T,p}\mu_i + \frac{1}{c_t RT}\left(c_i\overline{V}_i - \omega_i\right)\nabla p - \frac{\rho_i}{c_t RT}\left(\tilde{\mathbf{F}}_i - \sum_{i=1}^{n}\omega_i\tilde{\mathbf{F}}_i\right) \end{aligned} \tag{9-7}$$

As emphasized by Lightfoot,[137] the "fearsome" quantity $c_t RT\mathbf{d}_i$ has a very simple physical significance: $c_t RT\mathbf{d}_i$ = force per unit volume of solution tending to move species *i relative to the solution*. With this definition of the generalized driving force, the rate of entropy production is

$$\sigma = -c_t R\sum_{i=1}^{n}\mathbf{d}_i\bullet\left(\mathbf{u}_i - \mathbf{v}\right) \geq 0 \tag{9-8}$$

As noted by Lightfoot,[137] the rate of entropy production remains unchanged if any arbitrary reference velocity is chosen in place of the mass average reference velocity $\mathbf{v}$. With the molar average reference velocity $\mathbf{u}$ we write

$$\sigma = -c_t R\sum_{i=1}^{n}\mathbf{d}_i\bullet\left(\mathbf{u}_i - \mathbf{u}\right) = -R\sum_{i=1}^{n}\frac{\mathbf{d}_i}{x_i}\bullet\mathbf{J}_i \geq 0 \tag{9-9}$$

It follows from the Gibbs-Duhem equation that

$$\sum_{i=1}^{n}\mathbf{d}_i = 0 \tag{9-10}$$

Following the Onsager concepts of irreversible thermodynamics, we may set up linear relations between the driving forces $c_t RT\mathbf{d}_i$ and relative velocities $\left(\mathbf{u}_i - \mathbf{v}\right)$, taken as representative of "fluxes":

$$c_t RT\mathbf{d}_i = \sum_{j=1}^{n}\beta_{ij}\left(\mathbf{u}_j - \mathbf{v}\right); \quad i = 1,2,...n \tag{9-11}$$

**M-S formulation with generalized driving force**

The Onsager Reciprocal Relations assert the symmetry constraint

$$\beta_{ij} = \beta_{ji}; \quad i, j = 1, 2, ...n \tag{9-12}$$

It follows from the Gibb-Duhem constraint (9-10) that

$$\sum_{j=1}^{n}\sum_{i=1}^{n}\beta_{ij}\left(\mathbf{u}_j - \mathbf{v}\right) = 0 \tag{9-13}$$

Since the relative velocities $\left(\mathbf{u}_i - \mathbf{v}\right)$ are mathematically independent of one another it must also follow that

$$\sum_{i=1}^{n}\beta_{ij} = 0; \quad j = 1, 2, ...n \tag{9-14}$$

Due to the constraint imposed by equation (9-14), we may replace the mass average reference velocity $\mathbf{v}$ in equation (9-11), by any arbitrary velocity. We may replace the reference velocity $\mathbf{v}$ by the species velocity of any arbritrary species *k*, $\mathbf{u}_k$ and write equation (9-11) as

$$c_t RT\mathbf{d}_i = \sum_{j=1}^{n}\beta_{ij}\left(\mathbf{u}_j - \mathbf{u}_k\right); \quad i = 1, 2, ...n \tag{9-15}$$

Essentially, in the Maxwell-Stefan formulation, we take $\mathbf{u}_k = \mathbf{u}_i$ and $Đ_{ij} = \dfrac{x_i x_j}{\beta_{ij}} c_t RT; \quad i, j = 1, 2, ...n$;

this results in

$$\mathbf{d}_i \equiv \frac{x_i}{RT}\nabla_{T,p}\mu_i + \frac{1}{c_t RT}\left(c_i\overline{V}_i - \omega_i\right)\nabla p - \frac{\rho_i}{c_t RT}\left(\tilde{\mathbf{F}}_i - \sum_{i=1}^{n}\omega_i\tilde{\mathbf{F}}_i\right) = \sum_{j=1}^{n}\frac{x_i x_j}{Đ_{ij}}\left(\mathbf{u}_j - \mathbf{u}_i\right); \quad i = 1, 2, ...n$$

or

$$-\mathbf{d}_i = \sum_{j=1}^{n}\frac{x_i x_j}{Đ_{ij}}\left(\mathbf{u}_i - \mathbf{u}_j\right) == \sum_{\substack{j=1\\ j\neq i}}^{n}\frac{x_j\mathbf{N}_i - x_i\mathbf{N}_j}{c_t Đ_{ij}} = \sum_{j=1}^{n}\frac{x_j\mathbf{J}_i - x_i\mathbf{J}_j}{c_t Đ_{ij}}; \quad i = 1, 2, ...n \tag{9-16}$$

If the body forces $\mathbf{F}_i$ represent the force acting per mole of species *i*, the corresponding relations are

**M-S formulation with generalized driving force**

$$\mathbf{d}_i \equiv \frac{x_i}{RT}\nabla_{T,p}\mu_i + \frac{1}{c_t RT}\left(c_i\overline{V}_i - \omega_i\right)\nabla p - \frac{1}{c_t RT}\left(c_i\mathbf{F}_i - \omega_i\sum_{k=1}^{n}c_k\mathbf{F}_k\right) = \sum_{j=1}^{n}\frac{x_i x_j}{Đ_{ij}}\left(\mathbf{u}_j - \mathbf{u}_i\right);\quad i=1,2,...n$$

or

$$-\mathbf{d}_i = \sum_{j=1}^{n}\frac{x_i x_j}{Đ_{ij}}\left(\mathbf{u}_i - \mathbf{u}_j\right) = \sum_{\substack{j=1\\ j\neq i}}^{n}\frac{x_j\mathbf{N}_i - x_i\mathbf{N}_j}{c_t Đ_{ij}} = \sum_{j=1}^{n}\frac{x_j\mathbf{J}_i - x_i\mathbf{J}_j}{c_t Đ_{ij}};\quad i=1,2,...n \tag{9-17}$$

For transport in electrolyte systems, for example, the body force $\mathbf{F}_i$ acting per mol of species *i* is $\mathbf{F}_i = -z_i\mathrm{F}\nabla\Phi$ where $z_i$ is the ionic charge of species *i* and F is the Faraday constant. Except in regions close to electrode surfaces, where there will be charge separation (the double layer phenomena), the condition of electro-neutrality is met $\sum_{i=1}^{n}c_i z_i = 0$ and therefore $\sum_{k-1}^{n}c_k\mathbf{F}_k = \left(\sum_{k=1}^{n}c_k z_k\right)\mathrm{F}\nabla\Phi = 0$; the expression for the generalized driving force simplifies to yield

$$\mathbf{d}_i \equiv \frac{x_i}{RT}\nabla_{T,p}\mu_i + \frac{1}{c_t RT}\left(c_i\overline{V}_i - \omega_i\right)\nabla p + x_i z_i\mathrm{F}\nabla\Phi = \sum_{j=1}^{n}\frac{x_i x_j}{Đ_{ij}}\left(\mathbf{u}_j - \mathbf{u}_i\right);\quad i=1,2,...n$$

or

$$-\mathbf{d}_i = \sum_{j=1}^{n}\frac{x_i x_j}{Đ_{ij}}\left(\mathbf{u}_i - \mathbf{u}_j\right) = \sum_{\substack{j=1\\ j\neq i}}^{n}\frac{x_j\mathbf{N}_i - x_i\mathbf{N}_j}{c_t Đ_{ij}} = \sum_{j=1}^{n}\frac{x_j\mathbf{J}_i - x_i\mathbf{J}_j}{c_t Đ_{ij}};\quad i=1,2,...n \tag{9-18}$$

An important advantage of the use of the M-S formulation is that the addition of the driving forces $\nabla p$, and $\nabla\Phi$ has no influence on the M-S diffusivities of the constituent binary pairs, $Đ_{ij}$.

With the choice of $\mathbf{u}_i$ as reference velocity, substitution of equation (9-16) into equation (9-8) gives the following expression for the rate of entropy production

$$\sigma = \frac{1}{2}c_t R\sum_{i=1}^{n}\sum_{j=1}^{n}\frac{x_i x_j\left|\mathbf{u}_i - \mathbf{u}_j\right|^2}{Đ_{ij}} \geq 0 \tag{9-19}$$

## 9.2 Separations in an ultracentrifuge

Equation (9-16) is the appropriate starting point for the analysis of separations in an ultracentrifuge. The centrifugal force exerted per kg of component *i* in a multicomponent mixture is $\tilde{F}_i = \Omega^2 r$ where *r*

is the distance from the axis of rotation, and $\Omega$ is the angular velocity: $\Omega = 2\pi(\text{rotational speed expressed in revolutions per second})$. Equation (9-16) yields

$$d_i \equiv \frac{x_i}{RT}\frac{d\mu_i}{dr} + \frac{1}{c_t RT}\left(c_i\overline{V_i} - \omega_i\right)\frac{dp}{dr} - \frac{\rho_i}{c_t RT}\left(\Omega^2 r - \Omega^2 r\right) = \frac{x_i}{RT}\frac{d\mu_i}{dr} + \frac{1}{c_t RT}\left(c_i\overline{V_i} - \omega_i\right)\frac{dp}{dr} \tag{9-20}$$

Mechanical equilibrium is established quickly in relation to thermodynamic equilibrium in an ultracentrifuge. At mechanical equilibrium we have

$$\frac{dp}{dr} = \rho_t \sum_{i=1}^{n} \omega_i \tilde{F}_i = \rho_t \Omega^2 r \tag{9-21}$$

Substituting equation (9-21) into equation (9-20) reesults in

$$d_i \equiv \frac{x_i}{RT}\frac{d\mu_i}{dr} + \frac{1}{c_t RT}\left(c_i\overline{V_i} - \omega_i\right)\rho_t \Omega^2 r \tag{9-22}$$

We note that the contribution of the centrifugal force to the overall driving force is effective only when there is a difference between the volume fraction of component $i$, $c_i\overline{V_i}$, and its mass fraction, $\omega_i$; for a mixture where these differ the centrifugal force will cause relative motion of species. Components with a higher molar mass and mass density will experience a greater force and will therefore tend to congregate towards the periphery; this will cause a composition gradient $\nabla_{T,p}\mu_i$ directed inwards tending to cause re-distribution. At thermodynamic equilibrium, the driving forces vanish and therefore the composition distribution is described by

$$\frac{x_i}{RT}\frac{d\mu_i}{dr} = -\frac{1}{c_t RT}\left(c_i\overline{V_i} - \omega_i\right)\rho_t \Omega^2 r \tag{9-23}$$

The ultracentrifuge induces a separation provided that the volume fraction $c_i\overline{V_i}$ is different from the mass fraction $\omega_i$. As illustration, consider the separation of the gaseous isotopes $U^{235}F_6(1)/U^{238}F_6(2)$ at 293.15 K as described in Example 2.3.2 of Taylor and Krishna;[1]; see Figure 9-1. The molar masses are $M_1$=0.34915 kg mol$^{-1}$; $M_2$=0.35215 kg mol$^{-1}$. The centrifuge rotates at 40000 rpm. The separation takes place within the annular space between $r = r_0 = 10$ mm and $r = r_1 = 60$ mm. The mole fraction distribution of component 1 within the annular space as a function of the radial distance $r$ is

$$\frac{x_{r=r}}{1-x_{r=r}}\frac{1-x_{r=r0}}{x_{r=r0}}=\exp\left[\left(M_1-M_2\right)\frac{\Omega^2\left(r^2-r_0^2\right)}{2RT}\right] \tag{9-24}$$

The composition profiles within the annular space are shown in Figure 9-1; the heavier isotope concentrates near the periphery. An uranium enrichment industrial facility will have a few million centrifuges to achieve the desired degree of separation.[1] Separations in an ultracentrifuge may also be viewed as uphill diffusion, engendered by the centrifugal force.

## 9.3 Thermal diffusion or Soret effect

The Soret effect, also called thermal diffusion, is the tendency of a mixture of two or more components to separate due to a temperature gradient. In 1879 Charles Soret discovered that a salt solution contained in a tube with the two ends at different temperatures did not remain uniform in composition; the salt was more concentrated near the cold end than near the hot end of the tube; for a review of the history and applications see Platten.[140] When steep temperature gradients are encountered, such as in chemical vapor deposition processes, we need additionally to take account of the thermal diffusion contribution to the molar fluxes.[141]

The Maxwell-Stefan formulation can be augmented in the following form; see Kuiken[139] for detailed derivations

$$-\mathbf{d}_i=\sum_{\substack{j=1\\ j\neq i}}^{n}\frac{x_i x_j(\mathbf{u}_i^T-\mathbf{u}_j^T)}{Đ_{ij}};\qquad i=1,2,\ldots n \tag{9-25}$$

where $u_i^T$ is the augmented species velocity incorporating the thermal diffusion contribution

$$\mathbf{u}_i^T=\mathbf{u}_i+\left(\frac{D_i^T}{\rho_i}\right)\frac{\nabla T}{T};\qquad i=1,2,...n \tag{9-26}$$

The thermal diffusion coefficients $D_i^T$ have been defined in the manner of Hirschfelder et al.[13] and have the units kg m$^{-1}$ s$^{-1}$. In CVD processes, thermal diffusion causes large, heavy gas molecules like $WF_6$, whose $D_i^T > 0$, to concentrate in cold regions whereas small, light molecules like $H_2$, whose $D_i^T < 0$,

concentrate in hot regions. Kleijn and Hoogendoorn[141] have demonstrated the importance of the thermal diffusion contribution in the modelling of CVD processes.

In hydrocarbon reservoirs, the temperature gradient $\frac{dT}{dz} \approx -0.03$ K m$^{-1}$;[142] i.e. the temperature increases along the reservoir depth. Segregation is induced due to both gravity and thermal diffusion, described by combining equations (9-18), and (9-25)

$$-\frac{x_i}{RT}\frac{d\mu_i}{dz}-\frac{1}{c_t RT}\left(c_i\overline{V}_i-\omega_i\right)\frac{dp}{dz}=\sum_{\substack{j=1\\ j\neq i}}^{n}\frac{x_i x_j(u_i^T-u_j^T)}{Đ_{ij}};\qquad i=1,2,\ldots n \tag{9-27}$$

Inserting equation (9-26) into equation (9-27), we obtain after re-arranging

$$-\frac{x_i}{RT}\frac{d\mu_i}{dz}-\frac{1}{c_t RT}\left(c_i\overline{V}_i-\omega_i\right)\frac{dp}{dz}-\sum_{\substack{j=1\\ j\neq i}}^{n}\frac{x_i x_j}{Đ_{ij}}\left(\frac{D_i^T}{\rho_i}-\frac{D_j^T}{\rho_j}\right)\frac{1}{T}\frac{dT}{dz}=\sum_{\substack{j=1\\ j\neq i}}^{n}\frac{x_i x_j\left(u_i-u_j\right)}{Đ_{ij}};\qquad i=1,2,\ldots n \tag{9-28}$$

The terms $\frac{D_i^T}{\rho_i}$ have the units of m$^2$ s$^{-1}$. The thermal diffusion coefficients are not all independent; we have the constraint

$$\sum_{j=1}^{n} D_i^T = 0 \tag{9-29}$$

For the special case of a binary mixture, we write

$$-\frac{x_1}{RT}\frac{d\mu_1}{dz}-\frac{1}{c_t RT}\left(c_1\overline{V}_1-\omega_1\right)\frac{dp}{dz}-\frac{x_1x_2}{Đ_{12}}\left(\frac{D_1^T}{\rho_1}-\frac{D_2^T}{\rho_2}\right)\frac{1}{T}\frac{dT}{dz}=\frac{x_1x_2\left(u_1-u_2\right)}{Đ_{12}} \tag{9-30}$$

Introducing the constraint $D_1^T=-D_2^T$, we obtain

$$-\frac{x_1}{RT}\frac{d\mu_1}{dz}-\frac{1}{c_t RT}\left(c_1\overline{V}_1-\omega_1\right)\frac{dp}{dz}-\frac{x_1x_2D_1^T}{Đ_{12}}\left(\frac{\rho_t}{\rho_1\rho_2}\right)\frac{1}{T}\frac{dT}{dz}=\frac{x_1x_2\left(u_1-u_2\right)}{Đ_{12}} \tag{9-31}$$

Introducing the diffusion fluxes $J_1=c_t x_1\left(u_1-u\right)=-J_2=-c_t x_2\left(u_2-u\right)$, we derive

**M-S formulation with generalized driving force**

$$-\frac{x_1}{RT}\frac{d\mu_1}{dz}-\frac{1}{c_tRT}\left(c_1\overline{V_1}-\omega_1\right)\frac{dp}{dz}-\frac{x_1x_2D_1^T}{Đ_{12}}\left(\frac{\rho_t}{\rho_1\rho_2}\right)\frac{1}{T}\frac{dT}{dz}=\frac{J_1}{c_tĐ_{12}}$$
$$-\frac{x_1}{RT}\frac{d\mu_1}{dz}-\frac{1}{c_tRT}\left(c_1\overline{V_1}-\omega_1\right)\frac{dp}{dz}-\frac{x_1x_2D_1^T}{\rho_t\omega_1\omega_2Đ_{12}}\frac{1}{T}\frac{dT}{dz}=\frac{J_1}{c_tĐ_{12}} \quad (9\text{-}32)$$

Define the dimensionless thermal diffusion ratio

$$k_{T1}=\frac{x_1x_2D_1^T}{Đ_{12}}\left(\frac{\rho_t}{\rho_1\rho_2}\right)=\frac{D_1^T}{\rho_tĐ_{12}}\left(\frac{x_1x_2}{\omega_1\omega_2}\right) \quad (9\text{-}33)$$

Other quantities encountered are the thermal diffusion factor $\alpha_T$

$$\alpha_{T1}=\frac{k_{T1}}{x_1x_2}=\frac{D_1^T}{\rho_tĐ_{12}}\left(\frac{1}{\omega_1\omega_2}\right)=\frac{D_1^T}{Đ_{12}}\left(\frac{\rho_t}{\rho_1\rho_2}\right) \quad (9\text{-}34)$$

The Soret coefficient is defined as

$$S_{T1}=\frac{k_{T1}}{x_1x_2T}=\frac{D_1^T}{\rho_tĐ_{12}T}\left(\frac{1}{\omega_1\omega_2}\right)=\frac{D_1^T}{Đ_{12}T}\left(\frac{\rho_t}{\rho_1\rho_2}\right) \quad (9\text{-}35)$$

Equation (9-32) reduces to yield

$$-d_1=-\frac{x_1}{RT}\frac{d\mu_1}{dz}-\frac{1}{c_tRT}\left(c_1\overline{V_1}-\omega_1\right)\frac{dp}{dz}-k_{T1}\frac{1}{T}\frac{dT}{dz}=\frac{J_1}{c_tĐ_{12}} \quad (9\text{-}36)$$

For segregation due to both gravity and thermal diffusion, the flux expression is

$$J_1=-c_tĐ_{12}\left(\frac{x_1}{RT}\frac{d\mu_1}{dz}-\frac{1}{c_tRT}\left(c_1\overline{V_1}-\omega_1\right)\rho g+k_{T1}\frac{1}{T}\frac{dT}{dz}\right) \quad (9\text{-}37)$$

Setting the fluxes equal to zero, the steady-state the steady-state mole fraction profiles are described by

$$\frac{x_1}{RT}\frac{d\mu_1}{dz}=\frac{1}{c_tRT}\left(c_1\overline{V_1}-\omega_1\right)\rho g-k_{T1}\frac{1}{T}\frac{dT}{dz} \quad (9\text{-}38)$$

Introducing the thermodynamic correction factor $\Gamma\equiv\left(1+\frac{\partial\ln\phi_1}{\partial\ln x_1}\right)$ we write the steady-state mole fraction profile as

**M-S formulation with generalized driving force**

$$\Gamma \frac{dx_1}{dz} = \left(\rho_t \overline{V_1} - M_1\right)\frac{x_1 g}{RT} - k_{T1}\frac{1}{T}\frac{dT}{dz} \tag{9-39}$$

When $D_1^T > 0;\quad S_{T1} > 0;\quad k_{T1} > 0;\quad \frac{dx_1}{dT} < 0$; this implies that the component 1 segregates towards the cold end; in this scenario, thermal diffusion serves to enhance the gravitational segregation effect. Conversely, when $D_1^T < 0;\quad S_{T1} < 0;\quad k_{T1} < 0;\quad \frac{dx_1}{dT} > 0$, the component 1 segregates towards the hot end; in this scenario, thermal diffusion acts in a direction opposite to the gravitational segregation. +

In the absence of pressure gradients, equation (9-32) simplifies to

$$J_1 = -c_t Đ_{12}\frac{x_1}{RT}\frac{d\mu_1}{dz} - c_t \frac{x_1 x_2 D_1^T}{\rho_t \omega_1 \omega_2}\frac{1}{T}\frac{dT}{dz} \tag{9-40}$$

In view of the inter-relations in Table 9-1, and introducing the Fick diffusivity $D_{12} = Đ_{12}\Gamma \equiv Đ_{12}\left(1 + \frac{\partial \ln \gamma_1}{\partial \ln x_1}\right)$, we get

$$\begin{aligned} J_1 &= -c_t Đ_{12}\frac{x_1}{RT}\frac{d\mu_1}{dz} - D_1^T \frac{\overline{M}}{M_1 M_2}\frac{1}{T}\frac{dT}{dz} \\ J_1 &= -c_t D_{12}\frac{dx_1}{dz} - D_1^T \frac{\overline{M}}{M_1 M_2}\frac{1}{T}\frac{dT}{dz} \\ \frac{M_1 M_2}{\overline{M}} J_1 &= j_1 = -\rho_t D_{12}\frac{d\omega_1}{dz} - D_1^T \frac{1}{T}\frac{dT}{dz} \end{aligned} \tag{9-41}$$

## 9.4 List of Tables for M-S formulation with generalized driving force

Table 9-1. Inter-relationships between molar fluxes and mass fluxes

| Molar fluxes | Mass fluxes |
|---|---|
| $J_1 = c_t x_1 (u_1 - u); u = x_1 u_1 + x_2 u_2$<br>$J_1 = c_t x_1 (u_1 - x_1 u_1 - x_2 u_2) = c_t x_1 x_2 (u_1 - u_2)$<br>$x_1 = \frac{\omega_1}{M_1}\overline{M}; x_2 = \frac{\omega_2}{M_2}\overline{M}; c_t = \frac{\rho_t}{\overline{M}}$<br>$J_1 = c_t x_1 x_2 (u_1 - u_2)$<br>$J_1 = \rho_t \omega_1 \omega_2 \frac{\overline{M}}{M_1 M_2}(u_1 - u_2) = \frac{\overline{M}}{M_1 M_2} j_1$ | $j_1 = \rho_t \omega_1 (u_1 - v); v = \omega_1 u_1 + \omega_2 u_2$<br>$j_1 = \rho_t \omega_1 (u_1 - \omega_1 u_1 - \omega_2 u_2) = \rho_t \omega_1 \omega_2 (u_1 - u_2)$<br>$\omega_i = \frac{\rho_i}{\rho_t} = \frac{x_i M_i}{\sum_{i=1}^{n} x_i M_i} = \frac{x_i M_i}{\overline{M}}; \rho_t = c_t \overline{M}$<br>$j_1 = \rho_t \omega_1 \omega_2 (u_1 - u_2) = c_t x_1 x_2 (u_1 - u_2)$<br>$j_1 = c_t x_1 x_2 \frac{M_1 M_2}{\overline{M}}(u_1 - u_2) = \frac{M_1 M_2}{\overline{M}} J_1$ |
| $dx_1 = \frac{\frac{1}{\overline{M_1 M_2}}}{\left(\frac{\omega_1}{M_1} + \frac{\omega_2}{M_2}\right)^2} d\omega_1; \quad d\omega_1 = \frac{M_1 M_2}{(x_1 M_1 + x_2 M_2)^2} dx_1$<br>$\frac{1}{\overline{M}} = \frac{\omega_1}{M_1} + \frac{\omega_2}{M_2}; \overline{M} = x_1 M_1 + x_2 M_2$<br>$dx_1 = \frac{\overline{M}^2}{M_1 M_2} d\omega_1; \quad d\omega_1 = \frac{M_1 M_2}{\overline{M}^2} dx_1$<br>$\frac{c_t}{\rho_t}\frac{x_1 x_2}{\omega_1 \omega_2} = \frac{\overline{M}}{M_1 M_2}$ | |
| $J_1 = -c_t D_{12} \frac{dx_1}{dz};$<br>$dx_1 = \frac{\overline{M}^2}{M_1 M_2} d\omega_1; c_t = \frac{\rho_t}{\overline{M}}$<br>$J_1 = -\rho_t D_{12} \frac{\overline{M}}{M_1 M_2}\frac{d\omega_1}{dz}$<br>$\frac{M_1 M_2}{\overline{M}} J_1 = -\rho_t D_{12} \frac{d\omega_1}{dz} = j_1$ | $j_1 = -\rho_t D_{12} \frac{d\omega_1}{dz}$<br>$d\omega_1 = \frac{M_1 M_2}{\overline{M}^2} dx_1; \rho_t = c_t \overline{M}$<br>$j_1 = -c_t D_{12} \frac{M_1 M_2}{\overline{M}}\frac{dx_1}{dz}$<br>$\frac{\overline{M}}{M_1 M_2} j_1 = -c_t D_{12} \frac{dx_1}{dz} = J_1$ |

## 9.5 List of Figures for M-S formulation with generalized driving force

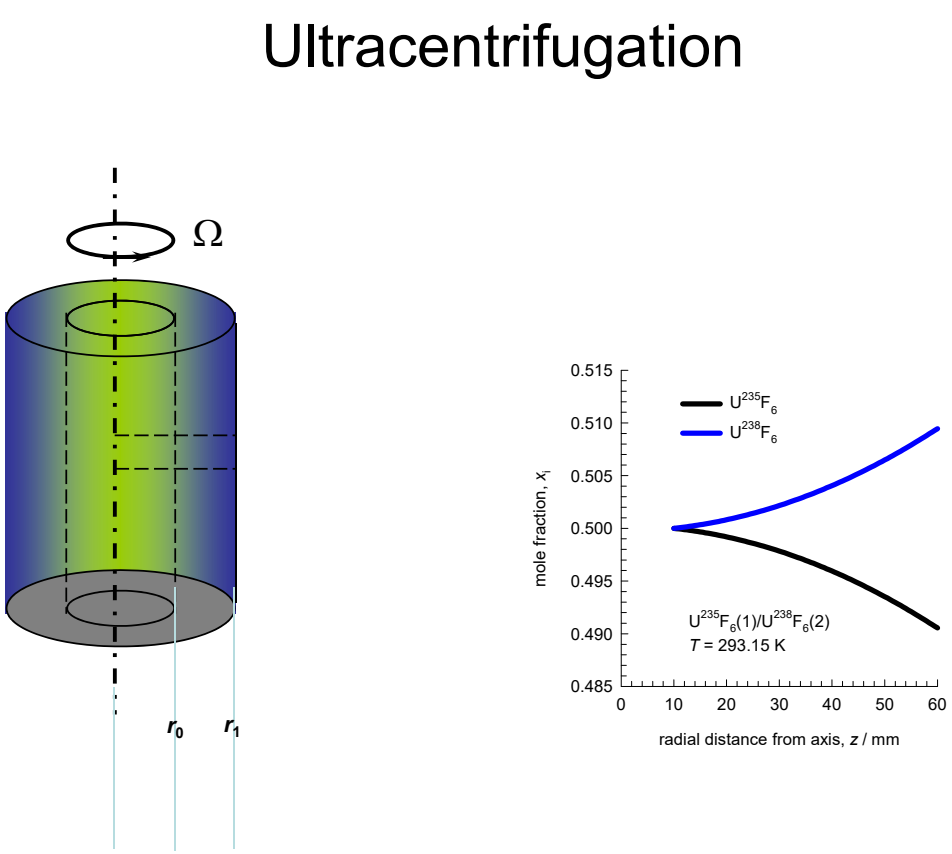


Figure 9-1. Separation of gaseous uranium isotopes $U^{235}F_6(1)/U^{238}F_6(2)$ by ultracentrifugation as described in Example 2.3.2 of Taylor and Krishna.[1]

# 10 Diffusion of Ionic Species

## 10.1 The Maxwell-Stefan diffusion formulation for ionic diffusion

For diffusion in *n*-component fluid mixtures consisting of neutral, uncharged species, the Maxwell-Stefan (M-S) equations[73, 99] are normally written as

$$-\frac{1}{RT}\frac{d\mu_i}{dz}=\sum_{\substack{j=1\\ j\neq i}}^{n}\frac{x_j\left(u_i-u_j\right)}{Đ_{ij}};\quad i=1,2,\ldots n \tag{10-1}$$

In equation (10-1), $u_i$ is the velocity of species *i* in a laboratory fixed reference frame, and $Đ_{ij}$ is the diffusivity of *i-j* pair in the *n*-component mixture. The M-S formulation is essentially a friction formulation, and $Đ_{ij}$ is to be interpreted as the inverse drag coefficient for the *i-j* pair. The Onsager reciprocal relations demand the symmetry constraint

$$Đ_{ij}=Đ_{ji};\quad i=1,2,\ldots n \tag{10-2}$$

We may also define the diffusion fluxes in the laboratory-fixed reference frame

$$N_i=c_iu_i;\quad i=1,2,\ldots n \tag{10-3}$$

where $c_i$ is the molar concentration of species *i*. The total molar concentration of the mixture, $c_t$, is also the inverse of the mean molar volume

$$c_t=\sum_{i=1}^{n}c_i=\frac{1}{\bar{V}} \tag{10-4}$$

A wide variety of processes of importance in the process industries involve the transport of ionic species in bulk electrolyte liquid mixtures, within charged particles, and across charged membranes. Examples include electrolysis, electrodialysis, ion exchange, and fuel cells.[50, 64, 137, 143-145] For design and development of such processes, it is essential to have adequate models to describe the transport fluxes.

**Diffusion of Ionic Species**

For transport of ionic species in electrolyte solutions, we need to consider as an additional driving force, expressed in Joules per mole of mixture, caused by the electrostatic potential gradient

$$F_i = -z_i \mathrm{F} \frac{d\Phi}{dz} \tag{10-5}$$

where $z_i$ is the ionic charge of species $i$ and F is the Faraday constant. Except in regions close to electrode surfaces, where there will be charge separation (the double layer phenomena), the condition of electro-neutrality is met

$$\sum_{i=1}^{n} c_i z_i = 0; \quad \text{electroneutrality constraint} \tag{10-6}$$

and therefore

$$\sum_{k-1}^{n} c_k F_k = \left( \sum_{k=1}^{n} c_k z_k \right) \mathrm{F} \frac{d\Phi}{\partial z} = 0 \tag{10-7}$$

Adding the contribution of the electrostatic potential gradients to the left member of equation (10-1) yields

$$-\frac{1}{RT} \frac{d\mu_i}{dz} - z_i \frac{\mathrm{F}}{RT} \frac{d\Phi}{dz} = \sum_{\substack{j=1 \\ j \neq i}}^{n} \frac{x_j \left( u_i - u_j \right)}{Đ_{ij}}; \quad i = 1, 2, \ldots n \tag{10-8}$$

It is convenient to define a generalized driving force

$$d_i \equiv \frac{x_i}{RT} \frac{d\mu_i}{dz} + x_i z_i \frac{\mathrm{F}}{RT} \frac{d\Phi}{dz} \tag{10-9}$$

The second law of thermodynamics demands that the rate of entropy production be positive definite[9]

$$\sigma = \frac{1}{2} c_t R \sum_{i=1}^{n} \sum_{j=1}^{n} \frac{x_i x_j \left| \left( u_i - u_j \right) \right|^2}{Đ_{ij}} \geq 0 \tag{10-10}$$

The division by 2 is required because of the application of the Onsager symmetry constraint in equation (10-2). The second law constraint does not require each of the pair M-S diffusivities to be positive definite. Indeed, Kraaijeveld and Wesselingh[146] experimental evidence to suggest that cation-cation diffusivities could assume negative values without violation of the second law of thermodynamics. For

molten salt mixtures LiF-$BeF_2$, the MD simulation data of Chakraborty[147] show negative values of the ion pair diffusivities, without violation of the second law constraint described by equation (10-10).

In terms of the fluxes, $N_i = c_i u_i$, we may re-write equation (10-8) as

$$-\frac{x_i}{RT}\frac{d\mu_i}{dz} - x_i z_i \frac{\mathrm{F}}{RT}\frac{d\Phi}{dz} = \sum_{\substack{j=1 \\ j\neq i}}^{n} \frac{x_j N_i - x_i N_j}{c_t Đ_{ij}}; \quad i = 1,2,\ldots n \tag{10-11}$$

The total current carried by the electrolyte is $\mathrm{F}\sum_{i=1}^{n} z_i N_i$. In many chemical process applications such as ion exchange, no external electrical field is imposed on the system, and also there is no flow of current, i.e.

$$\sum_{i=1}^{n} z_i N_i = \sum_{i=1}^{n} c_i z_i u_i = 0; \quad \text{no current prescription} \tag{10-12}$$

For electrolyte concentrations smaller than about 0.01 mol $L^{-1}$, the cation-anion friction is less than 20% of the ion - water friction and the following simplified equation holds for ionic species *i*

$$N_i = -Đ_i \frac{c_i}{RT}\frac{d\mu_i}{dz} - c_i z_i Đ_i \frac{\mathrm{F}}{RT}\frac{d\Phi}{dz} + c_i u_n; \quad i = 1,2,\ldots n-1 \tag{10-13}$$

where the $Đ_i$ in equation (10-13) are the ionic diffusivities. The three contributions to the molar flux of ionic species *i* are usually termed “diffusion”, “migration” and “convection”.

If we define the diffusion fluxes $J_i$ with respect to the solvent, species *n*:

$$J_i = c_i(u_i - u_n) = N_i - c_i u_n = -Đ_i \frac{c_i}{RT}\frac{d\mu_i}{dz} - c_i z_i Đ_i \frac{\mathrm{F}}{RT}\frac{d\Phi}{dz}; \quad i = 1,2,\ldots n-1 \tag{10-14}$$

The no-current constraint also applies to the diffusion fluxes $J_i$:

$$\sum_{i=1}^{n} z_i J_i = \sum_{i=1}^{n} c_i z_i u_i - \left(\sum_{i=1}^{n} c_i z_i\right) u_n = 0; \quad \text{no current prescription} \tag{10-15}$$

For aqueous electrolyte solutions, the n*th* component is usually taken to be water, that is often considered to be stagnant, i.e.

$$u_n = 0; \quad N_n = 0; \quad \text{stagnant solvent water prescription} \tag{10-16}$$

## 10.2 Diffusivity of binary electrolytes in concentrated solutions

Let us consider a binary electrolyte solution, containing cation (C), and anion (A) with charges, $z_C$, and $z_A$, respectively, and stoichiometric coefficients $\nu_C$, and $\nu_A$. The sum of the stoichiometric coefficients, $\nu = \nu_C + \nu_A$. The species 3 is water (solvent). Let us assume that the solvent is stagnant, i.e. $u_3$=0. Let the molar concentration of the binary electrolyte ("salt") be denoted as $c_s$, mol $L^{-1}$; this is also termed the *molarity*. The ionic concentrations of C and A are $c_C = \nu_C c_s = \nu_C c_t x_3; \quad c_A = \nu_A c_s = \nu_A c_t x_3$. Here $c_t$ is the total molar concentration of the mixture, $c_t = c_C + c_A + c_3$. Thermodynamic non-ideality effects are most commonly described using molalities, $m_C$, and $m_A$ expressed in terms of moles per kg of solvent (water). The ionic strength is $I = \frac{1}{2}\left(z_C^2 m_C + z_A^2 m_A\right)$.

The chemical potential of the electrolyte is

$$\mu_s = \nu_C \mu_C^m + \nu_A \mu_A^m + RT \ln\left(m_C^{\nu C} m_A^{\nu A} (\gamma_C)^{\nu C} (\gamma_A)^{\nu A}\right) \tag{10-17}$$

The $\mu_C^m$, and $\mu_A^m$ are chemical potentials of the cation and anion in the standard state; the superscript *m* serves as a reminder that this standard state is defined in terms of the ion *molalities*. A mean molality and a mean molal activity coefficient are defined. Both are given the subscript ± to indicate that this is an average (geometric mean) of the value for the cation and the anion. The mean molality is defined as $m_\pm = \left(m_C^{\nu C} m_A^{\nu A}\right)^{1/\nu}$. The mean molal activity coefficient is defined in a similar way $\gamma_\pm = \left((\gamma_C)^{\nu C} (\gamma_A)^{\nu A}\right)^{1/\nu}$. If the standard state chemical potential of the salt in solution is written as $\mu_S^m = \nu_C \mu_C^m + \nu_A \mu_A^m$, can re-write equation (10-17) as

$$\mu_s = \mu_s^m + RT \ln\left((m_\pm)^\nu (\gamma_\pm)^\nu\right) = \mu_s^m + \nu RT \ln\left((m_\pm)(\gamma_\pm)\right) \tag{10-18}$$

Figure 10-1(a) shows the experimental data of Moggia and Bianco[148] on the mean activity coefficient $\gamma_\pm$ of aqueous solutions of neutral electrolyte NaCl at 298.15 K. The deep valley in the molal activity coefficient at a mean molality $m_\pm \approx 1$ mol $kg^{-1}$ is particularly noteworthy. The dashed line represents

the calculations of the mean activity coefficient using the Pitzer-Mayorga[149] activity coefficient model. The Pitzer model is of good accuracy for the range of molalities considered.

Figure 10-1(b) shows the experimental data of Ananthaswamy and Atkinson[150] on the mean activity coefficient $\gamma_{\pm}$ of aqueous solutions of neutral electrolyte $CaCl_2$ at 298.15 K. Also for this electrolyte, the deep valley in the molal activity coefficient at a mean molality ≈ 1 mol kg$^{-1}$ is observed. The dashed line represents the calculations of the mean activity coefficient using the Pitzer-Mayorga[149] activity coefficient model. The Pitzer model is of good accuracy for the range of molalities considered. The Pitzer model is of good accuracy for molalities $m_{\pm} < 2$ mol kg$^{-1}$.

For both $NaCl/H_2O$ and $CaCl_2/H_2O$, calculations of the mean activity coefficient using the Deby-Hückel limiting law $\ln(\gamma_{\pm}) = -|z_C z_A| A\sqrt{I}$, where $A$ = 1.1717 kg$^{1/2}$ mol$^{-1/2}$ and the ionic strength $I = \frac{1}{2}\left(z_C^2 m_C + z_A^2 m_A\right)$ are only applicable for molalities $m_{\pm} < 0.01$ mol kg$^{-1}$; see comparisons with the Pitzer-Mayorga[149] activity coefficient model in Figure 10-1(a,b).

Let us define the Fick diffusivity of the binary electrolyte by the flux relation

$$N_s = -D\frac{dm_{\pm}}{dz} \tag{10-19}$$

The Maxwell-Stefan diffusivity of the electrolyte, *Đ*, is defined by

$$N_s = -Đ\left(\frac{m_{\pm}}{RT}\frac{d\mu_s}{dz}\right) = -Đ\left(1+\frac{\partial\ln(\gamma_{\pm})}{\partial\ln(m_{\pm})}\right)\frac{dm_{\pm}}{dz} = -Đ\Gamma\frac{dm_{\pm}}{dz} \tag{10-20}$$

The thermodynamic factor, Γ, accounts for non-ideal solution thermodynamics , The Fick diffusivity is related to the M-S diffusivity by

$$D = Đ\Gamma = Đ\left(1+\frac{\partial\ln(\gamma_{\pm})}{\partial\ln(m_{\pm})}\right) \tag{10-21}$$

At vanishingly small molalities, the Fick diffusivity of the electrolyte can be calculated on the basis of the individual ionic diffusivities and the species charge numbers

$$D = Đ = \frac{Đ_1 Đ_2 (z_1 - z_2)}{z_1 Đ_1 - z_2 Đ_2} \tag{10-22}$$

Figure 10-2(a,b) show the calculations of Rard and Miller[151] for the thermodynamic correction factor Γ for aqueous solutions of (a) NaCl, and (b) $CaCl_2$ at 298.15 K. In both cases, the thermodynamic correction factor Γ displays a minimum at a mean molality in the range $0.1 < m_{\pm} < 0.2$ mol kg$^{-1}$. For $CaCl_2$ we also note a maximum in the Γ factor at $m_{\pm} \approx 5.5$ mol kg$^{-1}$.

From equation (10-21), we anticipate that the Fick diffusivity will be influenced by the thermodynamic correction factor Γ. Figure 10-3(a) shows the experimental data of Rard and Miller,[151] and Chang and Myerson[152] for Fick diffusivity $D$ of aqueous solutions of neutral electrolyte NaCl at 298.15 K. Due to the influence of Γ, the Fick diffusivity shows both a minimum and a maximum. At saturation conditions, corresponding to $m_{\pm} \approx 6.2$ mol kg$^{-1}$, we have $\Gamma = Đ\left(1 + \frac{\partial \ln(\gamma_{\pm})}{\partial \ln(m_{\pm})}\right) \to 0$; consequently, the Fick diffusivity also tends to vanish at this spinodal composition; further discussions on this are provided in the paper by Chang and Myerson.[152]

Entirely analogous characteristics of the Fick diffusivity are also observed in the experimental data of Rard and Miller,[151] for aqueous solutions of neutral electrolyte $CaCl_2$ at 298.15 K; see Figure 10-3(b). The sharp reduction in the Fick diffusivity of the salts at concentrations approaching saturation, as witnessed in Figure 10-3 are of crucial importance in crystal growth.

## 10.3 Thermodynamic influences on the kinetics of crystal growth

By definition, crystallization processes operate under conditions close to supersaturation. Non-ideal thermodynamics will have a strong influence on diffusion fluxes and the kinetics of crystal growth. It is common practice to use chemical potential differences between the supersaturated solution (the transferring state) and the crystal (the transferred state), $\sigma = \Delta\mu / RT = \nu \ln\left(a_{\pm} / a_{\pm}^{*}\right)$, as the driving force to model crystal growth kinetics;[153, 154] here $\nu$ is the total number of mole of ions per mole of electrolyte.

As illustration, Figure 10-4(a,b,c) present calculations of thermodynamic non-idealities for Potassium Dihydrogen Phosphate (KDP)/Urea/$H_2O$ system at 303.15 K, using the parameters provided by Enqvist et al.;[155] the molality of urea is maintained constant at 5 mol $kg^{-1}$; the saturation molality of KDP in the solution, $m^*$ = 1.70 mol $kg^{-1}$. Figure 10-4(a) are calculations of the mean activity coefficient $\gamma_{\pm}$ of KDP. Figure 10-4(b) are calculations of the thermodynamic correction factor $\Gamma = \left(1 + \frac{\partial \ln(\gamma_{\pm})}{\partial \ln(m_{\pm})}\right)$. At the spinodal concentration, $m$ = 5.35 mol $kg^{-1}$, we have $\Gamma = 0$. Figure 10-4(c) presents calculations of the activity based supersaturation, $\sigma = \Delta\mu / RT = \nu \ln\left(a_{\pm} / a_{\pm}^{*}\right)$.

Figure 10-4(d) presents the experimental data of Enqvist et al.[155] on growth rate of KDP crystals, at the **[1 0 1]** face and expressed in units of nm $s^{-1}$, as a function of the supersaturation, $\sigma = \Delta\mu / RT = \nu \ln\left(a_{\pm} / a_{\pm}^{*}\right)$. As a good approximation, the growth rate is proportional to the activity based degree of supersaturation.

The process of purification by crystallization is important in the process industries. Using the data on activity coefficients provided in the paper by Louhi-Kultanen et al.,[153] we analyze thermodynamic non-idealities in $Na_2SO_4(1)/K_2SO_4(2)/H_2O(3)$ mixtures under conditions relevant to crystallization purification processes; the calculations of the activity coefficients are based on the model described in the papers of Pitzer and Mayorga,[149] and Pitzer and Kim.[156] Towards this end, we calculate the 2-dimensional matrix of thermodynamic factors, $[\Gamma]$, defined by

$$\Gamma_{ij} = \frac{m_i}{RT}\frac{\partial \mu_i}{\partial m_j} = \frac{m_i}{m_j}\frac{\partial \ln\left(\gamma_{\pm,i} m_i\right)}{\partial \ln m_j} = \delta_{ij} + \frac{m_i}{m_j}\frac{\partial \ln\left(\gamma_{\pm,i}\right)}{\partial \ln m_j}; \quad i, j = 1,2 \tag{10-23}$$

The input data for the calculation of the activity coefficients $\gamma_{\pm,1}, \gamma_{\pm,2}$ of the neutral electrolytes $Na_2SO_4(1)$, and $K_2SO_4(2)$, respectively, are provided in the paper by Louhi-Kultanen et al;[153] see equations (22) – (32), along with Table 1 of their paper.

Figure 10-5(a) presents calculations of the elements of the the 2-dimensional matrix of thermodynamic factors, $[\Gamma]$, $Na_2SO_4(1)/K_2SO_4(2)/H_2O(3)$ mixtures at 298.15 K. The $x$-axis in the

graph represents the total mixture molality, $m_t = m_1 + m_2$; in these calculations, the ratio of the molalities, $m_1/m_2$, of $Na_2SO_4(1)$ and $K_2SO_4(2)$ is held constant at the value of 0.25. The off-diagonal elements cannot be ignored, as is evidenced by the ratios of the elements $\frac{\Gamma_{12}}{\Gamma_{11}}$ and $\frac{\Gamma_{21}}{\Gamma_{22}}$, plotted in Figure 10-5(b). We note that at a total mixture molality, $m_t$ = 1 mol kg$^{-1}$, the ratio $\frac{\Gamma_{21}}{\Gamma_{22}} \approx 0.5$, indicating the diffusion fluxes will be strongly coupled.

Let us calculate $[\Gamma]$ for a set of conditions specified in Table 4 of Louhi-Kultanen et al.[153]

The molalities of neutral electrolytes $Na_2SO_4(1)$ and $K_2SO_4(2)$ in the bulk solution are $m_{10} = 0.201; \quad m_{20} = 0.632$ mol kg$^{-1}$.

The molalities of neutral electrolytes $Na_2SO_4(1)$ and $K_2SO_4(2)$ at the crystal surface are $m_{1\delta} = 0.202; \quad m_{2\delta} = 0.752$ mol kg$^{-1}$.

At the arithmetic average molalities, the matrix of thermodynamic factors is calculated as follows

$$[\Gamma] = \begin{bmatrix} 0.905 & -0.097 \\ -0.333 & 0.706 \end{bmatrix}$$

The influence of thermodynamic coupling on the diffusion fluxes will be discussed in a later section.

## 10.4 Diffusion in dilute electrolyte solutions

For dilute aqueous solutions of electrolytes, $m_{\pm}$ < 0.01 mol kg$^{-1}$, the thermodynamic correction factors are approximately unity, so $\frac{m_{\pm}}{RT}\frac{d\mu_s}{dz} \approx \frac{dm_{\pm}}{dz}$; $\frac{c_s}{RT}\frac{d\mu_s}{dz} \approx \frac{dc_s}{dz}$ for the electrolyte. For each individual ionic species, $n$-1 in number, also, we may approximate $\frac{c_i}{RT}\frac{d\mu_i}{dz} \approx \frac{dc_i}{dz}$. With these assumptions and simplifications, equation (10-13) reduces to the Nernst-Planck equation for the flux of individual ionic species

$$N_i = -Đ_i \frac{dc_i}{dz} - c_i z_i Đ_i \frac{\mathrm{F}}{RT}\frac{d\Phi}{dz}; \quad i = 1,2,\ldots n-1 \tag{10-24}$$

Combining equations (10-12), and (10-24) we obtain the following expression for the diffusion potential that is engendered due to ionic diffusion

$$\frac{d\Phi}{dz} = -\frac{\sum_{k=1}^{n-1} z_k Đ_k \frac{dc_k}{dz}}{\frac{\mathrm{F}}{RT}\sum_{j=1}^{n-1} c_j z_j^2 Đ_j} \tag{10-25}$$

Inserting equation (10-25) for the diffusion potential into equation (10-24) we obtain the following flux expressions for the $n$-1 ionic species (recall that species $n$ is water)

$$N_i = -Đ_i \frac{dc_i}{dz} + \frac{c_i z_i Đ_i}{\sum_{j=1}^{n-1} c_j z_j^2 Đ_j} \sum_{k=1}^{n-1} z_k Đ_k \frac{dc_k}{dz}; \quad i = 1,2,\ldots n-1 \tag{10-26}$$

The requirement of electro-neutrality places a constraint on the ionic concentration gradients

$$\sum_{i=1}^{n-1} z_i \frac{dc_i}{dz} = 0; \quad \text{electroneutrality constraint} \tag{10-27}$$

This means that the $(n\text{-}1)th$ concentration gradient can be eliminated

$$\sum_{i=1}^{n-2} z_i \frac{dc_i}{dz} = -z_{n-1} \frac{dc_{n-1}}{dz}; \quad \text{electroneutrality constraint} \tag{10-28}$$

The expression for the diffusion potential engendered due to ionic diffusion can be written in terms of the ($n$-2) independent concentration gradients

$$\frac{d\Phi}{dz} = -\frac{\sum_{k=1}^{n-2} z_k Đ_k \frac{dc_k}{dz} + z_{n-1} Đ_{n-1} \frac{dc_{n-1}}{dz}}{\frac{\mathrm{F}}{RT}\sum_{j=1}^{n-1} c_j z_j^2 Đ_j} = -\frac{\sum_{k=1}^{n-2} z_k \left(Đ_k - Đ_{n-1}\right)\frac{dc_k}{dz}}{\frac{\mathrm{F}}{RT}\sum_{j=1}^{n-1} c_j z_j^2 Đ_j} \tag{10-29}$$

Inserting equation (10-29) for the diffusion potential into equation (10-24) we obtain the following expression for the ionic fluxes

$$N_i = -Đ_i \frac{dc_i}{dz} + \frac{c_i z_i Đ_i}{\sum_{j=1}^{n-1} c_j z_j^2 Đ_j} \sum_{k=1}^{n-2} z_k \left(Đ_k - Đ_{n-1}\right)\frac{dc_k}{dz}; \quad i = 1,2,\ldots n-2 \tag{10-30}$$

Equation (10-30) can be conveniently cast into ($n$-2) dimensional matrix notation

$$(N) = -[D]\frac{d(c)}{dz} \tag{10-31}$$

The elements of the ($n$-2)×($n$-2) dimensional square matrix of Fick diffusivities are

$$D_{ik} = Đ_i\delta_{ik} - \frac{c_i z_i z_k Đ_i (Đ_k - Đ_{n-1})}{\sum_{j=1}^{n-1} c_j z_j^2 Đ_j}; \quad i,k = 1,2,\ldots n-2 \tag{10-32}$$

where $\delta_{ik}$ is the Kronecker delta. In the ensuing discussions equation (10-32) will also be considered to be a manifestation of the Nernst-Planck equations. The second member of the right of equation (10-32) quantifies the electrostatic "leash" that serves to enhance, or diminish, the ionic mobilities. Whether an ion is accelerated or decelerated depends on the species charges, $z_i$, and whether we have co-diffusion or counter-diffusion. The elements of the Fick diffusivity matrix [$D$] are strongly concentration dependent; the off-diagonal elements are non-zero, i.e. *ionic diffusion is always coupled even for dilute solutions*.

More generally, if the solvent (water) is not stagnant, we define the matrix of Fick diffusivities as follows

$$(J) = -[D]\frac{d(c)}{dz} \tag{10-33}$$

where we define the diffusion fluxes $J_i$ of each individual ionic species with respect to the solvent, species $n$ as $J_i = c_i(u_i - u_n) = N_i - c_i u_n$. If the $n$th component (water, say) is stagnant, then we have $u_n = 0; \quad J_i = N_i$.

The ionic concentrations $c_i$ are relatable to the concentrations $C_i$ of neutral electrolytes. Let $\nu_{ik}$ represent the number of moles of ionic species $i$ per mole of neutral electrolyte $k$. The gradients of the ionic concentrations are related to the gradients of the concentrations of the netural electrolytes by $\frac{dc_i}{dz} = \sum_{k=1}^{ne} \nu_{ik}\frac{dC_k}{dz}$, where $ne$ is the number of neutral electrolytes. In matrix notation we have $\frac{d(c)}{dz} = [\nu]\frac{d(C)}{dz}$, where $[\nu]$ is not a square matrix, in general. Therefore the ionic fluxes can be related to the gradients of the concentrations of neutral electrolytes by

$$(N) = -[D][\nu]\frac{d(C)}{dz} \tag{10-34}$$

## 10.5 Re-analysis of Vinograd-McBain experiments

Consider the experimental results of Vinograd and McBain[157] in a two-compartment diffusion cell, shown schematically in Figure 10-6. Diffusion takes place through the pores of a sintered glass disk that separate the two compartments. Each of the two compartments is well-mixed, and the concentration gradients are restricted to disk thickness, $\delta$. The bottom compartment contains pure water while the top compartment contains a mixture of aqueous solutions of HCl and $BaCl_2$. Let $c_{HCl}$ and $c_{BaCl2}$ denote the molar concentrations, expressed in mol $L^{-1}$ of solution. Total ionization takes place and the system is a quaternary mixture: 1 = $H^+$, 2 = $Cl^-$, 3 = $Ba^{++}$, 4 = $H_2O$. The concentrations of ions are: $c_{H+} = c_{HCl}$; $c_{Ba++} = c_{BaCl2}$; $c_{Cl-} = (c_{HCl} + 2\, c_{BaCl2})$. In one set of experiments reported by Vinograd and McBain,[157] the ratio of the concentrations $c_{HCl}/c_{BaCl2}$ was varied. By monitoring the concentrations of the three ionic species as a function of time, Vinograd and McBain[157] obtained the effective ionic diffusivities $D_{i,eff}$ for $H^+$, $Cl^-$ and $Ba^{2+}$. The experimentally observed ionic diffusivities are shown in Figure 10-6 as function of the square root of the ratio of the initial ionic concentrations of $H^+$ and $Ba^{2+}$ in the top compartment $\sqrt{c_{HCl}/c_{BaCl2}} = \sqrt{c_{H+}/c_{Ba++}}$. With increasing values of $\sqrt{c_{H+}/c_{Ba++}}$, it is observed that both $D_{H+}$ and $D_{Ba++}$ decrease while $D_{Cl-}$ increases. At the start of the diffusion process, the highly mobile $H^+$ diffuses ahead of its companion ions into the pure water compartment, creating an excess of positive charge. This induces a diffusion potential $\partial\Phi/\partial z$ which acts in such a way as to comply with the no-current and electro-neutrality prescriptions. The consequence is that the $Cl^-$ experiences an extra electrostatic "pull", enhancing its effective diffusivity value. The electrical potential gradient also serves to retard the motion of the positive ions $H^+$ and $Ba^{++}$ or in other words these ions experience a "push" in a direction opposite to that dictated by their composition gradient driving forces. For $\sqrt{c_{H+}/c_{Ba++}}$ =2, the

electrostatic "push" on $Ba^{++}$ is such as to result in a vanishing value for $D_{Ba2+}$. The continuous solid lines in Figure 10-6 are the calculations of the effective ionic diffusivities

$$D_{i,eff} = \frac{N_i}{-\frac{dc_i}{dz}}; \quad i = 1,2,..n-1 \tag{10-35}$$

wherein the fluxes are determined from Equation (10-30).The values of the effective diffusivities $D_{i,eff}$ for $H^+$, $Cl^-$ and $Ba^{++}$ can be determined by approximating the concentration gradients $-\frac{dc_i}{dz} = \frac{c_{i0} - c_{i\delta}}{\delta}; \quad i = 1,2,..n-1$. The concentrations $c_{i0}$ correspond to those in the top well-stirred compartment: $c_{10} = c_{HCl}; \quad c_{20} = c_{HCl} + 2c_{BaCl2}; \quad c_{30} = c_{BaCl2}$. In the bottom compartment, we have pure water; all the ionic concentrations are zero $c_{i\delta} = 0$.We use the ionic diffusivities provided in Example 2.4.2 of Taylor and Krishna:[1]

$$Đ_1 = 9.3\times10^{-9}; \quad Đ_2 = 2\times10^{-9}; \quad Đ_3 = 0.85\times10^{-9} \text{ m}^2 \text{ s}^{-1}.$$

The continuous solid lines in Figure 10-6 are the calculations of the effective ionic diffusivities using equations (10-31), (10-32), and (10-35). The elements of the matrix [*D*] are determined at the *average* concentration in the top and bottom compartments; this allows explicit evaluation of the fluxes and the effective ionic diffusivities. The essential diffusion characteristics for the $HCl/BaCl_2/H_2O$ mixture are properly captured by the linearized analytic solution to the Nernst-Planck equation.

The Nernst-Planck model calculations anticipate negative values of $D_{Ba2+}$ for $\sqrt{c_{H+}/c_{Ba2+}} > 2$ due to a strong electrostatic "push"; see Figure 10-6. Negative effective diffusivities signal the possibility of uphill diffusion for $Ba^{2+}$.

Figure 10-7 compares the experimental data of Vinograd and McBain[157] for effective ionic diffusivities of $H^+$, $K^+$, and $Cl^-$ in a two-compartment diffusion cell with the calculations using equations (10-31), (10-32), and (10-35). We use the ionic diffusivities[1] (1 = $H^+$, 2 = $Cl^-$, 3 = $K^+$)

$$Đ_1 = 9.3\times10^{-9}; \quad Đ_2 = 2\times10^{-9}; \quad Đ_3 = 2\times10^{-9} \text{ m}^2 \text{ s}^{-1}.$$

In this case, the $Cl^-$ is accelerated, while both cations $H^+$, and $K^+$ are retarded due to the electrostatic leash. The essential diffusion characteristics for the HCl/KCl/$H_2O$ mixture are properly captured by the linearized analytic solution to the Nernst-Planck equation.

## 10.6 Effective ionic diffusivities in HCl/$CaCl_2$/$H_2O$ system

In Figure 7 of their paper, Nakagaki and Kitagawa[158] have reported experimental data for effective ionic diffusivities of $H^+$, $Ca^{++}$, and $Cl^-$ in HCl/$CaCl_2$/$H_2O$ aqueous solutions. The experimental data are presented as function of the ratio $\frac{z_{Ca++}c_{Ca++}}{z_{H+}c_{H+}+z_{Ca++}c_{Ca++}}$ under conditions that the total cation concentration is constant in the diffusion layer; see. Their experimental data (indicated by symbols) has been replotted in Figure 10-8. Due to the electro-neutrality restraint $\sum_{i=1}^{n} c_i z_i = 0$, $z_{Cl-}c_{Cl-} = -\left(z_{H+}c_{H+}+z_{Ca++}c_{Ca++}\right)$. With increasing values of $\frac{z_{Ca++}c_{Ca++}}{z_{H+}c_{H+}+z_{Ca++}c_{Ca++}}$, it is observed that both $D_{\text{eff,H+}}$ and $D_{\text{eff,Ca++}}$ increase while $D_{\text{eff,Cl-}}$ decreases. The continuous solid lines in Figure 10-8 are the calculations of the effective diffusivities using $D_{i,eff} = \frac{N_i}{-\frac{dc_i}{dz}}$ wherein the fluxes are determined from equations (10-31), (10-32). The values of the effective ionic diffusivities $D_{\text{i,eff}}$ for $H^+$, $Cl^-$ and $Ca^{++}$ can be determined explicitly from equations (10-31), (10-32), and (10-35) by approximating the concentration gradients $-\frac{dc_i}{dz} \approx \frac{c_i}{\delta}$; $i = 1,2,..n-1$. The Nernst-Planck equations are able to capture, almost quantitatively, the variation of the effective ionic diffusivities as a function of $\frac{z_{Ca++}c_{Ca++}}{z_{H+}c_{H+}+z_{Ca++}c_{Ca++}}$. A particularly noteworthy feature of the Nernst-Planck equations is that the predicted effective diffusivities of $Ca^{++}$ approaches negative values for $\frac{z_{Ca++}c_{Ca++}}{z_{H+}c_{H+}+z_{Ca++}c_{Ca++}} < 0.4$. We now examine experimental data of Nakagaki and Kitagawa[158] that demonstrates the possibility of uphill diffusion.

## 10.7 Uphill diffusion and transient overshoots during inter-diffusion of mixed ions

Nakagaki and Kitagawa[158] have conducted transient inter-diffusion experiments in HCl(1)/$CaCl_2$(2)/$H_2O$ aqueous solutions in a diaphragm cell with two well-stirred compartments. The top and bottom comparments are initially filled with two distinctly different concentrations of the two electrolytes, HCl(1)/$CaCl_2$(2). The results of three experimental campaigns are reported; these are termed Examples 1, 2 and 3; see Table 3 of Nakagaki and Kitagawa;[158] the initial concentrations in the top and bottom compartments are specified in the schematics in Figure 10-9.

On the basis of the transient equilibration of ionic concentrations, Nakagaki and Kitagawa[158] have determined the effective ionic diffusivities of $H^+$, $Ca^{++}$, and $Cl^-$. Remarkably, the effective diffusivities, $D_{i,eff}$, as defined by equation (10-35), of $H^+$, $Ca^{++}$, and $Cl^-$ are negative for, respectively, Examples 2, 1, and 3; see Figure 10-9. Negative effective ionic diffusivities are indicative of uphill ionic transport, engendered by the electro-static "leash".

Our objective here is to model the transient inter-diffusion of $H^+$, $Ca^{++}$, and $Cl^-$ in the three sets of experiments to examine the origin and consequences of negative effective ionic diffusivities $D_{i,eff}$.

Let us consider first the transient equilibration in Example 1 in Figure 10-9. Initially, the top compartment contains HCl(1) and $CaCl_2$(2) with concentrations of 0.1488 mol $L^{-1}$ and 0.0263 mol $L^{-1}$, respectively. The initial concentrations of HCl(1) and $CaCl_2$(2) in the bottom compartment are 0.0521 mol $L^{-1}$ and 0.0242 mol $L^{-1}$, respectively. Each of the electrolytes will undergo complete dissociation. The final equilibrated concentrations of the three ions $H^+$, $Ca^{++}$, and $Cl^-$ are: 0.10045 mol $L^{-1}$ and 0.02525 mol $L^{-1}$, and 0.15095 mol $L^{-1}$. Due to the electro-neutrality restraint $\sum_{i=1}^{n} c_i z_i = 0$, only two of the ionic concentrations in each compartment are independently variable; we take 1 = $H^+$, and 2 = $Ca^{++}$ as the independent species.

The transient equilibration process in the top and bottom compartments (with volumes $V$, and interfacial area $A$) is described in 2-dimensional matrix notation by

$V\frac{d\left(c_{top}\right)}{dt}=-V\frac{d\left(c_{bottom}\right)}{dt}=-\left(N\right)A=\begin{pmatrix}N_1\\N_2\end{pmatrix}A$. The molar fluxes $N_i$ are taken to be positive if directed from top to bottom. At any instant of time, $t$, we have $V\frac{d\left(c_{top}\right)}{dt}=-\left[D\right]\frac{\left(c_{top}-c_{eq}\right)}{\delta}A$ where $\delta$ is the effective thickness of the diffusion layer, and $\left[D\right]$ is the ($n$-2)×($n$-2) dimensional square matrix of Fick diffusivities, defined by equation (10-32). The driving forces for ionic transport are $\left(c_{top}-c_{eq}\right)=\begin{pmatrix}0.04835\\0.00105\end{pmatrix}$. We note that the driving force for transport of $Ca^{++}$ is significantly lower, by a factor of about 50, than the driving force for $H^+$ transport. We define a cell constant $\beta=\frac{A\delta}{V}$, and write $\frac{d\left(c_{top}\right)}{dt}=-\beta\left[D\right]\left(c_{top}-c_{eq}\right)$. The Fick diffusivity matrix $\left[D\right]$ is calculable using equation (10-32). If the diffusivity matrix is evaluated at the final equilibrated composition and considered constant, this matrix differential equation may be integrated to obtain $\left(c_{top}-c_{eq}\right)=\exp\left[-\beta\left[D\right]t\right]\left(c_{top,0}-c_{eq}\right)$ where the vector $\left(c_{eq}\right)=\frac{\left(c_{top,0}+c_{bottom,0}\right)}{2}=\begin{pmatrix}0.10045\\0.02525\end{pmatrix}$ mol $L^{-1}$. An analogous expression holds for the bottom compartment, $\left(c_{bottom}-c_{eq}\right)=\exp\left[-\beta\left[D\right]t\right]\left(c_{bottom,0}-c_{eq}\right)$. The square matrix $\left[Q\right]=\exp\left[-\beta\left[D\right]t\right]$ quantifies the transient departure from equilibrium. The Sylvester theorem, detailed in Appendix A of Taylor and Krishna,[1] is required for explicit determination of $\left[Q\right]=\exp\left[-\beta\left[D\right]t\right]$. For the case of two distinct eigenvalues, $\lambda_1$, and $\lambda_2$, of the 2-dimensional square matrix $\left[D\right]$, the Sylvester theorem yields $\exp\left[-\beta\left[D\right]t\right]=\left(\exp\left(-\beta\lambda_1 t\right)\right)\frac{\left[\left[D\right]-\lambda_2\left[I\right]\right]}{\left(\lambda_1-\lambda_2\right)}+\exp\left(-\beta\lambda_2 t\right)\frac{\left[\left[D\right]-\lambda_1\left[I\right]\right]}{\left(\lambda_2-\lambda_1\right)}$ where $\left[I\right]$ is the identity matrix with elements $\delta_{ik}$, the Kronecker delta.

The concentration trajectories in the top and bottom compartments during transient equilibration are presented in Figure 10-10(a,b). The diffusion equilibration of $H^+$, and $Cl^-$ proceeds in a "normal"

manner, i.e. the transport is from higher to lower concentration regions with exponential decay. The equilibration of $Ca^{++}$ ions is remarkable in that a concentration overshoot is experienced in the top compartment with a concomitant undershoot in the bottom compartment. Let us explain the concentration overshoot in physical terms. The more mobile $H^{+}$ rapidly diffuses into the bottom compartment; this creates an excess of positive charge. This excess of positive charge serves to prevent the influx of $Ca^{++}$ ions into the bottom compartment even though its concentration is higher in the top compartment. Indeed, the requirement of electro-neutrality causes the $Ca^{++}$ ions to traverse uphill from bottom to top compartment in the interests of maintaining electro-neutrality. Uphill transport of $Ca^{++}$ ions leads to transient overshoots in the early stages of equilibration. There is a corresponding undershoot in the concentration of $Ca^{++}$ ions in the bottom compartment. Figure 10-10(b) also shows the equilibration trajectories for $Ca^{++}$ that are calculated without the influence of the electrostatic leash, i.e. ignoring the contribution of the second term to the right of equation (10-32) and taking $D_{ik} = Đ_i \delta_{ik}$ for all three ionic species. Clearly, the phenomenon of uphill diffusion for $Ca^{++}$ is engendered by the electro-static leash.

The equilibration process follows serpentine trajectories in composition space; see Figure 10-10(c).

Next, we consider the transient equilibration in Example 2 portrayed in Figure 10-9 of Nakagaki and Kitagawa.[158] Initially, the top compartment contains HCl(1) and $CaCl_2$(2) with concentrations of 0.0972 mol $L^{-1}$ and 0.0525 mol $L^{-1}$, respectively. The initial concentrations of HCl(1) and $CaCl_2$(2) in the bottom compartment are 0.1033 mol $L^{-1}$ and 0.0 mol $L^{-1}$, respectively. Each of the electrolytes will undergo complete dissociation. The final equilibrated concentrations of the three ions $H^{+}$, $Ca^{++}$, and $Cl^{-}$ are: 0.10025 mol $L^{-1}$ and 0.02513 mol $L^{-1}$, and 0.1505 mol $L^{-1}$. The driving forces for ionic transport are $\left(c_{top} - c_{eq}\right) = \begin{pmatrix} -0.00305 \\ 0.02513 \end{pmatrix}$. We note that the driving force for transport of $Ca^{++}$ is significantly higher, by a factor of about 8, than the driving force for $H^{+}$ transport.

The transient concentration equilibration trajectories in the top and bottom compartments transient equilibration are presented in Figure 10-11(a,b). The diffusion equilibration of $Ca^{++}$, and $Cl^{-}$ proceeds

in a "normal" manner, i.e. the transport is from higher to lower concentration regions with exponential decay. The equilibration of $H^+$ ions is remarkable in that a concentration overshoot is experienced in the bottom compartment with a concomitant undershoot in the top compartment. Let us explain the concentration overshoot in physical terms. Due to its large driving force, $Ca^+$ gets transported quickly into the bottom compartment where it creates an excess positive charge (recall that its charge number $z_2$ = + 2 is twice as high as for $H^+$). This excess positive charge causes the efflux of $H^+$ from the bottom compartment to be slowed down considerably. Figure 10-11(b) also shows the equilibration trajectories for $H^+$ that are calculated without the influence of the electrostatic leash, i.e. ignoring the contribution of the second term to the right of equation (10-32) and taking $D_{ik} = Đ_i \delta_{ik}$ for all three ionic species. It is evident that the phenomenon of uphill diffusion for $H^+$ is engendered by the electro-static leash. The influence of the electrostatic leash slow down the transfer of $H^+$ from the bottom compartment, causing an overshoot in the concentration. There is a concomitant undershoot in the concentration of $H^+$ ions in the top compartment.

The equilibration process follows serpentine trajectories in composition space; see in Figure 10-11(c). Next, we consider the transient equilibration in Example 3 in Figure 10-9 of Nakagaki and Kitagawa.[158] Initially, the top compartment contains HCl(1) and $CaCl_2$(2) with concentrations of 0.0878 mol $L^{-1}$ and 0.0327 mol $L^{-1}$, respectively. The initial concentrations of HCl(1) and $CaCl_2$(2) in the bottom compartment are 0.1116 mol $L^{-1}$ and 0.01765 mol $L^{-1}$, respectively. Each of the electrolytes will undergo complete dissociation. The final equilibrated concentrations of the three ions $H^+$, $Ca^{++}$, and $Cl^-$ are: 0.0997 mol $L^{-1}$ and 0.02517 mol $L^{-1}$, and 0.15005 mol $L^{-1}$. The driving forces for ionic transport are, respectively, $\begin{pmatrix} c_{1,top} - c_{1,eq} \\ c_{2,top} - c_{2,eq} \end{pmatrix} = \begin{pmatrix} -0.0119 \\ 0.007525 \end{pmatrix}$; $c_{3,top} - c_{3,eq} = 0.00315$ mol $L^{-1}$. We note that the driving force for transport of $Cl^-$ is significantly lower in magnitude than the other two driving forces. Also noteworthy is that the driving force of $H^+$ is opposite in sign to the driving forces of $Ca^{++}$ and $Cl^-$.

The transient concentration equilibration trajectories in the top and bottom compartments transient equilibration are presented in Figure 10-12(a,b). The diffusion equilibration of $H^+$ and $Ca^{++}$ proceeds in

a "normal" manner, i.e. the transport is from higher to lower concentration regions with exponential decay. The equilibration of $Cl^-$ ions is remarkable in that a concentration overshoot is experienced in the top compartment with a concomitant undershoot in the bottom compartment. Let us explain the concentration overshoot in physical terms. Due to its high mobility, $H^+$ gets transported quickly into the top compartment where it creates an excess positive charge. This excess positive charge causes the transfer of $Cl^-$ from the top compartment to be retarded down considerably, causing an overshoot in the $Cl^-$ concentration in the top compartment. Figure 10-12(b) also shows the equilibration trajectories for $Cl^-$ that are calculated without the influence of the electrostatic leash, i.e. ignoring the contribution of the second term to the right of equation (10-32) and taking $D_{ik} = Đ_i \delta_{ik}$ for all three ionic species. It is interesting to note that even ignoring the electrostatic leash leads to overshoots and undershoots; these over/undershoots are caused by the electro-neutrality restraint $\sum_{i=1}^{n} c_i z_i = 0$.

The equilibration process follows serpentine trajectories in composition space; see Figure 10-12(c).

## 10.8 Fick diffusivity matrix for $NaCl/Na_2SO_4/H_2O$ solutions

Rard et al.[159] report experimental data for elements of the Fick diffusivity matrix, $\begin{bmatrix} D_{11} & D_{12} \\ D_{21} & D_{22} \end{bmatrix}$, for the mixture of aqueous electrolytes NaCl (1), and $Na_2SO_4$ (2) at 298.15 K. The reported data are not for ionic diffusivities but for the neutral electrolytes NaCl (1), and $Na_2SO_4$ (2) respectively. The matrix [*D*] is defined in the *solvent-fixed reference frame*; see equation (10-33):

$$\begin{pmatrix} J_{NaCl} \\ J_{Na2SO4} \end{pmatrix} = -\begin{bmatrix} D_{11} & D_{12} \\ D_{21} & D_{22} \end{bmatrix} \begin{pmatrix} \frac{dc_{NaCl}}{dz} \\ \frac{dc_{Na2SO4}}{dz} \end{pmatrix} = -[D][\nu] \begin{pmatrix} \frac{dc_{NaCl}}{dz} \\ \frac{dc_{Na2SO4}}{dz} \end{pmatrix} \tag{10-36}$$

Clearly, if the water is considered to be stagnant, then we have $u_n = 0; \quad J_i = N_i$. For one set of conditions, the four elements of the Fick matrix $\begin{bmatrix} D_{11} & D_{12} \\ D_{21} & D_{22} \end{bmatrix}$, in the solvent fixed reference frame, are

shown in Figure 10-13(a); the plotted data are for the total molar concentration of the mixture $c_{\mathrm{NaCl}} + c_{\mathrm{Na2SO4}} = 0.5$ mol $\mathrm{L}^{-1}$. The $x$-axis represents the fraction $c_{NaCl}/\left(c_{NaCl}+c_{Na2SO4}\right)$ in the mixture of mixed electrolytes. We use $c_{\mathrm{NaCl}}$, and $c_{\mathrm{Na2SO4}}$ to denote the concentrations of *neutral electrolytes*. Let us examine the applicability of the Nernst-Planck equations for *ionic species* for estimation of the Fick matrix $\begin{bmatrix} D_{11} & D_{12} \\ D_{21} & D_{22} \end{bmatrix}$ for the two *neutral electrolytes* NaCl (1), and $Na_2SO_4$ (2).

Towards this end, we number the ionic species in equation (10-32) as follows:

1=$Cl^-$; 2=$SO_4^{--}$; 3=$Na^+$; $z_1$= -1, $z_2$= -2, $z_3$= 1. The ionic diffusivities are

$\mathcal{D}_1 = 2\times10^{-9}; \mathcal{D}_2 = 0.6\times10^{-9}; \mathcal{D}_3 = 1.3\times10^{-9}$ $\mathrm{m}^2\ \mathrm{s}^{-1}$.

The ionic concentrations $c_i$ can be related to the concentrations of the neutral electrolytes $c_{\mathrm{NaCl}}$, and $c_{\mathrm{Na2SO4}}$

$c_1 = c_{NaCl}; c_2 = c_{Na2SO4}; c_3 = c_{NaCl} + 2c_{Na2SO4}$. The two independent ionic concentrations are

$$\begin{pmatrix} c_1 \\ c_2 \end{pmatrix} = [\nu]\begin{pmatrix} c_{NaCl} \\ c_{Na2SO4} \end{pmatrix} = \begin{bmatrix} 1 & 0 \\ 0 & 1 \end{bmatrix}\begin{pmatrix} c_{NaCl} \\ c_{Na2SO4} \end{pmatrix}$$

The fluxes of the neutral electrolytes are relatable to the ionic fluxes as follows

$J_{NaCl} = J_{Cl} = J_1; \quad J_{Na2SO4} = J_{SO4} = J_2$

The Fick diffusivity matrix $\begin{bmatrix} D_{11} & D_{12} \\ D_{21} & D_{22} \end{bmatrix}$ for neutral electrolytes, defined by equation (10-36) is therefore $\begin{bmatrix} D_{11} & D_{12} \\ D_{21} & D_{22} \end{bmatrix} = [D][\nu] = [D]\begin{bmatrix} 1 & 0 \\ 0 & 1 \end{bmatrix}$ where the elements of the 2×2 matrix $[D]$ is determined from equation (10-32). The estimated values are shown by the continuous solid lines in Figure 10-13(b).

At $c_{NaCl}/\left(c_{NaCl}+c_{Na2SO4}\right)$ = 1, $D_{11}$ = the Fick diffusivity of the neutral electrolyte NaCl, $D_{11} = \dfrac{\mathcal{D}_3\mathcal{D}_1(z_3 - z_1)}{z_3\mathcal{D}_3 - z_1\mathcal{D}_1} = 1.576\times10^{-9}$ $\mathrm{m}^2\ \mathrm{s}^{-1}$. Also, at this composition, the non-diagonal element, $D_{21}$= 0.

At $c_{NaCl}/\left(c_{NaCl}+c_{Na2SO4}\right)$ = 0, $D_{22}$ = the Fick diffusivity of the neutral electrolyte $Na_2SO_4$, $D_{11}=\dfrac{\mathcal{D}_3\mathcal{D}_2\left(z_3-z_2\right)}{z_3\mathcal{D}_3-z_2\mathcal{D}_2}=0.936\times10^{-9}$ m$^2$ s$^{-1}$. Also, at this composition, the non-diagonal element, $D_{12}$= 0.

The Nernst-Plank equations are able to capture all the essential characteristics of the composition dependence of the Fick diffusivity matrix $\begin{bmatrix} D_{11} & D_{12} \\ D_{21} & D_{22} \end{bmatrix}$ for neutral electrolytes. For quantitative agreement with the experimental data, we need to take account of the influence of the thermodynamic non-idealities; further details are provided by Rard et al.[159]

## 10.9 Fick diffusivity matrix for $CaCl_2$/HCl/$H_2O$ solutions

Figure 10-14(a) shows the experimental data (symbols) of Leaist and Curtis[160] for the elements of the Fick diffusivity matrix $\begin{bmatrix} D_{11} & D_{12} \\ D_{21} & D_{22} \end{bmatrix}$ for the mixture of aqueous electrolytes $CaCl_2$ (1), and HCl (2) at 298.15 K. The total molar concentration of the mixture $c_{CaCl2}+c_{HCl}$ = 0.1 mol L$^{-1}$. The *x*-axis represents the fraction $c_{CaCl2}/\left(c_{CaCl2}+c_{HCl}\right)$.

The continuous solid lines in Figure 10-14(a) are the estimations using the Nernst-Planck equation (10-32). In these calculations, we number the ionic species in equation (10-32) as follows:

1=$Ca^{++}$; 2=$H^+$; 3=$Cl^-$; $z_1$= 2, $z_2$= 1, $z_3$= -1. The ionic diffusivities are $\mathcal{D}_1=0.792\times10^{-9};\mathcal{D}_2=9.315\times10^{-9};\mathcal{D}_3=2.0333\times10^{-9}$ m$^2$ s$^{-1}$.

The ionic concentrations $c_i$ can be related to the concentrations of the neutral electrolytes $c_{CaCl2}$, and $c_{HCl}$:

$$c_1=c_{CaCl2};c_2=c_{HCl};c_3=2c_{CaCl2}+c_{HCl}$$

The fluxes of the neutral electrolytes are relatable to the ionic fluxes as follows (if water is considered to be stagnant, then we have $u_n=0;\quad J_i=N_i$).

$$N_{CaCl2}=N_{Ca}=N_1;\quad N_{HCl}=N_H=N_2$$

At $c_{CaCl2}/\left(c_{CaCl2}+c_{HCl}\right)$ = 1, $D_{11}$ = the Fick diffusivity of the neutral electrolyte $CaCl_2$, $D_{11}=\dfrac{\mathcal{D}_3\mathcal{D}_1\left(z_3-z_1\right)}{z_3\mathcal{D}_3-z_1\mathcal{D}_1}=1.335\times10^{-9}$ m$^2$ s$^{-1}$. Also, at this composition, the non-diagonal element, $D_{21}$= 0.

At $c_{CaCl2}/\left(c_{CaCl2}+c_{HCl}\right)$ = 0, $D_{22}$ = the Fick diffusivity of the neutral electrolyte HCl, $D_{11}=\dfrac{\mathcal{D}_3\mathcal{D}_2\left(z_3-z_2\right)}{z_3\mathcal{D}_3-z_2\mathcal{D}_2}=3.338\times10^{-9}$ m$^2$ s$^{-1}$. Also, at this composition, the non-diagonal element, $D_{12}$= 0.

The Nernst-Plank equations (10-32) are able to capture all the essential characteristics of the composition dependence of the Fick diffusivity matrix $\begin{bmatrix} D_{11} & D_{12} \\ D_{21} & D_{22} \end{bmatrix}$ for neutral electrolytes.. For quantitative agreement with the experimental data, we need to take account of the influence of the thermodynamic non-idealities; see further discussions in Leaist and Curtis.[160]

In order to appreciate the influence of the electrostatic "leash", Figure 10-14(b) presents calculations of the contribution of the second term in the right member of equations (10-32) to each of the elements of [$D$]. The influence of the electrostatic leash is most severe on the "more mobile" HCl; this is evidenced by the large contribution of the electrostatic leash to $D_{22}$.

## 10.10 Fick diffusivity matrix for $K_2SO_4$/KOH/$H_2O$ solutions

Figure 10-15(a) shows the experimental data (symbols) of Leaist and Curtis[160] for the elements of the Fick diffusivity matrix $\begin{bmatrix} D_{11} & D_{12} \\ D_{21} & D_{22} \end{bmatrix}$ for the mixture of aqueous electrolytes $K_2SO_4$ (1), and KOH (2) at 298.15 K. The total molar concentration of the mixture $c_{K2SO4}+c_{KOH}$ = 0.1 mol L$^{-1}$. The $x$-axis represents the fraction $c_{K2SO4}/\left(c_{K2SO4}+c_{KOH}\right)$.

The continuous solid lines in Figure 10-15(a) are the estimations using the Nernst-Planck equations (10-32). In these calculations, we number the ionic species in equations (10-32) as follows: 1=$SO_4^{--}$; 2=$OH^-$; 3=$K^+$; $z_1$= -2, $z_2$= -1, $z_3$= 1. The ionic diffusivities are $\mathcal{D}_1=1.0652\times10^{-9};\mathcal{D}_2=5.281\times10^{-9};\mathcal{D}_3=1.9573\times10^{-9}$ m$^2$ s$^{-1}$.

The ionic concentrations $c_i$ can be related to the concentrations of the neutral electrolytes $c_{K2SO4}$, and $c_{KOH}$: $c_1 = c_{K2SO4}; c_2 = c_{KOH}; c_3 = 2c_{K2SO4} + c_{KOH}$ .

The fluxes of the neutral electrolytes are relatable to the ionic fluxes as follows (if water is considered to be stagnant, then we have $u_n = 0; \quad J_i = N_i$): $N_{K2SO4} = N_{SO4} = N_1; \quad N_{KOH} = N_{OH} = N_2$ .

At $c_{K2SO4}/(c_{K2SO4} + c_{KOH})$ = 1, $D_{11}$ = the Fick diffusivity of the neutral electrolyte $K_2SO_4$, $D_{11} = \dfrac{Đ_3 Đ_1 (z_3 - z_1)}{z_3 Đ_3 - z_1 Đ_1} = 1.53 \times 10^{-9}$ m$^2$ s$^{-1}$. Also, at this composition, the non-diagonal element, $D_{21}$= 0.

At $c_{K2SO4}/(c_{K2SO4} + c_{KOH})$= 0, $D_{22}$ = the Fick diffusivity of the neutral electrolyte KOH, $D_{22} = \dfrac{Đ_3 Đ_2 (z_3 - z_2)}{z_3 Đ_3 - z_2 Đ_2} = 2.856 \times 10^{-9}$ m$^2$ s$^{-1}$. Also, at this composition, the non-diagonal element, $D_{12}$= 0.

The Nernst-Plank equations (10-32) are able to capture all the essential characteristics of the composition dependence of the Fick diffusivity matrix. For quantitative agreement with the experimental data, we need to take account of the influence of the thermodynamic non-idealities; see further discussions in Leaist and Curtis.[160]

In order to appreciate the influence of the electrostatic "leash", Figure 10-15(a) presents calculations of the contribution of the second term in the right member of equations to each of the elements of [$D$]. The influence of the electrostatic leash is most severe on the "more mobile" KOH; this is evidenced by the large contribution of the electrostatic leash to $D_{22}$.

## 10.11 Fick diffusivity matrix for $Li_2SO_4$/LiOH/$H_2O$ solutions

Figure 10-16(a) shows the experimental data (symbols) of Leaist and Curtis[160] for the elements of the Fick diffusivity matrix $\begin{bmatrix} D_{11} & D_{12} \\ D_{21} & D_{22} \end{bmatrix}$ for the mixture of aqueous electrolytes $Li_2SO_4$ (1), and LiOH (2) at 298.15 K. The total molar concentration of the mixture $c_{Li2SO4} + c_{LiOH}$ = 0.1 mol L$^{-1}$. The $x$-axis represents the fraction $c_{Li2SO4}/(c_{Li2SO4} + c_{LiOH})$.

The continuous solid lines in Figure 10-16(a) are the estimations using the Nernst-Planck equations (10-32). In these calculations, we number the ionic species in equations (10-32) as follows: 1=$SO_4^{--}$; 2=$OH^-$; 3=$Li^+$; $z_1$= -2, $z_2$= -1, $z_3$= 1. The ionic diffusivities are $Đ_1 = 1.0652\times10^{-9}; Đ_2 = 5.281\times10^{-9}; Đ_3 = 1.03\times10^{-9}$ $m^2$ $s^{-1}$. The ionic concentrations $c_i$ can be related to the concentrations of the neutral electrolytes $c_{Li2SO4}$, and $c_{LiOH}$: $c_1 = c_{Li2SO4}; c_2 = c_{LiOH}; c_3 = 2c_{Li2SO4} + c_{LiOH}$.

The fluxes of the neutral electrolytes are relatable to the ionic fluxes as follows (if water is considered to be stagnant, then we have $u_n = 0; \quad J_i = N_i$): $N_{Li2SO4} = N_{SO4} = N_1; \quad N_{LiOH} = N_{OH} = N_2$

At $c_{Li2SO4}/(c_{Li2SO4} + c_{LiOH})$ = 1, $D_{11}$ = the Fick diffusivity of the neutral electrolyte $Li_2SO_4$, $D_{11} = \dfrac{Đ_3 Đ_1 (z_3 - z_1)}{z_3 Đ_3 - z_1 Đ_1} = 1.04\times10^{-9}$ $m^2$ $s^{-1}$. Also, at this composition, the non-diagonal element, $D_{21}$= 0.

At $c_{Li2SO4}/(c_{Li2SO4} + c_{LiOH})$= 0, $D_{22}$ = the Fick diffusivity of the neutral electrolyte LiOH, $D_{22} = \dfrac{Đ_3 Đ_2 (z_3 - z_2)}{z_3 Đ_3 - z_2 Đ_2} = 1.724\times10^{-9}$ $m^2$ $s^{-1}$. Also, at this composition, the non-diagonal element, $D_{12}$= 0.

The Nernst-Plank equations (10-32) are able to capture all the essential characteristics of the composition dependence of the Fick diffusivity matrix $\begin{bmatrix} D_{11} & D_{12} \\ D_{21} & D_{22} \end{bmatrix}$ for neutral electrolytes. For quantitative agreement with the experimental data, we need to take account of the influence of the thermodynamic non-idealities; see further discussions in Leaist and Curtis.[160]

In order to appreciate the influence of the electrostatic "leash", Figure 10-16(b) presents calculations of the contribution of the second term in the right member of (10-32) to each of the elements of [$D$]. The influence of the electrostatic leash is most severe on the "more mobile" LiOH; this is evidenced by the large contribution of the electrostatic leash to $D_{22}$.

## 10.12 Fick diffusivity matrix for NaCl/$MgCl_2$/$H_2O$ solutions

Figure 10-17 shows the experimental data (symbols) of Leaist and Al-Dhaher[161] for the elements of the Fick diffusivity matrix $\begin{bmatrix} D_{11}^V & D_{12}^V \\ D_{21}^V & D_{22}^V \end{bmatrix}_i$ for the mixture of aqueous electrolytes NaCl (1), and $MgCl_2$ (2) at 298.15 K. The experimental data are for the *volume averaged reference velocity* frame $u^V = \sum_{i=1}^{2} c_i \overline{V}_i u_i$ where $\overline{V_i}$ is the partial molar volume of species *i* in the mixture. The $\phi_i = c_i \overline{V_i}$ represent the volume fractions. The *x*-axis in Figure 10-17 represents the square root of the total mixture concentration $\sqrt{c_{NaCl} + c_{MgCl2}}$.

We number the ionic species in equations (10-32) as follows: 1=$Na^+$; 2=$Mg^{++}$; 3=$Cl^-$; $z_1$= 1, $z_2$= 2, $z_3$= -1. The ionic diffusivities are $Đ_1 = 1.334\times10^{-9}; Đ_2 = 0.7063\times10^{-9}; Đ_3 = 2.033\times10^{-9}$ $m^2$ $s^{-1}$. The ionic concentrations $c_i$ can be related to the concentrations of the neutral electrolytes $c_{NaCl}$ and $c_{MgCl2}$: $c_1 = c_{NaCl}; c_2 = c_{MgCl2}; c_3 = 2c_{MgCl2} + c_{NaCl}$.

The fluxes of the neutral electrolytes are relatable to the ionic fluxes as follows (if water is considered to be stagnant, then we have $u_n = 0; \quad J_i = N_i$): $N_{NaCl} = N_{Na} = N_1; \quad N_{MgCl2} = N_{Mg} = N_2$.

The expression for the Fick diffusivity matrix $\begin{bmatrix} D_{11} & D_{12} \\ D_{21} & D_{22} \end{bmatrix} = [D][\nu]$, used in conjunction with the Nernst-Planck equations (10-32) for $[D]$, yield diffusivities in the solvent (water = component 3) fixed reference velocity frame $\begin{bmatrix} D_{11} & D_{12} \\ D_{21} & D_{22} \end{bmatrix}_i$. To convert the Fick diffusivities to the volume-averaged reference velocity frame $\begin{bmatrix} D_{11}^V & D_{12}^V \\ D_{21}^V & D_{22}^V \end{bmatrix}_i$ we use the transformation (see the formulas in the Appendix to the paper by Rard et al.[159])

$$\begin{bmatrix} D_{11}^V & D_{12}^V \\ D_{21}^V & D_{22}^V \end{bmatrix} = \begin{bmatrix} 1-c_1\overline{V_1} & -c_1\overline{V_2} \\ -c_2\overline{V_1} & 1-c_2\overline{V_2} \end{bmatrix} \begin{bmatrix} D_{11} & D_{12} \\ D_{21} & D_{22} \end{bmatrix}$$

$$\begin{bmatrix} D_{11} & D_{12} \\ D_{21} & D_{22} \end{bmatrix} = \begin{bmatrix} 1+\dfrac{c_1\overline{V_1}}{c_3\overline{V_3}} & \dfrac{c_1\overline{V_2}}{c_3\overline{V_3}} \\ \dfrac{c_2\overline{V_1}}{c_3\overline{V_3}} & 1+\dfrac{c_2\overline{V_2}}{c_3\overline{V_3}} \end{bmatrix} \begin{bmatrix} D_{11}^V & D_{12}^V \\ D_{21}^V & D_{22}^V \end{bmatrix} \qquad (10\text{-}37)$$

$$\begin{bmatrix} 1-c_1\overline{V_1} & -c_1\overline{V_2} \\ -c_2\overline{V_1} & 1-c_2\overline{V_2} \end{bmatrix} \begin{bmatrix} 1+\dfrac{c_1\overline{V_1}}{c_3\overline{V_3}} & \dfrac{c_1\overline{V_2}}{c_3\overline{V_3}} \\ \dfrac{c_2\overline{V_1}}{c_3\overline{V_3}} & 1+\dfrac{c_2\overline{V_2}}{c_3\overline{V_3}} \end{bmatrix} = \begin{bmatrix} 1 & 0 \\ 0 & 1 \end{bmatrix}$$

where the partial molar volumes $\overline{V_i}$ are calculated using equations (16) of Leaist and Al-Dhaher.[161] The volume fraction of the solvent water (species 3) is calculated using $c_3\overline{V_3} = 1 - c_1\overline{V_1} - c_2\overline{V_2}$. The continuous solid lines in Figure 10-17 are the estimations, combining equations (10-32) and equation (10-37). We note that Nernst-Planck equations (10-32) of reasonably good accuracy for $\sqrt{c_{NaCl} + c_{MgCl2}} < 0.1 \quad (\text{mol/L})^{1/2}$. For higher electrolyte concentrations, there are significant deviations due to thermodynamic non-ideality effects. The paper by Leaist and Al-Dhaher[161] provide further discussions on the thermodynamic non-ideality effects that need to be included for better agreement with experimental data.

## 10.13 Fick diffusivity matrix for NaCl/$SrCl_2$/$H_2O$ solutions

Figure 10-18 shows the experimental data (symbols) of Leaist and Al-Dhaher[161] for the elements of the Fick diffusivity matrix [$D^v$] for the mixture of aqueous electrolytes NaCl (1), and $SrCl_2$ (2) at 298.15 K. The experimental data are for the *volume averaged reference velocity* frame $u^V = \sum_{i=1}^{2} c_i\overline{V_i}u_i$ where $\overline{V_i}$ is the partial molar volume of species *i* in the mixture. The $c_i\overline{V_i}$ represent the volume fractions. The *x*-axis represents the square root of the total mixture concentration $\sqrt{c_{NaCl} + c_{SrCl2}}$.

We number the ionic species as follows:1=$Na^+$; 2=$Sr^{++}$; 3=$Cl^-$; $z_1$= 1, $z_2$= 2, $z_3$= -1. The ionic diffusivities are $Đ_1 = 1.334\times10^{-9}; Đ_2 = 0.7915\times10^{-9}; Đ_3 = 2.033\times10^{-9}$ $m^2\ s^{-1}$.

The ionic concentrations $c_i$ can be related to the concentrations of the neutral electrolytes $c_{NaCl}$ and $c_{SrCl2}$: $c_1 = c_{NaCl}; c_2 = c_{SrCl2}; c_3 = 2c_{SrCl2} + c_{NaCl}$. The fluxes of the neutral electrolytes are relatable to the ionic fluxes: $N_{NaCl} = N_{Na} = N_1; \quad N_{SrCl2} = N_{Sr} = N_2$.

The expression for the Fick diffusivity matrix $\begin{bmatrix} D_{11} & D_{12} \\ D_{21} & D_{22} \end{bmatrix} = [D][\nu]$, used in conjunction with the Nernst-Planck equations (10-32) for $[D]$, yield diffusivities in the solvent (water = component 3) fixed reference velocity frame $\begin{bmatrix} D_{11} & D_{12} \\ D_{21} & D_{22} \end{bmatrix}_i$. To convert the Fick diffusivities to the volume-averaged reference velocity frame $\begin{bmatrix} D^V_{11} & D^V_{12} \\ D^V_{21} & D^V_{22} \end{bmatrix}_i$ we use the transformation equation (10-37). The continuous solid lines in Figure 10-18 are the estimations, combining equations (10-32) and (10-37).

The Nernst-Planck equations (10-32) are of reasonably good accuracy for $\sqrt{c_{NaCl} + c_{SrCl2}} < 0.1 \quad (\text{mol/L})^{1/2}$. For higher electrolyte concentrations, there are significant deviations due to thermodynamic non-ideality effects. The paper by Leaist and Al-Dhaher[161] provide further discussions on the thermodynamic non-ideality effects that need to be included for better agreement with experimental data.

## 10.14 Inter-diffusion without a common ion in aqueous solutions

Following Hao and Leaist,[162] we now consider inter-diffusion in mixed electrolytes systems without a common ion.

The following quotes from the paper by Hao and Leaist[162] provides a good summary of the discussions and calculations to follow.

*When a solution of electrolyte MX interdiffuses with a solution of electrolyte NY, the transport of four different ions (M, X, N, andY) is constrained only by eIectroneutrality. Because three degrees of freedom remain, the interdiffusion of two electrolytes without a common ion can produce an independent flow of a third electrolyte.*

**Diffusion of Ionic Species**

*At first glance the interdiffusion of electrolytes MX and NY is another two-electrolyte diffusion problem. But since ions M, X, N, and Y will in general have different mobilities and different diffusion speeds, ions M and X will not diffuse together as a single electrolyte component, nor will ions N and Y. Consequently, the interdiffusion of electrolytes MX and NY cannot be described in terms of fluxes of components MX and NY alone. Because fluxes of four different ions are constrained only by electroneutrality, three diffusional flows are independent. These considerations suggest that an accurate description of the interdiffusion of electrolytes MX and NY must include the flux of a third electrolyte component: MY or NX.*

For aqueous solutions of mixed electrolytes $NaCl/MgSO_4$, there are four different ionic species $Na^+$, $Cl^-$, $Mg^{2+}$, and $SO_4^{2-}$. Due to the electroneutrality $\sum_{i=1}^{n} c_i z_i = 0$ and no-current $\sum_{i=1}^{n} z_i N_i = \sum_{i=1}^{n} c_i z_i u_i = 0$ constraints there are three independent fluxes, three independent concentrations, and three independent concentration gradients. Inter-diffusion in aqueous solutions of mixed electrolytes $NaCl/MgSO_4$ engenders the flow of an additional neutral electrolyte $Na_2SO_4$, as evidenced in the experiments of Hao and Leaist.[162] The diffusion characteristics of the ternary electrolyte $NaCl(1)/Na_2SO_4(2)/MgSO_4(3)$ system is described a 3×3 dimensional Fick diffusivity matrix that is *linearly related* to the Fick diffusivity matrix for ionic diffusion (with elements given by equations (10-32)).

Figure 10-19(a) presents calculations of the elements of the 3×3 dimensional Fick diffusivity matrix for the ternary electrolyte $NaCl(1)/Na_2SO_4(2)/MgSO_4(3)$ system in the solvent (water) fixed reference frame. These elements can be compared with the experimental data presented in Figure 1 of Hao and Leaist.[162] Note, however, the experimental data in Figure 1 of Hao and Leaist[162] are for values in the volume-averaged reference velocity frame; consequently, the agreement of experimental data with Figure 10-19(a) is not perfect.

**Diffusion of Ionic Species**

Consider inter-diffusion of NaCl(1)/$Na_2SO_4$(2)/$MgSO_4$(3) mixtures between two compartments. The initial concentrations of the three neutral electrolytes in the left compartment is $(c_{L0}) = \begin{pmatrix} 0.1 \\ 0 \\ 0 \end{pmatrix}$ mol $L^{-1}$. The initial concentrations of the three neutral electrolytes in the right compartment is $(c_{R0}) = \begin{pmatrix} 0 \\ 0 \\ 0.1 \end{pmatrix}$ mol $L^{-1}$. Note that the concentration of $Na_2SO_4$(2) is zero in both compartments. The matrix of diffusivities [$D$] at the arithmentic average concentrations $\frac{(c_{L0})+(c_{R0})}{2} = \begin{pmatrix} 0.05 \\ 0 \\ 0.05 \end{pmatrix}$ mol $L^{-1}$ is calculated from the Nernst-Planck equations: $[D] = \begin{bmatrix} 1.897 & 0.105 & -0.14 \\ -0.237 & 1.247 & 0.116 \\ 0.094 & -0.073 & 0.803 \end{bmatrix} \times 10^{-9}$ $m^2$ $s^{-1}$. The transient development of concentrations of the ions in the Left and Right compartments (denoted by subscripts L and R) is described by the 3-dimensional matrix equation

$$(c(z,t)) = \frac{(c_{L0} + c_{R0})}{2} + erf\left[\frac{z}{\sqrt{4t}}[D]^{-1/2}\right]\frac{(c_{R0} - c_{L0})}{2} \tag{10-38}$$

The Sylvester theorem, detailed in Appendix A of Taylor and Krishna,[1] is required for explicit determination of the 3-dimensional square matrix $[Q] = erf\left[\frac{z}{\sqrt{4t}}[D]^{-1/2}\right]$. For the case of three distinct eigenvalues, $\lambda_1$, $\lambda_2$, and $\lambda_3$ of the 3×3 dimensional Fick diffusivity matrix $[D]$, the Sylvester theorem yields

$$[Q] = \frac{f(\lambda_1)[[D]-\lambda_2[I]][[D]-\lambda_3[I]]}{(\lambda_1-\lambda_2)(\lambda_1-\lambda_3)} + \frac{f(\lambda_2)[[D]-\lambda_1[I]][[D]-\lambda_3[I]]}{(\lambda_2-\lambda_1)(\lambda_2-\lambda_3)} + \frac{f(\lambda_3)[[D]-\lambda_1[I]][[D]-\lambda_2[I]]}{(\lambda_3-\lambda_1)(\lambda_3-\lambda_2)} \tag{10-39}$$

where $[I]$ is the identity matrix with elements $\delta_{ik}$, the Kronecker delta. The functions $f(\lambda_i)$ are calculated from $f(\lambda_i) = erf\left[\frac{z}{\sqrt{4t}}\lambda_i^{-1/2}\right]$.

Figure 10-19(b) shows the transient development of concentrations in the Left and Right compartments. It is interesting to note the negative concentrations of the neutral electrolyte $Na_2SO_4(2)$ are experienced in the right compartment; see further explanations in the paper by Hao and Leaist.[162]

A precisely analogous situation arises for diffusion in aqueous solutions of mixed electrolytes LiCl/NaOH, there are four different ionic species $Li^+$, $Cl^-$, $Na^+$, and $OH^-$. Due to the electroneutrality $\sum_{i=1}^{n} c_i z_i = 0$ and no-current $\sum_{i=1}^{n} z_i N_i = \sum_{i=1}^{n} c_i z_i u_i = 0$ constraints there are three independent fluxes, three independent concentrations, and three independent concentration gradients. Inter-diffusion in aqueous solutions of mixed electrolytes LiCl/NaOH engenders the flow of an additional neutral electrolyte NaCl, as evidenced in the experiments of Hao and Leaist.[162]

Figure 10-20(a) presents calculations of the elements of the 3×3 dimensional Fick diffusivity matrix for the ternary electrolyte LiCl(1)/NaCl(2)/NaOH(3) system in the solvent (water) fixed reference frame, using equations (10-32) for the Fick diffusivities in the corresponding ionic system, with three independent ionic species. These elements can be compared with the experimental data presented in Figure 3 of Hao and Leaist.[162] Note, however, the experimental data in Figure 3 of Hao and Leaist[162] are for values in the volume-averaged reference velocity frame; consequently, the agreement with Figure 10-20(a) is not perfect.

Consider inter-diffusion of LiCl(1)/NaCl(2)/NaOH(3) mixtures between two compartments. The initial concentrations of the three neutral electrolytes in the left compartment is $(c_{L0}) = \begin{pmatrix} 0.1 \\ 0 \\ 0 \end{pmatrix}$ mol $L^{-1}$.

The initial concentrations of the three neutral electrolytes in the right compartment is $(c_{R0}) = \begin{pmatrix} 0 \\ 0 \\ 0.1 \end{pmatrix}$ mol

$L^{-1}$. Note that the concentration of NaCl(2) is zero in both compartments. The matrix of diffusivities [*D*] at the arithmentic average concentrations, $\frac{(c_{L0})+(c_{R0})}{2}=\begin{pmatrix}0.05\\0\\0.05\end{pmatrix}$ mol $L^{-1}$, is calculated from the Nernst-Planck equations: $[D]=\begin{bmatrix}1.137 & 0.074 & 0.42\\0.686 & 1.812 & -1.249\\-0.547 & -0.381 & 3.127\end{bmatrix}\times 10^{-9}$ $m^2$ $s^{-1}$. The transient development of concentrations of the ions in the Left and Right compartments (denoted by subscripts L and R) is described by the 3-dimensional matrix equation (10-38).

Figure 10-20(b) shows the transient development of concentrations in the Left and Right compartments. It is interesting to note the negative concentrations of the neutral electrolyte NaCl(2) are experienced in the left compartment; see further explanations in the paper by Hao and Leaist.[162]

## 10.15 Fick diffusivity matrix for LiCl/KCl/$H_2O$ solutions

Figure 10-21(a,b,c,d) shows the experimental data, as reported in Table 3 of Leaist and Kanakos[163] for the elements of the Fick diffusivity matrix $\begin{bmatrix}D_{11}^V & D_{12}^V\\D_{21}^V & D_{22}^V\end{bmatrix}_i$, in the volume-averaged reference velocity frame, for mixtures of aqueous electrolytes LiCl (1), and KCl (2) at 298.15 K. The total molar concentration of the mixture $c_{LiCl}+c_{KCl}$ is (a) 0.5 mol $L^{-1}$, (b) 1 mol $L^{-1}$, (c) 2 mol $L^{-1}$, and (d) 3 mol $L^{-1}$, The *x*-axis represents the fraction $c_{LiCl}/(c_{LiCl}+c_{KCl})$. The *x*-axis represents the fraction $c_{LiCl}/(c_{LiCl}+c_{KCl})$.The experimental data are for the *volume averaged reference velocity* frame $u^V=\sum_{i=1}^{2}c_i\overline{V}_i u_i$ where $\overline{V}_i$ is the partial molar volume of species *i* in the mixture.

We number the ionic species as follows: 1=$Li^+$; 2=$K^+$; 3=$Cl^-$; $z_1$= 1, $z_2$= 1, $z_3$= -1. The ionic diffusivities are $Đ_1=1.03\times10^{-9}; Đ_2=1.957\times10^{-9}; Đ_3=2.033\times10^{-9}$ $m^2$ $s^{-1}$. The ionic concentrations $c_i$ can be related to the concentrations of the neutral electrolytes $c_{LiCl}$ and $c_{KCl}$: $c_1=c_{LiCl}; c_2=c_{KCl}; c_3=c_{LiCl}+c_{KCl}$.

The fluxes of the neutral electrolytes are relatable to the ionic fluxes as follows $N_{LiCl} = N_{Li} = N_1; \quad N_{KCl} = N_K = N_2$.

The expression for the Fick diffusivity matrix $\begin{bmatrix} D_{11} & D_{12} \\ D_{21} & D_{22} \end{bmatrix} = [D][\nu]$, used in conjunction with the Nernst-Planck equations (10-32) for $[D]$, yield diffusivities in the solvent (water = component 3) fixed reference velocity frame $\begin{bmatrix} D_{11} & D_{12} \\ D_{21} & D_{22} \end{bmatrix}_i$. To convert the Fick diffusivities to the volume-averaged reference velocity frame $\begin{bmatrix} D^V_{11} & D^V_{12} \\ D^V_{21} & D^V_{22} \end{bmatrix}_i$ we use the transformation equation (10-37). The continuous solid lines in Figure 10-21(a,b,c,d) are the estimations, combining equations (10-32) and equation (10-37).

We note that Nernst-Planck equations (10-32) provide estimates that are reasonably good when the total molar concenrations are lower than about 1 mol $L^{-1}$. At higher concentrations, thermodynamic non-ideality effects become increasingly important. The paper by Leaist and Kanakos[163] provide further discussions on the thermodynamic non-ideality effects that need to be included for better agreement with experimental data.

## 10.16 Taylor dispersion in LiCl/KCl/$H_2O$ solutions

We now demonstrate the influence of diffusional coupling effects for the mixture of aqueous electrolytes LiCl (1), and KCl (2) at 298.15 K. In order to illustrate the consequences of diffusional coupling, we consider Taylor dispersion for laminar flow in a circular tube. Taylor dispersion in a binary solution is initiated by injecting a small volume $\Delta V$ of solution containing solute at concentration $c_0 + \Delta c$ is injected into a carrier solution of concentration, $c_0$. For laminar flow in a circular tube of length $L$, and radius $R$ the concentration development following the (Dirac delta) $\delta$-pulse injection is

$$c(t)-c_0=\frac{\Delta c\Delta v}{2\pi R^2\sqrt{\pi\frac{u^2R^2}{48D}t}}\exp\left(-\frac{(L-ut)^2}{4\frac{u^2R^2}{48D}t}\right)=f(D,t)\Delta c;$$
$$f(D,t)=\frac{\Delta v}{2\pi R^2\sqrt{\pi\frac{u^2R^2}{48D}t}}\exp\left(-\frac{(L-ut)^2}{4\frac{u^2R^2}{48D}t}\right) \quad (10\text{-}40)$$

Equation (10-40) can be generalized for a binary electrolyte solution by using 2-dimensional matrix notation

$$\left(c(t)\right)-\left(c_0\right)=f\left(\left[D\right],t\right)\left(\Delta c\right) \quad (10\text{-}41)$$

The Sylvester theorem, detailed in Appendix A of Taylor and Krishna,[1] is required for explicit calculation of the 2-dimensional matrix $f\left(\left[D\right],t\right)$. For the case of distinct eigenvalues, $\lambda_1$ and $\lambda_2$ of the 2-dimensional square matrix $\left[D\right]$, the Sylvester theorem yields

$$f\left[\left[D\right],t\right]=f\left(\lambda_1,t\right)\frac{\left[\left[D\right]-\lambda_2\left[I\right]\right]}{\left(\lambda_1-\lambda_2\right)}+f\left(\lambda_2,t\right)\frac{\left[\left[D\right]-\lambda_1\left[I\right]\right]}{\left(\lambda_2-\lambda_1\right)} \quad (10\text{-}42)$$

Following, Chen and Leaist[164] the Taylor dispersion calculations are for the following set of conditions:

Length of tube, $L$ = 2 m;

Cross-sectional averaged velocity in tube, $u$ = 0.0025 m s$^{-1}$;

Radius of tube, $R$ = 0.4 mm

The injected pulse volume is $\Delta v = 2\times10^{-6}$ m$^3$.

The initial concentrations of electrolytes LiCl, KCl are $\begin{pmatrix}c_{10}\\c_{20}\end{pmatrix}=\begin{pmatrix}0.25\\0.75\end{pmatrix}$ mol L$^{-1}$.

At the concentrations $c_{10}$ =0.75 mol L$^{-1}$, $c_{20}$ =2.25 mol L$^{-1}$, Chen and Leaist[164] provide the values $\left[D\right]=\begin{bmatrix}1.23 & 0.09\\0.59 & 1.87\end{bmatrix}\times10^{-9}$ m$^2$ s$^{-1}$.

The eigenvalues of the matrix $[D]=\begin{bmatrix}1.23 & 0.09\\ 0.59 & 1.87\end{bmatrix}\times 10^{-9}$ are $\lambda_1 = 1.16\times 10^{-9}; \lambda_2 = 1.94\times 10^{-9}$ m$^2$ s$^{-1}$.

The excess concentrations in the pulse are $\begin{pmatrix}\Delta c_1\\ \Delta c_2\end{pmatrix}=\begin{pmatrix}0.05\\ 0\end{pmatrix}$ mol L$^{-1}$, implying that there is no alteration in the concentration of KCl.

Figure 10-22 shows the transient development of the excess concentrations $(c(t))-(c_0)=f([D],t)(\Delta c)$ . The Gaussian peak characteristics of LiCl is the "normal" behavior of Taylor dispersion. However, we note that KCl experiences undershoots, and overshoots despite the fact that there is no alteration in the KCl concentration in the injected pulse. The dispersion of KCl is strongly influenced by the driving force of LiCl due to the contribution of the off-diagonal element $D_{21}$.

## 10.17 Fick diffusivity matrix for HCl/NaOH/$H_2O$ solutions

Leaist and Wiens[165] have presented a detailed analysis of the Fick diffusivity matrix [$D$] for the mixture of aqueous electrolytes HCl (1), and NaOH (2) at 298.15 K. Their analysis includes the influence of thermodynamic non-idealities. We compare their model calculations with the estimations using the Nernst-Plank equations (10-32), that ignores thermodynamic non-idealities. The estimations of the elements of $\begin{bmatrix}D_{11} & D_{12}\\ D_{21} & D_{22}\end{bmatrix}=[D][\nu]$ are shown in Figure 10-23(a).

The total molar concentration of the mixture $c_{HCl}+c_{NaOH}$ = 0.05 mol L$^{-1}$. The $x$-axis represents the fraction $c_{HCl}/(c_{HCl}+c_{NaOH})$. In these calculations, we number the ionic species as follows: 1=$Cl^-$; 2=$Na^+$; 3=$H^+$; 4=$OH^-$; $z_1$= -1, $z_2$= 1, $z_3$= 1, $z_4$= -1. The ionic diffusivities are $Đ_1 = 2.03\times 10^{-9}; Đ_2 = 1.33\times 10^{-9}; Đ_3 = 9.31\times 10^{-9}\, Đ_2 = 5.3\times 10^{-9}$ m$^2$ s$^{-1}$. The fluxes of the neutral electrolytes are relatable to the ionic fluxes: $N_{HCl} = N_{Cl} = N_1$; $N_{NaOH} = N_{NaH} = N_2$.

The ionic concentrations of $H^+$ and $OH^-$ are related by $K_w = c_H c_{OH} \gamma_H \gamma_{OH}$. The value of the dissociation constant $K_w = 10^{-14}$ is taken from the literature. In mixed electrolyte solutions with excess

HCl, we have $c_H = c_{HCl} - c_{NaOH}$. In mixed electrolyte solutions with excess NaOH, we have $c_{OH} = c_{NaOH} - c_{HCl}$. Consequently, there is a discontinuity in the elements of [$D$] when the concentrations of the two neutral electrolytes are equal; see Figure 10-23(a).

Figure 10-23(b) presents the calculations of the elements of the Fick diffusivity matrix [$D$] including the influence of thermodynamic non-idealities, following the procedure as outlined in the Appendix to the paper by Leaist and Wiens.[165] The inclusion of thermodynamic non-idealities does not have a significant influence on the values of the elements of $\begin{bmatrix} D_{11} & D_{12} \\ D_{21} & D_{22} \end{bmatrix} = [D][\nu]$ because the total molar concentration of the system is only 0.05 mol L$^{-1}$.

In order to highlight the influence of coupling effects in ionic diffusion, we consider transient inter-diffusion of HCl (component 1) and NaOH (component 2) between between upper and lower compartments of a diaphragm cell as shown in the schematic in Figure 10-24(a). The experimental data corresponding to a set of 3 experiments has been reported in the paper by Leaist and Wiens.[165] We simulate one of these set of experiments in which the upper compartment initially contains the aqueous electrolyte HCl (1) with a molar concentration of 0.025 mol L$^{-1}$ and the lower compartment initiually contains aqueous NaOH (2) with a molar concentration of 0.075 mol L$^{-1}$. The initial driving forces for inter-diaphragm transport of HCl (1) and NaOH (2) are respectively, $\Delta c_{10} = 0.025; \Delta c_{20} = -0.075$ where $\Delta c_i$ is the concentration difference between the upper and lower compartments. The transient equilibration process is described by the two-dimensional matrix expression $(\Delta c) = \exp[-\beta[D]t](\Delta c_0)$, where $\beta$ is the cell constant. As $t \to \infty$, $(\Delta c) \to (0)$, and the concentrations of each electrolyte in the top and bottom compartments will be identical. The value of the integral average Fick diffusivity matrix for these set of conditions is provided in Table 2 of Leaist and Wiens:[165] $[D] = \begin{bmatrix} 2.59 & -0.68 \\ -0.83 & 2.19 \end{bmatrix} \times 10^{-9}$ m$^2$ s$^{-1}$. The Sylvester theorem, detailed in Appendix A of Taylor and Krishna,[1] is required for explicit

calculation of $\exp[-\beta[D]t]$. For the case of distinct eigenvalues, $\lambda_1$ and $\lambda_2$ of the 2-dimensional square matrix $[D]$, the Sylvester theorem yields

$$\exp[-\beta[D]t] = (\exp(-\beta\lambda_1 t))\frac{[[D]-\lambda_2[I]]}{(\lambda_1-\lambda_2)} + \exp(-\beta\lambda_2 t)\frac{[[D]-\lambda_1[I]]}{(\lambda_2-\lambda_1)} \tag{10-43}$$

The eigenvalues of the matrix $[D] = \begin{bmatrix} 2.59 & -0.68 \\ -0.83 & 2.19 \end{bmatrix} \times 10^{-9}$ are $\lambda_1 = 3.167\times10^{-9}; \lambda_2 = 1.613\times10^{-9}$ $m^2$ $s^{-1}$.

The transient approach to equilibrium of the concentration differences of HCl and NaOH are shown by the red lines in Figure 10-24(b,c). It is interesting to note a pronounced undershoot in the equilibration of HCl. This undershoot signifies the phenomenon of uphill diffusion, as explained by Leaist and Wiens.[165] Uphill diffusion is a common occurrence in coupled diffusion processes; see the papers by Krishna for general background to uphill diffusion.[99, 166, 167] The blue lines in Figure 10-24(b,c). represent correspond calculations for the transient *uncoupled* equilibration process in which ionic effects are ignored and each of the electrolytes HCl and NaOH are assumed to transfer at the diffusivities of the neutral electrolytes $D_{HCl} = 3.333\times10^{-9}; D_{NaOH} = 2.12\times10^{-9}$ $m^2$ $s^{-1}$. For uncoupled diffusion, there is no undershoot in the equilibration of HCl.

The enhancement in the equilibration of HCl due to counter-diffusion of NaOH has important consequence for gas absorption processes, as discussed hereunder.

## 10.18 Ion diffusion and rapid reaction of HCl and NaOH

Many industrial processes involve the absorption, and subsequent reaction, of dissolved gases into aqueous solutions. For example, absorption of gases into aqueous solutions is an important industrial process for removal of pollutants such as $SO_2$, $NH_3$, $CO_2$, and $H_2S$ from gaseous streams. The general mechanism of simultaneous mass transfer and chemical reaction was elucidated by S. Hatta in 1928. The reader is referred to Chapter 23 of Levenspiel[168] for background information on mass transfer with chemical reaction. Consider the absorption of solute A from a bulk gas phase, into a solvent containing

the reactant B with which A reacts; see schematic in Figure 10-25(a). Let the concentration of the solute A at the gas/liquid interface be $p$ mol $L^{-1}$. The concentration of reactant B in the bulk liquid phase is $q$ mol $L^{-1}$. In the special case of a rapid irreversible reaction between A and B, the reaction occurs at a reaction plane at a distance $x_1$ from the gas-liquid interface; at this reaction plane the concentrations of both A and B are zero. The overall rate of reaction is dictated entirely by diffusional considerations. A diffuses from the gas/liquid interface to the reaction plane due to the concentration gradient $(p-0)/x_1$, with diffusivity $D_A$, and flux $N_A = D_A(p-0)/x_1$. B diffuses from the bulk liquid to the reaction place as a result of the concentration gradient $(q-0)/x_2$, with diffusivity $D_B$, and flux $N_B = D_B(q-0)/x_2$. The flux across the interface is $N = (D_A p + D_B q)/x_L = (N_A x_1 + N_B x_2)/x_L$. We may also write $\frac{N x_L}{p} = (N_A x_1 + N_B x_2)/p = k_L x_L$ where $k_L$ is the effective phase mass transfer coefficient. The product $k_L x_L = \left( D_A + D_B \frac{q}{p} \right)$ is the effective diffusivity for transfer. This effective diffusivity is higher than the diffusivity of the reactant A. Put another way, there is an enhancement to the interphase mass transfer process due to chemical reaction within the diffusion film of thickness $x_L$. With increasing values of $\frac{q}{p}$, the reaction plane moves closer to the gas/liquid interface.

In their classic paper, Sherwood and Wei[169] have presented an analysis of the scenario in which the dissolved gas A and reactant B both undergo dissociation, partial or total dissociation, in the aqueous solution. For absorption of gaseous HCl into aqueous NaOH, both the reactants undergo complete dissociation in the aqueous phase, forming the ions $OH^-, H^+, Na^+, Cl^-$. The neutralization reaction is essentially represented by the reaction of the hydrogen ion with the hydroxyl ion $H^+ + OH^- \leftrightarrow H_2O$. Due to the constraints of electro-neutrality $\sum_{i=1}^{n} c_i z_i = 0$, and the no-current restriction

$\sum_{i=1}^{n} z_i N_i = \sum_{i=1}^{n} c_i z_i u_i = 0$, the diffusion of each of the four ions is strongly influenced by the transport of each of the partner ions in the solution.

Sherwood and Wei[169] used the Nernst-Planck equations to demonstrate the strong influence of diffusonal coupling effects on the transport of individual ions and the overall rate of absorption of HCl into aqueous NaOH. It is both illuminating, and instructive to reproduce the calculation results presented in their paper.

Figure 10-25(b) presents a schematic of the ionic concentrations in the "double film" for absorption of HCl into aqueous NaOH; This schematic is essentially identical to that presented in Figure 1 of Sherwood and Wei.[169] At the reaction plane, distance $x_1$ from the gas-liquid interface, we have the instantaneous neutralization reaction $H^+ + OH^- \leftrightarrow H_2O$. At this plane, the concentrations of both $H^+$ and $OH^-$ must vanish. Consequently, the concentrations of the partner ions $Na^+$ and $Cl^-$ must equal each other at the reaction plane; this concentration is denoted as *m*.

To the left of the reaction plane, we have the three ions $H^+, Na^+, Cl^-$. To the right of the reaction plane, we have the three ions $OH^-, Na^+, Cl^-$. Due to rapid influx of $H^+$ into the aqueous solution, $C1^-$ gets drawn into the liquid film in order to maintain electroneutrality.

The transfer fluxes of each of the ions in either of these two zones is described by equation (10-26). The ionic diffusivities are $\mathcal{D}_H = 9.317\times10^{-9}; \mathcal{D}_{Na} = 1.331\times10^{-9}; \mathcal{D}_{Cl} = 2.023\times10^{-9}; \mathcal{D}_{OH} = 5.271\times10^{-9}$ $m^2\ s^{-1}$. The ion concentrations in each of the two zones, left and right of the reaction plane, are taken to be the arithmetic average of the concentrations at either ends of the respective regions. There is no net transport of $Na^+$ across the gas liquid interface, and therefore its ionic flux must vanish in the region to the left of the reaction plane, i.e. $N_{Na} = 0$. Imposition of this condition results in the relation

$s = -\frac{p}{2} + \sqrt{\frac{p^2}{4} + m^2 + 4.61pm}$. The condition $N_{\mathrm{Na}} = 0$ also applies to the region towards the right of the reaction plane; imposition of this condition results in $m = n\sqrt{1.605\frac{q}{n} + 1}$.

The flux across the interface is $N = \left(Đ_H p + Đ_{OH} q\right)/x_L = \left(N_H x_1 + N_{OH} x_2\right)/x_L$ or $\frac{Nx_L}{p} = \left(N_H x_1 + N_{OH} x_2\right)/p = k_L x_L$ where $k_{\mathrm{L}}$ is the effective phase mass transfer coefficient.

Figure 10-26 presents a comparison of Nernst-Planck calculations for the parameter $k_{\mathrm{L}}x_{\mathrm{L}}$ with those using the classic Hatta model, assuming that the reaction takes place between "neutral" HCl and "neutral" NaOH: $k_L x_L = \left(D_{HCl} + D_{NaOH}\frac{q}{p}\right)$ where diffusivities of the neutral molecules are, respectively, $D_{HCl} = 3.32\times10^{-9}; D_{NaOH} = 2.12\times10^{-9}$. The calculations presented in Figure 10-26 are precisely identical to those presented in Figure 2 of Sherwood and Wei,[169] albeit presented in SI units. The following summary of the results is provided by Sherwood and Wei:[169] "the rapid diffusion of $H^+$ and $OH^-$ ions in the presence of $Na^+$ and $C1^-$ ions may lead to an absorption rate more than twice that predicted by the use of molecular diffusion concepts and the Hatta theory".

## 10.19 Ion diffusion and rapid reaction of HOAc and NaOH

Sherwood and Wei[169] have also presented an analysis of the scenario in which the dissolved gas A reacts with reactant B under conditions such that only B dissociates into ions; see Figure 10-27. This scenario is exemplified by the absorption of gaseous acetic acid (HOAc) into aqueous NaOH. HOAc remains practically undissociated, whereas NaOH and NaOAc undergoes complete dissociation, forming the ions $OH^-, Na^+, OAc^-$. Sherwood and Wei[169] used the Nernst-Planck equations to demonstrate the significant influence of electrostatic coupling effects on the transport of individual ions and the overall rate of absorption of HOAc into aqueous NaOH. We shall reproduce the calculation results presented in their paper.

Figure 10-27(b) presents a schematic of the ionic concentrations in the "double film" for absorption of HOAc into aqueous NaOH; This schematic is essentially identical to that presented in Figure 3 of Sherwood and Wei.[169] At the reaction plane, distance $x_1$ from the gas-liquid interface, we have the instantaneous reaction $HOAc + OH^- \leftrightarrow H_2O + OAc^-$. At this plane, the concentrations of both HOAc $H^+$ and $OH^-$ must vanish. Consequently, the concentrations of the partner ions $Na^+$ and $OAc^-$ must equal each other at the reaction plane; this concentration is denoted as *m*.

To the left of the reaction plane, we have the diffusion of neutral molecules HOAc and NaOAc. The transfer flux of HOAc is $N_{HOAc} = D_{HOAc}(p-0)/x_1$. The diffusivity of neutral, undissociated HOAc is $D_{HOAc} = 1.279\times10^{-9}$ $m^2$ $s^{-1}$.

To the right of the reaction plane, we have the three ions $OH^-, Na^+, OAc^-$. $OH^-$ is the most mobile of the ionic species, and the hydroxyl ion diffuses rapidly from the bulk aqueous solution to the reaction plan.

The transfer fluxes of each of the ions on the right side of the reaction plane is described by by equation (10-26). The ionic diffusivities are $Đ_{OAc} = 1.091\times10^{-9}; Đ_{Na} = 1.331\times10^{-9}; Đ_{OH} = 5.271\times10^{-9}$ $m^2$ $s^{-1}$.

The concentrations of each of the species to the right of the reaction plane are taken to be the arithmetic average of the concentrations at either ends of the respective regions. There is no net transport of $Na^+$ across the reaction plance, and therefore its ionic flux must vanish to the right of the reaction plane, i.e. $N_{Na} = 0$; imposition of this condition results in $m = n\sqrt{3.82\frac{q}{n}+1}$.

The flux across the interface is $N = (Đ_{HOAc}p + Đ_{OH}q)/x_L = (N_{HOAc}x_1 + N_{OH}x_2)/x_L$ or $\frac{Nx_L}{p} = (N_{HOAc}x_1 + N_{OH}x_2)/p = k_L x_L$ where $k_L$ is the effective phase mass transfer coefficient.

Figure 10-28 presents a comparison of Nernst-Planck calculations for the parameter $k_L x_L$ with those using the classic Hatta model, assuming that the reaction takes place between "neutral" HOAc and

"neutral" NaOH. $k_L x_L = \left( D_{HOAc} + D_{NaOH} \frac{q}{p} \right)$ where diffusivities of the neutral molecules are, respectively, $D_{HOAc} = 1.279 \times 10^{-9}; D_{NaOH} = 2.12 \times 10^{-9}$. The calculations presented in Figure 10-28 are precisely identical to those presented in Figure 4 of Sherwood and Wei,[169] albeit presented in SI units. The rates of reaction including ionic diffusion are about a factor 2 higher than the estimations of the classic Hatta model.

In many cases, the dissolved gas undergoes partial hydrolysis in the aqueous phase, e.g. $SO_2 + H_2O \leftrightarrow HSO_3^- + H^+$, $CO_2 + H_2O \leftrightarrow HSO_3^- + H^+$. Littel et al.[170] have modelled the absorption of $CO_2$ and $H_2S$ in alkanolamine solutions, taking proper account of ionic diffusion effects and the Nernst-Planck equations.

## 10.20 Diffusion of $SO_2$ in aqueous solutions

Leaist[171] has reported experimental data for diffusivity of $SO_2$ in water; see Figure 10-29(a). Noteworthy is the decrease in the diffusivity of increasing concentration of the solute. The proper description of the diffusion of $SO_2$ is described in the paper of Leaist.[171] We retrace the various essential elements of the diffusion process.

Firstly, we need to consider hydrolysis of $SO_2$ in aqueous solutions and is present either as molecular $SO_2$ or as bisulfite ion $HSO_3^-$: $SO_2 + H_2O \leftrightarrow HSO_3^- + H^+$. The degree of hydrolysis, $\alpha$, defined as, $\alpha = \frac{c_{HSO3}}{c_{HSO3} + c_{SO2}} = \frac{c_{HSO3}}{c}; c_{HSO3} = \alpha c; c_{SO2} = (1-\alpha)c$, can be calculated from $K_H = \frac{c_{HSO3} c_H}{c_{SO2}} \frac{\gamma_{HSO3} \gamma_H}{\gamma_{SO2}} = \frac{\alpha^2 c \gamma_\pm^2}{1-\alpha}$ where the mean activity coefficient is calculated from $\ln(\gamma_\pm) = -\frac{A\sqrt{I}}{1+\sqrt{I}}$ with $A$ = 1.175, and ionic strength $I = \alpha c$. The hydrolysis constant $K_H = 0.013$ mol $L^{-1}$ at 298.15 K. Figure 10-29(b) presents the calculations for the degree of hydrolysis as a function of

the concentration $c$ of the solute. At vanishingly small concentrations, the dissolved $SO_2$ is almost entirely hydrolyzed; the degree of hydrolysis decreases with increasing solute concentration.

Leaist[171] has derived the following expression for the Fick diffusivity of aqueous $SO_2$:

$D = \left( (1-\alpha) D_{SO2} + \frac{\alpha D_{\pm}}{2} \right) \Gamma; \quad \Gamma \equiv \frac{c}{RT} \frac{\partial \mu}{\partial c} = \frac{2}{2-\alpha} \left( 1 + \alpha \frac{\partial \ln \gamma_{\pm}}{\partial \ln c} \right)$ where $D_{SO2} = 1.77 \times 10^{-9}$ m$^2$ s$^{-1}$ is the diffusivity of molecular $SO_2$, and $D_{\pm} = \frac{2 Đ_{HSO3} Đ_H}{Đ_{HSO3} + Đ_H}$, can be estimated from the ionic diffusivities of $HSO_3^-$ and $H^+$.

Figure 10-29(c) shows the calculations for the thermodynamic correction factor, for two different scenarios: including or ignoring the correction for activity coefficients. Activity coefficient corrections are not significant for diffusion of $SO_2$.

The continuous solid lines in Figure 10-29(a) are the model estimations of the Fick diffusivity. At vanishingly small concentrations, $c \to 0; \quad D \to D_{\pm} = \frac{2 Đ_{HSO3} Đ_H}{Đ_{HSO3} + Đ_H}$; in dilute solutions where most of the dissolved gas is hydrolyzed, a sharp increase in the diffusivity of $SO_2$ is a consequence of the exceptionally high mobility of $H^+$.

## 10.21 Diffusion of Acetic Acid in aqueous solutions

Leaist and Lyons[172] has reported experimental data for diffusivity of acetic acid (HOAc) in water; see Figure 10-30(a). The analysis of the diffusion process is analogous to that of $SO_2$, discussed in the foregoing section.

HOAc undergoes dissociation in in aqueous solutions: $HOAc \leftrightarrow OAc^- + H^+$. The degree of dissociation, $\alpha$, can be calculated from $K_D = \frac{\alpha^2 c \gamma_{\pm}^2}{1-\alpha}$ where the mean activity coefficient is determined from $\ln(\gamma_{\pm}) = -\frac{A\sqrt{I}}{1+\sqrt{I}}$ with $A$ = 1.175, and ionic strength $I = \alpha c$. The dissociation constant $K_D = 1.753 \times 10^{-5}$ mol L$^{-1}$ at 298.15 K. Figure 10-30(b) presents the calculations for the degree of

dissociation as a function of the concentration *c* of the solute. The degree of dissociation is significantly lower than the degree of hydrolysis of $SO_2$ (cf. Figure 10-29(b). Consequently, ion diffusion effects have a significantly lower prominence for HOAc; this manifests in a weak reduction in the Fick diffusivity value with increased concentration of solute.

The expression for the Fick diffusivity of HOAc, presented by Leaist and Lyons[172] is formally the same as for $SO_2$:

$$D = \left( (1-\alpha) D_{HOAc} + \frac{\alpha D_{\pm}}{2} \right) \Gamma; \quad \Gamma \equiv \frac{c}{RT} \frac{\partial \mu}{\partial c} = \frac{2}{2-\alpha} \left( 1 + \alpha \frac{\partial \ln \gamma_{\pm}}{\partial \ln c} \right)$$ where $D_{HOAc} = 1.201 \times 10^{-9}$ $m^2$ $s^{-1}$ is

the diffusivity of molecular (undissociated) acetic acid, and $D_{\pm} = \frac{2 Đ_{OAc} Đ_H}{Đ_{OAc} + Đ_H} = 1.95 \times 10^{-9}$ $m^2$ $s^{-1}$, is

estimated from the ionic diffusivities of $OAc^-$ and $H^+$.

Figure 10-30(c) shows the calculations for the thermodynamic correction factor, for two different scenarios: including or ignoring the correction for activity coefficients. Activity coefficient corrections are insignificant for diffusion of acetic acid because of the small degree of dissociation.

## 10.22 Diffusion of $SO_2$ in aqueous $NaHSO_3$ solutions

The removal of $SO_2$ from gaseous streams by gas absorption in aqueous solutions is an important industrial process. In a previous section we had examined the diffusion of SO2 in aqueous solutions in order to demonstrate the importance of hydrolysis $SO_2 + H_2O \leftrightarrow HSO_3^- + H^+$ and inclusion of the proper description of ionic diffusion in the analysis. In this section we examine diffusion of SO2 in aqueous bisfulfite ($NaHSO_3$) solutions. The treatment here follows the model equations of Leaist,[173] and include thermodynamic non-ideality effects. Sodium bisulphite undergoes complete dissociation . $NaHSO_3 \leftrightarrow HSO_3^- + Na^+$ The system consists of five species: $SO_2$ (molecular), $HSO_3^-$, $H^+$, $Na^+$, and $H_2O$.

Figure 10-31(a) presents calculations of the elements of the Fick diffusivity matrix for the mixture of aqueous electrolytes $SO_2$(1), and $NaHSO_3$ (2) at 293.15 K. The *x*-axis represents the total molar

concentration of the mixture $c_{SO2} + c_{NaHSO3}$. In these calculations, we take the fraction $c_{SO2}/\left(c_{SO2} + c_{NaHSO3}\right)$ = 0.25. We note that the main coefficient $D_{11}$ increases significantly as the total concentration molar concentration $c_{SO2} + c_{NaHSO3}$ is lowered. This is due to the increased degree of hydrolysis $SO_2 + H_2O \leftrightarrow HSO_3^- + H^+$ at low concentrations; this behavior is precisely analogous to that observed in Figure 10-29(a).

For the calculations in Figure 10-31(b) we take the fraction $c_{SO2}/\left(c_{SO2} + c_{NaHSO3}\right)$ = 0.75. We note that the main coefficient $D_{11}$ is significantly lower than the corresponding values shown in Figure 10-31(a). We conclude that the coefficient $D_{11}$ is higher in solutions that contain a higher proportion of the bisulfite eolution. Ionic effects become increasingly significant at higher bisulfite concentrations. In order to further underscore this point, Figure 10-32(a) presents calculations of the elements of the Fick diffusivity matrix [$D$] for the mixture of aqueous electrolytes $SO_2$(1), and $NaHSO_3$ (2) at 293.15 K with varying fractions $c_{SO2}/\left(c_{SO2} + c_{NaHSO3}\right)$ for a total mixture concentration $c_{SO2} + c_{NaHSO3}$ = 0.001 mol $L^{-1}$. We note that the main coefficient $D_{11}$ progressively increases as the solution becomes increasingly dilute in $SO_2$. Figure 10-32(b) compares $D_{11}$ with the diffusivity of molecular $SO_2$, $D_{SO2} = 1.45 \times 10^{-9}$ $m^2$ $s^{-1}$. Due to ionic effects, there is about a five-fold increase in $D_{11}$. Ionic diffusion effects need to be taken into consideration in the design of gas absorption processes in which the solute undergoes hydrolysis or dissociation. Littel et al.[170] have modelled the absorption of $CO_2$ and $H_2S$ in alkanolamine solutions, taking proper account of ionic diffusion effects and using the Nernst-Planck equations.

In order to highlight the influence of coupling effects in ionic diffusion, we consider transient inter-diffusion of $SO_2$(1), and $NaHSO_3$ (2) at 293.15 K between upper and lower compartments of a diaphragm cell as shown in the schematic in Figure 10-33(a). We simulate a scenario in which the concentrations in the upper compartment are $c_{10,up}$ =0.01 mol $L^{-1}$, $c_{20,up}$ =0.1 mol $L^{-1}$. The initial concentrations in the bottom compartment are $c_{10,bottom}$ =0.001 mol $L^{-1}$, $c_{20,bottom}$ =1 mol $L^{-1}$. The transient equilibration of concentrations is described by the two-dimensional matrix expression

$(\Delta c) = \exp[-\beta[D]t](\Delta c_0)$, where $\beta$ is the cell constant. The initial driving forces for inter-diaphragm transport are respectively, $\Delta c_{10} = 0.01 - 0.001; \Delta c_{20} = 0.1 - 1$ where $\Delta c_i$ is the concentration difference between the upper and lower compartments. As $t \to \infty$, $(\Delta c) \to (0)$, and the concentrations of each electrolyte in the top and bottom compartments will be identical. The value of the Fick diffusivity matrix at the equilibrated composition is $[D] = \begin{bmatrix} 1.916 & -0.003827 \\ -0.249 & 1.021 \end{bmatrix} \times 10^{-9}$ m$^2$ s$^{-1}$. The Sylvester theorem, detailed in Appendix A of Taylor and Krishna,[1] is required for explicit calculation of $\exp[-\beta[D]t]$. For the case of distinct eigenvalues, $\lambda_1$ and $\lambda_2$ of the 2-dimensional square matrix $[D]$, the Sylvester theorem yields

$$\exp[-\beta[D]t] = (\exp(-\beta\lambda_1 t))\frac{[[D] - \lambda_2[I]]}{(\lambda_1 - \lambda_2)} + \exp(-\beta\lambda_2 t)\frac{[[D] - \lambda_1[I]]}{(\lambda_2 - \lambda_1)} \tag{10-44}$$

The eigenvalues of the matrix $[D] = \begin{bmatrix} 1.916 & -0.003827 \\ -0.249 & 1.021 \end{bmatrix} \times 10^{-9}$ are $\lambda_1 = 1.917 \times 10^{-9}; \lambda_2 = 1.02 \times 10^{-9}$ m$^2$ s$^{-1}$.

The transient approach to equilibrium are shown by the red lines in Figure 10-33(b,c). It is interesting to note a slight undershoot in the equilibration of $SO_2$. This undershoot signifies the phenomenon of uphill diffusion; see the papers by Krishna for general background to uphill diffusion.[99, 166, 167]

The blue lines in Figure 10-33(b,c) represent correspond calculations for the transient *uncoupled* equilibration process in which ionic effects are ignored both components are assumed to transfer at the diffusivities of molecular $SO_2$ $D_{SO2} = 1.45 \times 10^{-9}$ m$^2$ s$^{-1}$ and neutral electrolyte $D_{NaHSO3} = 1.19 \times 10^{-9}$ m$^2$ s$^{-1}$. For uncoupled diffusion, there is no undershoot in the equilibration of $SO_2$.

A further important point to note is that the counter-diffusion of $NaHSO_3$ serves to enhance the equilibration of $SO_2$.

## 10.23 Diffusion in aqueous solutions of $Na_2SO_4/K_2SO_4$

The process of purification by crystallization is important in the process industries. By definition, crystallization processes operate under conditions close to supersaturation. As evidenced by the calculations presented in Figure 10-5, thermodynamic correction factors cannot be ignored; the will have a strong influence on diffusion fluxes and the kinetics of crystal growth. Using the data on diffusivities and activity coefficients provided in the paper by Louhi-Kultanen et al.[153] we analyse diffusion in $Na_2SO_4(1)/K_2SO_4(2)/H_2O(3)$ mixtures under conditions relevant to crystallization processes.

Firstly, we estimate the matrix of Fick diffusivities [$D$] for the ternary $Na_2SO_4(1)/K_2SO_4(2)/H_2O(3)$ mixture using the Nernst-Planck equations that ignore thermodynamic non-idealities.

Towards this end, we number the ionic species as follows: 1=$Na^+$; 2=$K^+$; 3=$SO_4^{--}$; $z_1$= 1, $z_2$= 1, $z_3$= -1. The ionic diffusivities are $\mathcal{D}_1 = 1.334\times10^{-9}; \mathcal{D}_2 = 1.957\times10^{-9}; \mathcal{D}_3 = 1.065\times10^{-9}$ m$^2$ s$^{-1}$. The ionic molalities $m_i$ can be related to the molalities of the neutral electrolytes $m_{NaCl}$, and $m_{Na2SO4}$

$$m_1 = 2m_{Na2SO4}; m_2 = 2m_{K2SO4}; c_3 = c_{Na2SO4} + c_{K2SO4} \tag{10-45}$$

The fluxes of the neutral electrolytes $Na_2SO_4(1)$ and $K_2SO_4(2)$ are relatable to the ionic fluxes as follows

$$N_{Na2SO4} = \frac{N_1}{2}; \quad N_{K2SO4} = \frac{N_2}{2} \tag{10-46}$$

The Fick diffusivity matrix for neutral electrolytes can be estimated by combining equations (10-32) with equation (10-37) and invoking the equalities in equations (10-45), and (10-46).

Let us calculate the fluxes for a set of conditions specified in Table 4 of Louhi-Kultanen et al.[153]

The molalities of neutral electrolytes $Na_2SO_4(1)$ and $K_2SO_4(2)$ in the bulk solution are

$m_{10} = 0.201; \quad m_{20} = 0.632$ mol kg$^{-1}$.

The molalities of neutral electrolytes $Na_2SO_4(1)$ and $K_2SO_4(2)$ at the crystal surface are

$m_{1\delta} = 0.202; \quad m_{2\delta} = 0.752$ mol kg$^{-1}$.

At the arithmetic average molalities, the Fick diffusivity matrix is $[D]=\begin{bmatrix} 1.314 & -0.068 \\ -0.103 & 1.164 \end{bmatrix}\times 10^{-9}$ m$^2$ s$^{-1}$. In view of equations (10-45), and (10-46), the same values of the Fick diffusivity matrix for ionic species, calculated from equations (10-32), also applies for the binary $Na_2SO_4$(1)/$K_2SO_4$(2) mixture of neutral electrolytes. Ignoring thermodynamic correction factors, and assuming an effective film thickness $\delta = 10\times 10^{-6}$ m, the fluxes of $Na_2SO_4$(1) and $K_2SO_4$(2) are

$$\begin{pmatrix} N_1 \\ N_2 \end{pmatrix} = \frac{\begin{bmatrix} 1.314 & -0.068 \\ -0.103 & 1.164 \end{bmatrix}\times 10^{-9}}{10\times 10^{-6}} \begin{pmatrix} m_{10}-m_{1\delta} \\ m_{10}-m_{1\delta} \end{pmatrix} \times \frac{\text{kg water}}{\text{m}^3 \text{ solution}} = \begin{pmatrix} 6.624\times 10^{-4} \\ -0.018 \end{pmatrix} \text{ mol m}^{-2}\text{ s}^{-1}$$

. Taking into account the correction for the matrix thermodynamic correction factors $[\Gamma]=\begin{bmatrix} 0.905 & -0.097 \\ -0.333 & 0.706 \end{bmatrix}$, as calculated in an earlier section, we can re-calculate the fluxes

$$\begin{pmatrix} N_1 \\ N_2 \end{pmatrix} = \frac{\begin{bmatrix} 1.314 & -0.068 \\ -0.103 & 1.164 \end{bmatrix}\times 10^{-9}}{10\times 10^{-6}} \begin{bmatrix} 0.905 & -0.097 \\ -0.333 & 0.706 \end{bmatrix} \begin{pmatrix} m_{10}-m_{1\delta} \\ m_{10}-m_{1\delta} \end{pmatrix} \times \frac{\text{kg water}}{\text{m}^3 \text{ solution}} = \begin{pmatrix} 1.895\times 10^{-3} \\ -0.013 \end{pmatrix}$$

mol m$^{-2}$ s$^{-1}$. We note that the flux of $Na_2SO_4$(1) is significantly higher than for the case in which thermodynamic corrections are ignored. This is because of the coupling with the driving force of $K_2SO4$.

We conclude that thermodynamic corrections are of significant importance for describing the kinetics of crystal growth, and in particular the transport of impurities.

## 10.24 Transient permeation across cation exchange membranes

Yang and Pintauro[174] report an interesting set of experimental data for transient transport of $H^+$, $Na^+$, and $Cs^+$ ions across a Nafion cation exchange membrane separating the acid and salt compartments; see Figure 10-34(a). In the reported experiments, the initial concentrations are:

Left: salt compartment: $Na_2SO_4$ = 0.125 mol L$^{-1}$ ; $Cs_2SO_4$ = 0.0054 mol L$^{-1}$

Right: acid compartment: $H_2SO_4$ = 0.125 mol L$^{-1}$

The $H^+$ ions transfer from the acid to the salt compartment. Both $Na^+$, and $Cs^+$ ions transfer from the salt to the acid compartment. The $SO_4^{2-}$ ions cannot cross the membrane. Due to the significantly higher mobility of the $H^+$ ions, there is a significant influence of the diffusion potential $\frac{d\Phi}{dz}$ that tends to influence the mobility of the $Na^+$, and $Cs^+$ ions during the initial stages of the transience. Since the concentration driving force of $Cs^+$ ions is very small, the initial transience is strongly dictated by the diffusion potential $\frac{d\Phi}{dz}$; this results in the observed overshoot in the transient equilibration of $Cs^+$. Yang and Pintauro[174] present a detailed simulation model for the experiments. For our purposes here, we wish to demonstrate that the overshoot in the transient equilibration of $Cs^+$ ions can be rationalized by a simplified analytic solution of the Nernst-Planck equations using matrix calculus.

Assuming total ionization, the total ionic concentrations in the left and right compartments are (1 = $H^+$, 2 = $Na^+$; 3 = $Cs^+$, 4 = $SO_4^{2-}$)

$$c_{1L0} = 0; \quad c_{2L0} = 0.25; \quad c_{3L0} = 0.0108; \quad c_{4L0} = 0.1304$$
$$c_{1R0} = 0.25; \quad c_{2R0} = 0.0; \quad c_{3R0} = 0.0; \quad c_{4R0} = 0.125 \quad \text{mol L}^{-1}$$

The equilibrated ionic concentrations are the arithmetic averages: $c_{1eq} = 0.125; \quad c_{2eq} = 0.125; \quad c_{2eq} = 0.0054$ mol $L^{-1}$.

The cation exchange membrane prevents the transport of $SO_4^{2-}$ ions; and therefore the compositions in the left and right compartments of $SO_4^{2-}$ ions will remain 0.1304 and 0.125, respectively. In order to take account of the exclusion of $SO_4^{2-}$ ions from the matrix of the cation exchange membrane, we need to impose the additional constraint for the $(n\text{-}1)^{th}$ species, i.e. the $4^{th}$ species.

$$N_{n-1} = 0 \tag{10-47}$$

This implies that the no-current relation must simplify to

$$\sum_{i=1}^{n-2} z_i N_i = \sum_{i=1}^{n-2} c_i z_i u_i = 0; \quad \text{no current prescription} \tag{10-48}$$

The expression for the electrostatic potential gradient also reduces to

$$\frac{d\Phi}{dz} = -\frac{\sum_{k=1}^{n-2} z_k Đ_k \frac{dc_k}{dz}}{\frac{\mathrm{F}}{RT}\sum_{j=1}^{n-2} c_j z_j^2 Đ_j} \tag{10-49}$$

The ($n$-2) non-zero fluxes are

$$N_i = -Đ_i \frac{dc_i}{dz} + \frac{c_i z_i Đ_i}{\sum_{j=1}^{n-2} c_j z_j^2 Đ_j} \sum_{k=1}^{n-2} z_k Đ_k \frac{dc_k}{dz}; \quad i = 1,2,\ldots n-2 \tag{10-50}$$

We define a ($n$-2)×($n$-2) dimensional square matrix

$$D_{ik} = Đ_i \delta_{ik} - \frac{(c_i z_i Đ_i z_k Đ_k)}{\sum_{j=1}^{n-2} c_j z_j^2 Đ_j}; \quad i,k = 1,2,\ldots n-2 \tag{10-51}$$

The explicit expression for the ($n$-2) non-zero fluxes can be written in ($n$-2) dimensional matrix notation

$$(N) = -[D]\frac{d(c)}{dz} \tag{10-52}$$

The transient equilibration process in the left and right compartments is described by the ($n$-2) dimensional matrix equations $(c_L - c_{eq}) = \exp[-\beta[D]t](c_{L0} - c_{eq})$ where the vector $(c_{eq}) = \frac{(c_{L0} + c_{R0})}{2} = \begin{pmatrix} 0.125 \\ 0.125 \\ 0.0054 \end{pmatrix}$, and $\beta$ is the cell constant. The 3×3 dimensional square matrix $\exp[-\beta[D]t]$ quantifies the transient approach to equilibrium. In our calculations, we take $\beta = 2\times10^4$ m$^{-2}$, that is representative of the experimental set-up. The Sylvester theorem, detailed in Appendix A of Taylor and Krishna,[1] is required for explicit determination of $[Q] = \exp[-\beta[D]t]$. Equation (10-51) is used to determine the Fick diffusivity matrix [$D$].

For simulations of the transient equilibration process, we use the ionic diffusivities provided in Table 3 of Yang and Pintauro[174] (1 = $H^+$, 2 = $Na^+$; 3 = $Cs^+$, 4 = $SO_4^{2-}$)

$Đ_1 = 9.3\times10^{-9}$; $Đ_2 = 1.33\times10^{-9}$; $Đ_3 = 2.06\times10^{-9}$; $Đ_4 = 1.33\times10^{-9}$ m$^2$ s$^{-1}$.

The elements of the matrix [*D*] are determined at the *average* concentration in the left and right compartments at any instant of time. In other words, the solution to the matrix equation $\left(c_L - c_{eq}\right) = \exp\left[-\beta[D]t\right]\left(c_{L0} - c_{eq}\right)$ is carried out in time-discretized form. By choosing sufficiently small time intervals, a good accuracy in the calculations is achieved. The simulation results for transient approach to equilibration are shown in Figure 10-34(b). Our simple model is able to capture the overshoot in the transient equilibration of $Cs^+$ ions. The physical reasoning for the overshoot is as follows. The more mobile $H^+$ ions vacate the right (acid) compartment rapidly. This creates a rapid reduction in the positive charge in the right compartment. The $SO_4^{2-}$ are non-diffusing and cannot participate in redressing this charge imbalance. Electroneutrality is restored by the enhanced influx of $Na^+$, and $Cs^+$ from the salt compartment. Consequently, both $Na^+$, and $Cs^+$ get accelerated by electrostatic effects. The influence of the second member of the right of equation (10-51) is relatively large for $Cs^+$ because its concentration driving force is small.

The reasonably good match between model simulations and experiments is also indicative of the fact that the transmembrane permeation fluxes are dictated by diffusion in the electrolyte solutions in either compartment.

In Figure 10-35 the equilibration trajectories followed by $H^+$, $Na^+$, and $Cs^+$ in the salt and acid compartments, are plotted in composition space. In Figure 10-35(a), the left compartment contains $Na_2SO_4$ and $Cs_2SO_4$ and the right compartment contains $H_2SO_4$. The undershoot and overshoot in $Cs^+$ correspond to the Yang-Pintauro experimental observations.

We also carried out simulations for a set of different concentrations in the left and right compartments. The results are presented in Figure 10-35(b) for the scenario in which the left compartment contains $Na_2SO_4$ and the right compartment contains $H_2SO_4$ and $Cs_2SO_4$; in this case no overshoot or undershoot is experienced by $Cs^{++}$ because it diffuses in the same direction as $H^+$.

Transient overshoots for $Cs^+/Na^+$ permeation across a cation-exchange membrane have been reported by Sodaye et al.[175] These overshoots are most likely caused by a combination of electrostatic and thermodynamic coupling effects.

## 10.25 Uphill diffusion and transient overshoots in ion-exchange particles

Ion exchange is a sorption separation process that is carried out in fixed bed units in a transient manner. Most commonly, the ion-exchange resins are solid gels, consisting of a polymeric matrix produced by co-polymerization of styrene and a cross-linking agent, divinylbenzene, to produce a three-dimensional cross-linked structure with ionic functional groups attached to the polymeric network.[50] As illustration, Figure 10-36 shows a schematic showing an ion exchanger (IEX) particle with fixed $HSO_3^-$ charges. The liquid phase surrounding the particles consists of a bulk electrolyte solution e,g, HCl and NaCl. The electrolytes are fully ionized and the bulk liquid phase contains $H^+$, $Na^+$, $Cl^-$ ions along with unionized water molecules. The cation exchange particle is negative charged and disallows the influx of $Cl^-$ ions; only the positively charged cations, called counter-ions, are allowed to enter or leave the particle. If the styrene-divinylbenzene copolymer is chlormethylated and aminated, a strong-base, anionic exchange resin is formed that contain fixed positive charges, $RN^+$.[50]

We focus our attention to forward/reverse exchanges in which the diffusion resistance is within the particle. The IEX particle matrix consists of fixed negative charges. Let us assume that the total concentration of negative charges inside the matrix is $c_{\text{fixed}}$, expressed say as equivalent (mole) per volume of particle. Typically, the concentration of fixed negative charges is in the range of 1 to 4 equiv $L^{-1}$;[64] this value is considerably higher than the molar concentrations of ions in the bulk electrolyte solutions surrounding the particle. The concentration of counter ions within the particle must balance $c_{\text{fixed}}$ and therefore we have $\sum_{i=1}^{m} z_i c_i = c_{fixed}$. The quantity

$$\frac{z_i c_i}{c_{fixed}} \equiv X_i \tag{10-53}$$

is the ionic equivalent fraction. The ionic equivalent fractions of all the counter ions sum to unity $\sum_{i=1}^{m} X_i = 1$.

For HCl/NaCl exchange, the negative chloride ion is excluded from the particle. The fluxes of $H^+(1)$, and $Na^+(2)$ are

$$N_1 = -Đ_1 \frac{dc_1}{dz} - c_1 z_1 Đ_1 \frac{\mathrm{F}}{RT} \frac{d\Phi}{dz}$$
$$N_2 = -Đ_2 \frac{dc_2}{dz} - c_2 z_2 Đ_2 \frac{\mathrm{F}}{RT} \frac{d\Phi}{dz} \tag{10-54}$$

There is no flow of current

$$z_1 N_1 + z_2 N_2 = 0 \tag{10-55}$$

Combining equations (10-54), and (10-55) allows the determination of the electrostatatic potential gradient engendered by intra-particle diffusion

$$\frac{\mathrm{F}}{RT} \frac{d\Phi}{dz} = \frac{-z_1 Đ_1 \frac{dc_1}{\partial z} - z_2 Đ_2 \frac{dc_2}{dz}}{\left(c_1 z_1^2 Đ_1 + c_2 z_2^2 Đ_2\right)} \tag{10-56}$$

Introducing equation (10-56) into equation (10-54) yields the flux relations

$$N_1 = -Đ_1 \frac{dc_1}{dz} + c_1 z_1 Đ_1 \frac{z_1 Đ_1 \frac{dc_1}{dz} + z_2 Đ_2 \frac{dc_2}{dz}}{\left(c_1 z_1^2 Đ_1 + c_2 z_2^2 Đ_2\right)}$$
$$N_2 = -Đ_2 \frac{dc_2}{\partial z} + c_2 z_2 Đ_2 \frac{z_1 Đ_1 \frac{dc_1}{\partial z} + z_2 Đ_2 \frac{dc_2}{\partial z}}{\left(c_1 z_1^2 Đ_1 + c_2 z_2^2 Đ_2\right)} \tag{10-57}$$

For electro-neutrality:

$$z_1 \frac{dc_1}{dz} + z_2 \frac{dc_2}{dz} = 0 \tag{10-58}$$

In view of equation (10-58), we can simplify equations (10-57)

$$N_1 = -D_{1,eff} \frac{dc_1}{dz}; \quad N_2 = -D_{2,eff} \frac{dc_2}{dz} \tag{10-59}$$

where the effective ionic diffusivities are

$$D_{1,eff} = \frac{c_1 z_1^2 + c_2 z_2^2}{\left(c_1 z_1^2 Đ_1 + c_2 z_2^2 Đ_2\right)} Đ_1 Đ_2 = D_{2,eff} = D_{eff} = \frac{c_1 z_1^2 + c_2 z_2^2}{\left(\frac{c_1 z_1^2}{Đ_2} + \frac{c_2 z_2^2}{Đ_1}\right)} \tag{10-60}$$

Equation (10-60) is a remarkable result because the limiting values are:

$$\begin{aligned} &c_1 \to 0; \quad D_{eff} \to Đ_1 \\ &c_2 \to 0; \quad D_{eff} \to Đ_2 \end{aligned} \tag{10-61}$$

In other words, the intra-particle effective diffusivity corresponds to the diffusivity of the ion that is present in the *smaller* quantity. Helfferich, perhaps the most influential researcher, in ion exchange has termed this the "minority rule". To quote Helfferich[145] *binary interdiffusion is not a democratic process but, in the parlance of the activist 1960's, is ruled by a participating minority*!

For the exchange of ions with equal charge numbers such as for $H^+(1)/Na^+(2)$, in which $z_1 = z_2$, we obtain

$$D_{1,eff} = \frac{1}{\frac{c_1}{Đ_2} + \frac{c_2}{Đ_1}} = D_{2,eff} = D_{eff}; \quad \text{special case of equal charges } z_1 = z_2 \tag{10-62}$$

We can also extend the foregoing analysis to diffusion of *m* different counter ions within the IEX particle. Equation (10-54) is extended as follows

$$N_i = -Đ_i \frac{dc_i}{dz} - c_i z_i Đ_i \frac{\mathrm{F}}{RT} \frac{d\Phi}{dz}; \quad i = 1,2,..m \tag{10-63}$$

For no flow of current, the electrostatic diffusion potential gradient that is engendered by ion diffusion is

$$\frac{\mathrm{F}}{RT} \frac{d\Phi}{dz} = \frac{-z_1 Đ_1 \frac{dc_1}{dz} - z_2 Đ_2 \frac{dc_2}{dz} - .... - z_m Đ_m \frac{dc_m}{dz}}{\sum_{k=1}^{m} c_k z_k^2 Đ_k} \tag{10-64}$$

Electro-neutrality demands

$$z_1 \frac{dc_1}{dz} + z_2 \frac{dc_2}{dz} + ....z_m \frac{dc_m}{dz} = 0 \tag{10-65}$$

so we can eliminate the concentration gradient of the *m*th component and write

$$\frac{\mathrm{F}}{RT}\frac{d\Phi}{dz}=\frac{-\sum_{k=1}^{m-1}z_k\left(Đ_k-Đ_m\right)\frac{dc_k}{dz}}{\sum_{k=1}^{m}c_k z_k^2 Đ_k} \tag{10-66}$$

Combining equations (10-63), and (10-66)) we derive

$$N_i=-Đ_i\frac{dc_i}{dz}+c_i z_i Đ_i\frac{\sum_{j=1}^{m-1}z_k\left(Đ_k-Đ_m\right)\frac{dc_k}{dz}}{\sum_{j=1}^{m}c_k z_k^2 Đ_k};\quad i=1,2,...m-1 \tag{10-67}$$

We may cast equation (10-67) into ($m$-1)-dimensional matrix notation

$$\left(N\right)=-\left[D\right]\frac{d\left(c\right)}{dz} \tag{10-68}$$

where the elements of the ($m$-1)×($m$-1) dimensional square matrix [$D$] are

$$D_{ik}=Đ_i\delta_{ik}-\frac{\left(c_i z_i Đ_i\right)z_k\left(Đ_k-Đ_m\right)}{\sum_{j=1}^{m}c_j z_j^2 Đ_j};\quad i,k=1,2,\ldots m-1 \tag{10-69}$$

For the case in which we have 3 counter-ions within the IEX particle, $m$ = 3, equation degenerates (10-58) to yield

$$\begin{aligned}N_1&=-Đ_1\frac{dc_1}{dz}+c_1 z_1 Đ_1\frac{z_1\left(Đ_1-Đ_3\right)\frac{dc_1}{dz}+z_2\left(Đ_2-Đ_3\right)\frac{dc_2}{dz}}{\left(c_1 z_1^2 Đ_1+c_2 z_2^2 Đ_2+c_3 z_3^2 Đ_3\right)}\\ N_2&=-Đ_2\frac{dc_2}{dz}+c_2 z_2 Đ_2\frac{z_1\left(Đ_1-Đ_3\right)\frac{dc_1}{dz}+z_2\left(Đ_2-Đ_3\right)\frac{dc_2}{dz}}{\left(c_1 z_1^2 Đ_1+c_2 z_2^2 Đ_2+c_3 z_3^2 Đ_3\right)}\end{aligned} \tag{10-70}$$

We may cast equation (10-70) into 2-dimensional matrix notation

$$\left(N\right)=-\left[D\right]\frac{d\left(c\right)}{dz} \tag{10-71}$$

in which the 2×2 dimensional square matrix [$D$] has the elements

$$
\begin{aligned}
D_{11} &= Đ_1 - c_1 z_1 Đ_1 \frac{z_1\left(Đ_1 - Đ_3\right)}{\left(c_1 z_1^2 Đ_1 + c_2 z_2^2 Đ_2 + c_3 z_3^2 Đ_3\right)} \\
D_{12} &= -c_1 z_1 Đ_1 \frac{z_2\left(Đ_2 - Đ_3\right)}{\left(c_1 z_1^2 Đ_1 + c_2 z_2^2 Đ_2 + c_3 z_3^2 Đ_3\right)} \\
D_{21} &= -c_2 z_2 Đ_2 \frac{z_1\left(Đ_1 - Đ_3\right)}{\left(c_1 z_1^2 Đ_1 + c_2 z_2^2 Đ_2 + c_3 z_3^2 Đ_3\right)} \\
D_{22} &= Đ_2 - c_2 z_2 Đ_2 \frac{z_2\left(Đ_2 - Đ_3\right)}{\left(c_1 z_1^2 Đ_1 + c_2 z_2^2 Đ_2 + c_3 z_3^2 Đ_3\right)}
\end{aligned}
\tag{10-72}
$$

It is noteworthy that Yoshida and Kataoka[176] and Jones and Carta[177] have set up in a different manner using the gradients of the ionic equivalent fractions, $\frac{dX_k}{dz}$ as driving forces, where $\frac{z_k c_k}{c_{fixed}} \equiv X_k$ defined are the ion equivalent fractions

$$
z_i N_i = -c_{fixed} \sum_{k=1}^{m-1} D_{ik,eff} \frac{dX_k}{dz}; \quad i = 1,2,..m-1 \tag{10-73}
$$

The elements of the ($m$-1)×($m$-1) dimensional square matrix $\left[D_{eff}\right]$ is defined by

$$
D_{ik,eff} = Đ_i \delta_{ik} - \frac{\left(X_i z_i Đ_i\right)}{\sum_{j=1}^{m} X_j z_j Đ_j}\left(Đ_k - Đ_m\right); \quad i,k = 1,2,..m-1 \tag{10-74}
$$

For the case in which we have 3 counter-ions within the IEX particle, $m$ = 3, and equation (10-44) yields

$$
\begin{bmatrix} D_{11,eff} & D_{12,eff} \\ D_{21,eff} & D_{22,eff} \end{bmatrix} = \begin{bmatrix} Đ_1 & 0 \\ 0 & Đ_2 \end{bmatrix} - \frac{1}{\left(X_1 z_1 Đ_1 + X_2 z_2 Đ_2 + X_3 z_3 Đ_3\right)} \begin{bmatrix} X_1 z_1 Đ_1\left(Đ_1 - Đ_3\right) & X_1 z_1 Đ_1\left(Đ_2 - Đ_3\right) \\ X_2 z_2 Đ_2\left(Đ_1 - Đ_3\right) & X_2 z_2 Đ_2\left(Đ_2 - Đ_3\right) \end{bmatrix} \tag{10-75}
$$

For the special case $m$=2, we have only one independent flux, and equations (10-73), and (10-74) degenerate to yield

$$
\begin{aligned}
z_1 N_1 &= -c_{fixed} Đ_1 \frac{dX_1}{dz} - c_{fixed} X_1 z_1 Đ_1 \frac{\mathrm{F}}{RT}\frac{d\Phi}{dz} = -c_{fixed} D_{eff} \frac{dX_1}{dz};\\
z_2 N_2 &= -c_{fixed} Đ_2 \frac{dX_2}{dz} - c_{fixed} X_2 z_2 Đ_2 \frac{\mathrm{F}}{RT}\frac{d\Phi}{dz} = -c_{fixed} D_{eff} \frac{dX_2}{dz};\\
D_{eff} &= \frac{X_1 z_1 + X_2 z_2}{\left(\frac{X_1 z_1}{Đ_2} + \frac{X_2 z_2}{Đ_1}\right)}
\end{aligned}
\tag{10-76}
$$

The corrective action of the induced potential gradient $\frac{d\Phi}{dz}$ is mainly directed *against* the species that is present in the *higher* equivalent fraction $X_i$.

For the limiting scenario $X_1 \to 0$, Equation (10-76) yields the minority rule

$$
\begin{aligned}
&X_1 \to 0; \quad D_{eff} \to Đ_1\\
&X_2 \to 0; \quad D_{eff} \to Đ_2
\end{aligned}
\tag{10-77}
$$

For transient unary uptake within a spherical IEX particle of radius $r_c$, the radial distribution of ion concentrations, $c_i$, is obtained from a solution of a set of differential equations describing the uptake

$$
\frac{\partial c_i(r,t)}{\partial t} = -\frac{1}{r^2}\frac{\partial}{\partial r}\left(r^2 N_i\right) \tag{10-78}
$$

Combining equations (10-68), and (10-78)) we obtain the following differential equation describing the transient uptake

$$
\frac{\partial c_i(r,t)}{\partial t} = \frac{1}{r^2}\frac{\partial}{\partial r}\left(r^2 \sum_{k=1}^{m-1} D_{ik}\frac{\partial c_k}{\partial r}\right) \tag{10-79}
$$

where the elements of the ($m$-1)×($m$-1) dimensional square matrix [$D$] are given by equation (10-69).

Written in terms of the ionic mole fractions, equations (10-79) take the form

$$
\frac{\partial X_i(r,t)}{\partial t} = \frac{1}{r^2}\frac{\partial}{\partial r}\left(r^2 \sum_{k=1}^{m-1} D_{ik,eff}\frac{\partial X_k}{\partial r}\right) \tag{10-80}
$$

where the elements of the ($m$-1)×($m$-1) dimensional square matrix $\left[D_{eff}\right]$ are given by equation (10-74).

At any time $t$, during the transient approach to thermodynamic equilibrium, the spatially averaged concentration within the particle of radius $r_c$ is obtained by integration of the radial loading profile

$$\bar{c}_i(t) = \frac{3}{r_c^3}\int_0^{r_c} c_i(r,t) r^2 dr \tag{10-81}$$

An analytical solution to equation (10-79) is only possible for the special case in which the matrix [$D$], defined by equation (10-69) can be considered constant for the range of concentrations encountered within the particle. In our simulations, we calculate the matrix [$D$] at the spatially averaged value $\bar{x}_i(t)$, i.e. the diffusivity matrix is constantly updated in the time-discretized calculations.

Let us consider a particle that has the uniform concentrations ($c_0$). At time $t = 0$, the external surface is brought into contact with the bulk electrolyte solution with a different composition. The surface concentrations ($c_{r=rc}$) is maintained for the entire duration of the equilibration process; this concentration is dictated by the ion exchange equilibrium (for further details see Wesselingh and Krishna[64]).

The expression for fractional *departure* from equilibrium is given by the matrix equation

$$\left(\bar{c}(t) - c_{r=rc}\right) = [Q]\left(c_0 - c_{r=rc}\right); \quad [Q] \equiv \frac{6}{\pi^2}\sum_{m=1}^{\infty}\frac{1}{m^2}\exp\left[-m^2\pi^2\frac{[D]t}{r_c^2}\right] \tag{10-82}$$

Using time discretization, typically over a few thousand steps, the equation (10-82)can be written as $\left(\bar{c}(t_j)\right) = \left[Q_{j-1}\right]\left(c_0 - c_{r=rc}\right) + c_{r=rc}$ where $\left[Q_{j-1}\right]$ is evaluated using the concentrations at the time step $t_{j-1}$, $\left(c(t_{j-1})\right)$ that are known from the previous time step. The numerical procedure is easily implemented in MathCad 15. The same procedure applies to the determination of the spatial-averaged ionic equivalent fractions, $\left(\overline{X}(t_j)\right)$:

$$\left(\overline{X}(t) - X_{r=rc}\right) = [Q]\left(X_0 - X_{r=rc}\right); \quad [Q] \equiv \frac{6}{\pi^2}\sum_{m=1}^{\infty}\frac{1}{m^2}\exp\left[-m^2\pi^2\frac{\left[D_{eff}\right]t}{r_c^2}\right] \tag{10-83}$$

The accuracy of our methodology for determination of the spatial-averaged concentrations $\left(\overline{X}(t_j)\right)$ was established by comparison with the results of Hwang and Helfferich;[178] see Supporting Information of our earlier paper.[167]

We shall demonstrate the possibility of uphill diffusion and transient overshoots in ionic concentration during transient uptake of ternary counter-ions within cation exchanger particles.

The intra-particle diffusion is described by the 2×2 dimensional square matrix $\left[D_{eff}\right]$ with elements given by equation (10-75) The transient uptake of the three cations is described by a two-dimensional matrix equation (10-83) for the fractional departure from equilibrium; the matrix [$Q$] quantifies the departure from equilibrium. The Sylvester theorem, detailed in Appendix A of Taylor and Krishna,[1] is required for explicit calculation of the elements of [$Q$]. Using time discretization, typically over a few thousand steps, the equation equation (10-83) can be written as $\left(\overline{X}(t_j)\right) = \left[Q_{j-1}\right]\left(X_0 - X_{r=rc}\right) + X_{r=rc}$ where $\left[Q_{j-1}\right]$ is evaluated using the equivalent fractions at the time step $t_{j-1}$: $\left(\overline{X}(t_{j-1})\right)$ that are known from the previous time step.

The experimental data of Yoshida and Kataoka[176] for transient uptake of $H^+$, $Na^+$, and $Zn^{++}$ within DOWEX 50WX10 cation exchangers provide experimental confirmation of intra-particle overshoots and asymmetries in the forward/reverse ion exchanges. The ion exchanger particle is DOWEX 50WX10 with fixed $HSO_3^-$ charges. The cation exchange particle prevents the influx of anions from the bulk electrolyte surrounding the particle. The zero-flux constraint of Equation (10-47) applies to anions. The input data for the ionic diffusivities inside the pores of the ion exchanger are taken from Table III of Yoshida and Kataoka[176] $Đ_1 = 1.65\times10^{-9}$; $Đ_2 = 1.1\times10^{-10}$; $Đ_3 = 9.62\times10^{-12}$ $m^2$ $s^{-1}$. The ion diffusivity of $Zn^{2+}$ is about an order of magnitude lower than that of $H^+$, and $Na^+$.

We simulated two experimental data sets by using the matrix equation (10-83) to quantify the transient uptake of $H^+$, $Na^+$, and $Zn^{++}$. In our simulations we used a particle radius $r_c$ = 0.4 mm, an average value of the sizes reported in Table II of Yoshida and Kataoka.[176]

We first investigate the uptake of $H^+(1)/Na^+(2)/Zn^{2+}(3)$ in IEX particle, as reported in Figure 6 of Yoshida and Kataoka.[176] Initially the particle is loaded with Na+ and is replaced by $H^+/Zn^{2+}$

$$\frac{z_1 c_{1,0}}{c_{fixed}} = 0; \quad \frac{z_2 c_{2,0}}{c_{fixed}} = 1; \quad \frac{z_3 c_{3,0}}{c_{fixed}} = 0; \qquad \text{particle initially loaded with } Na^+$$

The surface of the particle in contact with bulk electrolytes such that the surface ion fractions are maintained at

$$\frac{z_1 c_{1,r=rc}}{c_{fixed}} = 0.; \quad \frac{z_2 c_{2,r=rc}}{c_{fixed}} = 0.0; \qquad \frac{z_2 c_{3,r=rc}}{c_{fixed}} = 0.5$$

The continuous solid lines in Figure 10-37(a) a shos the results of the simulation when the particle is loaded with Na+ and is replaced $H^+/Zn^{++}$. Also shown in Figure 10-37(a) are the experimental data (shown by the symbols) from Figure 6 of Yoshida and Kataoka[176] for this scenario. There is good agreement between the experimental data and the simulated uptakes; the transient overshoot in the uptake of $H^+$ that signals uphill diffusion is properly captured by the simulations.

Next we investigate the uptake of $H^+(1)/Na^+(2)/Zn^{2+}(3)$ in IEX particle, as reported in Figure 9 of Yoshida and Kataoka.[176] Initially the particle is loaded with $H^+/Zn^{2+}$ and is replaced by $Na^+$

$$\frac{z_1 c_{1,0}}{c_{fixed}} = 0.5; \quad \frac{z_2 c_{2,0}}{c_{fixed}} = 0; \quad \frac{z_3 c_{3,0}}{c_{fixed}} = 0.5; \quad \text{particle initially loaded with } H^+/Zn^{2+}$$

The surface of the particle in contact with bulk electrolytes such that the surface ion fractions are maintained at

$$\frac{z_1 c_{1,r=rc}}{c_{fixed}} = 0; \quad \frac{z_2 c_{2,r=rc}}{c_{fixed}} = 1; \qquad \frac{z_2 c_{3,r=rc}}{c_{fixed}} = 0$$

The continuous solid lines in Figure 10-37(b) shows the simulations for the scenario in which the particle is loaded with $H^+/Zn^{++}$ and is replaced $Na^+$. No overshoots or undershoots are experienced in this scenario. Also shown in Figure 10-37(b) are the experimental data in Figure 9 of Yoshida and Kataoka[176] for this scenario; there is good agreement between simulations and experiment. Figure 10-37(c) compares the diffusion equilibration trajectories in composition space. The two scenarios follow completely different paths in composition space.

## 10.26 List of Figures for Diffusion of Ionic Species

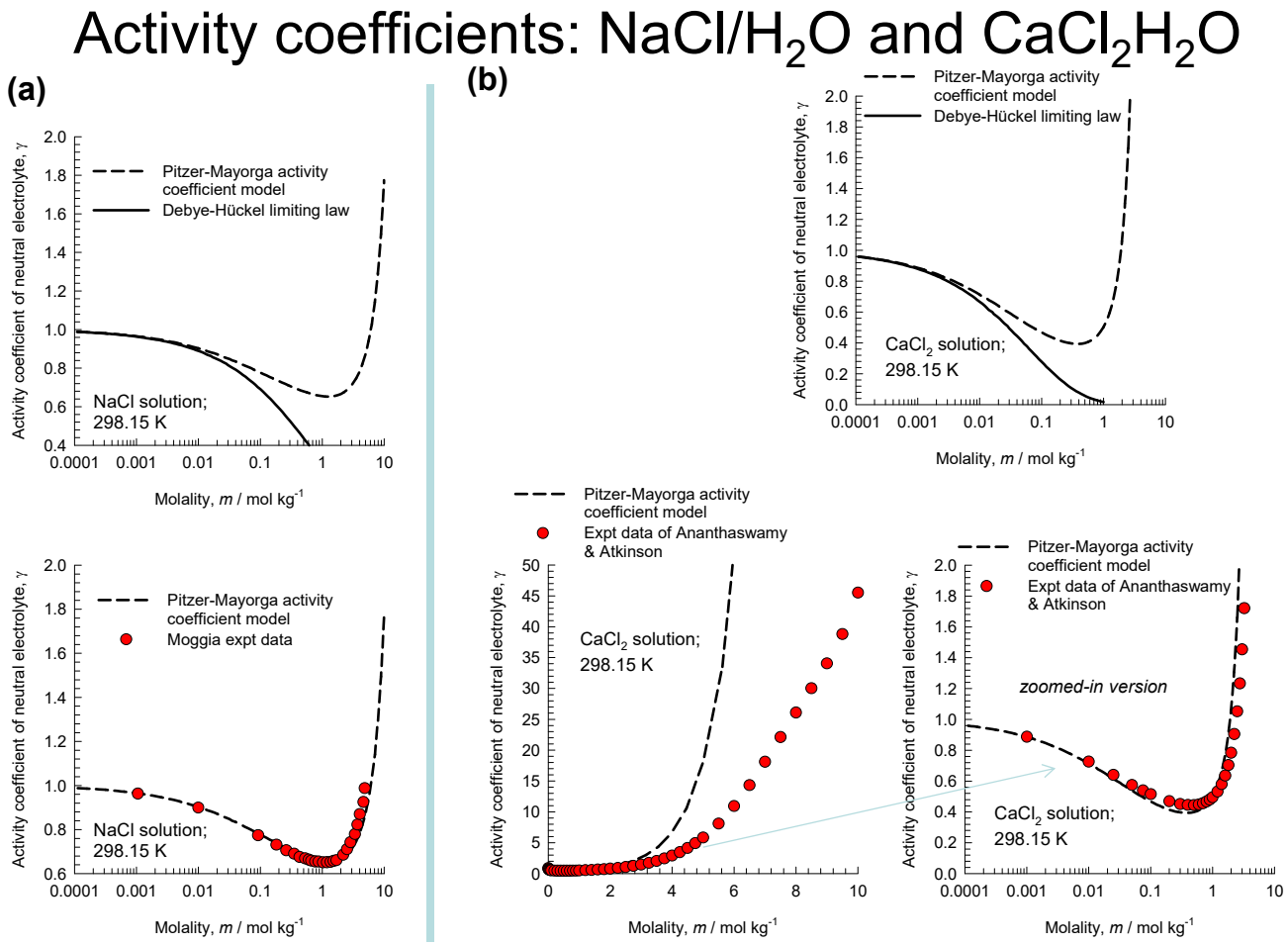


Figure 10-1. (a) Experimental data of Moggia and Bianco[148] on the mean activity coefficient of aqueous solutions of neutral electrolyte NaCl at 298.15 K. (b) Experimental data of Ananthaswamy and Atkinson[150] on the mean activity coefficient of aqueous solutions of neutral electrolyte $CaCl_2$ at 298.15 K. The dashed lines represent the calculations of the Pitzer-Mayorga[149] activity coefficient model.

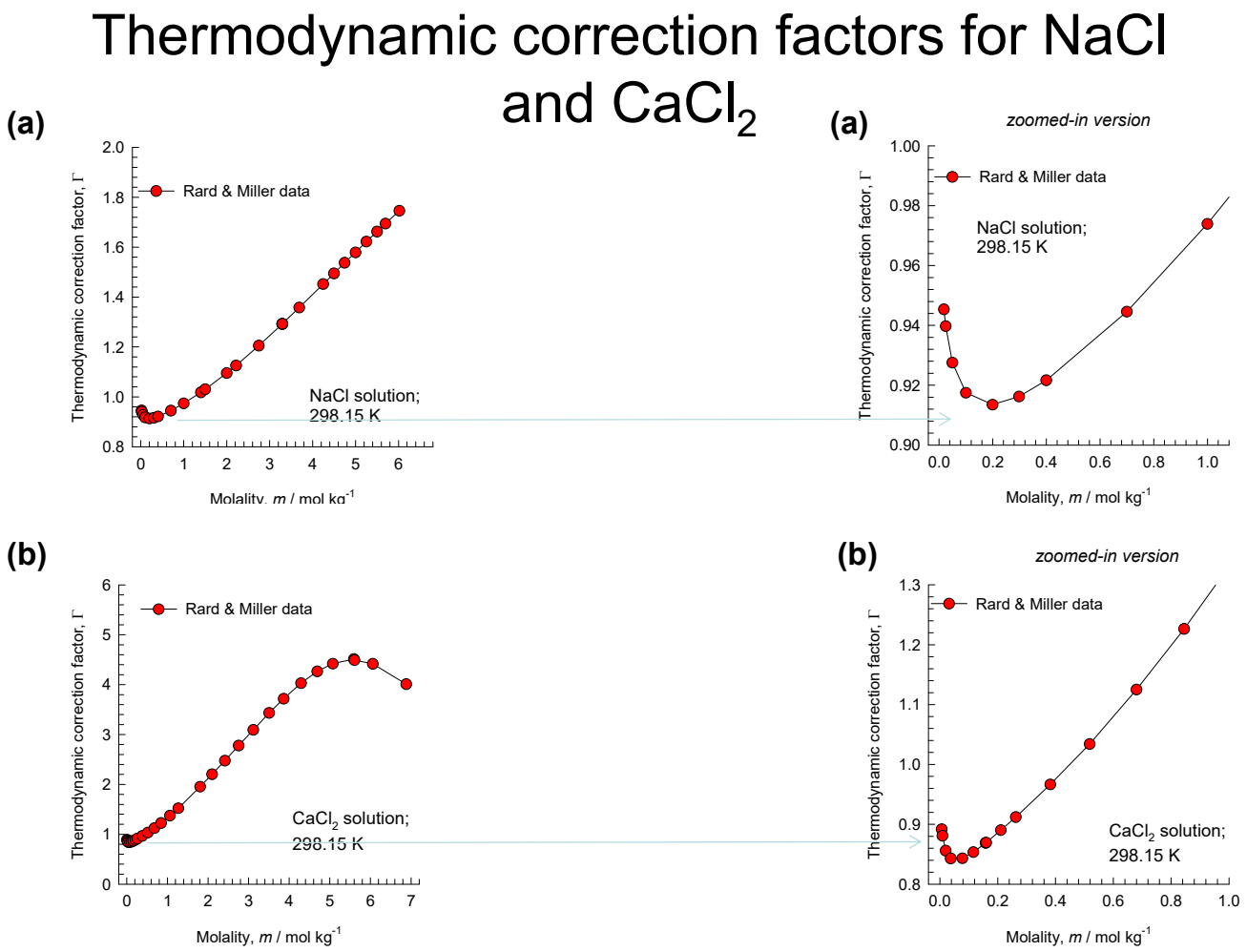


Figure 10-2. (a) Calculations of Rard and Miller[151] for the thermodynamic correction factor Γ for aqueous solutions of neutral electrolyte NaCl at 298.15 K. (b) Calculations of Rard and Miller[151] for the thermodynamic correction factor Γ for aqueous solutions of neutral electrolyte $CaCl_2$ at 298.15 K.

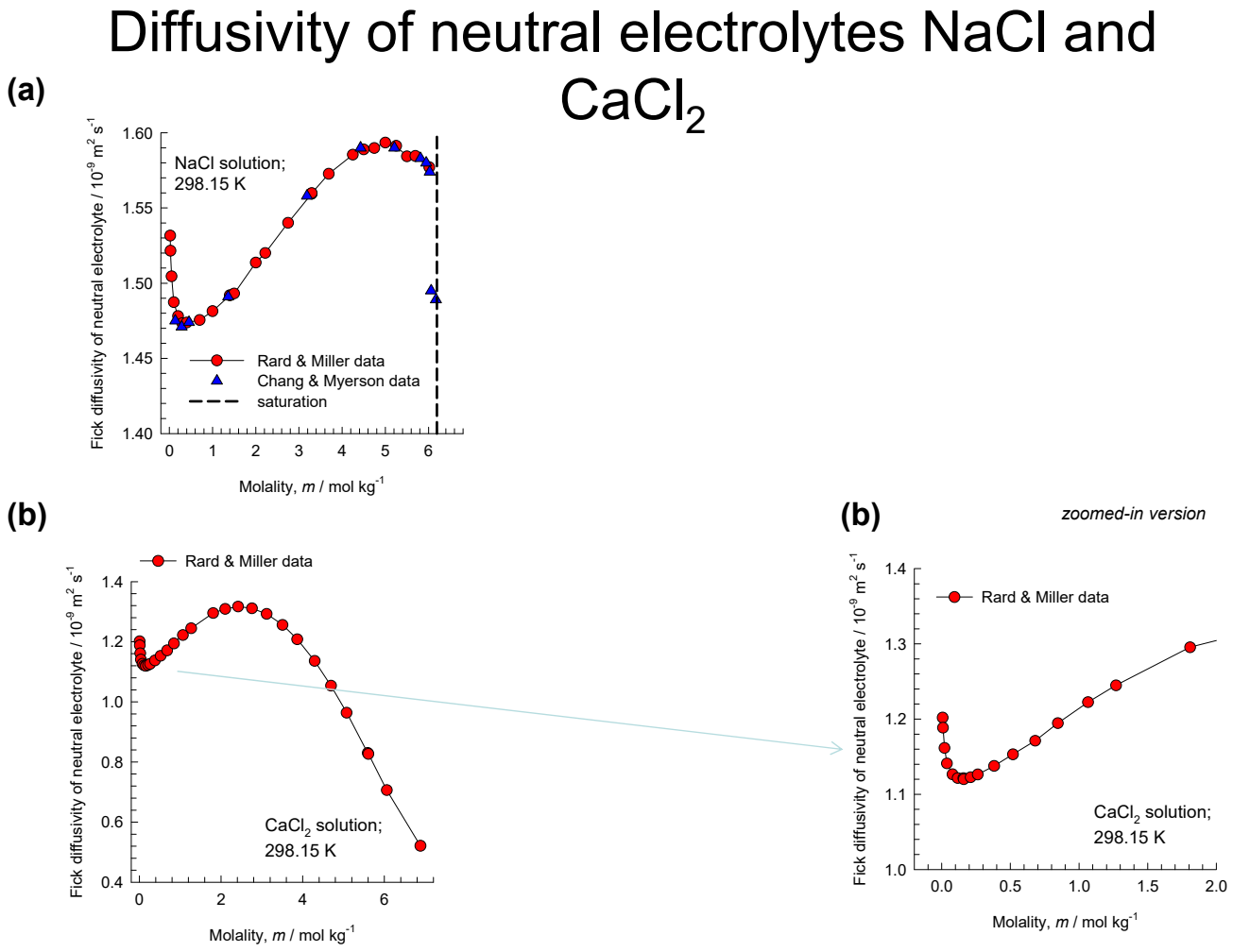


Figure 10-3. (a) Experimental data of Rard and Miller,[151] and Chang and Myerson[152] for Fick diffusivity $D$ of aqueous solutions of neutral electrolyte NaCl at 298.15 K. (b) Experimental data of Rard and Miller,[151] for Fick diffusivity $D$ of aqueous solutions of neutral electrolyte $CaCl_2$ at 298.15 K.

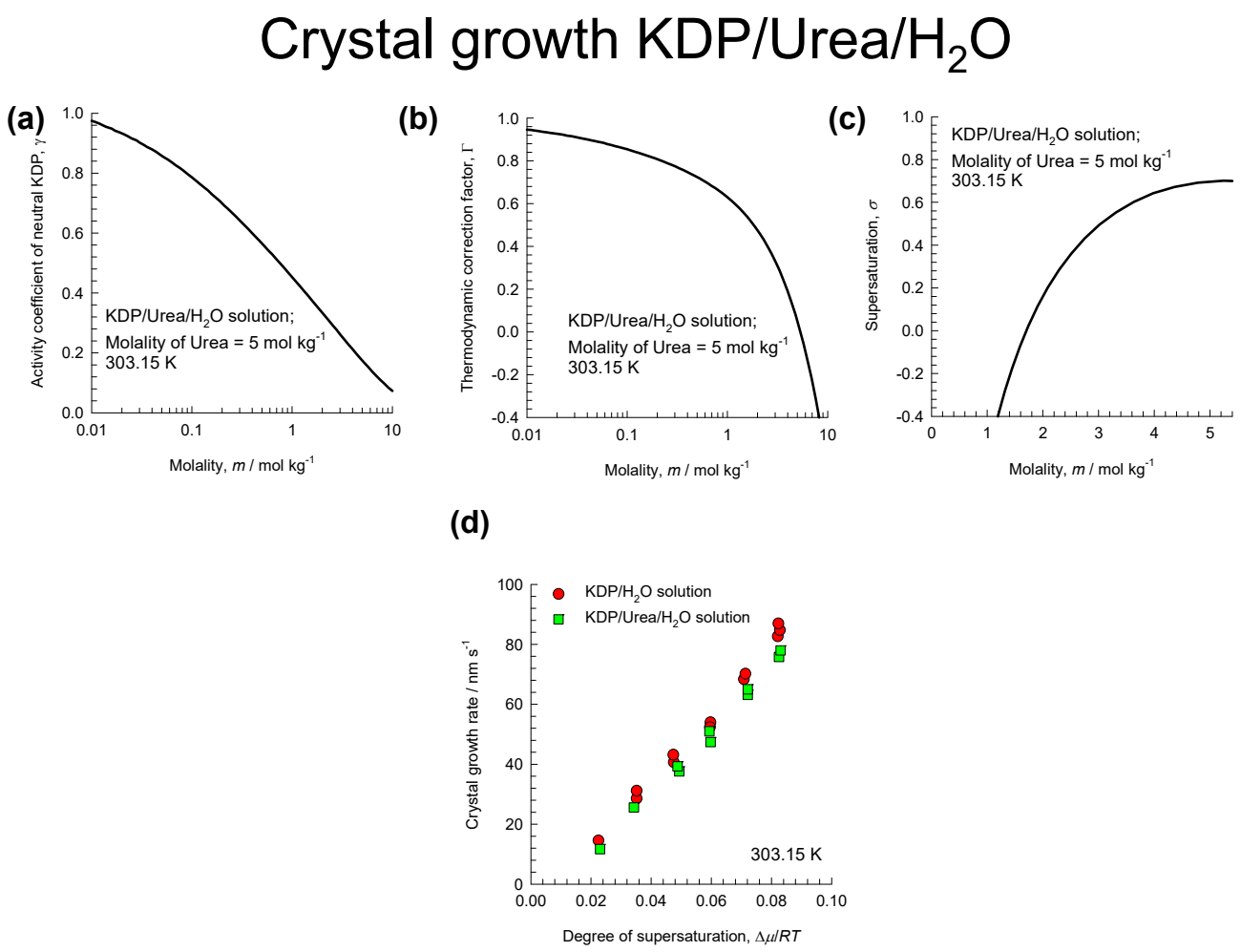


Figure 10-4. (a, b, c) Thermodynamics for KDP/Urea/$H_2O$ system at 303.15 K, calculated using the parameters provided by Enqvist et al.[155] The molality of urea is maintained constant at 5 mol $kg^{-1}$. (a) Activity coefficient, $\gamma$, of KDP. (b) Thermodynamic correction factor, $\Gamma$. (c) Supersaturation, activity based $\sigma$, as a function of the molality of KDP in solution. (d) Experimental data of Enqvist et al.[155] on growth rate of KDP crystals as a function of the supersaturation, $\sigma$.

# Thermodynamic correction factors for $Na_2SO_4/K_2SO_4/H2O$

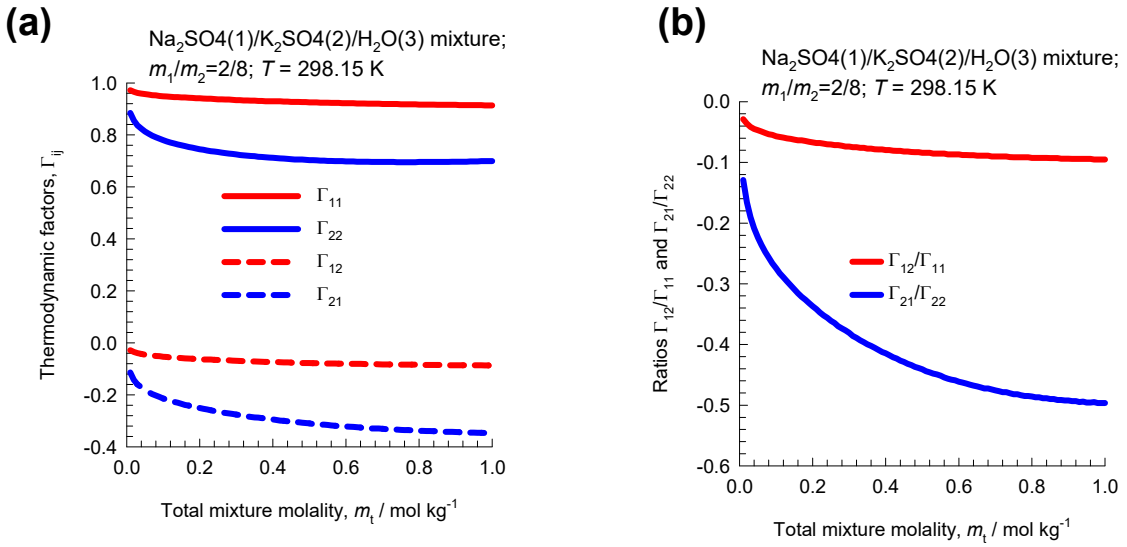


Figure 10-5. (a) Calculations of the elements of the the 2-dimensional matrix of thermodynamic factors, $[\Gamma]$, $Na_2SO_4(1)/K_2SO_4(2)/H_2O(3)$ mixtures at 298.15 K. The ratio of the molalities, $m_1/m_2$, of $Na_2SO_4(1)$ and $K_2SO_4(2)$ is held constant at the value of 0.25. (b) Ratio of the elements $\frac{\Gamma_{12}}{\Gamma_{11}}$ and $\frac{\Gamma_{21}}{\Gamma_{22}}$. The input data for the calculations are provided in the by paper by Louhi-Kultanen et al.[153]

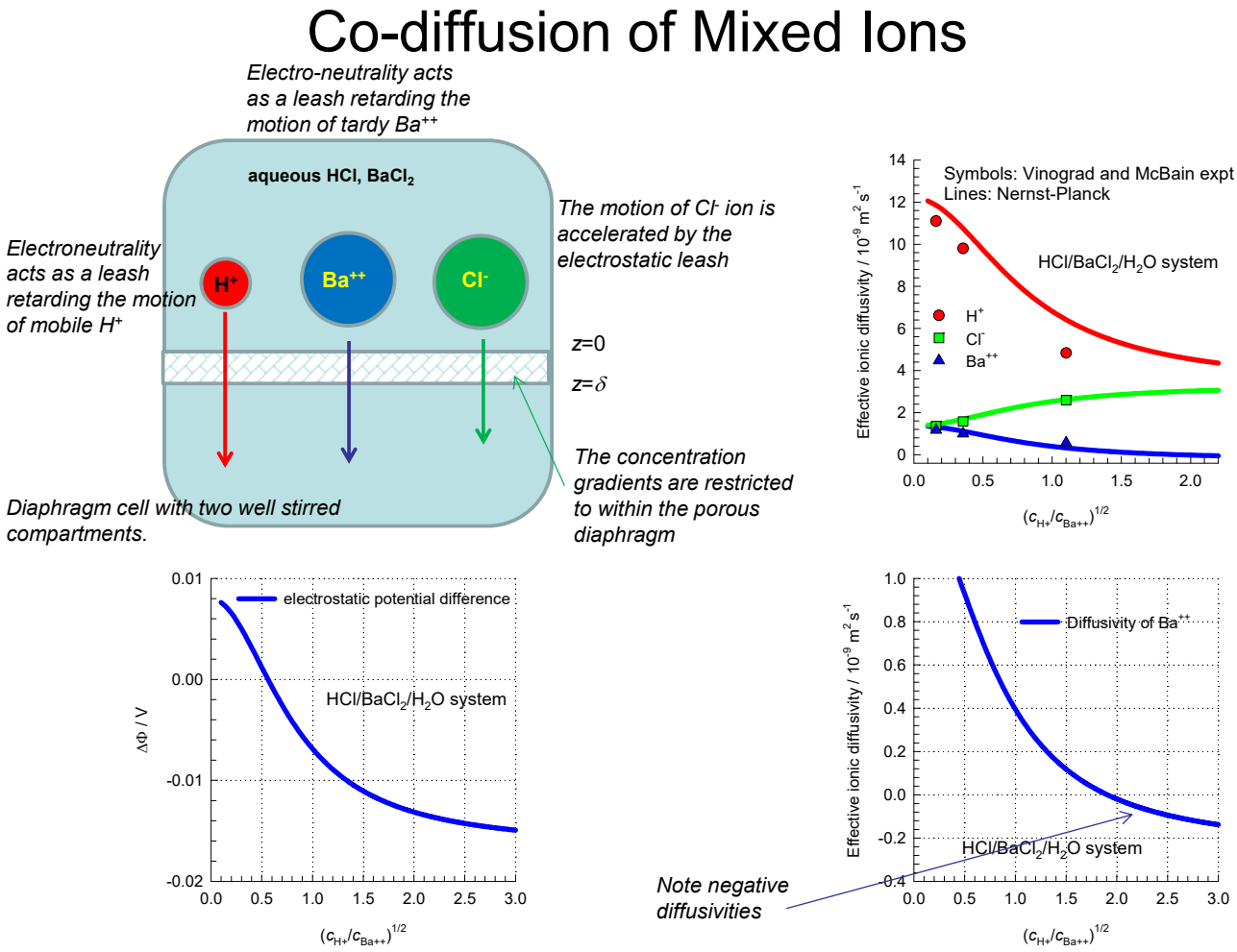


Figure 10-6. Co-diffusion of $H^+$, $Ba^{++}$, and $Cl^-$ between two well-mixed compartments. Experimental data of Vinograd and McBain[157] for ionic diffusivities of $H^+$, $Ba^{++}$, and $Cl^-$ in a two-compartment diffusion cell. The continuous solid lines are the simulations based on the Nernst-Planck equations.

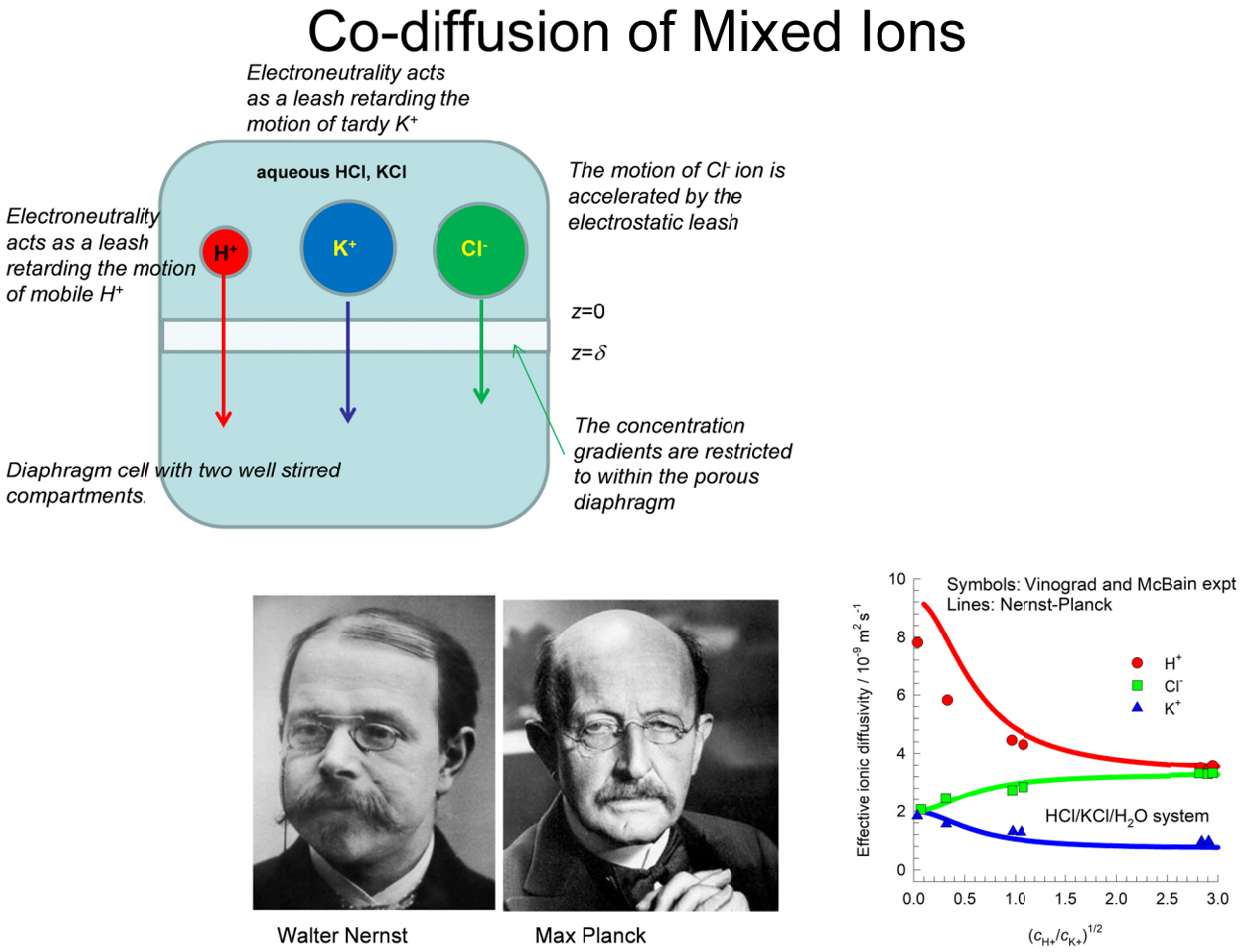


Figure 10-7. Co-diffusion of $H^+$, $K^+$, and $Cl^-$ between two well-mixed compartments. Experimental data of Vinograd and McBain[157] for ionic diffusivities of $H^+$, $K^+$, and $Cl^-$ in a two-compartment diffusion cell. The continuous solid lines are the calculations using the Nernst-Planck equations.

# Inter-diffusion HCl(1)/$CaCl_2$(2)/$H_2O$(3)

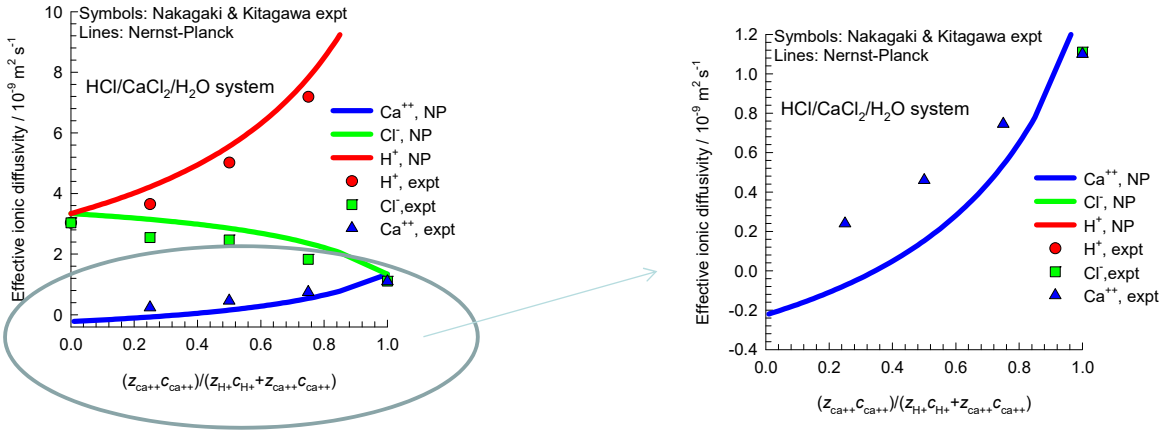


Figure 10-8. Experimental data (symbols) for effective ionic diffusivities of $H^+$, $Ca^{++}$, and $Cl^-$ in HCl/$CaCl_2$/$H_2O$ aqueous solutions, scanned from Figure 7 of the paper of Nakagaki and Kitagawa[158]. The *x*-axis is the ratio $\frac{z_{Ca++}c_{Ca++}}{z_{H+}c_{H+}+z_{Ca++}c_{Ca++}}$ under conditions that the total cation concentration is constant in the diffusion layer. The continuous solid lines are the calculations using the Nernst-Planck equations.

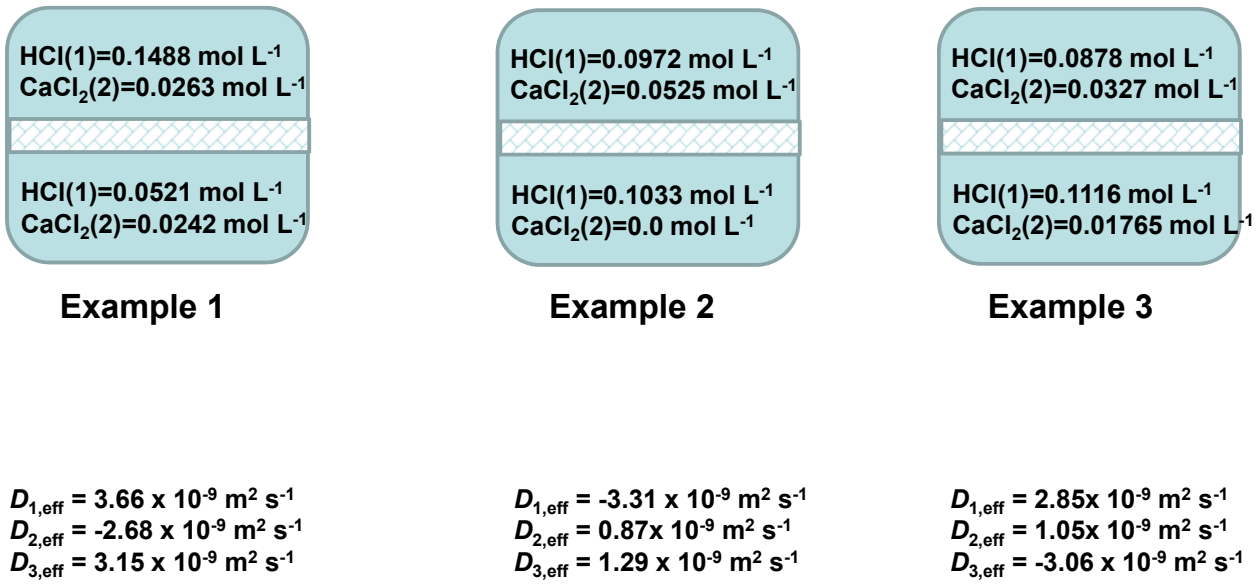


Figure 10-9. Experimental data for effective ionic diffusivities of $H^+$, $Ca^{++}$, and $Cl^-$ in $HCl/CaCl_2/H_2O$ aqueous solutions, reported in Table 3 of the paper of Nakagaki and Kitagawa[158] for three different sets (Examples 1, 2, and 3) of initial molar concentrations of the two electrolytes in the top and bottom compartments are as specified.

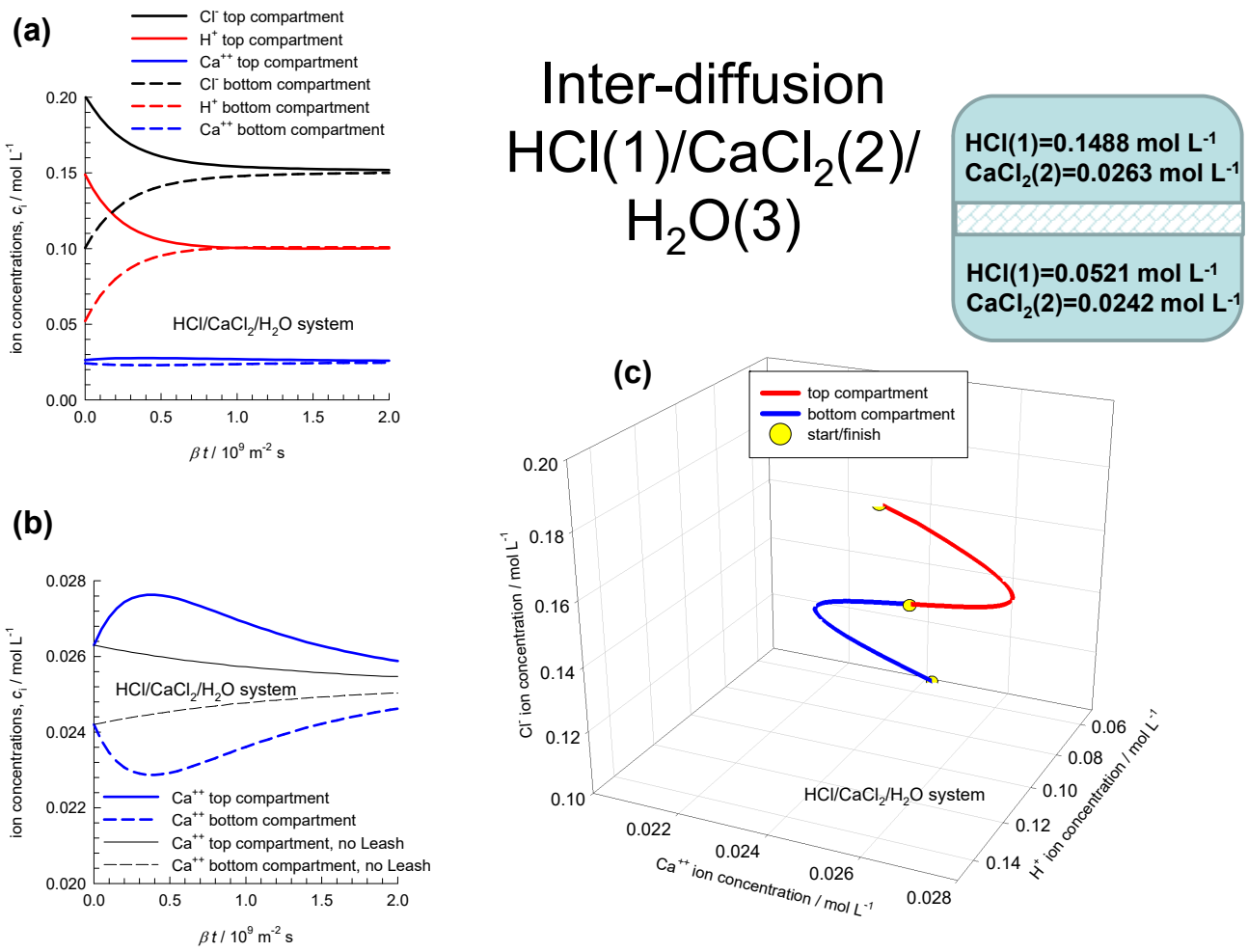


Figure 10-10. Inter-diffusion of $HCl(1)/CaCl_2(2)/H_2O$ between top and bottom, well-stirred compartments separated by a diaphragm. The initial molar concentrations of the two electrolytes in the top and bottom compartments correspond to Example 1 in Table 3 of Nakagaki and Kitagawa.[158] (a, b) Transient approach to equilibrium of the concentrations of $H^+$, $Ca^{++}$, and $Cl^-$ in the top and bottom compartments. (c) The equilibration trajectory plotted in concentration space.

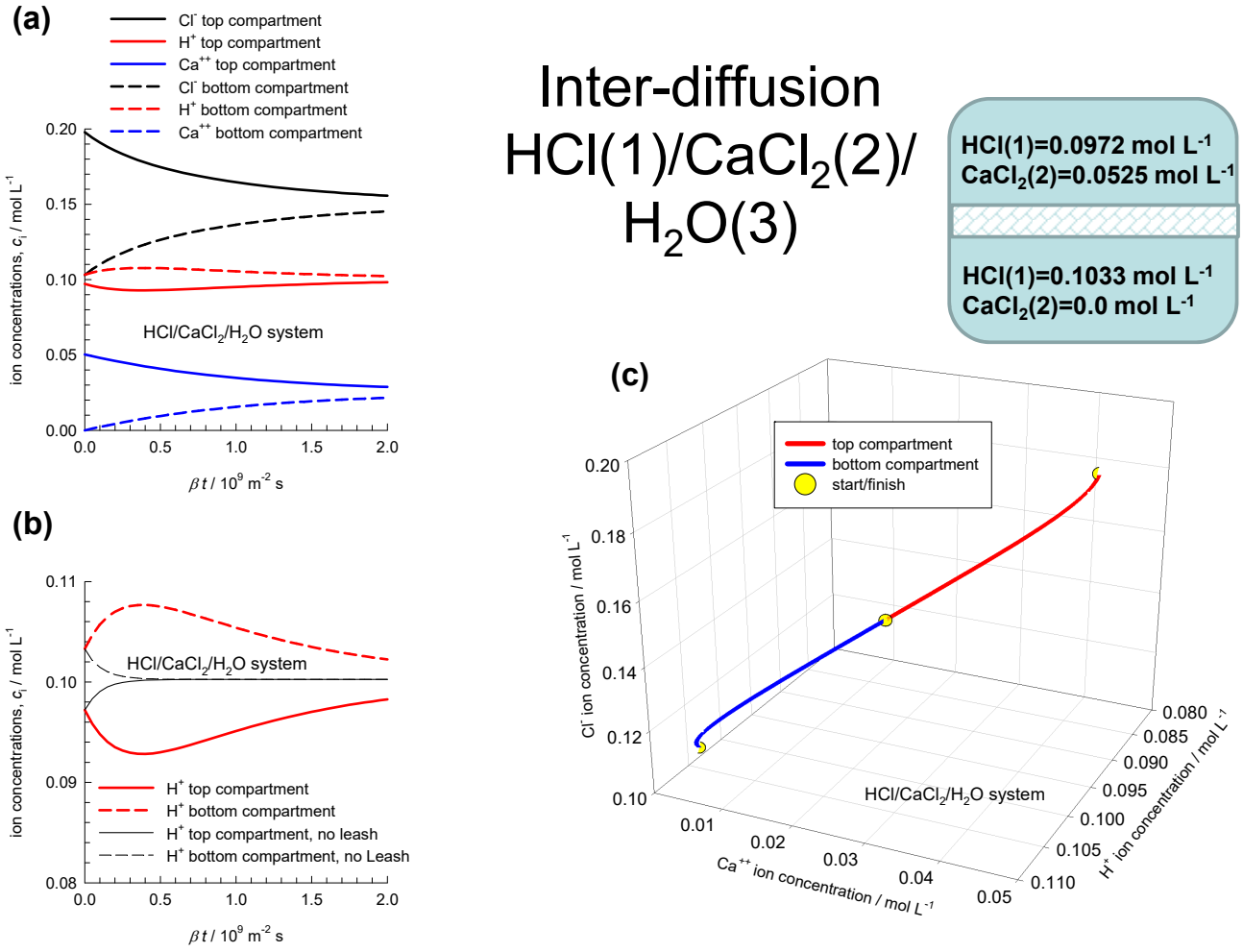


Figure 10-11. Inter-diffusion of $HCl(1)/CaCl_2(2)/H_2O$ between top and bottom, well-stirred compartments separated by a diaphragm. The initial molar concentrations of the two electrolytes in the top and bottom compartments correspond to Example 2 in Table 3 of Nakagaki and Kitagawa.[158] (a, b) Transient approach to equilibrium of the concentrations of $H^+$, $Ca^{++}$, and $Cl^-$ in the top and bottom compartments. (c) The equilibration trajectory plotted in concentration space.

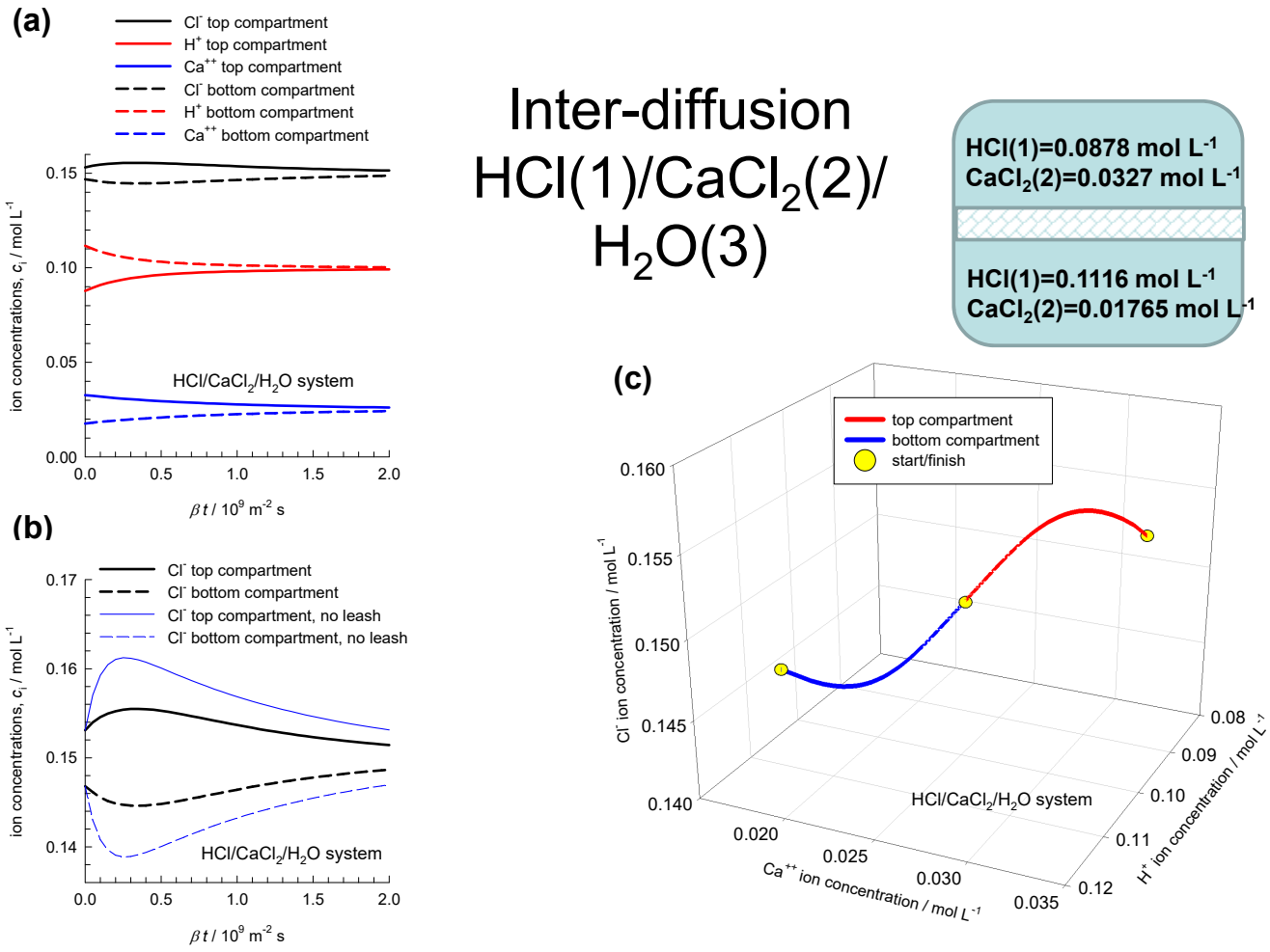


Figure 10-12. Inter-diffusion of HCl(1)/$CaCl_2$(2)/$H_2O$ between top and bottom, well-stirred compartments separated by a diaphragm. The initial molar concentrations of the two electrolytes in the top and bottom compartments correspond to Example 3 in Table 3 of Nakagaki and Kitagawa.[158] (a, b) Transient approach to equilibrium of the concentrations of $H^+$, $Ca^{++}$, and $Cl^-$ in the top and bottom compartments. (c) The equilibration trajectory plotted in concentration space.

# Fick [*D*] NaCl/$Na_2SO_4$/Water solution

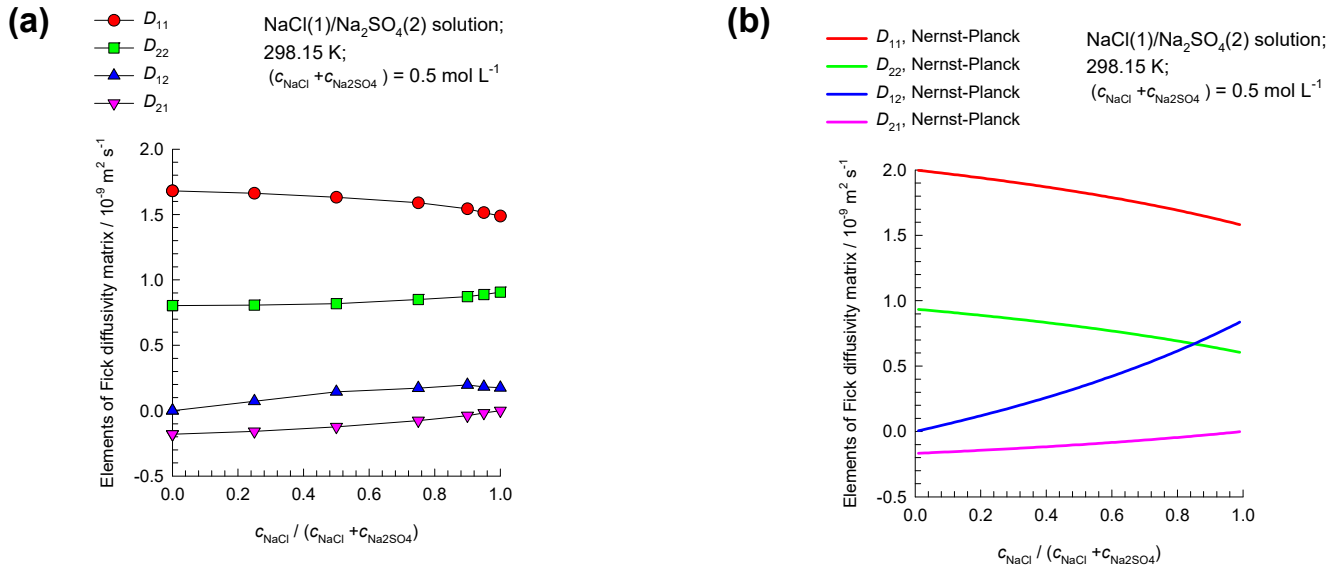


Figure 10-13. (a) Experimental data of Rard et al.[159] for elements of the Fick diffusivity matrix, [*D*], in the solvent fixed reference frame, for the mixture of aqueous electrolytes NaCl (1), and $Na_2SO_4$ (2) at 298.15 K. The total molar concentration of the mixture $c_{NaCl}+c_{Na2SO4}$= 0.5 mol $L^{-1}$. The *x*-axis represents the fraction $c_{NaCl}/(c_{NaCl}+c_{Na2SO4})$. (b) Calculations of the elements of the Fick diffusivity matrix [*D*] using the Nernst-Planck equations for dilute solutions.

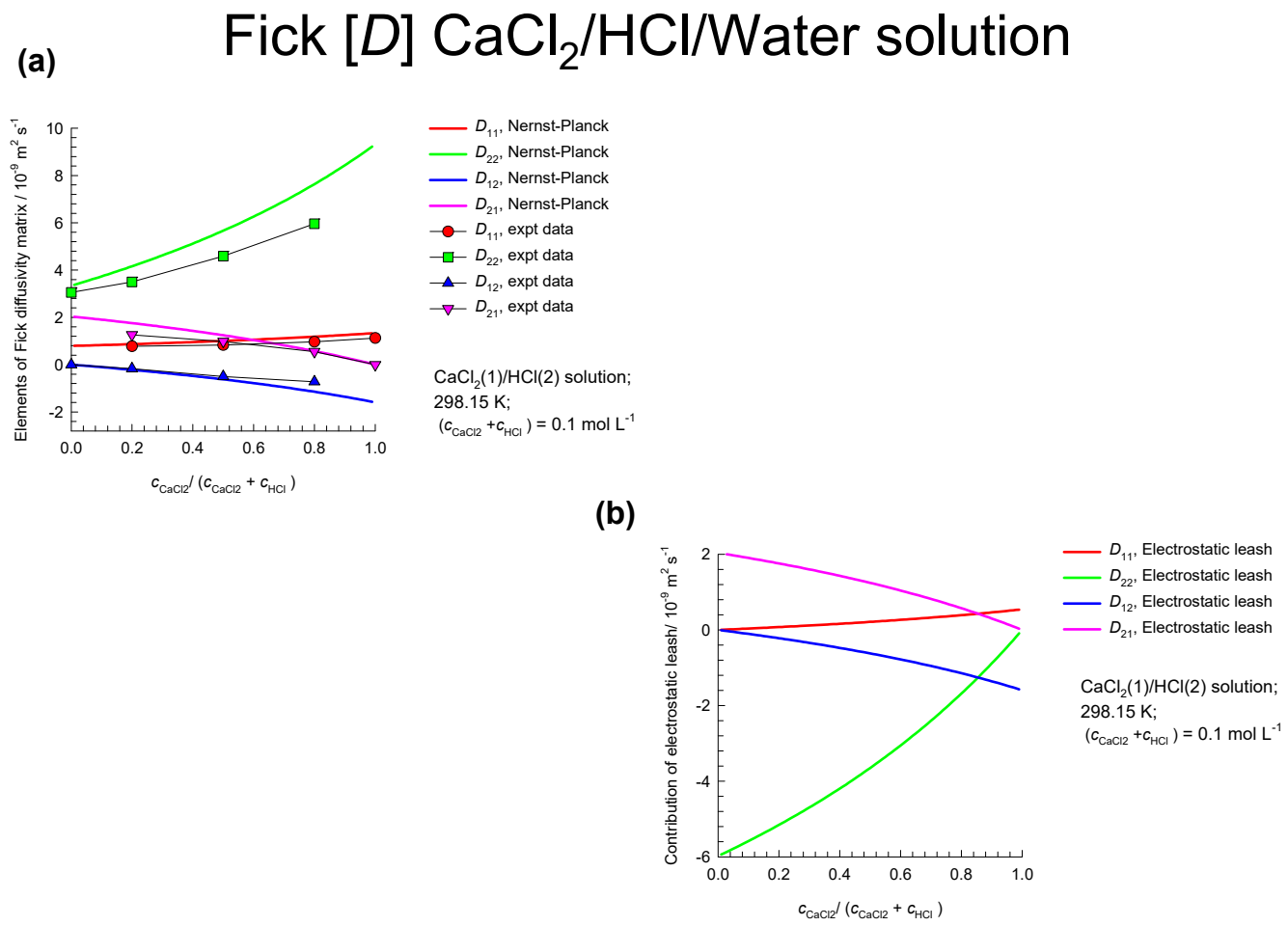


Figure 10-14. (a) Experimental data (symbols), taken from Table 1 of Leaist and Curtis,[160] for the elements of the Fick diffusivity matrix [$D$] for the mixture of aqueous electrolytes $CaCl_2$ (1), and HCl (2) at 298.15 K. The continuous solid lines are the estimations using the Nernst-Planck equations. The total molar concentration of the mixture $c_{CaCl2} + c_{HCl} = 0.1$ mol $L^{-1}$. The $x$-axis represents the fraction $c_{CaCl2}/(c_{CaCl2} + c_{HCl})$. (b) Contributions of the electrostatic leash to each of the four elements of [$D$].

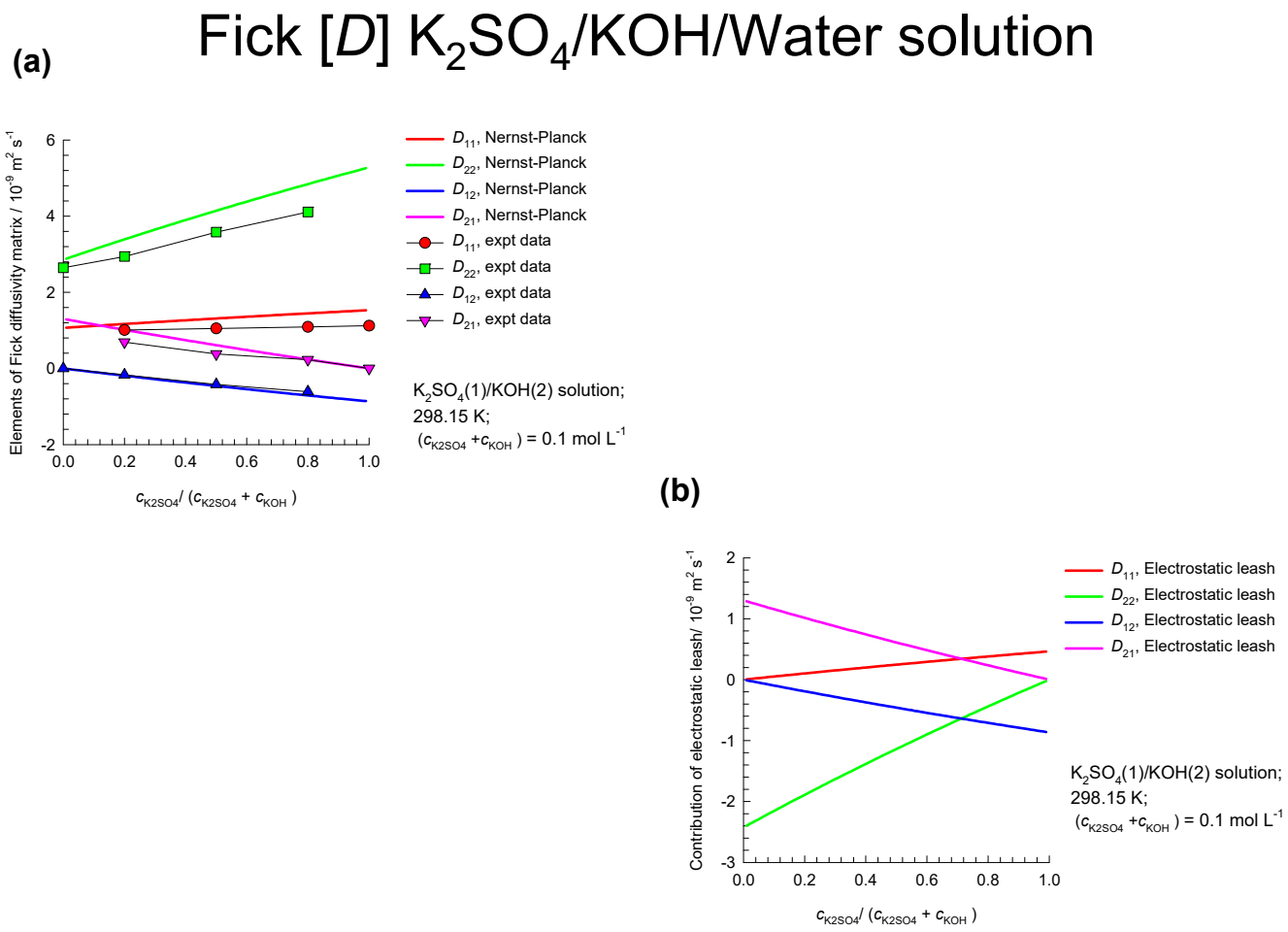


Figure 10-15. (a) Experimental data (symbols), taken from Table 1 of Leaist and Curtis,[160] for the elements of the Fick diffusivity matrix [*D*] for the mixture of aqueous electrolytes $K_2SO_4$ (1), and KOH (2) at 298.15 K. The continuous solid lines are the simulations using the Nernst-Planck equations. The total molar concentration of the mixture $c_{K2SO4} + c_{KOH}$ = 0.1 mol $L^{-1}$. The *x*-axis represents the fraction $c_{K2SO4}/(c_{K2SO4} + c_{KOH})$. (b) Contributions of the electrostatic leash to each of the four elements of [*D*].

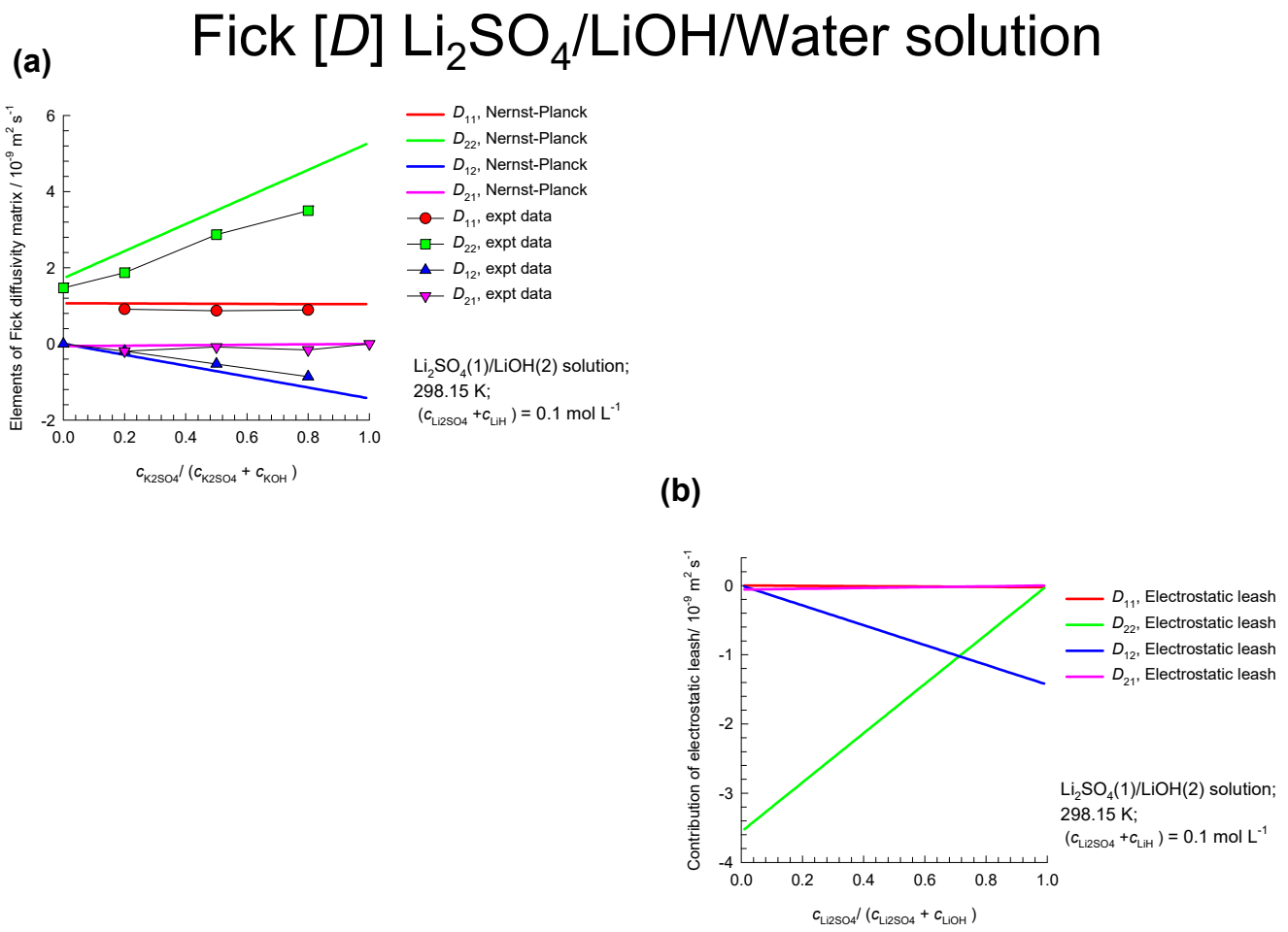


Figure 10-16. (a) Experimental data (symbols), taken from Table 1 of Leaist and Curtis,[160] for the elements of the Fick diffusivity matrix [$D$] for the mixture of aqueous electrolytes $Li_2SO_4$ (1), and LiOH (2) at 298.15 K. The continuous solid lines are the estimations using the Nernst-Planck equations. The total molar concentration of the mixture $c_{Li2SO4} + c_{LiOH} = 0.1$ mol $L^{-1}$. The $x$-axis represents the fraction $c_{Li2SO4}/(c_{Li2SO4} + c_{LiOH})$. (b) Contributions of the electrostatic leash to each of the four elements of [$D$].

# Fick [$D$] NaCl/$MgCl_2$/Water solution

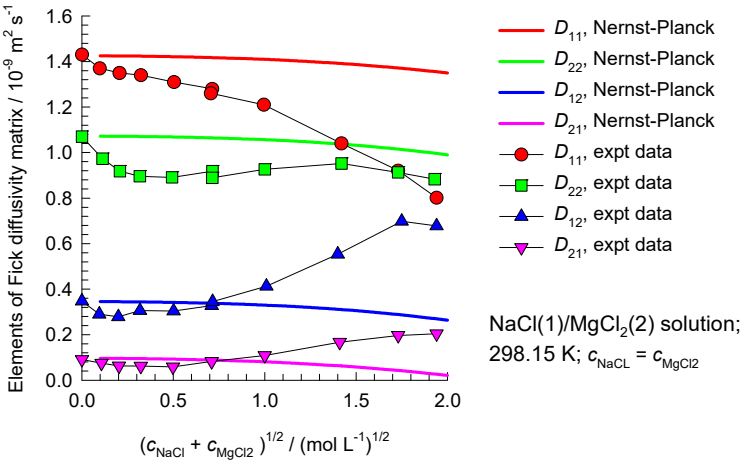


Figure 10-17. Experimental data (symbols), scanned from Figure 2 of Leaist and Al-Dhaher[161] for the elements of the Fick diffusivity matrix [$D^{V}$], in the volume-averaged reference velocity frame, for equimolar mixture of aqueous electrolytes NaCl (1), and $MgCl_2$ (2) at 298.15 K. The continuous solid lines are the estimations based on the Nernst-Planck equations. The $x$-axis represents the square root of the total mixture concentration $\sqrt{c_{NaCl} + c_{MgCl2}}$ .

# Fick [*D*] NaCl/$SrCl_2$/Water solution

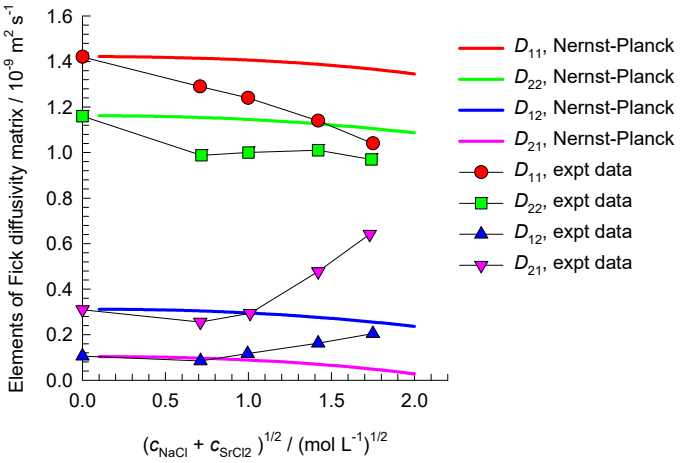


Figure 10-18. Experimental data (symbols), scanned from Figure 7 of Leaist and Al-Dhaher[161] for the elements of the Fick diffusivity matrix [$D^V$], in the volume-averaged reference velocity frame, for equimolar mixture of aqueous electrolytes NaCl (1), and $SrCl_2$ (2) at 298.15 K. The continuous solid lines are the estimations using the Nernst-Planck equations. The *x*-axis represents the square root of the total mixture concentration $\sqrt{c_{NaCl} + c_{SrCl2}}$ . It is to be noted that the labels $D_{12}$ and $D_{21}$ appear to have been interchanged in Figure 7 of Leaist and Al-Dhaher.[161]

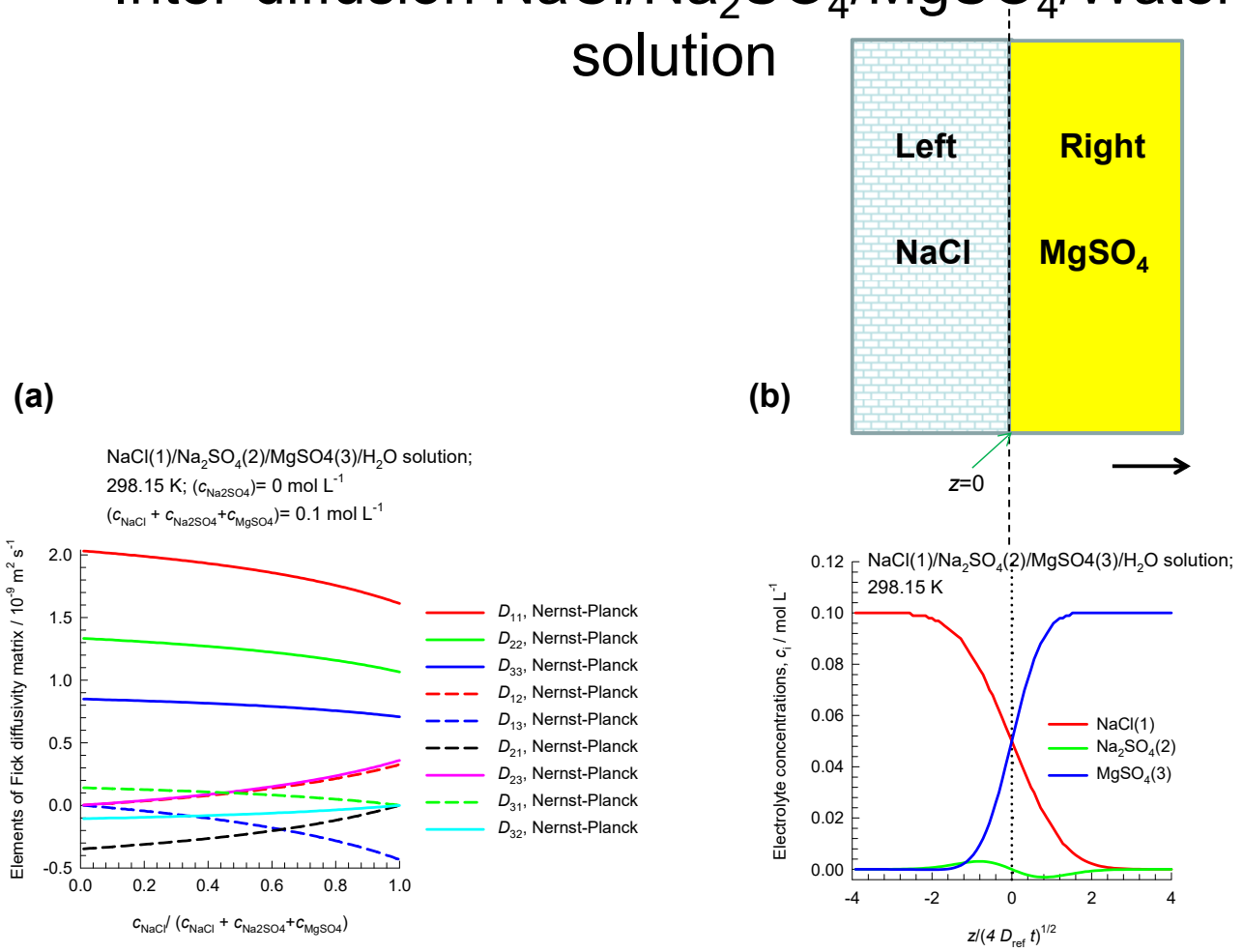


Figure 10-19. (a) Calculations of the elements of the 3×3 dimensional Fick diffusivity matrix for the ternary electrolyte NaCl(1)/$Na_2SO_4$(2)/$MgSO_4$(3) system in the solvent (water) fixed reference frame. (b) Transient inter-diffusion in NaCl(1)/$Na_2SO_4$(2)/$MgSO_4$(3) mixtures between two slabs (L and R). The reference diffusivity $D_{ref} = 10^{-9}$ m$^2$ s$^{-1}$.

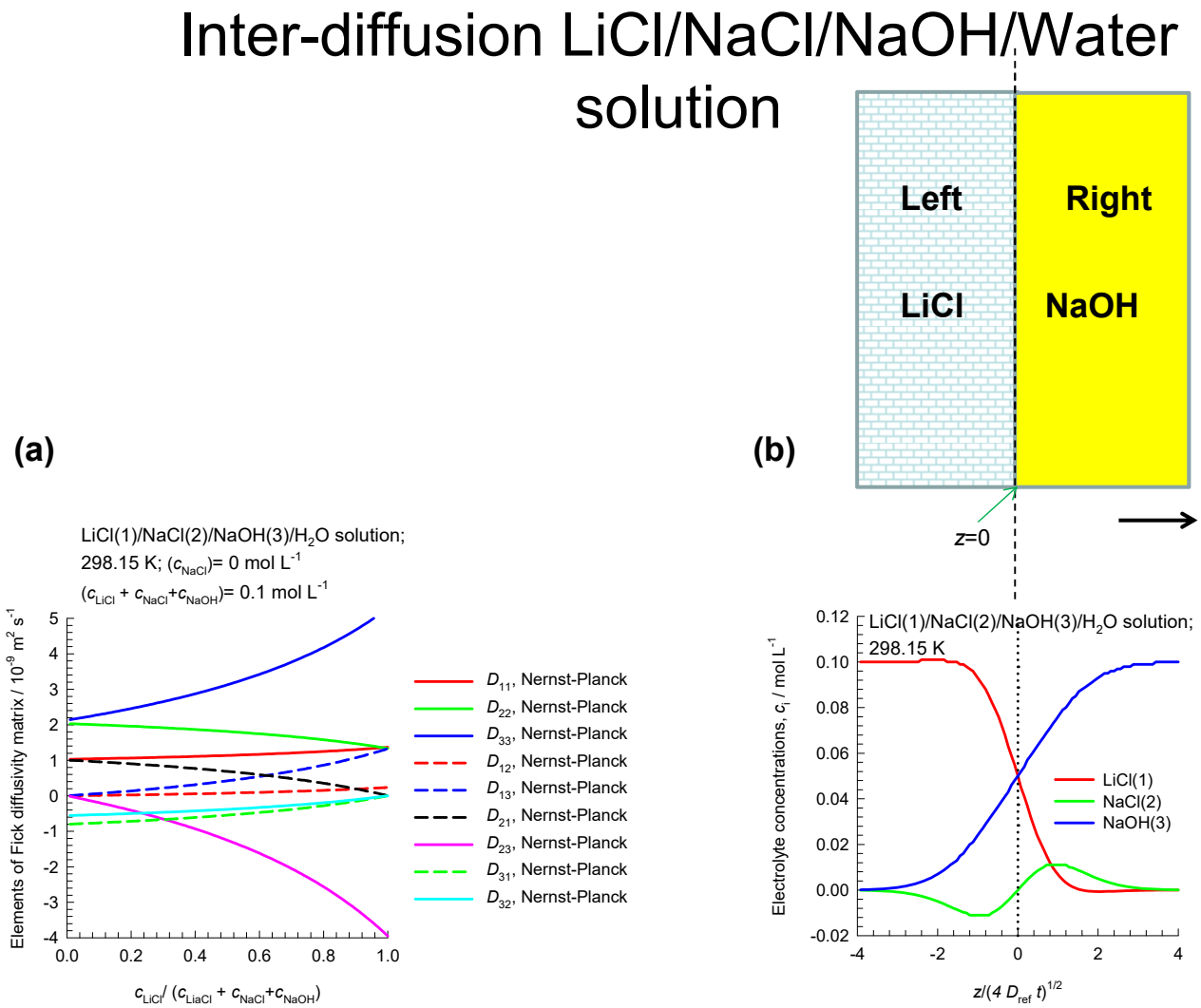


Figure 10-20. (a) Calculations of the elements of the 3×3 dimensional Fick diffusivity matrix for the ternary electrolyte LiCl(1)/NaCl(2)/NaOH(3) system in the solvent (water) fixed reference frame. (b) Transient inter-diffusion in LiCl(1)/NaCl(2)/NaOH(3) mixtures between two slabs (L and R). The reference diffusivity $D_{ref} = 10^{-9}$ m$^2$ s$^{-1}$.

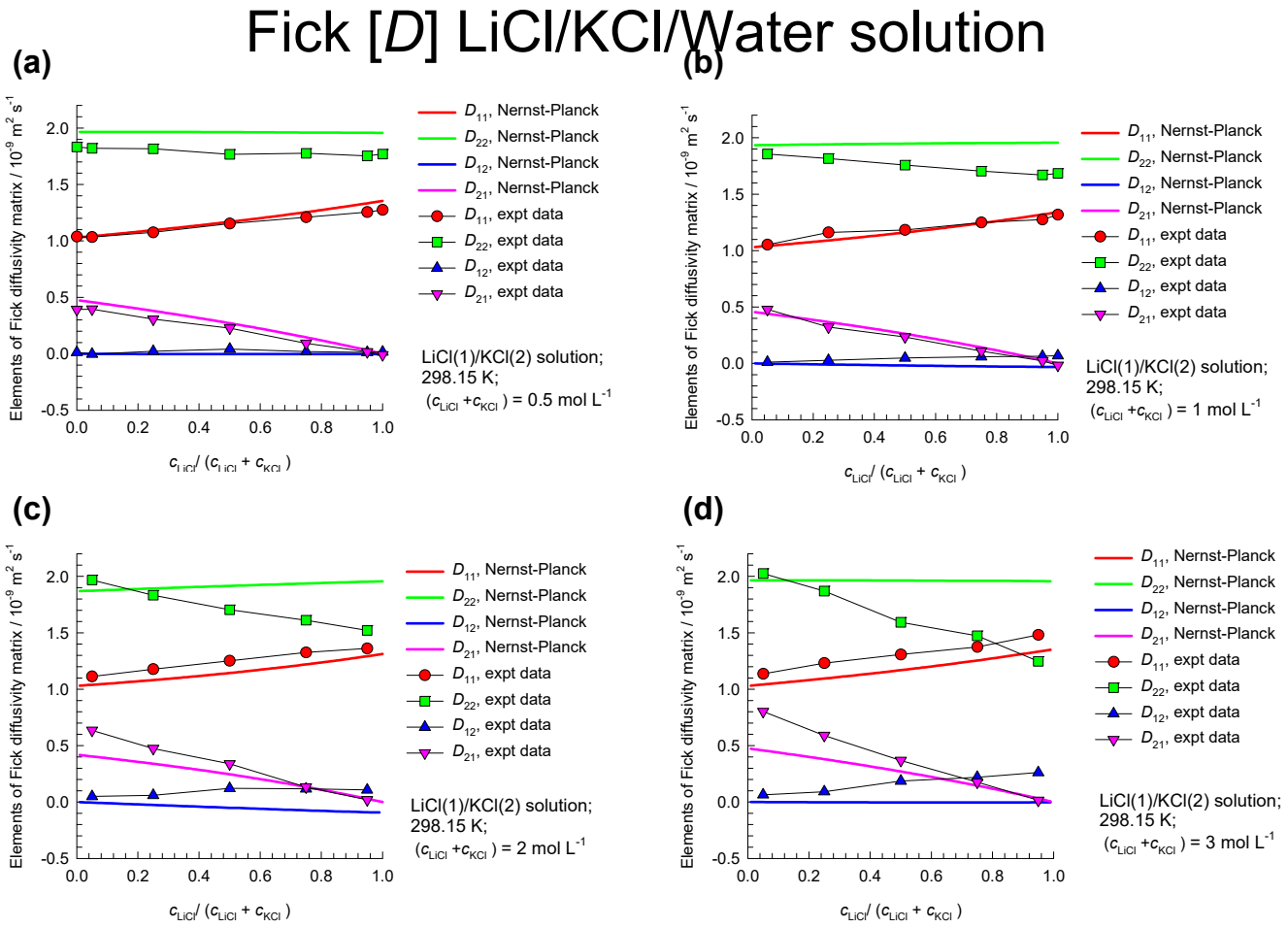


Figure 10-21. (a, b, c, d) Experimental data, as reported in Table 3 of Leaist and Kanakos[163] for the elements of the Fick diffusivity matrix [$D^{V}$], in the volume-averaged reference velocity frame, for mixtures of aqueous electrolytes LiCl (1), and KCl (2) at 298.15 K. The continuous solid lines are the estimations using the Nernst-Planck equations. The total molar concentration of the mixture $c_{LiCl}+c_{KCl}$ is (a) 0.5 mol $L^{-1}$, (b) 1 mol $L^{-1}$, (c) 2 mol $L^{-1}$, (d) 3 mol $L^{-1}$, The *x*-axis represents the fraction $c_{LiCl}/(c_{LiCl}+c_{KCl})$.

# Taylor dispersion LiCl/KCl/Water solution

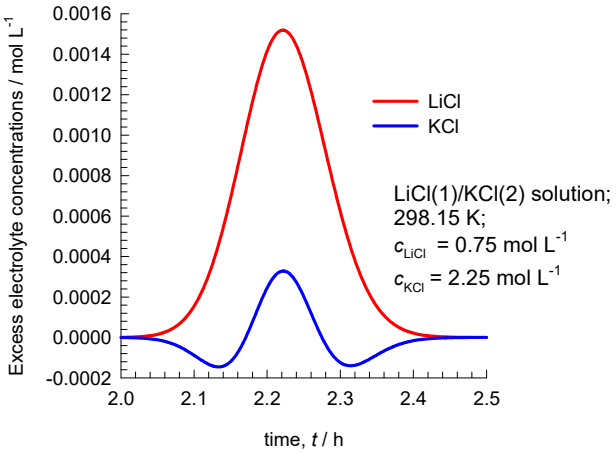


Figure 10-22. Taylor dispersion characteristics for the mixture of aqueous electrolytes LiCl (1), and KCl (2) at 298.15 K.

# Fick [*D*] HCl/NaOHWater solution

## (a) Nernst-Planck estimations

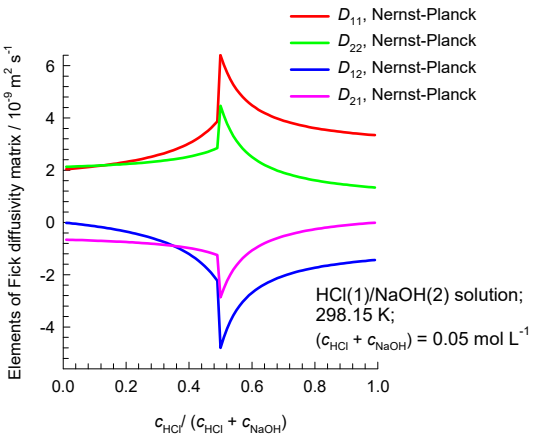


## (b) Calculations including activity coefficients

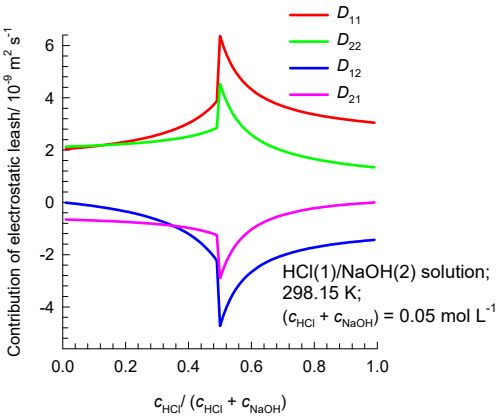


Figure 10-23. (a) Estimations using the Nernst-Planck equationsof the elements of the Fick diffusivity matrix [*D*] for the mixture of aqueous electrolytes HCl (1), and NaOH (2) at 298.15 K. T The total molar concentration of the mixture $c_{HCl} + c_{NaOH}$ = 0.05 mol L$^{-1}$. The *x*-axis represents the fraction $c_{HCl}/(c_{HCl} + c_{NaOH})$. (b) Elements of the Fick diffusivity matrix [*D*] including the influence of thermodynamic non-idealities, following the procedure as outlined in the Appendix to the paper by Leaist and Wiens.[165]

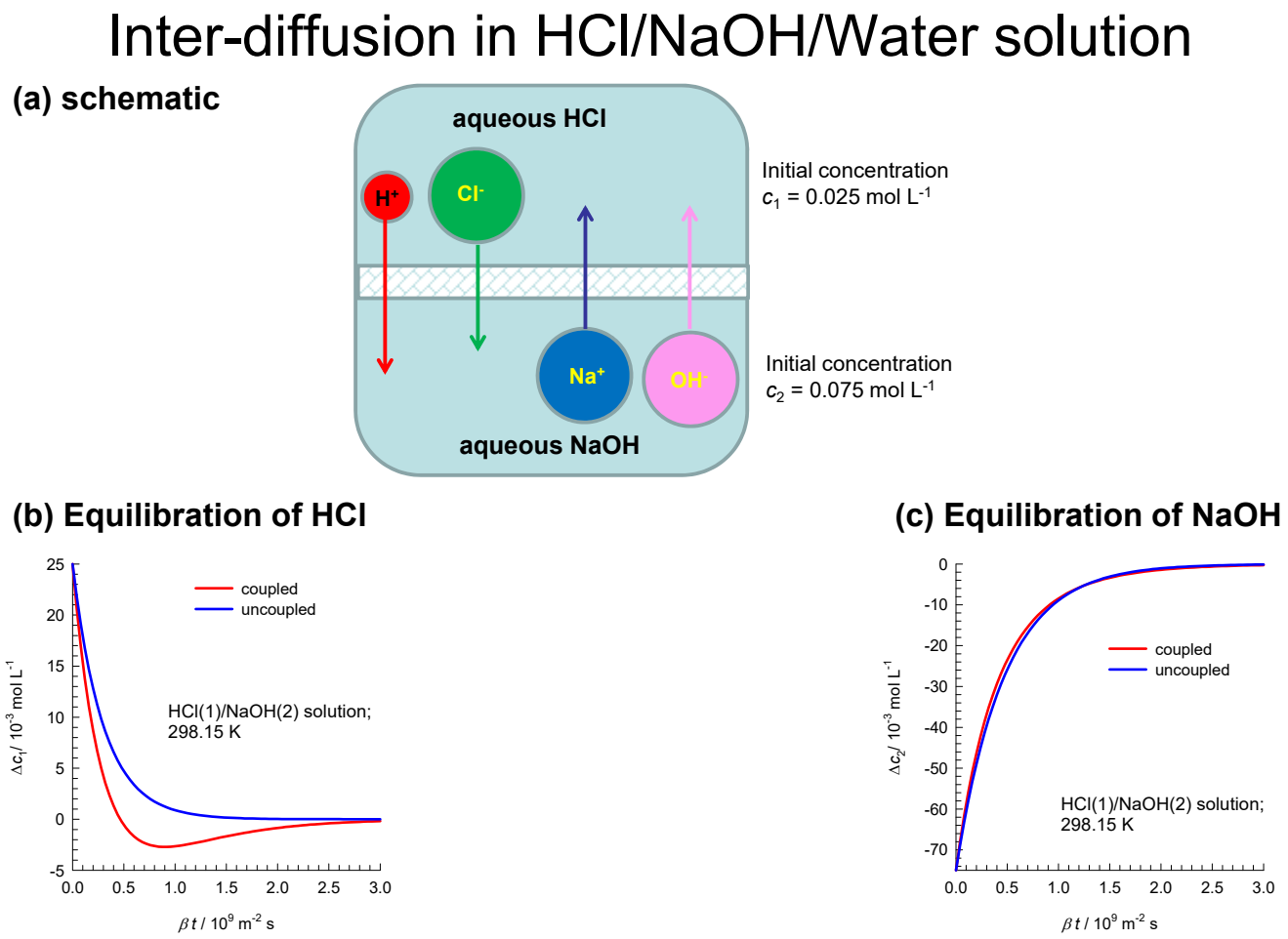


Figure 10-24. (a) Schematic showing the inter-diffusion of HCl (1), and NaOH (2) at 298.15 K between upper and lower compartments of a diaphragm cell, as discussed in the paper by Leaist and Wiens.[165] (b, c) Transient equilibration in the molar concentrations of HCl (1), and NaOH (2) in the upper and lower compartments, respectively.

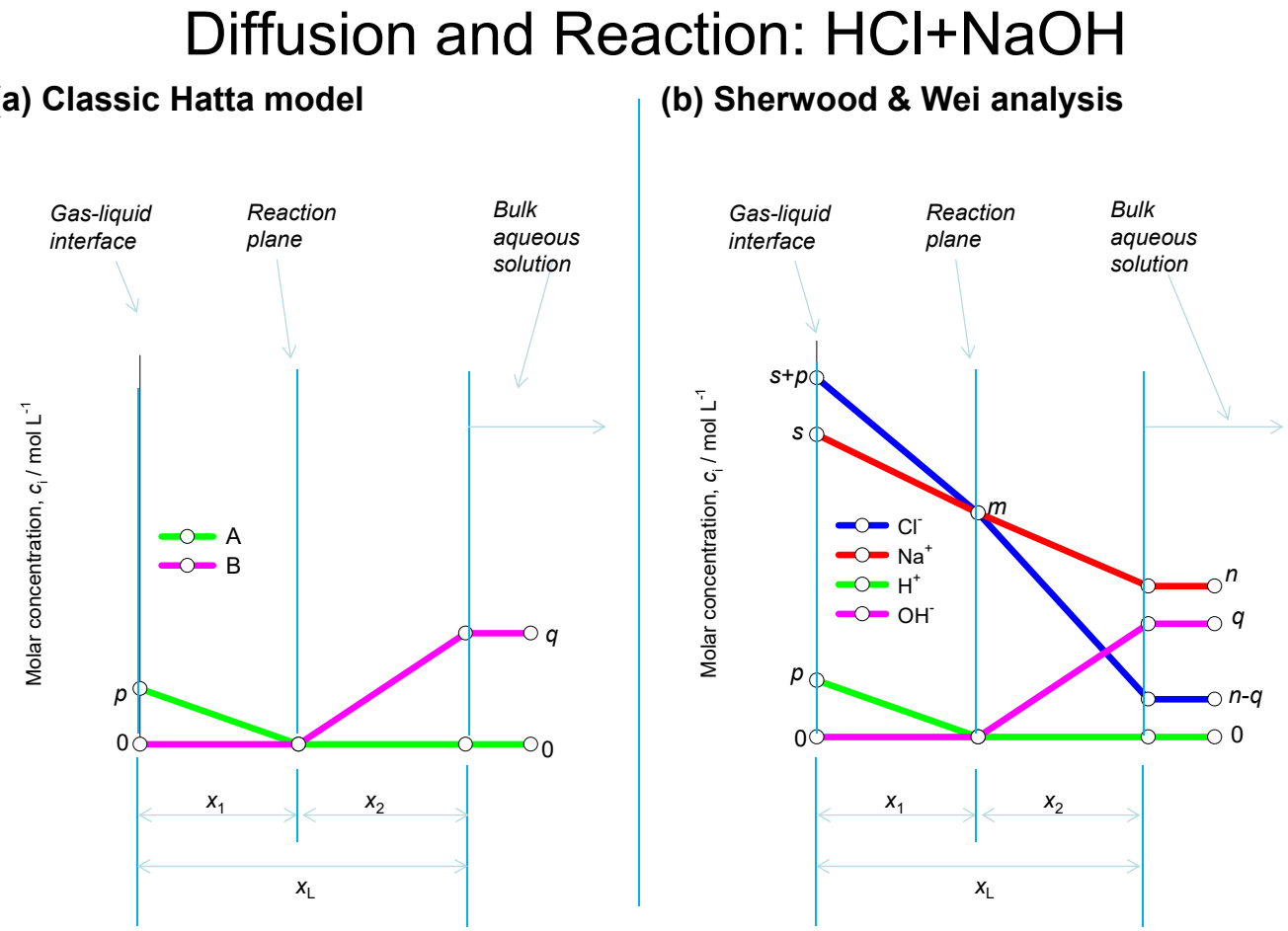


Figure 10-25. (a) Classic Hatta model for instantaneous reaction between "neutral" compounds A and B. Because the reaction is instantaneous it occurs at a reaction plane at a distance $x_1$ from the gas/liquid interface. (b) Ionic concentrations in the "double film" for absorption of HCl into aqueous NaOH. This schematic is essentially as presented in Figure 1 of Sherwood and Wei.[169]

# Comparison with Hatta model: HCl+NaOH

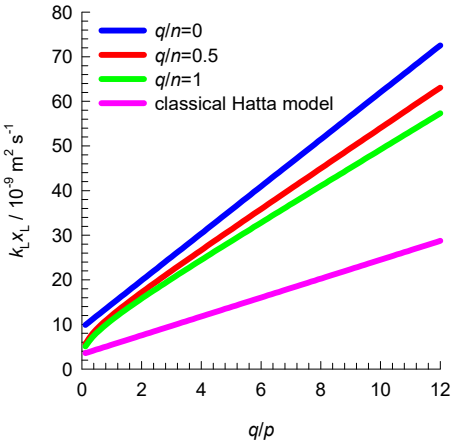


Figure 10-26. Comparison of Nernst-Planck calculations for the parameter $k_L x_L$ with those using the classic Hatta model, assuming that the reaction takes place between “neutral” HCl and “neutral” NaOH.

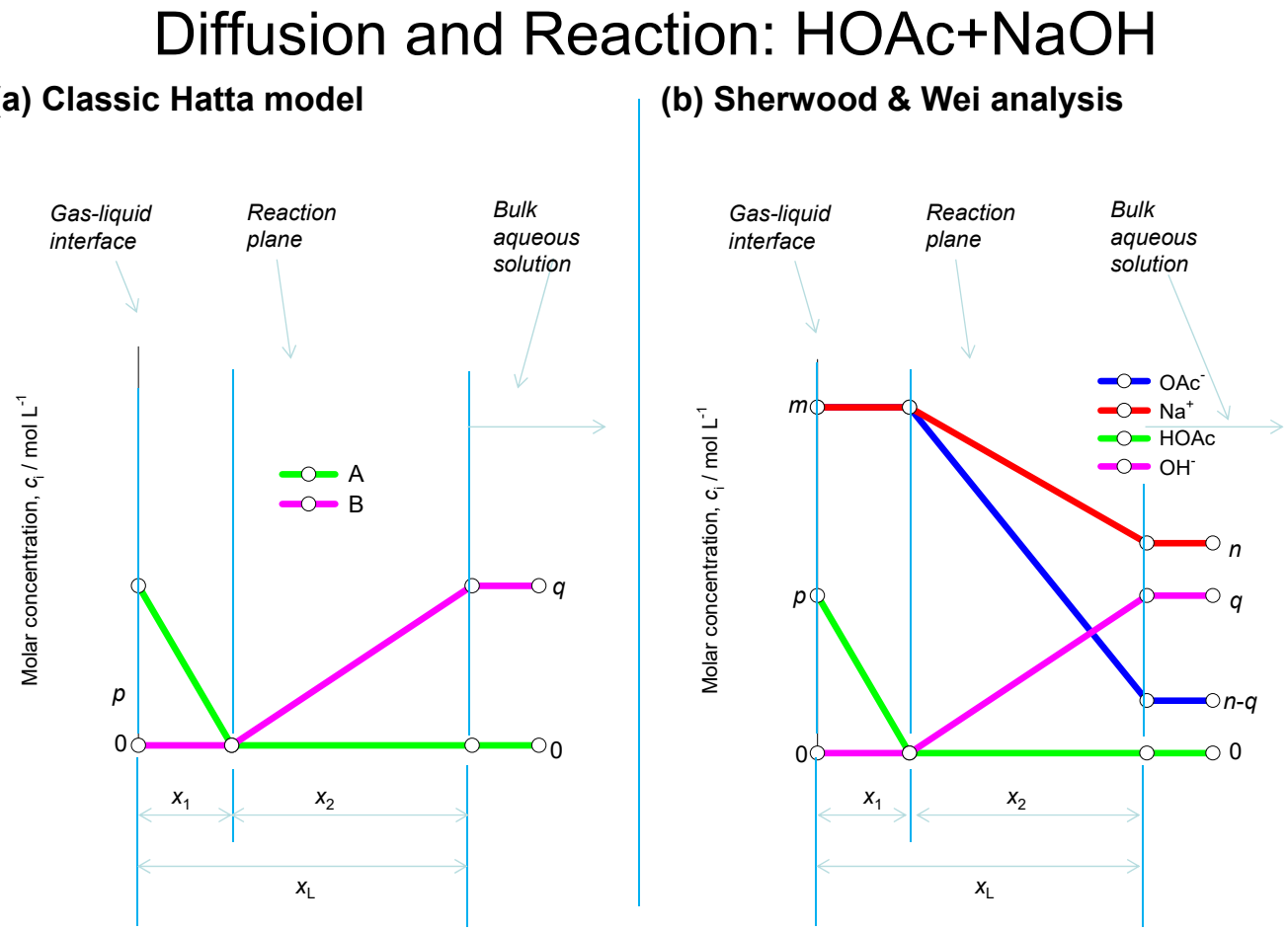


Figure 10-27. (a) Classic Hatta model for instantaneous reaction between "neutral" compounds A and B. Because the reaction is instantaneous it occurs at a reaction plane at a distance $x_1$ from the gas/liquid interface. (b) Ionic concentrations in the "double film" for absorption of HOAc into aqueous NaOH. This schematic is essentially as presented in Figure 3 of Sherwood and Wei.[169]

# Comparison with Hatta model: HOAc+NaOH

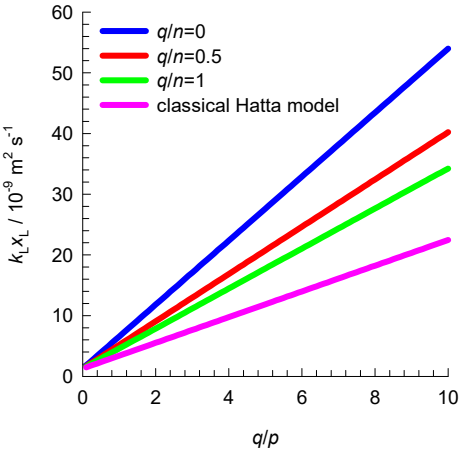


Figure 10-28. Comparison of Nernst-Planck calculations for the parameter $k_L x_L$ with those using the classic Hatta model, assuming that the reaction takes place between "neutral" HOAc and "neutral" NaOH.

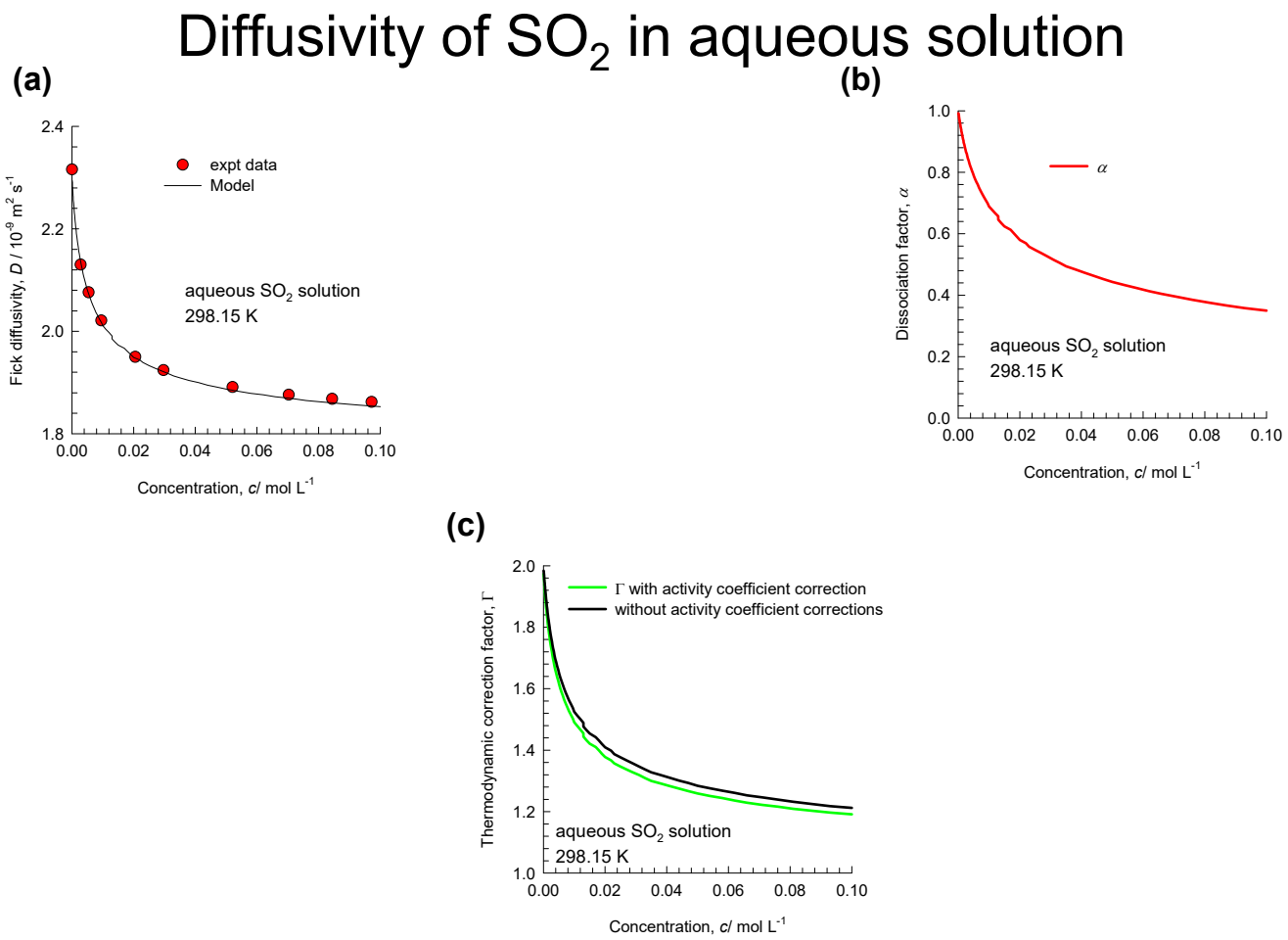


Figure 10-29. (a) Experimental data of Leaist[171] for diffusivity of $SO_2$ in aqueous solution at 298.15. (b) Calculation of the degree of hydrolysis, $\alpha$. (c) Calculation of the thermodynamic correction factor, $\Gamma$.

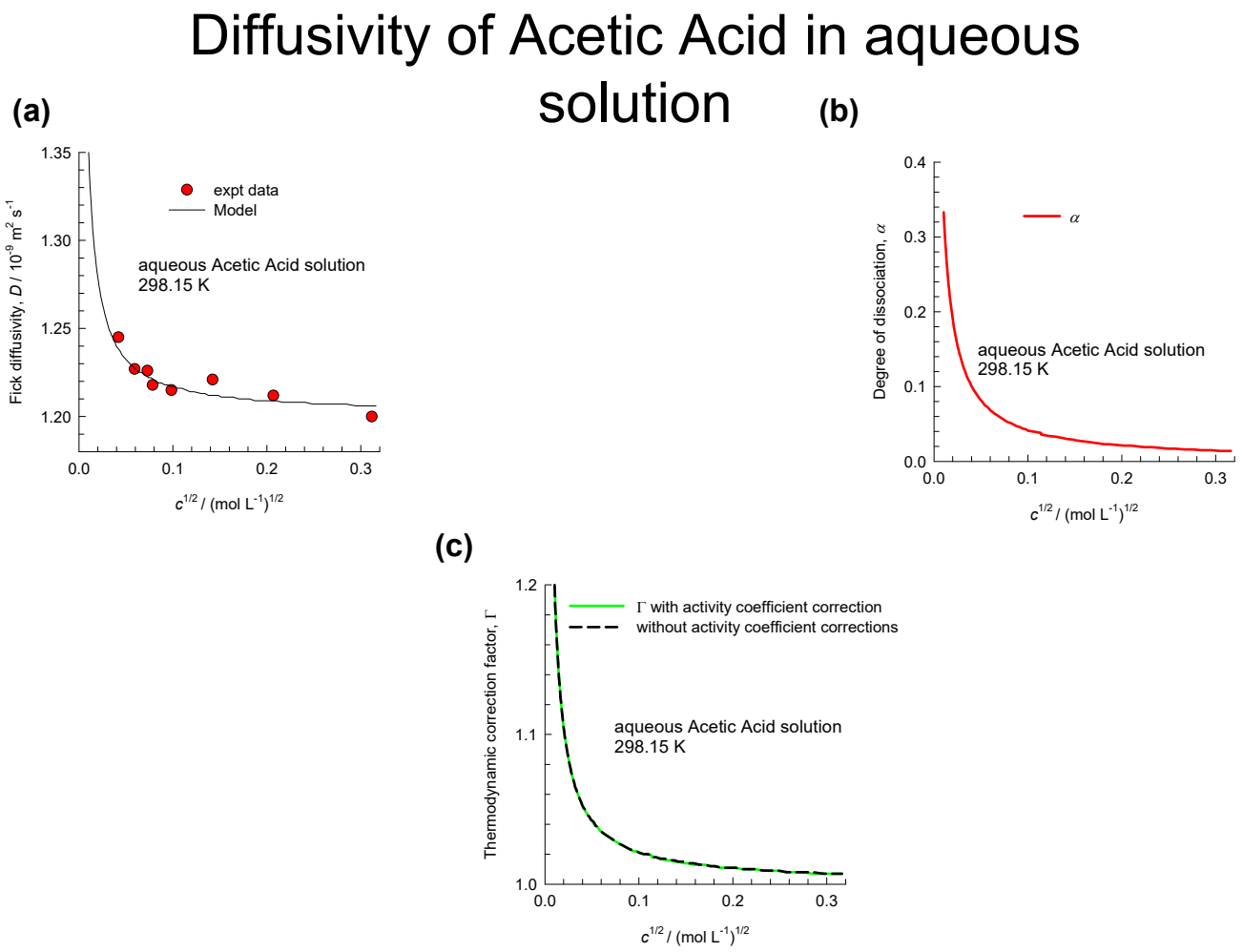


Figure 10-30. (a) Experimental data of Leaist and Lyons[172] for diffusivity of Acetic Acid in aqueous solution at 298.15. (b) Calculation of the degree of dissociation, $\alpha$. (c) Calculation of the thermodynamic correction factor, $\Gamma$.

# Fick Diffusivity $SO_2/NaHSO_3/H_2O$

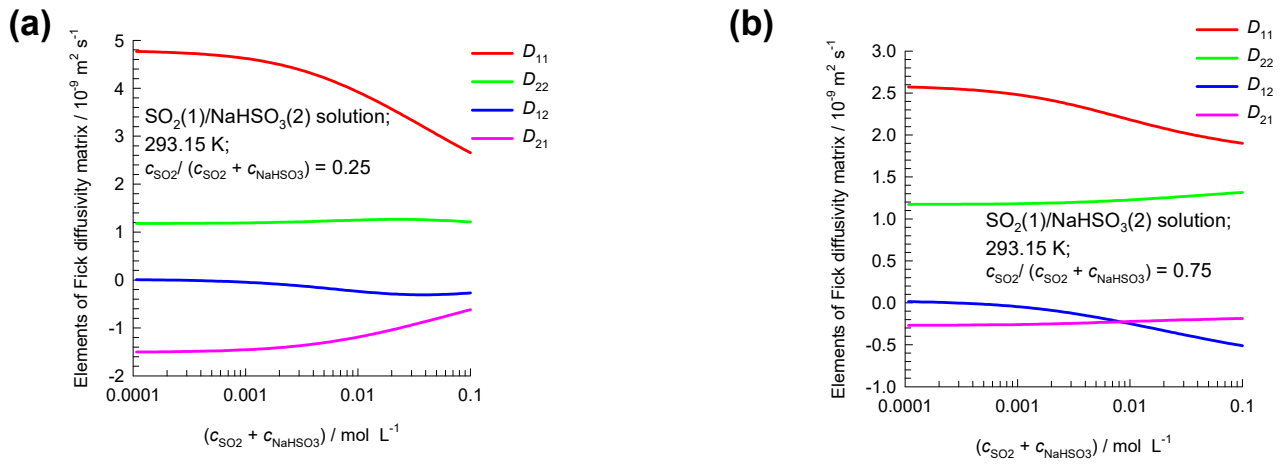


Figure 10-31. (a, b) Calculations of the elements of the Fick diffusivity matrix [$D$] for the mixture of aqueous electrolytes $SO_2$(1), and $NaHSO_3$ (2) at 293.15 K. The $x$-axis represents the total molar concentration of the mixture $c_{SO2} + c_{NaHSO3}$. For the calculations in (a) $c_{SO2}/\left(c_{SO2} + c_{NaHSO3}\right) = 0.25$. For the calculations in (b) $c_{SO2}/\left(c_{SO2} + c_{NaHSO3}\right) = 0.75$. The calculations follow the same procedure as described by Leaist,[173] and include thermodynamic non-ideality effects.

# Fick Diffusivity $SO_2/NaHSO_3/H_2O$

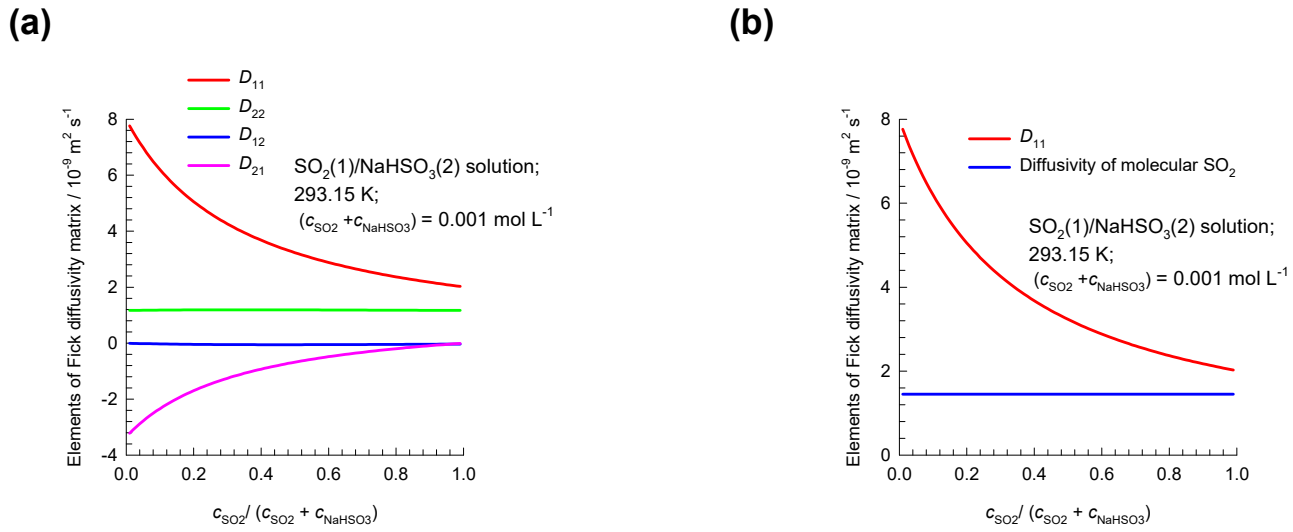


Figure 10-32. (a) Calculations of the elements of the Fick diffusivity matrix [$D$] for the mixture of aqueous electrolytes $SO_2(1)$, and $NaHSO_3$ (2) at 293.15 K for a total mixture concentration $c_{SO2} + c_{NaHSO3}$ = 0.001 mol $L^{-1}$. The $x$-axis represents the fraction $c_{SO2}/(c_{SO2} + c_{NaHSO3})$. (b) Comparison of $D_{11}$ with the diffusivity of molecular $SO_2$ for the same set of conditions as in (a). The calculations follow the same procedure as described by Leaist,[173] and include thermodynamic non-ideality effects.

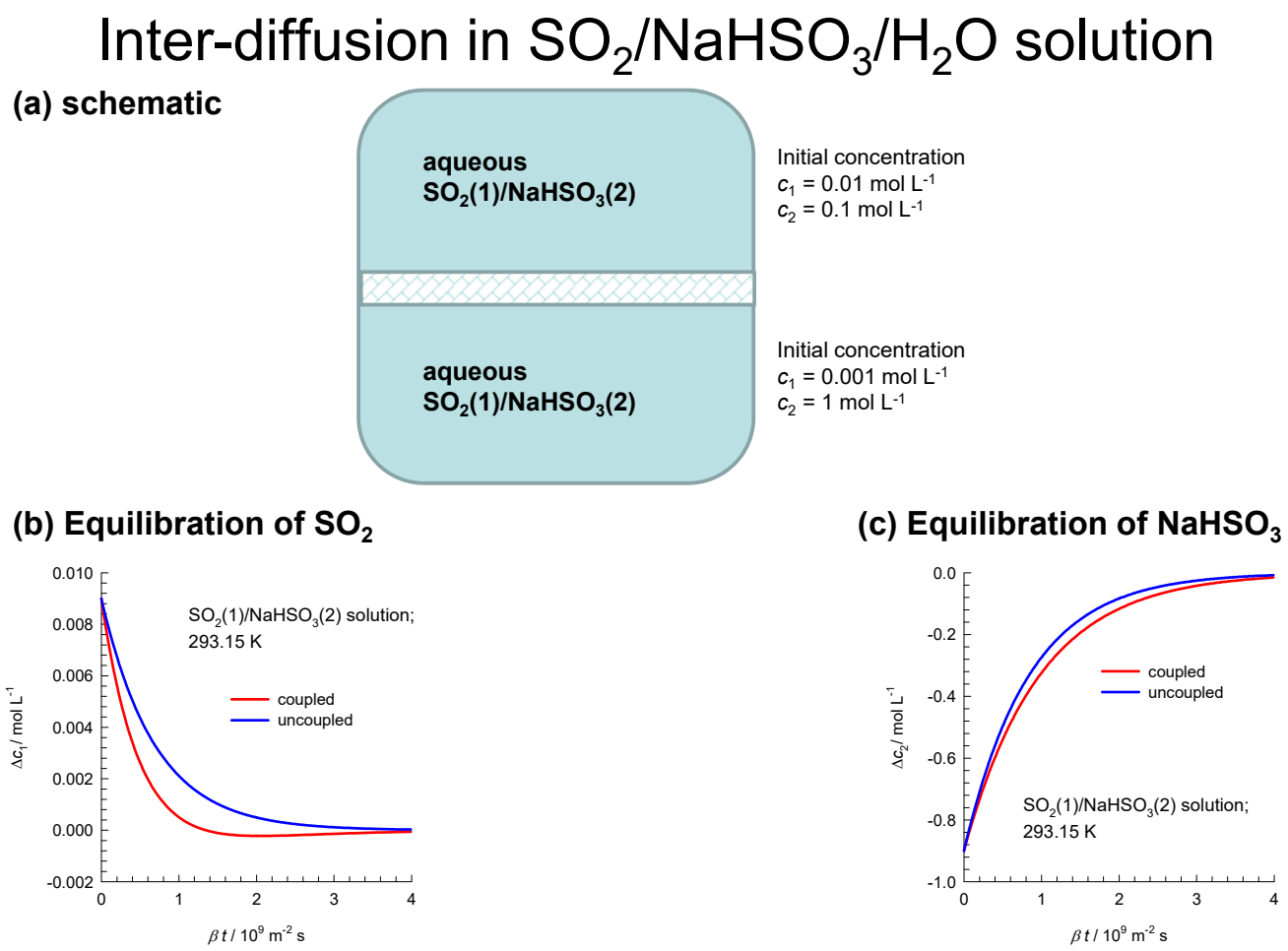


Figure 10-33. (a) Schematic showing the inter-diffusion of $SO_2$(1), and $NaHSO_3$ (2) at 293.15 K between upper and lower compartments of a diaphragm cell. (b, c) Transient equilibratrion of molar concentrations of (b) $SO_2$(1), and (c) $NaHSO_3$ (2), respectively.

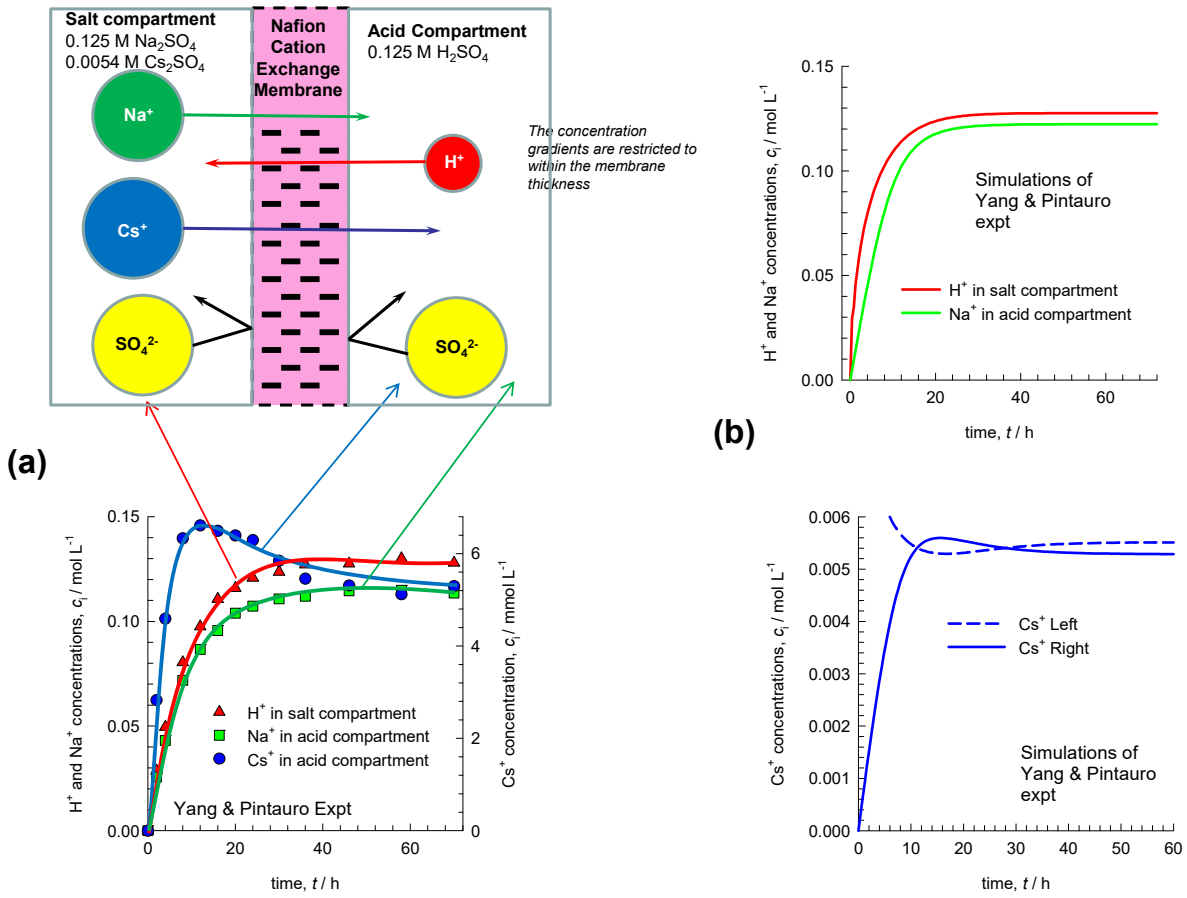


Figure 10-34. (a) Experimental data of Yang and Pintauro[174] for the transient equilibration of $H^+$, $Na^+$, and $Cs^+$ in the salt and acid compartments that are separated by a Nafion cation exchange membrane. (b) Simulations using the Nernst-Planck equations.

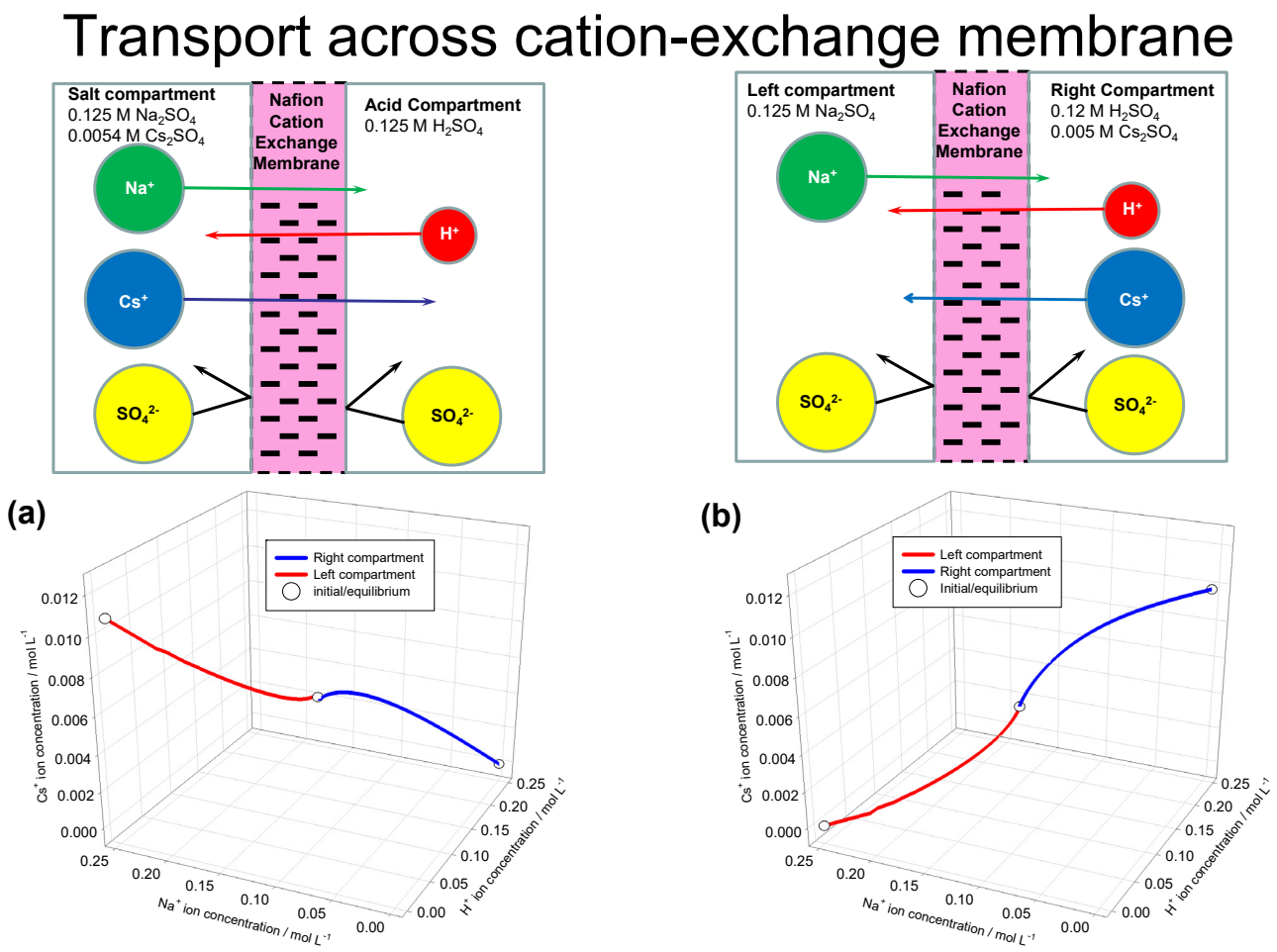


Figure 10-35. (a, b) Equilibration trajectories followed by $H^+$, $Na^+$, and $Cs^+$ in the left and right compartments, plotted in composition space. In (a) the left compartment contains $Na_2SO_4$ and $Cs_2SO_4$ and the right compartment contains $H_2SO_4$. In (b) the left compartment contains $Na_2SO_4$ and the right compartment contains $H_2SO_4$ and $Cs_2SO_4$.

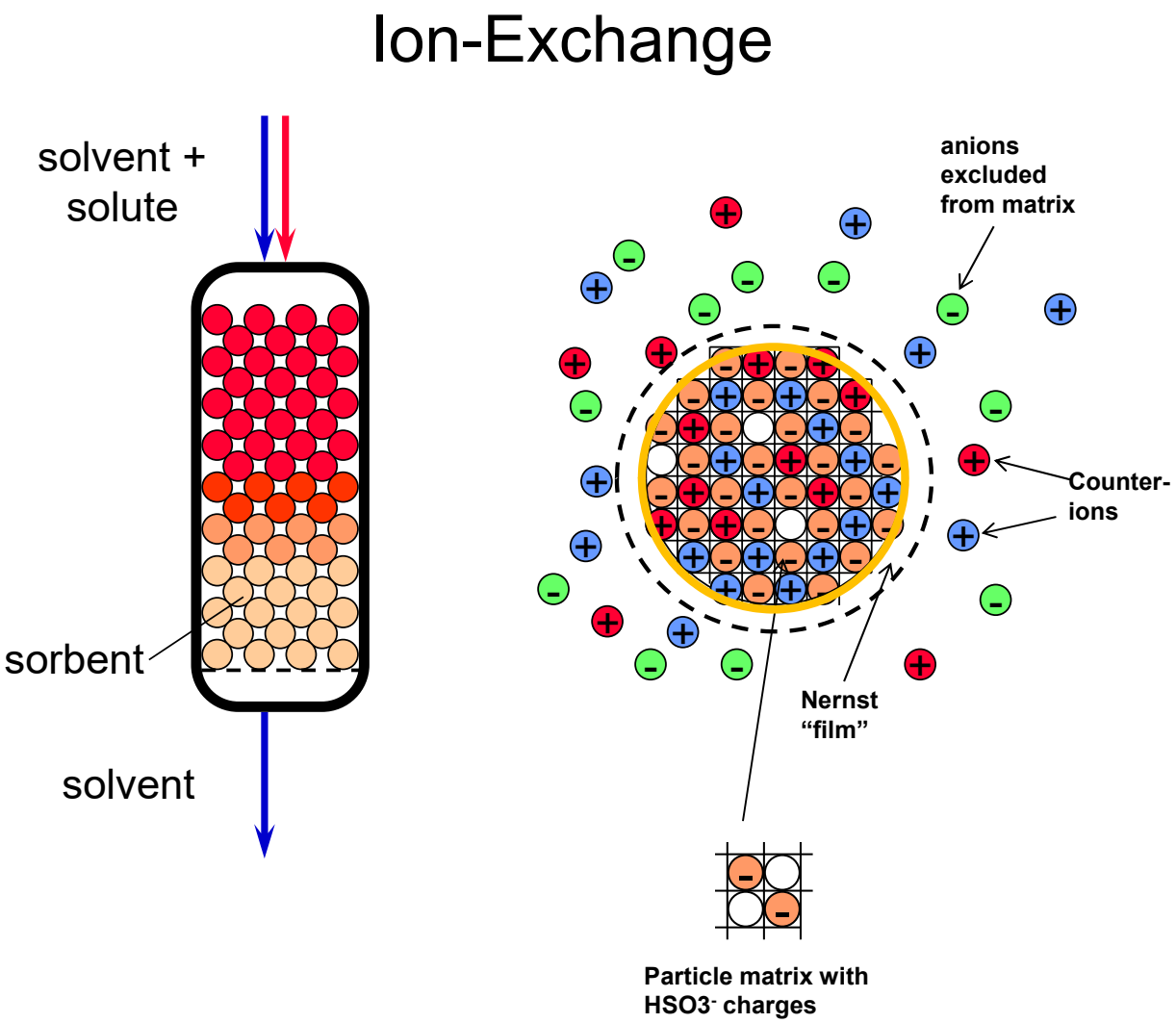


Figure 10-36. Schematic showing an ion exchanger particle with fixed $HSO3^-$ charges. The surrounding liquid phase consists of a mixture of electrolytes. The electrolytes are fully ionized and the bulk liquid phase contains anion, and two counter-ions along with unionized water molecules. The schematic is redrawn using the information contained in Wesselingh and Krishna[64]

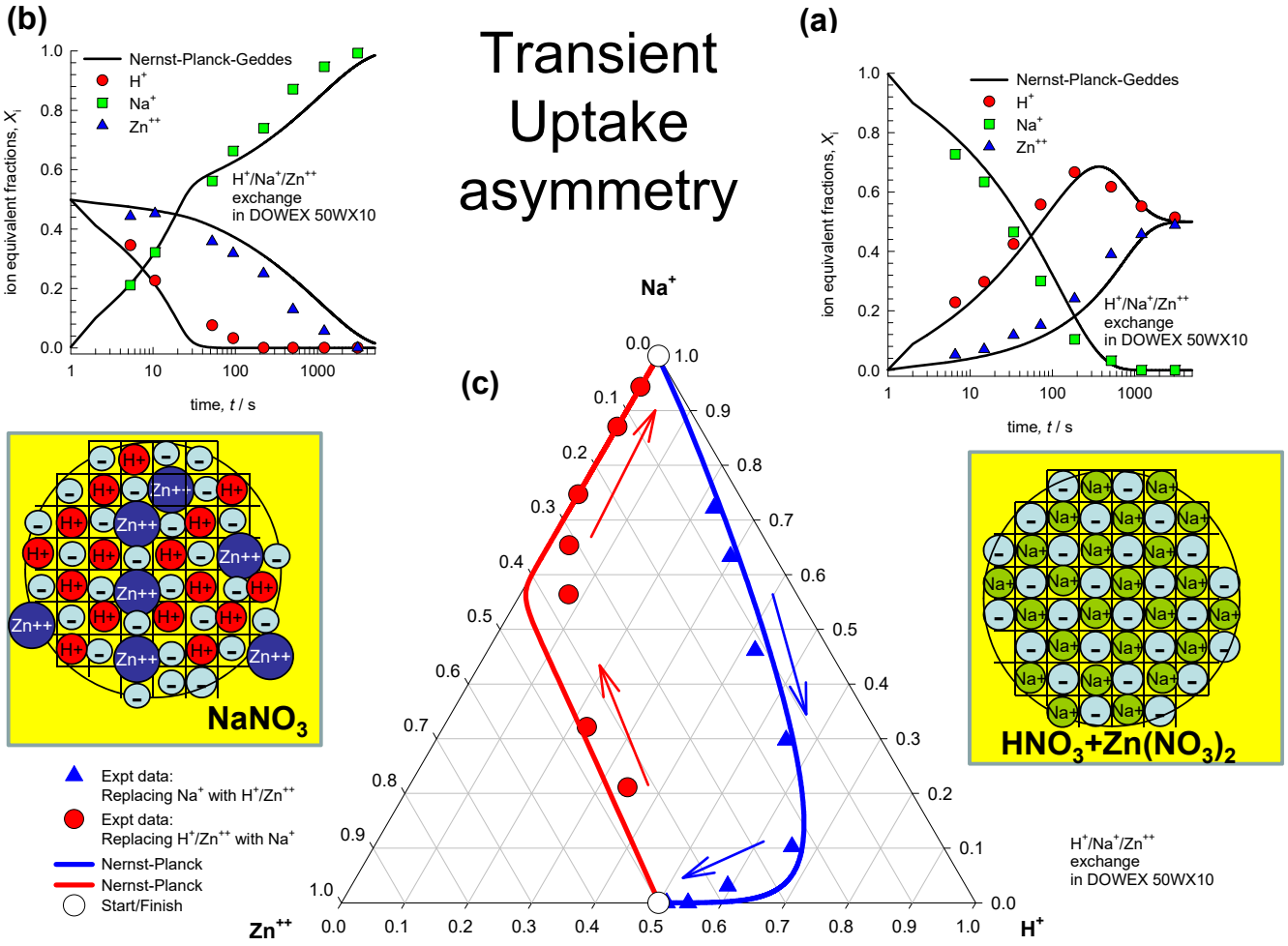


Figure 10-37. Transient exchange of $H^+/Na^+/Zn^{++}$ within DOWEX 50WX10 cation exchanger particle of radius 0.4 mm. Two scenarios are considered. (a) Initially the particle is loaded with $Na^+$ and is replaced $H^+/Zn^{++}$. (b) Initially the particle is loaded with $H^+/Zn^{++}$ and is replaced $Na^+$. (c) Plots of the ionic equivalent fractions $\frac{z_i c_i}{c_{fixed}}$ in ternary composition space for the two scenarios. The experimental data in Yoshida and Kataoka[176] are indicated by symbols. The Nernst-Planck-Geddes model simulations are indicated by the continuous solid lines.

# 11 Diffusion in Microporous Crystalline Materials

## 11.1 The Maxwell-Stefan (M-S) description of diffusion

Within micro-porous crystalline materials, such as zeolites, metal-organic frameworks (MOFs), and zeolitic imidazolate frameworks (ZIFs), the guest molecules exist in the adsorbed phase. The Maxwell-Stefan (M-S) equations for *n*-component diffusion in porous materials is applied in the following manner[60, 67, 179-184]

$$
\begin{aligned}
-\frac{d\mu_1}{dz} &= \frac{RT}{Đ_{12}} X_2(u_1-u_2) + \frac{RT}{Đ_{13}} X_3(u_1-u_3) + \ldots + \frac{RT}{Đ_{1m}} X_m(u_1-u_m) \\
-\frac{d\mu_2}{dz} &= \frac{RT}{Đ_{21}} X_1(u_2-u_1) + \frac{RT}{Đ_{23}} X_3(u_2-u_3) + \ldots + \frac{RT}{Đ_{2m}} X_m(u_2-u_m) \\
&\cdots\cdots \\
-\frac{d\mu_n}{dz} &= \frac{RT}{Đ_{n1}} X_1(u_n-u_1) + \frac{RT}{Đ_{n2}} X_2(u_n-u_3) + \ldots + \frac{RT}{Đ_{nm}} X_m(u_n-u_m)
\end{aligned}
\tag{11-1}
$$

The left members of equation (11-1) are the negative of the gradients of the chemical potentials, with the units N mol$^{-1}$; it represents the driving force acting per mole of species 1, 2, 3,..*n*. The $u_i$ represents the velocity of motion of the adsorbate, defined in a reference frame with respect to the framework material. The subscript m refers to the porous material, that is regarded as the (*n*+1) th component in the mixture; the crystalline framework is considered to be stationary, i.e., $u_m = 0$. The term $RT/Đ_{im}$ is interpreted as the drag or friction coefficient between the guest species *i* and the pore wall. The term $RT/Đ_{ij}$ is interpreted as the friction coefficient for the *i-j* pair of guest molecules. The multiplier $X_j$ in each of the right members represents a measure of the composition of component *j* in the mixture because we expect the friction to be dependent on the number of molecules of *j* relative to that of component *i*. Since the composition fraction $X_m$ of the material is undefined, we re-define the M-S diffusivity for interaction of the penetrant (i.e. guest molecule) *i* with the pore wall as $Đ_i \equiv Đ_{im}/X_m$ .

Two different choices of composition measures have been used in the literature: (a) using the fractional occupancies, $\theta_i \equiv q_i / q_{i,sat}$, and (b) using the mole fractions of the adsorbed mixture, $x_i = q_i / q_t$; these are discussed below in turn.

We start the analysis of diffusion in microporous materials by considering diffusion of adsorbed species on a 2D surface consisting of well defined adsorption sites, such as that on graphenes.

## 11.2 "Vacancy mediated" diffusion of adsorbed species on 2D surface

For diffusion of adsorbed species on a two-dimensional (2D) surface made up of distinct sites, the Maxwell-Stefan equations may be written as[123, 185]

$$-\frac{1}{RT}\frac{d\mu_i}{dz} = \sum_{\substack{j=1 \\ j\neq i}}^{n} \frac{\theta_j}{Đ_{ij}^{\theta}}\left(u_i - u_j\right) + \frac{\theta_V}{Đ_{iV}^{\theta}}\left(u_i - u_V\right); \quad i = 1, 2..n \tag{11-2}$$

In equation (11-2), $\theta_i$ is the fractional occupancy, and $\theta_V$ is the fractional vacancy. The fractional occupancies, $\theta_i$, of species *i* are determined from the molar loadings, $q_i$, expressed in moles per kg of material, and the saturation capacities, $q_{i,sat}$, for adsorption of each species

$$\theta_i = \frac{q_i}{q_{i,sat}}; \quad i = 1,2,..n \tag{11-3}$$

For the specific case of a binary mixture, the hopping of molecules from one site to another is depicted in Figure 11-1. Using a simple lattice model, the M-S diffusivity in the limit of vanishingly small occupancies, $Đ_{iV}^{\theta}(0) = \frac{1}{\zeta}\nu_i(0)\lambda^2$, where $\zeta = 4$ is the coordination number of the 2D array of lattice sites, $\lambda$ is the jump distance on the square lattice, and $\nu_i(0)$ is the jump frequency at vanishingly small occupancy.[185]

More generally, molecule-molecule interactions serve to influence the jump frequencies by a factor that depends on the energy of interaction, *w*. For repulsive interactions, $w > 0$, whereas for attractive interactions, $w < 0$. Using the quasi-chemical approach of Reed and Ehrlich[186] to quantify such

interactions, the following expression is obtained for the loading dependence of the M-S diffusivities [185, 187, 188]

$$Đ_{iV}^{\theta} = Đ_{iV}^{\theta}(0)\left(\frac{1+\beta_i}{2\,(1-\theta_i)}\right)^{-\zeta}\left(1+\frac{(\beta_i - 1 + 2\theta_i)\varphi}{2\,(1-\theta_i)}\right)^{\zeta-1} \tag{11-4}$$

In equation (11-4) the following dimensionless parameters are defined

$$\beta_i = \sqrt{1-4\,\theta_i(1-\theta_i)(1-1/\phi)}; \quad \phi = \exp(w/RT) \tag{11-5}$$

In the limiting case of negligible molecule-molecule interactions, $w = 0$, $\phi = 1$, $\beta_i = 1$ equation (11-4) yields

$$Đ_{iV}^{\theta} = Đ_{iV}^{\theta}(0)(1-\theta_i) \tag{11-6}$$

Equation (11-6) implies that the M-S diffusivity is proportional to the number of unoccupied sites.

The M-S diffusivities $Đ_{ij}^{\theta}$ quantify the correlation effects. Generally speaking, the hopping of the more-mobile-less-strongly-adsorbed species will be slowed-down by the tardier-more-strongly-adsorbed species. The Onsager reciprocal relations demand the symmetry

$$q_{j,sat}Đ_{ij}^{\theta} = q_{i,sat}Đ_{ji}^{\theta}; \quad i = 1,2..n \tag{11-7}$$

Consider the specific case of tracer diffusion; in this case the species 1 = tagged species 1*; 2 = untagged species 1; 3 = vacancy (V). Equation (11-2) simplifies to yield

$$\begin{aligned} -\frac{d\mu_{1*}}{dz} &= \frac{RT}{Đ_{1*1}}\theta_1(u_{1*}-u_1) + \frac{RT}{Đ_{1*V}}\theta_V(u_{1*}-u_V) \\ -\frac{d\mu_1}{dz} &= \frac{RT}{Đ_{11*}}\theta_{1*}(u_1-u_{1*}) + \frac{RT}{Đ_{1V}}\theta_V(u_1-u_V) \end{aligned} \tag{11-8}$$

The expression for the tracer diffusivity $D^*$ has been derived by Krishna[123]

$$D^* = \frac{1}{\dfrac{\theta_{1*}+\theta_1}{Đ_{11*}^{\theta}} + \dfrac{\theta_V}{Đ_{1V}^{\theta}}} \tag{11-9}$$

Equation (11-9) has been validated by Kinetic Monte Carlo simulations.[185]

An important characteristic of the foregoing description is that the vacancy flux is non-zero, and this description is essentially a 2D analog of the "vacancy mediated" diffusion in non-porous crystalline metal crystals, described in an earlier section. We now apply the "vacancy" description of diffusion to microporous materials in a slightly modified form.

## 11.3 "Vacancy" description of diffusion in micropores

In our earlier publications[179, 189-191] on *n*-component mixture diffusion in *micro*pores, equation (11-1) was applied in the following manner

$$-\frac{1}{RT}\frac{d\mu_i}{dz}=\sum_{\substack{j=1\\ j\neq i}}^{n}\frac{\theta_j}{Đ_{ij}^{\theta}}\left(u_i-u_j\right)+\frac{1}{Đ_i}\left(u_i\right);\quad i=1,2..n \tag{11-10}$$

In equation (11-10), $\theta_i$ is the fractional occupancy of species $i$ ; these are determined from the molar loadings, $q_i$, expressed in moles per kg of material, and the saturation capacities, $q_{i,sat}$, for adsorption of each species

$$\theta_i=\frac{q_i}{q_{i,sat}};\quad i=1,2,..n \tag{11-11}$$

The superscript $\theta$ on the exchange coefficients $Đ_{ij}^{\theta}$ serves as a reminder that these coefficients are defined in terms of the vacancies as composition measures in the Maxwell-Stefan description. The M-S diffusivities $Đ_{ij}^{\theta}$ quantify the correlation effects. Generally speaking, the hopping of the more-mobile-less-strongly-adsorbed species within the pores will be slowed-down by the tardier-more-strongly-adsorbed species. The $Đ_i$ may be interpreted as inverse drag coefficients between the species $i$ and the material surface. Indeed, an important persuasive advantage of the M-S equations is that the $Đ_i$ for mixture diffusion often retains the same magnitude and loading dependence as for unary diffusion;[67, 181, 182] we return to this point later in this article.

If $\rho$ represents the mass density of the framework material, expressed commonly in the units kg $m^{-3}$, and $q_i=q_{i,sat}\theta_i$ is the molar loading of the adsorbed species $i$ within the micropores, expressed in the

units of mol kg$^{-1}$, the intra-crystalline diffusion fluxes are $N_i = \rho q_i u_i$. Re-writing equation (11-10) in terms of the intracrystalline fluxes we get

$$-\rho \frac{\theta_i}{RT}\frac{d\mu_i}{dz} = \sum_{\substack{j=1 \\ j\neq i}}^{n}\left(\frac{q_j N_i - q_i N_j}{q_{i,sat} q_{j,sat} Đ_{ij}^{\theta}}\right) + \frac{N_i}{q_{i,sat} Đ_i}; \quad i = 1,2..n \tag{11-12}$$

The Onsager reciprocal relations demand the symmetry

$$q_{j,sat} Đ_{ij}^{\theta} = q_{i,sat} Đ_{ji}^{\theta}; \quad i = 1,2..n \tag{11-13}$$

If the saturation capacities of all of the individual species are (nearly) equal to one another, equation (11-12) simplifies to

$$-\rho \frac{q_i}{RT}\frac{d\mu_i}{dz} = \sum_{\substack{j=1 \\ j\neq i}}^{n}\left(\frac{\theta_j N_i - \theta_i N_j}{Đ_{ij}^{\theta}}\right) + \frac{N_i}{Đ_i}; \quad i = 1,2..n \tag{11-14}$$

The important advantage of the use of equations (11-14) is that these can be elegantly combined with the mixed-gas Langmuir model for mixture adsorption (equation (11-25)), and analytical solutions can be derived for the membrane permeation fluxes, and effectiveness factors.[192-195]

An important disadvantage of the use of the "vacancy description" of intra-crystalline diffusion is that the treatment is restricted to the case where all of the molecules exist in the adsorbed phase. This implies that equation (11-12) cannot be applied to describe diffusion in meso-porous and macro-porous materials, where a substantial portion of the molecules within the pores may exist in the "bulk" fluid phase, not adsorbed on the pore walls.

For a *unified* description of diffusion in micro-, meso-, and macro-porous materials, we abandon the "vacancy" concept and proceed using the mole fractions as composition measures.

## 11.4 Unified M-S description of diffusion in porous materials

For a unified description of diffusion in porous materials, it is convenient to use as composition measures the mole fractions of the components in the adsorbed phase, $x_i = q_i / q_t$ where $q_i$ is the molar loading of adsorbate, and $q_t$ is the *total* mixture loading $q_t = \sum_{i=1}^{n} q_i$.

In terms of mole fractions, equations (11-1) are modified as follows

$$
\begin{aligned}
-\frac{d\mu_1}{dz} &= \frac{RT}{Đ_{12}} x_2(u_1 - u_2) + \frac{RT}{Đ_{13}} x_3(u_1 - u_3) + \ldots + \frac{RT}{Đ_1}(u_1) \\
-\frac{d\mu_2}{dz} &= \frac{RT}{Đ_{21}} x_1(u_2 - u_1) + \frac{RT}{Đ_{23}} x_3(u_2 - u_3) + \ldots + \frac{RT}{Đ_2}(u_2) \\
&\cdots\cdots \\
-\frac{d\mu_n}{dz} &= \frac{RT}{Đ_{n1}} x_1(u_n - u_1) + \frac{RT}{Đ_{n2}} x_2(u_n - u_3) + \ldots + \frac{RT}{Đ_n}(u_n)
\end{aligned}
\tag{11-15}
$$

An important, persuasive, argument for the use of the M-S formulation for mixture diffusion is that the M-S diffusivity $Đ_i$ in mixtures can be estimated using information on the loading dependence of the corresponding unary diffusivity values. Put another way, the M-S diffusivity $Đ_i$ can be estimated from experimental data on *unary* diffusion in the porous material.

The M-S diffusivity $Đ_{ij}$ has the units $m^2\ s^{-1}$ and the physical significance of an *inverse* drag coefficient. The magnitudes of the M-S diffusivities $Đ_{ij}$ do not depend on the choice of the mixture reference velocity because equation (11-1) is set up in terms of velocity differences. At the molecular level, the $Đ_{ij}$ reflect how the facility for transport of species *i correlates* with that of species *j*; they are also termed *exchange coefficients*.

For *meso*porous materials with pores in the 20 Å to 100 Å size range the values of the exchange coefficient $Đ_{12}$ are the nearly the same as the binary *fluid phase* M-S diffusivity, $Đ_{12,fl}$, over the entire range of pore concentrations.[60, 108, 181, 182, 196] For micro-porous materials, the exchange coefficient $Đ_{12}$ cannot be directly identified with the corresponding fluid phase diffusivity $Đ_{12,fl}$ because the molecule-molecule interactions are also significantly influenced by molecule-wall interactions.

The Maxwell-Stefan diffusion formulation (11-15) is consistent with the theory of irreversible thermodynamics. The Onsager Reciprocal Relations imply that the M-S pair diffusivities are symmetric

$$Đ_{ij} = Đ_{ji} \tag{11-16}$$

We define $N_i$ as the number of moles of species *i* transported per $m^2$ of crystalline material per second

$$N_i \equiv \rho q_i u_i \tag{11-17}$$

where $\rho$ is the framework density with units of kg m$^{-3}$. Multiplying both sides of equation (11-15) by $\rho q_i$, the M-S equations for *n*-component diffusion in zeolites, MOFs, and ZIFs take the form [196-198]

$$-\rho \frac{q_i}{RT}\frac{d\mu_i}{dz} = \sum_{\substack{j=1 \\ j\neq i}}^{n} \frac{x_j N_i - x_i N_j}{Đ_{ij}} + \frac{N_i}{Đ_i}; \quad i = 1,2,..n \tag{11-18}$$

An entirely analogous manner of writing equation (11-18) is in terms of molar concentrations $c_i$, in the adsorbed phase, with units mol m$^{-3}$, based on the accessible pore volume, $V_p$ ( = m$^3$ pore volume per kg framework)

$$c_i = \frac{q_i}{V_p}; \quad c_t = \sum_{i=1}^{n} c_i = \frac{q_t}{V_p} \tag{11-19}$$

In terms of molar concentrations, the M-S description for intra-pore diffusion is

$$-\rho V_p \frac{c_i}{RT}\frac{d\mu_i}{dz} = \sum_{\substack{j=1 \\ j\neq i}}^{n} \left(\frac{x_j N_i - x_i N_j}{Đ_{ij}}\right) + \frac{N_i}{Đ_i}; \quad i = 1,2...n \tag{11-20}$$

The quantity $\rho V_p \equiv \varepsilon$ is the fractional pore volume,

$$\rho V_p = \left(\frac{\text{kg framework}}{\text{m}^3 \text{ framework}}\right)\left(\frac{\text{m}^3 \text{ pore volume}}{\text{kg framework}}\right) = \left(\frac{\text{m}^3 \text{ pore volume}}{\text{m}^3 \text{ framework}}\right) = \varepsilon \tag{11-21}$$

So, we re-write equation (11-20) in the form

$$-\varepsilon \frac{c_i}{RT}\frac{d\mu_i}{dz} = \sum_{\substack{j=1 \\ j\neq i}}^{n} \left(\frac{x_j N_i - x_i N_j}{Đ_{ij}}\right) + \frac{N_i}{Đ_i}; \quad i = 1,2...n \tag{11-22}$$

The formulation (11-22) has been employed to develop a unified theory of mixture diffusion in both micro-pores and meso-pores.[60, 181, 184, 199] The fluxes $N_i$ in equations (11-18), and (11-22) are defined in terms of the moles transported per m$^2$ of the *total surface of crystalline material*. Alternatively, if we just focus on fluxes inside a single pore, it is convenient to define the fluxes $N_i$ in terms of the moles transported per m$^2$ surface of the pore, then the factor $\rho V_p \equiv \varepsilon$ has to be omitted in the left member of equation (11-22).

## 11.5 Thermodynamic correction factors

At thermodynamic equilibrium, the chemical potential of component *i* in the bulk fluid mixture equals the chemical potential of that component in the adsorbed phase. For the bulk fluid phase mixture we have

$$\frac{1}{RT}\frac{d\mu_i}{dz}=\frac{d\ln f_i}{dz}=\frac{1}{f_i}\frac{df_i}{dz};\qquad i=1,2,..n \tag{11-23}$$

The chemical potential gradients $d\mu_i/dz$ can be related to the gradients of the molar loadings, $q_i$, by defining thermodynamic correction factors $\Gamma_{ij}$

$$\frac{q_i}{RT}\frac{d\mu_i}{dz}=\sum_{j=1}^{n}\Gamma_{ij}\frac{dq_j}{dz};\quad \frac{c_i}{RT}\frac{d\mu_i}{dz}=\sum_{j=1}^{n}\Gamma_{ij}\frac{dc_j}{dz};\qquad \Gamma_{ij}=\frac{q_i}{f_i}\frac{\partial f_i}{\partial q_j}=\frac{c_i}{p_i}\frac{\partial f_i}{\partial c_j};\qquad i,j=1,....n \tag{11-24}$$

The thermodynamic correction factors $\Gamma_{ij}$ can be calculated by differentiation of the model describing mixture adsorption equilibrium. Generally speaking, the Ideal Adsorbed Solution Theory (IAST) of Myers and Prausnitz[200] is the preferred method for estimation of mixture adsorption equilibrium. In some special case, the mixed-gas Langmuir model

$$\frac{q_i}{q_{i,sat}}=\theta_i=\frac{b_i f_i}{1+\sum_{i=1}^{n}b_i f_i};\quad i=1,2,...n \tag{11-25}$$

may be of adequate accuracy. Analytic differentiation of equation (11-25) yields

$$\Gamma_{ij}=\delta_{ij}+\left(\frac{q_{i,sat}}{q_{j,sat}}\right)\left(\frac{\theta_i}{\theta_V}\right);\quad i,j=1,2\ldots n \tag{11-26}$$

where the fractional vacancy $\theta_V$ is defined as

$$\theta_V=1-\theta_t=1-\sum_{i=1}^{n}\theta_i \tag{11-27}$$

The elements of the matrix of thermodynamic factors $\Gamma_{ij}$ can be calculated explicitly from information on the component loadings $q_i$ in the adsorbed phase; this is the persuasive advantage of the use of the

mixed-gas Langmuir model. By contrast, the IAST does not allow the calculation of $\Gamma_{ij}$ explicitly from knowledge on the component loadings $q_i$ in the adsorbed phase; a numerical procedure is required.

## 11.6 Explicit expression for the fluxes as function of loading gradients

By defining an $n$-dimensional square matrix $[B]$ with elements

$$B_{ii} = \frac{1}{Đ_i} + \sum_{\substack{j=1 \\ j\neq i}}^{n} \frac{x_j}{Đ_{ij}}; \qquad B_{ij} = -\frac{x_i}{Đ_{ij}}; \quad i, j = 1,2....n \tag{11-28}$$

we can recast equation (11-18), or equation (11-22), into the following form

$$-\rho \frac{q_i}{RT} \nabla \mu_i = -\varepsilon \frac{c_i}{RT} \frac{d\mu_i}{dz} = \sum_{j=1}^{n} B_{ij} N_j; \qquad i = 1,2,..n \tag{11-29}$$

Equation (11-29) can be re-written in $n$-dimensional matrix notation as

$$(N) = -\rho [B]^{-1} [\Gamma] \frac{d(q)}{dz} = -\rho [\Lambda][\Gamma] \frac{d(q)}{dz} = -\varepsilon [\Lambda][\Gamma] \frac{d(c)}{dz} \tag{11-30}$$

We denote the inverse of $[B]$ as $[\Lambda]$:

$$[B]^{-1} \equiv [\Lambda] \tag{11-31}$$

The elements of $[\Lambda]$ cannot be determined from experimental measurements. However, $\Lambda_{ij}$ are directly accessible from MD simulations[60, 67, 181, 199] by monitoring the individual molecular displacements

$$\Lambda_{ij} = \frac{1}{2} \lim_{\Delta t \to \infty} \frac{1}{n_j} \frac{1}{\Delta t} \left\langle \left( \sum_{l=1}^{n_i} \left( \mathbf{r}_{l,i}(t + \Delta t) - \mathbf{r}_{l,i}(t) \right) \right) \bullet \left( \sum_{k=1}^{n_j} \left( \mathbf{r}_{k,j}(t + \Delta t) - \mathbf{r}_{k,j}(t) \right) \right) \right\rangle \tag{11-32}$$

In this expression $n_i$ and $n_j$ represent the number of molecules of species $i$ and $j$ respectively, and $\mathbf{r}_{l,i}(t)$ is the position of molecule $l$ of species $i$ at any time $t$. In this context we note a typographical error in equation (11-32) as printed in earlier publications[201-203] wherein the denominator in the right member had $n_i$ instead of $n_j$. The simulation results presented in these publications are, however, correct as the proper formula given in equation (11-32) was used. Compliance with the Onsager Reciprocal Relations demands

$$n_j \Lambda_{ij} = n_i \Lambda_{ji}; \quad i, j = 1, 2, ....n \tag{11-33}$$

## 11.7 M-S formulation for binary mixture diffusion

For binary mixture diffusion inside microporous crystalline materials the Maxwell-Stefan equations (11-18) are written

$$\begin{aligned} -\rho \frac{q_1}{RT} \frac{d\mu_1}{dz} &= \frac{x_2 N_1 - x_1 N_2}{Đ_{12}} + \frac{N_1}{Đ_1} \\ -\rho \frac{q_2}{RT} \frac{d\mu_2}{dz} &= \frac{x_1 N_2 - x_2 N_1}{Đ_{12}} + \frac{N_2}{Đ_2} \end{aligned} \tag{11-34}$$

The first members on the right hand side of Equation (11-34) are required to quantify slowing-down effects that characterize binary mixture diffusion.[181, 182, 204] There is no experimental technique for direct determination of the exchange coefficients $Đ_{12}$, that quantify molecule-molecule interactions.

In two-dimensional matrix notation, equation (11-24) take the form

$$-\begin{pmatrix} \frac{q_1}{RT}\frac{d\mu_1}{dz} \\ \frac{q_2}{RT}\frac{d\mu_2}{dz} \end{pmatrix} = [\Gamma] \begin{pmatrix} \frac{dq_1}{dz} \\ \frac{dq_2}{dz} \end{pmatrix} \tag{11-35}$$

For the mixed-gas Langmuir model, equation (11-25), we can derive simple analytic expressions for the four elements of the matrix of thermodynamic factors:[189]

$$\begin{bmatrix} \Gamma_{11} & \Gamma_{12} \\ \Gamma_{21} & \Gamma_{22} \end{bmatrix} = \frac{1}{1-\theta_1-\theta_2} \begin{bmatrix} 1-\theta_2 & \frac{q_{1,sat}}{q_{2,sat}}\theta_1 \\ \frac{q_{2,sat}}{q_{1,sat}}\theta_2 & 1-\theta_1 \end{bmatrix} \tag{11-36}$$

where the fractional occupancies, $\theta_i$, are defined by equation (11-25).

Let us define the square matrix [$B$]

$$[B]=\begin{bmatrix}\frac{1}{Đ_1}+\frac{x_2}{Đ_{12}} & -\frac{x_1}{Đ_{12}}\\ -\frac{x_2}{Đ_{12}} & \frac{1}{Đ_2}+\frac{x_1}{Đ_{12}}\end{bmatrix};\quad [B]^{-1}=\frac{1}{1+\frac{x_1Đ_2}{Đ_{12}}+\frac{x_2Đ_1}{Đ_{12}}}\begin{bmatrix}Đ_1\left(1+\frac{x_1Đ_2}{Đ_{12}}\right) & \frac{x_1Đ_1Đ_2}{Đ_{12}}\\ \frac{x_2Đ_1Đ_2}{Đ_{12}} & Đ_2\left(1+\frac{x_2Đ_1}{Đ_{12}}\right)\end{bmatrix} \tag{11-37}$$

In proceeding further, it is convenient to define a 2×2 dimensional square matrix $[\Lambda]$:

$$[\Lambda]=\begin{bmatrix}\frac{1}{Đ_1}+\frac{x_2}{Đ_{12}} & -\frac{x_1}{Đ_{12}}\\ -\frac{x_2}{Đ_{12}} & \frac{1}{Đ_2}+\frac{x_1}{Đ_{12}}\end{bmatrix}^{-1}=\frac{1}{1+\frac{x_1Đ_2}{Đ_{12}}+\frac{x_2Đ_1}{Đ_{12}}}\begin{bmatrix}Đ_1\left(1+\frac{x_1Đ_2}{Đ_{12}}\right) & \frac{x_1Đ_1Đ_2}{Đ_{12}}\\ \frac{x_2Đ_1Đ_2}{Đ_{12}} & Đ_2\left(1+\frac{x_2Đ_1}{Đ_{12}}\right)\end{bmatrix} \tag{11-38}$$

Equation (11-34) can be re-cast into 2-dimensional matrix notation

$$(N)=-\rho[\Lambda][\Gamma]\frac{d(q)}{dz};$$

$$\begin{pmatrix}N_1\\ N_2\end{pmatrix}=-\frac{\rho}{1+\frac{x_1Đ_2}{Đ_{12}}+\frac{x_2Đ_1}{Đ_{12}}}\begin{bmatrix}Đ_1\left(1+\frac{x_1Đ_2}{Đ_{12}}\right) & \frac{x_1Đ_1Đ_2}{Đ_{12}}\\ \frac{x_2Đ_1Đ_2}{Đ_{12}} & Đ_2\left(1+\frac{x_2Đ_1}{Đ_{12}}\right)\end{bmatrix}\begin{bmatrix}\Gamma_{11} & \Gamma_{12}\\ \Gamma_{21} & \Gamma_{22}\end{bmatrix}\begin{pmatrix}\frac{dq_1}{dz}\\ \frac{dq_2}{dz}\end{pmatrix} \tag{11-39}$$

The elements of $[B]$ can be obtained by inverting the matrix $[\Lambda]$ determined using MD simulations using equation (11-32): $\begin{bmatrix}B_{11} & B_{12}\\ B_{21} & B_{22}\end{bmatrix}=\begin{bmatrix}\frac{1}{Đ_1}+\frac{x_2}{Đ_{12}} & -\frac{x_1}{Đ_{12}}\\ -\frac{x_2}{Đ_{12}} & \frac{1}{Đ_2}+\frac{x_1}{Đ_{12}}\end{bmatrix}=[\Lambda]^{-1}$ . The three M-S diffusivities can be backed-out from the four elements $\begin{bmatrix}B_{11} & B_{12}\\ B_{21} & B_{22}\end{bmatrix}$ using;

$$Đ_{12}=-\frac{x_2}{B_{21}};\quad Đ_1=\frac{1}{B_{11}-\frac{x_2}{Đ_{12}}};\quad Đ_2=\frac{1}{B_{22}-\frac{x_1}{Đ_{12}}} \tag{11-40}$$

For a wide variety of guest/host combinations we used MD simulations to determine the four elements $\Lambda_{11},\Lambda_{12},\Lambda_{21},\Lambda_{22}$ for equimolar ($q_1$=$q_2$; $c_1$=$c_2$) binary mixtures for a range of total mixture loadings, $q_t$= $q_1$+$q_2$, using equation (11-32). A small but representative selection of the MD simulated data culled from our previous publications [60, 67, 182, 191, 196, 201, 205-210] are presented in the following Figures:

Figure 11-2: $CO_2(1)/N_2(2)$ mixtures in MFI zeolite

Figure 11-3: $CO_2(1)/N_2(2)$ mixtures in FAU all-silica zeolite

Figure 11-4: Ne(1)/Ar(2) mixtures in CHA all-silica zeolite

Figure 11-5: Ne(1)/Ar(2) mixtures in DDR all-silica zeolite

Figure 11-6: $CH_4(1)/C_2H_6(2)$ mixtures in IRMOF-1

Figure 11-7: $CH_4(1)/H_2(2)$ mixtures in MgMOF-74

Figure 11-8: $CO_2(1)/H_2(2)$ mixtures in CuBTC

Also presented in Figure 11-2 to Figure 11-8, are the backed-out M-S diffusivities, $Đ_1, Đ_2$, using equation (11-40). A careful examination of presented MD data in Figure 11-2 to Figure 11-8 reveal a number of common characteristic features.

In the limit of vanishingly small loadings, or occupancies:

$$q_t \to 0; \quad \theta \to 0; \quad \Lambda_{11} \to Đ_1; \Lambda_{22} \to Đ_2; \Lambda_{12} \to 0; \Lambda_{21} \to 0 \tag{11-41}$$

With increasing mixture loadings, the diagonal elements $\Lambda_{11}, \Lambda_{22}$ are lowered below the corresponding values of the unary M-S diffusivities $Đ_1, Đ_2$.

$$q_t > 0; \quad \theta > 0; \quad \Lambda_{11} < Đ_1; \Lambda_{22} < Đ_2 \tag{11-42}$$

The extent of lowering, caused by correlation effects, is higher for the more mobile partner species. For the tardier species, the extent of lowering is significantly smaller.

As the total pore concentration approaches saturation, *all* diffusivities appear to converge to the same diffusivity values:

$$q_t \to q_{sat,mix}; \quad \theta \to 1; \quad \Lambda_{11} \approx Đ_1 \approx \Lambda_{22} \approx Đ_2 \approx \Lambda_{12} \approx \Lambda_{21} \tag{11-43}$$

The rationalization of Equation (11-43) is provided in a subsequent section entitled Correlations dominant scenario.

## 11.8 Self-diffusivity in *n*-component mixtures

The expression for the self-diffusivity in *n*-component mixtures can be derived by considering the mixture to be made of tagged and un-tagged species *i*, in the company of other partner molecules[211]

$$\frac{1}{D_{i,self}} = \frac{1}{Đ_i} + \frac{x_i}{Đ_{ii}} + \sum_{\substack{j=1 \\ j\neq i}}^{n} \frac{x_j}{Đ_{ij}}; \quad i = 1, 2, ...n \tag{11-44}$$

The self-diffusivity $D_{\mathrm{i,self}}$ within is dictated by (a) species *i* - wall, (b) species *i* – species *i*, and (c) species *i* – species *j* interactions. Specifically, for a binary mixture of species 1, and 2, we have

$$\frac{1}{D_{1,self}} = \frac{1}{Đ_1} + \frac{x_2}{Đ_{12}} + \frac{x_1}{Đ_{11}}; \quad \frac{1}{D_{2,self}} = \frac{1}{Đ_2} + \frac{x_1}{Đ_{12}} + \frac{x_2}{Đ_{22}} \tag{11-45}$$

In view of equation (11-37), we may relate the self-diffusivities to the diagonal elements of the matrix

$$[B] = \begin{bmatrix} \frac{1}{Đ_1} + \frac{x_2}{Đ_{12}} & -\frac{x_1}{Đ_{12}} \\ -\frac{x_2}{Đ_{12}} & \frac{1}{Đ_2} + \frac{x_1}{Đ_{12}} \end{bmatrix} :$$

$$\frac{1}{D_{1,self}} = B_{11} + \frac{x_1}{Đ_{11}}; \quad \frac{1}{D_{2,self}} = B_{22} + \frac{x_2}{Đ_{22}} \tag{11-46}$$

Equation (11-46) implies that the self-diffusivities experience correlation effects to a stronger extent than the elements of the matrices $[B] = \begin{bmatrix} \frac{1}{Đ_1} + \frac{x_2}{Đ_{12}} & -\frac{x_1}{Đ_{12}} \\ -\frac{x_2}{Đ_{12}} & \frac{1}{Đ_2} + \frac{x_1}{Đ_{12}} \end{bmatrix}$ and $[\Lambda] = \frac{1}{1 + \frac{x_1 Đ_2}{Đ_{12}} + \frac{x_2 Đ_1}{Đ_{12}}} \begin{bmatrix} Đ_1\left(1 + \frac{x_1 Đ_2}{Đ_{12}}\right) & \frac{x_1 Đ_1 Đ_2}{Đ_{12}} \\ \frac{x_2 Đ_1 Đ_2}{Đ_{12}} & Đ_2\left(1 + \frac{x_2 Đ_1}{Đ_{12}}\right) \end{bmatrix}$ that characterize binary mixture diffusion.

## 11.9 Degree of correlations

In order to appreciate the relative importance of correlations on the calculations of the fluxes for binary mixture diffusion, we define the *degrees of correlation*, $Đ_1/Đ_{12}$ , and $Đ_2/Đ_{12}$ ; the values can be determined from those backed-out from mixture MD simulations for earlier publications.[60, 67, 182, 191, 196, 201, 205-210] The magnitude of $Đ_1$, relative to that of $Đ_{12}$, determines the extent to which the flux of species 1 is influenced by the chemical potential gradient of species 2. The larger the degree of correlation, $Đ_1/Đ_{12}$, the stronger is the influence of coupling. Generally speaking, the more-strongly-adsorbed-tardier partner species will have the effect of slowing down the less-strongly-adsorbed-more-mobile partner in the mixture.

Figure 11-9 shows MD simulation data for the degree of correlations, $Đ_1/Đ_{12}$ , for diffusion of equimolar ($q_1 = q_2$) binary mixtures (a) $CO_2/CH_4$, (b) $H_2/CO_2$, (c) $N_2/CO_2$, (d) $Ne/CO_2$, (e) $CH_4/Ar$ (f) $H_2/CH_4$, (g) Ne/Ar, (h) $CH_4/C_2H_6$, and (i) $CH_4/C_3H_8$ at 300 K in a variety of host materials. For any guest/host combination, $Đ_1/Đ_{12}$ is seen to increase as the pore concentration increases; this implies that correlation effects are expected to be stronger for high pore occupancies.

The degree of correlations is weakest in cage-type structures such as CHA, DDR and LTA; the reason is that the molecules jump one-at-a-time across the narrow windows separating adjacent cages; $CO_2$ molecules jump length-wise across the windows. At the other end of the spectrum, correlations are strongest in one-dimensional (1D) channel structures (e.g. BTP-COF, MgMOF-74, NiMOF-74), intersecting channels (e.g. MFI), and "open" structures (e.g. IRMOF-1, FAU, NaY, NaX) consisting of large cages separated by wide windows.

## 11.10 Negligible correlations scenario for M-S diffusivities

For values of $Đ_1/Đ_{12} \to 0$ , and $Đ_2/Đ_{12} \to 0$ , the contribution of the first right member of M-S Equation (11-34) can be ignored and correlations can be considered to be of negligible importance; we derive

$$\frac{Đ_1}{Đ_{12}} \to 0; \quad \frac{Đ_2}{Đ_{12}} \to 0; \quad \begin{bmatrix} \Lambda_{11} & \Lambda_{12} \\ \Lambda_{21} & \Lambda_{22} \end{bmatrix} \to \begin{bmatrix} Đ_1 & 0 \\ 0 & Đ_2 \end{bmatrix} \tag{11-47}$$

Equation (11-47) is valid, as a first approximation, for diffusion in cage-type zeolites with 8-ring windows (CHA, LTA, DDR, ERI) and ZIF-8; see e.g. Figure 11-4, and Figure 11-5 and earlier publications.[67, 191, 196, 199, 201, 212-214]

When correlation effects are negligible, the diffusional coupling effects are solely traceable to mixture adsorption thermodynamics, embodied in the matrix $[\Gamma]$.

## 11.11 Correlations dominant scenario for M-S diffusivities

For the case in which correlation effects are dominant $\frac{Đ_1}{Đ_{12}} >> 1; \quad \frac{Đ_2}{Đ_{12}} >> 1;$ correlations dominant .

This also implies that $\frac{x_1 Đ_2 + x_2 Đ_1}{Đ_{12}} >> 1$ because the sum of the adsorbed phase mole fractions add to unity, i.e. $x_1+x_2 = 1$. Therefore, the term $1 + \frac{x_1 Đ_2}{Đ_{12}} + \frac{x_2 Đ_1}{Đ_{12}}$ in equation (11-38) can be simplified as $1 + \frac{x_1 Đ_2 + x_2 Đ_1}{Đ_{12}} \to \frac{x_1 Đ_2 + x_2 Đ_1}{Đ_{12}}$, and the matrix $[\Lambda]$ reduces to

$$[\Lambda] = \frac{1}{\frac{x_1 Đ_2 + x_2 Đ_1}{Đ_{12}}} \begin{bmatrix} Đ_1\left(1 + \frac{x_1 Đ_2}{Đ_{12}}\right) & Đ_1 \frac{x_1 Đ_2}{Đ_{12}} \\ Đ_2 \frac{x_2 Đ_1}{Đ_{12}} & Đ_2\left(1 + \frac{x_2 Đ_1}{Đ_{12}}\right) \end{bmatrix} \tag{11-48}$$

The expressions for $\Lambda_{12}$ and $\Lambda_{21}$ can be further simplified

$$\begin{aligned} \Lambda_{12} &= \frac{Đ_1\left(\frac{x_1 Đ_2}{Đ_{12}}\right)}{\frac{x_1 Đ_2}{Đ_{12}} + \frac{x_2 Đ_1}{Đ_{12}}} = \frac{Đ_1}{1 + \frac{x_2}{x_1}\frac{Đ_1}{Đ_2}} = \frac{x_1}{\frac{x_1}{Đ_1} + \frac{x_2}{Đ_2}}; \\ \Lambda_{21} &= \frac{Đ_2\left(\frac{x_2 Đ_1}{Đ_{12}}\right)}{\frac{x_1 Đ_2}{Đ_{12}} + \frac{x_2 Đ_1}{Đ_{12}}} = \frac{Đ_2}{1 + \frac{x_1}{x_2}\frac{Đ_2}{Đ_1}} = \frac{x_2}{\frac{x_1}{Đ_1} + \frac{x_2}{Đ_2}} \end{aligned} \tag{11-49}$$

The expressions for $\Lambda_{11}$ and $\Lambda_{22}$ for the correlations dominant scenario must be derived with more care. The diagonal elements must degenerate to the corresponding pure component $Đ_i$ values at either ends of the composition range, i.e.

$$\Lambda_{11} \to Đ_1; \quad x_1 \to 1; \quad x_2 \to 0 \tag{11-50}$$

and,

$$\Lambda_{22} \to Đ_2; \quad x_2 \to 1; \quad x_1 \to 0 \tag{11-51}$$

Equations (11-50), and (11-51) must be satisfied for *any* degree of correlations, not just in the Correlations Dominant scenario. Consider $\Lambda_{11}$. For equation (11-48) to satisfy equation (11-50) for $\frac{Đ_1}{Đ_{12}} >> 1; \quad \frac{Đ_2}{Đ_{12}} >> 1$ we must *also* satisfy the conditions

$$\frac{x_1 Đ_2}{Đ_{12}} >> 1; \quad \frac{x_2 Đ_1}{Đ_{12}} >> 1 \tag{11-52}$$

because, otherwise, (11-50) will be violated. Invoking equation (11-52) we obtain from equation (11-48)

$$\Lambda_{11} = \frac{Đ_1}{1+\frac{x_2}{x_1}\frac{Đ_1}{Đ_2}} = \frac{x_1}{\frac{x_1}{Đ_1}+\frac{x_2}{Đ_2}}; \quad \Lambda_{22} = \frac{Đ_2}{1+\frac{x_1}{x_2}\frac{Đ_2}{Đ_1}} = \frac{x_2}{\frac{x_1}{Đ_1}+\frac{x_2}{Đ_2}} \tag{11-53}$$

The M-S diffusivity matrix $[\Lambda]$ for the correlations dominant scenario yields the remarkably simple result

$$[\Lambda] = \frac{1}{\frac{x_1}{Đ_1}+\frac{x_2}{Đ_2}}\begin{bmatrix} x_1 & x_1 \\ x_2 & x_2 \end{bmatrix} = \frac{1}{\frac{q_1}{Đ_1}+\frac{q_2}{Đ_2}}\begin{bmatrix} q_1 & q_1 \\ q_2 & q_2 \end{bmatrix} \tag{11-54}$$

Remarkably, in this scenario, $\Lambda_{11} = \Lambda_{12}$, and $\Lambda_{21} = \Lambda_{22}$. For equimolar mixtures, $x_1 = x_2$, all the four elements of $[\Lambda]$ are equal to one another.

The dominant correlations scenario is a good approximation under pore saturation conditions.[199] An extensive and detailed validation of equation (11-54) at pore saturation conditions is provided in our earlier works.[199, 215]

## 11.12 Onsager formulation for diffusion in micropores

In the Onsager formulation, the fluxes are linearly related to the chemical potential gradients by defining a matrix of Onsager coefficients $[L]$

$$\begin{pmatrix} N_1 \\ N_2 \end{pmatrix} = -\frac{\rho}{RT} \begin{bmatrix} L_{11} & L_{12} \\ L_{21} & L_{22} \end{bmatrix} \begin{pmatrix} \frac{d\mu_1}{dz} \\ \frac{d\mu_2}{dz} \end{pmatrix}; \quad \text{Onsager formulation} \tag{11-55}$$

The Onsager Reciprocal Relations[67] prescribes the symmetry relation

$$L_{12} = L_{21} \tag{11-56}$$

The units of the elements of the Onsager matrix in microporous materials are mol kg$^{-1}$ m$^2$ s$^{-1}$. The Onsager formulation suffers from the major disadvantage that the diagonal elements $L_{11}$ and $L_{22}$ cannot be identified with the corresponding values $L_1$, and $L_2$ for unary transport of species 1 and 2.[67] The inter-relationship between $[\Lambda]$ and $[L]$ is

$$[L] = [\Lambda] \begin{bmatrix} q_1 & 0 \\ 0 & q_2 \end{bmatrix} \tag{11-57}$$

In the correlations dominant scenario, the elements of the Onsager matrix $[L] = [\Lambda] \begin{bmatrix} q_1 & 0 \\ 0 & q_2 \end{bmatrix}$ can be determined by combining equations (11-54), and (11-55):

$$[L] = [\Lambda] \begin{bmatrix} q_1 & 0 \\ 0 & q_2 \end{bmatrix} = \frac{1}{\frac{q_1}{Đ_1} + \frac{q_2}{Đ_2}} \begin{bmatrix} q_1^2 & q_1 q_2 \\ q_1 q_2 & q_2^2 \end{bmatrix}; \quad \text{correlations dominant} \tag{11-58}$$

## 11.13 List of Figures for Diffusion in Microporous Crystalline Materials

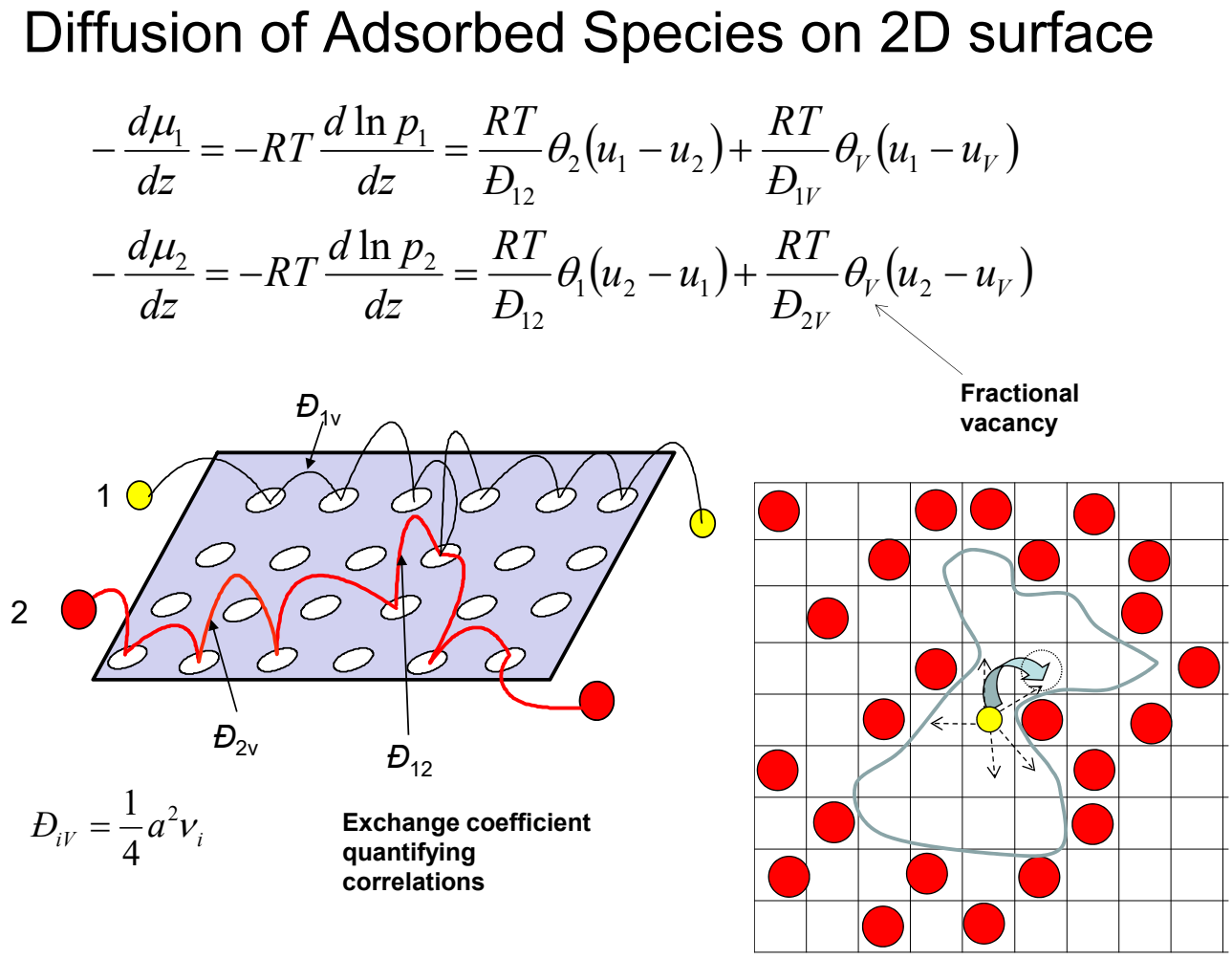


Figure 11-1. The Maxwell- Stefan description of hopping of molecules on a 2D surface.

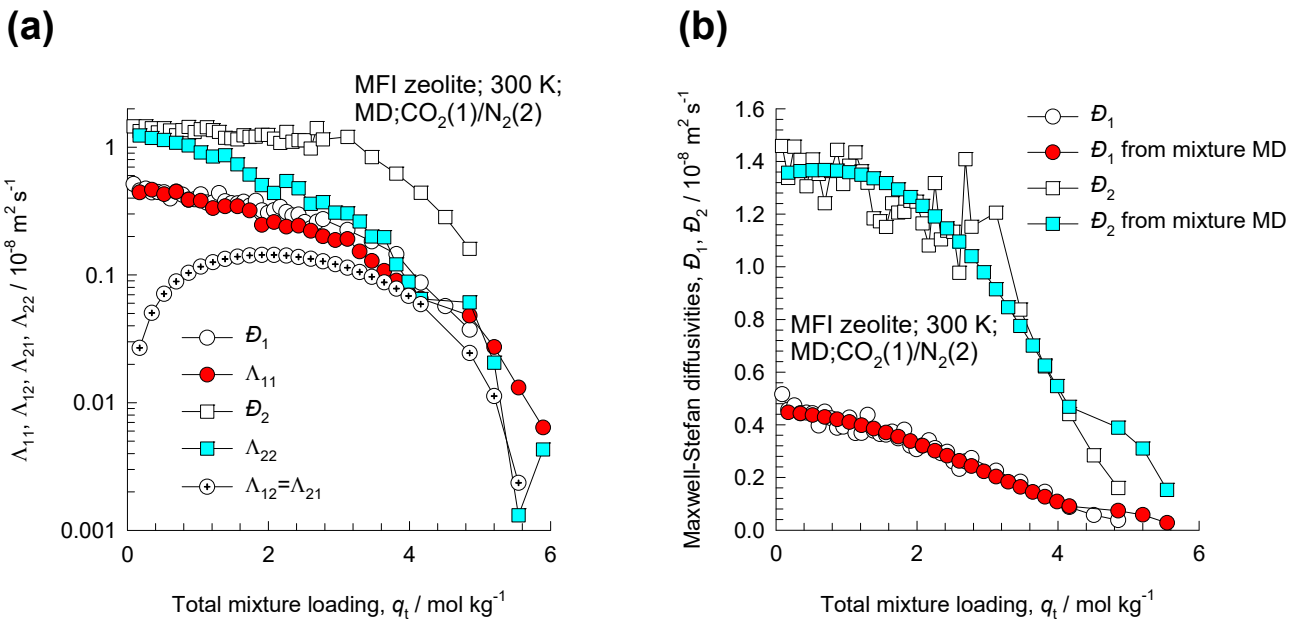


Figure 11-2. MD simulated values of $\Lambda_{11}, \Lambda_{12}, \Lambda_{22}$, along with the backed-out M-S diffusivities, $Đ_1, Đ_2$ for equimolar ($q_1$=$q_2$) binary $CO_2$(1)/$N_2$(2) mixtures in MFI zeolite at 300 K plotted as a function of the total mixture loading $q_t = q_1 + q_2$.

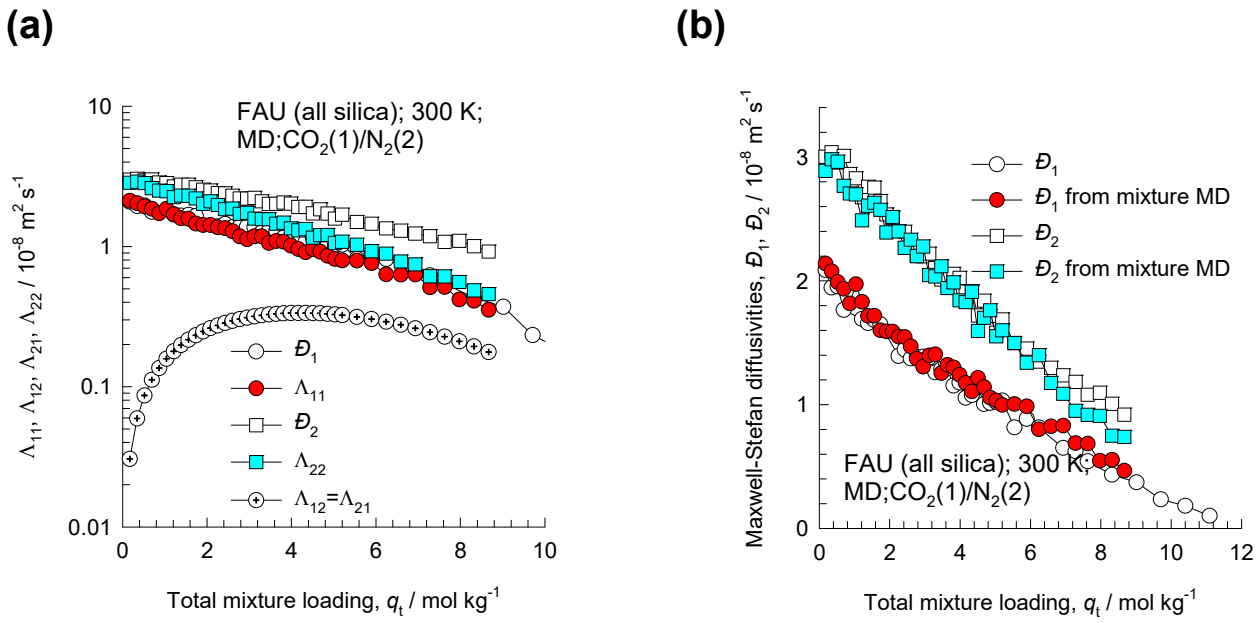


Figure 11-3. MD simulated values of $\Lambda_{11}, \Lambda_{12}, \Lambda_{22}$, along with the backed-out M-S diffusivities, $Đ_1, Đ_2$ for equimolar ($q_1$=$q_2$) binary $CO_2(1)/N_2(2)$ mixtures in FAU all-silica zeolite at 300 K plotted as a function of the total mixture loading $q_t = q_1+q_2$.

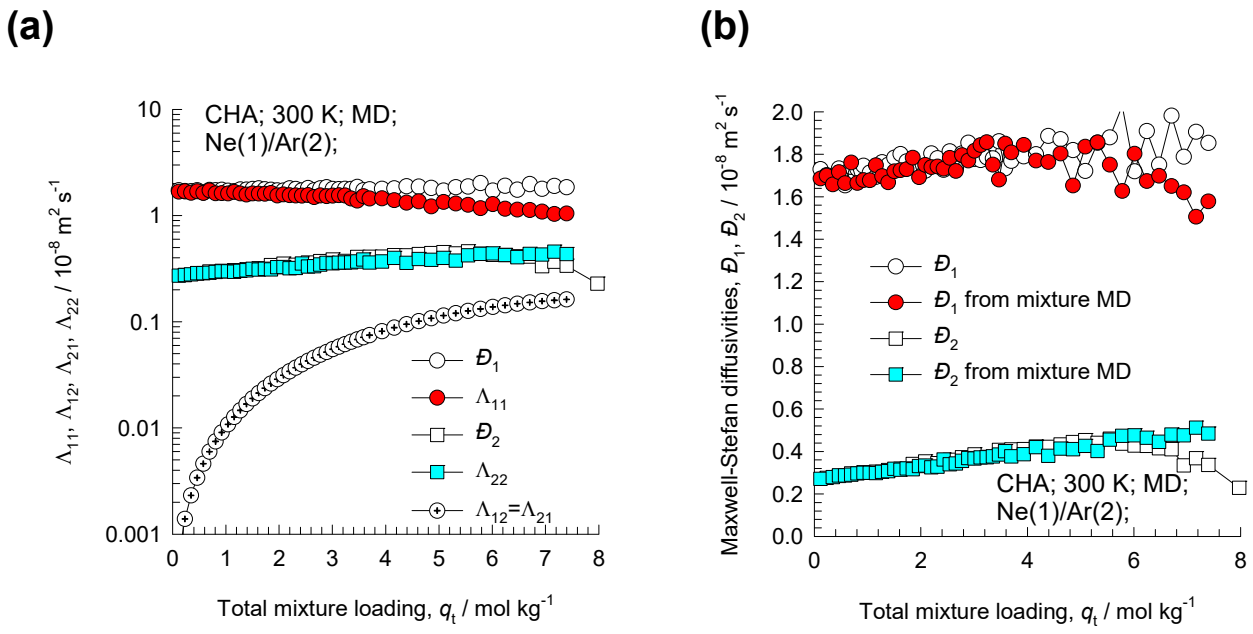


Figure 11-4. MD simulated values of $\Lambda_{11}, \Lambda_{12}, \Lambda_{22}$, along with the backed-out M-S diffusivities, $Đ_1, Đ_2$ for equimolar ($q_1$=$q_2$) Ne(1)/Ar(2) mixtures in CHA all-silica zeolite at 300 K plotted as a function of the total mixture loading $q_t$= $q_1$+$q_2$.

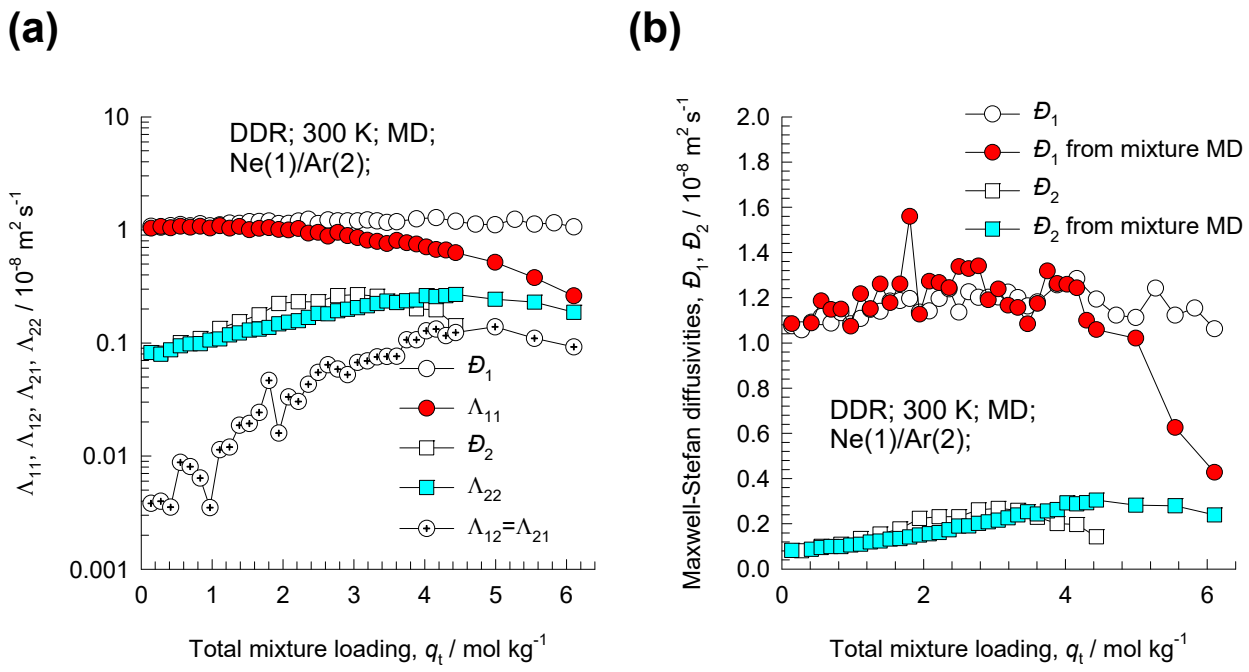


Figure 11-5. MD simulated values of $\Lambda_{11}, \Lambda_{12}, \Lambda_{22}$, along with the backed-out M-S diffusivities, $Đ_1, Đ_2$ for equimolar ($q_1$=$q_2$) binary Ne(1)/Ar(2) mixtures in DDR all-silica zeolite at 300 K plotted as a function of the total mixture loading $q_t$= $q_1$+$q_2$.

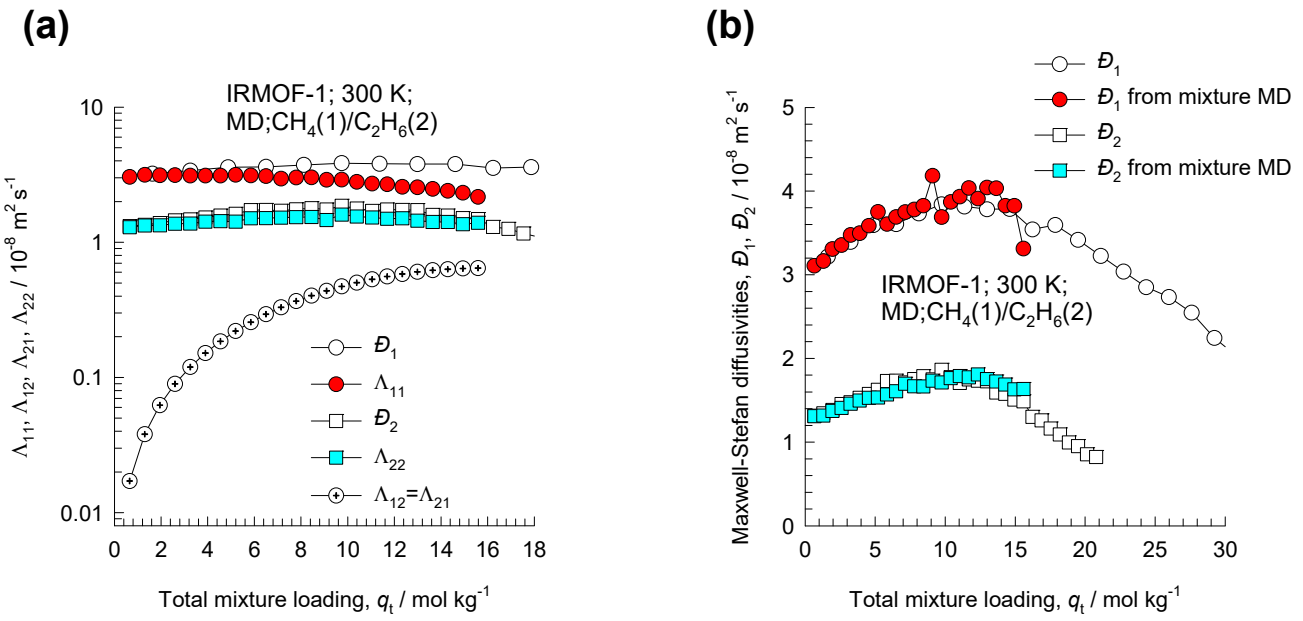


Figure 11-6. MD simulated values of $\Lambda_{11}, \Lambda_{12}, \Lambda_{22}$, along with the backed-out M-S diffusivities, $Đ_1, Đ_2$ for equimolar ($q_1$=$q_2$) binary $CH_4(1)/C_2H_6(2)$ mixtures in IRMOF-1 at 300 K plotted as a function of the total mixture loading $q_t = q_1+q_2$.

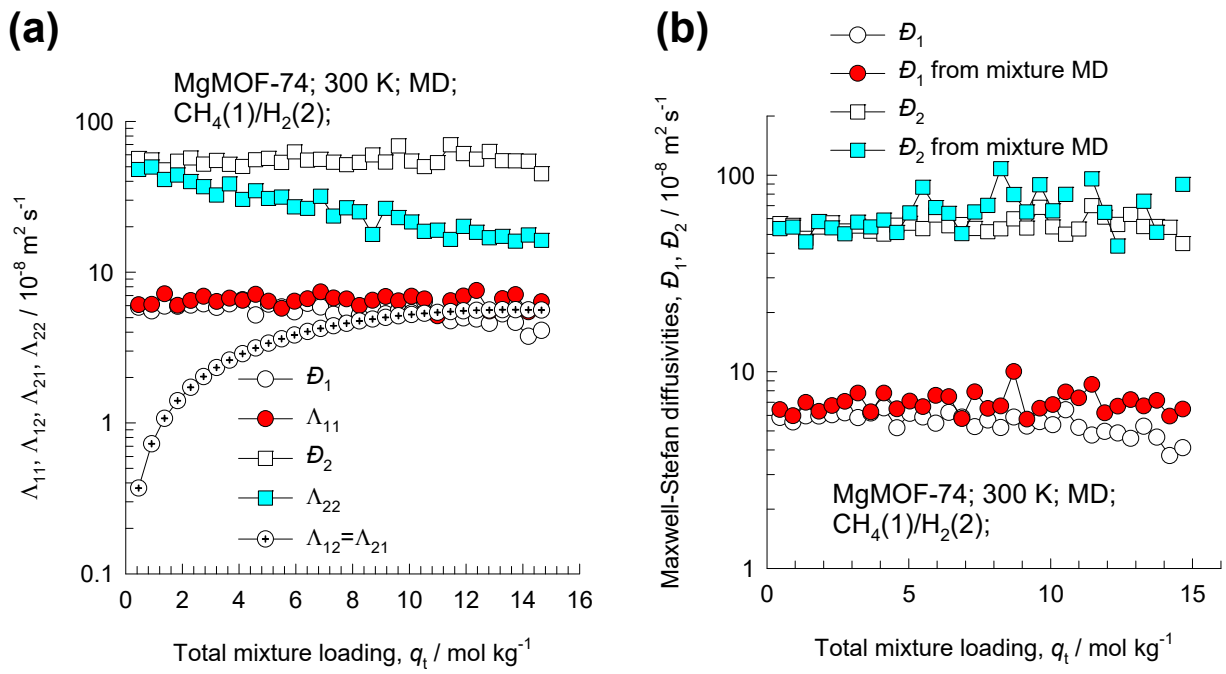


Figure 11-7. MD simulated values of $\Lambda_{11}, \Lambda_{12}, \Lambda_{22}$, along with the backed-out M-S diffusivities, $Đ_1, Đ_2$ for equimolar ($q_1$=$q_2$) binary $CH_4(1)/H_2(2)$ mixtures in MgMOF-74 at 300 K plotted as a function of the total mixture loading $q_t = q_1+q_2$.

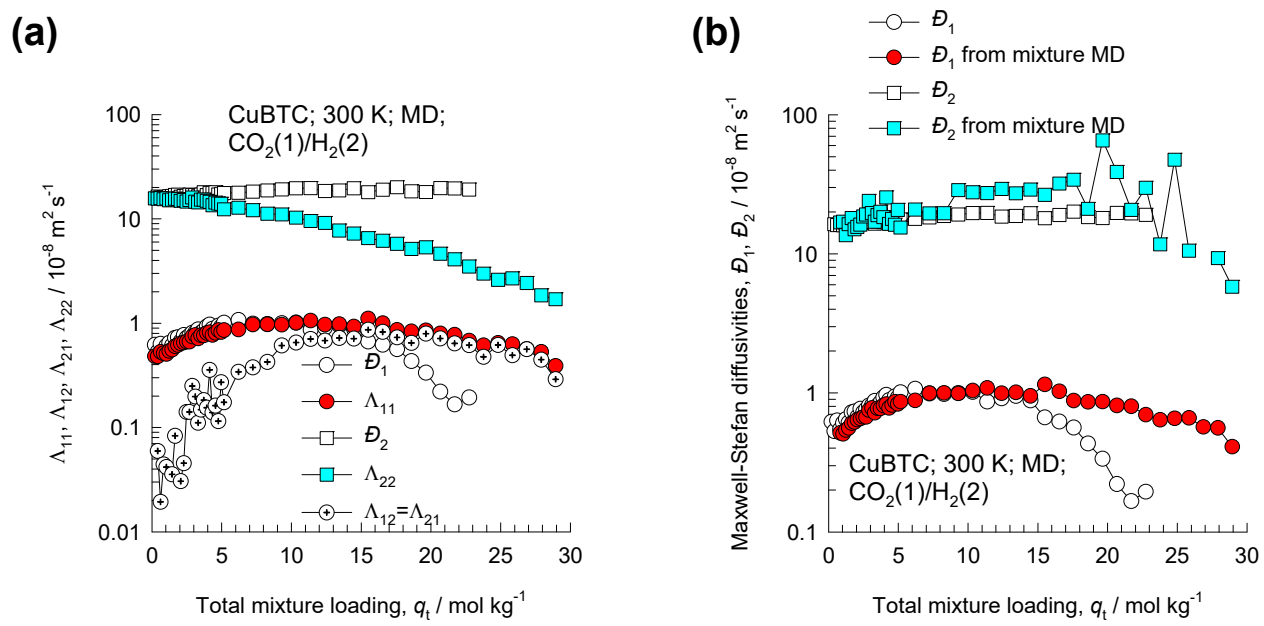


Figure 11-8. MD simulated values of $\Lambda_{11}, \Lambda_{12}, \Lambda_{22}$, along with the backed-out M-S diffusivities, $Đ_1, Đ_2$ for equimolar ($q_1$=$q_2$) binary $CO_2$(1)/$H_2$(2) mixtures in CuBTC at 300 K plotted as a function of the total mixture loading $q_t = q_1+q_2$.

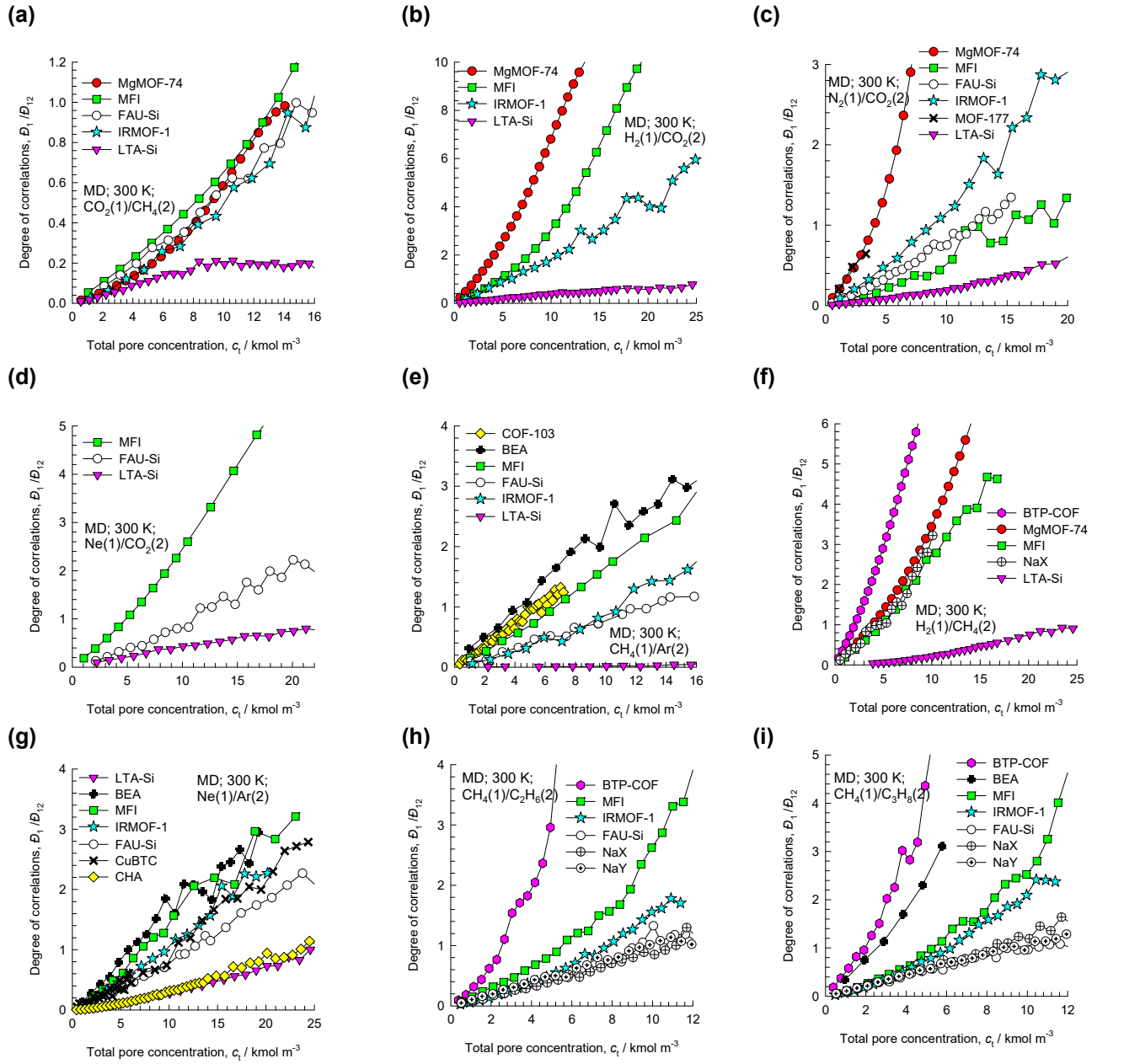


Figure 11-9. MD simulation data for the degree of correlations, $Đ_1/Đ_{12}$, for diffusion of equimolar ($q_1 = q_2$) binary mixtures (a) $CO_2/CH_4$, (b) $H_2/CO_2$, (c) $N_2/CO_2$, (d) $Ne/CO_2$, (e) $CH_4/Ar$ (f) $H_2/CH_4$, (g) Ne/Ar, (h) $CH_4/C_2H_6$, and (i) $CH_4/C_3H_8$ at 300 K in a variety of host materials. The *x*- axes represent the pore concentration, $c_i$, based on accessible pore volume.

# 12 Nomenclature

## Latin alphabet

| | |
|---|---|
| $a_i$ | component activity, dimensionless |
| $b_i$ | parameter in the pure component Langmuir adsorption isotherm, $Pa^{-1}$ |
| $[B]$ | matrix of inverse M-S coefficients, $m^{-2}$ s |
| $c_i$ | molar concentration of species *i*, mol $m^{-3}$ |
| $c_t$ | total molar concentration of mixture, mol $m^{-3}$ |
| $c_{fixed}$ | molar concentration of fixed charges in ion exchanger particle, equiv $m^{-3}$ |
| $d$ | generalized driving force, $m^{-1}$ |
| $d_{bubble}$ | bubble diameter, m |
| $d_{drop}$ | droplet diameter, m |
| $Đ_i$ | ion diffusivity, $m^2$ $s^{-1}$ |
| $Đ_i$ | diffusivity characterizing molecule-wall interactions, $m^2$ $s^{-1}$ |
| $Đ_i(0)$ | M-S diffusivity at zero-loading in microporous materials, $m^2$ $s^{-1}$ |
| $Đ_{12}$ | M-S exchange coefficient for binary mixture, $m^2$ $s^{-1}$ |
| $Đ_{ij}$ | M-S binary pair diffusivity, $m^2$ $s^{-1}$ |
| $Đ_{ij}^V$ | modified M-S diffusivity for binary penetrant pair *i*-*j*, $m^2$ $s^{-1}$ |
| $Đ_{im}^V$ | modified M-S diffusivity for penetrant *i* in polymer m, $m^2$ $s^{-1}$ |
| $D^*$ | tracer diffusivity, $m^2$ $s^{-1}$ |
| $D_{i,self}$ | self-diffusivity of species *i*, $m^2$ $s^{-1}$ |
| $D_{12}$ | Fick diffusivity for binary 1-2 mixture , $m^2$ $s^{-1}$ |

**Nomenclature**

| | |
|---|---|
| $[D]$ | Fick diffusivity matrix, $m^2\ s^{-1}$ |
| $\lvert D \rvert$ | Determinant of the Fick diffusivity matrix, $m^4\ s^{-2}$ |
| $\lvert D \rvert^{1/2}$ | Square-root of determinant of $[D]$, $m^2\ s^{-1}$ |
| $D_i^T$ | thermal diffusion coefficient, kg $m^{-1}\ s^{-1}$ |
| $E_i$ | Component Murphree efficiency, dimensionless |
| $f$ | correlation factor for diffusion crystalline metals, dimensionless |
| $f_i$ | partial fugacity of species *i*, Pa |
| $f_t$ | total fugacity of bulk fluid mixture, Pa |
| F | Faraday constant, $9.65\times10^4$ C $mol^{-1}$ |
| Fo | Fourier number, dimensionless |
| $h_f$ | froth height on distillation tray, m |
| $[I]$ | Identity matrix, dimensionless |
| $j_i$ | mass diffusion flux of species *i* with respect to $v$, kg $m^{-2}\ s^{-1}$ |
| $J_i$ | molar diffusion flux of species *i* with respect to $u$, mol $m^{-2}\ s^{-1}$ |
| $[L]$ | Onsager matrix, $m^2\ s^{-1}$ |
| $M_i$ | molar mass of species *i*, kg $mol^{-1}$ |
| $n$ | number of species in the mixture, dimensionless |
| $N_i$ | molar flux of species *i* in laboratory fixed reference frame, mol $m^{-2}\ s^{-1}$ |
| $N_i$ | molar flux of species *i* with respect to material framework, mol $m^{-2}\ s^{-1}$ |
| $N_t$ | molar flux of total mixture in laboratory fixed reference frame, mol $m^{-2}\ s^{-1}$ |
| $p_i$ | partial pressure of species *i* in mixture, Pa |
| $p_t$ | total system pressure, Pa |
| $q_i$ | molar loading of species *i*, mol $kg^{-1}$ |
| $q_{i,sat}$ | molar loading of species *i* at saturation, mol $kg^{-1}$ |

**Nomenclature**

| | |
|---|---|
| $q_t$ | total molar loading of mixture, mol kg$^{-1}$ |
| $[Q]$ | matrix quantifying fractional departure from equilibrium, dimensionless |
| $r$ | radial direction coordinate, m |
| $r_c$ | radius of particle m |
| $R$ | gas constant, 8.314 J mol$^{-1}$ K$^{-1}$ |
| $t$ | time, s |
| $T$ | absolute temperature, K |
| $x_i$ | mole fraction of component *i* in bulk fluid phase, dimensionless |
| $X_i$ | ionic equivalent fraction of species *i* inside IEX particle, dimensionless |
| $y_i$ | mole fraction of component *i* in bulk vapor phase, dimensionless |
| $u$ | molar average mixture velocity, m s$^{-1}$ |
| $u_i$ | velocity of motion of adsorbate species *i* with respect to the framework material, m s$^{-1}$ |
| $u_i^T$ | augmented species velocity to account for thermal diffusion, m s$^{-1}$ |
| $v$ | mass average mixture velocity, m s$^{-1}$ |
| $\overline{V_i}$ | partial molar volume of species *i,* m$^3$ mol$^{-1}$ |
| $\overline{V}$ | mean molar volume of mixture, m$^3$ mol$^{-1}$ |
| $V_{bubble}$ | bubble rise velocity, m s$^{-1}$ |
| $V_{drop}$ | droplet rise velocity, m s$^{-1}$ |
| $V_p$ | pore volume, m$^3$ kg$^{-1}$ |
| $z$ | direction coordinate, m |
| $z_i$ | charge on species *i*, dimensionless |
| $Z$ | compressibility factor, dimensionless |

**Greek alphabet**

**Nomenclature**

| | |
|---|---|
| $\beta$ | cell constant, dimension depends on the context |
| $\gamma_i$ | activity coefficient of component *i*, dimensionless |
| $\delta$ | length of diffusion path, m |
| $\delta_{ij}$ | Kronecker delta, dimensionless |
| $\varepsilon$ | fractional pore volume of microporous material, dimensionless |
| $\Gamma_{ij}$ | thermodynamic correction factors, dimensionless |
| $[\Gamma]$ | matrix of thermodynamic factors, dimensionless |
| $\lvert\Gamma\rvert^{1/2}$ | Square-root of determinant of $[\Gamma]$, dimensionless |
| $\theta_i$ | fractional occupancy of component *i*, dimensionless |
| $\theta_t$ | fractional occupancy of adsorbed mixture, dimensionless |
| $\theta_V$ | fractional vacancy, dimensionless |
| $[\Theta]$ | Hessian of the Gibbs free energy, dimensionless |
| $\lambda_i$ | eigenvalue of Fick diffusivity matrix, $m^2\ s^{-1}$ |
| $[\Lambda]=[B]^{-1}$ | matrix of M-S diffusivities, $m^2\ s^{-1}$ |
| $\lvert\Lambda\rvert^{1/2}$ | Square-root of determinant of $[\Lambda]$, $m^2\ s^{-1}$ |
| $\mu_i$ | molar chemical potential, $J\ mol^{-1}$ |
| $\pi_i$ | dimensionless partial pressures, $b_i p_i$, dimensionless |
| $\rho$ | framework density of adsorbent, $kg\ m^{-3}$ |
| $\sigma$ | rate of entropy production, $J\ m^{-3}\ s^{-1}\ K^{-1}$ |
| $\tau$ | stress tensor, Pa |
| $\phi_i$ | volume fraction of *i* , dimensionless |
| $\phi_i$ | fugacity coefficient of component *i*, dimensionless |
| $[\Phi]$ | matrix of dimensionless fluxes, dimensionless |

**Nomenclature**

| | |
|---|---|
| $\Phi$ | electrostatic potential, V |
| $\chi$ | interaction parameter in Flory-Huggins model, dimensionless |
| $\omega_i$ | mass fraction of component *i*, dimensionless |
| $\Omega$ | angular velocity, $s^{-1}$ |

**Subscript**

| | |
|---|---|
| eq | equilibrium value |
| E | entering stage |
| i | referring to component *i* |
| Inter | Inter-diffusion in metallic alloys |
| L | leaving stage |
| n | referring to component *n* |
| t | referring to total mixture |
| V | vacancy |

**Superscript**

| | |
|---|---|
| mass | mass average reference velocity frame |
| volume | volume average reference velocity frame |
| $\theta$ | coefficient defined using the M-S formulation in terms of vacancies |

**Matrix notation**

| | |
|---|---|
| ( ) | column matrix |
| [ ] | square matrix |

## Nomenclature

### Vector notation

| | |
|---|---|
| $\nabla$ | gradient |
| $\nabla \bullet$ | divergence |

# 13 References

(1) Taylor, R.; Krishna, R. *Multicomponent mass transfer*. John Wiley: New York, 1993.

(2) Leahy-Dios, A.; Bou-Ali, M. M.; Platten, J. K.; Firoozabadi, A. Measurements of molecular and thermal diffusion coefficients in ternary mixtures. *J. Chem. Phys.* **2005**, *122*, 234502.

(3) Alimadadian, A.; Colver, C. P. A New Technique for the Measurement of Ternary Diffusion Coefficients in Liquid Systems. *Can. J. Chem. Eng.* **1976**, *54*, 208-213.

(4) Onsager, L. Theories and Problems of Liquid Diffusion. *Annals N.Y. Acad. Sci.* **1945**, *46*, 241-265.

(5) de Groot, S. R.; Mazur, P. *Non-Equilibrium Thermodynamics*. North-Holland Publishing Co.: Amsterdam, 1962.

(6) Truesdell, C. A. *Rational Thermodynamics*. McGraw-Hill: New York, 1969.

(7) Maxwell, J. C. On the dynamical theory of gases. *Phil. Trans. Roy. Soc.* **1866**, *157*, 49-88.

(8) Stefan, J. Über das Gleichgewicht und die Bewegung insbesondere die Diffusion von Gasgemengen. *Sitzber. Akad. Wiss. Wien.* **1871**, *63*, 63-124.

(9) Standart, G. L.; Taylor, R.; Krishna, R. The Maxwell-Stefan formulation of irreversible thermodynamics for simultaneous heat and mass transfer. *Chem. Eng. Commun.* **1979**, *3*, 277-289.

(10) Krishna, R.; Low, C. Y.; Newsham, D. M. T.; Olivera Fuentes, C. G.; Paybarah, A. Liquid Liquid Equilibrium in the System Glycerol Water Acetone at 25 $^{o}$C. *Fluid Phase Equilib.* **1989**, *45*, 115-120.

(11) Krishna, R.; van Baten, J. M. Describing Diffusion in Fluid Mixtures at Elevated Pressures by Combining the Maxwell-Stefan Formulation with an Equation of State *Chem. Eng. Sci.* **2016**, *153*, 174-187.

(12) Tuan, D. Q.; Zollweg, J. A.; Rizvi, S. S. H. Concentration Dependence of the Diffusion Coefficient of Lipid in Supercritical Carbon Dioxide. *Ind. Eng. Chem. Res.* **1999**, *38*, 2787-2793.

(13) Hirschfelder, J. O.; Curtiss, C. F.; Bird, R. B. *Molecular theory of gases and liquids*. Second Corrected Printing, John Wiley: New York, USA, 1964.

(14) Fuller, E. N.; Schettler, P. D.; Giddings, J. C. A New Method for Prediction of Binary Gas-phase Diffusion Coefficients. *Ind. Eng. Chem.* **1966**, *58*, 19-27.

(15) Reid, R.C.; Prausnitz, J. M.; Poling, B. E. *The Properties of Gases and Liquids*. 4th Edition, McGraw-Hill: New York, 1986.

(16) Arnold, K. R.; Toor, H. L. Unsteady Diffusion in Ternary Gas Mixtures. *A.I.Ch.E.J.* **1967**, *13*, 909-914.

(17) Ravi, R. Mathematical Treatment of the Loschmidt Tube Experiment: Some Clarifications. *Chem. Eng. Commun.* **2007**, *194*, 170-176.

(18) Duncan, J. B.; Toor, H. L. An Experimental Study of Three Component Gas Diffusion. *A.I.Ch.E.J.* **1962**, *8*, 38-41.

(19) PTC MathCad 15.0. http://www.ptc.com/, PTC Corporate Headquarters, Needham, 3 November 2015.

(20) Taveira, P.; Cruz, P.; Mendes, A. A Maxwell-Stefan Experiment. *Chem. Eng. Education* **2000**, *Winter*, 90-93.

(21) Krishna, R.; Standart, G. L. A multicomponent film model incorporating a general matrix method of solution to the Maxwell-Stefan equations. *A.I.Ch.E.J.* **1976**, *22*, 383-389.

(22) Krishna, R. Highlighting Multiplicity in the Gilliland Solution to the Maxwell-Stefan Equations Describing Diffusion Distillation. *Chem. Eng. Sci.* **2017**, *164*, 63-70.

(23) Bres, M.; Hatzfeld, C. Three-Gas Diffusion - Experimental and Theoretical Study. *Pflügers Arch.* **1977**, *371*, 227-233.

(24) Tai, R. C. A Mathematical Study of Non-Equimolar Ternary Gas Diffusion. *Bulletin Math. Biol.* **1979**, *41*, 591-606.

(25) Chang, H.-K.; Farhi, L. E. On Mathematical Analysis of Gas Transport in the Lung. *Resp. Physiol.* **1973**, *18*, 370-385.

(26) Chang, H.-K.; Tai, R. C.; Farhi, L. E. Some Implications of Ternary Diffusion in the Lung. *Resp. Physiol.* **1975**, *23*, 109-120.

(27) Jebria, A. B. Simulations of Steady Quaternary Gas Diffusion between Alveolar and Blood Compartments. *Int. J. Bio-Medical Computing* **1987**, *20*, 97-105.

(28) Jebria, A. B.; Bres, M. Computer Simulation of Ternary Diffusion in Distal Airways. *Int. J. Bio-Medical Computing* **1982**, *13*, 403-419.

(29) Boudin, L.; Götz, D.; Grec, B. Diffusion Models of Multicomponent Mixtures in the Lung. *ESAIM: Proceedings* **2010**, *30*, 90-103. http://dx.doi.org/10.1051/proc/2010008.

(30) Chiappa, G. R.; Queiroga, F.; Meda, E.; Ferreira, L. F.; Diefenthaeler, F.; Nunes, M.; Vaz, M. A.; Machado, M. C. L.; Nery, L. E.; Neder, J. A. Heliox Improves Oxygen Delivery and Utilization during Dynamic Exercise in Patients with Chronic Obstructive Pulmonary Disease. *Am. J. Respir. Crit. Care. Med.* **2009**, *179*, 1004-1010.

(31) Chevrolet, J.-C. Helium oxygen mixtures in the intensive care unit. *Critical Care* **2001**, *5*, 179–181.

(32) Taylor, R.; Krishna, R.; Kooijman, H. Real-World Modeling of Distillation. *Chem. Eng. Prog.* **2003**, *99 (7)*, 28-39.

(33) Krishna, R.; Martinez, H. F.; Sreedhar, R.; Standart, G. L. Murphree point efficiencies in multicomponent systems. *Trans. Inst. Chem. Eng.* **1977**, *55*, 178-183.

(34) Krishna, R.; Standart, G. L. Mass and energy transfer in multicomponent systems. *Chem. Eng. Commun.* **1979**, *3*, 201-275.

(35) Springer, P. A. M.; Baur, R.; Krishna, R. Influence of interphase mass transfer on the composition trajectories and crossing of boundaries in ternary azeotropic distillation. *Sep. Purif. Technol.* **2002**, *29*, 1-13.

(36) Springer, P. A. M.; Baur, R.; Krishna, R. Composition trajectories for heterogeneous azeotropic distillation in a bubble-cap tray column: Influence of mass transfer. *Chem. Eng. Res. Des.* **2003**, *81*, 413-426.

(37) Springer, P. A. M.; Buttinger, B.; Baur, R.; Krishna, R. Crossing of the distillation boundary in homogeneous azeotropic distillation: Influence of interphase mass transfer. *Ind. Eng. Chem. Res.* **2002**, *41*, 1621-1631.

(38) Springer, P. A. M.; Krishna, R. Crossing of boundaries in ternary azeotropic distillation: Influence of interphase mass transfer. *Int. Commun. Heat Mass Transf.* **2001**, *28*, 347-356.

(39) Springer, P. A. M.; van der Molen, S.; Baur, R.; Krishna, R. Experimental verification of the necessity to use the Maxwell-Stefan formulation in describing trajectories during azeotropic distillation. *Chem. Eng. Res. Des.* **2002**, *80*, 654-666.

(40) Springer, P. A. M.; van der Molen, S.; Krishna, R. The need for using rigorous rate-based models for simulations of ternary azeotropic distillation. *Comput. Chem. Eng.* **2002**, *26*, 1265-1279.

(41) Baur, R.; Taylor, R.; Krishna, R.; Copati, J. A. Influence of mass transfer in distillation of mixtures with a distillation boundary. *Trans. Inst. Chem. Eng.* **1999**, *77, Part A*, 561-565.

(42) Levy, S. G.; Van Dongen, D. B.; Doherty, M. F. Design and synthesis of homogeneous azeotropic distillation. 2. Minimum reflux calculations for nonideal and azeotropic columns. *Ind. Eng. Chem. Fundamentals* **1985**, *24*, 463-474.

(43) Li, Y. H.; Chen, H. F.; Liu, J. Q. Composition profile of an azeotropic continuous distillation with feed composition on a ridge or in a valley. *Ind. Eng. Chem. Res.* **1999**, *38*, 2482-2484.

(44) Kooijman, H. A.; Taylor, R. *The ChemSep Book*. 2nd Edition, H.A. Kooijman and R. Taylor, www.chemsep.com: 2007.

(45) Krishna, R. Highlighting Diffusional Coupling Effects in Ternary Liquid Extraction and Comparisons with Distillation. *Ind. Eng. Chem. Res.* **2016**, *55*, 1053-1063.

(46) Geddes, R. L. Local efficiencies of bubble-plate fractionators. *Trans. Am. Inst. Chem. Engrs.* **1946**, *42*, 79-105.

(47) Krishna, R. Model for prediction of point efficiencies for multicomponent distillation. **1985**, *63*, 312-322.

(48) Treybal, R. E. *Mass-Transfer Operations*. 3rd Edition, McGraw-Hill: New York, 1980.

(49) Robbins, L. A.; Cusack, R. W. *Chaper 15, Liquid-Liquid Extraction Operations and Equipment*. Perry's Chemical Engineers' Handbook; 7th Edition, Edited by R.H. Perry and D.W. Green, McGraw-Hill: New York, 1999.

(50) Seader, J. D.; Henley, E. J.; Roper, D. K. *Separation Process Principles*. 3rd Edition, John Wiley: New York, 2011.

(51) Taylor, R.; Baur, R.; Krishna, R. Influence of Mass Transfer in Distillation: Residue Curves and Total Reflux. *A.I.Ch.E.J.* **2004**, *50*, 3134-3148.

(52) Pelkonen, S.; Kaesemann, R.; Gorak, A. Distillation lines for multicomponent separation in packed columns: Theory and comparison with experiment. *Ind. Eng. Chem. Res.* **1997**, *36*, 5392-5398.

(53) Pelkonen, S.; Gorak, A.; Ohligschlager, A.; Kaesemann, R. Experimental study on multicomponent distillation in packed columns. *Chem. Eng. Process.* **2001**, *40*, 235-243.

(54) Darken, L. S. Diffusion, Mobility and Their Interrelation through Free Energy in Binary Metallic Systems. *Trans. AIME* **1948**, *175*, 184-201.

(55) Darken, L. S. Diffusion of Carbon in Austenite with a Discontinuity in Composition. *Trans. AIME* **1949**, *180*, 430-438.

(56) Shieh, J. C.; Lyons, P. A. Transport Properties of Liquid n-Alkanes. *J. Phys. Chem.* **1969**, *73*, 3258-3264.

(57) Bidlack, D. L.; Anderson, D. K. Mutual diffusion in the system hexane-hexadecane. *J. Phys. Chem.* **1964**, *68*, 206-208.

(58) Helbaek, M.; Hafskjold, B.; Dysthe, D. K.; Sorland, G. H. Self-diffusion coefficients of methane or ethane mixtures with hydrocarbons at high pressure by NMR. *J. Chem. Eng. Data* **1996**, *41*, 598-603.

(59) Krishna, R.; van Baten, J. M. The Darken relation for multicomponent diffusion in liquid mixtures of linear alkanes. An investigation using Molecular Dynamics (MD) simulations. *Ind. Eng. Chem. Res.* **2005**, *44*, 6939-6947.

(60) Krishna, R.; van Baten, J. M. Unified Maxwell-Stefan Description of Binary Mixture Diffusion in Micro- and Meso- Porous Materials. *Chem. Eng. Sci.* **2009**, *64*, 3159-3178.

(61) Liu, X.; Bardow, A.; Vlugt, T. J. H. Multicomponent Maxwell-Stefan Diffusivities at Infinite Dilution. *Ind. Eng. Chem. Res.* **2011**, *50*, 4776-4782.

(62) Krishna, R.; van Baten, J. M. MD simulations of diffusivities in methanol – n-hexane mixtures near the liquid-liquid phase splitting region. *Chem Eng Technol* **2006**, *29*, 516-519.

(63) Krishna, R.; van Baten, J. M. Validating the Darken relation for diffusivities in fluid mixtures of varying densities by use of MD simulations. *Chem Eng Technol* **2006**, *29*, 761-765.

(64) Wesselingh, J. A.; Krishna, R. *Mass transfer in multicomponent mixtures*. VSSD: Delft, 2000.

(65) Hsu, Y.-D.; Chen, Y.-P. Correlation of the mutual diffusion coefficients of binary liquid mixtures. *Fluid Phase Equilibr.* **1998**, *152*, 149-168.

(66) Krishna, R. A Unified Theory of Separation Processes Based on Irreversible Thermodynamics. *Chem. Eng. Commun.* **1987**, *59*, 33-64.

(67) Krishna, R.; van Baten, J. M. Onsager coefficients for binary mixture diffusion in nanopores. *Chem. Eng. Sci.* **2008**, *63*, 3120-3140.

(68) Nishiumi, H.; Kubota, T. Fundamental behavior of benzene–$CO_2$ mutual diffusion coefficients in the critical region of $CO_2$. *Fluid Phase Equilib.* **2007**, *261*, 146-151.

(69) Leute, V. The Influence of Thermodynamics on the Interdiffusion in Quasibinary Systems. *Solid State Ion.* **2003**, *164*, 159-168.

(70) Chang, Y. C.; Myerson, A. S. Diffusivity of Glycine in Concentrated Solutions and Supersaturated Aqueous Solutions. *A.I.Ch.E.J.* **1986**, *32*, 1567-1569.

(71) Myerson, A. S.; Senol, D. Diffusion Coefficients near the Spinodal Curve. *A.I.Ch.E.J.* **1984**, *30*, 1004-1006.

(72) Wesselingh, J. A.; Bollen, A. M. Multicomponent diffusivities from the free volume theory. *Chem. Eng. Res. Des.* **1997**, *75*, 590-602.

(73) Krishna, R. Serpentine Diffusion Trajectories and the Ouzo Effect in Partially Miscible Ternary Liquid Mixtures. *Phys. Chem. Chem. Phys.* **2015**, *17*, 27428-27436.

(74) Grossmann, T.; Winkelmann, J. Ternary Diffusion Coefficients of Glycerol + Acetone + Water by Taylor Dispersion Measurements at 298.15 K. *J. Chem. Eng. Data* **2005**, *50*, 1396-1403.

(75) Grossmann, T.; Winkelmann, J. Ternary Diffusion Coefficients of Glycerol + Acetone + Water by Taylor Dispersion Measurements at 298.15 K. 2. Acetone-Rich Region. *J. Chem. Eng. Data* **2007**, *52*, 336-340.

(76) Grossmann, T.; Winkelmann, J. Ternary Diffusion Coefficients of Glycerol + Acetone + Water by Taylor Dispersion Measurements at 298.15 K. 3. Water-Rich Region. *J. Chem. Eng. Data* **2007**, *52*, 341-344.

(77) Vitagliano, V.; Sartorio, R.; Scala, S.; Spaduzzi, D. Diffusion in a Ternary System and the Critical Mixing Point. *J. Solution Chem.* **1978**, *7*, 605-621.

(78) Buzatu, D.; Buzatu, F. D.; Paduano, L.; Sartorio, R. Diffusion Coefficients for the Ternary System Water + Chloroform + Acetic Acid at 25 °C. *J. Solution Chem.* **2007**, *36*, 1373-1384.

(79) Pertler, M. *Die Mehrkomponenten-Diffuson in nicht vollständig mischbaren Flüssigkeiten*. Technische Universität München, München, 1996.

(80) Lo, P. Y.; Myerson, A. S. Ternary Diffusion Coefficients in Metastable Solutions of Glycine-Valine-H,O. *A.I.Ch.E.J.* **1989**, *35*, 676-678.

(81) Othmer, D. F.; Ku, P. L. Solubility Data for Ternary Liquid Systems. Acetic Acid and Formic Acid Distributed between Chloroform and Water. *J. Chem. Eng. Data* **1960**, *5*, 42-44.

(82) Tyn, M. T.; Calus, W. F. Temperature and Concentration Dependence of Mutual Diffusion Coefficients of Some Binary Liquid Systems. *J. Chem. Eng. Data* **1975**, *20*, 310-316.

(83) Königer, A.; Meier, B.; Köhler, W. Measurement of the Soret, diffusion, and thermal diffusion coefficients of three binary organic benchmark mixtures and of ethanol–water mixtures using a beam deflection technique. *Philos. Mag.* **2009**, *89*, 907-923.

(84) Clark, W. M.; Rowley, R. L. The mutual diffusion coefficient of methanol - n-hexane near the consolute point. *A.I.Ch.E.J.* **1986**, *32*, 1125-1131.

(85) Haeberl, M.; Blass, E. Multicomponent Effects in Liquid-Liquid Extraction. *Trans. I. Chem. E.* **1999**, *77*, 647-655.

(86) Lewis, W. K. The principles of countercurrent extraction. *J. Ind. Eng. Chem.* **1916**, *8*, 825-833.

(87) Wankat, P. C. *Separation Process Engineering*. 3rd Edition, Prentice-Hall: Upper Saddle River, New Jersey, USA, 2012.

(88) Sherwood, T. K.; Pigford, R. L.; Wilke, C. R. *Mass Transfer*. Mc-Graw Hill: New York, U.S.A., 1975.

(89) Bart, H.-J. *Reactive Extraction*. Springer-Verlag: Berlin, 2001.

(90) Meindersma, G. W.; de Haan, A. Conceptual process design for aromatic/aliphatic separation with ionic liquids. *Chem. Eng. Res. Des.* **2008**, *86*, 745-752.

(91) Meindersma, G. W. *Extraction of Aromatics from Naphtha with Ionic Liquids*. Ph.D. Dissertation, University of Twente, The Nethelands, Enschede, 2005.

(92) Rodriguez, N. R.; Requejo, P. F.; Kroon, M. C. Aliphatic-aromatic separation using deep eutectic solvents as extracting agents. *Ind. Eng. Chem. Res.* **2015**, *54*, 11404-11412.

(93) Krishna, R.; Goswami, A. N.; Nanoti, S. M.; Rawat, B. S.; Khanna, M. K.; Dobhal, J. Extraction of aromatics from 63-69 $^{o}$C Naphtha fraction for food grade hexane production using sulpholane and NMP as solvents. *Indian Journal of Technology* **1987**, *25*, 602-606.

(94) Al-Jimaz, A. S.; Fandary, M. S.; Al-Kandary, J. A.; Fahim, M. A. Liquid–liquid equilibria for n-alkanes (C12, C14,C17) + propylbenzene +NMP mixtures at temperatures between 298 and 328K. *Fluid Phase Equilib.* **2005**, *231*, 163-170.

(95) Lao, M. Z.; Kingsley, J. P.; Krishnamurthy, R.; Taylor, R. A Nonequilibrium Stage Model of Multicomponent Separation Processes .6. Simulation of Liquid Liquid Extraction. *Chem. Eng. Commun.* **1989**, *86*, 73-89.

(96) Krishna, R.; Nanoti, S. M.; Goswami, A. N. Mass-Transfer Efficiency of Sieve Tray Extraction Columns. *Ind. Eng. Chem. Res.* **1989**, *28*, 642-644.

(97) Krishna, R.; Low, C. Y.; Newsham, D. M. T.; Olivera-Fuentes, C. G.; Standart, G. L. Ternary mass transfer in liquid-liquid extraction. *Chem. Eng. Sci.* **1985**, *40*, 893-903.

(98) Sun, Y.; Zhao, Q.; Zhang, L.; Jiang, B. Measurement and Correlation of the Mass-Transfer Coefficient for the Methyl Isobutyl Ketone−Water−Phenol System. *Ind. Eng. Chem. Res.* **2014**, *53*, 3654-3661.

(99) Krishna, R. Uphill Diffusion in Multicomponent Mixtures. *Chem. Soc. Rev.* **2015**, *44*, 2812-2836.

(100) Bollen, A. M. *Collected tales on mass transfer in liquids*. Ph.D. Dissertation, Rijksuniversiteit Groningen, Groningen, 1999. http://dissertations.ub.rug.nl/faculties/science/1999/a.m.bollen/

(101) Kärger, J.; Ruthven, D. M.; Theodorou, D. N. *Diffusion in Nanoporous Materials*. Wiley - VCH: Weinheim, 2012.

(102) Resa, J. M.; Goenaga, J. M. Liquid-Liquid Equilibrium Diagrams of Ethanol + Water + (Ethyl Acetate or 1-Pentanol) at Several Temperatures. *J. Chem. Eng. Data* **2006**, *51*, 1300-1305.

(103) Reyes-Labarta, J. A.; Olaya, M. M.; Velasco, R.; Serrano, M. D.; Marcilla, A. Correlation of the liquid–liquid equilibrium data for specific ternary systems with one or two partially miscible binary subsystems. *Fluid Phase Equilib.* **2009**, *278*, 9-14.

(104) Ribeiro, C. P.; Freeman, B. D.; Paul, D. R. Modeling of Multicomponent Mass Transfer across Polymer Films using a Thermodynamically Consistent Formulation of the Maxwell-Stefan Equations in terms of Volume Fractions. *Polymer* **2011**, *52*, 3970-3983.

(105) Fornasiero, F.; Prausnitz, J. M.; Radke, C. J. Multicomponent Diffusion in Highly Asymmetric Systems. An Extended Maxwell-Stefan Model for Starkly Different-Sized, Segment-Accessible Chain Molecules. *Macromolecules* **2005**, *38*, 1364-1370.

(106) Varady, M. J.; Pearl, T. P.; Stevenson, S. M.; Mantooth, B. A. Decontamination of VX from Silicone: Characterization of Multicomponent Diffusion Effects. *Ind. Eng. Chem. Res.* **2016**, *55*, 3139-3149.

(107) Krishna, R. Describing Mixture Permeation across Polymeric Membranes by a Combination of Maxwell-Stefan and Flory-Huggins Models. *Polymer* **2016**, *103*, 124-131.

(108) Krishna, R. Using the Maxwell-Stefan formulation for Highlighting the Influence of Interspecies (1-2) Friction on Binary Mixture Permeation across Microporous and Polymeric Membranes. *J. Membr. Sci.* **2017**, *540*, 261-276.

(109) van den Berg, G. B.; Smolders, C. A. Diffusional phenomena in membrane separation processes. *J. Membr. Sci.* **1992**, *73*, 103-118.

(110) Reuvers, A. J.; Smolders, C. A. Formation of membranes by means of immersion precipitation Part II. The mechanism of formation of membranes prepared from the system cellulose acetate - acetone - water. *J. Membr. Sci.* **1987**, *34*, 67-86.

(111) Tsay, C. S.; McHugh, A. J. Mass Transfer Modeling of Asymmetric Membrane Formation by Phase Inversion. *J. Polym. Sci.: Part B: Polym. Phys.* **1990**, *28*, 1327-1365.

(112) Mulder, M. H. V.; Smolders, C. A. On the Mechanism of Separation of Ethanol/Water Mixtures by Pervaporation. I. Calculation of Concentration Profiles *J. Membr. Sci.* **1984**, *17*, 289-307.

(113) Altena, F. W.; Smolders, C. A. Calculation of Liquid-Liquid Phase Separation in a Ternary System of a Polymer in a Mixture of a Solvent and a Nonsolvent. *Macromolecules* **1982**, *15*, 1491-1497.

(114) Altinkaya, S. A.; Ozbas, B. Modeling of Asymmetric Membrane Formation by Dry-casting Method. *J. Membr. Sci.* **2004**, *230*, 71-89.

(115) Wilkinson, D. S. *Mass Transport in Solids and Fluids*. Cambridge University Press: Cambridge, 2000.

(116) Glicksman, M. E. *Diffusion in Solids: Field Theory, Solid-state Principles, and Applications*. John Wiley: New York, 2000.

(117) Paul, A.; Laurila, T.; Vuorinen, V.; Divinski, S. V. *Thermodynamics, Diffusion and the Kirkendall Effect in Solids*. Springer International Publishing Switzerland: Heidelberg, 2014.

(118) Belova, I. V.; Murch, G. E. Expressions for Vacancy-wind Factors Occurring in Interdiffusion in Ternary and Higher-order Alloys. *Acta Materialia* **2007**, *55*, 627-634.

(119) Belova, I. V.; Murch, G. E.; Filipek, R.; Danielewski, M. Theoretical Analysis of Experimental Tracer and Interdiffusion Data in Cu–Ni–Fe Alloys. *Acta Materialia* **2005**, *53*, 4613-4622.

(120) Manning, J. R. Correlation Factors for Diffusion in Nondilute Alloys. *Phys. Rev. B* **1971**, *4*, 1111-1121.

(121) Van der Ven, A.; Yu, H.-C.; Ceder, G.; Thornton, K. Vacancy Mediated Substitutional Diffusion in Binary Crystalline Solids. *Progess in Materials Science* **2010**, *55*, 61-105.

(122) Gupta, P. K.; Cooper, A. R. The [*D*] Matrix for Multicomponent Diffusion. *Physica* **1971**, *54*, 39-59.

(123) Krishna, R. Multicomponent Surface Diffusion of Adsorbed Species - A Description Based on the Generalized Maxwell-Stefan Equations. *Chem. Eng. Sci.* **1990**, *45*, 1779-1791.

(124) Reynolds, J. E.; Averbach, B. L.; Cohen, M. Self-diffusion and Interdiffusion in Gold-Nickel Alloys. *Acta Metallurgica* **1957**, *5*, 29-40.

(125) Rönkä, K. J.; Kodentsov, A. A.; Van Loon, P. J. J.; Kivilahti, J. K.; Van Loo, F. J. J. Thermodynamic and Kinetic Study of Diffusion Paths in the System Cu-Fe-Ni. *Metall. Mater. Trans. A* **1996**, *27A*, 2229-2238.

(126) Ugaste, Ü.; Kodentsov, A. A.; Van Loo, F. J. J. Concentration Dependence of Interdiffusion Coefficients in Cu–Fe–Ni System. *The Physics of Metals and Metallography* **2013**, *114*, 54-62.

(127) Kokkonis, P.; Leute, V. Simulation of Interdiffusion Processes in Quasiternary Systems of type MX/MY/MZ (β-class). *Solid State Ion.* **2006**, *177*, 1267-1274.

(128) Imai, T. *Thermodynamic Data from Multi-component Metallic Diffusion Couples*. Massachusetts Institute of Technology, Cambridge, Massachusetts, 1997.

(129) Kirkaldy, J. S. Diffusion in Multicomponent Metallic Systems. *Canad. J. Phys.* **1957**, *35*, 435-440.

(130) Vignes, A.; Sabatier, J. P. Ternary Diffusion in Fe-Co-Ni Alloys. *Trans. Met. Soc. A.I.M.E.* **1969**, *245*, 1795-1802.

(131) Sabatier, J. P.; Vignes, A. Etude des Phénomènes de Diffusion dans le Systéme Ternaire Fe-Ni-Co. *Mem. Sci. Rev. Metallurg.* **1967**, *64*, 225-240.

(132) Divya , V. D.; Ramamurty, U.; Paul, A. Interdiffusion and Solid Solution Strengthening in Ni–Co–Pt and Ni–Co–Fe Ternary Systems. *Philos. Mag.* **2013**, *93*, 2190-2206.

(133) Varshneya, A. K.; Cooper, A. R. Diffusion in the System $K_2O$-SrO-$SiO_2$: III, Interdiffusion Coefficients. *J. Am. Ceram.. Soc.* **1972**, *55*, 312-317.

(134) Christensen, N. H. Multiphase Ternary Diffusion Couples. *J. Am. Ceram.. Soc.* **1977**, *60*, 293-296.

(135) Vielzeuf, D.; Saúl, A. Uphill diffusion, zero-flux planes and transient chemical solitary waves in garnet. *Contrib. Mineral. Petrol.* **2011**, *161*, 683-702.

(136) Krishna, R.; Wesselingh, J. A. The Maxwell-Stefan Approach to Mass Transfer. *Chem. Eng. Sci.* **1997**, *52*, 861-911.

(137) Lightfoot, E. N. *Transport phenomena and living systems*. John Wiley: New York, 1974.

(138) Prigogine, I. *Thermodynamics of Irreversible Processes*. Interscience: New York, U.S.A., 1961.

(139) Kuiken, G. D. C. *Thermodynamics of irreversible processes: Applications to diffusion and rheology*. John Wiley: Chichester, UK, 1994.

(140) Platten, J. K. The Soret Effect: A Review of Recent Experimental Results. *J. Appl. Mech.* **2006**, *73*, 5-15.

(141) Kleijn, C. R.; Hoogendoorn, C. J. A study of 2- and 3-D transport phenomena in horizontal chemical vapor deposition reactors. *Chem. Eng. Sci.* **1991**, *46*, 321-334.

(142) Touzet, M.; Galliero, G.; Lazzeri, V.; Saghir, M. Z.; Montel, F.; Legros, J.-C. Thermodiffusion: From microgravity experiments to the initial state of petroleum reservoirs. *C.R. Mecanique* **2011**, *339*, 318-323.

(143) Newman, J.; Thomas-Alyea, K. E. *Electrochemical Systems*. 3rd Edition, Hoboken, New Jersey: John Wiley & Sons, Inc., 2004.

(144) Helfferich, F. G. Ion Exchange Kinetics. III. Experimental Test of the Theory of Particle-Diffusion Controlled Ion Exchange. *J. Phys. Chem.* **1962**, *66*, 39-42.

(145) Helfferich, F. G. *Ion Exchange Kinetics - Evolution of a Theory*. Mass Transfer and Kinetics of Ion Exchange; Edited by L. Liberti and F.G. Helfferich, Martinus Nijhoff Publishers: The Hague, 1983.

(146) Kraaijeveld, G.; Wesselingh, J. A. Negative Maxwell-Stefan Diffusion Coefficients. *Ind. Eng. Chem. Res.* **1993**, *32*, 738-742.

(147) Chakraborty, B. Sign Crossover in All Maxwell−Stefan Diffusivities for Molten Salt LiF-BeF2: A Molecular Dynamics Study. *J. Phys. Chem. B* **2015**, *119*, 10652-10663.

(148) Moggia, E.; Bianco, B. Mean Activity Coefficient of Electrolyte Solutions. *J. Phys. Chem.* **2007**, *111*, 3183-3191.

(149) Pitzer, K. S.; Mayorga, G. Thermodynamics of Electrolytes. II. Activity and Osmotic Coefficients for Strong Electrolytes with One or Both Ions Univalent. *J. Phys. Chem.* **1973**, *77*, 2300-2308.

(150) Ananthaswamy, J.; Atklnson, G. Thermodynamics of Concentrated Electrolyte Mixtures. 5. A Review of the Thermodynamic Properties of Aqueous Calcium Chloride in the Temperature Range 273.15-373.15 K. *J. Chem. Eng. Data* **1985**, *30*, 120-128.

(151) Rard, J. A.; Miller, D. G. The Mutual Diffusion Coefficients of NaCI-$H_2O$ and $CaCI_2$-$H_2O$ at 25 $^oC$ from Rayleigh Interferometry. *J. Solution Chem.* **1979**, *8*, 701-716.

(152) Chang, Y. C.; Myerson, A. S. The Diffusivity of Potassium Chloride and Sodium Chloride in Concentrated, Saturated, and Supersaturated Aqueous Solutions. *A.I.Ch.E.J.* **1985**, *31*, 890-894.

(153) Louhi-Kultanen, M.; Kallas, J.; Partanen, J.; Sha, Z.; Oinas, P.; Palosaari, S. The influence of multicomponent diffusion on crystal growth in electrolyte solutions. *Chem. Eng. Sci.* **2001**, *56*, 3505-3515.

(154) Kim, S.; Myerson, A. S. Metastable Solution Thermodynamic Properties and Crystal Growth Kinetics. *Ind. Eng. Chem. Res.* **1996**, *35*, 1078-1084.

(155) Enqvist, Y.; Partanen, J.; Louhi-Kultanen, M.; Kallas, J. Thermodynamics and Kinetics of KDP Crystal Growth from Binary and Ternary Solutions. *Trans. Inst. Chem. Eng.* **2003**, *81, Part A*, 1354-1362.

(156) Pitzer, K. S.; Kim, J. J. Thermodynamics of Electrolytes. IV. Activity and Osmotic Coefficients for Mixed Electrolytes. *J. Am. Chem. Soc.* **1974**, *96*, 5701-5707.

(157) Vinograd, J. R.; McBain, J. W. Diffusion of Electrolytes and Ions in their Mixtures. *J. Am. Chem. Soc.* **1941**, *63*, 2008-2015.

(158) Nakagaki, M.; Kitagawa, s. The Theory of the Reverse Diffusion of Ions in Mixed Electrolyte Solutions and Experimental Results on the HCl-$CaCl_2$-$H_2O$ Ternary System. *Bull. Chem. Soc. Japan* **1976**, *49*, 1748-1753.

(159) Rard, J. A.; Albright, J. G.; Miller, D. G. Diffusion Onsager Coefficients $L_{ij}$ for the NaCl + $Na_2SO_4$ + H2O System at 298.15 K. *J. Chem. Eng. Data* **2009**, *54*, 636-651.

(160) Leaist, D. G.; Curtis, N. Hartley-Crank Equations for Coupled Diffusion in Concentrated Mixed Electrolyte Solutions. The $CaC_{l2}$ + HCl + $H_2O$ System. *J. Solution Chem.* **1999**, *28*, 341-366.

(161) Leaist, D. G.; Al-Dhaher, F. F. Predicting the Diffusion Coefficients of Concentrated Mixed Electrolyte Solutions from Binary Solution Data. NaCl + $MgCl_2$ + $H_2O$ and NaCl + $SrCl_2$ + $H_2O$ at 25 °C. *J. Chem. Eng. Data* **2000**, *45*, 308-314.

(162) Hao, L.; Leaist, D. G. Interdiffusion Without a Common Ion in Aqueous NaCl-$MgSO_4$ and LiCl-NaOH Mixed Electrolytes. *J. Solution Chem.* **1995**, *24*, 523-535.

(163) Leaist, D. G.; Kanakos, M. A. Measured and predicted ternary diffusion coefficients for concentrated aqueous LiCl + KCl solutions over a wide range of compositions. *Phys. Chem. Chem. Phys.* **2000**, *2*, 1015-1021.

(164) Chen, L.; Leaist, D. G. Multicomponent Taylor Dispersion Coefficients. *J. Solution Chem.* **2014**, *43*, 2224-2237.

(165) Leaist, D. G.; Wiens, B. Interdiffusion of acids and bases. HCl and NaOH in aqueous solution. *Canad. J. Chem.* **1986**, *64*, 1007-1011.

(166) Krishna, R. Diffusing Uphill with James Clerk Maxwell and Josef Stefan. *Curr. Opin. Chem. Eng.* **2016**, *12*, 106-119.

(167) Krishna, R. Highlighting Coupling Effects in Ionic Diffusion. *Chem. Eng. Res. Des.* **2016**, *114*, 1-12.

(168) Levenspiel, O. *Chemical Reaction Engineering*. 3rd Edition, John Wiley: New York, 1999.

(169) Sherwood, T. K.; Wei, J. C. Ion Diffusion in Mass Transfer Between Phases. *A.I.Ch.E.J.* **1955**, *1*, 522-527.

(170) Littel, R. J.; Filmer, B.; Versteeg, G. F.; Van Swaaij, W. P. M. Modelling of Simultaneous Absorption of $H_2S$ and $CO_2$ in Alkanolamine Solutions: The Influence of Parallel and Consecutive Reversible Reactions and the Coupled Diffusion of Ionic Species. *Chem. Eng. Sci.* **1991**, *46*, 2303-2313.

(171) Leaist, D. G. Diffusion Coefficient of Aqueious Sulfur Dioxide at 25 $^{o}$C. *J. Chem. Eng. Data* **1984**, *29*, 281-282.

(172) Leaist, D. G.; Lyons, P. A. Diffusion in Dilute Aqueous Acetic Acid Solutions at 25 $^{o}$C. *J. Solution Chem.* **1984**, *13*, 77-85.

(173) Leaist, D. G. Gas Absorption with Instantaneous Chemical Reaction. Absorption of Sulfur Dioxide by Aqueous Sodium Bisulfite. *J. Phys. Chem.* **1983**, *87*, 4936-4939.

(174) Yang, Y.; Pintauro, P. N. Multicomponent Space-Charge Transport Model for Ion-Exchange Membranes. *A.I.Ch.E.J.* **2000**, *46*, 1177-1190.

(175) Sodaye, S.; Agarwal, C.; Goswami, A. N. Study on multicomponent diffusion of ions in poly(perfluorosulfonated) ion-exchange membrane using radiotracers *J. Membr. Sci.* **2006**, *314*, 221-225.

(176) Yoshida, H.; Kataoka, T. Intraparticle Ion-Exchange Mass Transfer in Ternary System. *Ind. Eng. Chem. Res.* **1987**, *26*, 1179-1184.

(177) Jones, I. L.; Carta, G. Ion Exchange of Amino Acids and Dipeptides on Cation Resins with Varying Degree of Cross-Linking. 2. Intraparticle Transport. *Ind. Eng. Chem. Res.* **1993**, *32*, 117-125.

(178) Hwang, Y.-L.; Helfferich, F. G. Generalized Model for Multispecies Ion-Exchange Kinetics Including Fast Reversible Reactions. *Reactive Polymers* **1987**, *5*, 237-253.

(179) Skoulidas, A. I.; Sholl, D. S.; Krishna, R. Correlation effects in diffusion of $CH_4$/$CF_4$ mixtures in MFI zeolite. A study linking MD simulations with the Maxwell-Stefan formulation. *Langmuir* **2003**, *19*, 7977-7988.

(180) Chempath, S.; Krishna, R.; Snurr, R. Q. Nonequilibrium MD simulations of difusion of binary mixtures containing short n-alkanes in faujasite. *J. Phys. Chem. B* **2004**, *108*, 13481-13491.

(181) Krishna, R. Describing the Diffusion of Guest Molecules inside Porous Structures. *J. Phys. Chem. C* **2009**, *113*, 19756-19781.

(182) Krishna, R. Diffusion in Porous Crystalline Materials. *Chem. Soc. Rev.* **2012**, *41*, 3099-3118.

(183) Hansen, N.; Keil, F. J. Multiscale modeling of reaction and diffusion in zeolites: from the molecular level to the reactor. *Soft Mater.* **2012**, *10*, 179-201.

(184) Krishna, R.; van Baten, J. M. An Investigation of the Characteristics of Maxwell-Stefan Diffusivities of Binary Mixtures in Silica Nanopores. *Chem. Eng. Sci.* **2009**, *64*, 870-882.

(185) Krishna, R. The Maxwell-Stefan Description of Mixture Permeation across Nanoporous Graphene Membranes. *Chem. Eng. Res. Des.* **2018**, *133*, 316-325. https://doi.org/10.1016/j.cherd.2018.03.033.

(186) Reed, D. A.; Ehrlich, G. Surface diffusion, atomic jump rates and thermodynamics. *Surf. Sci.* **1981**, *102*, 588-609.

(187) Krishna, R.; Paschek, D.; Baur, R. Modelling the occupancy dependence of diffusivities in zeolites. *Microporous Mesoporous Mater.* **2004**, *76*, 233-246.

(188) Krishna, R.; van Baten, J. M. A molecular dynamics investigation of a variety of influences of temperature on diffusion in zeolites. *Microporous Mesoporous Mater.* **2009**, *125*, 126-134.

(189) Krishna, R.; Baur, R. Modelling Issues in Zeolite Based Separation Processes. *Sep. Purif. Technol.* **2003**, *33*, 213-254.

(190) Kapteijn, F.; Moulijn, J. A.; Krishna, R. The generalized Maxwell-Stefan model for diffusion in zeolites: sorbate molecules with different saturation loadings. *Chem. Eng. Sci.* **2000**, *55*, 2923-2930.

(191) Krishna, R.; van Baten, J. M. Insights into diffusion of gases in zeolites gained from molecular dynamics simulations. *Microporous Mesoporous Mater.* **2008**, *109*, 91-108.

(192) Baur, R.; Krishna, R. Effectiveness factor for zeolite catalysed isomerization reactions. *Chem. Eng. J.* **2004**, *99*, 105-116.

(193) Baur, R.; Krishna, R. The effectiveness factor for zeolite catalysed reactions. *Catal. Today* **2005**, *105*, 173-179.

(194) Baur, R.; Krishna, R. A moving bed reactor concept for alkane isomerization. *Chem. Eng. J.* **2005**, *109*, 107-113.

(195) Krishna, R.; Baur, R. Analytic solution of the Maxwell-Stefan equations for multicomponent permeation across a zeolite membrane. *Chem. Eng. J.* **2004**, *97*, 37-45.

(196) Krishna, R.; van Baten, J. M. Maxwell-Stefan modeling of slowing-down effects in mixed gas permeation across porous membranes. *J. Membr. Sci.* **2011**, *383*, 289-300.

(197) Krishna, R. The Maxwell-Stefan Description of Mixture Diffusion in Nanoporous Crystalline Materials. *Microporous Mesoporous Mater.* **2014**, *185*, 30-50.

(198) Krishna, R. Tracing the Origins of Transient Overshoots for Binary Mixture Diffusion in Microporous Crystalline Materials. *Phys. Chem. Chem. Phys.* **2016**, *18*, 15482-15495.

(199) Krishna, R.; van Baten, J. M. Describing Mixture Diffusion in Microporous Materials under Conditions of Pore Saturation. *J. Phys. Chem. C* **2010**, *114*, 11557-11563.

(200) Myers, A. L.; Prausnitz, J. M. Thermodynamics of Mixed Gas Adsorption. *A.I.Ch.E.J.* **1965**, *11*, 121-130.

(201) Krishna, R.; van Baten, J. M. Diffusion of alkane mixtures in zeolites. Validating the Maxwell-Stefan formulation using MD simulations. *J. Phys. Chem. B* **2005**, *109*, 6386-6396.

(202) van Baten, J. M.; Krishna, R. Entropy effects in adsorption and diffusion of alkane isomers in mordenite: An investigation using CBMC and MD simulations. *Microporous Mesoporous Mater.* **2005**, *84*, 179-191.

(203) Krishna, R.; van Baten, J. M. Describing binary mixture diffusion in carbon nanotubes with the Maxwell-Stefan equations. An investigation using molecular dynamics simulations. *Ind. Eng. Chem. Res.* **2006**, *45*, 2084-2093.

(204) Krishna, R.; van Baten, J. M. Investigating the Influence of Diffusional Coupling on Mixture Permeation across Porous Membranes *J. Membr. Sci.* **2013**, *430*, 113-128.

(205) Krishna, R. Adsorptive separation of $CO_2/CH_4/CO$ gas mixtures at high pressures. *Microporous Mesoporous Mater.* **2012**, *156*, 217-223.

(206) Krishna, R.; van Baten, J. M. Diffusion of alkane mixtures in MFI zeolite. *Microporous Mesoporous Mater.* **2008**, *107*, 296-298.

(207) Krishna, R.; van Baten, J. M. Investigating the Relative Influences of Molecular Dimensions and Binding Energies on Diffusivities of Guest Species Inside Nanoporous Crystalline Materials *J. Phys. Chem. C* **2012**, *116*, 23556-23568.

(208) Krishna, R.; van Baten, J. M. Investigating the potential of MgMOF-74 membranes for $CO_2$ capture. *J. Membr. Sci.* **2011**, *377*, 249-260.

(209) Krishna, R.; van Baten, J. M. Investigating the Validity of the Knudsen Prescription for Diffusivities in a Mesoporous Covalent Organic Framework. *Ind. Eng. Chem. Res.* **2011**, *50*, 7083-7087.

(210) Krishna, R.; van Baten, J. M. Investigating the Validity of the Bosanquet Formula for Estimation of Diffusivities in Mesopores. *Chem. Eng. Sci.* **2012**, *69*, 684-688.

(211) Krishna, R.; Paschek, D. Self-diffusivities in multicomponent mixtures in zeolites. *Phys. Chem. Chem. Phys.* **2002**, *4*, 1891-1898.

(212) Krishna, R.; van Baten, J. M. Influence of segregated adsorption on mixture diffusion in DDR zeolite. *Chem. Phys. Lett.* **2007**, *446*, 344-349.

(213) Krishna, R.; van Baten, J. M. Segregation effects in adsorption of $CO_2$ containing mixtures and their consequences for separation selectivities in cage-type zeolites. *Sep. Purif. Technol.* **2008**, *61*, 414-423.

(214) Krishna, R.; van Baten, J. M. A molecular dynamics investigation of the diffusion characteristics of cavity-type zeolites with 8-ring windows. *Microporous Mesoporous Mater.* **2011**, *137*, 83-91.

(215) Krishna, R.; van Baten, J. M. Letter to the Editor. *A.I.Ch.E.J.* **2010**, *56*, 3288-3289.